SAIP
CONFERENCE PROCEEDINGS

Edited by: Prof. Makaiko Chithambo

SAIP 2019

64TH ANNUAL CONFERENCE OF THE SOUTH AFRICAN INSTITUTE OF PHYSICS

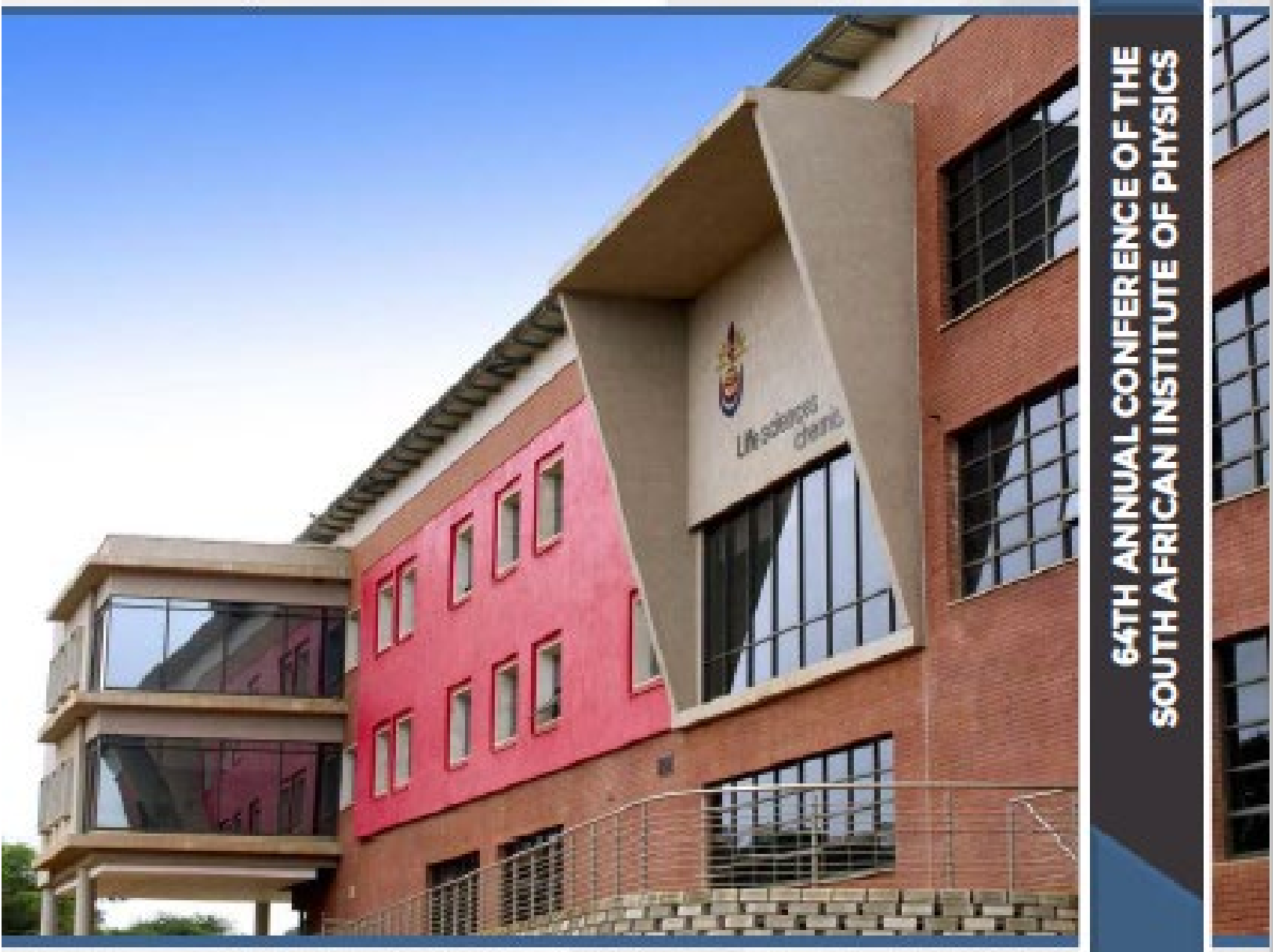

SOUTH AFRICAN INSTITUTE OF PHYSICS

University of Venda
Creating Future Leaders

PROCEEDINGS EDITOR-IN-CHIEF: Prof. Makaiko Chithambo, Rhodes University

PUBLISHER: The South African Institute of Physics

The Proceedings of SAIP2019, the 64th Annual Conference of the South African Institute of Physics (SAIP) will be available electronically only on the SAIP website www.saip.org.za.

ISBN: 978-0-620-88875-2

SAIP2019

Proceedings of SAIP2019

The 64th Annual Conference of the South African Institute of Physics

Hosted by the Department of Physics of the University of Venda.

08 July 2019 to 12 July 2019

Protea Hotel Ranch Resort – Polokwane, South Africa

Edited By

Prof. Makaiko Chithambo

SA Institute of Physics *ISBN: 978-0-620-88875-2*

TABLE OF CONTENTS

Contents

Editorial....1

SAIP2019 Conference Group Photo....2

Message from The Conference Chair....3

Conference, Divisions and Editorial Board details....4

Editorial Board....6

List of reviewers....8

DIVISION A – DIVISION FOR PHYSICS OF CONDENSED MATTER AND MATERIALS....10

Ab initio studies of sperrylite, platarsite and palladoarsenide bulk and surface stabilities....11

Structural, thermodynamic, electronic and mechanical properties of MCO3 (M: Ca, Fe) precursor materials for Li-ion batteries....17

Ab Initio Study of Ti50Pt50-xHfx (= 6.25, 18.75, 25) Potential Shape Memory Alloys....23

Computer simulation studies of HF adsorption on TiO2 (001) and (110) surfaces....28

First principle studies on lattice thermal conductivity and thermoelectric properties of LiYSe2....34

Investigation of beta Ti-Mo phase stability employing the first principle approach....40

Stability of lithium manganese oxide (LiMn2O4) surfaces during charge/discharge processes....46

Structural, electronic, elasticstability and optical properties of rare-earth copper chalcogenides LaCuX2 (X =S and Se), a first principless tudy....53

The effect of iron-particles on the electrical properties of n- GaSb semiconductor material....59

Magnetic properties and magnetocaloric effect of a distorted Kagom elattice:Gd3Os4Al12....65

Large magnetocaloric effect in Dy2NiSi3....70

Structural stability and electronic properties of bulk, bilayer and monolayer PtX2 (X = Se and Te)....76

Effect of Co addition on the structural, electronic and magnetic properties of Fe16N2 employing first principles approach....82

Study of lattice defects in BaF2 at elevated temperatures using positron annihilation and X-ray diffraction methods....87

Magnetic and thermodynamic properties of the CeRhGa4 compound....93

Structural and magnetic characterization of Sm3+ ion substituted Zn-Mn nanoferrites synthesized by glycol-thermal method.....99

TRACK B – NUCLEAR, PARTICLE AND RADIATION PHYSICS.....105

Electronic Stopping Force of 16O and 28Si Heavy Ions in Tantalum Nitride by Time of Flight Spectroscopy 106

Testing and Simulating the Response of a New Tracking Sensor for the ATLAS Detector.....111

Background estimation in the measurement of the top quark mass using J/ψ mesons with 13 TeV proton-proton collision data from the ATLAS experiment.....117

Radiological Assessment of Weenen Agricultural Fields Samples.....123

Compatibility of a simplified BSM model with the observed excesses in multi-lepton production at the LHC.....129

High mass VBF categorization for narrow-width resonance searches in the H → ZZ → 4 channel with the ATLAS detector.....135

Search for a resonance in the diphoton plus b-jet final states in the ttH and bbH production.....141

Top-quark background estimation for BSM physics search H → Sh → 2 + 2 jets with the ATLAS detector at LHC.....147

A Deep Neural Network for Missing Transverse Momentum Reconstruction in ATLAS.....153

Anomalies in the production of multiple leptons at the LHC.....159

Geant4 in a new role - Reactor Physics.....165

DIVISION D1 – DIVISION OF ASTROPHYSICS PHYSICS.....171

Multi-messenger hunts for heavy WIMPs.....172

Constraining f(R)-gravity models with recent cosmological data.....178

Multi-wavelength study of large-scale outflows from the Circinus galaxy.....184

A radiative transfer model for hydrogen recombination line masers.....190

Surface brightness profiles of nearby central group galaxies.....196

Phenomenology of axion-like particles coupling with photons in the jets of active galactic nuclei.....202

Unifying Dark Matter and Dark Energy in Chaplygin Gas Cosmology.....208

Perturbations in a Chaplygin gas Cosmology.....214

DIVISION E – DIVISION OF PHYSICS EDUCATION.....220

An evaluation of the impact of scientific explanation model on pre-service teachers' understanding of basic concepts in electricity 221

DIVISION F– DIVISION OF APPLIED PHYSICS.....227

Density functional theory study of copper zinc tin sulphide (Cu2ZnSnS4) doped with calcium and barium 228

Construction and testing of a magneto-optical trap for laser cooling of rubidium atoms.....234

Density functional theory study of Cyanidin (Cy) dye molecule adsorbed on (100) TiO2 anatase surface for application in DSSCs 240

Development and testing of a photon detector for Quantum optics experiments 246

The Diagnostics and Verification System for the Tile Calorimeter Trigger and Data Acquisition framework of the ATLAS Detector 251

The development of test stations for the ATLAS Tile Calorimeter Low Voltage Power Supplies 256

Low Voltage Power Supply production, hardware upgrade and testing for the ATLAS TileCal Front-End Electronics system 262

A case study on monitoring Potential Induced Degradation (PID) recovery in multi-crystalline modules 268

Investigating the feasibility of using neutron activation to measure elemental pollution in the Richards Bay area 274

Investigating the feasibility of using neutron activation to measure elemental pollution in the Richards Bay area 280

DIVISION G – DIVISION OF THEORETICAL & COMPUTATIONAL PHYSICS 286

The Equation of State (EoS) of hadronic matter from the microscopic Ultra-relativistic Quantum Molecular Dynamics (UrQMD) model.....287

Computation of the effective potential in the gauge-Higgs unification model with an SU(3) representation.....293

The ubiquitous pseudo-scalar in composite Higgs models.....299

Third order dissipative fluid dynamics and the Bjorken scaling solution.....305

Fluctuating open heavy flavour energy loss in a strongly coupled plasma with observables from rhic and the lhc.....311

Impact-response study of lattice waves and phonons in metallic FCC nanoclusters using the Sutton-Chen potential.....317

Modified hummers synthesis and structural characterisation of graphene oxide 323

Bottomonia suppression in heavy-ion collisions from AdS/CFT 329

Non-Abelian Corrections for Radiation in QCD.....335

Quantum secret sharing with Greenberger Horne Zeilinger states.....341

Solving the Schr¨odinger Equation using Sinc Functions in one and two dimensions, employing Python and Numpy.....347

A 2+1D Monte Carlo generator for jets in heavy ion collisions.....353

Editorial

The picturesque The Ranch and the voluminous blue skies of Limpopo provided the backdrop for a memorable 64th in a series of annual conferences of the SAIP. Some papers from that meeting are collected in this peer-reviewed volume. Submissions for the proceedings of SAIP2019 were, for the first time, handled by an Editorial Board headed by an Editor-in-Chief and Associate Editors with responsibility for submissions in different subject tracks. Ideally, the period between submission and publication should be reasonably brief but the reality is far different. Publication of proceedings depends as much on the goodwill of reviewers as it does on the efficiency of editors. Evaluating papers is onerous and many of our reviewers made commendable efforts to produce proper reports for which we are grateful. Indeed, several reviewers read more than one paper. The Associate Editors spent much time on papers and reports to ensure that acceptable academic standards were met during peer-review for the proceedings to be credible. The cost of all this is a delay between submission and publication and a test of patience for many authors who otherwise usually expect a quick turn-around after submission. These proceedings have been produced in 2020, a year in which this country, as the world, has had to contend with COVID-19 and that is no small feat. We are extremely grateful to reviewers who gave up their valuable time to devote themselves to these proceedings and to all the authors for their patience as we toiled behind the scenes to produce these proceedings in good time despite the odds.

The SAIP was pleased to welcome Professor Deena Naidoo as its new president coming in to replace Patrick Woudt whose term of office had come to an end. The conference gratefully acknowledged the commitment and inspiration with which Prof Woudt has led the institute. The new president, Prof Naidoo, a condensed matter physicist, also serves as the Head of the School of Physics at the University of the Witwatersrand.

We received 87 papers. Of the number that was eventually reviewed, 68% were accepted for publication. On behalf of the Editorial Board, I thank all authors for submitting their work to SAIP2019 proceedings.

Makaiko Chithambo

Editor-in-Chief

Delegates to the 2019 South African Institute of Physics conference. What of the warrior in battle garb and stance on the far right? Unlike the statue of the Commendatore in Don Giovanni, the warrior never left his pedestal and remained a sculpture throughout the conference.

 ISBN: 978-0-620-88875-2

Message from The Conference Chair

The Department of Physics, University of Venda, was pleased to welcome delegates to the 64th South African Institute of Physics Annual Conference. The Department was overwhelmed with joy to be the host of this conference. To have hosted an SAIP conference is a piece of history we will always be proud of.

It was a journey for our department to organize this important event. Due to circumstances beyond our control, we chose the Ranch Protea Hotel in Polokwane as the venue for the conference. Our department focusses on computational physics, atmospheric phyics, renewable energy and energy materials all which we hope will play a role in the future progress of humankind.

I would like to thank all participants, sponsors and the LOC members who made this event a success. Specifically, I would like to appreciate plenary speakers and delegates who enriched this conference through their presentations and discussions. At this conference, 90% of the plenary speakers were women. Special thanks go to the University of Venda and other organisations for their financial support for the conference.

I appreciate the finalization of the proceedings of the 64th SAIP annual conference. I would like to thank all delegates who sent their papers for publication, the reviewers and editors who were guided by Prof Makaiko Chithambo (Rhodes University Department of Physics).

Dr. Eric Maluta
HoD Physics
University of Venda

Conference, Divisions and Editorial Board details

SAIP2019 Conference Chairperson

Eric Maluta; Head, Department of Physics, University of Venda

Local organising Committee

IP Matamba

V Khomunala

TS Mulaudzi

P Nemaangani

W Mabongo

VM Nekhubvi

D Tinarwo

JK Kirui

TS Ravhengani

TT Khedzi

L Jhamba

F Nemangwele

J Netshaulu J

RS Dima

K Mashavhathaka

W Mabogo

SAIP2019 Division Chairs

Division for Particle and Condensed Matter and Materials Physics

Rudolph Erasmus, University of the Witwatersrand

Division for Nuclear and Particle Physics

Rudolph Nchodu, iThemba LABS

Bruce Mellado, University of the Witwatersrand

Division for Photonics:

Herman Uys, Stellenbosch University

Division for Astrophysics and Space Science

Brian Van Soelen, University of the Free State

Division for Space Science

Zama Katamzi, South African National Space Agency

Brian Van Soelen, University of the Free State

Division for Physics Education

Sam Ramaila, University of Johannesburg

Division for Applied Physics

Phil Ferrer, University of the Witwatersrand

Division Theoretical and Computational Physics

Alan Cornell, University of Johannesburg

SAIP2019 Division Chairs

Editor-in-Chief Makaiko Chithambo, Rhodes University

Associate Editors

Theoretical and Computational Physics	W A Horowitz, University of Cape Town
Nuclear,Particle and Radiation Physics	Iyabo Usman, University of Witwatersrand
Astrophysics	Patrick Woudt, University of Cape Town
Applied Physics	Ernest E van Dyk, Nelson Mandela University
Physics of Condensed Matter and Materials	Aletta Prinsloo, University of Johannesburg
Physics of Condensed Matter and Materials	Charles Sheppard, University of Johannesburg

Proceedings Online Administration

Tebogo Mokhine (South African Institute Of Physics)

Editorial Board

Proceedings of SAIP2019

Editor-in-Chief
Makaiko Chithambo

Makaiko Chithambo is a Professor of Physics and Head of the Department of Physics at Rhodes University. He is an NRF B2 rated research physicist with research interests in Experimental Solid State Physics specialising in the study of point defects in insulators using time-resolved luminescence and other allied methods. Makaiko Chithambo is the author of An Introduction to Time-resolved Optically Stimulated Luminescence published by Morgan & Claypool Publishers and IOP(UK). He is currently the Deputy President of the SAIP.

Associate Editors

Ernest E van Dyk

Ernest van Dyk is Professor of Physics at Nelson Mandela University. In addition to teaching Physics, his research interests are in the field of Solar Energy, specialising in Photovoltaics. He leads the Photovoltaics Research Group (PVRG) in the Department of Physics and is also Director of the university spin-off company, PVinsight (Pty) Ltd.

W A Horowitz

W A Horowitz is an Associate Professor of Physics at the University of Cape Town and Associate Faculty at the African Institute of Mathematical Sciences. He is the Head of the Theory Pillar of the SA-CERN Collaboration and the Associates' Representative at the National Institute of Theoretical Physics. He's an expert in theoretical high-energy nuclear physics whose publications have over 3000 citations.

Charles Sheppard

Charles. J. Sheppard is an Associate Professor in the Department of Physics, University of Johannesburg. His research interests are in the magnetism of chromium-based alloys, thin films and nano-materials.

Iyabo Usman

Iyabo Tinuola Usman is an Associate Professor at the University of the Witwatersrand, Johannesburg. Her specialist field of research is Experimental Nuclear Physics.

Aletta Prinsloo

Aletta R.E. Prinsloo is a Professor of Physics at the University of Johannesburg. Her research interests are on magnetism of chromium-based alloys, thin films and nanomaterials.

Patrick Woudt

Patrick Woudt is a Professor in the Department of Astronomy, University of Cape Town. His research specialisations are on the physics of accretion onto white dwarfs in mass-transferring close binaries with particular focus on 1) the study of rapid oscillations in cataclysmic variables, 2) the study of ultracompact helium-transferring binaries, and 3) optical and radio transient surveys using MeerLICHT and MeerKAT, respectively. He is a member of the Council of the SAIP and its past President.

List of reviewers

Dr. Jules Mba several - University of Johannesburg.

Dr. Geoff Beck - University of Witwatersrand.

Dr. Lianliang Ma - Shandong University, China.

Dr. Rachid Mazini - Academia Sinica, Taipei.

Dr. Jon Shock - University of Cape Town.

Mr. Ryan Sweke - Freie Universität Berlin.

Dr. Dawit Worku - Cape Peninsula University of Technology.

Dr. William Horowitz - University of Cape Town.

Dr. Benjamin Fuks - LPTHE Jussieu - Sorbonne Université.

Dr. Giacomo Cacciapaglia - Institut de Physique des 2 Infinis de Lyon.

Dr. Ulrich Heinz - Ohio State University.

Mr. Jean Jules Mboukam - University of Johannesburg.

Dr. Thulani Hlatshwayo - University of Pretoria.

Prof. Konstantinos Zoubos University of Pretoria

Dr. Makhamisa Senekane - Department of Physics and Electronics, National University of Lesotho.

Prof. Jean Cleymans - University of Cape Town.

Mr. Kingsley Obodo - University of Pretoria, South Africa.

Dr. Deepak Kar - University of Witwatersrand.

Dr. Bryan Doyle - University of Johannesburg.

Prof. Wiets Roos - University of the Free State.

Dr. Robert Warmbier - University of Johannesburg.

Dr Pankaj Mohanty - University of Johanneburg.

Mrs. Bincy Susan Jacobs - University Of Johannesburg.

Prof. Emanuela Carleschi - Department of Physics, University of Johannesburg.

Dr. Moise Bertin Tchoula Tchokonte - Department of Physics, University of the Western Cape.

Dr. Buyi Sondezi - University of Johannesburg.

Dr. Andrew Venter - Necsa Limited.

Dr. Thomas Moyo - University of KwaZulu-Natal.

Dr. Bidhubhusan Sahu - KIIT University.

Prof. Hendrik Swart - University of the Free State.

Dr. Timothy Gibbon - NMMU Physics Department.

Dr. Alan Matthews - UKZN.

Prof. Martin Mtwaeaeborwa - Wits University.

Dr. Frederik Vorster - NMMU.

Dr. Aletta Karsten - NMISA.

Mr. Ryan Atkin - University of Cape Town.

Prof. Simon Connell - University of Johannesburg.

Prof. JJ (Koos) Terblans - University of the Free State.

Dr. Phil Ferrer - University of Witwatersrand.

Dr. Mmantsae Diale - University of Pretoria.

Prof. Aletta Prinsloo - University of Johannesburg.

Prof. Charles Sheppard - Department of Physics, University of Johannesburg.

Dr. Frikkie De Beer - Necsa.

Dr. R. Mavunda - UJ / Necsa.

Dr. Xifeng Ruang - University of the Witwatersrand.

Prof. Manny Mathuthu - North West University- Mafikeng.

Prof. Alan Cornell - University of Johannesburg.

Dr. Mukesh Kumar - University of the Witwatersrand.

Prof. Bruce Mellado - University of the Witwatersrand.

Ms. Linina Bedhesi - NECSA.

Prof. Sam Chikwembani - Walter Sisulu University.

Dr. Maleho Letloenyane.

Dr. Frank Komati - Central University of Technology

Dr Geoff Beck - University of the Witwatersrand

DIVISION A – DIVISION FOR PHYSICS OF CONDENSED MATTER AND MATERIALS

Ab initio studies of sperrylite, platarsite and palladoarsenide bulk and surface stabilities

B Nemutudi, P P Mkhonto and P E Ngoepe

Materials Modelling Centre, University of Limpopo, Private Bag x1106, Sovenga 0727, South Africa

Email: bradley.nemutudi@ul.ac.za

Abstract. In this study we employed the Vienna *Ab-initio* Simulation Package (VASP) along with the projector augmented wave (PAW) pseudopotential method to investigate the bulk structural and surface stabilities of sperrylite ($PtAs_2$), platarsite (PtAsS) and palladoarsenide (Pd_2As) minerals. The phase stability of PtAsS was obtained using cluster expansion. The phonon dispersion curves showed no soft modes for all the structures, suggesting stability. The calculated surface energies indicated that the (100) surface was the most stable amongst the low miller index (100), (110) and (111) surfaces for $PtAs_2$, PtAsS and Pd_2As. The order of surface energies increased as: (100) < (111) < (110) for $PtAs_2$ and PtAsS and (100) < (110) < (111) for Pd_2As. The calculated thermodynamically equilibrium morphologies of the relaxed surface structures indicated that the (100) surface was the most dominant for all the studied structures. The findings offered more insights on the stability of these minerals which may be applicable in their recovery.

1. Introduction

South Africa is one of the leading countries with high percentage of platinum group metal (PGM) in the igneous intrusion of Platreef Bushveld Complex [1]. The most predominant PGMs are platinum (Pt) and palladium (Pd) which consist of about 21% of arsenides [2]. Platinum is extremely resistant to physical and chemical degradation and has exceptional catalytic properties. These properties have led to extensive utilization of jewelry, high temperature industrial and automobile markets [3]. The stability of $PtAs_2$, PtAsS and Pd_2As is important in understanding their mineralogy formation which lead to their recovery. Furthermore, PGMs which contain both sulphur and arsenide are complex and needs a detailed understanding in their stability and for better extraction. First principle calculations have become an important tool for surface scientist as they can determine facet-specific surface energies, surface electronic structures and crystal morphologies [4].

In this paper, we performed density functional theory (DFT) calculations to study structural and vibrational stability of $PtAs_2$, PtAsS and Pd_2As models. The cluster expansion was implemented to generate the platarsite (PtAsS) mix bulk model. The surface calculations were computed to identify the most stable surface (working surface) for $PtAs_2$, PtAsS and Pd_2As minerals. These will be complemented with surface morphology in order to identify the preferred plane cleavages.

2. Computational methodology

The bulk and surface stability calculations were performed within the framework of *ab-initio* quantum mechanical density functional theory [5]. The plane-wave (PW) projector augmented wave

pseudopotential with the generalized gradient approximation of Perdew-Burke-Ernzerhof (GGA-PBE) exchange-correlation [6], implemented within the VASP code [7], were employed. The plane-wave cut-off energy was set to 450 and 500 eV for ($PtAs_2$, PtAsS) and Pd_2As bulk models, respectively. The Brillouin zone k-points sampling for bulk model were performed on a grid of $4 \times 4 \times 4$ and $7 \times 7 \times 14$ and for surfaces the $4 \times 4 \times 1$ and $5 \times 3 \times 1$ were used for ($PtAs_2$, PtAsS) and Pd_2As. This was chosen according to the scheme proposed by Monkhorst-Pack [8]. The phonon dispersion spectra were computed using PHONON code [9]. The interaction range of 10.0 Å for phonon dispersion were used for all the models. These were used to investigate the structural and vibrational properties of $PtAs_2$, PtAsS and Pd_2As minerals. In addition, cluster expansion within MedeA-UNCLE was performed to generate new stable phase of PtAsS model [10].

To model surface of periodic boundary conditions, a slab of finite thickness perpendicular to the surface but infinite extension was used. These slabs surfaces were obtained by cleaving the optimized bulk $PtAs_2$, PtAsS and Pd_2As structures. Slabs were separated from replicas repeating by a vacuum width of 20 Å. Different terminations were tested and only less reactive (low positive surface energy) for (100), (110) and (111) surfaces were considered.

3. Results and discussion

3.1. Cluster expansion and ground state structures of PtAsS model

In order to minimize the sensitivity of the cluster expansion to the user choices, and to make cluster expansion applicable beyond simple binary systems, a new program package under the name UNiversal CLuster Expansion (UNCLE) [11] has been developed. The UNCLE code [12] predicts the ground states of systems containing up to three and more elements.

For the cluster expansion method we started by searching for the ground state of the PtAsS system of the DFT energy formation. Our initial starting point was $PtAs_2$, where the sulphur atoms were added at the same position as arsenic atoms. The X, Y and Z parameters were also fitted to be equivalent for both As and S atoms.

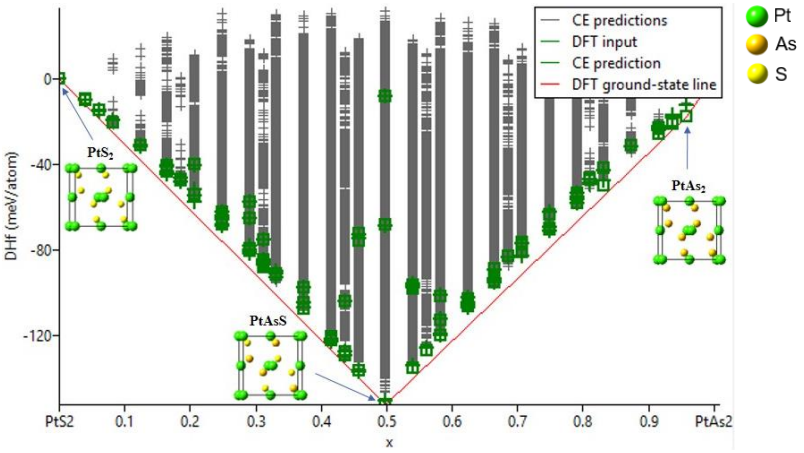

Figure 1: The cluster expansion calculated ground states structure determination of Pt-As-S. The energies of formation are with reference to Pt, As and S.

The binary ground state diagram in Figure 1 shows that all generated structures have negative heats of formation (ΔH_f), hence they are thermodynamically stable. Moreover, the cluster expansion showed a greater stability at 50/50 percentage (x = 0.5) where arsenic and sulphur atoms are equal with symmetry of the same structure. All structures between PtS_2 and $PtAs_2$ are more stable than PtS_2 and $PtAs_2$. However, some stoichiometries have multiple DFT inputs. Only three stable structures PtS_2, PtAsS and $PtAs_2$ were shown in Figure 1.

3.2. Bulk properties of $PtAs_2$, PtAsS and Pd_2As

The crystal structures of sperrylite, platarsite are cubic with space group Pa-3 [13] and 12 atoms, while palladoarsenide is monoclinic with space group of P-62m [14] and contain 9 atoms. The full structural relaxation of the bulk models were performed and the calculated structural lattice parameters of the bulk structures are given in Table 1. We found that the lattice constants were in good agreement with the experimental data. These comparisons confirm that our computational parameters are reasonably satisfactory and the DFT was able to predict the bulk structural properties.

Table 1. The relaxed lattice constants for $PtAs_2$, PtAsS and Pd_2As bulk structures.

	Lattice parameters (Å)	
Structure	Calculated	Experimental
$PtAs_2$	a = b = c = 6.061	a = b = c = 5.970 [15]
PtAsS	a = b = c = 6.024	a = b = c = 5.790 [13]
Pd_2As	a = b = 6.737, c = 3.664	a = b = 6.620, c =3.600 [16]

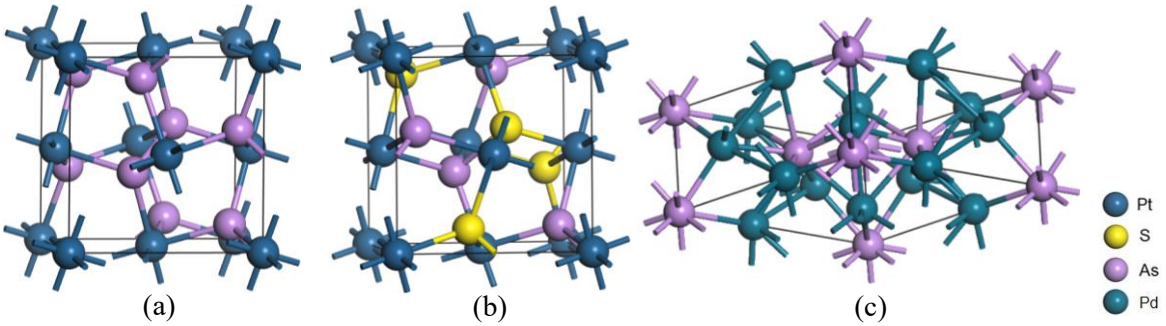

(a) (b) (c)

Figure 2: The relaxed bulk structure: (a) Sperrylite ($PtAs_2$), (b) platarsite (PtAsS) and (c) palladoarsenide (Pd_2As).

3.3. Vibrational properties of $PtAs_2$, PtAsS and Pd_2As

The analysis of vibrational properties of $PtAs_2$, PtAsS and Pd_2As phases with respect to the phonon dispersion are shown in Figure 3. The vibrational stability of the structures $PtAs_2$, PtAsS and Pd_2As were carried out along the symmetry directions within the first Brillouin zones.

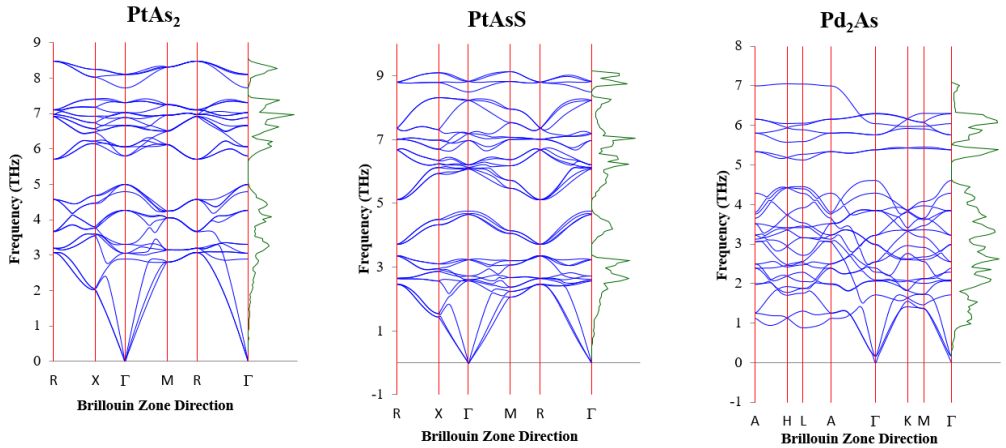

(a) (b) (c)

Figure 3: The phonon dispersion curves: (a) $PtAs_2$, (b) PtAsS and (c) Pd_2As structures.

We observed positive frequencies in all the Brillouin zone directions. As such, our phonon dispersion calculations confirm that $PtAs_2$, PtAsS and Pd_2As structures are vibrationally stable due to the absence

of negative vibrations (soft modes). However, in Figures 3(b) and (c) the scale of the graph goes to -1, which suggests that the frequencies do actually go negative.

3.4. Surface terminations and slab convergence

Considerations must be given to the large number of the Miller index planes (MI), and within each plane, all possible bulk terminations that exist. To reduce the search for working surfaces to a computationally tractable problem, whilst also ensuring that the most likely surfaces were surveyed, only the bulk terminations on the three low MI planes (100), (110) and (111) that are less reactive were considered. The desired surface terminations precisely were cleaved considering all possible terminations that are less reactive.

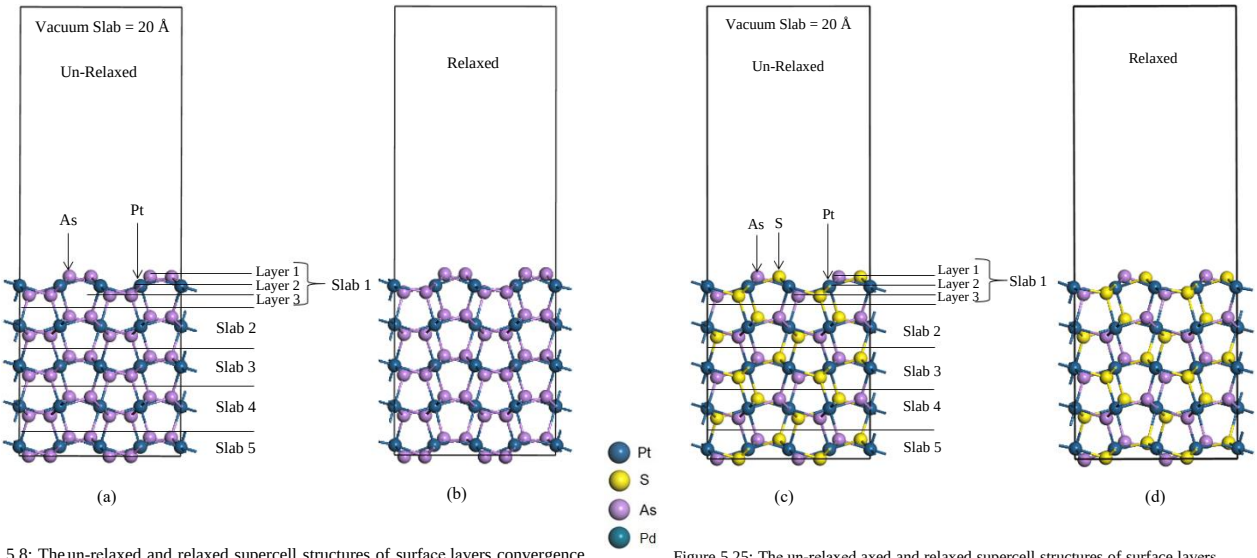

Figure 5.8: The un-relaxed and relaxed supercell structures of surface layers convergence for $PtAs_2$ (100) surface.

Figure 5.25: The un-relaxed axed and relaxed supercell structures of surface layers convergence for cluster expansion PtAsS (100) surface.

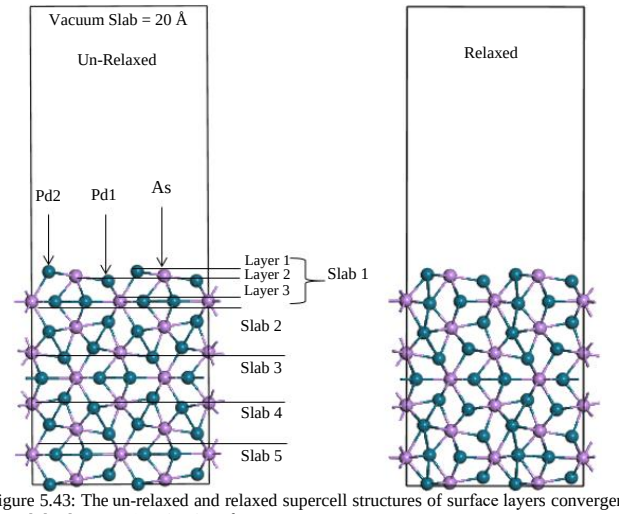

Figure 5.43: The un-relaxed and relaxed supercell structures of surface layers convergence for solid solution PtAsS (100) surface.

Figure 4: The un-relaxed and relaxed supercell structures of surface layers convergence for (a) and (b) $PtAs_2$, (c) and (d) PtAsS and (e) and (f) Pd_2As (100) surface.

The slab depth was varied and the 15-layer slab depth was chosen and considered as thick enough for adsorption. It was used to create a 2x2 supercell structures, which was then optimized allowing only the atom position to relax. Figure 4 shows the un-relaxed and relaxed supercell structures for (100) surface of $PtAs_2$, PtAsS and Pd_2As structures. The $PtAs_2$ and PtAsS supercell structures have 120 atoms while Pd_2As have 108 atoms. Figure 4(e) showed the slabs that are not identical due to the stacking configuration. The surface stabilities for different terminations were determined from the surface energies using equation 1:

$$E_{surface} = \left(\frac{1}{2A}\right)[E_{slab} - (n_{slab})(E_{bulk})] \quad (1)$$

where E_{slab} is the total energy of the cell containing the surface slab, n_{slab} is the number of atoms in the slab, E_{bulk} is the total energy per atom of the bulk and A is the surface area. A low positive value of $E_{surface}$ indicates stability of the surface termination.

Table 2 shows the supercell surface energies after relaxation for $PtAs_2$, PtAsS and Pd_2AS structures. The computed surface energies increase as: (100) < (111) < (110) for $PtAs_2$ and PtAsS and as (100) < (110) < (111) for Pd_2As. The (100) surface was identified as the most stable surface (working surface) since it displayed the lowest positive energies. Similar working surface for $PtAs_2$ was reported by Waterson et al. [3].

Table 2. The relaxed surface energies for $PtAs_2$ PtAsS and Pd_2As structures.

	Surface energy (eV/Å^2)		
Surface slab	**$PtAs_2$**	**PtAsS**	**Pd_2As**
100	0.065	0.035	0.070
111	0.085	0.062	0.109
110	0.091	0.717	0.097

3.5. Surface morphologies

The crystal morphology of $PtAs_2$, PtAsS and Pd_2As structures were predicted by using calculated surface energies within the METADISE code [17]. The calculated thermodynamical equilibrium morphologies of the relaxed (100), (110) and (111) surfaces are shown in Figure 5. Our surface morphologies results indicated that (100) surface was the most dominant surface exposed, followed by (111) and (110) surface for $PtAs_2$ model, with the (110) plane being the smallest. For PtAsS, the surface morphology showed that the mineral preferred to cleave only along the (100) surface plane, since the (110) and (111) surface plane did not appear on the morphology. Furthermore, the (100) surface was the dominant surface exposed on surface morphologies for Pd_2As model. However, in this case the (110) and (111) were also exposed largely, suggesting that these planes may cleave during mineral crushing.

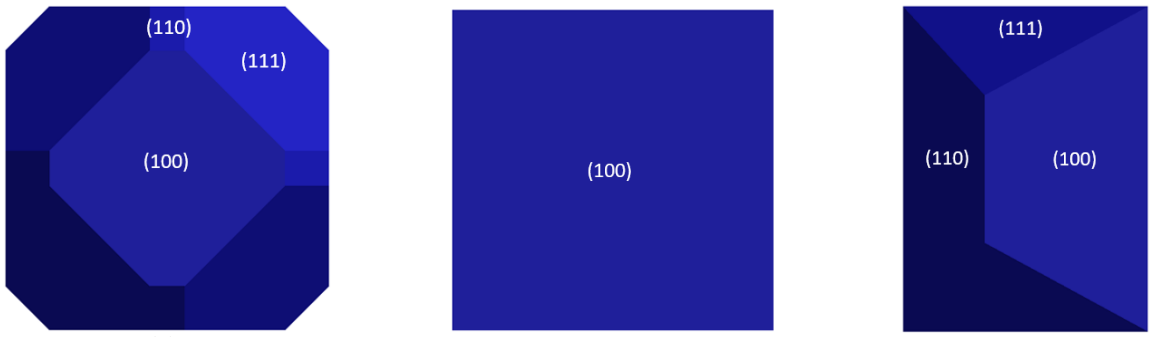

(a) (b) (c)

Figure 5: The calculated equilibrium morphologies. (a) $PtAs_2$, (b) PtAsS, and (c) Pd_2As surface structures.

4. Conclusion

In this study, we have performed *ab-initio* DFT calculations to investigate the bulk structural, vibrational and surface properties of $PtAs_2$, PtAsS and Pd_2As minerals. The optimized bulk structural lattice parameters were in agreement with the available experimental values. The PtAsS cluster expansion generated structures were found thermodynamically stable, with the 50:50 (x = 0.5) being the most stable phase. The phonon dispersion curves showed no soft modes along high symmetry direction suggesting stability for all structures. The calculated surface energies indicated that the (100) surface for $PtAs_2$, PtAsS and Pd_2As structures was the most stable amongst the low miller index (100), (110) and (111). Thermodynamical equilibrium morphologies of the relaxed structures indicated that (100)

surface was the most dominant surface. These findings gave more insights on the bulk and surface stability of these minerals which demonstrated the preferred plane cleavage of these minerals that may be applicable in their recovery.

Acknowledgements

This work was supported and performed at the Materials Modelling Centre (MMC), University of Limpopo. Computing resources were provided by the Centre for High Performance Computing (CHPC). We acknowledge the National Research Foundation (NRF) for financial support.

References

[1] Schouwstra R P, Kinloch E D and Lee C A 2000 Platinum excavation on the UG-2 reef in South Africa *Platinum Met. Rev.* **44** 33–39

[2] Viljoen M J and Schurmann L W 1998 Platinum-group metals *Miner. Resources. S. Afr.* **23** 532–568

[3] Waterson C N, Tasker P A, Farinato R, Nagaraj D R, Shacklenton N and Morrison C A 2016 A computational and experimental study on the binding of dithioligands to sperrylite, pentlandite and platinum *J. Phys. Chem.* **120** 22476–22488

[4] Manassidis I, De Vita A and Gillan M J 1993 Structure of the (0001) surface of Al_2O_3 from first principles calculations *Surf. Sci. Lett.* **285** 517–521

[5] Hohenberg P and Kohn W 1965 Inhomogeneous electron gas *Phys. Rev.* **136** 864–871

[6] Perdew J, Burke K and Ernzerhof M 1996 Generalized gradient approximation made simple *Phys. Rev. Lett.* **77** 3865–3868

[7] Kresse G and Furthmüller J 1996 Efficient iterative schemes for ab-initio total-energy calculations using a plane-wave basis set *Phys. Rev. B.* **54** 11169–11186

[8] Monkhorst H F and Pack J D 1976 Special points for Brillouin-zone integrations *Phys. Rev. B.* **13** 5188–5192

[9] Parlinski K, Li Z Q and Kawazoe Y 1997 First-principles determination of the soft mode in cubic ZrO_2 *Phys. Rev. Lett.* **78** 4063–4066

[10] Lee R and Raich J 1972 Cluster expansion for solid orthohydrogen *Phys. Rev. B.* **5** 1591–1604

[11] Sanchez J M, Ducastelle F and Gratias D 1984 Generalzed cluster description of multicomponent systems *Physica A: Stat. Mech. Appl.* **128** 334–350

[12] Lerch D, Wieckhorst O, Hart G L W, Forcade R W and Muller S 2009 UNCLE: a code for constructing cluster expansions for arbitrary lattices with minimal user-input *Modelling Simul. Mater. Sci. Eng.* **17** 1–19

[13] Cabri L J, Laflamme J H G and Stewart J M 1977 Platinum group minerals from the onverwacht *Can. Mineral.* **15** 385–388

[14] Cabri L J, Laflamme J H G, Stewart J M, Rowland J F and Chen T T 1975 New data on some palladium arsenides and antimonides *Can. Mineral.* **13** 321–335

[15] Ngoepe P E, Ntoahae P S, Mangwenjane S S, Sithole H M, Parker S C, Wright K V and de Leeuw N H 2005 Atomistic simulation studies of iron sulphide, platinum antimonide and platinum arsenide *J. Sci.* **101** 480–483

[16] Olowolafe J O, Ho P S, Hovel H J, Lewis J E and Woodall J M 1979 Contact reactions in Pd/GaAs junctions *J. Appl. Phys.* **50** 955–962

[17] Watson G W, Kesley E T, de Leeuw N H, Harris D J and Parker S C 1996 Atomistic simulation of dislocations, surfaces and interfaces in MgO *J. Chem. Soc. Faraday. Trans.* **92** 433–438

Structural, thermodynamic, electronic and mechanical properties of MCO_3 (M: Ca, Fe) precursor materials for Li-ion batteries

M T Morukuladi[1], N L Lethole[1], M C Masedi[1], N N Ngoepe[1]and P E Ngoepe[1]
[1]Materials Modelling Centre, University of Limpopo, Private Bag x1106, Sovenga, 0727, South Africa

Email address: tebogo.morukuladi@ul.ac.za

Abstract. First principle calculations were carried out on the structural, thermodynamic, electronic and mechanical properties of MCO_3 precursor materials at 0K to investigate their possible application as cathodes in Li-ion batteries. Li-ion batteries are the most crucial power sources for portable electronic devices. However, their performance greatly depends on the cathode materials, which serves as a host structure for Li ions. In this study we have performed DFT+U calculations using the plane-wave pseudopotential method framed within Perdew Burke Ernzerhof general gradient approximation (PBE-GGA) approach as embedded in the VASP code. The structural lattice parameters were calculated to 95% agreement with the experimental data, ensuring robustness of the approach employed. The calculated heats of formation are relatively low, suggesting thermodynamic stability. The electronic density of states showed that $CaCO_3$ is an insulator whereas $FeCO_3$ is predicted to be metallic, suggesting good electric conductivity on the latter.

1. Introduction

Lithium ion batteries have been widely investigated in the last decades for their application in energy storage due to their excellent cathode materials [1]. Li-ion batteries have different available cathode materials such as lithium iron phosphate, lithium cobalt oxide, lithium manganese oxide etc. Amongst all these cathode materials, lithium cobalt oxide ($LiCoO_2$) was reported as a better cathode material as compared to other cathode materials due to the high energy density translating into a long run-time for portable devices such as cell phones, tablets, laptops and cameras [2]. However, it was later reported that the very same $LiCoO_2$ cathode material was expensive and toxic [3]. As such, various transition metals were largely investigated alternative to the current widely used cathode materials. These include lithium and manganese rich composite $Li_{1+x}M_{1-x}O_2$ which are known for their high capacity (>200mAh/g) and improved structural stability [4]. However, the electrochemical performance of $Li_{1+x}M_{1-x}O_2$ compound depends on physical properties of the precursor materials which serve as a source of lithium. Hence, in this work we performed preliminary studies on the transition metal carbonate precursor materials namely calcium carbonate ($CaCO_3$) and iron carbonate ($FeCO_3$), to investigate their potential application as cathode materials in Li-Ion batteries. We have calculated their equilibrium cell parameters, heats of formations, elastic constants, band structures and densities of states to mimic stabilities at 0K. In Figure 1 we present the schematic atomic arrangement in the MCO_3 crystal system. MCO_3 compound crystallises in the R3cH space group. The transition metal atoms occupy the octahedral positions whilst the carbon atoms are in tetrahedral coordination with oxygen atoms.

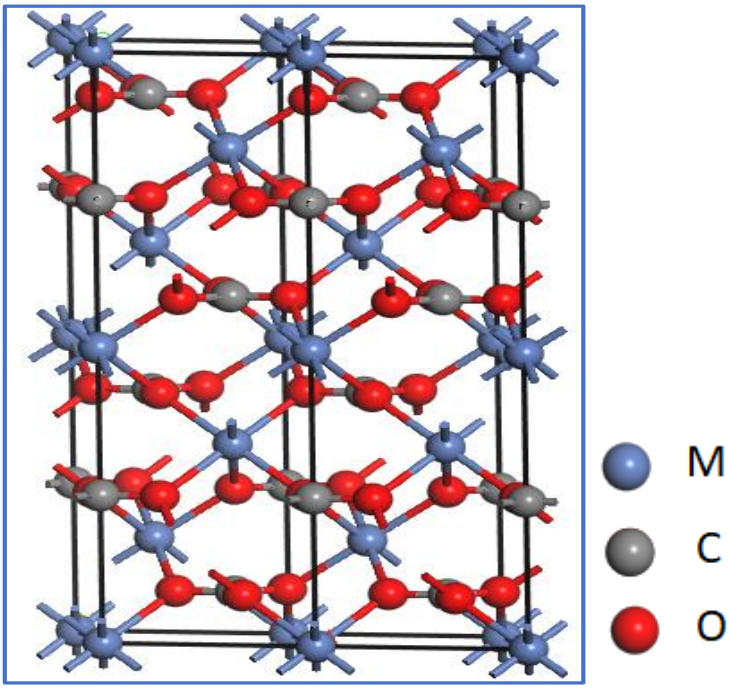

Figure 1. Schematic representation of atomic arrangements in MCO_3 system.

2. Computational Methodology

The first principle calculations based on the pseudopotential plane-wave within density functional theory (DFT) were performed using the Vienna *ab-initio* Simulation Package (VASP) code [5]. The ultrasoft pseudopotential was adopted to simulate the ion-electron interaction [6]. The generalised gradient approximation (GGA) with Hubbard parameter (U) [7] within the Perdew-Burke-Ernzerhof (PBE) functional [8, 9] was utilised to model the exchange-correlation. The plane-wave cut-off energy of 500 eV and Monkhorst and Pack k-points [10] mesh parameter of 4x4x4 were sufficient to converge the total energy of MCO_3 system to within 0.01 eV. Structure optimisation was first performed on the ionic positions and the unit cell size using GGA-PBE exchange correlation, followed by self-consistent calculations of heats of formation, density of states (DOS), band structure and elastic constants with a fixed unit cell volume.

3. Results and Discussions

3.1. Structural, Thermodynamic and Mechanical Properties

In Table 1 we show the DFT+U calculated equilibrium cell parameters, heats of formation, elastic constants and Pugh ratio (B/G) for MCO_3 systems. The available experimental data is also given. The equilibrium cell parameters were obtained by performing full geometry optimisations of atomic positions. The calculated cell parameters for $CaCO_3$ and $FeCO_3$ were found to be in good agreement with the experimental values to within 3.4% and 1.36% respectively. This suggests the quality of the approach employed. The calculated heats of formations for all MCO_3 structures are negative, suggesting thermodynamic stability. However, the experimental heats of formations are not available for comparison hence our results can be used for benchmarking in the future. Moreover, we calculated the elastic properties for $CaCO_3$ and $FeCO_3$ to determine their mechanical stability and compressibility. The elastic constants are basic parameters closely related to the hardness of the material, which inherently depends on the bond distance and microstructure. To describe the elastic behaviour of trigonal systems completely, six single-crystal elastic constants ($C_{11}, C_{12}, C_{13}, C_{14}, C_{33}, C_{44}$) [11] are

needed. For trigonal crystal systems to be considered mechanically stable, the following Born necessary stability conditions must be satisfied [12].

$$C_{11} - |C_{12}| > 0, (C_{44} + C_{12})C_{33} - 2C_{13}^2 > 0, (C_{11} + C_{12})C_{44} - 2C_{14}^2 > 0 \quad (1)$$

We note that the necessary stability condition for $CaCO_3$ are satisfied, indicating mechanical stability. On the other hand, the stability conditions for $FeCO_3$, in particular $(C_{44} + C_{12})C_{33} - 2C_{13}^2 > 0\ and\ (C_{11} + C_{12})C_{44} - 2C_{14}^2 > 0$ are not satisfied, suggesting mechanical instability. Furthermore, the bulk (B), shear (G) and Young's (E) moduli were calculated using the Voigt-Ruess-Hill approximation method from the obtained elastic constants. The bulk (B) modulus determines the hardness of materials, shear (G) modulus describes the response of materials to deformation and Young modulus (E) determine stiffness of materials. In order to determine the brittleness and ductility of MCO_3 materials, we have calculated the B/G ratio proposed by Pugh [13]. Materials are considered ductile if the Pugh's value is greater than 1.75, and brittle if less than 1.75. We note that our calculated B/G ratio is less than 1.75, suggesting brittleness (i.e. structural deformation after bending).

Table 1. Calculated and experimental lattice parameters, heats of formations, elastic constants and Pugh ratio for MCO_3 system.

	$CaCO_3$	Experimental [14]	$FeCO_3$	Experimental [15]
a (Å)	5.162	4.989	4.732	4.668
c (Å)	17.711	17.044	15.207	15.372
V (Å^3)	411.322	367.32	294.842	292.570
ΔH_f (kJ/mol)	-1030.902		-583.246	
		C_{ij} (GPa)		
C_{11}	125.57		703.63	
C_{12}	40.73		-588.10	
C_{13}	30.07		82.41	
C_{14}	12.03		101.32	
C_{33}	68.06		135.88	
C_{44}	31.44		-152.80	
B	55.05		57.04	
G	33.36		111.44	
E	83.25		190.09	
B/G	1.6402		0.5118	

3.2. Electronic Properties

3.2.1. Density of States. In order to gain knowledge on the electronic properties of $CaCO_3$ and $FeCO_3$, we have calculated their densities of states (DOS) and band structures (BS). In Figure 2 we present the total density of state (TDOS) and partial density of states (PDOS) for $CaCO_3$ and $FeCO_3$. The Fermi level (E_F) is taken as zero energy in total density of state and partial density of state spectra. We observe that the $CaCO_3$ system is characterised by a relatively wide energy band gap of -4.818eV near the Fermi level suggesting insulator behaviour and poor electronic conductivity. On the other hand, $FeCO_3$ shows non energy band gap. Moreover, the Fermi level falls on the spin–down *Fe 3d* band suggesting metallic behaviour and good electronic conductivity. The partial DOS for $CaCO_3$ (Figure 2a) show that the states around Fermi level are predominately *O 2p* with minimum contribution from Ca and C, whereas $FeCO_3$ (Figure 2b) is dominated by *Fe 3d* states.

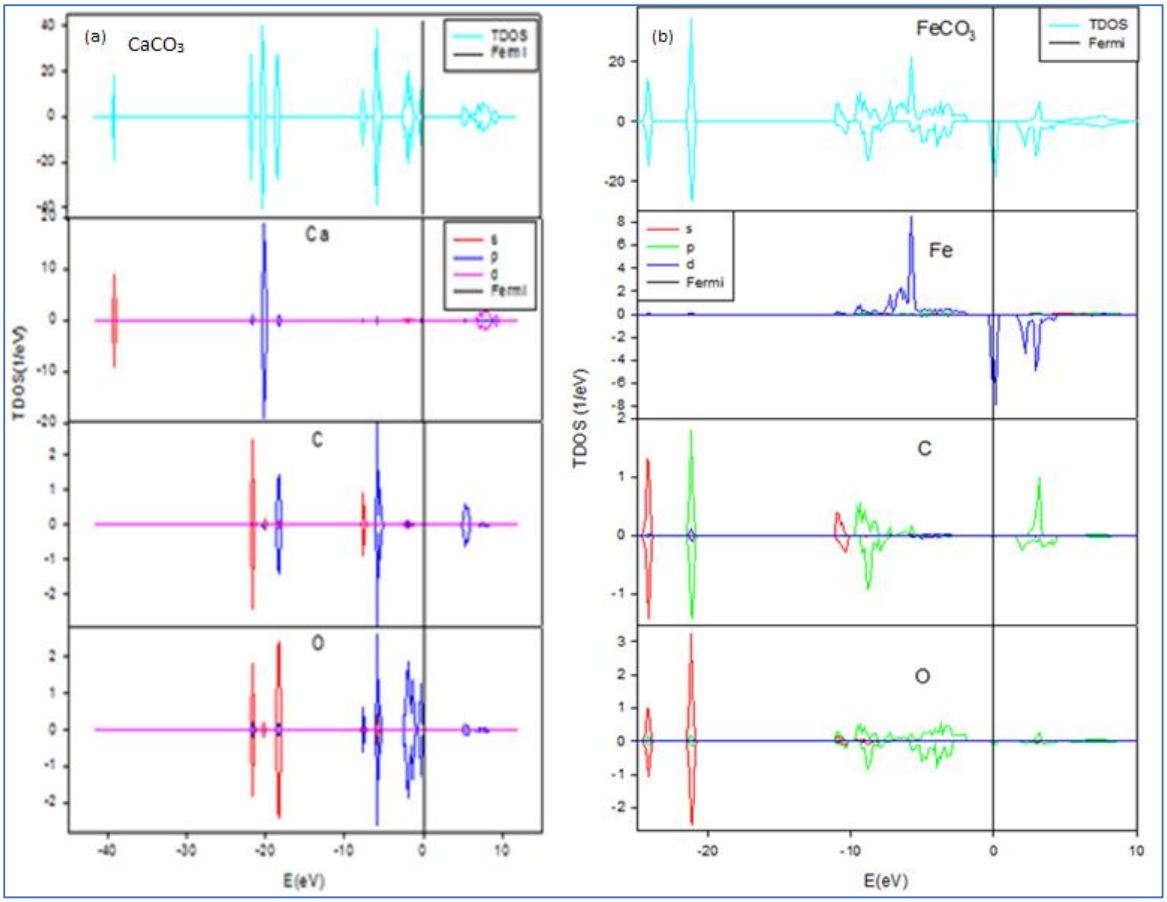

Figure 2. Total and partial DOS for (a) $CaCO_3$ and (b) $FeCO_3$ systems.

3.2.2. Band Structures. The calculations of electronic band structures along the symmetry lines of the Brillouin zone are shown in Figure 3. The band structure plot for $CaCO_3$ (Figure 3a) shows an indirect energy band gap of 4.824eV along high symmetry lines Γ (0,0,0) and L(1/2,1/2,1/2), suggesting that the system is a magnetic insulator. The valence maximum is located near the middle of an edge joining a trigonal face at -0.071eV while the conduction band minimum is located near the centre of the Brillouin zone (Γ) at 4.754eV with respect to the Fermi level. Moreover, band structure plot for $FeCO_3$ (Figure 3b) display no energy band gap at the Fermi level, suggesting a metallic characteristic and good electronic conductivity, the valence band states overlap the Fermi level to the conduction band.

 ISBN: 978-0-620-88875-2

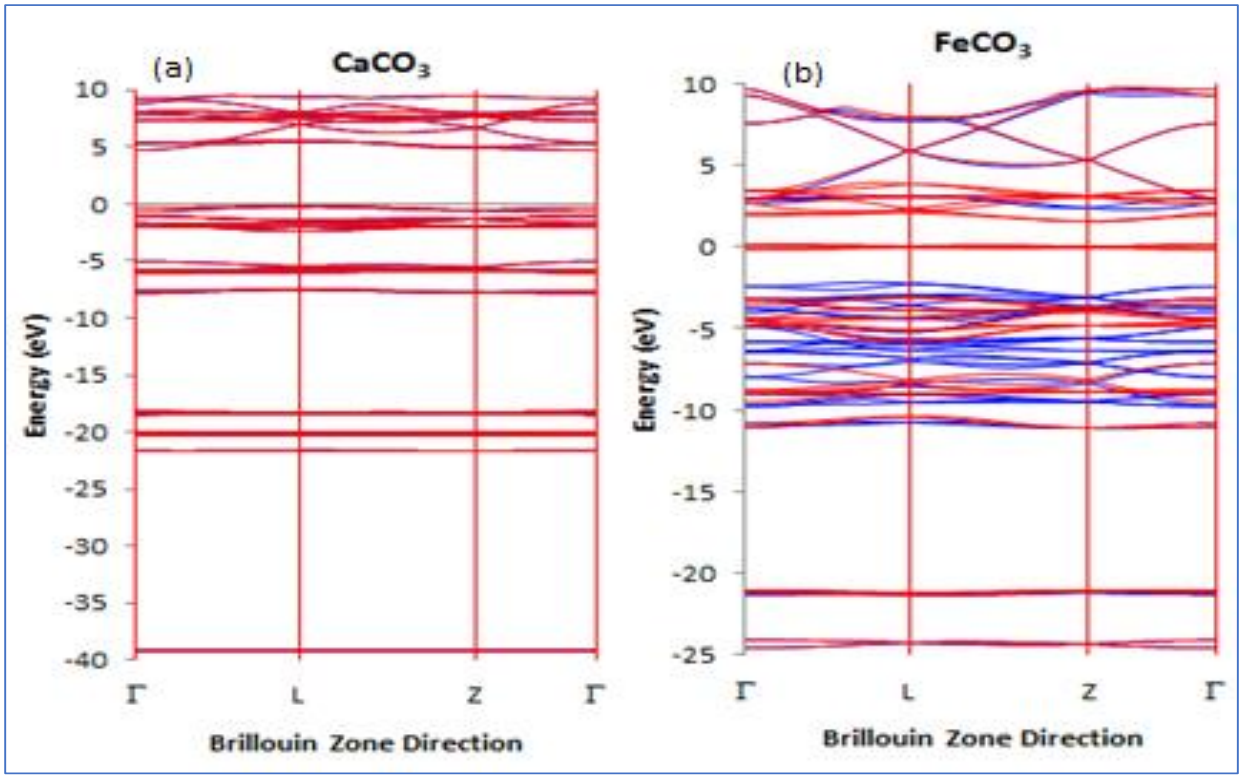

Figure 3. The electronic band structure plots for (a) $CaCO_3$ and (b) $FeCO_3$.

4. onclusions

The structural, thermodynamic, electronic and mechanical properties of MCO_3 (M: Ca and Fe) compounds have been investigated using the first principle calculations. Structural properties were found to be in good agreement with the experimental data which validate the approach employed. The calculated heats of formation have shown that MCO_3 systems are thermodynamically stable since they have negative values. Moreover, the calculated electronic density of states and band structures predicted that $CaCO_3$ is an insulator whereas $FeCO_3$ is metallic. Lastly, the mechanical properties for MCO_3 compounds showed that $CaCO_3$ satisfy the necessary stability criteria indicating that it is mechanically stable, while on the other hand $FeCO_3$ did not satisfy all the stability criterion for trigonal systems indicating mechanical instability.

Acknowledgement: This work was performed at the University of Limpopo Materials Modelling Centre and is sponsored by the National Research Foundation (NRF).

5. eferences

1. Liu K, Liu Y, Lin D, Pei A and Cui Y 2018 Materials for lithium-ion battery safety *Sci. Adv.* **4** 9820.
2. Mizushima K, Jones PC, Wiseman PJ and Goodenough JB 1980 LixCoO2 (0 < x < 1): A new cathode material for batteries of high energy density *Mater. Res.***15** 789.
3. Yoshio M, Brodd RJ and Kozawa A 2009 Lithium ion batteries *J. Sci. Technol.* ***46*** 299.
4. Lu Z, Macneil DD and Dahn JR 2001 Layered cathode materials Li[NixLi(1/3.2x/3) Mn(3/3.x/3)] O_2 for lithium ion batteries *Electrochem. Solid-State Lett* **4** 194.
5. Kresse G, Marsman M and Furthmuller J 2018 Computational materials physics *Fac. Phys.* **12** 1090.
6. Vanderbilt D 1990 Soft self-consistent pseudopotentials in a generalized eigenvalue formalism *Phys. Rev. B* **41** 7895.

7. Kulik J 2015 Perspective: treating electron over-delocalization with the DFT + U method, *J. Chem. Phys.* **142** 240901.
8. Perdew JP and Wang Y 1992 Accurate and simple analytic representation of the electron-gas correlation energy *Phys. Rev. B* **45** 13244.
9. Perdew JP, Burke K and Ernzerhof M 1996 Generalized gradient approximation made Simple Phys. *Rev. Lett* **77** 3865.
10. Monkhorst HJ and Pack JD 1976 Special points for brillouin-zone integrations *Phys. Rev. B* **13** 5188.
11. Chinh PD 2007 Estimates for the elastic moduli of random trigonal polycrystals and their macroscopic uncertainty *Int. J. Solid-Struct.* **44** 2772.
12. Mei Y, Pang D and Cheng N 2018 Electronic and mechanical properties of trigonal boron nitride by first-principles calculations *Physica E Low Dimens. Syst. Nanostruct.* **101** 385.
13. Pugh SF 1954 Relations between the elastic moduli and the plastic properties of polycrystalline pure metal J. Sci. **45** 843.
14. Zhang J and Reeder RJ 1999 Comparative compressibilities of calcite-structure carbonates: deviations from empirical relations Am. Mineral.**84** 870.
15. Navrotsky A and Chai L 1993 Thermochemistry of carbonate-pyroxene equilibria," contributions to mineralogy and petrology *Cont. Mineral. Petro.* **114** 147.

Ab Initio Study of $Ti_{50}Pt_{50-x}Hf_x$ (x = 6.25, 18.75, 25) Potential Shape Memory Alloys

M E Baloyi[1], R Modiba[2], P E Ngoepe[1] and H R Chauke[1]

[1] Materials Modelling Centre, University of Limpopo, Private Bag X1106, Sovenga, South Africa
[2] Future Production: Manufacturing, CSIR, PO Box 395, Pretoria, 0001, South Africa

Email: mphamela.baloyi@ul.ac.za

Abstract. *Ab initio* density functional theory approach was employed to study the effect of Hf addition to the TiPt binary shape memory alloys (SMAs). SMAs have the ability to retain their original shapes after deformation when heated above a certain temperature. They have been widely used in the fields of engineering and medicine due to their shape memory effect (SME) and super-plasticity which are displayed in martensitic transformations. In this work, a supercell approach method in VASP was used to substitute Pt with 6.25, 18.75 and 25 at.% Hf in the TiPt. The calculated heats of formation predicted that 6.25 at.% Hf to be the most stable structure and the elastic properties showed that $Ti_{50}Pt_{50-x}Hf_x$ is mechanically stable for all the concentrations. It is seen that hafnium addition stabilizes the B2 TiPt with all the Cij´s being positive. Moreover, phonon dispersion curves indicate that increasing the Hf content in the system stabilizes the structure.

1. Introduction

Shape memory alloys (SMAs) have the ability to recover their original shape after being deformed when heated above a certain temperature. They exhibit two interesting properties, shape memory effect (SME) and superelasticity [1]. Titanium-based SMAs have attracted significant attention due to its distinctive properties for extensive applications such as actuators and sensors [2]. TiNi has been extensively studied for various applications because it exhibits significant shape memory effect (SME) and excellent superelasticity [3]. However, some NiTi applications are greatly limited by its low martensitic transformation temperatures, T_m, lower than 373 K [4]. The development of SMAs which can operate at high temperature has been studied to improve SME properties and application areas [5].

High-temperature shape memory alloys (HTSMAs) with T_m greater than 373 K have numerous potential applications. TiPt and TiPd alloys are potential alloys to be used at high temperature due to their high T_m [6]. Moreover, TiPt has a higher T_m of about 1300 K rendering it suitable for HTSMAs development [7]. Previously, density functional theory (DFT) results on TiPt showed B2 phase to be unstable at 0 K due to negative C' shear modulus [8, 9]. In order to enhance the shape memory properties and stability of TiPt, ternary alloys are being considered. In the previous work, Zr, Ru, and Co were reported to enhance the shape recovery ratio [10]. However, martensitic transformation temperature of TiPt decreased with the addition of the Zr, Ru, Co and V [11, 12, 13].

In this work, the density functional theory (DFT) technique was used to demonstrate the effect of alloying elements (Hf) on the stability in $Ti_{50}Pt_{50-x}M_x$ shape memory alloys. Stabilities of B2 $Ti_{50}Pt_{50-x}Hf_x$ (x= 6.25, 18.75, 25) were investigated with respect to their equilibrium lattice parameters, heats of

formation, elastic and vibrational properties of the structures. The structures of TiPt is shown in Figure 1 below. It is a cubic B2 structure also known as a high temperature beta phase with the space group of Pm-3m. Its equilibrium lattice parameter is 3.192 Å. The supercell with 16 atoms was built using substitutional search embedded in MedeA and Pt atoms substituted with 6.25, 18.75, and 25 at.% Hf.

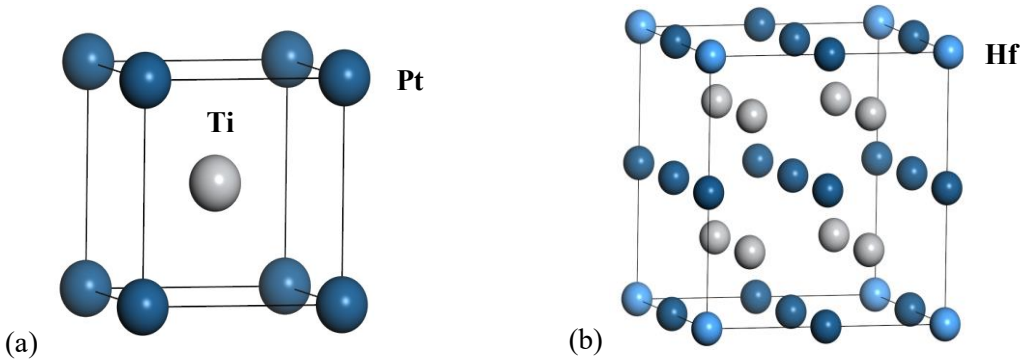

Figure 1. The atomic arrangement unit cell of (a) B2 TiPt system with a space group Pm-3m. Supercell of 2X2X2 for (b) B2 TiPt-Hf structures with 16 atoms.

2. Methodology

The calculations were carried out using *ab initio* density functional theory (DFT) [14, 15] formalism as implemented in the Vienna *ab initio* simulation package VASP [16] with the projector augmented wave (PAW) [17]. An energy cut-off of 500 eV was used, as it was sufficient to converge the total energy of the cubic B2 TiPt alloys. For the exchange-correlation functional, the generalized gradient approximation of Perdew, Burke, and Enzerhof (GGA-PBE) [18] was chosen. The Brillouin zone integrations were performed for suitably large sets of *k*-points according to Monkhorst and Pack [19]. A 2X2X2 supercell of cubic B2 TiPt with 16 atoms was used. The substitutional search tool embedded in VASP was used to substitute Pt with Ta. The phonon dispersion spectra were evaluated using PHONON code [20] as implemented in MedeA software.

3. Results and discussion

3.1. Structural and thermodynamic properties

The calculated DFT results on equilibrium lattice parameters and heats of formation of the $Ti_{50}Pt_{50-x}Hf_x$ (x = 6.25, 18.75, 25) are shown in Table 1. The calculated results show that the partial substitution of Pt with Hf increases the lattice parameters of the $Ti_{50}Pt_{50-x}Hf_x$. This implies that the structure becomes larger in volume. The volume of the structures increases since the atomic radius of Hf is larger than that of Ti and Pt atoms. The lattice parameters obtained for the ternary alloys are comparable to lattice parameter obtained by Bozollo *et al* [21] at 5 at.% Hf (a=3.17 Å).

Heats of formation were calculated to determine the stability of the structure. The equation for determining heats of formation (ΔH_f) is discussed by Baloyi *et al* [22]. The lowest and highest heats of formation show the most and least stable material, respectively. $Ti_{50}Pt_{43.75}Hf_{6.25}$ is found to be the most stable with the lowest predicted ΔH_f of -0.82 eV/atom. The systems become less favourable as the Hf content increases to 18.75 and 25 at.%, which indicates that the phase stabilities of the structures become worse (unstable).

Table 1. Lattice parameters (a) and heats of formation (ΔH_f) of the $Ti_{50}Pt_{50-x}Hf_x$ ternary alloys.

Structures	Lattice parameter (Å)	ΔH_f (eV/atoms)
$Ti_{50}Pt_{50}$ [8]	a = 3.18	-0.796
$Ti_{50}Pt_{43.75}Hf_{6.25}$	a = 3.19	-0.82
$Ti_{50}Pt_{31.25}Hf_{18.75}$	a = 3.22	-0.54
$Ti_{50}Pt_{25}Hf_{25}$	a = 3.25	-0.50

3.2. Elastic constants

The elastic constants (C_{ij}), anisotropy (A) and Pugh's ratio (B/G) of $Ti_{50}Pt_{50-x}Hf_x$ alloys were calculated as shown in Table 2. The elastic properties investigation is considered in this study to understand the martensitic transformation behaviour of these alloys [11]. The mechanical stability criterion of a cubic crystal is given as [8, 23]:

$$C_{44}>0,\ C_{11}>|C_{12}| \text{ and } C_{11} + 2C_{12}>0.$$

The positive C' designates the mechanical stability of the crystal, otherwise unstable. Elastic constants of the B2 structures are positive, thus satisfying mechanical stability criteria set for cubic crystals. Therefore, B2 structures are mechanically stable. $Ti_{50}Pt_{25}Hf_{25}$ are considered to be anisotropic since A is approximately 1 ($A \approx 1$, a less micro crack in the material). To investigate the ductility of these alloys, bulk (B) and shear (G) moduli are considered. All ternary alloys in this study are ductile due to Pugh's ratio greater than the critical value (B/G>1.75) [24].

Table 2. Elastic properties of $Ti_{50}Pt_{50-x}Hf_x$ (x = 6.25, 18.75, 25) ternary alloys and their anisotropy A.

Elasticity (GPa)	$Ti_{50}Pt_{50}$ [8]	$Ti_{50}Pt_{43.75}Hf_{6.25}$	$Ti_{50}Pt_{31.25}Hf_{18.75}$	$Ti_{50}Pt_{25}Hf_{25}$
C_{11}	145	189	197	196
C_{12}	210	175	151	124
C_{44}	45	53	53	67
C'	-32	7	23	36
$A = 2C_{44}/(C_{11}-C_{12})$		7.48	2.26	1.87
B/G		7.34	4.44	2.82

3.3. Phonon dispersions

Phonon dispersion calculations were performed to investigate the vibrational properties of $Ti_{50}Pt_{50-x}Hf_x$ ternary alloys at different concentration and are shown in Figure 2. In this section, we deduce the influence of Hf on the presence of soft modes in the negative frequency of TiPt binaries by the way of phonon dispersion and phonon DOS. These curves display interesting behaviour as we increase Hf concentration in the system. $Ti_{50}Pt_{43.75}Hf_{6.25}$ is unstable due to observed vibrations in the negative frequency along with the high symmetry directions, displayed by phonon dispersion curves. The observed soft modes are due to the high vibration of Pt atoms in the system. The vibrations are observed at a frequency of approximately -2 THz. The soft modes observed are along R, M, X and Γ directions on the phonon spectra. It is interesting to note that at higher content of Hf (x = 18.75 and 25), the material becomes vibrationally stable with no soft modes observed on the phonon dispersion

curves in the negative frequency. $Ti_{50}Pt_{31.25}Hf_{18.75}$ and $Ti_{50}Pt_{25}Hf_{25}$ are vibrational stable due to the absence of soft modes in the negative frequency of phonon dispersion curves. These results show that as Hf content increases in the system, the material becomes stable which is in good agreement with the predicted elastic constants.

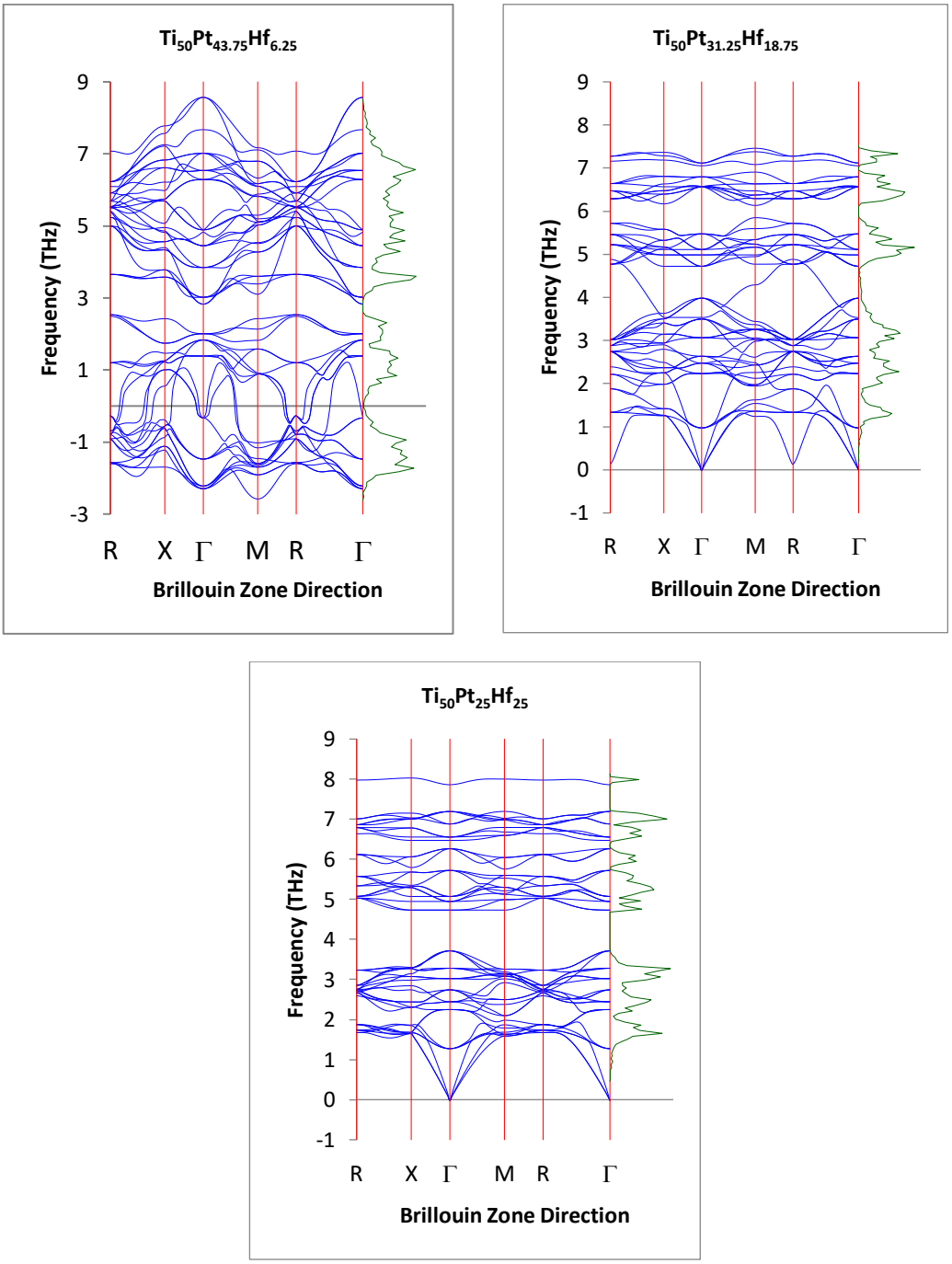

Figure 2. Phonon dispersions of $Ti_{50}Pt_{50-x}Hf_x$ (x= 6.25, 18.75, 25) ternary alloys.

4. Summary and conclusion

A first principle approach was used to study the stability of the $Ti_{50}Pt_{50-x}Hf_x$ atomic composition using the supercell approach. The ternary structures were found to be thermodynamically stable with $Ti_{50}Pt_{43.75}Hf_{6.25}$ being the most stable (lowest heats of formation). Elastic constants showed the stability of $Ti_{50}Pt_{50-x}Hf_x$ since all the C_{ij}'s were found to be positive and obey the elastic stability criterion of the cubic lattice. Interestingly, all the ternary alloys under study are ductile. $Ti_{50}Pt_{43.75}Hf_{6.25}$ was found to be vibrationally unstable due to observed soft modes at the negative frequency, whereas at 18.75 and 25 at.% Hf the system becomes more stable. Phonon dispersion curves predicted the stability of ternaries as Hf content increases. TiPtHf has shown potential for high temperature shape memory alloy (HTSMA) development since the alloy displayed elastic and vibrational stability properties.

Acknowledgements

I would like to thank NRF and CSIR for financial support. The work was carried at the Materials Modelling Centre, University of Limpopo and the Centre for High performance computing (CHPC) in South Africa. The support of the South African Research Chair Initiative of the Department of Science and Technology, DST is highly recognized.

References

[1] Mashamaite M P, Chauke H R and Ngoepe P E 2018 *Material Sci. and Eng.* ***430*** *012022*
[2] Kubo H, Hamabe A and Shimizi K 1975 *Scr. Metall*. **9** 1083-1087
[3] Chang-Long T, Wei C and Jing-Chuan Z 2006 *Chinese Phys. Lett.* **23** 2863-2866
[4] Otsuka K and Kakeshita T 2002 *MRS Bull*. **27** 91-100
[5] Van Humbeeck J 1999 *Mater. Sci. Eng*. A **273–275** 134-148
[6] Otsuka and X. Ren 2005 *Prog. Mater. Sci.* **50** 511-678
[7] Yamabe-Mitarai Y et al. 2015 Materials Today: Proceedings **2S** S517-S522
[8] Mahlangu R, Phasha M J, Chauke H R, Ngoepe P E 2013 *Intermetallics* **33** 27-32
[9] Baloyi M E, Modiba R, Chauke H R and Ngoepe P E 2018 *Material Sci. and Eng.* **430** 012020
[10] Takahashi Y, Inamura T, Sakurai J, Hosoda H, Wakashima K and Miyazaki S 2004, *Trans*. *MRS-J*. **29** 3005–3008
[11] Chauke H R, Mashamaite M, Modiba R and Ngoepe P E 2017 *Key Eng. Materials* **770** 230-238
[12] Chikosha S, Mahlatji M L, Modiba R and Chikwanda H K 2018 *Material Sci. and Eng.* **430** 012020
[13] Modiba R, Baloyi E, Chikosha S, Chauke H R and Ngoepe P E 2018 *Material Sci. and Eng.* **430** 012021
[14] Hohenberg P and Kohn W 1964 *Phys. Rev.* B **136** 864-871
[15] Kohn W and Sham L J 1965 *Phys. Rev.* A **140** 1133-1138
[16] Kresse G and Hafner J 1993 *Phys. Rev. B* **47** 558-561
[17] Blöchl P E 1994 *Phys. Rev. B* **50** 17953-17979
[18] Perdew J P, Burke K and Enzerhof M 1996 *Phys. Rev. Lett.* **77** 88-92
[19] Monkhorst H J and Pack J D 1976 *Phys. Rev.* B **13** 5188-5192
[20] Parlinski K, Li Z Q and Kawazoe Y 1997 *Phys. Rev. Lett.* **78** 4063-4066
[21] Bozollo G, Mosca H O and Noebe R D 2007 *Intermetallics* **15** 901-911
[22] Zhou X W and Zimmerman J A 2008 *Phys. Rev. Lett.* **23** 704-718
[23] Zhang J M and Guo G Y 1997 *Phys. Rev. Lett.* **78** 4789-4792
[24] Pugh S F 1954 *J. of Physics,* **45** 823-843

Computer simulation studies of HF adsorption on TiO_2 (001) and (110) surfaces

D M Tshwane[1,2*], R Modiba[1,2], H R Chauke[2], G Govender[1] and P E Ngoepe[2]

[1] Materials Science and Manufacturing, Advanced Materials and Engineering, CSIR, PO Box 395, Pretoria, 0001, South Africa

[2] Materials Modelling Centre, University of Limpopo, Private Bag X1106, Sovenga, South Africa

*DTshwane@csir.co.za

Abstract. Hydrogen fluoride molecule is a candidate used for etching metal oxide surface due to its strong corrosive qualities. However, the etching phenomenon is not well understood at the atomistic level. Investigation of HF interaction with TiO_2 (001) and (110) surfaces is important for enhancing the etching mechanism. Adsorption geometries and energies of HF on TiO_2 (001) and (110) surfaces have been investigated using density functional theory employing CASTEP code. It was found that HF chemically adsorbed to TiO_2 (001) and (110) surfaces to form Ti-F bond and hydroxyl molecule. The adsorption of HF molecule on TiO_2 (001) and (110) surfaces is by physisorption than chemisorption process. HF molecule prefers (001) surface with lower adsorption energy than on (110) surface. Besides, all these surfaces were found to have higher adsorption ability with increasing number of HF molecules. Mulliken charge analysis indicates that the dissociation of F atom attract electrons, due to the higher electronegativity of the fluorine atom.

1. Introduction

Titanium and its alloyed components are extensively used materials for a large variety of applications [1]. The adsorption of oxygen during the manufacturing of these metal components remain a big concern that results in the formation alpha case layer [2]. Surface modification is required due to the spontaneous growth of alpha case layer. Recently, wet chemical etching process remains a widely applied technique for surface modification using hydrogen fluoride (HF) as an etchant [3, 4]. HF is a colorless fuming liquid or gas molecule materials mainly used for industrial purpose such as metal surface etching. Metal surface etching by HF is one of the most important material tailoring technique in the manufacturing of metal-based alloyed components [5] therefore, it is very important to understand the interaction of HF with TiO_2 surfaces. Adsorption of HF by suitable solid adsorbents seems to offer an interesting and practical atomic interaction.

Considerable research effort has been expended for HF adsorption on the metal oxide surface [6, 7]. These studies, however, tend to have a focus on the Al_2O_2 [8], SiO_2 [9] surfaces and adsorption of a single prone molecule. Recently, Yang *et al* [10] showed that the adsorption of fluorine (F) ion on the surfaces of anatase-TiO_2 makes (100) surface energetically preferable than (101) surface. Wang *et al* [11] investigated selective etching phenomenon on (001) surface faceted anatase titanium dioxide. Their

results indicated that etching mechanism is energetically permitted and the surface etching can merely occur on the (100) surface under high HF concentrations. In this work density functional theory (DFT) approach is used to study the adsorption behavior of HF on TiO_2 (110) and (001) surfaces at different coverages. The adsorption energy, charge density difference and Mulliken charge are analyzed.

2. Computational methodology

First-principle calculations were performed using CASTEP code as implemented in Material Studio [12] on the basis of density functional theory (DFT). The electron-exchange and correlation were described by the Perdew-Burke-Ernzerhof (PBE) functional of the generalized gradient approximation (GGA) [13]. The GGA-PBE functional is well known to underestimate the band-gap which reduces photo-induced electron transfer during reactions [14]. To correct the strong electronic correlation problem, DFT+U method which was first initiated by Dudarev *et al* [15] was utilized with a U parameter of 5.0 eV for Ti in TiO_2 as proposed by Dompablo *et al* [16]. Brillouin-zone integrations are implemented using the Monkhorst-Pack approach [17] with K-point sampling grids of 4×4×1 for geometry calculation with cut-off energy of 400 eV. The TiO_2 (001) and (110) surfaces were represented by p(2×2) and p(3×3) supercell with five and seven atomic layers, respectively. In order to eliminate the interaction between two adjacent TiO_2, a vacuum of 30 Å was adopted. The interaction strength of HF molecule with the TiO_2 (001) and (110) surfaces is given by the adsorption energy, calculated using the equation below:

$$E_{ads} = [E_{HF/slab} - (E_{slab} + E_{HF})] \quad (1)$$

where $E_{HF/slab}$ is the total energy of the surface slab with molecule, E_{slab} is the energy of the surface slab and E_{HF} is the energy of the isolated molecule.

3. Results and discussion

3.1 Surface geometry and HF Adsorption

Pure surface slabs were initially optimized to obtain surface energetic minima and examine chemical properties. Figure 1 (a-b) shows the optimized surface slabs with designated atom coordination, (a) TiO_2 (110) surface consisting of three coordinating oxygen atom (O3c) and both titanium five- and six-coordination atoms (Ti5c and Ti6c), respectively. (b) TiO_2 (001) surface consist of two coordinate oxygen atoms (O2c) and five coordinates titanium (Ti5c). Surface optimization reveal that TiO_2 (110) surface is much more stable with a lower surface energy of (1.98 Jm^{-2}) than TiO_2 (001) surface (2.81 Jm^{-2}).

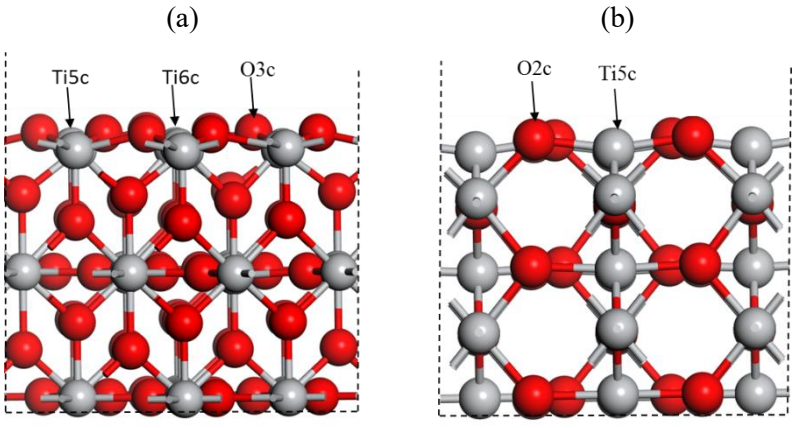

Figure 1: TiO_2 model surface slabs: (a) (110) and (b) (001) surface.

Calculated surface energies are well comparable with the results by Idrizz *et al* [18] and Tshwane *et al* [19]. The significant differences on the surface energy of TiO_2 (110) obtained by Tshwane *et al* [19], is due to different surface slabs. Adsorption process involves the interaction of HF molecule with TiO_2 (001) and (110) surfaces and one of the most fundamental characteristics of the process is the adsorption energy. Table 1 present the adsorption energies and the optimized parameters of HF molecule interacting with TiO_2 (110) and (001) surfaces. The negative value of adsorption energies indicates that the adsorption of HF molecule on Ti (001) and (110) surfaces is energetically favourable. TiO_2 (001) surface was found to be the most favourable adsorption surface than TiO_2 (110) surface with adsorption energy of -5.92 eV and -5.43 eV, respectively. The smaller E_{ads} value suggest very large exothermicity of the adsorption process. The relative difference in adsorption energy with a different surface is due to atom surface interaction and bonding.

Table 1: The optimized structure parameters and adsorption energies of HF on the TiO_2 (110) and (001) surfaces.

Surface slab	E_{ads} physisorption	E_{ads} chemisorption	Bond length Å		
			Ti-F	Ti-O	O-H
(001)-Ti5c	-5.92	-2.79	1.927	2.075	0.997
(110)-Ti5c	-5.43	-2.67	1.965	2.059	1.015
(110)-Ti6c	-4.93		1.984	2.086	1.022

Both physisorption and chemisorption were considered to investigate the nature of HF adsorption. The physisorption is the adsorption by bonding, whereas chemisorption is the adsorption without bonding. Comparing the adsorption energies, it was found that HF adsorption is by physisorption than chemisorption process. Figure 2 (a-b) present the optimized geometric structures of HF adsorption on Ti (110) and (001) surfaces. It was observed that HF dissociates completely when adsorbed on the TiO_2 (110) and (001) surfaces, with a hydrogen atom bonded to the oxygen atom forming hydroxyl while fluorine is bonded to five- and six-fold coordinated Ti atoms (Ti-F). The bond length of hydroxyl is about 0.99-1.022 Å and bond length of Ti-F is approximately 1.927-1.984 Å.

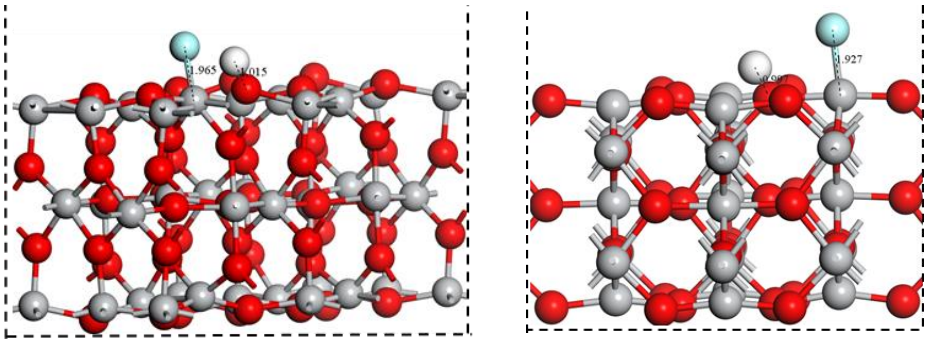

Figure 2: Optimized geometric structures of (a) HF-TiO_2 (110) and (b) HF-TiO_2 (001) surface.

The adsorption energies are shown to be the most thermodynamically favorable configuration. Figure 3 shows the dependence of adsorption energies per HF coverage on TiO_2 (110) and (001) surfaces. Results revealed that the adsorption energy become more stable with increasing HF coverage, this trend has been observed in several systems in the past [20]. However, the adsorption energies on (001) surface were found to be more stable than on (110) surface for all HF coverages. Therefore, attractive interaction between the HF molecules with the surface contribute to this phenomenon.

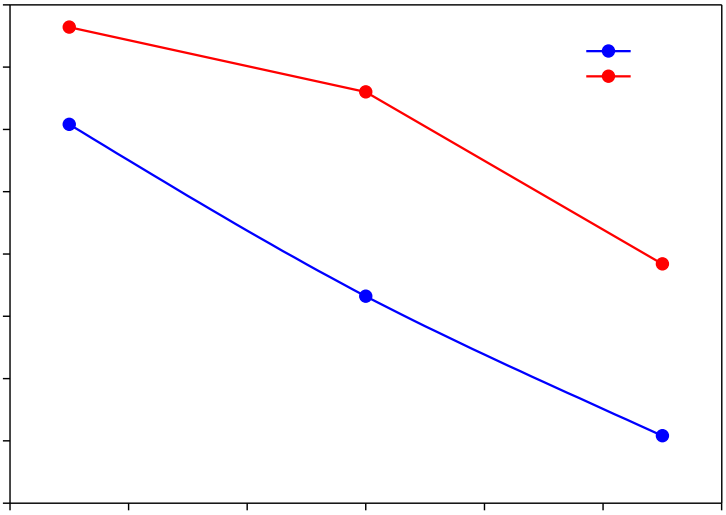

Figure 3: The adsorption energy of HF on TiO_2 (110) and (001) surfaces at different coverages.

3.2 *Charge density difference and Mulliken Charge analysis*

The interaction between the adsorbate and adsorbent implies a significant charge transfer. Charge density difference (CDD) between HF molecule with TiO_2 (001) and (110) surfaces were calculated using equation below:

$$\Delta\rho = \rho_{\frac{adsorbate}{slab}} - \rho_{slab} - \rho_{adsorbate} \quad (2)$$

where $\rho_{\frac{adsorbate}{slab}}$ is the charge density for the adsorbate system while ρ_{slab} and $\rho_{absorbate}$ are the charge densities for the non-interacting slab surface and adsorbate, respectively. Charge transfer influences the distribution of active species involved in the surface reaction, it becomes necessary to analyze the charge redistribution. The charge transfers between HF-TiO_2 (001) and (110) surfaces are visualized by plotting the 3D charge density difference as shown in figure 4. The blue and yellow iso-surface region represents the charge accumulation and depletion, respectively. A significant charge accumulation is established around the F atom forming electron rich region, whereas charge depletion is found around Ti atom.

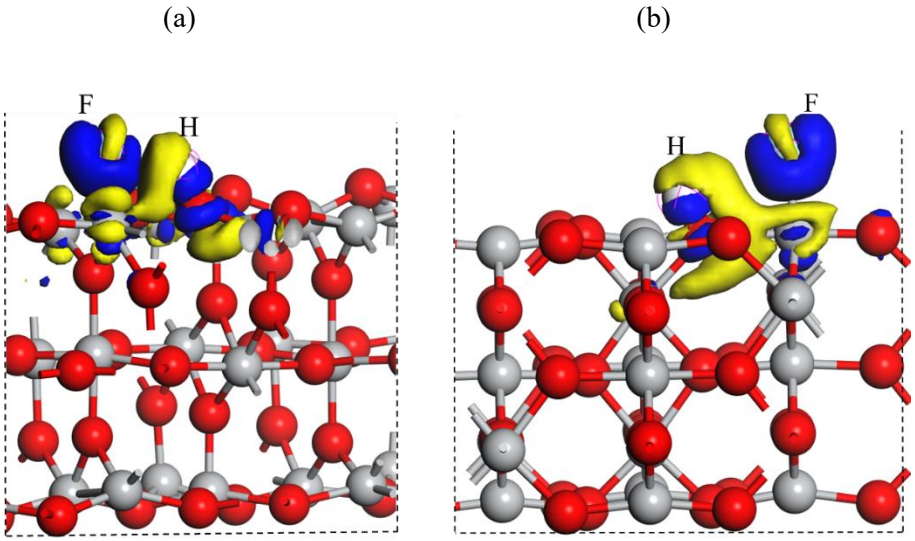

Figure 4: The charge density difference of HF adsorption on TiO_2 (a) (110) and (b) (001) surfaces with iso-surface value of 0.05 eV/Å^3.

Table 2 present Mulliken charge analysis for pure and adsorbed TiO_2 (110) and (001) surfaces. The Mulliken charge of Ti atoms in (001) and (110) surface are 1.34 e and 1.00 e, respectively. However, after adsorption Mulliken charge of Ti atoms increased to 1.47 e and 1.11 e for (001) and (110) surfaces, respectively. Comparing Mulliken charge analysis of clean surfaces and after adsorption, it is seen that electrons are transferred between HF molecule and TiO_2 (001) and (110) surfaces via F-Ti bonding. The electron transferred between F-Ti interaction for (001) surface is -0.13 e while for (110) surface is -0.11 e. This is due to the higher electronegativity of F atom than Ti atom.

Table 2: Mulliken charge analysis for Ti and F/Ti atoms.

surfaces	Mulliken Charge Analysis (|e|)		
	Ti	F/Ti	Δe^-
(001)	1.34	-0.49/1.47	-0.13
(110)	1.00	-0.51/1.11	-0.11

4. Conclusion

DFT calculations were employed to investigate the adsorption behaviour of HF molecule on TiO_2 (001) and (110) surfaces. It was found that HF molecule dissociates completely to form Ti-F and O-H bond. Adsorption behaviour of HF molecule is energetically favourable on TiO_2 (001) surface than on TiO_2 (110) surface. The adsorption energy value reveals that adsorption of HF molecule on TiO_2 (001) and (110) surfaces is by physisorption than chemisorption process, due to the stronger interaction between the F- ion and Ti atoms. The adsorption energy becomes more stable with increasing HF molecule coverage indicating that HF molecule coverage is thermodynamically stable. The interaction induced charge redistribution, according to charge density difference and Mulliken charge analysis it shows that HF-TiO_2 (001) and (110) surfaces have charge transferred process. Specifically, the electrons on the Ti atoms were transferred to HF molecule. This analysis showed patterns of electron accumulation and

depletion at the Ti-F interaction. Mulliken charge analysis indicated that titanium atom loses electrons whereas fluorine gains an additional electron during the interaction.

Acknowledgement

The authors acknowledge Department of Science and Innovation (DSI) and Council of Scientific Industrial Research (CSIR) for their financial support. Centre for High Performance Computing (CHPC) and Material Modelling Centre, University of Limpopo for computing resources.

References

[1] Trevisan F, Calignano F, Aversa A, Marchese G, Lombardi M, Biamino S, Ugues D and Manfredi D 2017 *Journal of Applied Biomaterials and Functional Material* **16** 57-67
[2] Sung S Y, Choi B J, Han B S, Oh H J and Kim Y J 2008 *Journal of Material Science and Technology* **24** 70-74
[3] David M, Muhida R, Roman T, Nakanishi H, Diño W, Kasai H, Takano F, Shima H and Akinaga H 2008 *Vacuum* **83** 599-601
[4] Natarajan S K and Elloitt S D 2018 *Chemistry of Materials* **30** 5912-5922
[5] Suratwala T I *et al.* 2011 *Journal of the American Ceramic Society* **94** 416-428
[6] Lee Y and George S M 2015 *American Chemical Society NANO* **9** 2061-2070
[7] Song E H, Zhu Y F and Jiang Q 2013 *Thin Solid Films* **546** 124-127
[8] Quan J L,Teng B T, Wen X D, Zhao Y, Liu R and Luo M F 2012 *Journal of Chemical Physics* ***136*** 114701(1)-114701(7)
[9] Chowdhury T, Hidayat R, Mayangsari T R, Gu J, Kim H L, Jung J and Lee W J 2019 *Journal of Vacuum Science and Technology A* **37** 021001(1)-021001(8)
[10] Yang H G, Sun C H, Qian S Z, Zou J, Liu G, Smith S C, Cheng H M and Lu G Q 2008 *Nature* **453** 638-641
[11] Wang Y, Zhang H, Han Y, Liu P, Yao X and Zhao H 2011 *Chemical Communications* **47** 2829-2831
[12] Segall M D, Philip J D L, Probert M J, Pickard C J, Hasnip P J, Clark S J and Payne M C 2002 *Journal of Physics: Condensed Matter* **14** 2717-2744
[13] Perdew J P and Wang Y 1992 *Physical Review B* **45** 13244-13249
[14] Di-Valentin C, Pacchioni G and Selloni A 2016 *Physical Review Letter* **97** 1-9
[15] Dudarev S, Botton G, Savrasov S, Humphreys C and Sutton A 1998 *Physical Review B* **57** 1505-1509
[16] Arroyo-de Dompablo M E, Morales-García A and Taravillo M 2011 *Journal of Chemical Physics* **135** 054503(1)-054503(9)
[17] Monkhorst H J and Pack J D 1976 *Physical Review B* **13** 5188-5192
[18] Waterhouse G I N and Idriss H 2009 Asia, John Wiley and Sons 78-89
[19] Tshwane D M, Modiba R, Chauke H R, Govender G and Ngoepe P E 2019 *IOP Conference Series: Materials Science and Engineering* **655** 012043(1)-012043(10)
[20] Samin A J and Taylor C D 2018 *Colloids and Surface A* **539** 92-100

First principle studies on lattice thermal conductivity and thermoelectric properties of $LiYSe_2$.

Elkana Rugut[1], Daniel Joubert[1] and Glenn Jones[2]

[1] The National Institute for Theoretical Physics, School of Physics and Mandelstam Institute for Theoretical Physics, University of the Witwatersrand, Johannesburg, Wits 2050, South Africa.

[2] Johnson Matthey Research (PTY) Limited, Scientia, CSIR Campus, Meiring Naude Road, Brummeria, Pretoria, South Africa.

E-mail: elkanatawich@gmail.com

Abstract. Thermoelectric materials can convert heat into electricity, hence these materials can play an important role in the efficient use of energy. In this study, we investigate the structural, dynamical and mechanical stability of lithium yttrium selenide ($LiYSe_2$) alongside its lattice thermal conductivity, electronic transport and thermoelectric properties for the first time. The potential of a material to be used as the active component in the design of a thermoelectric device is based on the value of its figure of merit (ZT), which requires information on the lattice and electronic transport properties. We computed the ZT value within density functional theory using linearized Boltzmann transport equations in a relaxation time approximation. From our findings, $LiYSe_2$ is stable and exhibit a semiconducting character having an indirect band gap of 1.80 eV. The predicted values of the anisotropic lattice thermal conductivity at 300 K are 2.63, 2.58 and 1.09 W/mK for x-,y- and z-axis, respectively, which is favorable for thermoelectric applications. Highest value of the predicted ZT is 0.6 at high temperature of 1000 K when the hole concentration is 10^{19} cm^{-3}, which indicates that with further tuning, $LiYSe_2$ holds potential in high temperature thermoelectric applications.

1. Introduction

Thermoelectricity is perceived as one of the possible solutions to deal with the global energy crisis [1]. The grand challenge in this field is that near room temperature; alloys of bismuth telluride [2] which are dominantly used in fabricating thermoelectric devices for commercial applications have dimensionless figure of merit (ZT) of about unity, which translates to a relatively low efficiency in thermal to electrical energy conversion without any mechanical component. Hence, comprehensive studies [1] have been vigorously explored in the recent years to uncover new potentially viable materials, or to engineer the existing ones in such a way that their ZT is improved beyond unity for efficient large scale production as well as applications.

Regarding the ternary compound of interest; Ohtani *et. al* [3] carried out synthesis of $LiYSe_2$ among other ternary chalcogenides whereby they reported that $LiYSe_2$ can adopt two different types of structures, a NaCl type and α-$NaFeO_2$, depending on the ratio of lanthanide ion (Y) to alkali metal (Li) radius ratio whereby for large (small) radius ratio values, the compound crystallizes in a disordered NaCl structure (α-$NaFeO_2$). Besides the cation radius ratio, the two crystals types are also dictated by the quenching temperatures whereby the NaCl structure is attained when quenched from the higher temperatures whereas α-$NaFeO_2$ structure is obtained when cooled slowly at room temperature [3]. The figure of merit is a quantitative parameter

that describes how efficient a thermoelectric material is in the direct conversion of temperature differences (thermal energy) to electric voltage and vice versa [4]. It is a dimensionless quantity that is related to the Carnot efficiency of a system (η) and is expressed as [5, 6];

$$ZT = \frac{S^2\sigma T}{\kappa} = \frac{S^2\sigma T}{\kappa_e + \kappa_l}; \qquad \eta = \frac{T_h - T_c}{T_h}\frac{\sqrt{1+ZT}-1}{\sqrt{1+ZT}+1} \tag{1}$$

The Seebeck coefficient, electrical conductivity, temperature in Kelvin scale and the total thermal conductivity are denoted by S, σ, T and κ, respectively. The total lattice thermal conductivity has two components, namely the electronic contribution (κ_e) and the lattice contribution (κ_l). For the Carnot efficiency, T_h and T_c denotes the temperature of the hot and cold part of the thermoelectric generator, respectively. Hence for us to gauge how efficient $LiYSe_2$ is; we computed its figure of merit based on first principles within Density Functional Theory (DFT).

2. Methodology

We describe the structural, vibrational, energetic, mechanical, electronic, thermal, transport and thermoelectric properties of lithium yttrium selenide based on numerical simulations conducted using the Vienna *ab initio* simulation package (VASP) [7] that applies the formalism of density functional theory. In order to test the reliability of our results, structural, energetic and mechanical studies were carried out using three functionals namely: local density approximation (LDA) [8], generalized gradient approximation with the Perdew-Burke-Ernzerhof (PBE) [9], as well as PBEsol [10]. The energy cut-off for the plane wave expansion was fixed at 520 eV. The atomic forces and energies were converged within 10^{-4} eV/Å and 10^{-8} eV, respectively, for structural calculations. For elastic constant calculations, the stress-strain technique proposed by Shang *et al.* was applied [11].

Vibrational studies were performed using the Phonopy code [12] where a finite displacement technique was applied on a 3×3×3 supercell with a Monkorst-Pack grid of size 3×3×3 used to sample the Brillouin zone in order to obtain the second and third order inter-atomic force constants from Phonopy and Phono3py [13], respectively. A mesh size of 38×38×24 was found sufficient to obtain converged values of lattice thermal conductivity. We computed the electronic transport coefficients by solving Boltzmann transport equations based on DFT under the mode dependent relaxation time approximation as implemented in BoltzTraP2 [14]. Both lattice thermal conductivity results and transport coefficients were then incorporated onto equation (1) as also indicated in the step by step work flow provided in Figure 1 (center) in order to predict the dimensionless figure of merit of $LiYSe_2$.

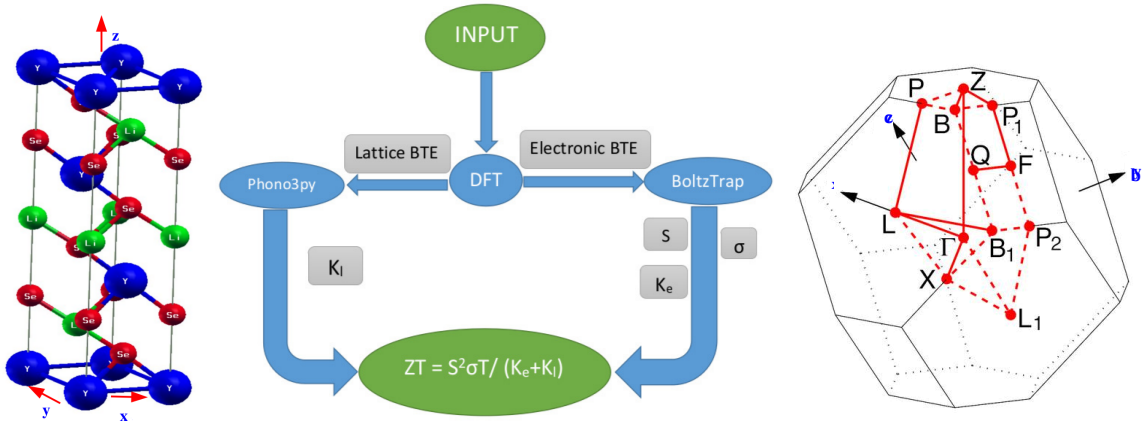

Figure 1. Crystal stucture of $LiYSe_2$ (left), work flow (center) and its Brillouin zone [15] (right)

3. Results and discussion

Structural, energetic and mechanical studies of $YCuSe_2$ were conducted using three functionals, as shown in Table 1. By comparing the obtained values of structural properties with the existing experimental data; we deduced that among the three functionals considered, PBEsol describes the structural behavior of $LiYSe_2$ better relative to PBE and LDA. Hence, further in-depth studies of lattice thermal conductivity and transport properties were investigated using PBEsol. The negative values obtained for cohesive energies signify that $LiYSe_2$ is an energetically stable.

Table 1. Structural parameters and cohesive energy.

	a (Å)	c (Å)	V_o (Å^3)	α (°)	γ (°)	B (GPa)	E_{coh} (eV/atom)
PBE	4.078	19.583	282.036	90	120	40.76	-2.471
LDA	3.985	19.135	263.157	90	120	48.95	-5.125
PBEsol	4.031	19.357	272.392	90	120	44.43	-4.801
Exp [3]	4.048	19.440	275.870	90	120	-	-

3.1. Mechanical properties

The elastic coefficients, bulk modulus, shear modulus and Young's modulus provided in Table 2 are in gigapascals (Gpa). Basically, $LiYSe_2$ belongs to the trigonal crystal system as shown in Figure 1 (left) of point group $\bar{3}$, Hermann Mauguin R$\bar{3}$m and space group number 166 falling under Rhombohedral (I) class as per classification of Coudert and Mouhat [16].

Table 2. Mechanical properties.

Functional	C_{11}	C_{12}	C_{13}	C_{14}	C_{33}	C_{44}	B	G	E	ν	G/B
PBE	101.15	27.82	23.19	-0.22	77.87	26.70	46.55	31.51	76.57	0.23	0.68
PBEsol	97.57	26.07	21.03	0.03	72.92	25.94	44.40	30.47	74.39	0.22	0.69
LDA	95.88	25.55	19.07	-1.64	71.29	23.28	42.81	29.02	71.01	0.22	0.68

Therefore, six independent elastic coefficients were obtained as indicated in Table 2. Thus, in order to attain mechanical stability; it has to fulfill the following necessary and sufficient conditions [16].

$$C_{11} > |C_{12}|; C_{44} > 0; C_{13}^2 < \frac{1}{2}C_{33}(C_{11} + C_{12}); C_{14}^2 < \frac{1}{2}C_{44}(C_{11} - C_{12}) = C_{44}C_{66} \quad (2)$$

Since all the four conditions were satisfied, our calculations confirm that lithium yttrium selenide is mechanically stable. Thermoelectric devices should possess exceptional mechanical properties as they might be used in environments where temperature keeps fluctuating. Moreover, their Fratserich's ratio (G/B) [17] is greater than 0.571 for all the three functionals, indicating that $LiYSe_2$ is a brittle material. From the values of Poisson's ratio obtained (≈ 0.22), it indicates the bonding in $LiYSe_2$ is most likely ionic in nature [18].

3.2. Dynamical and electronic properties

From the phonon dispersion curves shown in Figure 2, there is an absence of imaginary frequencies indicating $LiYSe_2$ is thermodynamically stable [12]. From the partial density of states (PDOS), vibration of selenium atoms dominates the acoustic phonons whereas lithium atoms are major heat carriers in the optical region as they propagate actively at higher frequencies. On the other hand, yttrium contributes to both acoustic and optical modes.

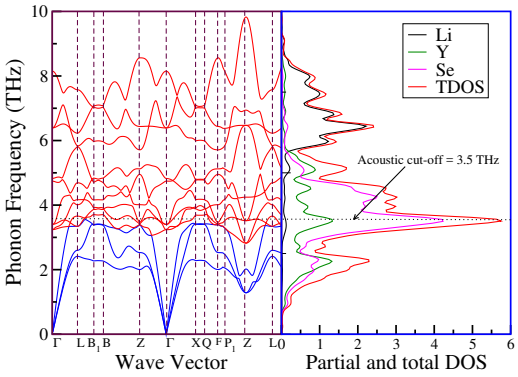

Figure 2. Phonon dispersion.

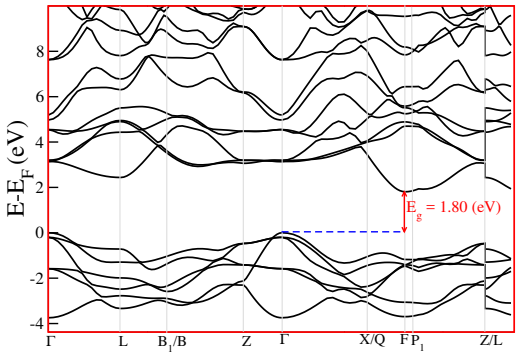

Figure 3. Electronic bands.

The modified Becke-Johnson potential (mBJ) [19] was used in determining the electronic band structure of $LiYSe_2$ in order to open the fundamental gap that is often underestimated when computed using DFT-GGA's. $LiYSe_2$ exhibited a semiconducting character having an indirect band gap of 1.80 eV; whose valence band maxima is situated at Γ whereas the conduction band minima is at F-point in the Brillouin zone as shown in Figure 3.

3.3. Lattice thermal conductivity

Figure 4 shows the lattice thermal conductivity of $LiYSe_2$ which confirms that there is slight thermal anisotropy in that the lattice thermal conductivity is comparable in x- and y-axis (in-plane) but different in the z-axis (out-of-plane).

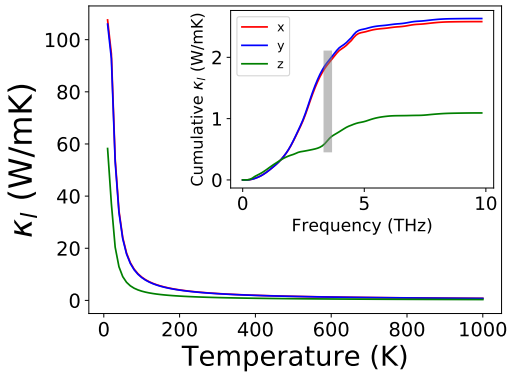

Figure 4. Lattice thermal conductivity and its cumulative.

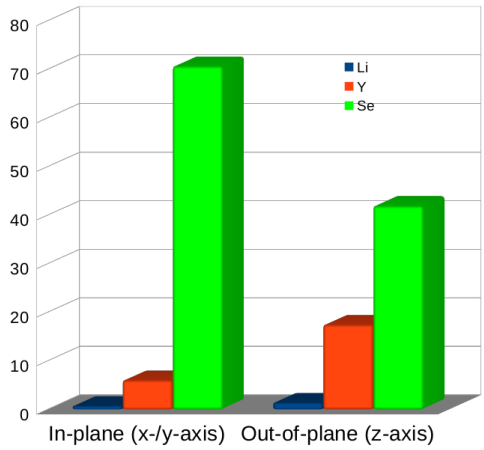

Figure 5. Estimates of percentage elemental contributions.

Similar anisotropic behavior is also visible in the cumulative lattice thermal conductivity as shown in the inset plot. The acoustic cut-off frequency (≈3.5 THz), indicated with the shadowed grey region in the inset plot that highlights the upper bound of acoustic phonon branches in Figure 2, the cumulative lattice thermal conductivity is almost flat at higher frequencies, which signify that acoustic phonon branches dominates heat transport in $LiYSe_2$ compared to the optical phonons. The predicted values of lattice thermal conductivity are 2.63, 2.58 and 1.09 W/mK for x-,y- and z-axis, respectively, at 300 K which is favorable for thermoelectric applications.

 ISBN: 978-0-620-88875-2

In Figure 5; after realizing that acoustic phonons are dominant heat carriers, we further narrow down to examine and approximately quantify the elemental contributions to the total cumulative lattice thermal at the acoustic phonon region at a temperature of 300 K. It is clear that among the three elements; selenium (Se) contributes significantly, followed by yttrium (Y) whereas contribution from lithium (Li) is almost insignificant. In addition; for the case of selenium, it indicates that a lot of heat is generated when selenium atoms are propagating in the x-/y-axis ($\approx$ 70%) as compared to the case when they are propagating along the z-axis ($\approx$ 40%). This information is crucial in thermal engineering of $LiYSe_2$ when tuning its lattice thermal conductivity as it indicates which element vibrates a lot relative to other elemental components in this ternary compound.

3.4. Transport and thermoelectric properties

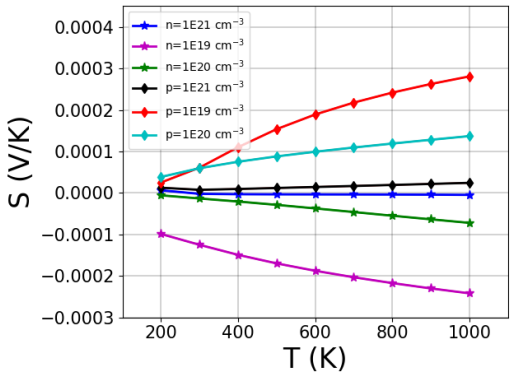

Figure 6. Seebeck coefficient (S) vs. temperature.

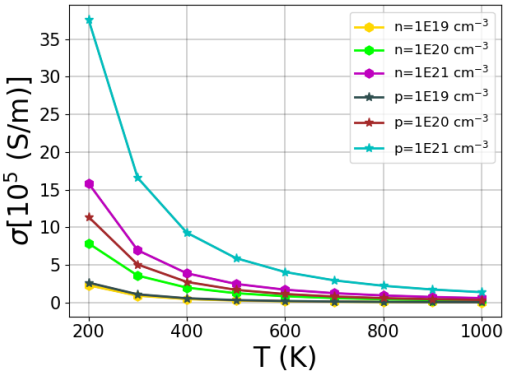

Figure 7. Electrical conductivity (σ) vs. temperature.

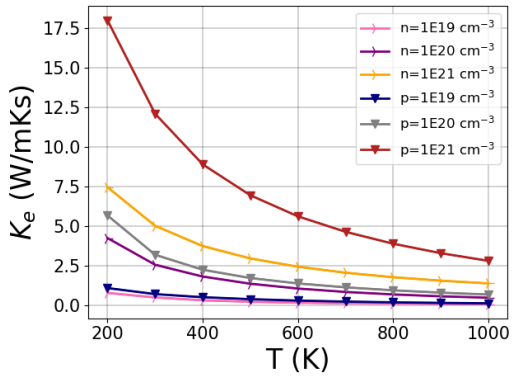

Figure 8. Electronic contribution to thermal conductivity (κ_e) vs. temperature.

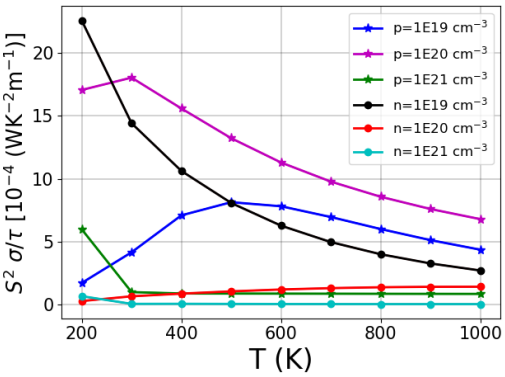

Figure 9. Power factor ($S^2\sigma$) vs. temperature.

Figures 6 to 11 shows the Seebeck coefficient (S), electrical conductivity (σ), electronic contribution to thermal conductivity (κ_e), power factor ($S^2\sigma$) and figure of merit (ZT) as function of tempereture, for various electron and hole concentrations. The highest value of Seebeck coefficient is attained when hole concentration is 10^{19} cm^{-3}, as displayed in Figure 6. Highest value of electrical conductivity is obtained when hole concentration is 10^{21} cm^{-3}

 ISBN: 978-0-620-88875-2

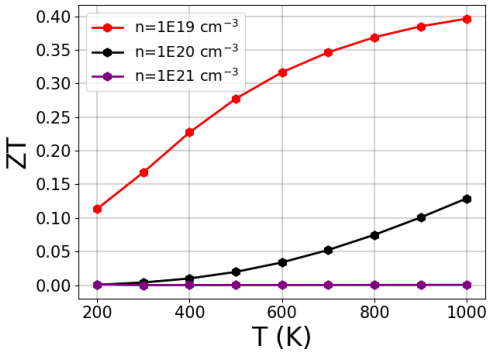

Figure 10. ZT for electrons.

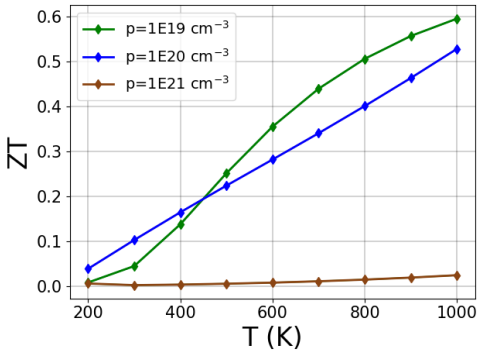

Figure 11. ZT for holes.

as presented in Figure 7. Lowest value of κ_e is attained when charge carrier concentration is 10^{19} cm^{-3} as shown in Figure 8. Above 300 K; highest power factor is obtained when hole concentration is 10^{20} cm^{-3} as provided in Figure 9. Generally, the magnitude of figure of merit is larger for holes relative to electrons as can be seen in Figures 10 and 11. Highest ZT of 0.6 obtained when hole concentration is 10^{19} cm^{-3} could be attributed to its high Seebeck coefficient and low values of electronic contribution to thermal conductivity (κ_e).

4. Summary and conclusion

We have performed a comprehensive study on structural, vibrational, energetic, mechanical, electronic, thermal, transport and thermoelectric properties of $LiYSe_2$ based on the first principles. We confirm that it is a stable ternary compound. From the value of ZT obtained (0.6); with further tailoring, $LiYSe_2$ holds promising potential in thermoelectric applications in that via thermal engineering i.e through creation of selenium (Se) vacancy defects; its ZT can be tuned towards unity.

Acknowledgments

We are grateful to Johnson Matthey Technology Centre (Pretoria) for financial support and Centre for High Computing (Cape Town) for computational resources.

References

[1] T. Tritt, Annual review of materials research. **41**, (2011) 433-448.
[2] L. Hu, T. Zhu, Y. Wang, H. Xie, Z. Xu, X. Zhao, NPG Asia Materials. **6**, (2014) e88.
[3] T. Ohtani, H. Honjo and H. Wada, Materials research bulletin. **22**, (1987) 829-840.
[4] J.P. Heremans *et al.*, Science **321**, (2008) 554-557.
[5] M. M. Rull-Bravo, J. F. Fernandez and M. Martin-Gonzalez, Rsc Advances. **5**, (2015) 41653-41667.
[6] B. Sherman, R. R. Heikes and R. W. Ure , Journal of Applied Physics. **31**, (1960) 1-16.
[7] G. Kresse, J. Hafner, Physical Review B. **47**, (1993) 558.
[8] A. D. Becke, Physical review A. **38**, (1988) 3098.
[9] J. P. Perdew, K. Burke and M. Matthias, Physical review letters. **77**, (1996) 3865.
[10] M. Ropo, K. Kokko, and L. Vitos, Physical Review B. **77**, 195445.
[11] Shang S, Wang Y and Zi-Kui L 2007 *Appl. Phys. Lett* **90** 101909.
[12] A. Togo and I. Tanaka, Scripta Materialia. **108** (2015) 1-5.
[13] A. Togo, L. Chaput and I. Tanaka, Physical Review B. **91**, (2015) 094306.
[14] M. K. Georg, C. Jesús and M. J. Verstraete, Computer Physics Communications. **231**, (2018) 140-145.
[15] S. Curtarolo *et. al*, Computational Materials Science.**58**, (2012) 218-226.
[16] F. Mouhat and F. Coudert, Physical Review B. **90**, (2014) 224104.
[17] Tariq S, Ahmed A, Saad S and Tariq S 2015 *AIP Adv.* **5** 077111.
[18] J. Haines, J. M. Leger and G. Bocquillon, Annual Review of Materials Research. **31**, (2001) 1-23.
[19] F. Tran and P. Blaha, Physical review letters. **102**, (2009) 226401.

Investigation of beta Ti-Mo phase stability employing the first principle approach

VC Mnisi[1, a*], ME Sithole[1, b], R Modiba[2,c] and R Machaka[2,d]

[1]Department of Physics, Sefako Makgatho Health Science University, P. O. Box 94, Medunsa, 0204, South Africa

[2] Materials Science and Manufacturing, CSIR, PO Box 395, Pretoria, 0001, South Africa

Email: Mnisi.charmain@yahoo.com

Abstract. The improvement for load bearing dental and orthopaedic implants of Titanium (Ti) based alloys have become significant in the medical industry, this is due to the increase of knee and hip replacement amongst younger individuals and the deterioration of body parts by increasing human age. Hence the need for developing low modulus Ti-based alloys with biocompatible properties and low elastic modulus close to that of bone. This study aims to investigate the stability of Ti-based alloys for biomedical applications using the first-principles approach. The stability of β $Ti_{100-x}Mo_x$ (x=0-10) alloys was investigated with respect to their equilibrium lattice parameters, elastic constants and the density of states. The study employed the density functional theory (DFT) within the generalized gradient approximation (GGA). Addition of the alloying element was achieved employing the visual crystal approximation embedded in CASTEP. Interestingly, the Molybdenum (Mo) addition stabilizes the β-phase with an increasing C′ moduli and the density of states suggest that the phase is being stabilized at a higher content of Mo.

1. Introduction

The use of Titanium (Ti) and Ti-based alloys implantable device has become a great part of modern medicine [1]. Compared to other metallic implants (stainless steel and cobalt-chromium) Ti-based alloys stands out with its unique properties which makes it more probable for prosthetic applications [2]. In biomedical applications, Ti and Ti-based alloys are the best choices for replacing or repairing damaged hard tissues such as bone plate, since they have excellent characteristics such as biocompatibility, Osseointegration, high wear, and corrosion resistance, low compatibility issues, and high strength [3]. Ti-alloys also exhibit low modulus of elasticity (100-110 GPa) that is lower compared to other materials but more than that of a bone in the range of (20-40GPa) [4]. Ti-based alloys have become significant in the medical industry due to the increase in knee and hip replacement amongst younger individuals and there has been a dramatic increase of the use of biomedical implants because of the deterioration of body parts by increasing human age. With this rise, the need for the development of Ti-alloys implants that can withstand physiological loads and can serve for a lifetime without failure has become crucial[5].

Most research on titanium alloys for biomedical implantable devices has focused on β-phase Ti- alloys because of the bcc structure. The body centered cubic (bcc) structure can be manipulated to enhance properties such as lower elastic modulus, high wear and corrosion resistance. β-phase Ti alloys containing Mo are the safest alloying metals which has been used for orthopaedic implants applications due to their unique combination of excellent mechanical properties, low elastic modulus, and superior bio-corrosion resistance, low allergenic and non-toxic properties, which give rise to excellent biocompatibility [6-7].

Previous studies have found that elastic modulus can significantly be reduced by adjusting the concentration of β stabilizing element such as Molybdenum [8-9]. Zhao et al [10] investigated β-phase Ti-Mo alloys with changeable Young's modulus for spinal fixation application. In their study it was found that increasing the concentration of Mo the stability of β-phase increases. Further studies done on Ti-Mo binary systems have reported Young's modulus between the ranges of 60-100 GPa which is still not

low enough for biomedical applications [8-10]. There are a few reported studies [8-10] on Ti-Mo for biomedical application, the main objective of this study is to investigate the stability of Ti-Mo alloys with different Mo concentration varying from 0-10% and carry out structural properties such as heats of formation, elastic constants and density of state using first principle approach.

2. Methodology

First principle calculations were performed using Cambridge Serial Total Energy Package (CASTEP) code as implemented in Material Studio [11] based on density functional theory (DFT). The Perdew-Burke-Ernzerhof (PBE) functional of the generalized gradient approximation (GGA) [12] described the electron-exchange and correlation. The CASTEP code performed a variation solution to the Kohn-Sham equations by using a density mixing scheme [13] to minimize the total energy and conjugate gradients to relax the ions under the influence of the Hellmann-Feynman forces. After the convergence test, an energy cut-off of 400 eV and the k-mash of 6x6x6 were chosen since they were sufficient to converge our structures. The Brillouin zone integrations were performed for suitably large sets of *k*-points according to Monkhorst and Pack [14]. The solid solution approach employing visual crystal approximation (VCA) [15] embedded in CASTEP was used to substitute Ti with Mo atoms. It is a much simpler and computationally less expensive approach in which one studies a crystal with the primitive periodicity but composed of fictitious ‘‘virtual’’ atoms that interpolate between the behavior of the atoms in the parent compounds. This technique has seen wide use in band structure calculations [16, 17, 18]

3. Results and Discussions

3.1. Structural and elastic properties of $Ti_{100-x}Mo_x$ *(x: 0, 6, 8, 10)*

3.2. In Fig. 1, the investigated structure is shown which is a β-phase having a space group of Im-3m bcc crystal with two atoms which was generated using tungsten (W) as a prototype. Using VCA the β-phase Ti was doped with Mo as illustrated in fig 1 below. The B2 Ti structure was subjected to full geometry optimization, allowing both the lattice parameters and volume to change. The calculated equilibrium lattice parameters of the structures are shown in Table 1. The β Ti lattice was found to be a=3.165 and in good comparison with the available experimental value of 3.26 [19]. As the Mo content is added on the Ti, the lattice parameter increases as shown in Table 1, which is due to the larger atomic radius of Mo (1.90 Å) than that of Ti (1.76 Å).

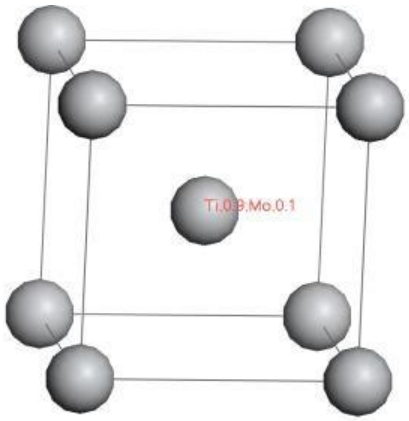

Figure 1: *Structure of β-phase Ti-Mo.*

Table1: The equilibrium lattice parameters and elastic constants for the $Ti_{100-x}Mo_x$ (x: 0, 6, 8, 10)

Structure	Lattice parameter	C_{11}	C_{44}	C_{12}	C′	Y(GPa)
Ti	3.165	96	46	160	-32	
$Ti_{94}Mo_6$	3.233	89	33	112	-11.5	42
$Ti_{92}Mo_8$	3.230	109	35	108	0.5	61
$Ti_{90}Mo_{10}$	3.222	128	36	100	14	75

In addition, the elastic properties of the structures were calculated and are also shown in Table 1. The accurate calculations of elasticity are important for gaining an insight into the mechanical and elastic properties of solids. There are three (C_{11}, C_{12} and C_{44}) independent elastic constants for cubic structure [20]. The mechanical stability criterion given by Born's [20] for a cubic crystal is as follows:

$$C_{11} + 2C_{12} > 0,\ C_{11} > |C_{12}| \text{ and } C_{44} > 0$$

Wherein the C′ is calculated using this equation: $C' = (C_{11}-C_{12})/2$

For a structure to be considered mechanically stable, the stability criterion for the elastic constants should all be satisfied. The pure Ti β is found to be unstable at 0 K with a negative C′ of -32 which is due to the C_{11} being less than C_{12} (i.e. 96 < 160). As the 6 at. % Mo is added, C′ modulus increases but still remains negative. Lower C_{11} reflects weak resistance to shear deformation, which is observed on Table 1 above for Mo concentration less than 6 at. %. The C′ is stabilized at Mo > 8 at % wherein the C_{11} is found to be greater than C_{12}. The calculated Young's modulus exhibits a similar trend to the elastic constants, indicating hardening of C′ which results in high Young's modulus of β-phase with increasing Mo content.

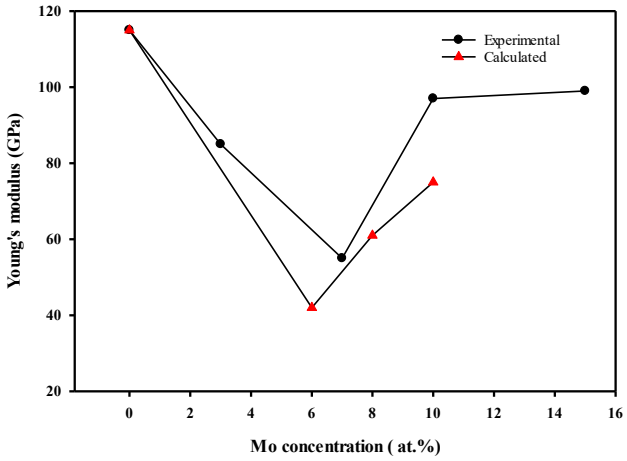

Figure 2: *Experimental [21] and calculated Young's modulus of $Ti_{100-x}Mo_x$*

Figure 2 represent the Young's moduli of the calculated and experimental Ti-Mo with respect to the varying Mo concentration. In fig 2 the experimental Young's modulus decreased with the addition of Mo, although the actual value of the modulus fluctuated with different Mo concentration which was due to the presence of metastable phases α″ and ω in some of the samples during the XRD and TEM investigation [21]. Interestingly the theoretical and experimental Young modulus show a similar trend, they both increase with increasing Mo content showing structural stability. It is also observed that the

Youngs modulus of $Ti_{92}Mo_8$ in the reported study was low (61GPa) which was in good agreement with Sung experimental observations [21]. It is noted that the Young's modulus of the experimental result was larger than that of the theoretical calculations this is because the theoretical calculations were restricted to bulk single crystals, while the real samples are polycrystalline [21-22]. The difference might also be due to the difference in temperature (0K for all calculations and 298K for experimental).

3.3. Density of states

In order to further understand the chemical bonding and β-phase stability, we calculated the DOS of all the $Ti_{100-x}Mo_x$ structures (fig 3). Structural instability is related to the Fermi level (E_f) which is represented by the vertical line in fig 3 below. According to Mahlangu et al [23] structures with the highest and lowest density of states at E_f is considered the least and most stable, respectively. It is very clear from fig 3 that the s and p orbitals peaks are much broader than sharp peaks observed for the d orbital at E_f. We also observe in fig 3b, c and d that d-orbital of Mo has the major contribution to the TDOS near Fermi level.

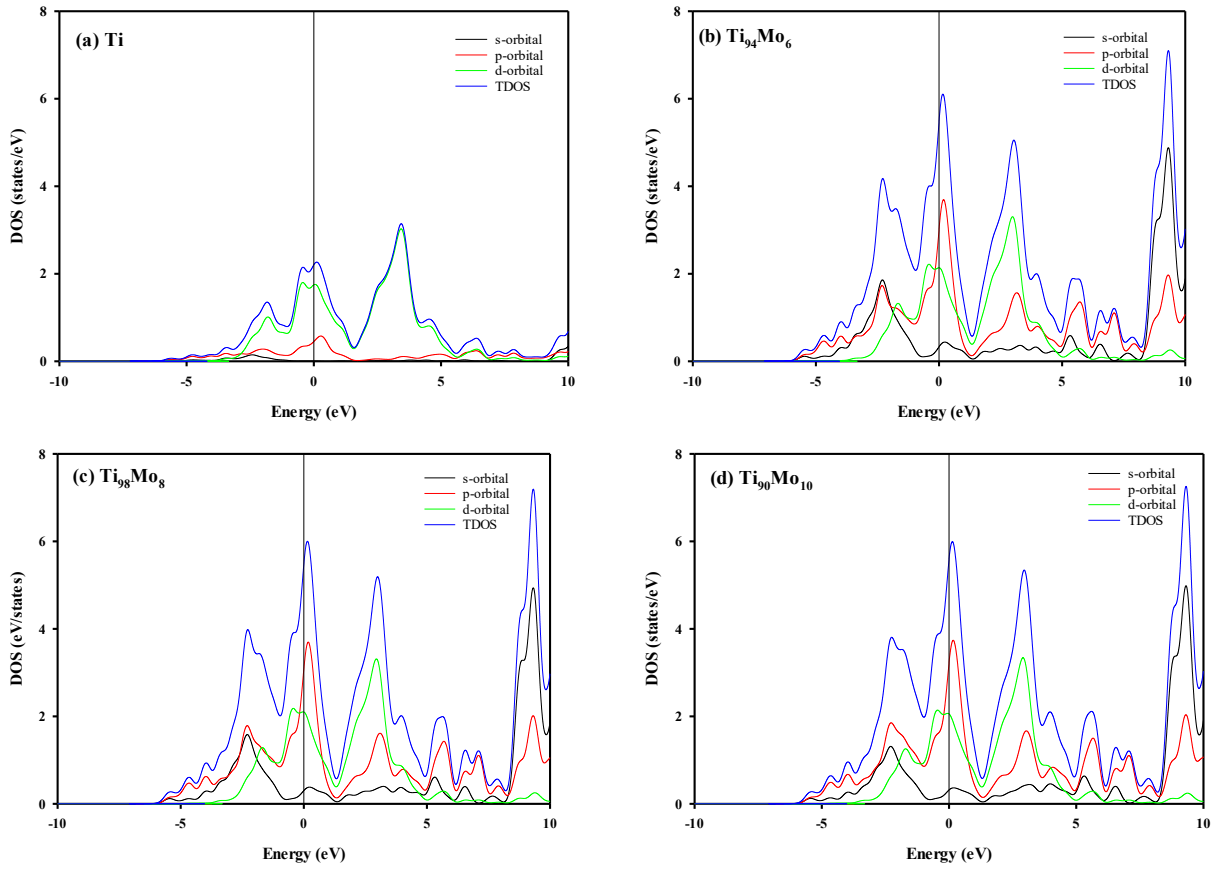

Figure 3: *Density of states curves of β-phase for Ti-Mo alloys with different Mo contents (0-10%).*

ISBN: 978-0-620-88875-2

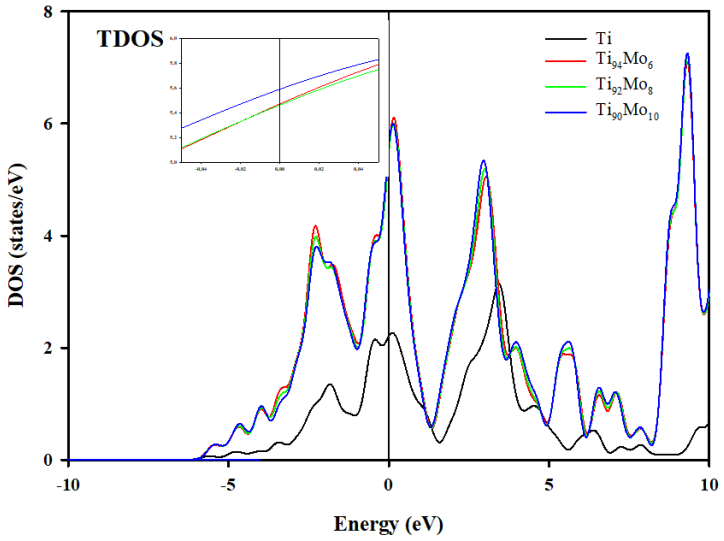

Figure 4: *Total Density of states curves of β-phase for Ti-Mo alloys with different Mo contents (0-10%).*

The embedded total density of states is represented in figure 4. We note that the TDOS peak of pure titanium although with lower density of states near E_f it is much broader than the other peaks and located in the antibonding region. Interestingly at 8 at. % Mo concentration, the dip of the TDOS at E_f was observed to slightly move away from the antibonding region suggesting β-phase stability increased gradually. Lower number of density of states was observed for $Ti_{92}Mo_8$ plot at E_f compared to the other structures confirming it to be the most stable structure. However, it was noted that $Ti_{90}Mo_{10}$ is the least stable structure since it has the highest number of density of states at E_f. Our DOS analysis is in good agreement with some theoretical studies which suggest that the DOS at E_f decreased with increasing Mo content for ordered cells, indicating that the β-phase stability. The opposite is observed for distorted cells where by Li et al observed that higher Mo content produces the most stable structure [24].

4. Conclusions

In this study the stability of Ti-Mo alloys was investigated with respect to their equilibrium lattice parameters, elastic constants and density of states employing DFT embedded in CASTEP code. The lattice parameters were found to be increasing with increase in Mo content. The elastic properties results were found to be in good agreement with the available experimental and theoretical findings. The C′ moduli of β Ti was found to be unstable with a negative value. Interestingly as Mo was added in the system C′ increased resulting in a positive C′ at higher Mo content. It was observed that the elastic constants obeyed the stability criterion since the addition Mo content stabilized the β-phase with an increasing C′ moduli suggesting that the phase is being stabilized at a higher content of Mo. The density of states suggests that the β-phase stabilizes at higher Mo content. As more Mo is added the structure becomes unstable as seen by the highest number of states of the highest content of Mo.

5. Acknowledgements

The authors acknowledge Sefako Makgatho Health Science University and NRF for their financial support. The support of the CSIR and national research foundation is highly recognized. The calculations were carried out using computer resources at the center for high-performance computing (CHPC) in Cape Town.

References

[1] Niinomi, M 2003 “Recent research and development in titanium alloys for biomedical applications and healthcare goods”, *Science and Technology of Advanced Materials*, **4**, no. 5, pp. 445-454.

[2] Li Y, Yang C, Zhao H, Qu S, Li X and Li Y 2014 “New Developments of Ti-Based Alloys for Biomedical Applications”, *Materials*, **7**, pp. 1709-1800.

[3] Hou Y P, Guo S, Zhao X Q 2016 J. *Mechanical Behavior Biomedical Materials*, **59**, pp. 220-225.

[4] Niinomi M 1998 *Material. Science and. Engineering*. A. **243**, pp. 231-236.

[5] Kurtz S 2007 *The Journal of Bone and Joint Surgery (American)*, **89**, no. 4, pp. 780-785.

[6] Abdel-Hady Gepreel M, Niinomi M 2013 J. *Mechanical Behavior Biomedical Materials,* **20**, pp. 407-415.

[7] Hao Y L, Li S J, Sun S Y, Zheng C Y, Yang R 2007 *Acta Biomaterialia*, **3**, pp. 277-286.

[8] Kumar S, Sankara T S N 2008 *Journal of Dentistry*, **7**, pp. 500 -507.

[9] Ying-Long Z, Dong-Mei L 2011 *Material Characterization*, **62**, pp. 931-937.

[10] Zhao M X, Niinomi M, Nakai M 2012 *Acta Biometerialia*, **8**, pp 1990-1997.

[11] Segall M D, Philip J D L, Probert M J, Pickard C J, Hasnip P J, Clark S J, Payne M C 2002 "First-principles simulation: ideas, illustrations and the CASTEP code," *Journal of Physic: Condensed Matter,* **14**, pp. 2717-2744.

[12] Perdew J P and Wang Y 1992 " Accurate and simple analytic representation of the electron-gas correlation energy," *Physical Review B,* **45**, pp. 13244-13249.

[13] Kohn W and Sham L J 1965 *Physical Review.* **140**, 1138.

[14] Monkhorst H J and Pack J D 1976 *Physical Review B*, **13**, no. 13, pp. 5188.

[15] Ramer N J and Rappe A M 2000 "Application of a New Virtual Crystal Approach for the Study of Disordered Perovskites," *Journal of Physics and Chemistry of Solids,* **61**, no. 2, pp. 315-320.

[16] Nordheim L 1931 "To the Electron Theory of Metals," *Annals of Physics (Leipzig)*, **401**, pp. 607-640.

[17] De Gironcoli S, Giannozzi P and Baroni S 1991 "Structure and Thermodynamics of Si x Ge 1-x Alloys from ab initio Monte Carlo Simulations," *Physical Review Letter.,* **66**, no. 16, pp. 2116-2119.

[18] Segall M D, Philip J D L, Probert M J, Pickard C J, Hasnip P J, Clark S J and Payne M C 2002 "First-principles simulation: ideas, illustrations and the CASTEP code," *Journal of Physic: Condensed Matter,* **14**, pp. 2717-2744.

[19] Joris O P J Diffraction Experiments on superelastic Beta Titanium alloys.

[20] Born M and Huang K 1998 Dynamical Theory of Crystal Lattices, Oxford University Press.

[21] Sung B S, Park T E, and Yun Y H 2015 “Microstructures and electrochemical behavior of Ti-Mo alloys for biomaterials,” *Advances in Materials Science and Engineering*, pp. 1-7.

[22] Zhang W D Y, Liu H, Wu M, Song T Y, Zhang X D and Yao T H 2015 “Elastic modulus of phases in Ti-Mo alloys,” *Materials Characterization*, **106**, pp. 302-307.

[23] Boyer R G, Welsch and Collings E 1994 “Materials Properties Handbook: Titanium Alloys,” ASM International, Materials Park, OH.

[24] Mahlangu R, Phasha M J, Chauke H R, Ngoepe P E 2013 *Intermetallics,* **33,** pp. 27-32.

[25] Li M, Min X, Ye F, Li P, Cheng C and Zhao J 2018 “First-principles study of phase stability and elastic properties in metastable Ti-Mo alloys with cluster structure”, *Molecular Simulation*.

Stability of lithium manganese oxide ($LiMn_2O_4$) surfaces during charge/discharge processes.

Brian Ramogayana[1], Khomotso P. Maenetja[1], David Dantos-Carballal[1, 2], Nora H. de eeuw[2, 3] and Phuti E. Ngoepe[1]

[1]Materials Modelling Centre, University of Limpopo, Private Bag x1106, Sovenga, 0727, South Africa

[2]School of Chemistry, Cardiff University, Main Building, Park Place, Cardiff CF10 3AT, United Kingdom

[3]Department of Earth Sciences, Utrecht University, Budapestlaan 4, 3584 CD Utrecht, The Netherlands

E-mail: brian.ramogayana@ul.ac.za

Abstract. Surface stability and reactivity of cathode materials is one of the key aspects in improving the electrochemical performance of secondary Li-ion batteries. Lithium manganese oxide spinel attracted the most attention as a potential cathode material for lithium-ion batteries because of its three-dimensional crystal structure that allows a smooth diffusion of Li^+ in and out of the material. However, its application as a cathode material is limited by irreversible capacity fading due to manganese dissolution In the current paper, we employ the spin-polarized density functional theory calculations with on-site Coulomb interactions and long-range dispersion corrections [DFT+U−D3− (BJ)] to investigate the stability of (001), (011) and (111) surfaces during charge/discharge processes. Based on the calculated surface energies, it was observed that the Li-terminated (001) surface is the most stable with γ_r = 0.04 eV/Å^2, which is in agreement with the reported literature. To mimic charge/discharge processes, delithiated surfaces were modelled from the most stable surfaces terminations, and their stabilities were evaluated by calculating the surface free energies. As compared to the surface energies of the pure pristine facets, we observed an increase in energy during delithiation process, which indicate that the surfaces are destabilizing. However, the most stable surface upon delithiation was the (111) surface with the most dominant plane on the particle morphologies. Our work gives an insight about the surface stability and particle morphologies during charge/discharge processes.

1. Introduction

Alternative energy sources became the world's leading technology due to global warming and depleting natural resources. Although there have been many studies aimed to facilitate the movement away from the reliance on fossil fuels [1], there is still no replacement for commercially used lithium-ion batteries. Li-ion batteries are widely used because of their high-power density, long cycle life, and low self-discharge property [2]. However, recent Li-ion batteries have a limited cycling life which cannot keep up with the current advanced technologies. An improvement of the positive electrodes can facilitate the implementations of Li-ion batteries in the currently used electronic devices, electric vehicles and storage

systems. Many cathode materials such as $LiCoO_2$ [3], $LiMn_2O_4$ [4], $LiFePO_4$ [5], etc. were studied and gave an improved electrochemical performance.

Lithium manganese oxide ($LiMn_2O_4$) spinel attracted the most attention as potential cathode material because of its 3D crystal structure that allows a smooth movement of Li ions in and out of the cathode materials [6, 7]. It was considered as a suitable cathode material for Li-ion batteries because of its environmental friendliness, affordability, thermal stability, high energy density and high earth abundance of manganese [8]. However, it suffers from capacity fading due to manganese dissolution caused by the presence of the highly corrosive hydrofluoric acid continuously produced by degradation of the common $LiPF_6$-based electrolytes [9].

Various strategies were implemented to reduce Mn^{2+} dissolution into the electrolyte, which including cation doping [10, 11], replacement of commercially used electrolyte component [12] and surface coating to create an artificial barrier that limits the direct electrode-electrolyte contact [13]. Most recently, studies focused on exposing the (111) surface since it is resistant to Mn dissolution [14, 15, 16]. However, the effect of surface delithiation on the fully $LiMn_2O_4$ spinel is not completely understood. In this paper, we study the effect of delithiation on the $LiMn_2O_4$ low Miller index (001), (011) and (111) surfaces using spin-polarised density functional theory calculations. We investigate the effect of surface delithiation by calculating surface free energies of surface as we reduce the Li content and constructing their respective particle morphologies.

2. Method

The density functional theory (DFT) calculations as implemented in the Vienna Ab-initio Simulation Package (VASP) [17] was used to investigate the effect of surface delithiation on the surface stability. All calculations were carried out within the generalized gradient approximation (GGA) using the Perdew, Burke, and Ernzerhof (PBE) exchange-correlation functional [18]. We used the kinetic energy cut-off of 560 eV and the *k*-points of 5×5×5 for the integration of the reciprocal space. The projector augmented-wave (PAW) method [19] in the implemented by Kresse and Joubert [20] was used to describe the core electrons and their interaction with the valence electrons. To improve the description of the localized 3*d* electrons, we used the Hubbard correction [21] in the formulation of Dudarev *et al.* [22] and the *U* parameter was set at 4.0 eV, which was in the range of values reported in the literature [23]. We also included the semi-empirical method to model the long-range interactions [24]. We set a Gaussian smearing width of 0.05 eV to improve the convergence of the Brillion zone integrations during geometry optimizations [24].

Lithium manganese oxide ($LiMn_2O_4$) commonly known as spinel is a face-centered cubic structure with a space group *Fd*-3*m* (No. 227) and the lattice parameter of a = 8.247 Å [25]. The lithium atoms occupy the 8*a* tetrahedral sites, manganese atoms at the 16*d* octahedral sites and oxygen atoms at the 32*e* sites [26].

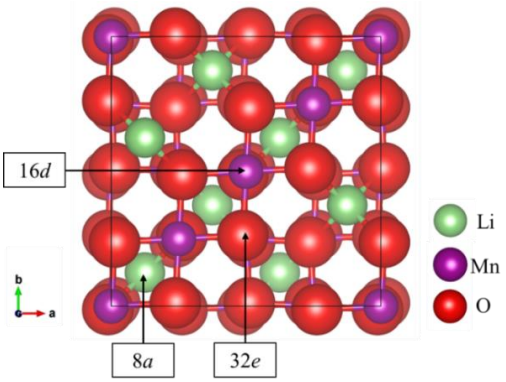

Figure 1: The crystal structure of lithium manganese oxide ($LiMn_2O_4$) spinel.

 ISBN: 978-0-620-88875-2

3. Results

3.1. Surface models

All the surfaces modelled in this study were created by cutting the fully optimised bulk using the dipole method implemented in METADISE code [27]. The resulting surfaces were represented by keeping fixed the bottom atoms at their *ab-initio* relaxed bulk positions while the rest of the atoms were allowed to relax during geometry optimization to simulate the half-relaxed slabs. The surfaces composed of the same 56 atoms (8 formula units) as in the bulk structure, with 8 Li, 16 Mn and 32 O atoms. The $LiMn_2O_4$ (001), (011) and (111) surfaces were modelled with slabs have surface areas 69.72, 48.30 and 60.38 $Å^2$, respectively.

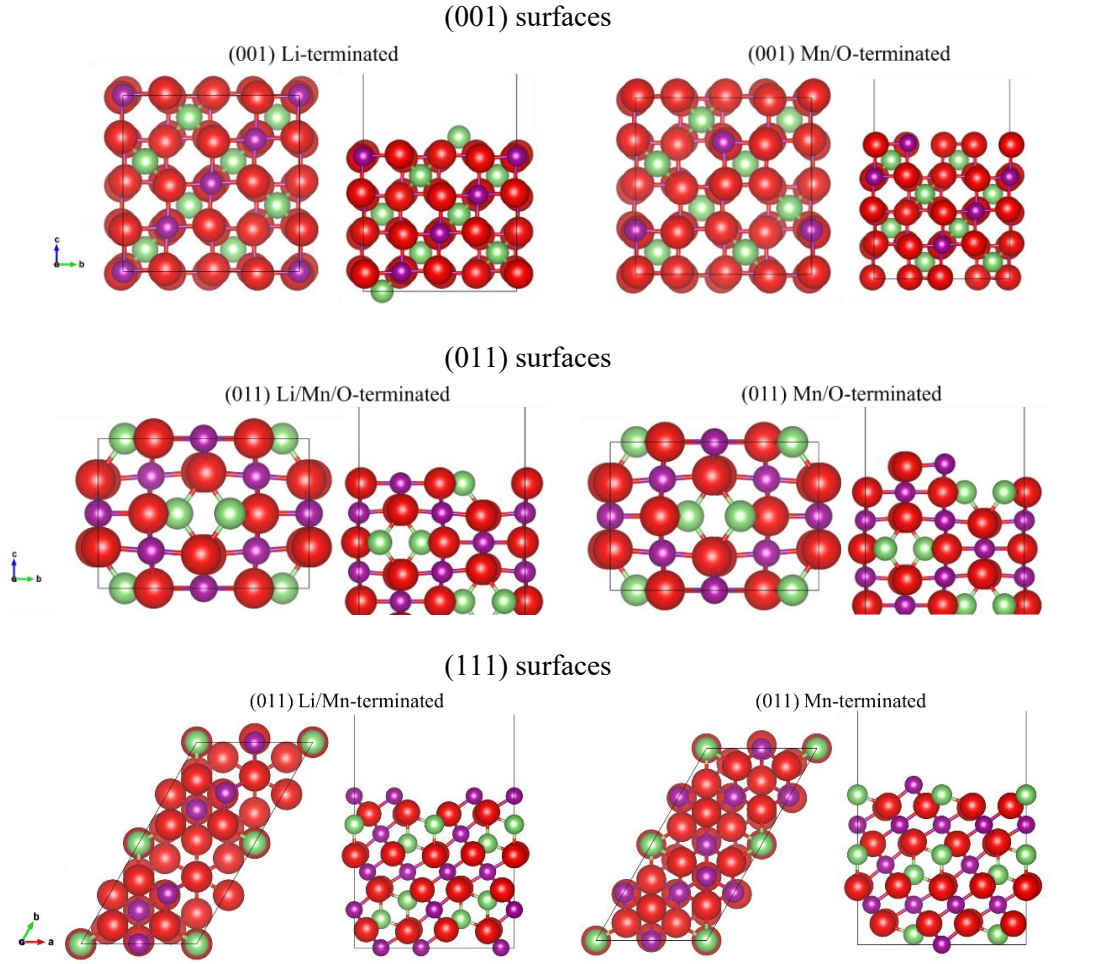

Figure 2. Top and side view of the modelled low Miller index surfaces from a fully optimized $LiMn_2O_4$ bulk structure. Crystallographic directions for the top view of (001) surface terminations is [100] for the abscissae towards the right, for the (011) surface terminations it is $[0\bar{1}1]$ for the abscissae towards the right, and for the (111) surface terminations it is $[0\bar{1}1]$ for the longest axis towards the top.

In each surface termination, a vacuum region of 15 Å was added perpendicularly to avoid interactions with the successive slabs. Various slabs, vacuum thickness and number of relaxed layers were tested until the convergence was within 1 eV per cell. In each surface orientation, we modelled two terminations which were both symmetrical and non-polar as outlined by Tasker [28]. The (001), (011) and (111) surfaces composed on two terminations, which are the Li and Mn/O-terminated slabs for

(001), Li/Mn/O and Mn/O-terminated for (011), and Li/Mn and Mn-terminated slabs for (111) surfaces (see Figure 2).

3.2. Surface energies

Energy minimization of (001), (011) and (111) surfaces were carried out to obtain their respective surface energies. We determined the surface energies for the unrelaxed surface from a single point calculations of the slabs before relaxation. The unrelaxed surfaces energies (γ_u) were calculated as:

$$\gamma_{\mathrm{u}} = \frac{E_{\mathrm{u}} - E_{\mathrm{b}}}{2A} \quad (1)$$

where E_{u} is the total energy of unrelaxed facet, E_{b} is the energy of the fully optimized bulk with the same number of formula units as in the slabs and A is the surface area of each slab. During surface relaxation, the uppermost atoms were allowed to relax and the bottom atoms were kept fixed at bulk positions. The relaxed surface energies (γ_r) for these half-relaxed slabs were calculated using:

$$\gamma_r = \frac{E_{\mathrm{r}} - E_{\mathrm{b}}}{A} - \gamma_{\mathrm{u}} \quad (2)$$

where E_{r} is the energy of half relaxed surface. The degree of relaxation (R) was also calculated for all the surfaces as:

$$R = \frac{\gamma_{\mathrm{u}} - \gamma_{\mathrm{r}}}{\gamma_{\mathrm{u}}} \times 100 \quad (3)$$

Table I. Surface energies of the low Miller index surface for the relaxed (γ_r) and unrelaxed (γ_u) slab.

Surface	Termination	γ_u (eV/Å^2)	γ_r (eV/Å^2)	R (%)
(001)	Li	0.07	0.04	43.7
	Mn/O	0.15	0.11	28.7
(011)	Li/Mn/O	0.10	0.05	50.0
	Mn/O	0.10	0.07	37.2
(111)	Li/Mn	0.08	0.05	38.0
	Mn	0.21	0.09	57.9

Table 1 summarizes the surface energies (for both unrelaxed and relaxed slabs) and the degree relaxation for the modelled surface shown in Figure 2. Considering the most stable surface as the one with the lowest surface energy, the (001) surface is observed as the most stable in both relaxed and unrelaxed slabs. The calculated surface energies indicated that the Li-terminated (001) surface has the lowest surface energy of γ_r = 0.04 eV/Å^2 compared to other facets. With reference to the reported literature, the calculated surface energy for the Li-terminated (001) facet was in the range between 0.26-0.96 J/m^2 (0.02 and 0.06 eV/Å^2) [29]. Surface energies of both the relaxed and unrelaxed slabs show an increasing trend for the most stable termination, {(001) < (011) < (111)}, and therefore a decreasing surface stability. The most stable surface terminations for (001), (011) and (111) facets are the Li, Li/Mn/O and Li/Mn-terminated slabs, respectively. The relaxation percentages indicate that the (111) Mn–terminated (111) surface had the highest geometry relaxation while the Mn/O-terminated (001) had the lowest geometry relaxation percentage.

3.3. Surface free energies

To mimic the Li intercalation during charge/discharge processes, we modelled the partially delithiated surfaces by removing the Li atoms from the uppermost atomic layer of the most stable surface terminations. The delithiated surfaces were modelled by removing only the Li atoms from the atomic layers which were allowed to move during geometry optimization. The stability of the modelled

delithiated surfaces were investigated by calculating surface energies for different Li concentrations using equation:

$$\sigma = \gamma_{\mathrm{r}} + \frac{E_{\mathrm{d}} - E_{\mathrm{r}} + (8 - N_{\mathrm{Li}})E_{\mathrm{Li}}}{A} \quad (3)$$

where E_{d} is the energy of the delithiated slab, E_{r} is the energy of the pristine slab, $8-N_{\mathrm{Li}}$ is the number of lithium atoms removed from the slab and E_{Li} is the energy of one atom in the bulk of the body-centered cubic (*bcc*) lithium. Table II summarize the surface free energies (σ) for slabs with different Li concentration. Note that when there are no surface modifications (such as surface doping, adsorption or delithiation), the surface energies and the surface free energies have the same magnitude [30]. In every surface orientation, we modelled slabs with compositions $Li_8Mn_{16}O_{32}$, $Li_7Mn_{16}O_{32}$ and $Li_6Mn_{16}O_{32}$. Generally, we observe an increase in surface free energies upon delithiation compared to the surface energy for the fully lithiated surfaces, indicating surface destabilizing effect. After removing a single Li atom (x = 0.125), we observe that the (001) surface destabilises but still remain the most stable surface with σ = 0.12 eV/ Å^2, followed by the (111) facet with σ = 0.14 eV/ Å^2 and then (001) surface with the highest surface free energy of σ = 0.31 eV/ Å^2. Upon the removal of two Li atoms (x = 0.250), the lowest surface free energy was the (111) facet with σ = 0.09 eV/Å^2, while the slab with the highest surface free energy was the (001) facet with σ = 0.10 eV/Å^2.

Table II. Surface free energies (σ) for the partially delithiated surfaces at different Li content, showing the surface compositions and the number of Li atoms removed (x). Note that for x = 0, the surface free energy is equivalent to the surface energy ($\sigma = \gamma$).

Surface	Composition	x	σ (eV/ Å^2)
(001)	$Li_8Mn_{16}O_{32}$	0	0.04
	$Li_7Mn_{16}O_{32}$	0.125	0.12
	$Li_6Mn_{16}O_{32}$	0.250	0.10
(011)	$Li_8Mn_{16}O_{32}$	0	0.05
	$Li_7Mn_{16}O_{32}$	0.125	0.31
	$Li_6Mn_{16}O_{32}$	0.250	0.14
(111)	$Li_8Mn_{16}O_{32}$	0	0.05
	$Li_7Mn_{16}O_{32}$	0.125	0.14
	$Li_6Mn_{16}O_{32}$	0.250	0.09

3.4. Particle morphologies

The Wulff construction for particle morphologies was based on the famous paper on the heterogeneous substances by J.W. Gibbs [31]. Figure 3 summarizes the constructed particle morphology for the fully lithiated and partially delithiated surfaces. The particle morphologies were constructed from the surface free energies of respective Li concentrations. The fully lithiated particle morphologies are dominated by the (001) Li terminated surface, which is similar to the octahedron-shaped observed in literature [25]. Upon delithiation, the morphology clearly indicates that as we reduce the Li content, the (001) surface plane decreases, while the (111) plane becomes the most dominant facet. The (011) surface turn to disappear in the Wulff morphology upon delithiation because of its higher surface free energy with respect to the (001) and (111) planes.

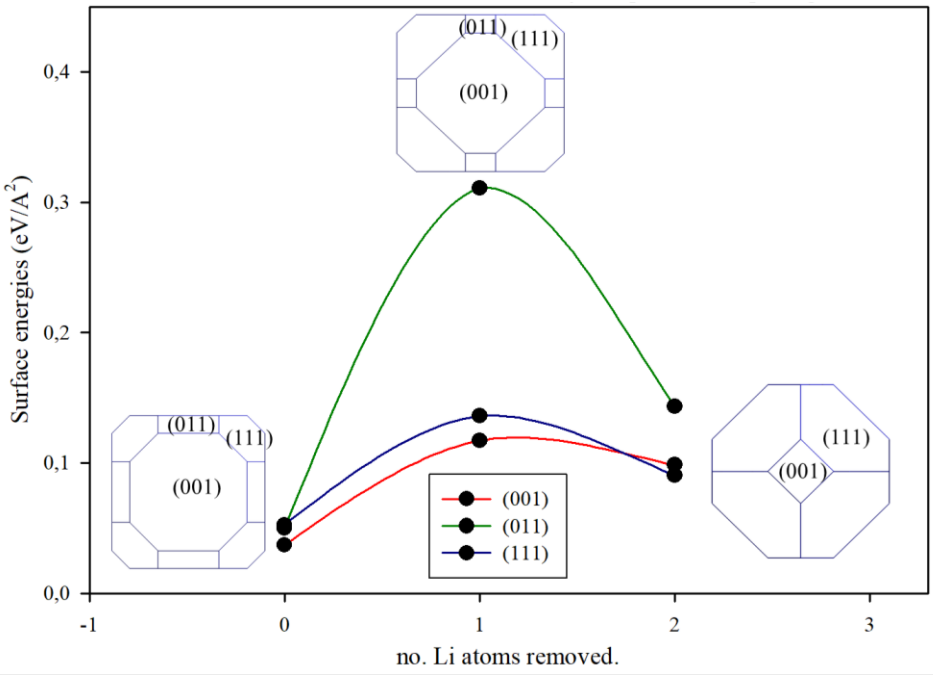

Figure 3. The effect of delithiation onto the $LiMn_2O_4$ spinel surfaces at different Li content. This was investigated by calculating the surface free energies of partially delithiated surfaces at various Li concentrations and contracting their respective particle morphologies.

4. Conclusion

Using the density functional theory calculations, we successfully investigated the effect of delithiation on the three low Miller index (001), (011) and (111) Surfaces. We modelled the fully lithiated and partially delithiated surfaces from an optimised bulk and the most stable surface terminations, respectively. The calculated surface energies show that Li-terminated (001) facet is the most stable surface with γ_r = 0.04 eV/Å^2, which is in agreement with the reported literature. To mimic the charge/discharge surfaces, we modelled the delithiated surfaces from the most stable termination by removing the Li atoms from the uppermost atomic layers. The surface free energies (σ) calculated for the modelled partially delithiated surface were higher as compared to the surface energies of the fully lithiated facets, which indicated that the surfaces were destabilising as the Li content decreases. Furthermore, we observed a decrease in (001) plane on the particle morphologies, while (111) surface become the most dominant slab upon delithiation.

Acknowledgement

This work was performed using the computational facilities of the Advanced Research Computing @ Cardiff (ARCCA) Division, Cardiff University. We acknowledge the South African Research Chair Initiative of the Department of Science and Technology, the National Research Foundation in Pretoria and the Centre for High-Performance Computing in Cape Town. Part of the study was undertaken using the Supercomputing Facilities at Cardiff University operated by ARCCA on behalf of the HPC Wales and Supercomputing Wales (SCW) projects. The authors also wish to thank the collaboration between the Material Modelling Centre (MMC), University of Limpopo and Advanced Research Computing @ Cardiff (ARCCA) Division, Cardiff University.

5. References

[1] S.k. Nandi and H.R. Ghosh 2010 *Energy* **35** 3040.

[2] S. Goriparti, E. Miele, F. De Angelis, E. Di Fabrizio, R.P. Zaccaria and C. Capiglia 2014 *J. Power sources* **257** 421.

[3] P. Byeon, H.B. Bae, H.S. Chung, S.G. Lee, J.G. Kim, H.J. Lee, J.W. Choi and S.Y. Chung 2018 *Adv. Funct.l Mater.* **28** 1804564.

[4] C.Y. Ouyang, S.Q. Shi, Z.X. Wang, H. Li, X.J Huang and L.Q. Chen 2004 *Europhy. Lett.* **67** 28.

[5] T. Mueller, G. Hautier, A. Jain and G. Ceder 2011 *Chem. Mater.* **23** 3854.

[6] J. Kim and A. Marnthiram 1997 *Nature* **390** 265.

[7] S.T. Lee, K. Raveendranath, R.M. Tomy, N.A. George, S. Jayalekshmi and J. Ravi 2007 *J. Phys. D: Appl. Phys.* **40** 3807.

[8] K.R. Ragavendran, H. Xia, G. Yang, D. Vasudevan, B. Emmanuel, D. Sherwood and A.K. Arof 2014 *PCCP* **16** 2553.

[9] M. Wohlfahrt-Mehrens, C. Vogler and J. Garche 2004 *J. Power sources* **127** 58.

[10] M. Michalska, D.A. Ziółkowska, J.B. Jasiński, P.-H. Lee, P. Ławniczak, B. Andrzejewski, A. Ostrowski, W. Bednarski, S.H. Wu and J.Y. Lin 2018 *Electrochim. Acta* **276** 37.

[11] A. M. Kannan and A. Manthiram 2002 *Electrochem. Solid-State Lett.* **5** 167.

[12] G. Xu, Z. Liu, C. Zhang, G. Cui and L. Chen 2015 *J. Mater. Chem. A* **3** 4092.

[13] D. Guan, J.A. Jeevarajan and Y. Wang 2011 *Nanoscale* **3** 1465.

[14] C.J. Jafta, F. Nkosi, L. le Roux, M.K. Mathe, M. Kebede, K. Makgopa, Y. Song, D. Tong, M. Oyama, N. Manyala and S. Chen 2013 *Electrochim. Acta* **110** 228.

[15] F.P. Nkosi, C.J. Jafta, M. Kebede, L. Le Roux, M.K. Mathe and K.I. Ozoemena 2015 *RSC Adv.* **5** 32256.

[16] Y. Xiao, X.D. Zhang, Y.F. Zhu, P.F. Wang, Y.X. Yin, X. Yang, J.L. Shi, J. Liu, H. Li, X.D. Guo and B.H. Zhong 2019 *Adv. Sci.* **6** 1801908.

[17] G. Kresse and J. Furthmüller 1996 *Phys. Rev. B* **54** 11169.

[18] J.P. Perdew, K. Burke and M. Ernzerhof 1996 *Phys. Rev. lett.* **77** 11169.

[19] P.E. Blöchl 1994 *Phys. Rev. B* **50** 17953.

[20] G. Kresse and D. Joubert 1999 *Phys. Rev. B* **19** 1758.

[21] V.I. Anisimov, M.A. Korotin, J. Zaanen and O.K. Andersen 1992 *Phys. Rev. lett.* **68** 345.

[22] S.L. Dudarev, G.A Botton, S.Y. Savrasov, C.J. Humphreys and A.P. Sutton 1998 *Phys. Rev. B* **57** 1505.

[23] D. Santos-Carballal, P.E. Ngoepe and N.H. de Leeuw 2018 *Phys. Rev. B* **97** 085126.

[24] S. Grimme, J. Antony, S. Ehrlich and H. Krieg 2010 *J. Chem. Phys.* **132** 154104.

[25] J.S. Kim, K. Kim, W. Cho, W. H. Shin, R. Kanno and J. W.Choi 2012 *Nano lett.* **12** 6358.

[26] S. K. Mishra and G. Ceder 1999 *Phys. Rev. B* **59** 6120.

[27] G. W. Watson, E. T. Kelsey, N. H. de Leeuw, D. J. Harris and S. C. Parker 1996 *J. Chem. Soc. Faraday Trans.* **92** 433.

[28] P.W. Tasker 1979 *J. Phys. C: Solid State Phys.* **12** 4977.

[29] A. Karim, S. Fosse, and K. A. Persson 2013 *Phys. Rev. B* **87** 075322.

[30] V. Postica, A. Vahl, J. Strobel, D. Santos-Carballal, O. Lupan, A. Cadi-Essadek, N.H. de Leeuw, F. chütt, O. Polonskyi, T. Strunskus and M. Baum 2018 *J. Mater. Chem. A* **6** 23669.

[31] J.W. Gibbs 1875 *Trans. Conn. Acad. Arts Sci.* **3** 108.

Structural, electronic, elastic stability and optical properties of rare-earth copper chalcogenides $LaCuX_2$ (X = S and Se), a first principles study

Abdu Barde[1,2] and Daniel P Joubert[1]

[1] The National Institute for Theoretical Physics, School of Physics and Mandelstam Institute for Theoretical Physics, University of the Witwatersrand, Johannesburg, Wits 2050, South Africa
[2] College of Science and Technology, Jigawa state Polytechnic, Dutse - Jigawa state, Nigeria.

E-mail: abdubarde@gmail.com

Abstract. Structural, electronic, and optical properties of rare-earth copper chalcogenides $LaCuX_2$ (X = S, Se) were investigated with density functional theory (DFT). The calculated structural properties agree reasonably well with previous results and experimental data. Calculated elastic constants satisfy the stability conditions for monoclinic structures, which confirms mechanical stability for the compounds. DFT band structure and density of states calculations reveal that the $LaCuX_2$ (X = S, Se) compounds are direct band gap semiconductors. The fundamental gaps were determined at the many-body perturbation theory G_0W_0 level of approximation, while optical parameters such as dielectric functions, refractive indices, reflectivity and absorption coefficients were examined by solving the TammDancoff-Bethe-Salpeter approximation. The calculated optical energy gaps are between 1.52 and 2.04 eV. From the results obtained, $LaCuX_2$ are stable compounds and posses energy gaps suitable for photo-electrochemical and photovoltaic applications.

1. Introduction

The ternary rare earth metal copper chalcogenides with chemical formula $LnCuX_2$ (Ln = rare-earth metals and X = S, Se), have been studied by various researchers. Investigations include the synthesis and structural characterizations of $LnCuX_2$ (Ln = rare-earth metals, X = S Se) [1, 2, 3]. In others studies the structural diversity and potential applications as promising optical and thermoelectric [4], photo-catalytic [5] and magnetic [6] materials have been reported for the $LnCuX_2$ compounds. Their counterparts, the delafossite rare earth/transition metal copper dioxides, are well studied theoretically and experimentally and have been identified as p-type transparent conducting oxide (TCO) [7, 8] materials.

Synthesis and single crystal determination of the ternary compounds $LaCuS_2$ and $LaCuSe_2$ were reported by Julien-Pouzol [1] and Ijjaal et al. [2] respectively. $LaCuS_2$ crystallizes in a monoclinic $P2_1/b$ structure which is built up of sheets of pair arrangements of tetrahedral La_2S and CuS_2 parallel to the b and c-axis. From x-ray powder diffraction [3] study, $LaCuS_2$ is isostructural to $YCuSe_2$. Similarly, $LaCuSe_2$, which is isostructural to $LaCuS_2$, crystallizes in monoclinic, space group $P2_1/c$ structure, with four formula (Z=4) units per cell [2]. The structure consists of layers of $CuSe_4$ tetrahedral units separeted by double layers of $LaSe_7$, and monocapped trigonal prism structures along the a-axis.

Most of the investigations carried out on $LaCuS_2$ and $LaCuSe_2$ are experimental studies of the crystal structure and lattice parameters. Recently Nguyen et al. [5] carried out an experimental study of $LaCuS_2$ combined with mesoporous silica and graphine oxide to investigate photo-catalytic

applications. Also, Li [9] identified $LaCuS_2$ as a potentially good candidate for a transparent p-type conductor considering its gap-modulation when doped with Yttrium (Y). Theoretical studies of physical properties of these materials such as structural, elastic stability, electronic, dynamic and optical properties are lacking in the literature despite their potential technological importance. We are motivated by this to carry out $ab-initio$ calculations to explore the physical, electronic and optical properties of $LaCuS_2$ and $LaCuSe_2$.

In this work, we study the structural, elastic stability and electronic properties of $LaCuX_2$ (X = S, Se) using the density functional theory (DFT) in the Kohn-Sham formulation [10] within the generalized gradient approximation (GGA) PBEsol [11], semi-local modified Becker-Jonhson potential (MBJ) [12] and the hybrid HeydScuseriaErnzerhof (HSE) [13] approximation. Optical properties, including absorption coefficient, absorbance, refractive index, reflectivity and energy loss were studied at the level of G_0W_0-BSE approximation [14, 15].

We consider this work important because simulated electronic structure and optical property studies is a useful tool [16] for identifying potential photovoltaic materials.

2. Method of calculations

All calculations of structural, mechanical, electronic and optical properties of $LaCuX_2$ were carried out within the framework of density functional theory (DFT) as implemented in the Vienna *ab initio* simulation package (VASP) [10, 17]. VASP implements a plane-wave basis set and a projected-augmented-wave (PAW) [18] formulation for the description of electron-ion interactions. Groundstate energies were calculated within the Perdew-Burke-Ernzehof generalized gradient approximation as revised for solids and their surfaces, PBEsol [11], for the electron exchange-correlation energy. Equilibrium structure optimization was conducted on the primitive cell structure with energy cut-off of 520 eV and a 4×4×4 Monkhorst-pack mesh [19] for sampling the Brillouin zone. The k-point mesh sampling was chosen to achieve convergence energies within less than 1 meV/atom. The elastic tensor was calculated for the fully relaxed equilibrium geometry with PBEsol. From the optimized structure DFT band structure calculations were performed PBEsol as well as with the Modified Johnson Becker MBJ [12] potential and hybrid functional Heyd-Scuseria-Ernzerhof (HSE06) [13], to estimate DFT fundamental band gaps. MBJ and HSE normally give better estimates of the fundamental band gap when compared to conventional DFT calculations with local or semi-local exchange-correlation functions. The fundamental gaps were also determined from the so called many-body Green's function approximation G_0W_0 [14, 15]. The optical absorption spectrum was obtained by including excitonic effects using the Tamm-Dancoff, G_0W_0 + BSE [14, 15, 20, 21] approximation. From the optical absorption spectra, the optical band gaps were determined using Tauc plots [22].

3. Results and discussion

3.1. Structural properties

The structural optimization of $LaCuS_2$ and $LaCuSe_2$ units cells by means of total energy minimization for unit cell and atomic position were performed to obtain equilibrium lattice constants. Synthesis and characterizations of structural lattice parameters have been reported and it is known that $LaCuS_2$ and $LaCuSe_2$ both crystallize in a monoclinic crystal, space group $P2_1/b$, with four formula units (Z=4) per cell, [1] and $P2_1/c$ [2] respectively. The numerically optimized crystal unit cells and first Brillouin zone are shown in Figure 1 and 2. From the fully optimized structure of $LaCuS_2$ and $LaCuSe_2$ we derived the ground state properties. The optimized volume, bulk modulus and its pressure derivatives are determined by fitting the total energy to the well-known 3^{rd} order Murnaghan's equation of state (EOS) [23] for this purpose. The energy volume relationship are depicted in Figure 3 and 4. Lattice parameters, angle β for monoclinic crystals, optimized volume, bulk modulus and it's pressure derivative compared to available experimental values are listed in Table 1.

The PBEsol is well-known to describe accurately the behavior of solid [11]. Hence, our calculated structural parameters agree reasonably with experimentally reported [1, 2] values within 2%. Computed cohesive energies have negative values indicating that $LaCuX_2$ are energetically stable compounds.

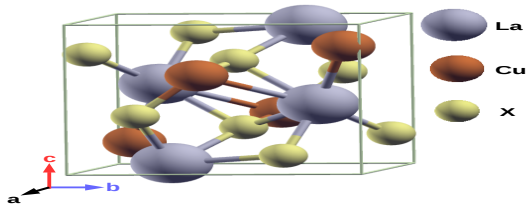

Figure 1. Craystal structure of $LaCuX_2$.

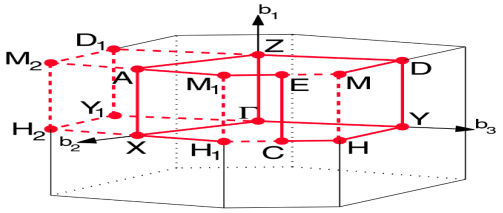

Figure 2. First Brillious zone of $LaCuX_2$ unit cells.

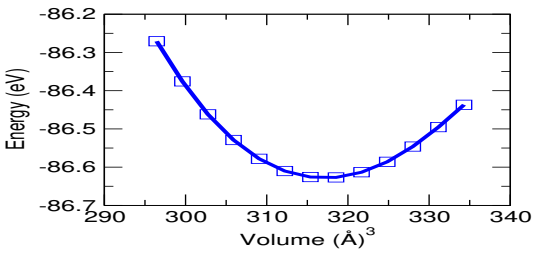

Figure 3. Variation of total energy as a function of volume of $LaCuS_2$.

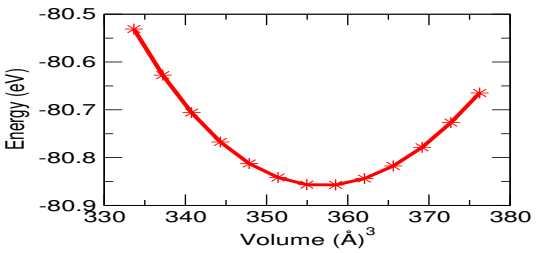

Figure 4. Variation of total energy as a function of volume of $LaCuSe_2$.

Table 1. Computed and experimental lattice parameters a, b, c (Å), volume V_0 (Å^3), angle β, bulk modulus B_0 (GPa), pressure derivatives of bulk modulus B_0' and cohesive energy E_{coh} (eV/atom).

	a	b	c	V	β	B_0	B_0'	E_{coh}
$LaCuS_2$	6.49,6.65[1]	6.82,6.94[1]	7.23,7.33[1]	317.12	82.13,98.73[1]	73.90	5.56	-5.41
$LaCuSe_2$	6.70,6.81[2]	7.51,7.58[2]	7.14,7.20[2]	356.8,369[2]	83.12,97.12[2]	63.44	3.29	-5.05

3.2. Elastic stability

We calculated the elastic constants from the PBEsol optimized structures of $LaCuS_2$ and $LaCuSe_2$ to check their mechanical stability. $LaCuX_2$ are monoclinic crystal structure with 13 independent elastic stiffness constants C_{ij}. The calculated values of the elastic constants are listed in Table 2. All monoclinic stability criteria [24] are satisfied and hence the compounds are mechanically stable. There are no available theoretical or experimental C_{ij} values for comparison. Using Hill'S approximation [25] the bulk moduli (B_0) are 79.12, 66.32 (GPa), shear moduli (G) 105.31, 86 (GPa) and Poisson's ratio (ν) both as 0.28 for $LaCuS_2$ and $LaCuSe_2$, respectively. Bulk and shear moduli are measures of a material's response to applied stress. Substituting Sulfur (S) by Selenium (Se) atom bring considerable decrease in bulk moduli and it's pressure derivatives, as well as the shear modulus. This indicates that compressibility increases and resistance to plastic deformations decreases with substitution of Se atom in $LaCuX_2$. The ratio B/G describes the ductility or brittleness behavior of a material. Our calculated values of B_0/G, 1.92 and 1.98 for $LaCuS_2$ and $LaCuSe_2$, respectively, show that the compounds are ductile [26]. Similarly, Poisson's ratio ν values of 0.28 reveal that the compounds are materials with good plasticity, and that the inter-atomic forces are central with an ionic bonding characteristic [27].

3.3. Electronic properties

The fundamental band gaps of $LaCuS_2$ and $LaCuSe_2$ were estimated with PBEsol, MBJ, HSE06 and G_0W_0 for better estimates and comparisons. The band structure calculated with PBEsol along high symmetry directions, with total (TDOS) and partial densities of states (PDOS), are shown in

Table 2. The computed thirteen independent elastic constant of $LaCuX_2$.

	C_{11}	C_{12}	C_{13}	C_{15}	C_{22}	C_{23}	C_{25}	C_{33}	C_{35}	C_{44}	C_{46}	C_{55}	C_{66}
$LaCuS_2$	159.82	60.9	56.80	4.04	104.7	49.52	-3.25	127.55	-4.47	55.41	6.68	35.46	46.51
$LaCuSe_2$	132.89	48.09	48.25	2.26	80.58	46.43	-0.07	113.3	-2.39	42.83	4.20	29.56	39.96

Table 3. Calculated and experimental band gap (eV) of $LaCuX_2$ compounds.

	PBEsol	MBJ	HSE06	G_0W_0	BSE			Exp.
					a	*b*	*c*	
$LaCuS_2$	1.24	1.56	2.31	2.39	2.04	1.97	1.98	2.23[9]
$LaCuSe_2$	0.85	1.41	1.87	1.85	1.64	1.52	1.52	

Figure 5 and Figure 6. The calculated band structures reveal that $LaCuX_2$ are direct band gaps semiconductors with gaps at the Γ point. The upper valence band (VBM), or Fermi-level is adjusted to zero. For the $LaCuX_2$ materials the VBM is dominated by hybridization of Cu(d) and Se(s) with a small contribution from La(d), while the lower conduction band (CBM) is dominated by La(d). The computed and available experimental band gaps are listed in Table 3. Our computed minimum fundamental band gaps for $LaCuS_2$ from PBEsol, MBJ, HSE06 and G_0W_0 are 1.24, 1.56, 2.31 and 2.39 eV, respectively. As expected, the GGA-PBEsol value under-estimates the experimental optical gap of 2.23 eV, while G_0W_0 gives a value which is larger than the measured optical gap. MBJ and HSE06 give values closer to the experimental value than PBEsol, as is commonly expected [28]. For the G_0W_0-BSE estimates (see discussion in next section), polarization of incident radiation is taken into account and optical anisotropy is evident. The best estimate we have for the optical gap, 1.97-2.04 eV, compares well with the experimental value. The results suggest that our calculated G_0W_0-BSE estimate of the optical band gap for $LaCuSe_2$ will be a good indicator of the value of this compound. We believe that one of the goals of material design is to tailor the band gap for desired applications. The substitutions of sulfur (S) by selenium (Se) atom in $LaCuX_2$ narrows the band gap to an energy around the recommended Shockley-Quiesse [29] equation band gap limit for ideal solar cell devices. These results are encouraging and suggest further study of the $LaCuSe_2$ compounds.

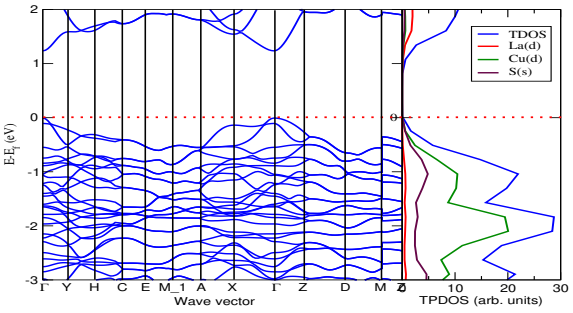

Figure 5. Electronic band structure, TDOS and PDOS of $LaCuS_2$.

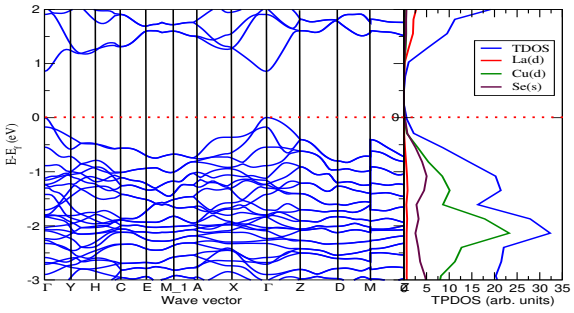

Figure 6. Electronic band structure, TDOS and PDOS of $LaCuSe_2$.

3.4. Optical properties

We investigated the optical properties of $LaCuS_2$ and $LaCuSe_2$ from the complex dielectric function $\epsilon(\omega)=\epsilon_1(\omega)+i\epsilon_2(\omega)$. The absorptive part, which is the imaginary dielectric function $\epsilon_2(\omega)$ can be calculated from momentum matrix elements between the occupied and unoccupied wave function [30]. The dispersive part, the real dielectric function $\epsilon_1(\omega)$, can be evaluated from the imaginary

Table 4. Computed static dielectric $\epsilon_1(0)$x, $\epsilon_1(0)$y, $\epsilon_1(0)$x), refractive index $n(0)$x, $n(0)$y, $n(0)$z and reflectivity $R(0)$x, $R(0)$y, $R(0)$z of $LaCuS_2$ and $LaCuSe_2$ compounds.

	$\epsilon_1(\omega)$			Refractive index			Reflectivity		
Compounds	$\epsilon_1(0)$x	$\epsilon_1(0)$y	$\epsilon_1(0)$z	$n(0)$x	$n(0)$y	$n(0)$z	$R(0)$x	$R(0)$y	$R(0)$z
$LaCuS_2$	4.11	3.45	4.48	2.03	1.85	2.11	0.33	0.20	0.23
$LaCuSe_2$	5.61	4.47	6.45	2.38	2.12	2.55	0.33	0.20	0.23

part the $\epsilon_2(\omega)$ using the Kramers-Kronig relations. Here we report the absorption coefficient ($\alpha(\omega)$) from which we estimated the directional x, y and z spectral absorption using the Tauc approach applied to the G_0W_0+BSE results. The band gap values are listed in Table 3, while the Tauc plots are shown in Figures 9 and 10. For the study of $LaCuX_2$ compounds the imaginary dielectric function $\epsilon_2(\omega)$ which is a frequency dependent is calculated using the G_0W_0+BSE approach in the energy range 0 - 8 eV depicted in Figure 7 and 8. This approach provides a reliable two particle interaction and electronic excitonic description [32]. The $\epsilon_2(\omega)$ optical spectra are obtained from the inter-band transition which are found to be consistent with our computed band structure. Optical spectra absorption peaks arises because of inter-band transition from top valence band (VB) to the bottom of the conduction band (CB). In Figure 7 and 8 the onset peaks of strong absorption occur at about 2.0 eV and 1.60 eV for $LaCuS_2$ and $LaCuSe_2$ respectively, which are consistent with our calculated band gaps from HSE06, G_0W_0, BSE and experiment. The static refractive index and reflectivity, which can also be derived from the imaginary and real parts of the dielectric functions using equations from reference [31], are listed in Table 4.

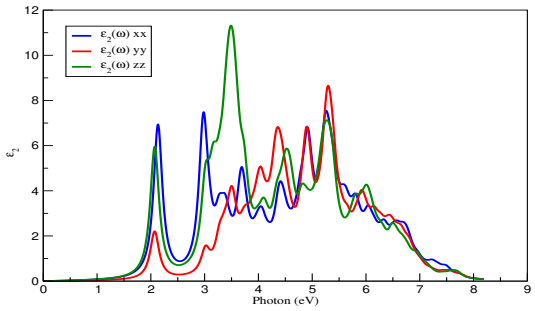

Figure 7. Imaginary dielectric $\epsilon_2(\omega)$ of $LaCuS_2$.

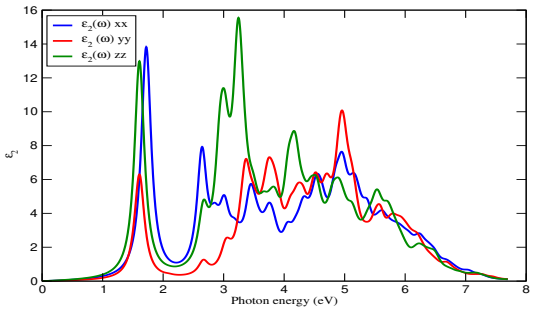

Figure 8. Imaginary dielectric $\epsilon_2(\omega)$ of $LaCuSe_2$.

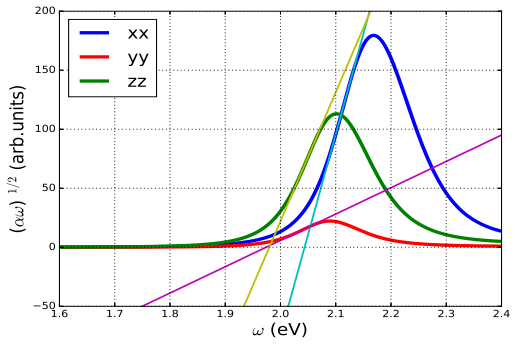

Figure 9. Tauc plot of absorption spectra of $LaCuS_2$.

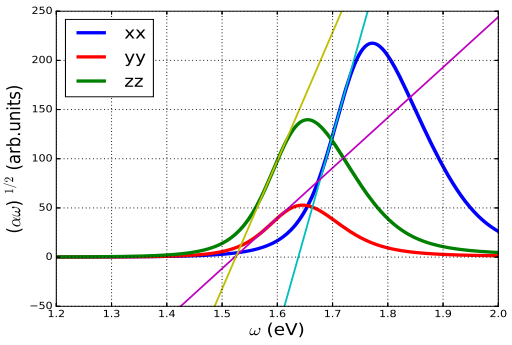

Figure 10. Tauc plot of absorption spectra of $LaCuSe_2$.

 ISBN: 978-0-620-88875-2

4. Conclusions

We use DFT and post-DFT techniques successfully study structural, electronic, elastic stability and optical properties of $LaCuS_2$ and $LaCuSe_2$ to fill the gap in the literature. Electronic band structures calculated from the DFT-PBEsol approximation show that $LaCuS_2$ and $LaCuSe_2$ are Γ point direct band gap semi-conductors. Calculated elastic constants verify the mechanical stability of $LaCuS_2$ and $LaCuSe_2$. Study of optical properties from many-body perturbation theory reveals that $LaCuSe_2$ has potential to absorption in the visible range. The computed energy gap from BSE calculations are 2.04 and 1.64 eV of $LaCuS_2$ and $LaCuSe_2$ respectively. This is favorable for photo-electrochemical and photovoltaic applications. $LaCuSe_2$ has potential for absorbing in the visible region, while $LaCuS_2$ has potential as a complementary absorber in a multi-junction solar cell.

5. Aknowledgements

We acknowledge the TETfund-Nigeria for financial support and the authors acknowledge the Centre for High Performance Computing (CHPC), South Africa, for providing computational resources to this research project.

6. References

[1] Ijjaali I, Mitchell K and Ibers J A 2004 *J. Solid State Chem.* **177** 760–764
[2] Julien-Pouzol M, Jaulmes S, Mazurier A and Guittard M 1981 *Acta Cryst. B* **37** 1901–1903
[3] Gulay L D and Olekseyuk I D 2005 *J. Alloys Compd.* **402** 89–94
[4] Esmaeili M, Tseng Y C and Mozharivskyj Y 2014 *J Alloys Compd.* **610** 555–560
[5] Nguyen D C T, Woo J H, Cho K Y, Jung C H and Oh W C 2018 *Sep. Sci. Technol.* **205** 11–21
[6] Wakeshima M, Furuuchi F and Hinatsu Y 2004 *J. Phys. Condens. Matter* **16** 5503
[7] Huda M N, Yanfa Y, Aron W, Su-Huai W and Mowafak M A 2009 *Phys. Rev. B* **80** 035205
[8] Wang X, Meng W and Yan, Y 2017 *J. Appl. Phys.* **122** 085104
[9] Wu L B and Huang F Q 2007 *Ceram. int.* **33** 1053–1055
[10] Kohn W and Sham L J 1968 *Phys. Rev.* **140** A1133
[11] Perdew J P *et al.* 2008 *Phys. Rev. Lett.* **100** 136406
[12] Tran F and Blaha P (2009) *Phys. Rev. Lett.* **102** 226401
[13] Heyd J, Scuseria G E and Ernzerhof M 2003 *J. Chem. Phys.* **118** 8207–8215
[14] Hanke W and Sham L J 1980 *Phys. Rev. B* **21** 4656
[15] Aryasetiawan F and Gunnarsson O 1998 *REP. PROG. PHYS.* **61** 237
[16] Curtarolo S, Hart G L, Nardelli M B, Mingo N, Sanvito S and Levy O 2013 *Nat. mater.* **12** 191
[17] Kresse G and Furthmller J 1996 *Comput. mater. sci.* **6** 15-50
[18] Kresse G and Joubert D 1999 *Phys. Rev. B* **59** 1758
[19] Monkhorst H J and Pack J D 1976 *Phys. Rev. B* **13** 5188
[20] Salpeter E E and Bethe H A 1951 *Phys. Rev.* **84** 1232
[21] Onida G, Reining L and Rubio A 2002 *Rev. Mod. Phys.* **74** 601
[22] Tauc J, Grigorovici R and Vancu A 1966 *Phys. Status Solidi B* **15** 627–637
[23] Murnaghan F D 1944 *Proc. Natl. Acad. Sci. U.S.A.* **30** 244
[24] Wu Zhi-Jian *et al.* 2007 *Phys. Rev. B* **76** 054115
[25] Hill R 1952 *Proc. Phys. Soc.* **65** 349
[26] Pugh S F 1954 *Philos. Mag.* **45** 823–843
[27] Haines J, Leger J M and Bocquillon G 2001 *Annu. Rev. Mater. Sci* **31** 1–23
[28] Garza A J and Scuseria G E 2016 *J. Phys. Chem. Lett.* **7** 4165–4170
[29] Shockley W and Queisser H J 1961 *J. Appl. Phys.* **32** 510–519
[30] Ambrosch-Draxl C and Sofo J O 2006 *Comput. Phys. Commun.* **175** 1–14
[31] Fox, M *Optical properties of solid* (Oxford University press, 2001)
[32] Rohlfing M. and Louie S G 2000 *Phys. Rev. B* **62** 4927

The effect of iron-particles on the electrical properties of n-GaSb semiconductor material

A Bele[1], LT Selepe[1], ME Sithole[1]

[1] Department of Physics, Sefako Makgatho Health Science University, P. O. Box 94, Medunsa, 0204, South Africa

E-mail address: abongile.bele@smu.ac.za

Abstract: Semiconductor material are characterized with the Schottky barrier diodes (SBDs) as a basic structure. The study was conducted in order to check the effect of iron (Fe^{+}) ions on the electrical properties of Gallium antimonide (n-GaSb) semiconductor material. GaSb was implanted with iron ions at various ion fluences ranging from 1.2 x 10^{15} ion.cm^{-2} to 1.2 x 10^{17} ions.cm^{-2} while keeping the ion energy at 90 keV. Aluminium (Al) SBDs were fabricated on the n-GaSb with Fe^{+} at various fluences. Structural and electrical properties have been investigated using the Raman spectroscopy and I-V characterization, respectively. Raman spectroscopy showed a slight amorphization at fluences higher than 1.2 x 10^{15} ions.cm^{-2}. The ideality factor (n) increased from 1.3 for the un-implanted to 2.0 for 1.2 x 10^{17} ions.cm^{-2}. The barrier height was found to decrease from 0.74 eV for the non-implanted to 0.64 eV for 1.2 x 10^{17} ions.cm^{-2}. Generally, the barrier height decreased with the increasing implantation fluences while the ideality factor increased with the increasing doping fluences.

1. Introduction

Gallium antimonide have been used in a wide range of applications such as developing radiation detector diodes [1]. These semiconductor materials are also used for radiation detection in a nuclear reactor [2]. The other applications include the use in radio detectors, transistors, lasers and light emitting diodes. The elemental semiconductors have been preferred for the detection in X-ray and gamma-ray spectroscopy but were later faced with limitations because of their radiation intolerance [3]. The semiconductors usually improve their functioning if there are adequate impurities that are added on them [4]. The semiconductor materials can be grown at different temperature conditions but the highest growth temperature is 520 ^{o}C [5]. The electrical characteristics of the semiconductor materials differ especially when subjected to different temperature conditions. These characteristics also differ when different impurities are added on the semiconductor materials. It is important that we know what impurity material improve the electrical properties of the semiconductor materials.

The Schottky barrier height and the ideality factor that assumes the thermionic emission (TE) theory shows a strong dependence on temperature [6]. In the investigation of the effect caused by the annealing temperature to the electrical and structural properties of a fabricated W/p-lnP Schottky barrier diodes, it was found that these diodes exhibit the good rectification behaviour. The barrier height increases at 300 ^{o}C but decreases at 400 ^{o}C. The maximum barrier height is reached at 300^{o}C. The overall

surface morphology of the SBD does not change significantly at elevated temperatures [7]. The fabrication of Cp/p-type Si Schottky barrier diodes at various annealing temperatures from 200-600 °C shows that the barrier height fluctuates. It slightly decreases from 200-300 °C but it also increases from 400-600 °C [8]. During the study of Pd/ZnO Schottky barrier diodes with temperature, it was found that the ideality factor decreased with increasing temperature between 30-300 K while on the other hand the barrier height increased with increasing temperature [9].

The current-transport mechanism for the Au/Zn-doped PVA/n-GaAs Schottky barrier diodes shows that the ideality factor decreases while the Schottky barrier height increases for the investigated temperature dependency from 80-300 K [10]. The capacitance and conductance are strong functions of frequency and applied bias voltage. The conductance increases with increasing applied bias voltage while the capacitance decreases. The same happens with an increase in frequency [11]. The annealing temperature affect the electronic parameters and carrier transport mechanism of the Pt/n-type Ge Schottky diode. The diodes were annealed at temperatures between 183-303K and it was discovered that the zero-bias barrier height increased but the ideality factor decreased with increasing temperature [12]. The capacitance and conductance are strong functions of frequency and temperature. The capacitance and conductance for the Au/n-GaAs Schottky barrier diodes increases at low frequency [13]. The transport characteristics of Pd/epixial n-GaSb:Te Schottky barrier diodes were studied with current-voltage measurements between 80 and 300K. The barrier height and ideality factor apparently increased with decreasing temperature. SBDs have remarkable low and saturating reverse current-of the lowest ever reported for GaSb [14]. The Hall effect measurements show a decrease in carrier mobility as the hole concentration increases on a silicon doped GaSb. The study shows the decrease in inter-band gap energy of the semiconductor material. The thermal conductivities become very low due to a high thermal resistivity [15]. In the study, the electrical properties of the Fe^+ implanted n-GaSb were studied.

2. Experimental procedure

Fe^+ ions were implanted in the n-GaSb semiconductor samples using an ion implanter system. The Fe^+ implantation was conducted at different fluencies of 1.2×10^{15}, 1.2×10^{16} and 1.2×10^{17} ions.cm^{-2} at the energy of 90 keV. Raman spectra were measured by a Thermal micro-Raman system at room temperature for both non-implanted and implanted n-GaSb samples. The excitation was at 520 nm from a semiconductor diode laser. The electrical characterization of the SBDs fabricated on n-GaSb was performed by *I-V* at room temperature (300 K). The HP4141B pico Amp meter was used for *I-V* measurements. When measurements were performed, the voltage was varied from -0.5V to 0.5 V with the steps of 0.1 V. The *I-V* system measured the parameters including saturation current (Is), the ideality factor (n), the Schottky barrier height (Φ_b).

3. Results and Discussion

3.1. Raman Spectroscopy

Raman spectra of the un-implanted and the implanted GaSb samples at different fluencies of 1.2×10^{15}, 1.2×10^{16} and 1.2×10^{17} ions.cm^{-2} at the energy of 90 keV are discussed. Figure 1 shows the comparison of Raman spectra for un-implanted and Fe^+ implanted n-GaSb at different fluencies.

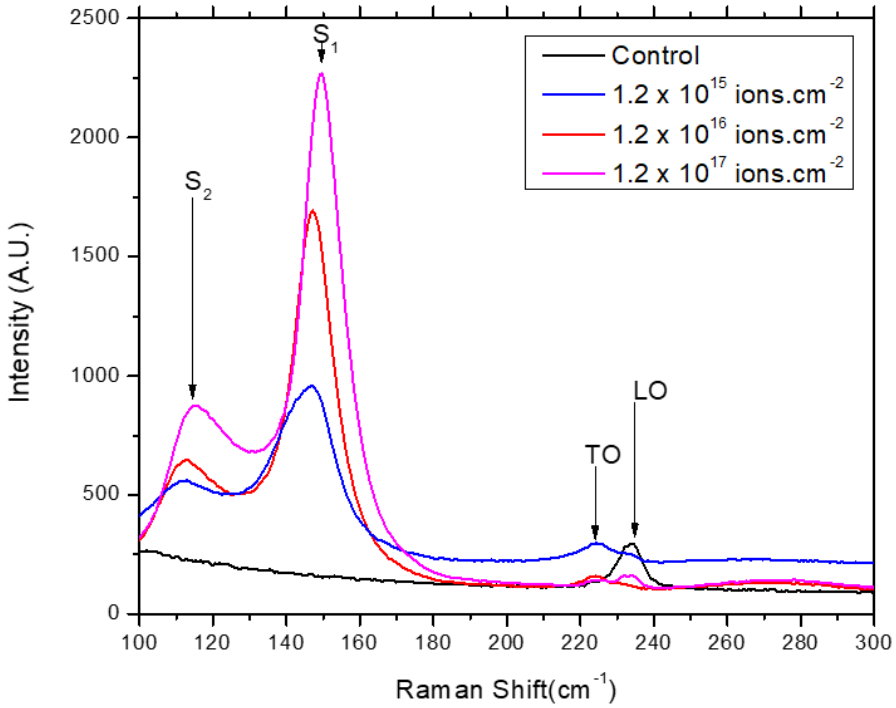

Figure 1. *Raman spectra for un-implanted and Fe^+ implanted n-GaSb at different fluences.*

The spectrum for the control sample shows a peak at 232.74 cm^{-1}. The peak correspond to the longitudinal optical (LO), which is an expected spectrum for the (100) plane [13]. In the sample implanted with 1.2×10^{15} Fe^+ ions.cm^{-2}, the LO phonons peak have been reduced and now a new peak emerges at 224.38 cm^{-1} which correspond to the Transverse optical (TO) phonons. In addition to the TO peak, new peaks were observed at 111.24 cm^{-1} (S_1) and 146.69 cm^{-1} (S_2). The reduction of LO phonons peak by ion implantation is associated with the disorder of crystalline structure of GaSb [16]. Nonetheless, the new peaks might be as a result of selective sputtering of Sb atoms during the ion implantation damage [17]. Regarding the sample implanted with 1.2×10^{16} Fe^+ ions.cm^{-2}, the LO phonons peak is not visible and the TO phonons peak is reduced and the new peaks are sharpening more. This might be due to ion implantation damage. For the sample implanted with 1.2×10^{16} Fe^+ ions.cm^{-2}, the LO phonons and TO phonons peaks have re-appeared but, however the new peaks are sharper. The comparison clearly illustrates the change in the structure of n-GaSb [16]. The change in the structure is due to the induced defects caused by Fe^+ ions. The GaSb is transformed into an amorphous state by Fe^+ implantation exceeding 1.2×10^{15} Fe^+ ions.cm^{-2}. This is also confirmed by [18].

3.2 I-V measurements

In this section, the *I-V* measurements of Al/n-GaSb Schottky barrier diodes (SBDs) at room temperature are presented. The current transport in the Schottky barrier diode is explained by majority carriers [6]. It may be described by thermionic emission (TE) mechanism over the interface barrier. The Schottky barrier height (ϕ_b) and the ideality factor (n) were determined by using the thermionic emission current voltage expression [19]:

$$I = I_s\left[\exp\left(\frac{q(V - IR_s}{nkT}\right) - 1\right]. \quad (1)$$

where

$$I_s = AT^2 A^* \exp\left(\frac{-q\phi_b}{kT}\right), \quad (2)$$

where, R_s is the series resistance of the diode, V is the applied voltage, q is the electronic charge, k is the Boltzmann constant, T is the absolute temperature, A is the area of the diode. A^* is the effective Richardson constant, ϕ_b is the effective barrier height at zero bias and n is the ideality factor. A theoretical value of A^* used was 5.16 A cm^{-2} K^{-2} for GaSb [20]. The values of the ideality factor were derived from the following equation 3

$$n = \frac{q}{kT}\left(\frac{dV}{d(\ln I)}\right). \quad (3)$$

$$\phi_b = \frac{kT}{q}\ln\left(\frac{AA^*T^2}{I_s}\right). \quad (4)$$

ϕ_b was determined using equation 4 above.

Figure 2 shows the semi-log plot of the forward and reverse current as a function of applied voltage. The graphs represent Al/n-GaSb Schottky barrier diodes for the non-implanted and implanted samples with a fluences of 1.2 × 10^{15}, 1.2 × 10^{16} and 1.2 × 10^{17} Fe$^+$ ions.cm^{-2}.

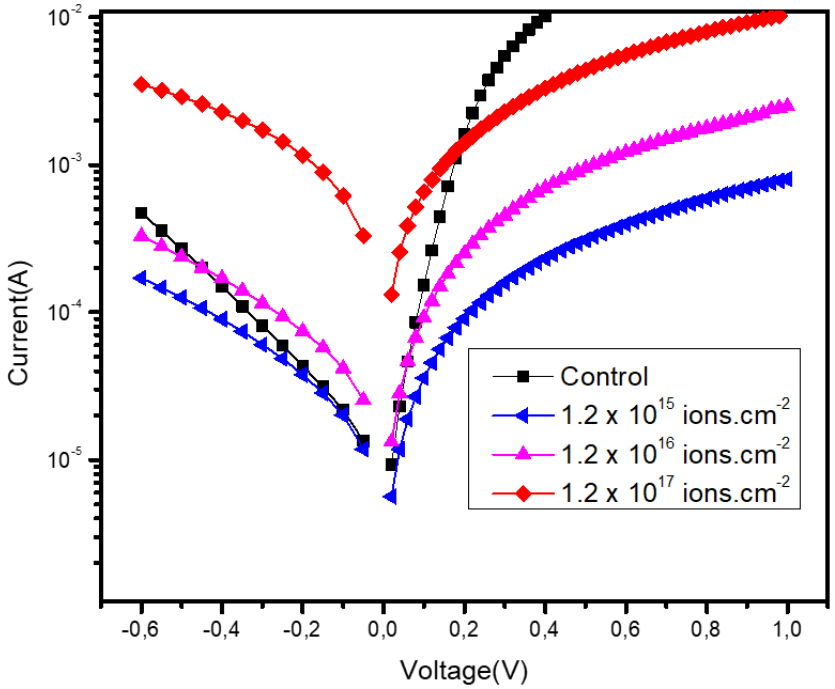

Figure 2: *The I-V characteristics of the un-implanted and implanted n-GaSb*

The as-deposited SBD showed good rectification properties which are attributed to the cleaning procedure used before deposition [21]. This curve shows two distinct linear regions as was also observed [21]. These regions are attributed by barrier height inhomogeneity; this is according to [9]. The Schottky barrier height evaluated on Al/n-GaSb was found to be 0.72 eV. This was higher than the 0.59 eV measured by [22], this might be due to the different material properties e.g. carrier concentration which is 10^{17}. The ideality factor was found to be 1.22 for the sample implanted with 1.2 × 10^{15} ion.cm^{-2}. The

ideality factor close to unity implies that the current transport is dominated by the thermionic emission mechanism [23]. It can be seen from the graphs that the gap between the forward and the reverse current decreases with an increase in the particle fluence. The curves deviate from linearity in the forward region which indicated that other current mechanisms contributes to the leakage current. These results show the evidence of generation-recombination current at low voltages and dominance of the thermionic emission at greater voltages [6]. Similar results were found by [24]. These SBDs are the same as the ones observed in Ge by [25]. The high ideality factor can be attributed to the surface damage by ion implantation.

The Schottky barrier height was observed to decrease with increasing the particle fluence, 0.73. 0.71 and 0,64 eV for particle fluence of 1.2×10^{15}, 1.2×10^{16} and 1.2×10^{17} ions/cm^2, respectively. The saturated current was increasing from 4.23×10^{-6} A to 1.05×10^{-4} A. The ideality factor decreased from 1.75 at 1.2×10^{15} to 1.64 at 1.2×10^{16} and then increased with the increasing particle fluence. This is consistent to the results that were found by [6].

4. Conclusion

This study was focused on the electrical properties of the n-GaSb semiconductor material. This semiconductor material was successfully implanted with Fe^+ ions at different ion fluencies while keeping the ion energy constant. These Fe^+ ions were implanted into the n-GaSb samples using a 350D ion implanter system. The Raman spectroscopy was used to check for the Raman activity. Raman spectroscopy showed that the material amorphized at fluences higher than 1.2×10^{15} ions.cm^{-2}. The aluminium Schottky contact as well as the gold-germanium ohmic contact have been successfully fabricated through electron beam deposition system on the front and the backsides of n-GaSb semiconductor material grown by LEC. All the samples including the implanted and non-implanted samples were analysed by *I-V* at room temperature. Generally, the barrier height decreased with the increasing implantation fluences while the ideality factor increased with the increasing implantation fluences.

Acknowledgements

This work was supported by National Research Foundation.

References

[1] Msimanga, M. McPherson, M. Theron C 2004 *Radiation Physics and Chemistry technology* **71** 2070-2073.
[2] Holland AD, Short ADT, Cross T 1994 *Nuclear Instruments and Methods Section A* **346** 366-371.
[3] Pitzl D, Cartiglia N, Hubbard B, Hutchinson D, Leslie J, O'Shaughnessy K, Rowe W, Sadrozinski HW, Seiden A, Spencer E, Ziock HJ, Ferguson P, Holzscheiter K, Sommer WF 1992 *Nuclear Instruments and Methods Section A* **311** 98-104.
[4] Jones BK, Santana J, McPherson M 1997 *Nuclear Instruments* and *Methods Section A* **395** 81-87.
[5] Keorperk E, Murray LM, Norton DT, Boggess TF, Prineas JP 2010 *Journal of Crystal Growth* **312** 185-191.
[6] Huang WC, Lin TC, Horng CT, Lin YH 2013 *Materials science and semiconductor processing* **16** 418.
[7] Reddy VR, Silpa DS, Hyung-Jong Y, Chel-Jong C 2014 *Superlattices and Microstructures* **71** 134-146.
[8] Guler G, Karastas S, Bakkaloglu OF 2009 *Physics B: Condensed Matter* **404** 1494-1497.
[9] Mayimele MA, Diale M, Mtangi W, Auret FD 2015 *Materials Science and Semiconductor Processing* **34** 359-364.

[10] Teamer H, Turut A, Uslu H, Altindal S, Uslu I 2013 *Sensors and Actuators A: Physical* **199** 194-201.
[11] Bilkan C, Gumus A, Altindal S 2015 *Materials Science and Semiconductor Processing* **39** 484-491.
[12] Guo E, Zeng Z, Zhang Y, Leng X, Zhou H 2016 Wang X, *Microelectronics Reliability* 63-69.
[13] Demirezen S, Ozavci E, Altindal S 2014 *Materials Science and Semiconductor Processing* **23** 1-6.
[14] Venter A, Murape DM, Botha JR, Auret FD 2015 *Thin Solid Films* **574** 32-37.
[15] Abroug S, Saadallah F, Genty F, Yacoubi N 2009 *Physics Procedia* **2** 787-795.
[16] Jadhav V, Dubey SK, Dubey RL, Yadav AD. Kanjilal D 2009 *Surface and Coatings* **203** 2670-2673
[17] Kim SG, Asahi H, Seta M, Takizawa J, Emura S, Soni RK, Gonda S, Tanoque H 1993 *Journal of Applied Physics* **74** 579.
[18] Morehead Jr FF, Crowder BL 1970 *Radiat. Eff.* **6** 27
[19] Rhoderick EH, Williams RH 1988 *Semiconductor Contacts*, 2nd ed. (Clarendon Press: Oxford).
[20] Liu ZY, Saulys DA, Kuecha 2004 *Appl. Phys. Letter* **85** 1023-1033.
[21] Ozavc E, Demirezen S, Aydemir U, Altndal S 2013 *Sensors and Actuators A: Physical* **194** 259-268.
[22] Ramelan AH, Harjana, Pepen A, Goldys E 2010 *J Mater Dan Sains*. **15** 136.
[23] Sze, SM 1998 *Physics of Semiconductor devices*, 1st ed. (New York: Wiley)
[24] Chen JF, Chen NC, Liu HS 1996 *J. Electronic materials* **25** 1790-1800.
[25] Coelho SMM, Auret FD, Janse van Rensburg PJ, Nele JM 2014 *Physica B: Condensed matter* **439** 97-100.

Magnetic properties and magnetocaloric effect of a distorted Kagomé lattice: $Gd_3Os_4Al_{12}$

R. Djoumessi Fobasso[1], B.N. Sahu[1], A.M. Strydom[1],

[1] *Highly Correlated Matter Research Group, Physics Department, University of Johannesburg, PO Box 524, Auckland Park 2006, South Africa*

E-mail: redrisse.djoumessi@aims-cameroon.org

Abstract. We report on the magnetic properties and magnetocaloric effect of a new distorted Kagomé lattice compound $Gd_3Os_4Al_{12}$. The temperature dependent dc-magnetic susceptibility ($\chi(T)$) reveals that the compound undergoes successive ferromagnetic and antiferromagnetic orderings below 30 K. The estimated effective magnetic moment from magnetic susceptibility confirmed that the 4f-shell fully contributes to the magnetic properties. The obtained positive paramagnetic Weiss temperature indicates the presence of strong ferromagnetic interactions. The isothermal magnetic entropy change was evaluated from the magnetization isotherms and yielded a value of 4.6 J/kg-K at 9 T.

1. Introduction

Magnetocaloric effect is an interesting topic in the physics of rare-earth based magnetic compound due to the application in refrigeration and the environmental friendly application of materials with large magnetocaloric effect (MCE). Gadolinium (Gd) and Gd-based compounds have drawn particular attention on this regard, because Gd - itself shows a large MCE around room temperature. Typically, a good MCE material has large isothermal magnetic entropy change, adiabatic temperature change and cooling power close to a magnetic phase transition temperature. It is also proposed that emerging large MCE can be obtained in some magnetically frustrated systems [1, 2]. In these latter systems, the magnetic spin type of ordering is frustrated due to aspects of symmetries in the lattice. The system is unable to satisfy all the pairwise interactions simultaneously. In a certain class of frustrated system, the rare-earth atom form distorted Kagomé nets and triangles. For this purpose, we have synthesized a Gd - based distorted Kagomé lattice compound namely $Gd_3Os_4Al_{12}$ which was first reported by J. Niermann and W. Jeitschko in 2002 [3]. The magnetic properties and magnetocaloric effect were investigated using dc-magnetization measurements and the results are reported in details.

2. Synthesis and Experimental Details

A polycrystalline sample was synthesized by arc-melting stoichiometric amounts of high - purity (99.99 mass % purity or better) elements (Gd, Os and Al) under argon atmosphere in an Edmund Buhler arc-melting furnace. The Rietveld refinement of the powder x-ray diffraction pattern indicated that the compound crystallizes in the $Gd_3Ru_4Al_{12}$ type hexagonal structure with space group $P6_3/mmc$ (not shown in this paper). DC-magnetic susceptibility and isothermal magnetization measurements were performed using a commercial Dynacool physical properties

measurement system from Quantum Design, USA. The measurement was carried out in the temperature range between 1.8 K to 300 K and fields upto a maximum value of 9 T.

3. Results and Discussion

Figure 1 shows the dc-magnetic susceptibility as function of temperature (left axis). The data was obtained during the cooling process from 300 K to 1.8 K under a magnetic field of 0.1 T. As seen in the inset of figure 1, the compound exhibits two magnetic phase transitions at approximately 6 K and 18 K and is marked by arrows in the inset. It is also observed that the $\chi(T)$ has another transition around 150 K. Further investigation is required to find the details for that transition at high temperatures.

The inverse of $\chi(T)$ is plotted and shown on the right axis. As seen from the same figure, the high-temperature region T > 200 K is followed by the Curie-Weiss law, which is given by: $\chi = N_A\mu_{eff}^2/3k_B(T-\theta_P)$ where N_A and k_B are respectively the Avogadro number and Boltzmann constant. The fitting is shown as a black line on the $\chi^{-1}(T)$ data. The least-squares fit yields an effective magnetic moment $\mu_{eff} = 8.0\ \mu_B/Gd^{3+}$. This results indicate that the 4f-shell of Gd^{3+} is fully contributing towards the magnetic state of this compound. The positive sign of the paramagnetic Curie temperature $\theta_P = 60$ K suggests the presence of dominant ferromagnetic exchange interactions in the paramagnetic region. A strong deviation from the high-T Curie-Weiss behavior is observed at about 200 K as the temperature is lowered. This is due to the gradual presence of short-range correlations.

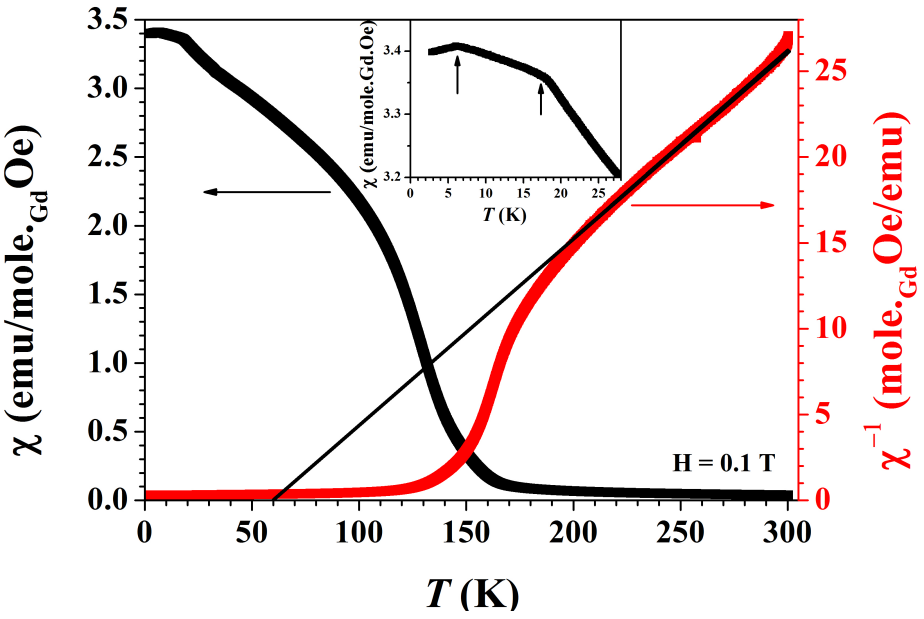

Figure 1. Left axis: temperature dependence of dc-magnetic susceptibility of $Gd_3Os_4Al_{12}$ in the temperature range 1.8 K - 300 K measured in a magnetic field of 0.1 T. Right axis: the inverse magnetic susceptibility of $Gd_3Os_4Al_{12}$. The black solid line represents the Curie-Weiss fit as described in the text.

 ISBN: 978-0-620-88875-2

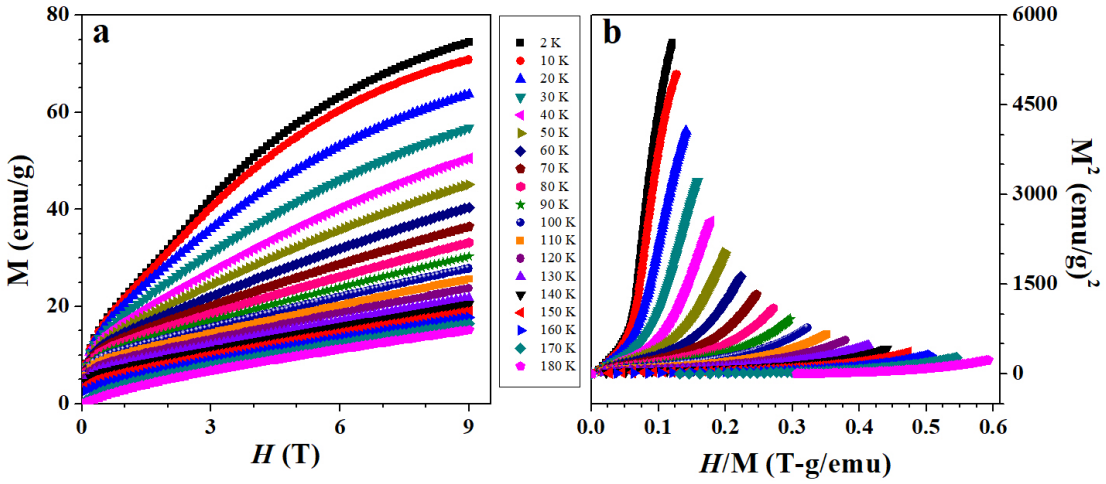

Figure 2. **a**) Isothermal magnetization curves of $Gd_3Os_4Al_{12}$ as function of magnetic field measured at selected temperatures up to 180 K. **b**) Standard Arrott - plots of isotherms corresponding to those in (a).

To further investigate the magnetic behavior of the compound, the isothermal magnetization measurements were performed from 2 K to 180 K in fields up to 9 T and is shown in figure 2**a**. As seen from the figure, the magnetization curves below 20 K have a tendency to saturate in high magnetic fields. The obtained magnetic moment reaches approximately 7.0 μ_B/Gd^{3+} at 2 K for 9 T, which is equal to the saturation magnetic moment of Gd^{3+}. This indicates that the magnetic moments of Gd^{3+} are nearly fully aligned parallel to the applied field. Arrott plots (M^2 *vs.* H/M) were derived from the magnetization isotherm curves to find the order of magnetic phase transitions. According to the Banarjee criterion [4]; a positive slope in the M^2 *vs.* H/M plots indicates second order magnetic phase transition, whereas, negative slope represents first order magnetic phase transition. In this case, positive slopes are observed (see figure 2**b**) meaning that the transition in this compound is of second order.

The isothermal magnetic entropy change ($-\Delta S_M$) was estimated from the isothermal magnetization curve using the Maxwell relation [5]; $\Delta S(T,H) = \int_0^H (\partial M/\partial T)_H dH$, where H is the applied magnetic field. Figure 3 shows the $-\Delta S_M$ changes as function of temperature for different magnetic fields. The maximum value of $-\Delta S_M$ is 4.6 J/kg-K for the change of field 9 T around 20 K. Another important factor is the refrigeration capacity (RC), which measure the amount of heat transfer between the cold and hot reservoir in an ideal refrigerator cycle [6, 7]. This RC value was calculated by integrating the area under the curve of $-\Delta S_M$ *vs.* T using the formula RC = $\int_{T_1}^{T_2}(-\Delta S_M)dT$, where T_1 and T_2 are the temperature corresponding to the left and right side at the half-maximum value of $-\Delta S_M$ respectively [8]. The obtained value of RC for a field change of 9 T is 177.804 J/kg. These obtained results are relatively small in comparison with other Gd-based ternary compounds [9, 10, 11].

 ISBN: 978-0-620-88875-2

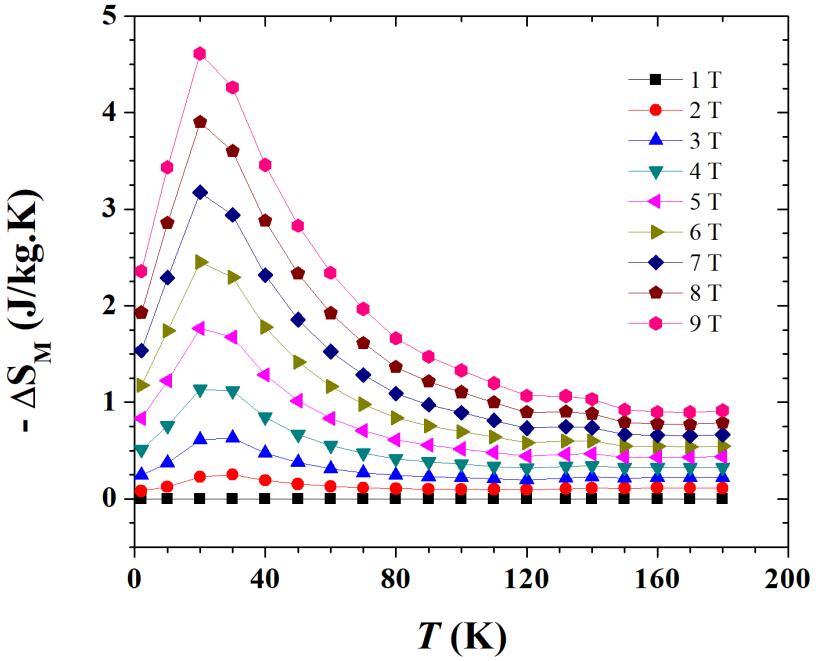

Figure 3. Temperature dependence of the isothermal entropy changes measured in fields up to 9 T as described in the text.

4. Conclusion

In summary, the magnetic properties and magnetocaloric effect of the compound $Gd_3Os_4Al_{12}$ have been studied experimentally. The initial magnetic study revealed that it possesses two magnetic transitions below 30 K and another transition above 150 K more likely being a structural transition. The Arrott - plots of magnetization suggest that the transition is of second order. The magnetocaloric effect of this compound shows a relatively small value of $-\Delta S_M = 4.6$ J/kg-K for a change of field 9 T compared to other Gd compounds [11, 12] with comparable values to profitable magnetic refrigerant materials. As the structure is likely to be subject to geometrical frustration, further investigations on this compound may lead to a better understanding of distorted Kagomé lattice and frustrated magnetism.

Acknowledgements

DFR thanks OWSD and SIDA for the fellowship towards PhD studies. B. Sahu thanks the UJ-GES, University of Johannesburg, South Africa for the postdoctoral fellowship. AMS thanks the URC/FRC of UJ for financial assistance.

References

[1] Zhitomirsky M 2003 *Physical Review B* **67** 104421
[2] Schnack J, Schmidt R and Richter J 2007 *Physical Review B* **76** 054413
[3] Niermann J and Jeitschko W 2002 *Zeitschrift für anorganische und allgemeine Chemie* **628** 2549–2556
[4] Banerjee B 1964 *Physics Letters* **12** 16–17
[5] Pecharsky V and Gschneidner Jr K 1999 *Journal of Applied Physics* **86** 565–575
[6] Gschneidner Jr K and Pecharsky V K 2000 *Annual Review of Materials Science* **30** 387–429
[7] Tishin A M and Spichkin Y I 2016 *The magnetocaloric effect and its applications* (CRC Press)
[8] Pecharsky V and Gschneidner Jr K 2001 *Journal of Applied Physics* **90** 4614–4622

[9] Kumar P, Singh N K, Suresh K and Nigam A 2008 *Physical Review B* **77** 184411
[10] Yang Y, Zhang Y, Xu X, Geng S, Hou L, Li X, Ren Z and Wilde G 2017 *Journal of Alloys and Compounds* **692** 665–669
[11] Kumar K, Nair H, Sahu B, Xhakaza S and Strydom A 2018 *Europhysics Letters* **122** 17003
[12] Pakhira S, Mazumdar C, Ranganathan R, Giri S and Avdeev M 2016 *Physical Review B* **94** 104414

Large magnetocaloric effect in Dy_2NiSi_3

Jean J Mboukam, Baidyanath Sahu, André M Strydom

Highly Correlated Matter Research Group, Physics Department, University of Johannesburg, PO Box 524, Auckland Park 2006, South Africa

E-mail: jules.mboukam@gmail.com

Abstract. The intermetallic ternary compound Dy_2NiSi_3 crystallizes in the AlB_2 type of hexagonal structure with the space group P6/mmm. The magnetic properties were studied by measuring magnetization as a function of temperature, and magnetic field and heat capacity ($C_p(T)$) in magnetic fields up to 7 T. Temperature dependent magnetization and heat capacity results revealed that Dy_2NiSi_3 shows an antiferromagnetic (AFM) ordering with Néel temperature at 5.9 K. Below the magnetic phase transition, $C_p(T)$ data is described by a spin wave spectrum with an energy gap of $\Delta = E/k_B = 1.96(4)$ K. The magnetocaloric effect (MCE) of the compound has been evaluated from heat capacity measurements and maximum values of magnetic entropy change and adiabatic temperature change are found to be 20.3 J/kg.K and 11.3 K respectively for a field change up to 7 T.

1. Introduction

Rare-earth based intermetallic compounds are attractive due to their novel magnetic properties such as: magnetocrystalline anisotropy and metamagnetism, spin-glass, heavy fermion behaviour, magnetoresistance effect, and magnetocaloric effect (MCE). In particular, there is great interest on the topic of MCE for magnetic refrigeration. MCE has advantages for environmental-friendly, energy-generation features [1, 2], which can replace the traditional vapour compressor technology and carbon-based fuels in the future. MCE is defined as the isothermal entropy change ($-\Delta S_M$) or adiabatic temperature change ($\Delta T_{\rm ad}$) of magnetic materials upon application of a magnetic field. MCE is a magneto-thermodynamic phenomenon which is observed in practically all magnetic materials when the material is cooled down sufficiently under magnetic field. RE_2NiSi_3 (where RE stands for rare-earth elements) compounds crystallize in the hexagonal AlB_2-type structure. One of the interesting features in these compounds is the co-existence of long-range AFM ordering and magnetically frustrated spin-glass behaviours [3, 4, 5, 6]. Beside these behaviours, several members in this system exhibit large MCE over a wide temperature range due to spin fluctuation [6, 7]. It is also reported that the MCE of RE_2NiSi_3 compounds may become enhanced in a defect structure [6].

In this work, single-phase sample material of polycrystalline Dy_2NiSi_3 was prepared. The magnetic properties, specific heat and MCE derived from calorimetric measurements of the compound have been systematically studied.

2. Experimental Details

Polycrystalline Dy_2NiSi_3 was prepared under high purity argon gas by a standard arc-furnace melting technique using stoichiometric amounts of high purity elements of Dy (99.99%), Ni

(99.999%) and Si (99.99%). The sample was turned over and remelted several times in order to ensure homogeneity. The sample was then wrapped in a tantalum foil and encapsulated in an evacuated quartz tube under 6.3 $\times 10^{-6}$ mbar pressure. The ingot was then heat treated at 1123 K for 7 days in a Carbolite box furnace followed by room-temperature water quenching. Powder x-ray diffraction measurements were carried out at room temperature using a Rigaku diffractometer employing the CuKα_1 radiation (λ = 1.540598 Å). Structural and phase purity analyses were confirmed by refinement of the powder x-ray diffraction patterns using the FullProf programme [8]. Temperature dependent dc-magnetic susceptibility was measured using a commercial Dynacool Physical Property Measurement System from Quantum Design (San Diego) with a vibrating sample magnetometer from 1.8 K to 50 K in applied magnetic field of 0.1 T. The heat capacity measurements were carried out in the temperature range between 1.8 K to 20 K in different fields of 0, 1, 3, 5 and 7 T using the same Dynacool PPMS system.

3. Results and discussion

The XRD-pattern of Dy_2NiSi_3 measured at room temperature is shown in Fig. 1 along with the Rietveld least-square refinement. All the diffraction peaks can be indexed in the hexagonal AlB_2-type structure with space group $P6/mmm$ (No. 191). In this refinement, the Dy (blue balls) atoms occupy the crystallographic 1a position while Ni and Si (red and white balls, respectivelly) atoms share the 2d site (see inset of Fig. 1). This was as also reported in [9]. The obtained refinement was clear with no impurity phase detectable on the patterns as shown in Fig. 1. The obtained lattice parameters and unit cell volume are: a = 3.9607(2) Å, c = 4.0258(3) Å and V = 54.69(2) Å^3, respectively. These values are in agreement with the previous study [10].

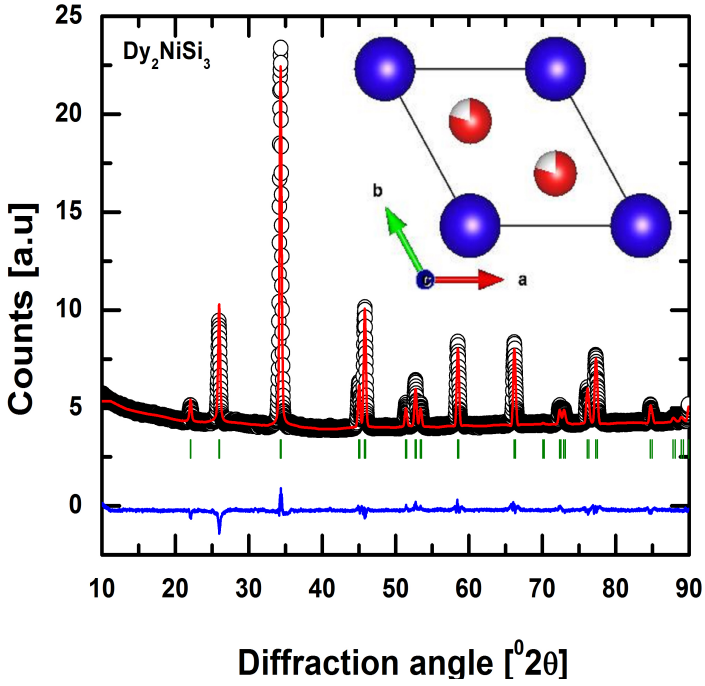

Figure 1: (Color online) The X-ray diffraction pattern (black symbols) of Dy_2NiSi_3 collected at room temperature and its Rietveld refinement (red curve). The bottom blue curve represents the difference between the experimental and calculated patterns. The vertical (green) ticks represent the calculated Bragg's reflection positions. The inset shows the crystal structure of Dy_2NiSi_3 with Dy, Ni and Si atoms at their crystallographic positions.

 ISBN: 978-0-620-88875-2

Fig. 2a shows the temperature dependence of dc-magnetic susceptibility, $\chi(T)$ (left axis) and inverse dc-magnetic susceptibility, $\chi^{-1}(T)$ (right axis) of Dy_2NiSi_3 compound measured from 1.8 K - 50 K under an applied magnetic field of 0.1 T. $\chi(T)$ data of Dy_2NiSi_3 displays a phase transition at around $T_N = 5.9$ K as indicating by the arrow, probably of AFM origin. Above the magnetic transition, $\chi^{-1}(T)$ data are linear in temperature and follow the Curie-Weiss relation:

$$\chi^{-1} = \frac{3k_B(T - \theta_P)}{N_A \mu_{eff}^2}, \tag{1}$$

where k_B and N_A are respectively the Boltzmann and Avogadro constant, θ_P is the paramagnetic Weiss temperature and μ_{eff} is the effective magnetic moment. The black line on $\chi^{-1}(T)$ data represents the least-square fit using Eq.1. This yielded $\theta_P = -0.81(1)$ K and $\mu_{eff} = 10.46(2)$ μ_B. The obtained μ_{eff} is very close to that expected for the free trivalent Dy ion (10.63 μ_B). The negative θ_P hints to an AFM exchange interactions. In Fig. 2b, the magnetization, $M(\mu_0 H)$ (blue symbols) measured at 2 K for field change up to 7 T shows a linear behaviour up to the critical field $\mu_0 H_{meta} = 0.8$ T where a weak field-induced metamagnetic transition occurs, and a tendency of saturation at high field. These can be connected to a complex (metamagnetic interactions) and or multiple type of interactions such as ferromagnetic (FM) and AFM interactions in the compound. Such type of analysis has also been performed on other reported compounds [9, 11, 12, 13]. The critical field ($\mu_0 H_{met}$) was estimated from the derivative of $dM(\mu_0 H)/dH$ and was taken at its maximum (see black symbols) as shown by the arrow. In order to study the nature of the magnetic phase transition, Arrott plots for the mean field model were made as shown in Fig. 2c. According to Banerjee's criterion, the negative slopes (see inset Fig. 2c) observed in low magnetic field and below T_N indicate the first order nature of the magnetic transition, whereas the positive slopes correspond to a second order magnetic phase transition [14].

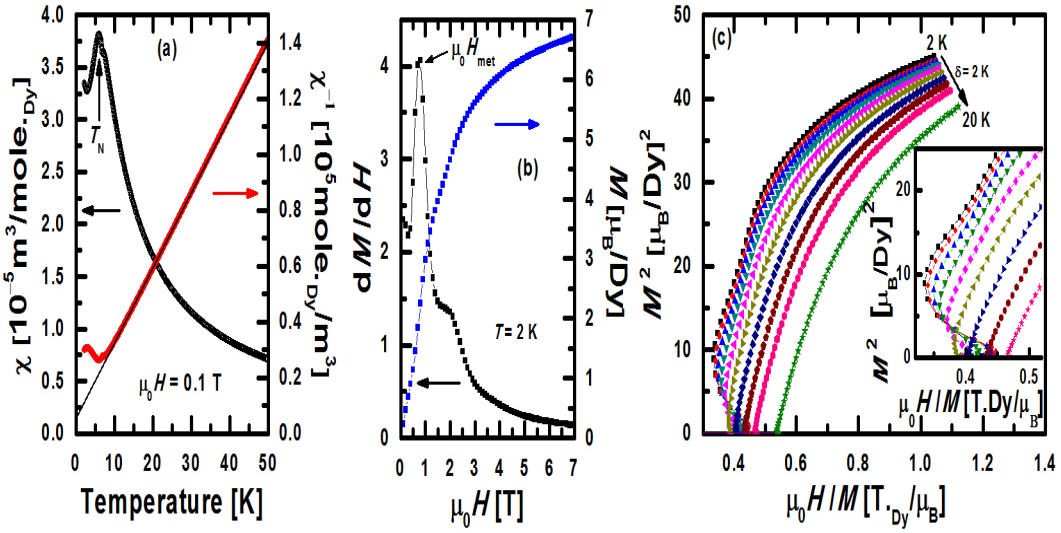

Figure 2: (a) Temperature dependence of the magnetic susceptibility of Dy_2NiSi_3 measured from 1.8 K - 50 K under an applied magnetic field of 0.1 T (left axis). Plot on the right hand axis shows the inverse magnetic susceptibility with the Curie-Weiss fit (black line) as described in the text. (b) Magnetization data measured at 2 K (blue symbols) along with dM/dH (black symbols). (c) Arrott plots for the mean field theory measured in the temperature range 2 K - 20 K in step of 2 K. The inset shows an expanded view of M^2 versus $\mu_0 H/M$.

The heat capacity of Dy_2NiSi_3 as a function of temperature measured in different magnetic fields of 0, 1 3, 5, and 7 T are shown in Fig. 3a and Fig. 3b, respectively. As seen in Fig. 3a,

$C_{\rm p}(T)$ data at 0 T show a peak that is plausibly associated with an AFM phase transition at $T_N = 5.9$ K. The obtained transition temperature is in agreement with T_N obtained from $\chi(T)$ measurements (see section **??**). This peak indicates the presence of long-range magnetic order, similar to that observed for the other reported compounds [6, 15, 16, 17]. The ordered region ($T<T_N$) of $C_p(T)$ is described by the AFM spin wave spectrum, which was fitted (see line in Fig. 3a) using the expression [18]:

$$C_{\rm p}(T) = \gamma_{AFM} T + BT^3 exp\left(-\frac{\Delta}{T}\right), \tag{2}$$

which takes into account the magnon contribution described by an energy gap ($\Delta = E/k_B$, where E is the energy). B is a constant. The fit yielded the values of the Sommerfeld coefficient γ_{AFM} = 1.39(5) J/mole.$_{\rm Dy}$.K^2, B = 0.055(5) J/mole.$_{\rm Dy}$.K^4 and Δ = 1.96(4) K. As seen in Fig. 3b, an increasing of magnetic field gradually suppresses T_N, which shifts toward low-temperatures as expected for AFM materials.

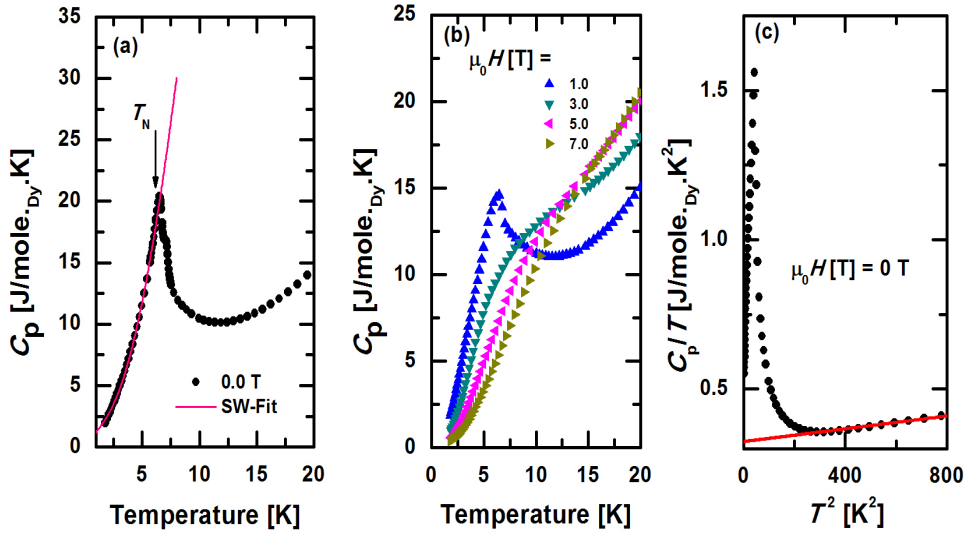

Figure 3: Temperature variation of $C_{\rm p}(T)$, of Dy_2NiSi_3 measured (a) in 0 T and (b) in different applied magnetic field of 1, 3, 5 and 7 T, where the arrow indicated the position of T_N. (c) Shows the linear dependence of $C_{\rm p}(T)/T$ versus T^2 in the paramagnetic region, above $\sim$ 20 K.

Fig. 3c shows $C_p(T)/T$ versus T^2 with a linear dependence in the paramagnetic region ($T>T_N$), indicating the electronic contribution to the heat capacity. The red curve is the least-square fit using the expression:

$$C_{\rm p}(T)/T = \gamma_P + \beta T^2. \tag{3}$$

The obtained values from the fit are: γ_P = 0.32(3) J/mole.$_{\rm Dy}$.K^2, $\beta = 1.07 \times 10^{-4}(5)$ J/mole.$_{\rm Dy}$.K^2 and $\theta_{\rm D}$ = 224.73 K derived from $\theta_D = (12\pi^4 nR/5\beta)^{1/3}$, where n and R in this latter equation represent the number of atoms ($n = 6$) per formula unit and the gas constant, respectively. The greater value of the Sommerfeld coefficient γ_{AFM} in the AFM region which is about 4 times greater than γ_P may be due to the electron-electron interactions when the 4f spins engage in AFM order below T_N.

In order to investigate the MCE properties from the calorimetric measurements of Dy_2NiSi_3, $C_{\rm p}(T)$ was measured at different magnetic fields up to 7 T. MCE refers to a change of the

magnetic entropy $(-\Delta S)$ induced by an applied field that can be evaluated from $C_{\rm p}(T)$ using the Maxwell thermodynamic relationship [1]:

$$\Delta S(T, \mu_0 H) = \int_0^T \left(\frac{C_{\rm p}(T')_{\mu_0 H} - C_{\rm p}(T')_0}{T'} \right) d(T'), \tag{4}$$

where $C_{\rm p}(T)_{\mu_0 H}$ and $C_{\rm p}(T)_0$ represent the heat capacity measured at applied and zero magnetic field respectively.

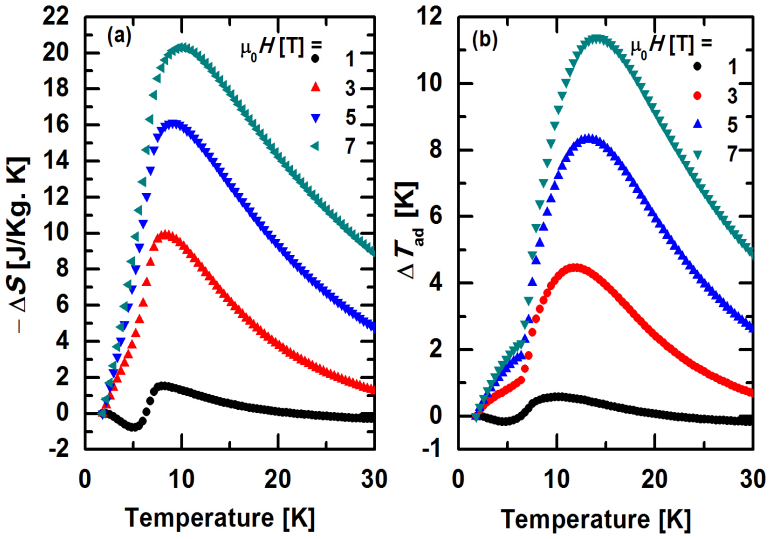

Figure 4: (a) Temperature dependencies of the entropy change $-\Delta S(T)$ calculated in fields of 0, 1, 3, 5 and 7 T, together with their respective adiabatic temperature change $\Delta T_{\rm ad}$ in (b).

Fig. 4a displays $-\Delta S(T)$ of Dy_2NiSi_3 as a function of temperature for different applied magnetic field changes up to 7 T. This was calculated using Eq. 4. It is clearly seen that relatively small negative $-\Delta S(T)$ values are observed below T_N for low magnetic field change. This is in agreement with field-induced metamagnetic behaviour [19, 20]. The obtained maximum values of $-\Delta S(T)$ evaluated using Eq.4 are 1.8, 10.1, 16.02 and 20.3 J/kg.K at $T = 5.9$ K, for fields change of 1, 3, 5 and 7 T, respectively. $-\Delta S(T)$ obtained at 7 T for this compound is higher than those of various promising magnetic refrigerant materials [13, 21, 22, 23, 24] and very close to that obtained from the isothermal magnetization studies in a defect structure of the same compound [9].

Another important factor for good refrigerant materials is the adiabatic temperature change $(\Delta T_{ad}(T))$ defined as:

$$\Delta T_{\rm ad} = [T(S, \mu_0 H) - T(S, 0)]_S \,, \tag{5}$$

where $T(S, \mu_0 H)$ and $T(S, 0)$ denote the temperature at applied and zero magnetic field for the particular $-\Delta S^{max}(T)$, respectively. The value of $\Delta T_{\rm ad}(T)$ was evaluated using $-\Delta S(T, \mu_0 H)$ and zero field heat capacity data. Fig. 4b displays the adiabatic temperature change $\Delta T_{ad}(T)$ for Dy_2NiSi_3. The obtained maximum value of $\Delta T_{\rm ad}(T)$ is 11.3 K for Dy_2NiSi_3 under a field change of 7 T. Even for a low field change of 5 T, $\Delta T_{\rm ad}(T)$ is 8.3 K, which is beneficial for application purpose. This value is comparable to the one of his counterpart metamagnetic $Ho_2Ni_{0.93}Si_{2.93}$ material obtained at 7 T [11] and other good magnetic materials [25, 26]. The nature of $\Delta T_{\rm ad}(T)$

 ISBN: 978-0-620-88875-2

is almost similar to $-\Delta S(T)$. Large positive values of $-\Delta S(T)$ and $\Delta T_{\rm ad}(T)$ are also observed above a field change of 1 T. This is due to the field induced first order metamagnetic transition as it was also reported in other metamagnetic compounds [9, 11, 12, 26].

4. Summary

A synthesized polycrystalline compound of Dy_2NiSi_3 was found to crystallize with the hexagonal AlB_2 type structure with the space group P6/mmm. The compound exhibits a first order nature of the magnetic phase transition as confirmed in an Arrott plots construction. The ordered region of $C_p(T)$ is characterized by a spin wave spectrum with an energy gap, $\Delta = 1.96(4)$ K. $-\Delta S(T)$ and $\Delta T_{\rm ad}$ measured from the heat capacity measurements reach the values of 20.3 J/kg.K and 11.3 K, respectively for a field change of 7 T. These obtained values are higher or similar to the same isostructural systems, RE_2CuSi_3 with RE = Pr and Gd [25] and in defect crystal structure $Tm_2Ni_{0.93}Si_{2.93}$ [26]. The obtained MCE values can classify Dy_2NiSi_3 amongst promising candidates for magnetic refrigerants.

Acknowledgments

AMS thanks the FRC/URC of UJ and the National Research Foundation (NRF) for financial support. Baidyanath Sahu thanks the UJ-GES postdoctoral fellowship for the support.

References

[1] Tishin AM, Spichkin YI, *The magnetocaloric effect and its application*. Eds. Coey JMD, Tilley DR, Vij DR (Institute of Physics Publishing, Bristol, 2003)
[2] Gschneidner Jr KA, Pecharsky VK, Tsokol AO, 2005 Rep. *Prog. Phys.* **68** 1479
[3] Li DX, Nimori S, Yamamura T, Shiokawa Y, 2008 *J. Appl. Phys.* **103** 07B715
[4] Pan ZY, Cao CD, Bai XJ, Song RB, Zheng JB, Duan LB, 2013 *Chinese Phys. B.* **22** 056102
[5] Hwang JS, Lin KJ, Tien C, 1996 *Solid State Commun.* **169** 100
[6] Pakhira S, Mazumdar C, Ranganathan R, Giri S, 2016 *Phys. Rev.* B. **94** 104414
[7] Zhitomirsky ME, 2003 *Phys. Rev.* B. **67** 104421
[8] Roisnel T, Rodrquez-Carvajal J, 1999 *Mater. Sci. Forum* 2001 **378** 118
[9] Pakhira S, Mazumdar C, Choudhury D, Ranganathan R, Giri, 2018 *Phys. Chem. Chem. Phys.* B. **20** 13580
[10] Chen X, Zhuang Y, 2016 *Phase Transit.* **90** 742
[11] Pakhira S, Mazumdar C, Ranganathan R, Avdeev M, 2017 *Sci. Rep.* **7** 7367
[12] Mboukam JJ, Tchoula Tchokonte MT, Bashir AK, Sondezi BM, Sahu BN, Strydom AM, Kaczorowski D, 2020 *J. Alloys Compd.* **814** 152228
[13] Samanta T, Das I, Banerjee S, 2007 *Appl. Phys. Lett.* **91** 152506
[14] Banerjee SK, 1964 *Phys. Lett.* **12** 16
[15] Tien C, Fen CH, Wur CS, Lu JJ, 2000 *Phys. Rev.* B. **61** 12151
[16] Jona YM, Sakai O, Higashinaka R, Fukazawa, H, Maeno Y, Dasgupta P, Ghosh D, 2003 *Phys. Rev.* B. **68** 174413
[17] Anand VK, Adroja DT, Hillier AD, Taylor J, Andre G, 2011 *Phys. Rev.* B. **84** 064440
[18] Tari A *The specific heat of matter at low temperatures*. (Imperial College Press, 2003)
[19] Alho BP, Nbrega EP, De Sousa VS, Carvalho AM, De Oliveira NA, Von Ranke PJ, 2011 *J. Appl. Phys.* **109** 083942.
[20] Wang YX, Zhang H, Wu ML, Tao K, Li YW, Yan T, Long KW, Long T, Pang Z, Long Y, 2016 *Chin. Phys. B.* **25** 127104
[21] Hu WJ, Du J, Li B, Zhang Q, Zhang ZG T, Das I, Banerjee S, 2008 *Appl. Phys. Lett.* **92** 192505
[22] Gupta S, Rawat R, Suresh KG, 2014 *Appl. Phys. Lett.* **105** 012403
[23] Mboukam JJ, Sondezi BM, Tchoula Tchokonte MB, Bashir AKH, Strydom AM, Britz D, Kaczorowski D, 2018 *Physica B.* **536** 505
[24] Tchoula Tchokonte MB, Mboukam JJ, Bashir AKH, Sondezi BM, Ramesh Kumar K, Strydom AM, Kaczorowski D, 2018 *Physica B.* **753** 41
[25] Wang F, Yuan FY, Wang JZ, Feng TF, Hu GQ, 2014 *J. Alloys Compd.* **592** 63
[26] Pakhira S, Mazumdar C, Ranganathan R, 2017 *J. Phys. Condens. Matter* **29** 505801

Structural stability and electronic properties of bulk, bilayer and monolayer PtX_2 (X = Se and Te)

Hamza A H Mohammed[1,2*], G M Dongho-Nguimdo[3] and Daniel P Joubert[1]

[1]The National Institute for Theoretical Physics, School of Physics and Mandelstam Institute for Theoretical Physics, University of the Witwatersrand, Johannesburg, Wits 2050, South Africa.
[2]Department of Physics, Shendi University, Shendi, Sudan
[3]College of Science, Engineering and Technology, University of South Africa, P.O. Box 392, UNISA 0003 Pretoria, South Africa

E-mail: hamzad00@gmail.com

Abstract. Using first-principles density functional theory, we investigate the structural, stability and electronic properties of the layered bulk, bilayer and monolayer platinum dichalcogenides $PtSe_2$ and $PtTe_2$ compounds in the CdI_2 structure. Our calculations confirm that these compounds are mechanically and dynamically stable. Band structure calculations show that bilayer and monolayer $PtSe_2$ and $PtTe_2$ are indirect band gap semiconductors whereas the bulk structures are semi-metal. The calculated band structure and density of states show that the band gaps decrease when the number of layers increases, which allows band gap engineering for optimal photovoltaic applications.

1. Introduction

Conducting research on clean and renewable energy sources has become necessary nowadays because of concerns about depleting reserves of fossil fuels and environmental pollution. Three-dimensional (3D) and two-dimensional (2D) transition metal dichalcogenides (TMDs) are potential materials for applications in energy conversion devices [1, 2, 3]. Few and multi-layer TMDs are promising as solar energy absorbers since the variation in band gap with the number of layers allows band gap engineering. Monolayer $PtSe_2$ is a semiconductor with a measured band gap of 1.22 eV [4, 5]. Yim C. *et al* [6] demonstrated that multilayer $PtSe_2$ is easy to synthesize and showed that vertically stacked heterostructures of $PtSe_2$ on Si can be used as photodiodes and in photovoltaic cells. The electronic structure of monolayer and bilayer $PtSe_2$ has been calculated using the Perdew-Burke-Ernzerhof (PBE) exchange-correlation approximation with density functional band (DFT) gaps of 1.39 and 0.99 eV for $PtSe_2$ and $PtTe_2$, respectively [7]. Experimental measurements confirm that bulk $PtSe_2$ and $PtTe_2$ are semi-metal [8], while monolayer and bilayer structures are semiconductors with a band gaps of 1.2 eV and 0.21 eV, respectively [4]. Phonon dispersion and electronic properties of bulk, monolayer, and bilayer $PtSe_2$, were also calculated using DFT with the Tkatchenko and Scheffler van der Waal's correction (DFT-TS) [9], that confirmed that the bulk is semi-metallic while monolayer and bilayer configurations are semiconductors with an indirect band gap of $\sim$1.6 eV and $\sim$0.8 eV, respectively. The investigation of electronic and transport properties for monolayer $PtSe_2$ and $PtTe_2$

reported in reference [10] suggest that these compounds have promising properties for thermoelectric applications.
In this study, we investigated the structural, mechanical and dynamical stability and electronic properties of bulk, bilayer, and monolayer $PtTe_2$ and $PtSe_2$. The results showed that the two compounds are stable, and that the band gap increases as the number of layers decreases

2. Computational details

The calculations were performed using Density Functional Theory (DFT), with the projector-augmented wave (PAW) pseudopotential approach as implemented in the VASP package [11, 12]. The generalized gradient approximation (GGA) of Perdew-Burke-Ernzerhof (PBE) [13] was used as an exchange-correlation approximation. We performed calculations using converged an energy cutoff of 520 eV for bulk and 350 eV for bilayer and monolayer calculations. We set a vacuum of 15 Å between the periodically repeated layers in the z direction for the monolayer and bilayer system. The self-consistent total energies were converged to 1.0×10^{-8} eV/atom and the residual forces per atom were less than 1m eV/Å. For the integration over the Brillouin zone, a Γ-centred Monkhorst-pack grid [14] of 8×8×6 for bulk and 12×12×1 for the single and double layer were found to be sufficient. A 3×3×3 supercell for bulk and 5×5×1 bilayer and monolayer were used for displacive phonon calculations [15].

3. Results and discussions

3.1. Structural parameters

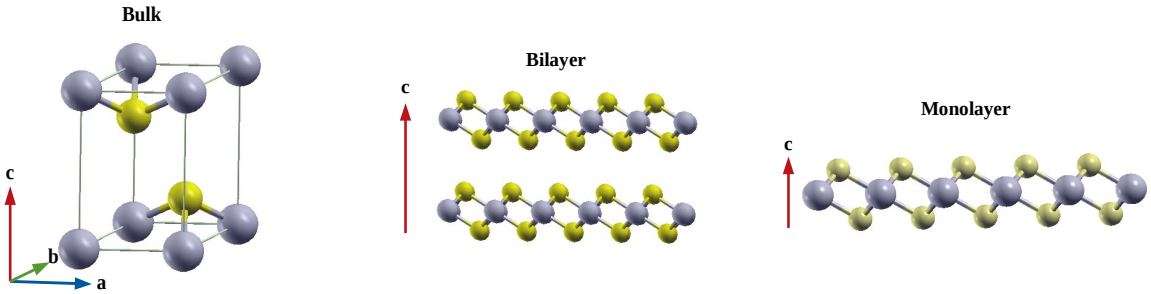

Figure 1. Crystal structure of bulk, bilayer and monolayer $PtTe_2$ and $PtSe_2$. The grey and yellow balls represent the Pt and Se/Te atoms, respectively.

In Figure 1 the bulk, bilayer and monolayer $PtTe_2$ and $PtSe_2$ crystal structures are shown. Our relaxed structural parameters for bulk, bilayer and monolayer, collected in Table 1, is consistent with the available experimental data. Atomic positions in the bilayer and monolayer do not deviate appreciably from the corresponding bulk positions, indicative of strong bonding between the Pt and chalcogen atoms. The calculated cohesive and formation energies of bulk, bilayer and monolayer, also listed in Table 1, are all negative, which suggests that the compounds are stable with respect to decomposition into their constituent atoms or solid components.

3.2. Elastic stability

To obtain the mechanical stability of bulk, bilayer and monolayer $PtTe_2$ and $PtSe_2$, we calculated the elastic constant tensor C_{ij} (i and j are tensor coordinates). $PtTe_2$ and $PtSe_2$ crystallise in

 ISBN: 978-0-620-88875-2

Table 1. Calculated equilibrium lattice parameters, cohesive energy (E_{coh}) and formation energy (E_{form}) per atom, together with the available experimental data.

		$a(\AA)$	$c(\AA)$	$V_o(\AA^3)$	$E_{coh}(eV)$	$E_{form}(eV)$
$PtTe_2$						
	Bulk	4.05	5.11	72.04	-4.43	-0.40
	Exp.[16]	4.01	5.20	72.43	–	–
	Bilayer	4.09	–	–	-3.81	-0.37
	Monolayer	4.05	–	–	-3.80	-0.36
$PtSe_2$						
	Bulk	3.77	4.98	61.11	-4.55	-0.43
	Exp.[17]	3.73	5.08	61.15	–	–
	Bilayer	3.76	–	–	-3.95	-0.39
	Monolayer	3.81	–	–	-3.96	-0.38

a trigonal $P\bar{3}m1$ symmetry, which has six independent elastic constants. The elastic constants listed in Table 2, fulfil the Born stability criteria [18], thus, confirming that bulk, bilayer and monolayer $PtTe_2$ and $PtSe_2$ are mechanically stable. Young's moduli (Y) indicate the resistance of a material to deform when subjected to opposing forces. Bulk moduli (B), describe the ability of a material to resist to volume change. Shear moduli (E), describe the materials respond to shear strain (the deformation of constant volume dimensions) opposing forces are applied. Poisson's ratio (ν), is related to the atomic bonding nature of a material. Our results show that the Young's moduli for bulk are greater than monolayer and bilayer, means Young's moduli is depended on the number of layers. The bulk moduli, shear moduli, Young's moduli and Poisson's ratio for bulk $PtTe_2$ and $PtSe_2$, obtained by the Hill's approach [19]. Young's moduli of the bulk structure depend on the volume, while Young's moduli of bilayer and monolayer depend on the area (called stiffness). Young's moduli increase with the increase of the number of layers, indicative of increased resistance to deformation under the application of opposing forces as the number of layers are increased.

Table 2. Elastic constants C_{ij} (GPa), elastic bulk moduli B_V (GPa), shear moduli E (GPa), Young's moduli Y (GPa) and Poisson's ratio ν for $PtTe_2$ and $PtSe_2$.

		C_{11}	C_{12}	C_{13}	C_{33}	C_{44}	C_{66}	B_V	Y	E	ν
$PtTe_2$											
	Bulk	170.5	53.80	42.07	67.62	45.00	58.31	68.42	105.2	42.26	0.24
	Bilayer	65.32	15.99	–	–	-	–	–	64.11	–	0.24
	Monolayer	64.61	22.89	–	–	–	–	–	56.50	–	0.35
$PtSe_2$											
	Bulk	197.7	67.89	41.32	51.39	40.73	64.91	66.75	102.97	41.42	0.24
	Bilayer	76.52	18.19	–	–	–	–	–	72.19	–	0.24
	Monolayer	65.38	19.37	–	–	–	–	–	59.64	–	0.29

3.3. Dynamical stability

The harmonic phonon dispersion relations were computed along the high symmetry directions. The phonon band structure, total density of states and partial density of states, for bulk, bilayer

and monolayer $PtTe_2$ and $PtSe_2$ are presented in Figure 2 and Figure 3, respectively. The phonon partial density of states shows the atomic contribution to the total phonon density. The increase in the range from $PtTe_2$ to $PtSe_2$ can be attributed to the relative atomic weights of Te and Se, with the lighter Se atom contributing to the higher frequencies. All the phonon frequencies are positive, which indicates that the bulk, bilayer and monolayer of $PtTe_2$ and $PtSe_2$ are dynamically stable. Note, the bilayer phonon band structure appear dense compared to the bulk and monolayer. This is due to the increase in the number of atoms per unit cell while the frequency range is almost unchanged for all three configurations.

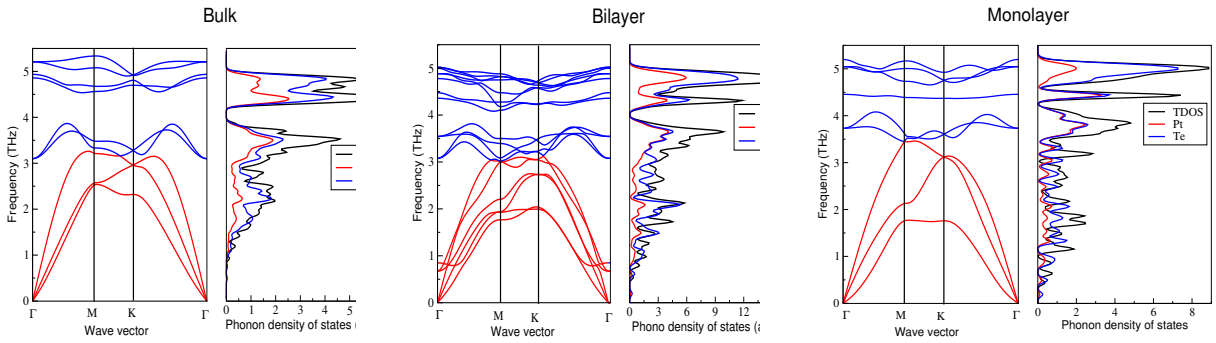

Figure 2. Phonon band structure and density of states of bulk, bilayer and monolayer $PtTe_2$

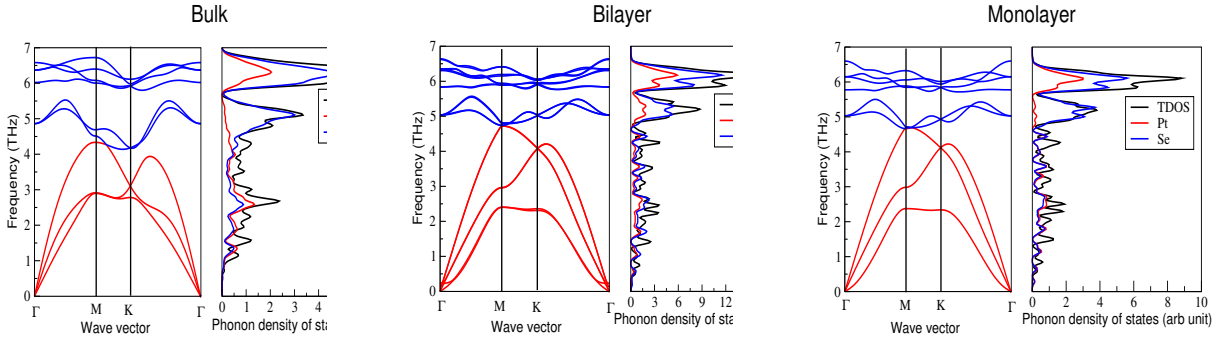

Figure 3. Phonon band structure and density of states of bulk, bilayer and monolayer $PtSe_2$.

3.4. Electronic structure properties

The electronic band structure and density of states (total and partial) of the bulk, bilayer and monolayer $PtTe_2$ and $PtSe_2$ are shown in Figure 4 and Figure 5, respectively. Note that the bilayer band structure appears dense relative to bulk and monolayer due to the doubling of the number of atoms in the unit cell. The electronic structure calculation proved that the bulk phase of both compounds shows overlap between valence and conduction band (semi-metal behaviour), while the bilayer and monolayer are semiconducting with an indirect band gap in both compounds. The conduction band minima (CBM) are located between Γ and M, while the valance band maxima (VBM) are at the Γ point, of the Brillouin zone. In Table 3, we present the band gap values for bulk, bilayer and monolayer for $PtTe_2$ and $PtSe_2$. Our calculated results agreed with some of the previous studies [8, 7, 9]. We find that the band gaps decrease with the increasing number of layers as it was previously reported by the references [3, 20].

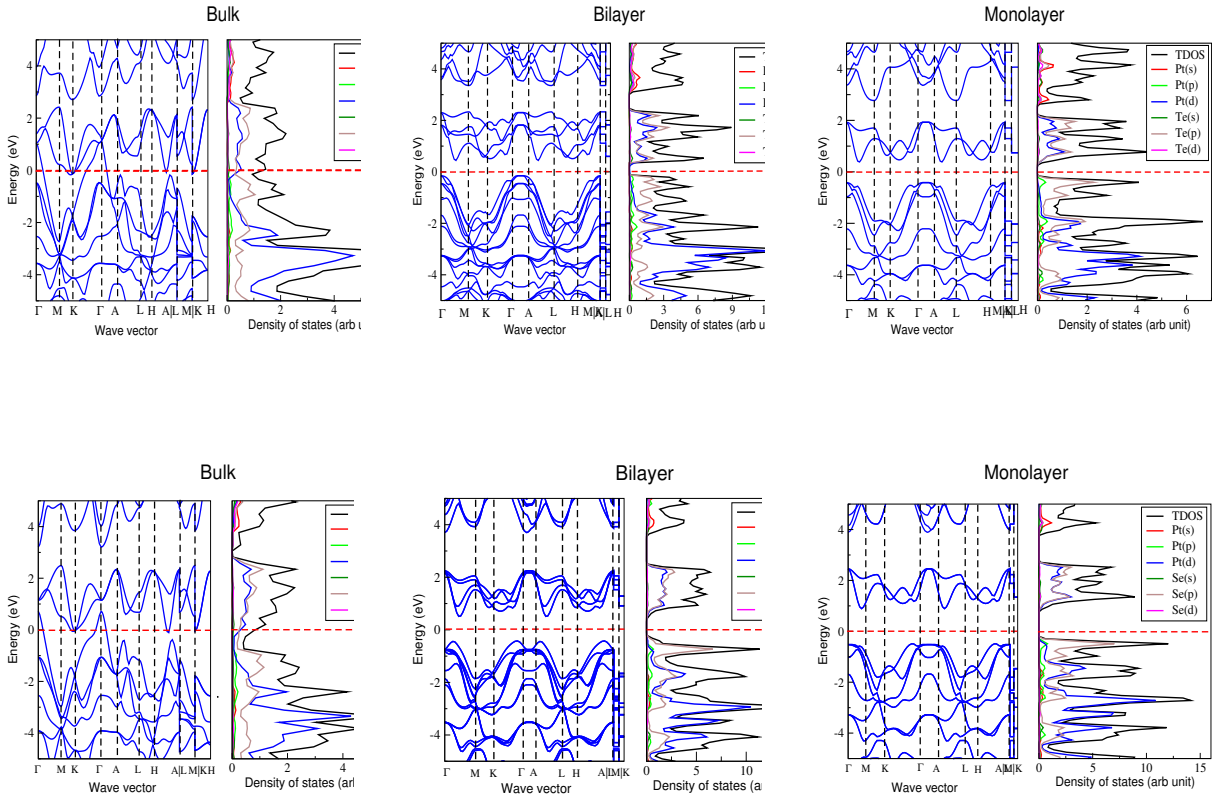

Figure 5. The band structure and density of states of $PtSe_2$ bulk, bilayer and monolayer.

Table 3. Calculated band gap values (in eV) of bulk, bilayer and monolayer $PtTe_2$ and $PtSe_2$.

		bulk	Bilayer	monolayer
$PtTe_2$				
	This study	semi-metal	0.46	0.80
	Other study	semi-metal[8]	—	0.38[10]
$PtSe_2$				
	This study	semi-metal	0.93	1.38
	Other study	semi-metal[8]	0.21[4],0.99[7],∼0.80[9]	1.22[4],1.39[7],∼1.60[9]

4. Conclusion

We studied the structural parameters, mechanical, dynamical and electronic properties of bulk, bilayer and monolayer $PtTe_2$ and $PtSe_2$ using the first-principles Density Functional Theory approach. Our results are in good agreement with available experimental data and previous studies of the structural and electronic properties. Our calculations confirm that the compounds are mechanically and dynamically stable. We found that the bilayer and the monolayer phases of these compounds have an indirect band gap. Our calculations also predicted that the size band gap strongly depends on the number of layers take into consideration in the calculations.

Acknowledgements
We like to acknowledge the all financial support received from University of Shendi, Shendi, Sudan. The authors acknowledge the Centre for High-Performance Computing (CHPC), South Africa, for providing computational resources to this research project.

References
[1] Ferrari A, et al 2015 *Nanoscale* **7** 4598–4810.
[2] Novoselov K S, Fal V, Colombo L, Gellert P R, Schwab M G and Kim K 2012 *Nature* **490** 192.
[3] Xu M, Liang T, Shi M and Chen H 2013 *Chem. Rev.* **113** 3766–3798.
[4] Wang Y *et al* 2015 *Nano Lett.* **15** 4013–4018.
[5] Zulfiqar M, Zhao Y, Li G, Nazir S and Ni J 2016 *J. Phys. Chem. C* **120** 25030–25036.
[6] Yim C, *et al* 2016 *ACS Nano* **10** 9550–9558.
[7] Li P, Li L and Zeng X C 2016 *J. Mater. Chem. C* **4** 3106–3112.
[8] Guo G and Liang W 1986 *J. Phys. C: Solid State Phys.* **19** 995.
[9] O'Brien M, *et al* 2016 *2D Mater.* **3** 021004.
[10] Guo S D and Wang Y 2017 *Semicond. Sci. Technol.* **32** 055004.
[11] Kresse G, and Joubert D 1999 *Phys. Rev. B* **59** 1758.
[12] Kresse G and Furthmüller J. 1996 *Comput. Mater. Sci.* **6** 15-50.
[13] Perdew P, Burke K and Ernzerhof M 1996 *Phys. Rev. Lett.* **77** 3865.
[14] Monkhorst J and Pack D 1976 *Phys. Rev. B* **13** 5188.
[15] Togo A, Chaput L and Tanaka I 2015 *Phys. Rev. B* **91** 094306.
[16] Thomassen L 1929 *J. Phys. Chem.* **2** 349–379.
[17] Furuseth S, Selte K and Kjekshus A 1965 *Acta Chemica Scandinavica* **19** 257.
[18] Mouhat F and Coudert X 2014 *Phys. Rev. B* **90** 224104.
[19] Hill R, 1952 *J. Proc. Phys. Soc.* **65** 349.
[20] Mohammed H A H, Dongho N G M and Joubert D 2019 *Mater. Today Commun.* **21** 100661.

Effect of Co addition on the structural, electronic and magnetic properties of $Fe_{16}N_2$ employing first principles approach

R Modiba*[1]and P E Ngoepe[2]

[1] Materials Modelling Centre, University of Limpopo, Private Bag X1106, Sovenga, South Africa
[2] Materials Science and Manufacturing, CSIR, PO Box 395, Pretoria, 0001, South Africa

Email: *Rmahlangu1@csir.co.za

Abstract. Improvements in energy efficiency and reduction of greenhouse gas emissions have been some of the central topics in recent years in environment and climate change. The advantages of using permanent magnets in many different types of electromagnetic drive and static magnetic field applications are compelling. Seemingly, demand is bound to increase substantially in coming years. There are significant challenges associated with coming up with new alloys or composite materials that can be used for bulk permanent magnets with an energy product in excess of 460 kJ m^{-3}. In this study, first-principles approach employing the density of states within the generalized gradient approximation is employed. The structural, electronic and magnetic properties of $Fe_{16-x}N_2Co$ for the development of permanent magnets are investigated. Firstly, geometry optimization was performed to reach the equilibrium state of the structures and the results compared well with the available experimental results. Interestingly, the density of states at the Fermi level decreases suggesting the stability of $Fe_{16}N_2$ with Co addition.

1. Introduction

Improvements in energy efficiency and reduction of greenhouse gas emissions have been some of the central topics in recent years in environment and climate change [1]. The advantages of using permanent magnets in many different types of electromagnetic drive and static magnetic field applications are compelling. It seems demand is bound to increase substantially in coming years. There are significant challenges associated with coming up with new alloys or composite materials that can be used for bulk permanent magnets with an energy product in excess of 460 kJ m^{-3}.

The large quantity of permanent magnets needed in contemporary technology, especially with the increased interest in alternative energy sources, transmission and conversions, also causes ecological concerns and economic problems, that have been discussed in detail by Alonso et al [2]. A complete and direct (one-by-one) replacement of all critical and rare elements in permanent magnets by other more readily available elements without decreasing product performance, raising the price or both, has limitations [3]. However, the substitution of rare earths and other critical materials appears to be a feasible solution.

It is of great importance for the theoretical search for hard-magnetic materials to gain detailed insight into the most relevant physical mechanisms, which determine the intrinsic properties of the hard-

magnetic materials [4]. In almost all modern hard-magnetic materials, the intrinsic material parameters are achieved as desired [5, 6] by combining transitional metals and rare earth elements in particular proportions. This results in a large class of possible chemical compositions and crystal structures. It is therefore well established that combining these two types of elements one can get materials with both high magnetic anisotropy and high Curie temperature [4]. In this study, electronic and magnetic properties of $(Fe_{16-x}Co_x)N_2$ (x = 0, 2, 4) for the development of permanent magnets are investigated using the first principle approach.

2. Methodology

The calculations were carried out using *ab initio* density functional theory (DFT) [7, 8] formalism as implemented in Cambridge *ab initio* simulation total energy package (CASTEP) [9] with the projector-augmented wave (PAW) [10]. An energy cutoff of 520 eV and 4x4x4 *k*-points were used, as they were sufficient to converge the total energy of the structures. For the exchange-correlation functional, the generalized gradient approximation of Perdew and Wang (GGA-PBE) [11] was chosen. The Brillouin zone integrations were performed for suitably large sets of *k*-points according to Monkhorst and Pack [12]. The convergence criteria for structure optimization and energy calculation were set to fine quality with the tolerance for the stress concentration factor (SCF), energy, maximum force and maximum displacement set to 1.0×10^{-5} eV/atom, 0.03 eV/ Å, 0.001 Å; respectively. Spin polarization was included using the formal spin as initial in the calculations to correctly account for its magnetic properties owing to the great effect of Fe, N and Co on magnetic systems. All the calculation were performed at 0 K.

3. Results and discussion

3.1. Structural and magnetic properties of $Fe_{16-x}Co_xN_2$

In this section the structural and magnetic properties of the $Fe_{16-x}Co_xN_2$ (x = 0, 2 and 4) are discussed. In Figure 1, the structures of the $Fe_{16-x}Co_xN_2$ wherein in (a) the pure $Fe_{16}N_2$ and (b) doped $Fe_{14}Co_2N_2$ are shown . We studied the tetragonal $F_{16}N_2$ with a space group of I4/MMM with 18 of atoms. The structure was optimized and Fe substituted with Co resulting in $Fe_{14}Co_2N_2$ and $Fe_{12}Co_4N_2$.

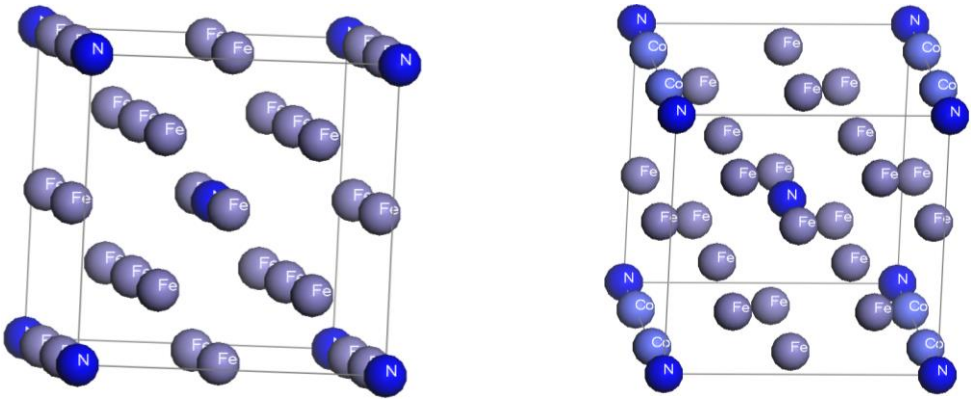

Figure 1. The structures of (a) Pure $Fe_{16}N_2$ and (b) doped $Fe_{14}Co_2N_2$ wherein the dark blue represents N, purple Fe and light blue Co atoms.

In Table 1, the structural and magnetic properties of the $Fe_{16-x}Co_xN_2$ structures are shown wherein all the structures were subjected to full geometry optimization. The c/a ratio of $Fe_{14}Co_2N_2$ was found to be smaller than that of $F_{16}N_2$ and $F_{12}Co_4N_2$. The magnetic moment of both Fe1and Fe2 for the $Fe_{14}Co_2N_2$ is found to be smaller than that of $Fe_{12}Co_4N_2$ whereas Fe3 and Fe4 are larger. The total magnetic of $Fe_{14}Co_2N_2$ was also found to be larger than that of the other two structures and is predicted as the metallic magnet whereas the other structures as half-metallic ferromagnetic.

3.2. Density of states

In Figure 2, the graph of total density of states (tDOS) for the $Fe_{16-x}Co_xN_2$ structures is shown. We observe the exchange splitting of spin-up and spin-down separated by Fermi level (E_f). The tDOS were found to be similar in shape to the $Fe_{16}N_2$ except that when Co is added there is a shift of peaks observed. The $Fe_{14}Co_2N_2$ was found to have the highest peak at E_f as compared to the other structures. The peak above the E_f is seen to be shifting to the right towards the E_f which behaves like a metal as predicted by the magnetic properties. The same behaviour is observed with $Fe_{12}Co_4N_2$ which has a higher peak as compared to the pure $Fe_{16}N_2$. On the spin down curves, the E_f hits the $Fe_{16}N_2$ at the pseudo and shifts to the lower energy with an increase in Co content.

Table 1: Lattice parameters (Å) and magnetic moment Bohr magnetons (μB) of $Fe_{16-x}Co_xN_2$

Structure	a	c	c/a	Atom	Magnetic moments	Total
$Fe_{16}N_2$	5.633	6.222	1.10	Fe1	2.311	18.7546
				Fe2	2.096	
				Fe3	2.799	
				N	-0.054	
$Fe_{14}Co_2N_2$	5.656	6.207	1.09	Fe1	2.789	36.019
				Co	1.284	
				Fe2	2.015	
				Fe3	2.288	
				Fe4	2.423	
				N	-0.056	
				N2	-0.057	
$Fe_{12}Co_4N_2$	5.616	6.241	1.11	Fe1	2.908	34.922
				Fe2	1.887	
				Fe3	2.25	
				Co	1.583	
				Fe4	2.286	
				N	-0.019	
				N2	-0.04	

 ISBN: 978-0-620-88875-2

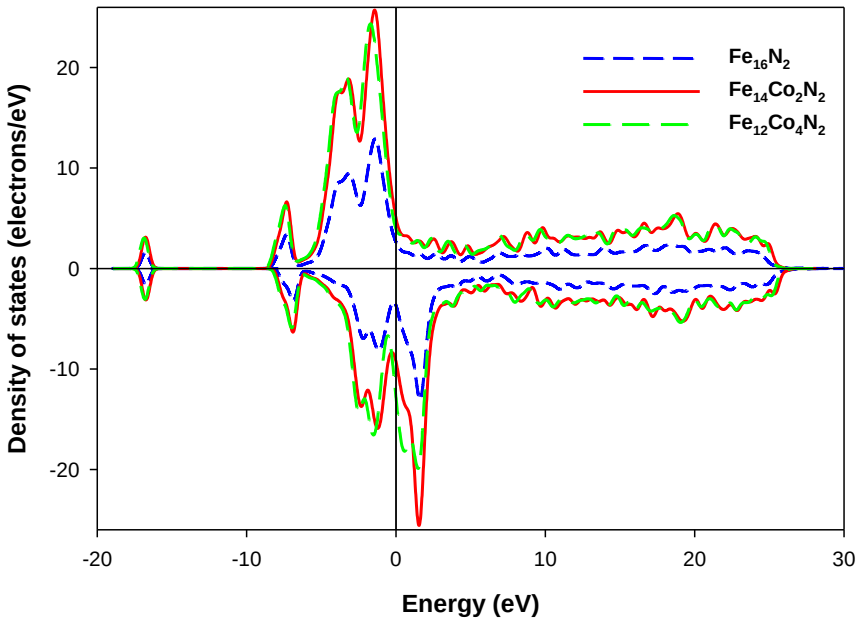

Figure 2. Comparison of the total density of states (tDOS) for the $Fe_{16-x}Co_xN_2$ (x=0, 2, 4) structures. The Fermi energy is taken as the energy zero ($E-E_f=0$).

4. Summary and Conclusions

$Fe_{16-x}Co_xN_2$ magnetic properties were investigated using ab initio techniques. The $Fe_{14}Co_2N_2$ was found to have high magnetic moment of 36 μB, which is good for strong magnets. Moreover, the structure is considered to be magnetic metallic as depicted by the tDOS at Fermi level. Both $Fe_{16}N_2$ and $Fe_{12}Co_4N_2$ were found to be half-metallic ferromagnets with the lowest total magnetic moment of the systems. This was found to be agreeing with the density of states wherein the $Fe_{14}Co_2N_2$ had the highest spin up and down tDOS; respectively. In future, the magnetic saturation and electronic transport properties of the structures will be investigated to further understand this material.

Acknowledgements

The authors acknowledge the CSIR and DSI for their financial support. The calculations were carried out using computer resources at the Materials Modelling Centre (MMC) at the University of Limpopo and the Centre for High Performance Computing (CHPC) in Cape Town.

References

[1] Ziervogel G *et. al.* 2014 *WIREs Clim. Change* **5** 605-620.
[2] Alonso E *et. al*. 2012 *Environ. Sci. Technol.* **46** 3406-3414.
[3] Graedel T E, Harper E M, Nassar N T and Reck B K 2015 *PNAS* **112** 6295-6300.
[4] Fähnle M, Hummler K, Liebs M and Beuerle T 1993 *Appl. Phys.* **A57** 67-76.
[5] Buschow K 1991 *Rep. Prog. Phys.* **54** 1123.
[6] Coey J M D 1996 *Phys. Scr.* **T66** 60-69.
[7] Hohenberg P and Kohn W 1964 *Phys. Rev.* B **136** 864-871.
[8] Kohn W and Sham L J 1965 *Phys. Rev.* A **140** 1133-1138.

[9] Clark S J et. al 2005 *Z. Kristallographie* **220** 567-570.
[10] Blöchl P E 1994 *Phys. Rev. B* **50** 17953-17979.
[11] Perdew J P, Burke K and Enzerhof M 1996 *Phys. Rev. Lett.* **77** 88-92.
[12] Monkhorst H J and Pack J D 1976 *Phys. Rev.* B **13** 5188-5192.

Study of lattice defects in BaF_2 at elevated temperatures using positron annihilation and X-ray diffraction methods

T P Jili[1,2], E Sideras-Haddad[2], D Wamwangi[2], D Billing[2], C L Ndlangamandla[1] and M Khulu[1]

[1]Physics Department, University of Zululand, P/B X1001, Kwadlangezwa, 3886, South Africa
[2]School of Physics, University of the Witwatersrand, P/B 3, Wits, 2050, South Africa

E-mail: jilip@unizulu.ac.za

Abstract. Different experimental techniques used in this study have clearly demonstrated that the predominant intrinsic point defects in ionic barium fluoride are anion Frenkel pairs. We utilized the positron annihilation technique in obtaining Doppler broadening spectra in the temperature range 300 – 900 K from which the ratios of the central annihilation areas to the total area of the annihilation curves (S-parameters) are extracted. Generalized gradient approximation in the framework of local density functional theory is used to calculate the Doppler broadening spectra. We found that the positron annihilations with barium valence electrons, especially 5p and 6s electrons, contributed immensely in the electron-positron annihilation momentum density. The rate of disordering of the fluorine sub-structure is found to increase non-linearly from a temperature of 580 K without observing any appreciable ionic conductivity. The X-ray diffraction method gave a lattice constant of (0.629 ± 0.003) nm at 693 K, corresponding to the S-parameter of 0.509 ± 0.002, through which an appreciable ionic conductivity of 4.64×10^{-7} Ohm^{-1} cm^{-1} is first observed. This is demonstrated through the correlation between the lattice constants and the ionic conductivity values at elevated temperatures.

1. Introduction

Alkaline-earth fluorides of space group Fm3m have demonstrated interesting properties and they constitute a wide range of applications. Barium fluoride and calcium fluoride exhibiting a wide band gap, meaning that their electronic properties fall between the insulators and the conventional semiconductors, are strongly ionic and have been studied partly because of their use in precision vacuum ultraviolet lithography [1], in fast scintillation detection and also in crystalline lens material for precision in vacuum ultra violet optics [2]. Han *et al* [3] have recently studied the light emission from barium fluoride as a scintillation detector with the aim of reducing the intensity of the slow component (~310 nm) with a decay constant of around 630 ns which hinders fast timing experiments.

Barium fluoride is an ionic conductor whose electrical properties are strongly dependent on temperature because of the migration of anion interstitials. Anion Frenkel pairs and ionic transport is understood through the migration of both anion vacancies and anion interstitials [4, 5]. Figueroa *et al* [6] investigated two possible diffusion mechanisms from the fluorite lattice, involving interstitial ions, namely the direct interstitial mechanism and the non-collinear interstitialcy mechanism. They concluded that non-collinear interstitialcy is more probable as it requires much lower energy to produce ionic displacements.

The present paper explores and demonstrates that at elevated temperatures (well below the melting point) the anion vacancy and the anion interstitial (Frenkel pairs) can well exist without any notable change in ionic conductivity. This is investigated by the positron annihilation technique both experimentally and theoretically to obtain the S-parameters in the temperature range (300 – 900) K. The lattice parameter as a function of temperature, which plays a pivotal role in the calculation of S-parameters, is obtained from the measured X-ray diffraction patterns.

2. Method of calculation

Two-component density functional theory (TCDFT) is used to obtain both positron and electron densities necessary to estimate positron lifetimes and positron-electron momentum densities. Local density approximation (LDA) in the framework of TCDFT is normally used but it does not depend on the variation of charge density and this tends to overestimate the positron-electron correlation energy functional and thus affecting the calculation of the enhancement factor. This deficiency in LDA is corrected through the generalized gradient approximation (GGA). The MIKA Doppler code [7] used in this work, corrects this deficiency through the enhancement function

$$g_{GGA} = 1 + (g_{LDA} - 1)e^{-\alpha\epsilon} \tag{1}$$

where α is an adjustable parameter designed to give better annihilation rates. In our case α is set at 0.22. Note that α = 0 gives the LDA enhancement factor. ϵ (the variation in electron charge density) is given by

$$\epsilon = \frac{|\nabla n_-|^2}{(n_{-qtf})^2} \tag{2}$$

where n_{-qtf} is the local Thomas-Fermi screening length and ∇n_- is the change in the electron density.

The Arponen –Parjane enhancement function [8] given by

$$g_{LDA-AP} = 1 + 1.23r_s - 0.0742r_s^2 + \frac{1}{6}r_s^3 \tag{3}$$

is substituted in equation (1) for GGA enhancement factor. $\boldsymbol{r_s}$ is the measure of the density of the system and is the radius of a sphere whose volume equals the volume per electron. Momentum distributions are calculated separately for each electronic state described by ψ_j as

$$\rho_j(\mathbf{p}) = \pi r_o^2 c u_j^2(0)\left|\int d\boldsymbol{r} e^{-i\boldsymbol{p}\cdot\boldsymbol{r}}\psi_+(\boldsymbol{r})\psi_j(\boldsymbol{r})\right|^2 \tag{4}$$

where u_j, ψ_+ and ψ_j are the state dependent enhancement factors, positron wavefunction and electron wavefunction respectively. r_o is the classical radius of electron.

The total electron-positron momentum density within the GGA is obtained by summing partial enhancement factors in equation (4) as

$$\rho(\mathbf{p}) = \pi r_o^2 c \sum_j \gamma_j \left|\int e^{-i\boldsymbol{p}\cdot\boldsymbol{r}}\psi_j(r)\psi_+(r)dr\right|^2 \tag{5}$$

The S-parameter which is defined as the ratio of the central annihilation area to the total annihilation area, is calculated from the electron-positron momentum density as

$$S = \frac{\int_0^{p2} f(p_z)dp_z}{\int_0^{\infty} p_z\, dp_z} \tag{6}$$

where the numerator is the central annihilation are and the denominator denotes the total annihilation area. f is the positron-electron momentum density function. The momentum window used in our theoretical and experimental calculations is (0-3) × 10^{-3} $m_o c$.

3. Experiment

The experimental setup for the positron annihilation investigation is shown in figure 1 and comprises a positron source (^{22}NaCl), sealed between two electron-welded nickel foils each of thickness 7 μm, with activity of 15 μCi, was sandwiched between two equal sized samples of barium fluoride each of dimensions 10 mm × 8 mm × 2 mm. The coincidence circuit diagram showing detector positions is shown in figure 1.

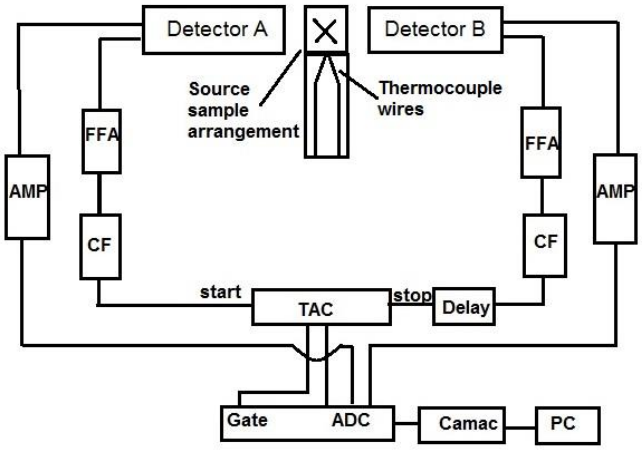

Figure 1. Setup used for positron annihilation investigation. Circuit diagram shows a two-detector system that was used. The two detectors measured the electron-positron annihilation radiation (511 ± ΔE) KeV at defects and in bulk.

A K-type (Chromel-alumen) thermocouple was utilized to obtain the temperature of the source-sample sandwich arrangement. A standard coincidence arrangement (two detector system), in which two high purity germanium detectors (HPGe) with energy resolution of 1.4 keV (FWHM) at 511 keV, was employed.

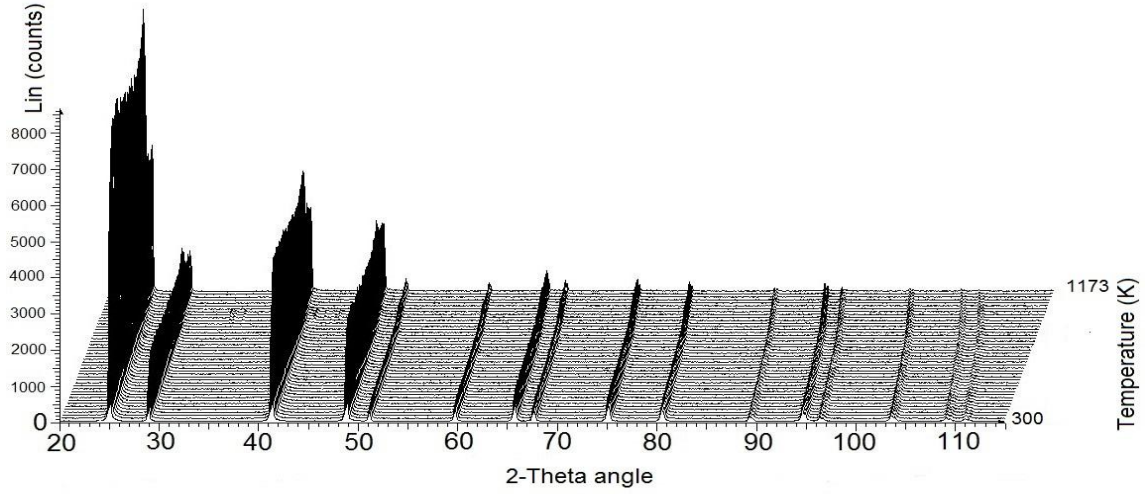

Figure 2. Measured X-ray diffraction patterns in BaF_2 in the temperature range 300 – 1173 K**.**

Two detectors are separated by a distance of 10 cm in a collinear arrangement. Accumulation average count rate of about 300 counts/second was achieved with peak-to-background ratio of ~10^4. Source-sample-heater system was kept at a pressure of 2×10^{-5} Torr. Doppler broadening spectra at different temperature values were obtained following the background subtraction. A source correction was conducted since (10-15) % of the annihilations occurs in the source material and in the foils. Additional lifetimes and intensities corresponding to source and foil were subtracted.

In order to obtain lattice parameters at elevated temperatures of BaF_2, an X-ray diffraction (XRD) method using Bruker D8 Advance, equipped with a Goebel Mirror for pseudo parallel beam optics, a Vantec detector and an Anton Paar XRK-900 reaction chamber was employed. Diffractometer utilized Cu-K_α radiation. Collected X-ray diffraction patterns of barium fluoride in the temperature range 300 – 1173 K is represented in figure 2. The data represents 45 diffraction pattern measurements from 300 K to 1173 K at regular temperature intervals of 30 K. The XRD patterns were compared with the reference pattern of BaF_2 from Inorganic Crystal Structure Database – Karlsruhe (ICDS) [9] for peak identification.

Rietveld refinements were done on the diffraction data using TOPAS 4.2 and EVA program (for phase analysis) to extract lattice parameters as a function of temperature. Lattice parameters obtained at different temperatures were then incorporated in the theoretical calculations of the positron-electron annihilation momentum density using the MIKADoppler program.

4. Results and discussion

The formation energy for a fluorine vacancy (F^- - vacancy) is -1.06 eV, which is more negative than the formation energy for a Ba^{2+} vacancy, which is positive at 21.27 eV [10]. Therefore the migration of an anion is energetically preferred to that of a cation and throughout the experiment, in the temperature range 300-800 K, anion vacancy formation is considered. For interstitial formation energies, the octahedral sites in the face-centered cubic fluorites are the most stable sites for anion and cation interstitials [11], a fact we took into consideration in this work.

X-ray diffraction analysis was performed on the barium fluoride over a temperature range 300-1173 K, below the melting point, in order to deduce the variation of the lattice constant with temperature from results shown in figure 3.

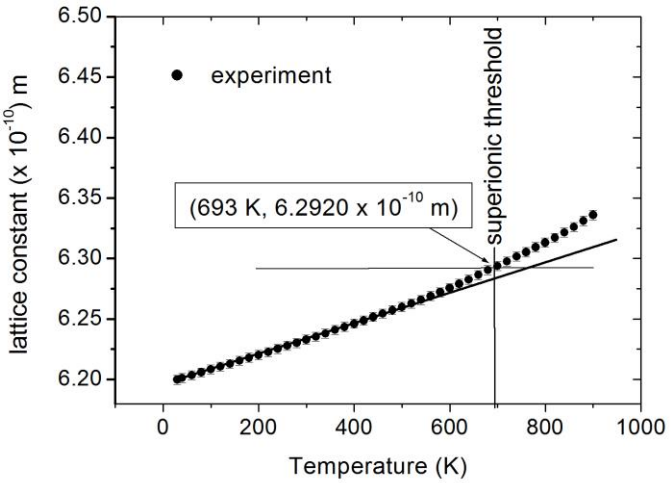

Figure 3. Variation of lattice constant in BaF_2 as a function of temperature.

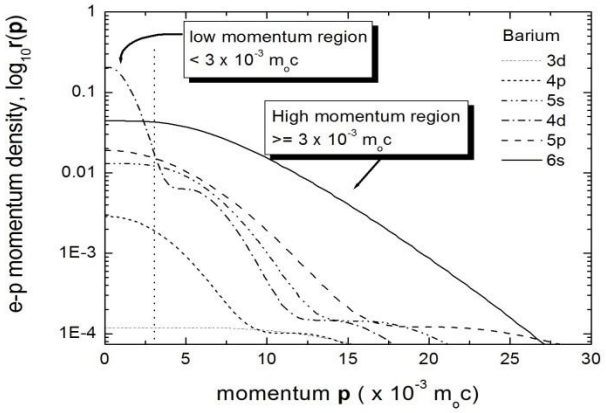

Figure 4. Barium decomposition shows two regions of interest. Most positron annihilations take place with low momentum electrons in the region $0 < p \leq 3 \times 10^{-3}$ $m_o c$, i.e. to the left of the vertical dotted line.

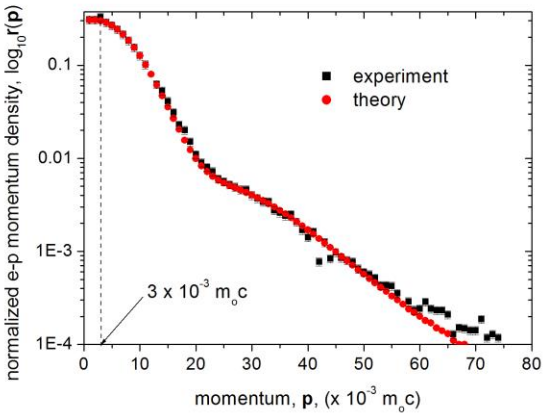

Figure 5. Low momentum window (0 to 3×10^{-3} $m_o c$) is chosen for both theory and experiment for consistency. Low momentum window represents the area of the annihilation centroid.

In the temperaure range between 300 – 580 K, we observe a linear behaviour of the lattice constant as a function of temperature. In contrast, between 580 K and 1173 K, a non-linear behaviour of the lattice constant becomes evident. Our detemined experimental values of the lattice parameters compare well with other values in the literature [12, 13]. Each lattice constant is used to construct a 124 atoms supercell for the calculation of s-parameters.

Partial electron-positron annihilation momentum distributions are derived from equation 4 and are shown in figure 4. The GGA in the framework of density functional theory (DFT) confirms that most contributors towards electron-positron annihilation momentum density are from the low momentum Ba-5p valence electrons rather than the Ba – 6s, as shown in figure 4. The total momentum distribution is calculated from equation 5 and compares well with experimental e-p momentum density as shown in figure 5 as normalized electron-positron momentum densities. For each spectrum, a fixed momentum window, $0 < p \leq 3 \times 10^{-3}$ $m_o c$ (low momentum range) around the centroid of the photopeak was used for both experimental and theoretical spectra for the calculation of S-parameters as shown in figure 6. The deviation of experimental S-parameter values from a theoretical values commencing at about 600 K is not of major concern since both experiment and theory deviate from observed linear trend at about the same temperature. This corresponds with the trend on the lattice constant. The deviation is probably due to the tail of specific heat anomaly which begins between 600 and 700 K and which is not incorporated in the MIKA code. This is interpreted as a transition from a normal fluorite structure at low temperatures, to a highly disordered state in which F^- ions are distributed between normal anion and interstitial sites.

Using the positron annihilation parameters, there is an agreement between the theory and the experiment regarding the thermal values at which both S-parameters (experiment and theory) begin to deviate from linear trend as shown in figure 6. The ionic conductivity measurements shown in figure 7 in relation to figure 3 suggest that a small threshold ionic conductivity (or a small noticeable disordering of F- sub-lattice), as probed by positrons, appears at the threshold lattice constant and temperature of a_o = 0.6292 nm and T = 693 K respectively. This minimum anionic interstitial transportation takes place at octahedral sites of the sample.

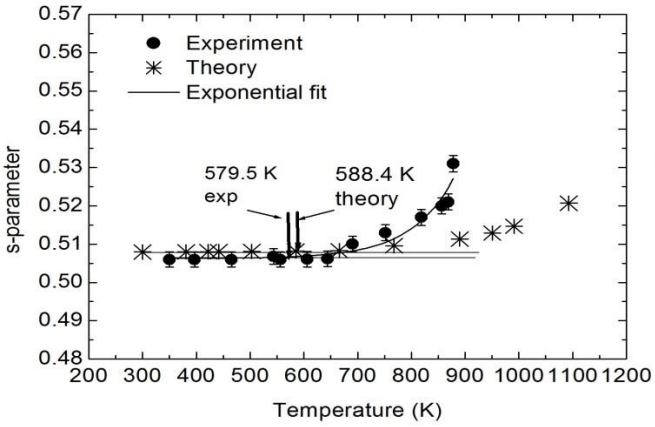

Figure 6. Comparison between theoretically and experimentally determined s-parameters. The experimental large deviation of which begins at ~579.5 K compares well with a theoretically calculated deviation.

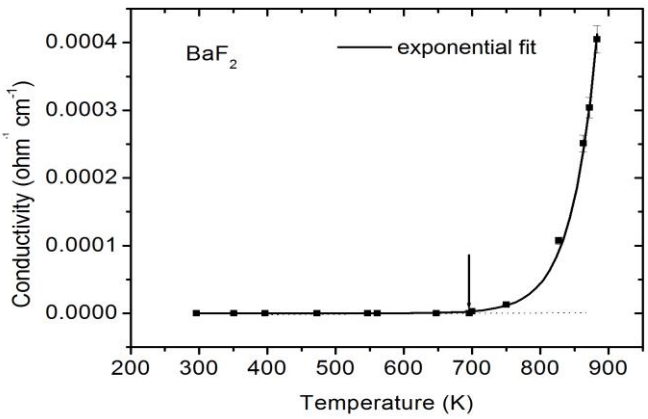

Figure 7. Measured ionic conductivity as a Function of temperature. The minimum threshold temperature for ionic conduction is ~693 K and corresponds to the conductivity of 4.64×10^{-7} $ohm^{-1}cm^{-1}$.

5. onclusion

Using both the positron annihilation and X-ray diffraction techniques, we found that the annihilation fractions of positrons interacting with low momentum electrons slightly differ with an increase of temperature. We also observed that creating an anion di-vacancy can largely increase the annihilation fractions with barium low momentum electrons due to an increase of intensity of positron wavefunction around barium atom. It was of no interest to consider cationic Frenkel defects since in reality the formation energy (21.27 eV) is very large and positive compare to the Fermi gap energy (~10 eV). We also see that charged anionic Frenkel interstitials are more stable than neutral anion Frenkels and that the minimum lattice constant required to establish a noticeable anion Frenkel defects formation is 0.62341 nm at ~580 K. The minimum ionic conductivity at octahedral sites occurs at threshold lattice constant of 0.62920 nm (corresponding to a temperature of 693 K).

Acknowledgement

We greatfully acknowledge financial support from the Research Committe of the University of Zululand and School of Physics at the University of the Witwatersrand.

References

[1] Burnett JH, Levine ZH and Shirley EL 2003 *Phys. Rev.* **B68** 155120/1-12
[2] Katsika-Tsigourakou JV and Skordas E 2010 *Cent. Eur. Phys*. **8** 900-904
[3] Han H, Zhang Z, Weng X, Liu J, Guan X, Zhang K and Li G 2013 *Rev. Sci. Instrm*. **84** 073503/1-5
[4] Chandra S 1981 *Superionic Solids : Principles and Applications* (North Holland, Amsterdam)
[5] Liliard AB, Hayes W (Eds) 1974 *Crystals with Fluoride Structure* (Clarendon Press, Oxford)
[6] Figueroa DR, Chadwick AV and Strange JH 1978 *J. Phys. C: Solid State Physics* **11** 55-73
[7] Hakala T 2001 *Special Assignment*, Helsinki University of Technology, Espoo
[8] Barbiellini B, Puska MJ, Torsti T and Nieminen RM 1995 *Phys. Rev*. **B51** 7341-7344
[9] ICDS: FIZ – Karlsruhe-Leibniz Institute for Information Infrastructure
[10] Bollman W 1981 *Cryst. Res. Technol* **16 9** 1039-1050
[11] Li K, Xiao HY and Wang LM 2008 *Nucl. Instrum. Meth* **B266**, 2698-2701
[12] Leger JM, Haines J, Atouf A, Schulte O and Hull S 1995 *Phys. Rev*. **B52**, 13247-13256
[13] Nyawere P, Scandolo S, Makau M and Amolo G 2014 *Solid State Commun.* **179**, 25-28

Magnetic and thermodynamic properties of the $CeRhGa_4$ compound

Precious M Mabidi, Buyisiwe M Sondezi, Baidyanath N Sahu and André M Strydom

Highly Correlated Matter Research Group, Physics Department, University of Johannesburg, P. O. Box 524, Auckland Park 2006, South Africa.

E-mail: pmabidi@uj.ac.za

Abstract. $CeRhGa_4$ is reported in this work for the first time to crystallize in an orthorhombic structure having the $CeOsGa_4$ structure type belonging to the space group *Pmma*. The physical and magnetic properties of this compound were studied by specific heat $C_p(T)$, magnetization $M(\mu_0 H)$ and magnetic susceptibility $\chi(T)$. $\chi(T)$ and $C_p(T)$ results indicated that there is no magnetic transition above 2 K. The effective magnetic moment μ_{eff} obtained by fitting the Curie-Weiss law on the $\chi^{-1}(T)$ data is $\mu_{eff} = 2.32(3)\ \mu_B$, which is close to the theoretical value for a free Ce^{3+} ion. The negative value of the Weiss temperature, $\theta p = -40.562(4)$ K indicates that antiferromagnetic interactions at high temperatures are dominant. After $M(\mu_0 H)$ shows simple paramagnetic behaviour above 10 K, where M is linear in $\mu_0 H$ up to 20 K. The $C_p(T)/T$ increases sharply below 10 K to reach a very high value of 700 mJ/mol.K^2at 0.5 K. Future studies will focus upon the low temperature region to search for a possible magnetic phase transition.

1. Introduction

Ce-based intermetallic compounds have produced a huge amount of literature for the past four decades and still remain of great interest in the current research, depending on the valence state of Ce ion, see for example the published volume of international conference proceedings on Strongly Correlated Electron System 2017 [1]. The interaction between the single $4f$ electron of cerium and the conduction electrons of transition metals belonging to group 3, 4 and 5, produce fascinating behaviours, especially near the ground state at low temperatures [2]. The behaviours shown by these compounds include the Kondo behaviour observed in for example $CeRh_2Al_{10}$ [3], the noncentrosymmetric heavy fermion superconductor in $CeIrGe_3$ [4] and quantum criticality in $CeCu_2Si_2$ [5]. However, temperature is usually the driving force behind the valence state of the Ce ion, therefore it is for this reason why we observe such behaviours in these compounds. Hence, Ce based compounds are unconventional and interesting to study.

Here we report on exploratory studies on a new Ce compound namely $CeRhGa_4$. This compound crystallizes in an orthorhombic structure having structure type $CeOsGa_4$ belonging to the space group *Pmma* number 51. This structure of the 1:1:4 systems was first reported in 2002 [6].

2. Experimental Details

A polycrystalline sample of $CeRhGa_4$ was prepared from high-purity elements of Ce (99.999 %), Rh (99.97 %) and Ga (99.999 %). The rhodium powder was cold pressed to pellets. The 3

 ISBN: 978-0-620-88875-2

elements with a total weight of 2.0 g were mixed in the ratio of Ce:Rh:Ga = 1:1:4. These elements were placed on a water-cooled copper plate in arc-melting furnace (MAM-1 system manufactured by Edmund B*ü*hler GmbH) under ultra-high purity argon atmosphere. The elements were heated to reach melting point and turned over and re-melted several times to ensure homogeneity. The mass loss was calculated and found to be less than 2 %. The sample was characterized by powder X-ray diffraction (XRD), which was followed by Rietveld refinement profile using the Fullprof program [7]. This was necessary to investigate whether the sample was formed in the desired crystal structure as well as to check for possible impurities and parasitic phases. The sample was confirmed to be homogeneous using Energy Dispersive X-Ray Spectroscopy, with only minor inclusions which deviate from the desired stoichiometry. Since ascast-sample was found to be of a good quality, no annealing process was carried out. The $C_{\mathrm{p}}(T)$ was measured in a Physical Property Measurement System (PPMS) from Quantum Design (San Diego), which presents high stability controlled temperature (1.9 K - 390 K) and magnetic field (0 T - 9 T) environments. $M(\mu_0 H)$ and $\chi(T)$ measurements were conducted on the vibrating - sample magnetometer (VSM) platform of the same equipment over the temperature range of 1.9 K - 300 K.

3. Structural Properties

Figure 1 shows the XRD pattern along with the refinement fitting on XRD data of $CeRhGa_4$.

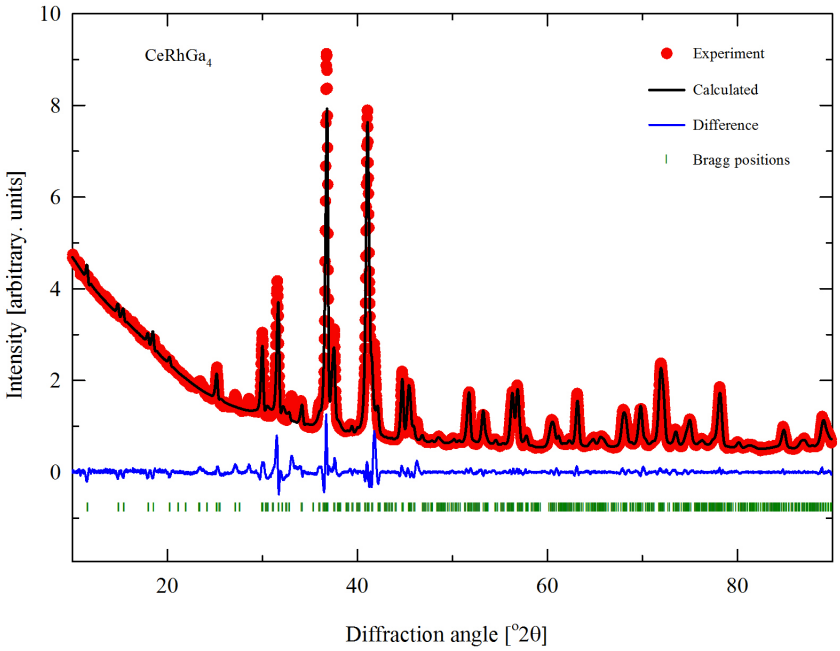

Figure 1. Powder X-ray diffraction pattern of $CeRhGa_4$ (red symbols) showing the Rietveld refinement profile shown by a black line, the difference between the calculated and the experimental intensities is indicated by a blue line and green vertical lines are the theoretical Bragg peak positions.

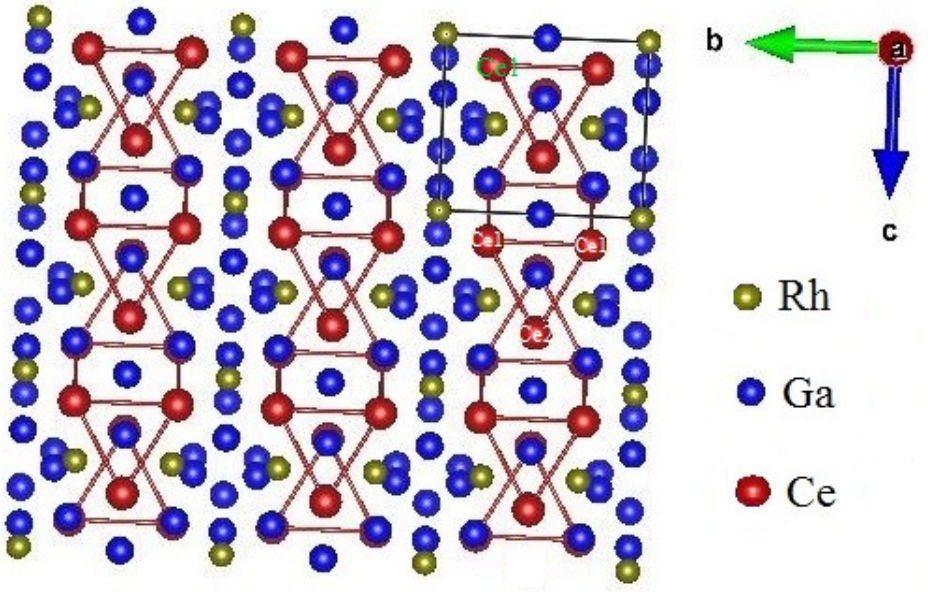

Figure 2. Crystal structure of $CeRhGa_4$ showing the location of atoms: cerium atoms are indicated by red spheres, blue spheres indicate gallium atoms and yellow spheres are rhodium atoms.

The refinement confirms that the compound is an orthorhombic structure with the $CeOsGa_4$ structure type [6]. The least-square refinement fit on XRD data yield the values of lattice parameters and are listed in Table 1. Figure 2 shows the crystal structure of the compound, having two Ce sites with their interatomic distances listed in Table 2, whilst the atomic coordinates are listed in Table 3.

Table 1. Crystal structure lattice parameters of $CeRhGa_4$ obtained from Rietveld refinement of the Powder X-ray diffraction pattern.

a (Å)	b (Å)	c (Å)	V (Å)^3
9. 5593(2)	8. 7441(2)	7. 6126(2)	636.3180(3)

Table 2. Interatomic distances in the structure of $CeRhGa_4$.

Atom	Interatomic distances (Å)
Ce1-Ce1	4.5053(0)
Ce1-Ce2	4.5512(0)
Ce1-Ga	3.1474(0)
Ce1-Rh	3.4740(0)
Ce2-Ga	2.9860(0)
Ce2-Rh	3.4773(0)

 ISBN: 978-0-620-88875-2

Table 3. The atomic coordinates and Wyckoff site locations of $CeRhGa_4$ obtained from Rietveld refinement of the Powder X-ray diffraction pattern.

Atom	sites	x	y	z
Ce1	4 k	1/4	0.2598(3)	0.8251(3)
Ce2	2 f	1/4	1/2	0.3229(4)
Ga3	8 l	0.0753(1)	0.2520(5)	0.1714(5)
Ga4	4 k	1/4	0.1585(1)	0.5417(5)
Ga5	4 j	0.0597(5)	1/2	0.6277(5)
Ga6	4 i	0.0580(5)	0	0.3257(3)
Ga7	2 e	1/4	0	0.1382(4)
Ga8	2 b	0	1/2	0
Rh9	4 h	0	0.2556(2)	1/2
Rh10	2 a	0	0	0

4. Magnetic properties

The magnetic susceptibility, $\chi(T)$, of $CeRhGa_4$ measured in the temperature range of 2 to 300 K and in the field of 1 T is shown in Figure 2 (main panel).

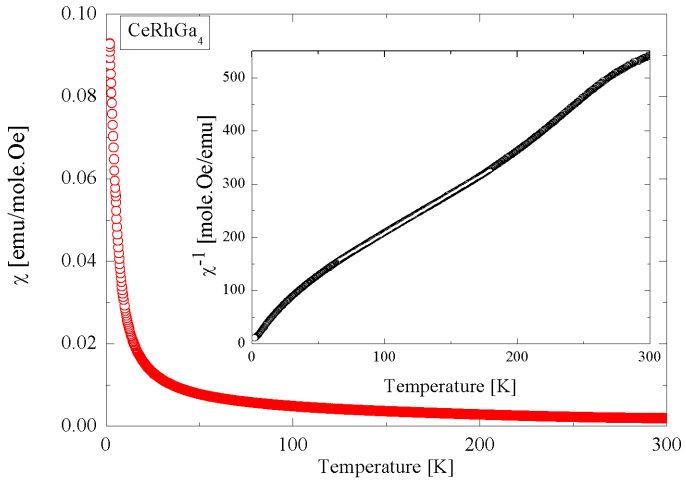

Figure 3. (Main panel) Temperature dependence of magnetic susceptibility, $\chi(T)$, of $CeRhGa_4$ measured in a field of 1 T. The inset shows the inverse magnetic susceptibility, with a white solid line representing a Curie-Weiss fit.

The data between 2 and 80 K, show no evidence of magnetic ordering, although a curvature deviating from Curie-Weiss behaviour is observed in this region. The inset shows the graph of $\chi^{-1}(T)$ in the temperature range, 2 to 300 K. The white solid line shows the Curie-Weiss fit for data in the temperature range ($80 > T < 180$ K), according to the expression $\chi^{-1}(T) = 3k_B(T - \theta_p)/\ N_A\mu^2{}_{eff}$. Data above 180 K deviates from the Curie-Weiss law and it is probably Crystal

 ISBN: 978-0-620-88875-2

Electric Field. The parameters; k_B is the Boltzman constant, θ_p is the Weiss temperature, N_A is the Avogadro number and $\mu^2{}_{eff}$ is the effective magnetic moment. The data obey Curie-Weiss behaviour and resulted in the fitted Weiss temperature $\theta_p = -40.562(4)$ K and the effective magnetic moment $\mu_{eff} = 2.32(3)\ \mu_B$. The negative value of θ_p indicates that antiferromagnetic interactions are dominant at high temperatures. The fitted value of μ_{eff} is close to the theoretical value of the free Ce^{3+} ion, which is 2.54 μ_B/Ce.

Figure 4 (a) shows the magnetic field dependence of magnetization, increased curvature towards low temperature isotherms is observed. Furthermore, at 2 K it is observed that there is a tendency to saturate in high magnetic fields, whilst for isotherms between 10 and 20 K a simple paramagnetism is observed. Figure 4 (b) shows the saturation magnetization that decreases with an increase in temperature. These values were simply extrapolated from the slope (shown by black solid line in Figure 4 (a)) of the highest magnetic field measured to the obtained magnetization value. The saturation magnetization in this compound at 2 K is 0.35 μ_B/Ce, which is much less than the theoretical expected value of $g_J J = 2.14\ \mu_B$ for a free Ce^{3+} ion, which involves the entire six-fold J= 5/2 multiplet [8].

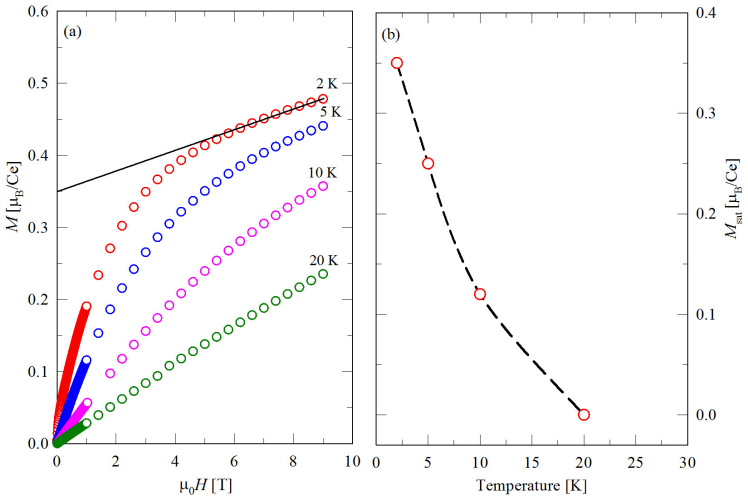

Figure 4. (a) Isothermal magnetization as a function of magnetic field upto 9 T within a temperature range of $T = 2$ and 30 K. (b) Variation of saturation magnetization as a function of temperature (2 to 30 K) evaluated from isotherm magnetization.

5. Specific heat

Figure 5 (a) presents the temperature dependence of specific heat, $C_p(T)$, measured in zero field showing a monotonous decrease of specific heat down to 2 K with no evidence of magnetic ordering. The dashed horizontal line represents the Dulong-Petit value $3NR$, where N is the number of atoms per formula unit and R is the universal gas constant. This data reached the Dulong-Petit value at 149.58 J/mol.K and it corresponds with the maximum specific heat obtained at room temperature, which is 150 J/mol.K. Figure 5 (b) shows the $C_p(T)/T$ vs T^2 data, with a Sommerfeld fit represented by a red solid line according to the expression $C_p(T)/T = \gamma + \beta T^2$, where γ is the Sommerfeld coefficient and β is the constant related to Debye temperature, θ_D, by $\beta = 12\pi^4 NR/5\theta_D$. The Sommerfeld coefficient was found to be γ = 0.1094(1) J/mol.K^2, whilst the calculated Debye temperature, $\theta_D = 268(1)$ K. The θ_D value

indicates the total phonon contribution to the specific heat. The Sommerfeld coefficient value obtained confirms that this compound is not a usual metal as it is 150 times greater than the coefficient of the normal metal, for example, $\gamma_{Cu} = 0.69$ mJ/mol.K^2 [8]. Figure 5 (c) plots $C_p(T)/T$ vs T at different magnetic fields, throughout the measured temperature range the data confirms the absence of the magnetic ordering. Below $T = 5$ K, an upturn is observed in each measured field, further investigations using Helium-3 measurements are planned.

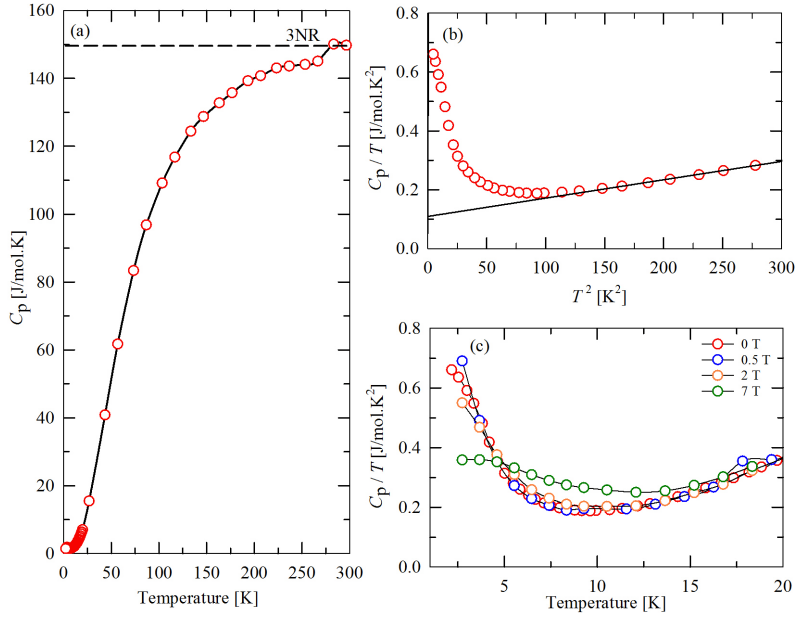

Figure 5. (a) Temperature dependence of specific heat measured under zero field. (b) $C_p(T)$ vs T^2 at zero-magnetic field with a black solid line showing a linear fit. (c) shows $C_p(T)/T$ vs T data measured at different fields.

6. Conclusions

$CeRhGa_4$ was confirmed to crystallize in an orthorhombic $CeOsGa_4$ type structure belonging to the space group *Pmma*, number 51. There is no detectable magnetic ordering observed from both $C_p(T)$ and $\chi(T)$ from room temperature to 2 K. Further measurements will be done towards lower temperatures to investigate the possible existence of magnetic ordering.

Acknowledgments

PMM thanks Vacuquip Solutions and SA-NRF Block Grant (118693). AMS thanks the FRC/URC of UJ for financial assistance.

References

[1] URL `http://www.sciencedirect.com/science/article/abs/pii/S0921452618302011`
[2] Szytuła A and Leciejewicz J 1994 *Handbook of crystal structures and magnetic properties of rare earth intermetallics* (CRC press)
[3] Tursina A, Nesterenko S, Avzuragova V and Strydom A 2017 *Journal of Alloys and Compounds* **728** 752
[4] Anand V, Hillier A, Adroja D, Khalyavin D, Manuel P, Andre G, Rols S and Koza M 2018 *Physical Review B* **97** 184422
[5] Yuan H, Grosche F, Deppe M, Geibel C, Sparn G and Steglich F 2003 *Science* **302** 2104
[6] Schlüter M and Jeitschko W 2002 *Zeitschrift für anorganische und allgemeine Chemie* **628** 1505
[7] Rodríguez-Carvajal J 1993 *Physica B: Condensed Matter* **192** 55
[8] Jensen J and Mackintosh A R 1991 *Rare earth magnetism* (Clarendon Press Oxford)

Structural and magnetic characterization of Sm^{3+} ion substituted Zn-Mn nanoferrites synthesized by glycol-thermal method

T. A. Nhlapo[1], J. Z. Msomi[2], T. Moyo[3]
[1]Department of Medical Physics, Sefako Makgatho Health Sciences University, P. O. Box 146, Medunsa 0204, South Africa.
[2]Department of Physics & Engineering, University of Zululand, Private Bag X1001, KwaDlangezwa 3886, South Africa.
[3]School of Chemistry and Physics, University of KwaZulu-Natal, Private Bag X54001, Durban 4000, South Africa

E-mail address: amos.nhlapo@smu.ac.za

Abstract. The magnetic properties of $Zn_{0.5}Mn_{0.5}Sm_xFe_{2-x}O_4$ ($0 \leq x \leq 0.05$) nanosized produced by glycol thermal methods. Crystallite size in the range 12-17 nm were investigated. XRD analysis confirmed a single phase cubic spinel structure in all the compounds investigated. The elemental composition was confirmed by EDX analysis and microstructure were examined by TEM and SEM measurements. TEM and SEM images showed nearly spherical particles with uniform particle size distributions. The Mössbauer spectra of $Zn_{0.5}Mn_{0.5}Fe_2O_4$ ($x = 0$) oxide could be resolved into two quadrupole doublets indicative of paramagnetic spin state. Sm^{3+} substituted $Zn_{0.5}Mn_{0.5}Sm_xFe_{2-x}O_4$ ($0.01 \leq x \leq 0.05$) fine powders show weak sextets in addition to broad doublets attributed some particles' magnetic moments in an ordered magnetic phase. The compounds have small coercive fields and high saturation magnetization (40 emu/g to 60 emu/g) which reduces with increasing Sm^{3+} content due to the paramagnetic nature of Sm ions. Results show that $Zn_{0.5}Mn_{0.5}Sm_xFe_{2-x}O_4$ substituted Sm are suitable for applications in electronic devices requiring high frequencies.

1. Introduction

Nano crystalline ferrites are a group of magnetic nanoparticles with the general chemical formula MFe_2O_4 where M are divalent ions such as Zn^{2+}, Cd^{2+}, Co^{2+}, Mn^{2+} etc. or a mixture. Their properties such as chemical stability at high temperature, high dc resistivity, mechanical hardness, high Curie temperature, and high permeability make them good materials for technology and industry [1]. Zn substituted Mn ferrites have low resistivity, high power loses making them suitable for applications in electronic devices such as transformers, inductor cores, converters, magnetic heads and electromagnetic wave absorbers [2, 3]. Substitution by low concentrations of rare earth ions can improve the ferrite properties [4, 5]. V. J. Angadi et al [4] prepared $Zn_{0.5}Mn_{0.5}Sm_xFe_{2-x}O_4$ ($0 \leq x \leq 0.05$) by combustion method and carried out Mössbauer spectral studies. Sm^{3+} doped Zn-Mn ferrites were found to have potential applications in electronic devices requiring high frequency [4]. The room temperature Mössbauer spectra of the $Zn_{0.5}Mn_{0.5}Sm_xFe_{2-x}O_4$ ($0 \leq x \leq 0.05$) compounds were indicative of paramagnetic spin phase [4].

La ions were found to have preference for octahedral (B) sites in Ni-Zn ferrites produced by sol-gel method [5]. The distribution of metal cations in A and B sites is sensitive to the sample preparation method and can affect the properties [6]. Magnetization data can reveal additional information such as superparamagnetism which cannot be clearly observed from only Mössbauer studies. However, no studies were done on the low temperature hysteresis loops for these compounds. The information deduced from *M (H)* curves will provide more understanding of the magnetic behaviour of these compounds at low temperature.

In this study we aim to synthesize materials suitable for high frequency electronic devices. Moreover to investigate the effect of Sm^{3+} ion substitution on structural and temperature-dependent magnetic properties of $Zn_{0.5}Mn_{0.5}Sm_xFe_{2-x}O_4$ ($0 \leq x \leq 0.05$) ferrite nano materials produced by glycol-thermal process. To achieve this, the study was done using several techniques such as XRD, TEM, SEM, EDX and Mössbauer spectroscopy, VSM and a mini- cryogenic free system.

2. Experimental details

Materials used to synthesize nano crystalline $Zn_{0.5}Mn_{0.5}Sm_xFe_{2-x}O_4$ ($0 \leq x \leq 0.05$) were of high purity (98+) and supplied by Aldrich Sigma Company of South Africa. The samples were prepared by glycol-thermal process from metal chlorides $FeCl_3{\cdot}6H_2O$, $MnCl_2{\cdot}6H_2O$, $SmCl_3{\cdot}6H_2O$ and $ZnCl_2$ following procedures reported previously [7]. The XRD analysis was done by using a monochromatic beam of Co K_α radiation (λ = 1.7903 Å) on a model PANalytical Empyrean diffractometer. The morphology and micro-structure were investigated on a high-resolution scanning electron microscope (HRSEM, Ultra Plus ZEISS-FEG HRSEM instrument) and high resolution transmission electron microscope (HRTEM, type: Jeol_JEM-1010), respectively. The Mössbauer spectra were recorded at about 300 K using a conventional constant acceleration Mössbauer spectrometer with a ^{57}Co source sealed in Rh matrix. The room temperature magnetization measurements were performed by using a Lake-Shore model 735 vibrating sample magnetometer and temperature-dependent magnetization measurements were performed by Cryogenic Ltd mini-cryogen free system from 2 – 300 K.

3. esults and discussions

The XRD patterns for the as-synthesized $Zn_{0.5}Mn_{0.5}Sm_xFe_{2-x}O_4$ ($0 \leq x \leq 0.05$) fine powders are shown in figure 1. The XRD patterns of all samples exhibit typical reflections of (111), (220), (311), (400), (422), (511) and (440) planes of a cubic spinel lattice with no traces of impurity phases. The broad peaks observed are indicative of fine particles. The average crystallite sizes listed in Table 1 were computed from the most intense (311) XRD peak using the Debye Scherer formula [8]. The reaction pressure has an efficient effect on crystallite sizes. The crystallite size fluctuates between 12 nm and 17 nm. The fluctuation is caused by reaction pressure during sample preparation process. It is observed from the table that a higher reaction pressure results in a higher particles size and vice versa. A typical TEM image is shown in Figure 2 for the sample x = 0.05. The particles are nearly spherical in shape with average particle diameter of about 15 nm, comparable to about 13 nm estimated from XRD data. The distributions of particle sizes are shown in Figures 3 sample x = 0.05 show narrow particle size distributions. The typical SEM image for sample x = 0.05 shown in Figure 4 (a) which also reveal nearly spherical agglomerated fine particles with homogeneous surface morphology. The elemental composition was confirmed by EDX shown in Figure 4 (b) and reveals the presence of characteristics peaks of Mn, Zn, Fe and Sm for x = 0.05 sample.

The Mössbauer spectra for $Zn_{0.5}Mn_{0.5}Sm_xFe_{2-x}O_4$ nanosized oxides are shown in Figure 5. The best fit to the experimental data for the compound $Zn_{0.5}Mn_{0.5}Fe_2O_4$ (x = 0) was obtained with two doublets associated with paramagnetic spin state. The Mössbauer spectra of Sm substituted Zn-Mn in the current work show weak sextets which were not observed in same compounds produced by combustion method [4]. This shows the effect of sample preparation method on the magnetic properties. The weak sextets (2-22 %) may be due to single domain particles with ordered magnetic phase and the redistribution of cations in tetrahedral (A) or octahedral (B). The fine powders of $Zn_{0.5}Mn_{0.5}Sm_xFe_{2-x}O_4$ ($0.01 \leq x \leq 0.05$) could be fitted with two sextets and two quadrupole doublets associated with ^{57}Fe nuclei distributed

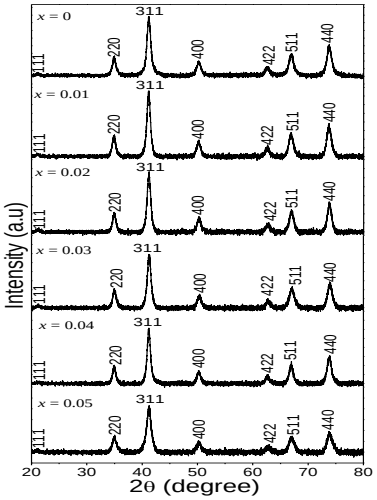

Figure 1. XRD patterns for as-prepared $Zn_{0.5}Mn_{0.5}Sm_xFe_{2-x}O_4$ oxides.

Table 1. Crystallite size (D), reaction pressures (P), lattice parameter (a) and X-ray density (ρ) for $Zn_{0.5}Mn_{0.5}Sm_xFe_{2-x}O_4$ oxides as function.

	D_{XRD} (nm)	P (psi)	a (Å)	ρ (g/cm^3)
x	± 0.2		±0.001	±0.003
0.00	14.7	90	8.439	5.213
0.01	15.1	80	8.440	5.223
0.02	14.4	40	8.435	5.262
0.03	14.0	30	8.425	5.302
0.04	16.5	60	8.436	5.268
0.05	12.5	20	8.430	5.336

within A and B sites. The spectrum for sample $x = 0.04$ with larger particles (~17 nm) that resulted from reaction highest pressure, shows stronger sextets (~42 %) due to ferromagnetic ordering large particles. The average isomer shift was about 0.35 mm/s for the whole composition range. The s electron charge distribution of Fe ions was therefore weakly affected by Sm ion substitution. The A site quadrupole splitting and line width were generally lower compared to B sites. This behaviour is attributed to high symmetry at A site.

The typical room temperature magnetization curves are presented in Figure 6 for $x = 0$, $x = 0.03$ and $x = 0.05$ oxides. The insert shows the magnified view at low magnetic field. $Zn_{0.5}Mn_{0.5}Sm_xFe_{2-x}O_4$ ($0.01 \leq x \leq 0.05$) samples have small coercive fields and high saturation magnetization which are relevant microwave properties [8]. Very small coercive magnetic fields and remnant magnetization are indicative of superparamagnetic nanoparticles [9]. Saturation magnetization values can be computed by fitting initial magnetization curves with the empirical law of approach to saturation based on the relation $M_S(H) = M_S(0)(1-a/H-b/h^2) + \chi H$ [10, 11], where a and b are the fitting parameters and χ is the high-field susceptibility due to field induced band splitting and are shown in Figure 7. Magnetization reduces from 58.9 emu/g at $x = 0$ to 47.2 emu/g at $x = 0.05$, with increasing Sm^{3+} ion content. This can be explained by the weakening of the super-exchange interactions between the B sites magnetic moments due to substitution of Fe^{3+} ions by paramagnetic Sm^{3+} ions. The magnitude of the magnetization in ferrites is

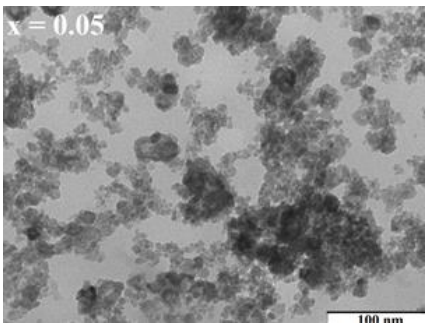

Figure 2. TEM image for as-prepared $Zn_{0.5}Mn_{0.5}Sm_{0.05}Fe_{1.95}O_4$ ($x = 0.05$).

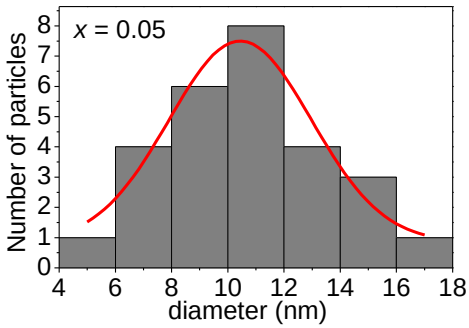

Figure 3. Particle size distribution for as-prepared $Zn_{0.5}Mn_{0.5}Sm_{0.05}Fe_{1.95}O_4$ (x=0.05).

 ISBN: 978-0-620-88875-2

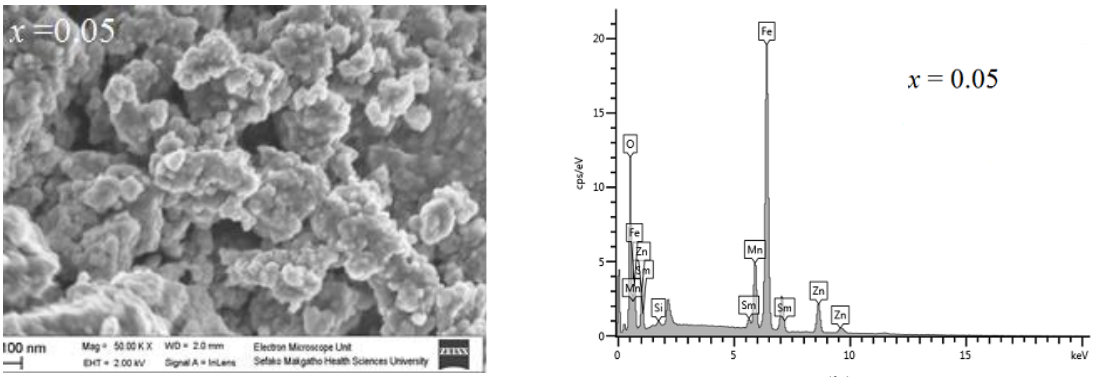

(a) (b)

Figure 4. SEM image (a) and EDX image (b) for $Zn_{0.5}Mn_{0.5}Sm_{0.05}Fe_{1.95}O_4$ (x = 0.05).

due to the difference between the magnetization at A- and B sub-lattices ($M = |M_B - M_A|$) [12]. For the $Zn_{0.5}Mn_{0.5}Fe_2O_4$ (x = 0) oxide magnetization is due to the magnetic Mn and Fe ions in A and B sites. Dilution of the B site magnetic neighbors by paramagnetic Sm^{3+} ions causes weaker super-exchange interactions between magnetic moments (B-O-B) and thus low B site magnetization (M_B). These results are well in agreement with Mössbauer results. The values of the magnetic moment per formula unit (magneton number*)* were calculated using the relation $\eta_B = MM_S/5585$ [11]. Where M is the molecular weight of the ample and M_s is the saturation magnetization. A general decrease in η_B relates well with reduction in saturation magnetization observed with increasing concentration of Sm^{3+} ions. This can be explained by the Neel's theory of ferrimagnetism [13] due to the nonmagnetic nature of Sm ions.

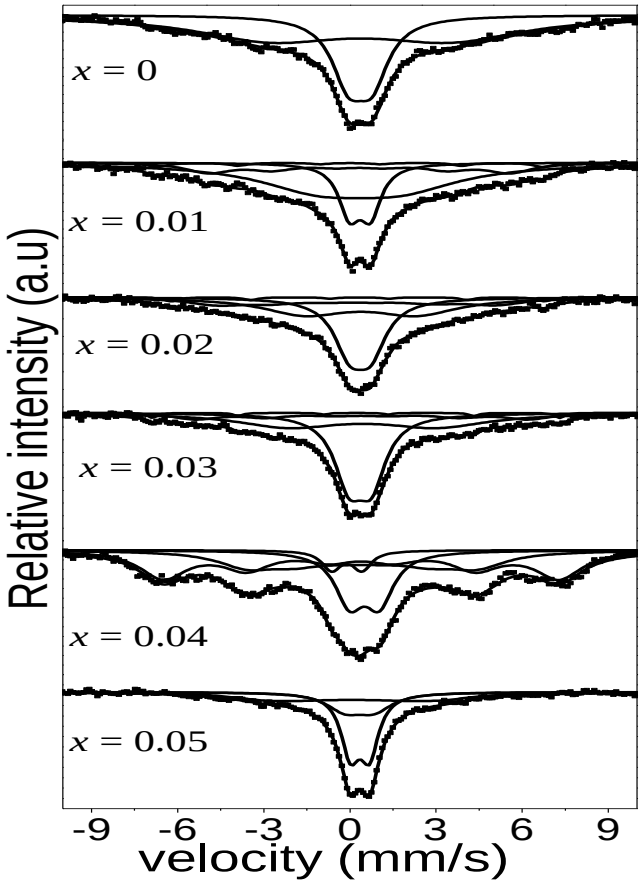

Figure 5. Room temperature Mössbauer spectra for the as-prepared $Zn_{0.5}Mn_{0.5}Sm_xFe_{2-x}O_4$ oxides indicating paramagnetic nature of compounds.

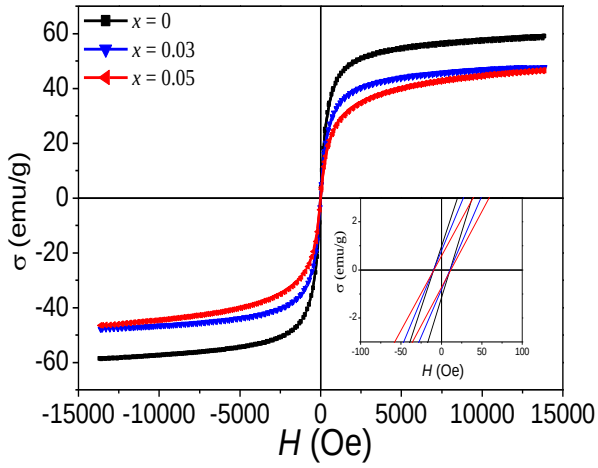

Figure 6. Room temperature hysteresis loops for $Zn_{0.5}Mn_{0.5}Sm_xFe_{2-x}O_4$ oxides.

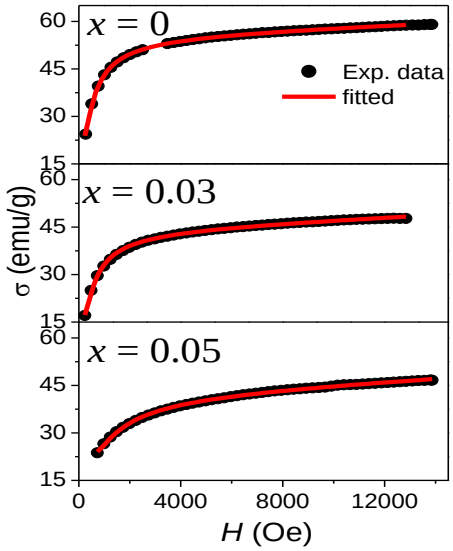

Figure 7. Initial magnetization with best fit curves based on empirical law approach to saturation magnetization.

The ratios of remnant (M_R) to saturation magnetizations (M_S) are listed in Table 2. M_R/M_S ratio is called the squareness of a hysteresis loop. It was about 2 % for samples $Zn_{0.5}Mn_{0.5}Sm_xFe_{2-x}O_4$ ($0.01 \leq x \leq 0.04$). An increase to about 5 % has been observed for sample $x = 0.05$. Small squareness is associated with non-interacting single domain particles [14]. The smaller values observed in the current study are in agreement with the Mossbauer data which shows paramagnetic spin state in the $Zn_{0.5}Mn_{0.5}Sm_xFe_{2-x}O_4$ ($0 \leq x \leq 0.05$) fine powders. The typical hysteresis loops recorded at different isothermal temperature from 2 K - 300 K to 2 k are shown in Figure 8 for sample $x = 0.05$. Small coercive fields are observed even at low temperatures. Magnetization increases with reducing temperature due to spin freezing of the magnetic moments [15]. Small coercive fields are observed for these samples even at lower temperatures. A plot of the variation of the magnetization for different compositions with increasing temperature is also shown in Figure 9. Reduction in magnetization with increasing temperature is due to increasing thermal energies resulting in disordered magnetic spin phase.

Table 2. Room temperature magnetization parameters (deduced from Figure 7) and magneton number (η_B) for $Zn_{0.5}Mn_{0.5}Sm_xFe_{2-x}O_4$ oxides.

X	M_r (emu/g)	M_s (emu/g)	*SQR*	μ_B *(emu/g)*
0	1.082	58.9	0.0184	2.49
0.03	0.808	44.6	0.0169	1.91
0.05	0.651	42.7	0.0525	1.84

 ISBN: 978-0-620-88875-2

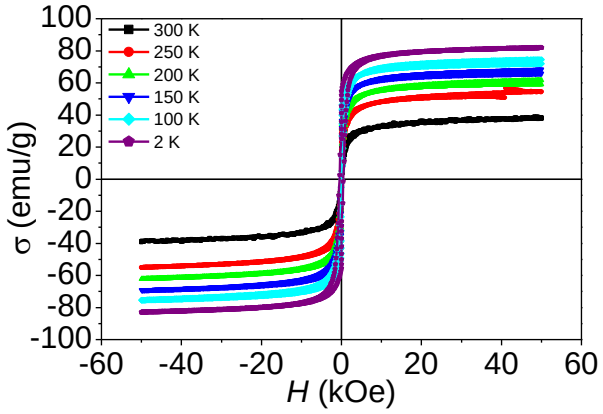

Figure 8. Temperature-dependent magnetization curves for $Zn_{0.5}Mn_{0.5}Sm_{0.05}Fe_{1.95}O_4$ oxide.

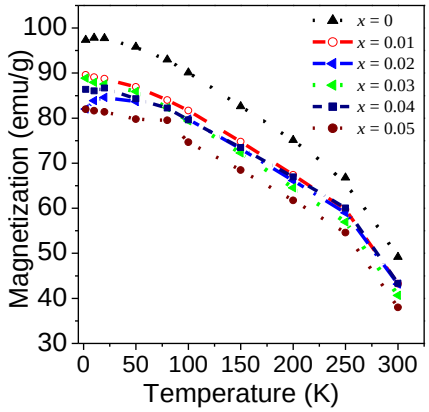

Figure 9. Highest magnetizations deduced from different isothermal temperatures.

4. Conclusions

Nanostructured $Zn_{0.5}Mn_{0.5}Sm_xFe_{2-x}O_4$ ($0 \leq x \leq 0.05$) were successfully prepared by glycol thermal technique. Synthesis route have significant effect on the structural and magnetic properties. Room temperature Mössbauer spectra of the samples investigated in the current study show weak sextet superimposed with paramagnetic doublets. Magnetization data revealed superparamagnetic nature of the compounds investigated. Slight change in coercive fields are observed at lower measuring temperatures. A reduction in saturation magnetization with increasing Sm content associated with the paramagnetic nature of Sm^{3+} ion has been observed. These properties make the compounds suitable for high frequency applications.

Acknowledgements

T. A. Nhlapo wishes to thank NRF of South Africa for financial support. Electron Microscope Unit of Sefako Makhatho Health Sciences University (SMU) for TEM measurements.

References

[1] S. Hcni, N. Kouki, A. Omri, A. Dhahri, M. L. Bouazizi, J. Magn. Magn. Mater. 464 (2018) 91.
[2] W.R. Agami J. Phys. Condens. Mater. 534 (2018) 17.
[3] Md. D. Rahaman, Md. D. Dalim Mia, M.N.I. Khan, A.K.M A. Hossain, J. Magn. Magn. Mater. 404 (2016) 238.
[4] V. J. Angadia, S. P. Kubrin, D. A. Sarychev, S. Matteppanavar, B. Rudraswamy, H. Liu, K. Praveena, J. Magn. Magn. Mater. 441 (2017) 348.
[5] Y. Wang, X Wu, W. Zhang, W. Chen, J. Magn. Magn. Mater. 398 (2016) 90.
[6] J. Hua, Y. Liu, L. Wang, M. Feng, J. Zhao, H. Li, J. Magn. Magn. Mater. 402 (2016) 166.
[7] J. Z. Msomi, Nhlapo T. A, T. Moyo; J. Snyman, A. M. Strydom, J. Magn. Magn. Mater. 373 (2015) 74.
[8] I. Sadiq, S.Naseem, M. N. Ashiq, M. A. Iqbal, I. Ali, J. Magn. Magn.Mater. 395 (2015) 159.
[9] J. Wang, X. Shao, G. Tian, Z. Li, W. Bao, J. Mater. Lett. 192 (2017) 36.
[10] P. T. Phuong, P. H. Nam, D. H. Man, In-Jab Lee J. Magn. Magn. Mater. 433 (2017) 76.
[11] J. M. D. Coey, Magnetism and Magnetic Materials, Cambridge University press, UK, 2010, pp. 218-244.
[12] M. Gupta, Anu, R. K. Mudsainiyan, B. S Randhawa J. Analyt Appl. Pyrol. 116 (2015) 75.
[13] M. Gupta, B.S. Randhawa, J. Alloys Compd. 626 (2015) 421.
[14] A. V. Raut, D. V. Kurmude, D. R. Shangule, K. M. Jadhav, Mater. Res. Bull. 63 (2015) 123.
[15] P. Masina, T. Moyo, H. M. I. Abdallah J. Magn. Magn. Mater. 381 (2015) 41.

TRACK B – NUCLEAR, PARTICLE AND RADIATION PHYSICS

Electronic Stopping Force of ^{16}O and ^{28}Si Heavy Ions in Tantalum Nitride by Time of Flight Spectroscopy

T Nkwashu[1], M Msimanga[2, 3] and S J Moloi[1]

[1] Department of Physics, University of South Africa, Florida Campus, South Africa
[2] Department of Physics, Tshwane University of Technology, Acadia Campus, South Africa
[3] Ithemba LABS, National Research Foundation, South Africa

t.nkwashu@gmail.com; MsimangaM@tut.ac.za; Moloisj@unisa.ac.za

Abstract. Accurate stopping force data of energetic ions in matter is important not just in the study of fundamental ion-matter interactions but also in practical applications that depend on particle-matter interactions. The work presented here describes the measurement of energy loss of heavy ions (O and Si) through a thin metallic film (TaN) using a Time of Flight – Energy spectrometer (ToF-E). Energy loss measurements are then used to calculate the stopping force. It is shown from the results, that the experimental and theoretical stopping force show the same trend of variation with energy, although there is a clear discrepancy between the experimental and theoretical data. The difference between the experimental results and theory is explained in terms of possible ion-atom interaction mechanisms.

1. Introduction

Knowledge of stopping force in matter is important for applications that are dependent on ion transport in matter. These applications include ion beam materials analysis, materials modification and ion implantation, ionization radiation dosimetry and tumour suppression in medicine, and validation of theoretical and experimental data [1, 2, 3, 4].

Electronic stopping force of ions in matter has been studied extensively over the years [5, 6, 7]. Although a lot of research on light ion ($Z<3$) stopping has been done in this field, not much work has been done on heavy ions [1, 8]. This has led to the need for further research in the stopping of heavy ions in matter, especially in the Bragg peak region, where the maximum stopping force lies. The Bragg peak region is of special importance in ion beam analysis work, because it corresponds to the energy region in which most measurements are carried out. This work presents measurements carried out to determine energy lost by an ion beam while moving through a thin film by using a Time of Flight – spectrometer and a silicon surface barrier detector (SBD). The energy lost and the thickness of the film were used to calculate the stopping force of heavy ions through the film.

 ISBN: 978-0-620-88875-2

2. Stopping Force

When an ion beam penetrates solid matter, a series of collisions occur between the incident ions and the atoms' nuclei and/or electrons of the target material. Once the ion beam enters the target material, energy and momentum is transferred from the projectiles to the target material [1, 5, 9]. The projectiles interact with the target nuclei or electrons in one of two general mechanisms at a time: nuclear energy loss or electronic energy loss [9]. Nuclear energy loss is dominant for low energy heavy ions (stopping force in the eV/Å range) [9]. Nuclear energy losses occur due to elastic collisions where energy is imparted from the projectile to the target atom by momentum transfer [10]. Electronic energy loss is dominant for light ions at any energy and high energy heavy ions (stopping force in the KeV/Å range) [9]. Electronic energy loss occurs due to inelastic scattering, where the electrons of the projectile interact with the electrons of the target atom [10].

Energetic ions penetrating a material collide with target atoms, thus losing a fraction of their energy with each and every successive collision. The ions will eventually lose all their energy and come to a complete stop [9]. The stopping force is defined as the rate at which ions lose energy in a target material and is given by dE/dx [5].

3. Experimental Method

Figure 1 is a schematic of the experimental set up used in this work. The incident ion beam, bombards a suitable target sample film that contains elements of interest. The incident beam ejects or recoils target atoms of different masses and energies, from the target sample, and some travel towards the detector system. In other instances, depending on the mass of the target atoms, some of the incident ions are forward scattered towards the detector system. Energy lost by each detected projectile that passes through the target foil as shown in Fig 1, is measured with the aid of a Time of Flight (ToF) spectrometer and a silicon Surface Barrier Detector (SBD). The ToF spectrometer measures the energy of the particle *before* it enters the stopping foil. After passing through the foil, the particle comes to a complete stop in the SBD energy detector where it deposits all of its residual energy. The particle's residual energy is measured by the SBD.

The energy lost, ΔE, is given by:

$$\Delta E = E_1 - E_2 \quad [1]$$

Where E_1 is the energy of the projectile before interaction with the foil (measured by the ToF spectrometer) and E_2 is the energy of the projectile after passing through the foil (tagged by the SBD).

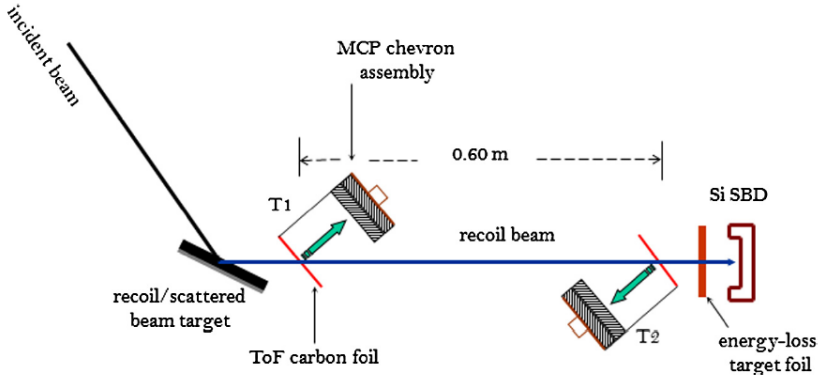

***Figure 1**: schematic representation of the experimental setup [7]*

The ToF spectrometer is an energy spectrometer that uses two detectors, to measure the time of flight of the particle of choice. Both detectors should be transparent and not alter the energy and/or trajectory of the particle of interest [13, 14]. Knowing the distance between the two detectors ($l = 0.6$

m), the ToF of the projectile particle of interest (t_1), and the mass of the projectile (m), the incident energy (E_1) of the particle is then given by the non-relativistic formula:

$$E_1 = \frac{m}{2}\left\{\frac{l}{t_1}\right\}^2 \quad [2]$$

Due to the known non-linearities of silicon SBDs in the detection of heavy charged particles, the ToF spectrometer is used to provide a 1-1 channel-to-energy calibration of the SBD, for each atomic species. That is, a measurement carried out *without* the stopper foil inserted in the particle path means that the energy determined from the ToF is the same as that measured by the SBD. Therefore, two measurement runs are actually carried out; with and without the stopper foil in place – from which the incident energy E_1 and the residual energy E_2 are obtained, respectively. Equation 1 then becomes

$$\Delta E = \frac{m}{2}\left\{\left(\frac{l}{t_1}\right)^2 - \left(\frac{l}{t_2}\right)^2\right\} \quad [3],$$

And the stopping force, the energy loss per unit depth, is given by

$$S = \frac{\Delta E}{\Delta x} \quad [4],$$

Where Δx is the thickness of the target foil.

To determine energy loss from the raw data, the exit energy is determined from a ToF–E measurement without any stopper foil between timing detector t_2 and the SBD. The energy signal from the SBD is used to tag events of a similar energy on two ToF curves; before and after the stopper foil is inserted and the corresponding ToF then used to calculate the energy in each instance using the known atomic mass and flight length. The procedure is then repeated for a series of different energies along the energy axis to generate a continuous energy loss curve [6]. Figure 2 is an example showing results from a measurement set up where the target sample was a film of Al_2O_3 [11]. Two measurement runs, with and without a stopper foil were carried out and the coincidence measurement of the ToF and Energy for each detected particle generated the 2-D ToF vs Energy scatter plot shown. From this plot, projections on to the ToF axis gave t_1 and t_2 values used in Eq. 3, for both ^{27}Al and ^{16}O species.

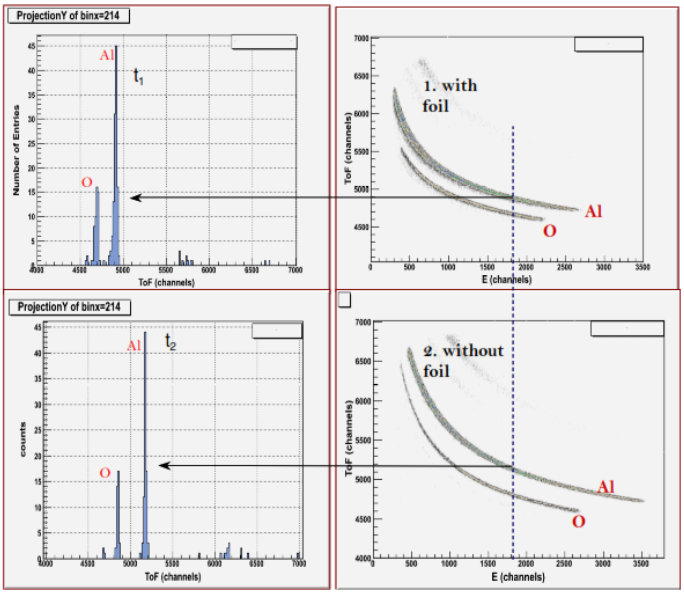

Figure 2. An example of raw data from measurements carried out with and without a stopper foil. The projections show ToF slices used to calculate energy before and after the Al ion passes through the foil

 ISBN: 978-0-620-88875-2

4. Results and Discussion

In this work the initial energy of the projectile was 26 MeV Cu^{7+}, and the target was a thick quartz (SiO_2) sample, from which recoils of ^{28}Si and ^{16}O were obtained. The stopper foil consisted of a thin film of TaN on a Si_3N_4 backing membrane. The energy loss measured, E_1-E_2, was therefore across the entire foil. In order to calculate stopping force across the TaN film, it was important to use the stopping force (S_M) of the backing membrane for ^{28}Si and ^{16}O ions, to account for the energy loss in the membrane. For this work, previous experimental data was used for the stopping force of Si_3N_4 for ^{28}Si and ^{16}O ions [7]

Correcting for energy loss in the Si_3N_4, the stopping force (S_F) in the TaN was then given by:

$$S_F = \frac{E_1 - (S_M \times \Delta x_M + E_2)}{\Delta x_F}$$

Where Δx_F is the thickness of the film of interest and Δx_M is the thickness of the backing membrane.

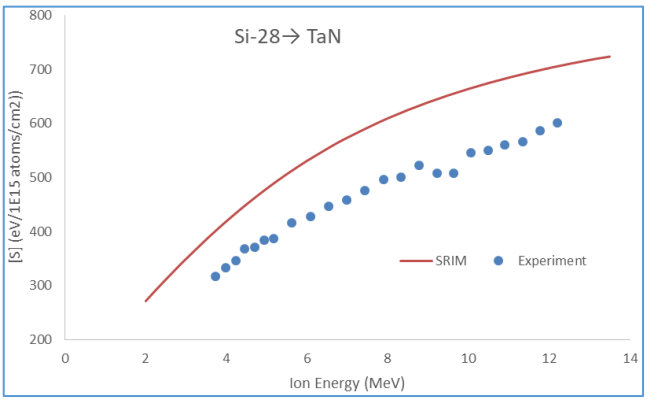

Figure 3

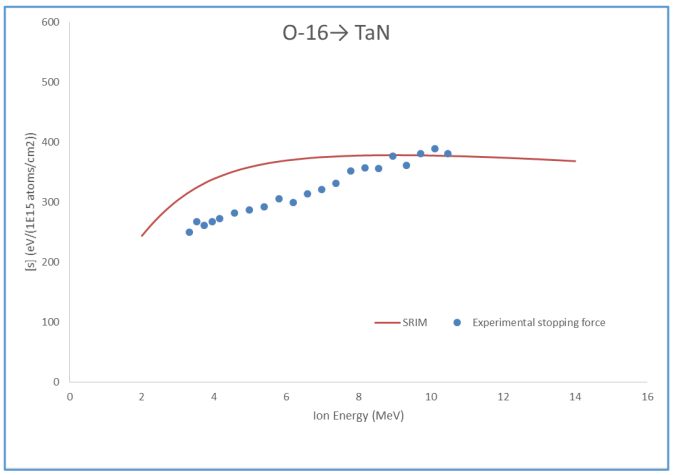

Figure 4

Figures 3 and 4 show the stopping force of Silicon and oxygen across a wide range of energies. Experimental data is compared to predictions of the semi-empirical code *Stopping and Range of Ions in Matter* (SRIM) [5]. Both plots show that SRIM overestimates experimental data around the Bragg peak region. The deviation between the experimental and theoretical data is about 24% for ^{28}Si in TaN and 22% for ^{16}O in TaN. This may be due to a lack of experimental data for the O-TaN and Si-TaN collision systems and/or a lack of proper accounting for charge-exchange of the projectile ion as it

traverses the target. Incidentally no other experimental data could be found in the literature for these collision systems.

5. Conclusion

The electronic stopping force of silicon and oxygen in TaN have been determined as described above. The measurement method and data analysis procedure facilitate spanning a wide range of energies in one measurement run. Results obtained show clear discrepancies between experiment and theory and point to a need for more measurements to validate our data for further testing of theoretical predictions.

6. Acknowledgements

The authors would like to thank the NRF (iThemba LABS TAMS), UNISA and Tshwane University of Technology for material and financial support, and to acknowledge Prof Daniel Wamwangi of WITS University for assistance with foil fabrication. T. Nkwashu would also like to acknowledge ARMSCOR for his study bursary.

References

[1] R. Miksova, V. Hnatowicz, A. Mackova, P. Malinsky and P. Selpicka, "The Stopping power and Energy Straggling of Heavy Ions In Silicone," *Nuclear Instruments and Methods in Physics Research B,* vol. 354, pp. 205-209, 2015.

[2] R. Mikšová, V. Hnatowicz, A. Macková, P. Malinsky and P. Slepicˇka, "The stopping power and energy straggling of heavy ions in silicon nitride," *struments and Methods in Physics Research B,* vol. 354, pp. 205-209, 2015.

[3] R. Hellborg, H. J. Whitlow and Y. Zhang, Ion Beam in Nanoscienc and Technology, Heidelberg: Springer, 2009.

[4] R. C. Brundle, C. A. Evans, Jr and S. Wilson, ENCYCLOPEDIA OF MLATERIALS CHARACTERIZATION, Greenwich: Manning Publications Co, 1992.

[5] J. F. Ziegler, M. D. Ziegler and J. P. Biersack, "SRIM - The stopping and range of ions in matter (2010)," *Nuclear Instruments and Methods in Physics Research Section B,* vol. 268, no. 11-12, pp. 1818-1823, 2010.

[6] M. Msimanga, C. Pineda-Vargas, T. Hlatshwayo, C. Comrie, H. Ammi and M. Nkosi, "Electronic stopping force of C^12, Si^28 and Cu^63 in HfO2 and SiO2 dielectric films," *Nuclear Instruments and Methods in Physics Research B ,* no. 322, pp. 54-58, 2014.

[7] M. Msimanga, C. M. Comrie, C. A. Pineda-Vargas, S. Murray, R. Bark and G. Dollinger, "A Time of Flight-Energy spectrometer for stopping power measurements in Heavy Ion-ERD analysis at iThemba LABS," *Nuclear Instruments and Methods in Physics Research,* vol. 267, pp. 2671-2674, 2009.

[8] M. Mayer, SIMNRA User's Guide, Garching: Max-Planck-Institut für Plasmaphysik, 1997.

[9] D. Fink and L. T. Chadderton, "Ion-Solid Interaction: Status and Perspectives," *Brazilan Journal of Physics,* vol. 35, no. 3B, pp. 735-740, 2005.

[10] L. A. Giannuzzi, B. I. Prenitzer and B. W. Kempshall, ION - Solid Interactions, Hillsboro: Nanospective inc, 200.

[11] M. Msimanga, Development of a Time of Flight – Energy spectrometer for applications in Heavy Ion – Elastic Recoil Detection thin film analysis, Cape Town, 2010.

Testing and Simulating the Response of a New Tracking Sensor for the ATLAS Detector

Ryan Justin Atkin

Department of Physics, University of Cape Town, Private Bag X3, Rondebosch 7701, Cape Town, South Africa

E-mail: rjatkin93@gmail.com

Abstract. The Large Hadron Collider (LHC) will undergo upgrades to the High Luminosity LHC (HL-LHC) in 2024, increasing the instantaneous luminosity almost four fold. This will require the detectors to be upgraded in order to cope with the large increase in data rates and radiation as well as improving the tracking and particle reconstruction in the higher occupancy environment. A major upgrade to the ATLAS detector will be replacing the current Inner Detector (ID) with a fully silicon semiconductor-based Inner Tracker (ITk). The sensors in the ITk strip forward region will use radial geometries, however until now the testbeam simulation and reconstruction software packages were designed with cartesian geometries. Presented is the work behind implementing a radial geometry and co-ordinate system, as well as a charge propagation model for one of the ITk strip forward sensors, the R0 module, in these testbeam software packages. The data from the EUDET testbeam telescope at DESY, Hamburg, and the simulated data both undergo the same reconstruction. A comparison between the two is performed in order to validate the radial geometry and charge propagation model.

1. Introduction

With new physics searches pushing the limits of the current Large Hadron Collider (LHC) [1] and its detectors, an upgrade of the LHC to the High Luminosity LHC (HL-LHC) [2] has been planned. The principal upgrade will occur during the third Long Shutdown (LS3) starting at the beginning of 2024 [3]. The upgrade will increase the instantaneous luminosity to an ultimate value of $\mathscr{L}_{ins} = 75\text{nb}^{-1}.\text{s}^{-1}$ [3], around 7.5 times the design luminosity. This will result in a total integrated luminosity of around $\mathscr{L} = 4000\text{fb}^{-1}$ during the 10 years of operation and up to an average of $\mu = 200$ collisions per bunch crossing. These improvements will greatly increase the statistics available for analysis while at the same time exceeding the current detectors' design capabilities with respect to pile-up management and radiation tolerance. Therefore the detectors will require an upgrade themselves. In particular, the ATLAS detector's main upgrades (phase-2 upgrades) will occur during LS3 (2024-2026) as laid out in the Letter of Intent (LoI) [4]. The focus will be on upgrading the current Inner tracking Detector (ID) to the full silicon semiconductor Inner Tracker (ITk) [3]. The purpose of the ID upgrade is to improve the tracking resolution as well as cope with the higher occupancy environment and radiation doses.

1.1. ITk

The current ID was designed to deal with an average of 23 proton-proton collisions per bunch crossing, not the proposed 200 during the HL-LHC phase [3]. The current resolution of the

Table 1. The specifications of the R0 module [5]. Rows 0 and 1 were read out by one hybrid, while rows 2 and 3 were read out by another hybrid. The pitch is the distance from the centre of a strip to the centre of the next strip.

Row number	nChips	nStrips	Inner Radius [mm]	Length [mm]	Angular Pitch [μrad]	Min/Max pitch [μm]
0	8	1026	384.500	18.981	193.3	74.3/78
1	8	1026	403.481	23.981	193.3	78/82.6
2	9	1154	427.462	28.980	171.8	73.5/78.4
3	9	1154	456.442	31.981	171.8	78.4/83.9

ID would make pattern recognition difficult and provide a poor track finding efficiency in the higher occupancy environment. The ITk will be a full silicon semiconductor tracker with forward (endcap, $|\eta| > 1.8$) and central (barrel, $|\eta| < 1.8$) regions divided into the strip detector (elongated read-outs capable of measuring 1 spatial co-ordinate) and the pixel detector (square read-outs capable of measuring 2 spatial co-ordinates). The tracking pseudorapidity range will be increased to $|\eta| < 4$, which will be important for electro-weak and new physics searches, as well as improving missing transverse momentum resolution and pile-up jet rejection [3].

2. R0 module

The R0 module is located in the ITk strip endcap, and is the closest module in that region to the interaction region [3]. A module is a composite device composed of a power board and one or two hybrids (kapton board with read-out chips) glued to a silicon semiconductor sensor. An image of the R0 module showing the sensor and hybrids is given in Fig. 2. The shape of the R0 sensor is known as a stereo annulus; it has the inner and outer curved edges concentric to the interaction region while the straight sides converge to a point offset in (x, y) from the interaction point. The strips are placed parallel to the straight sides and focus on the same offset point, providing the strips an angle of 20 mrad off the radial line (stereo angle) [3]. As the strips are only capable of measuring 1 spatial co-ordinate, the combination of strip sensors on either side of a petal with the stereo angle allows for the measurement of the second spatial co-ordinate. The R0 module has two hybrids each reading out two rows of strips. The two inner rows will have a different angular pitch to the two outer rows [5], where the pitch is the distance from the center of one strip to the next. Some of the R0 specifics are given in Table 1. The readout chips provide a 1-bit digital output that only stores a yes or no if the charge collected in a strip is over a predefined threshold charge.

3. Testbeam

The testbeam telescope is a EUDET-type telescope [6] operated by the EUDAQ framework and is located at DESY in Hamburg, Germany. A carbon fibre target in the DESY II e^+/e^- accelerator produces bremsstrahlung radiation that passes through a metal plate converter, producing more e^+/e^- pairs [6]. These electrons pass through a dipole magnet which selects 4.4 GeV electrons to be used as the test beam. The telescope comprises of six Mimosa26 high granularity pixel detectors [7], as shown in Fig. 2, that are used for track finding. The sensor that is being tested is known as a Device Under Test (DUT) and is placed between the third and fourth mimosa detectors. An additional FE-I4 sensor is used to improve the timing of the triggers.

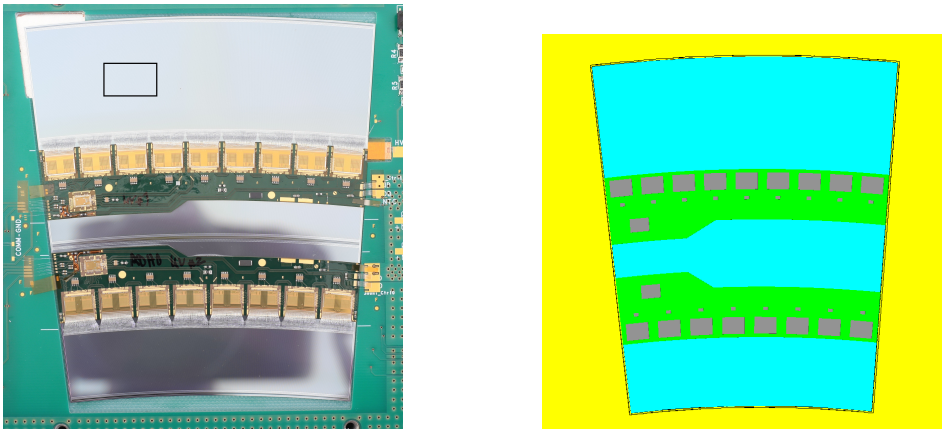

(a) (b)

Figure 1. An image of the R0 module tested in the testbeam (a) and the simulation of that module (b). The green boards going across the sensor are the hybrids, with the readout chips and hybrid controller chip. The black square in (a) is roughly the position and size of the beam for this study.

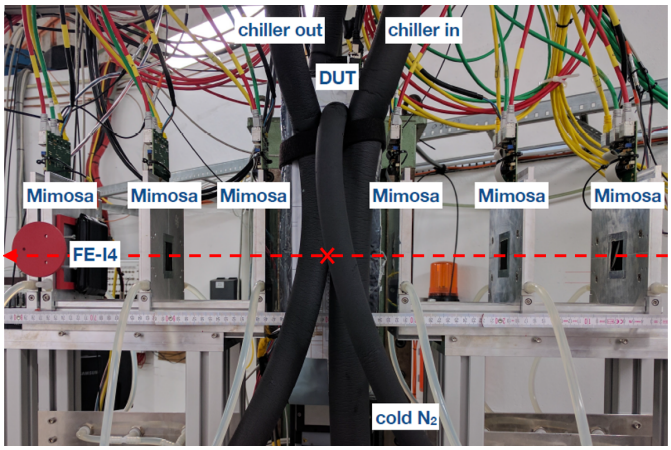

Figure 2. Image of the EUDET testbeam telescope at DESY. Shown are the six mimosa pixel detectors used for beam tracking, the Device Under Test (DUT) and the FE-I4 timing detector. The beam follows the red dashed line from right to left, and the interaction with the DUT occurs at the cross.

4. Simulation, Reconstruction and Analysis

The simulation of the R0 sensor in the testbeam telescope was performed using AllPix [8], a Geant4 [9] based simulator dedicated to the study of solid state detectors. AllPix was developed as a generic simulator for pixel detectors, although it has an important application in the simulation of EUDET-type testbeam telescopes due to the pre-defined detectors and telescope setups. AllPix not only defines the geometries of the sensors, but also simulates the response of the readout chips to the deposited charge for each specific detector. Strips with a deposited charge above a threshold are readout as hits. The reconstruction is performed using EUTelescope [10], a generic pixel-telescope data analysis framework. The software is used to reconstruct the tracks from both the testbeam telescope as well as the AllPix simulation data. Adjacent hits

on each sensor are clustered, and only the clusters across all six mimosa planes are fit to create proto-tracks, which are then used to align all the sensors. After alignment, a final fit of the mimosa clusters is performed to create the final tracks. The final tracks are extrapolated to find the (x, y) position of that track on the DUT. A cluster on the DUT is matched to the track if it lies within a particular distance from the track. The output of the reconstruction is the cluster and track positions in each sensors' local reference frame. This output underwent further analysis to calculate the phi residuals, interstrip clustering and interstrip efficiencies. The phi residual is the distance between the clusters' and reconstructed tracks' phi co-ordinates. The interstrip clustering shows how the probability of a cluster size being greater than 1 changes as we move from one side of a strip to the other. In other words, the probability that the deposited charge in the sensor is shared between neighbouring strips and is over threshold in those strips.

5. Results

This study looked at 4 different thresholds at a position in the fourth row of strips on the R0 sensor, shown in Fig. 1(a). A summary of the phi residuals and charge sharing for the different thresholds is given in Table 2. The uncertainties are purely statistical and are calculated assuming Poisson distributions. The systematic uncertainties from the charge propagation model were not taken into account. Before comparing the effects of different thresholds, a comparison between experiment and simulation is discussed at the threshold of 0.75 fC. The interstrip sharing, shown in Fig. 3(b), matches well between experiment and simulation, however the simulation is slightly higher near the strip edges and lower at the points of curvature around ± 0.3 from the centre of the strip. This is most likely due to the simulation having no noise or random effects added in the propagation of the charges. The interstrip sharing also shows how the probability of sharing in the central region of the strip is consistently very low and that it increases as the incident particle gets closer to the edge. The phi residual is given in Fig. 3(a). The experiment and simulation match very well, and both have a clear secondary peak from clusters of size greater than one due to the lower threshold of this run. The expected phi resolution for the strips in this row, based on single strip clusters, is ~ 49 μrad. The standard deviation of both simulation and experiment residuals are slightly lower than this, as seen in Table 2, since the threshold is low and sharing is relatively high. The plots comparing the different thresholds for the residuals and interstrip clustering are given in Fig. 4 and 5 respectively. As the threshold increases, the secondary peak in the residuals for experiment and simulation gets smaller and eventually disappears. The 3.05 fC threshold samples have almost all clusters as 1 strip clusters, and so have residual resolutions very close to the expected value of ~ 49 μrad. The experimental residual has started to round off at the centre for the 3.05 fC threshold data, becoming more gaussian, while the simulation has flat topped. This is most likely due to some of the electrons in the experiment depositing charge lower than the threshold which does not occur in the simulation since noise is not simulated. The peaks in the sharing plots also drop as the threshold increases, since the threshold becomes larger than the amount of charge shared between the strips. The difference in the values for sharing between experiment and simulation could be due to the one dimensional electric field modeling and no use of noise or random gaussian spreads in the threshold. The conversion of the threshold into femtocoulombs was an approximate fit and so may not be very accurate as well.

6. Conclusion

Due to the HL-LHC upgrade, the ATLAS detector will require an upgrade to cope with the new high pile-up environment. Part of the R&D for this upgrade was the testing and simulation of one of the ITk forward strip modules in a testbeam telescope.

The simulation of the testbeam telescope was compared to the results from the actual experiment. The experimental data performs as was expected for the R0 sensor based on

Table 2. Summary of the experimental (Exp) and simulation (Sim) results for the different thresholds. Shown is the resolution from the residuals, the probability of sharing, and the efficiency. All uncertainties are statistical.

Threshold [fC]	Residual [μrad]		Sharing [%]	
	Exp	Sim	Exp	Sim
0.75	48.78 ± 0.13	47.89 ± 0.07	12.80 ± 0.18	12.48 ± 0.08
1.62	51.19 ± 0.13	51.18 ± 0.08	4.92 ± 0.1	5.66 ± 0.05
2.33	49.90 ± 0.14	51.3 ± 0.08	2.78 ± 0.08	2.98 ± 0.04
3.05	48.66 ± 0.20	49.43 ± 0.08	2.31 ± 0.1	2.10 ± 0.03

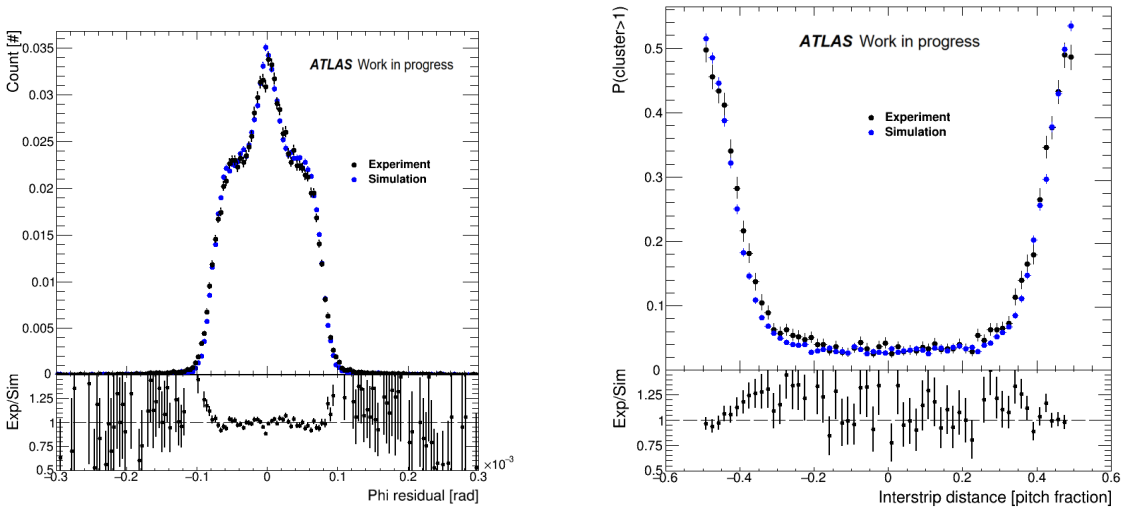

(a) (b)

Figure 3. The interstrip clustering (a) and phi residuals normalised to one (b) for the 0.75 fC run. The black points represent the experimental data while the blue points represent the simulated data. The secondary peaks in (b) are due to clusters of size 2.

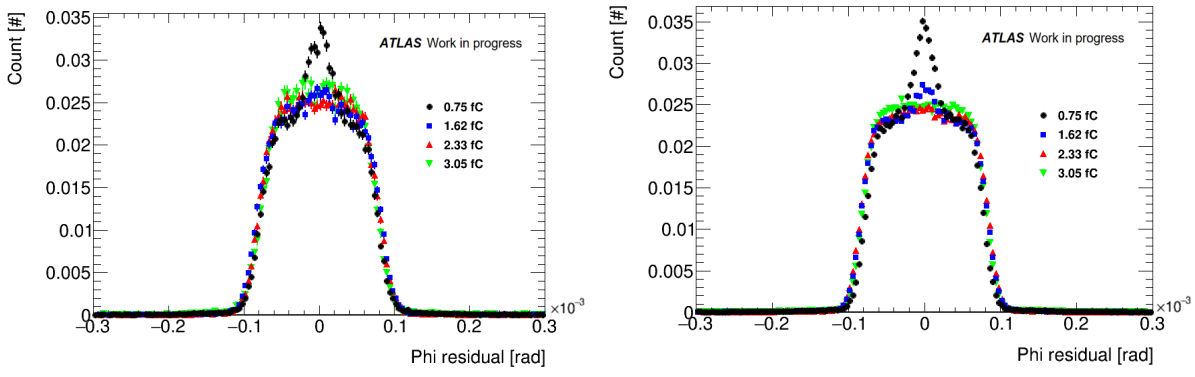

(a) (b)

Figure 4. The phi residuals normalised to one for the experiment (a) and simulation (b) at four different thresholds. The secondary peaks at the lower thresholds are due to clusters of size 2.

 ISBN: 978-0-620-88875-2

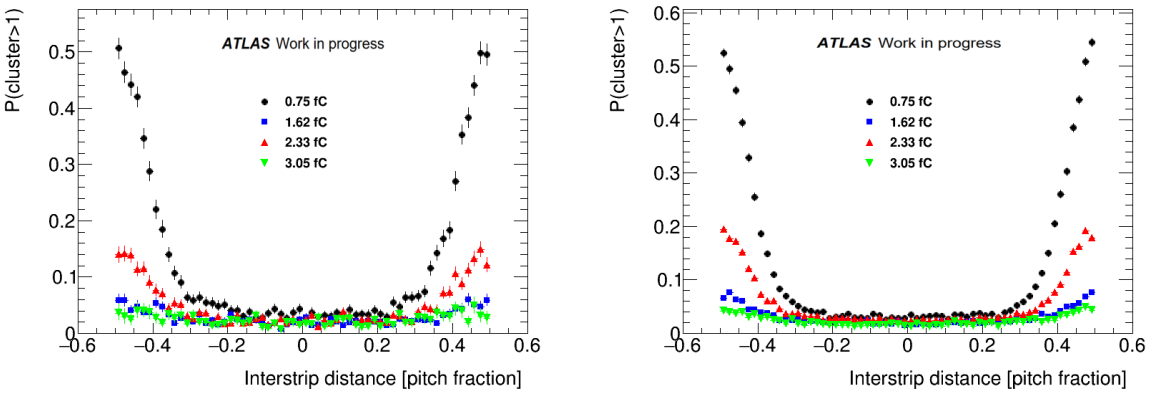

Figure 5. The interstrip clustering for the experiment (a) and simulation (b) at four different thresholds. Interstrip clustering is the probability of a cluster having a size greater than one as a function of the position of a track within a strip.

previous tests done on other strip sensors. This indicates that the radial geometry definitions in EUTelescope provides very good reconstruction of radial data, and that the sensors can go into full production. The simulation of the R0 sensor in terms of both the geometry and the charge propagation works well, predicting how the actual R0 sensor would behave in the testbeam telescope. Improvements to these results would be the inclusion of electronic noise during the digitisation stage of the R0 simulation, more accurately simulating the non-silicon material in the testbeam telescope and having a more accurate threshold conversion.

Acknowledgments

I would like to thank my supervisor Dr. Sahal Yacoob as well as my co-supervisors Dr. Kenneth G. Wraight, Dr. Stephen W. Peterson and Dr. Andrew Blue for their important input and assistance, the NRF for funding my MSc studies and as part of the AIDA2020 project: This project has received funding from the European Unions Horizon 2020 Research and Innovation programme under Grant Agreement no. 654168.

References

[1] Lyndon Evans and Philip Bryant. LHC Machine. *Journal of Instrumentation*, **3**(08):S08001, 2008.
[2] I Bejar Alonso and L Rossi. HiLumi LHC Technical Design Report: Deliverable: D1.10. Technical Report CERN-ACC-2015-0140, Nov 2015.
[3] ATLAS Collaboration. Technical Design Report for the ATLAS Inner Tracker Strip Detector. Technical Report CERN-LHCC-2017-005. ATLAS-TDR-025, CERN, Geneva, Apr 2017.
[4] ATLAS Collaboration. Letter of Intent for the Phase-II Upgrade of the ATLAS Experiment. Technical Report CERN-LHCC-2012-022. LHCC-I-023, CERN, Geneva, Dec 2012.
[5] ATLAS Upgrade Strip Sensor Collaboration. Supply of Silicon Microstrip Sensors of ATLAS12EC specifications. Technical report, 2016.
[6] Hendrik et al. Jansen. Performance of the eudet-type beam telescopes. *EPJ Techniques and Instrumentation*, 3(1):7, 2016.
[7] M. Winter. Development of Swift, High Resolution, Pixel Sensor Systems for a High Precision Vertex Detector suited to the ILC Running Conditions. Technical Report DESY PRC R&D Nr 01/04, 2009.
[8] M. Benoit and J. Idarraga. The AllPix Simulation Framework, 2014.
[9] Geant4 Collaboration. GEANT4: A Simulation toolkit. *Nucl. Instrum. Meth.*, A506:250–303, 2003.
[10] A. Bulgheroni, T. Klimkovich, P. Roloff, and A.F. Zarnecki. EUTelescope: tracking software. Technical Report EUDET Memo-2007-20, 2007.

Background estimation in the measurement of the top quark mass using J/ψ mesons with 13 TeV proton-proton collision data from the ATLAS experiment

Kevin Nicholas Barends

Department of Physics, University of Cape Town, Private Bag X3, Rondebosch 7701, South Africa

E-mail: brnkev010@myuct.ac.za

Abstract. High precision measurements of the top quark mass, m_t, are crucial to probe internal consistency of the Standard Model and increase the precision of predictions of processes involving top quarks. The kinematic properties of the top quark's decay products are correlated to m_t. The best current measurements are predominantly limited by uncertainties related to the reconstruction of jets. However, there is a top quark decay mode which are largely independent of the aforementioned uncertainty but require large amounts of data due to their low production rate. This decay mode includes a J/ψ meson originating from a b-hadron. Background J/ψ mesons contribute and negatively impact the mass measurement. These background contributions can be distinguished from signal J/ψ mesons by exploiting the mass of a J/ψ meson and the unique displaced decay vertex feature of b-hadrons. This paper describes a data-driven technique to determine the contributions from signal and background J/ψ mesons and highlight kinematic regions which limit the contamination of background J/ψ mesons in preparation for the large data-set that will be available at the end of the next data-taking period.

1. Introduction

The top quark's mass, m_t, is a very important quantity as it's not only the heaviest fundamental particle in the Standard Model (SM), but also plays a significant role in a number of areas in the SM as well as in physics Beyond the SM (BSM) [1–3]. The precision of m_t is crucial to probe the consistency of the SM and hence, help constrain scenarios of new physics. The current average top mass of 173.0 $\pm$ 0.4 GeV [4] (also known as the Monte Carlo mass) was determined by combining the kinematics of the top quark's decay products, i.e. jets [5] and leptons. These jets and leptons originated from a primary decay of the top quark (i.e. into a W boson and a b quark) which has a branching fraction of 95.7$\pm$3.4% [4]. There are other ways to measure the top mass which utilize top quark cross section measurements [2] and different ways to quote the top mass depending on the renormalization scheme [6].

Using the kinematics of the jets relies on jet reconstruction which proved to be one of the largest sources of uncertainty in previous mass measurements [7–10]. However, there are other top quark decay signatures that depend less on jet momenta and may produce a more precise measurement of the top mass. As these signatures are very rare, their study is only now

becoming possible due to the large datasets recorded by the Large Hadron Collider (LHC) experiments. One such signature consists of a lepton originating from a W boson signatures and two oppositely charged muons decaying from a J/ψ meson which originated from the b quark. However, this signature is sensitive to lepton backgrounds originating from mis-reconstructed jets or non-prompt processes [11] and J/ψ background originating from non-top quark b-/c-hadron decays (non-prompt background J/ψ), directly from the proton-proton collision (prompt J/ψ) or random combinations of two oppositely charged muons (combinatorial background) [12].

This paper describes a data-driven technique to estimate the contribution from background J/ψ mesons in the lepton+J/ψ top quark decay signature using proton-proton collision data at $\sqrt{s} = 13$ TeV, corresponding to an integrated luminosity of 36.1 fb^{-1}.

2. ATLAS Detector

ATLAS [13] is a general-purpose detector designed to capitalize on the full potential of the LHC [14]. The magnet system consists of a superconducting solenoid surrounding the Inner Detector (ID) and three large superconducting toroids, one barrel and two end-caps, arranged azimuthally symmetric outside the calorimeters and within the Muon Spectrometer (MS). The ID performs precise particle reconstruction and identification of the collision point over $|\eta| < 2.5$, while the calorimeters measure the energy and position of particles over $|\eta| < 4.9$. The MS surrounds the calorimeters and identifies and measures muon up to $|\eta| < 2.7$. These components are integrated with a Trigger and Data Acquisition system and a computing system which selects events which consist of high transverse momenta particles or large missing transverse energy, and stores them for further analysis.

3. Event Selection

The ℓ+J/ψ top quark decay signature requires the W boson to decay leptonically into either an electron or a muon, at least 2 b-tagged jets and two oppositely charged muons with an invariant mass around that of a J/ψ meson (i.e. 3096.900 $\pm$ 0.006 MeV). To enhance the selection of a lepton originating from a real W boson, a quantity known as the transverse mass of the W boson, $\mathrm{m_T(lepton,E_T^{miss})} = \sqrt{2p_\mathrm{T}(\mathrm{lepton})\mathrm{E_T^{miss}}(1-\cos(\phi(\mathrm{lepton})-\phi(\mathrm{E_T^{miss}})))}$, was used. This quantity combines the kinematics of the lepton and the missing transverse energy (which represents the transverse kinematics of the neutrino). The kinematic requirements to extract the ℓ+J/ψ top quark decay signature is summarized in Table 1, where the definitions of the different observables can be found in reference [15–18].

Description	Kinematic criteria
Electron (Muon) selection	Exactly 1 lepton with $\mathrm{p_T} > 25$ GeV, $\lvert\eta\rvert < 2.5$
	$\lvert\Delta z_0 \sin\theta\rvert < 0.5$ mm, $\lvert d_0\rvert/\sigma_{d_0} < 5$ (3), Isolation Gradient
Jet selection	At least 2 b-tagged jets with $\mathrm{p_T} > 40$ GeV
Missing transverse momentum selection	$\mathrm{E_T^{miss}} > 20$ GeV
Real W boson selection	$\mathrm{m_T(lepton,E_T^{miss})} > 40$ GeV
J/ψ muon selection	$\mathrm{p_T} > 2.5$ GeV if $\lvert\eta\rvert < 1.3$, $\mathrm{p_T} > 3.5$ GeV if $1.3 < \lvert\eta\rvert < 2.5$
J/ψ selection	$\mathrm{p_T} > 8.5$ GeV, $\lvert y\rvert < 2.1$, $2 < \mathrm{m}(\mu^+\mu^-) < 3.6$ GeV

Table 1. A table with the kinematic criteria for t $\to \ell$+J/ψ events is shown.

4. Determination of J/ψ backgrounds

The origin of the J/ψ mesons passing the kinematic criteria in Table 1 is unknown. These J/ψ mesons could be prompt J/ψ (i.e. background), non-prompt background J/ψ, combinatorial background or they could have originated from top quark b-hadron decays (non-prompt signal).

The following section describes an approach to determine the different J/ψ mesons in ℓ+J/ψ events. A similar approach was described in reference [19] and may be consulted for more information.

Due to the lifetime of b-hadrons [4], b-hadrons will travel before decaying, i.e. the decay vertex will be located away from the primary vertex. Therefore, prompt and non-prompt J/ψ mesons can be distinguished by studying the position of the decay vertices. This can be done by using a pseudo-proper time variable which makes use of time dilation and length contraction since the proton bunches collide at speeds near that of light. The proper decay time of b-hadrons is related to its proper decay length through $\tau = l/\mathrm{v}$, where l is the contracted length, v is the speed of the b-hadrons and τ is the dilated time variable. The proper decay length can be represented by its actual decay length undergoing time dilation through $l = \mathrm{L}/\gamma$, where L is the decay distance between the primary vertex and the b-hadrons decay vertex. Therefore, the proper decay time is related to the decay distance of the b-hadrons through $\tau = \mathrm{L}/(\gamma\mathrm{v})$. Using the relativistic momentum relation, i.e. $\mathrm{p} = \gamma\mathrm{mv}$, where m is the mass and p is the momentum of the b-hadrons, the proper decay time can be written as $\tau = \mathrm{Lm}/\mathrm{p}$. However, since the ATLAS detector cannot fully reconstruct the momentum of b-hadrons, a good approximation would be to use the transverse momentum (and the mass) of the J/ψ mesons coming from b-hadrons. This will also aid in approximating the decay distance description since the decay distance L can be projected onto the direction of the J/ψ mesons using the reconstructed transverse momentum. Thus, a "pseudo-proper time" variable τ can be used to represent the decay lifetime of b-hadrons, i.e.

$$\tau \equiv \frac{\vec{L} \cdot \vec{p_T}(J/\psi)}{p_T(J/\psi)} \frac{m_{\mu^+\mu^-}}{p_T(J/\psi)} \tag{1}$$

where $\vec{L}$ is the displacement vector from the primary vertex to the J/ψ decay vertex and $\mathrm{m}_{\mu^+\mu^-}$ is the reconstructed mass of the J/ψ mesons (using the invariant mass of the dimuon pair). Non-prompt J/ψ decay vertices will have a $\tau > 0$ (which represents a displaced vertex) whereas prompt J/ψ decay vertices will have a $\tau = 0$, within the position and momentum resolution of the detector.

4.1. Signal J/ψ determination

Since the invariant mass and pseudo-proper time of the J/ψ mesons can be used to distinguish signal and background prompt and non-prompt J/ψ mesons, a simultaneous two-dimensional fit was applied to these distributions to determine the individual contributions. In the invariant mass distribution, the probability density functions for the non-prompt signal and prompt J/ψ mesons were modelled by Gaussian distributions while background processes were modelled by exponential functions. In the pseudo-proper time distribution, the prompt components were modelled by the sum of a delta-function distribution and a double-sided exponential function convoluted with a Gaussian function. However, the non-prompt were modelled by an exponential function convoluted with a Gaussian function. These probability density functions were defined in reference [19] as

$$
\begin{aligned}
M_{J/\psi}(m_{\mu^+\mu^-}) &= G(m_{\mu^+\mu^-}; m_{J/\psi}^{PDG}, \sigma_m) \\
T_{\text{prompt } J/\psi}(\tau) &= G(\tau; 0, \sigma_\tau) \otimes \left((1-a)\delta(\tau) + ae^{-|\tau|/\tau_0}\right) \\
T_{\text{non-prompt } J/\psi}(\tau) &= G(\tau; 0, \sigma_\tau) \otimes \left(\Theta(\tau)e^{-\tau/\tau_1}\right) \\
M_{\text{prompt bkg}}(m_{\mu^+\mu^-}) &= e^{-m_{\mu^+\mu^-}/k_0} \\
M_{\text{non-prompt bkg}}(m_{\mu^+\mu^-}) &= e^{-m_{\mu^+\mu^-}/k_1} \\
T_{\text{prompt bkg}}(\tau) &= G(\tau; 0, \sigma_\tau) \otimes \left((1-b)\delta(\tau) + be^{-|\tau|/\tau_2}\right) \\
T_{\text{non-prompt bkg}}(\tau) &= G(\tau; 0, \sigma_\tau) \otimes \left(\Theta(\tau)e^{-\tau/\tau_3}\right),
\end{aligned}
$$

where $\mathrm{m}_{J/\psi}^{PDG}$ is the mass of the J/ψ meson in the Particle Data Group (PDG, i.e. reference [4]). The a, b, σ_m, σ_τ, k_i and τ_i are nuisance parameters with limits designed to produce a convergence. The total probability density function was defined in reference [19] as

$$
\begin{aligned}
\mathrm{p}_{\text{total}}(m_{\mu^+\mu^-}, \tau) = N_{\text{signal } J/\psi}[&N_{\text{prompt } J/\psi} M_{J/\psi}(m_{\mu^+\mu^-}) T_{\text{prompt } J/\psi}(\tau) \\
&+ (1 - N_{\text{prompt } J/\psi}) M_{J/\psi}(m_{\mu^+\mu^-}) T_{\text{non-prompt } J/\psi}(\tau)] \\
+ (1 - N_{\text{signal } J/\psi})[&N_{\text{prompt bkg}} M_{\text{prompt bkg}}(m_{\mu^+\mu^-}) T_{\text{prompt bkg}}(\tau) \\
&+ (1 - N_{\text{prompt bkg}}) M_{\text{non-prompt bkg}}(m_{\mu^+\mu^-}) T_{\text{non-prompt bkg}}(\tau)]
\end{aligned}
\tag{2}
$$

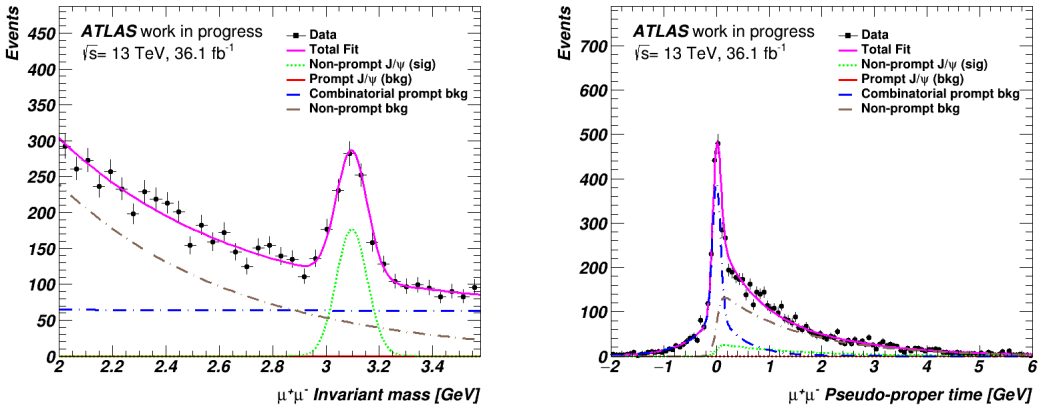

(a) (b)

Figure 1. The invariant mass (a) and pseudo-proper time (b) distribution of the dimuon pair with the contributions from each individual process as well as the total contribution. The prompt J/ψ contribution comes out to be very small and can be seen by the red projections.

After fitting the total probability density function, the total and individual fit results in the invariant mass and pseudo-proper time distributions of the selected J/ψ mesons can be seen in Figure 1 (a) and (b), respectively. In the invariant mass distribution, the peak around the J/ψ mass is dominated by non-prompt signal J/ψ mesons with an almost negligible contribution from prompt J/ψ mesons. There are, however, sizeable contributions from both prompt and non-prompt background with the majority coming from the non-prompt background. In the pseudo-proper time distribution, the background contributions dominate and there is a reasonable

contribution coming from non-prompt signal J/ψ mesons. Once again, there is an almost negligible contribution from the prompt J/ψ mesons. However, these fit results show that the original mass selection between 2 GeV and 3.6 GeV is too loose and a tighter selection cut on the mass (i.e. 2.9 GeV to 3.3 GeV) should be applied as all the non-prompt signal J/ψ mesons are contained within this kinematic region. It is unclear from the pseudo-proper time distribution where to apply cuts in order to improve the signal to background ratio. This can be done, however, by looking at the ratio between the cumulative signal over the cumulative total (see Figure 2). The negative gradient in these distributions show regions where the background contribution dominates over the signal. From the results in Figure 2, selecting J/ψ mesons with a pseudo-proper time between 0.2 and 4.6 ps (i.e. the peaks), the signal to background ratio could improve.

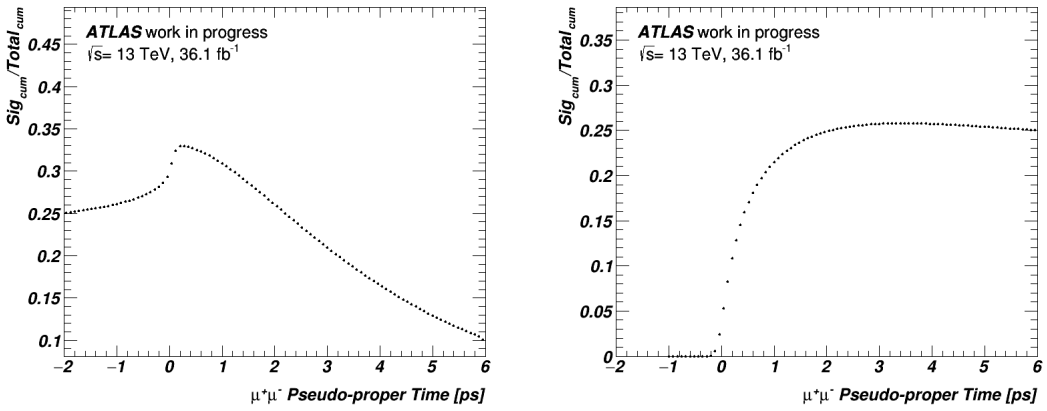

(a) (b)

Figure 2. The ratio between the cumulative signal over the cumulative total is shown for accumulating from left to right (a) and right to left (b) as a function of pseudo-proper time. The peaks occur at 0.2 ps and 4.6 ps, respectively.

4.2. J/ψ background reduction

From the results in Figure 1 and 2, tighter selection criteria on the J/ψ mesons should improve the signal to background ratio. The invariant mass distribution of the J/ψ mesons before, (a), and after, (b), applying a tighter pseudo-proper time selection on the is shown in Figure 3. The signal to background ratio can be quantified by using $S/\sqrt{S+B}$, where S is the non-prompt J/ψ contribution and $S+B$ is the total contribution. Using the yields determined from the fits, this quantity is 0.40 before the pseudo-proper time cut and 0.58 after. Thus, showing an improvement in the signal to background ratio.

5. Conclusion

Measuring the (Monte Carlo) mass of the top quark using the ℓ+J/ψ decay signature reduces the dependency on jet reconstruction. However, this signature consists of background which originates from non-prompt or misidentified jets (i.e. lepton background) and from random muon pairings, b-hadron decays not originating from top quarks, or directly from the proton-proton collision (i.e. J/ψ background). This J/ψ background was determined using a data-driven technique which capitalized on the mass of the J/ψ and the displaced decay vertex of b-hadrons.

The results showed that the extracted ℓ+J/ψ events were dominated by background J/ψ mesons. These top quark events therefore consist of J/ψ mesons not originating from the top

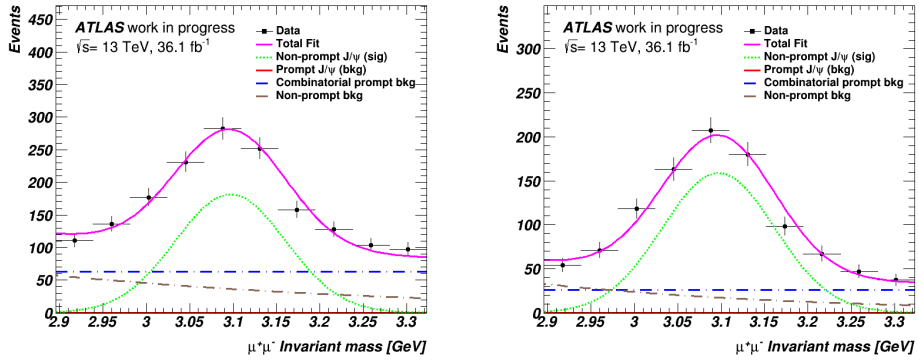

(a) (b)

Figure 3. The invariant mass distribution of the dimuon pair in the mass window 2.9 GeV-3.3 GeV before (a) and after (b) a pseudo-proper time selection cut of 0.2 ps $< \tau <$ 4.6 ps was applied. In each distribution, the contributions from the individual processes as well as the total contribution is shown. The prompt J/ψ contribution comes out to be very small and can be seen by the red projection.

quark's primary decay, reducing the precision of the top mass measurement. However, the results from this data-driven technique showed kinematic regions where these background contributions could be significantly reduced (i.e. 2.9 GeV $< m_{\mu^+\mu^-} <$ 3.3 GeV and 0.2 ps $< \tau <$ 4.6 ps). After applying these tighter selection cuts on the J/ψ mesons, the signal to background ratio improved which should result in a more precise mass measurement.

6. Acknowledgements

I would like to thank the NRF for their financial support and Dr Sahal Yacoob, Prof. Peter Onyisi and Assist. Prof. Tim Andeen for their guidance and continuous support.

7. References

[1] Heinemeyer S, Kraml S, Porod W and Weiglein G 2003 *JHEP* **09** 075 (*Preprint* hep-ph/0306181)
[2] Cortiana G 2016 *Rev. Phys.* **1** 60–76 (*Preprint* 1510.04483)
[3] Degrassi G, Di Vita S, Elias-Miro J, Espinosa J R, Giudice G F, Isidori G and Strumia A 2012 *JHEP* **08** 098 (*Preprint* 1205.6497)
[4] Patrignani C *et al.* (Particle Data Group) 2016 *Chin. Phys.* **C40** 100001
[5] Seymour M H 1995 *AIP Conf. Proc.* **357** 568–587. 20 p URL https://cds.cern.ch/record/283896
[6] Melnikov K and Ritbergen T v 2000 *Phys. Lett.* **B482** 99–108 (*Preprint* hep-ph/9912391)
[7] Sirunyan A M *et al.* (CMS) 2017 *Eur. Phys. J.* **C77** 354 (*Preprint* 1703.02530)
[8] Aaboud M *et al.* (ATLAS) 2016 *Phys. Lett.* **B761** 350–371 (*Preprint* 1606.02179)
[9] Khachatryan V *et al.* (CMS) 2016 *Phys. Rev.* **D93** 072004 (*Preprint* 1509.04044)
[10] Tevatron E W G and Aaltonen T (CD and D0) 2016 (*Preprint* 1608.01881)
[11] Aad G *et al.* (ATLAS) 2014 URL https://cds.cern.ch/record/1951336
[12] Aad G *et al.* (ATLAS) 2015 URL https://cds.cern.ch/record/2046216
[13] Aad G *et al.* (ATLAS) 2008 *JINST* **3** S08003
[14] Voss R and Breskin A (eds) 2009 *The CERN Large Hadron Collider, accelerator and experiments* URL http://www-spires.fnal.gov/spires/find/books/www?cl=QC787.P73C37::2009
[15] Aad G *et al.* (ATLAS) 2016 URL http://cds.cern.ch/record/2157687
[16] Aad G *et al.* (ATLAS) 2016 *Eur. Phys. J.* **C76** 292 (*Preprint* 1603.05598)
[17] Cacciari M, Salam G P and Soyez G 2008 *JHEP* **04** 063 (*Preprint* 0802.1189)
[18] Aad G *et al.* (ATLAS) 2015 URL https://cds.cern.ch/record/2037697
[19] Aad G *et al.* (ATLAS) 2014 *JHEP* **04** 172 (*Preprint* 1401.2831)

Radiological Assessment of Weenen Agricultural Fields Samples

MJ Mvelase[1], PL Masiteng[1], RD Mavunda[1,3], PP Maleka [3]

[1]Physics Department, University of Johannesburg, P.O.Box 524. Auckland Park 2006, Johannesburg, RSA

[2] Radiation Protection Training Centre, South African Nuclear Energy Corporation (Necsa), P.O. Box 582, 0001, RSA a

[3] Department of Subatomic Physics, iThemba LABS, National Research Foundation, P.O. Box 722, Somerset West 7129, RSA

E-mail: emjay.mvelase@gmail.com

Abstract. The radiological hazards were evaluated in the agricultural fields of Weenen, province of KwaZulu-Natal, South Africa. In this study, gamma spectroscopy was used to measure the activity concentrations of the radionuclides in field representative soil samples and two representative soil samples from the control area. The mean equivalent activity concentrations for field samples of ^{238}U, ^{232}Th, and ^{40}K were found to be 23.2±3.9, 44.5±3.5 and 552.5±21.4 Bq.kg-1, respectively. On the other hand, the mean activity concentrations for ^{238}U, ^{232}Th, and ^{40}K from the control area were found to be 19.5±0.9 Bq.kg-1, 39.4±2.9 Bq.kg-1 and 427±30 Bq.kg-1, respectively. Radiological hazard indices calculated from these activity concentrations were lower than recommended safe limits. In particular, calculated mean values for the radium equivalent (Raeq), absorbed dose (D_R), external hazard (H_{Ex}), and Annual effective dose equivalent (D_{Eff}), respectively. All these values were lower than unity, posing a lower health risk to the farm workers in the area.

1. Introduction

Radioactivity is a natural phenomenon that has existed since the formation of earth [1, 2]. The human population is constantly exposed to cosmogenic, primordial and anthropogenic radiations [2, 3, 4] . The natural radionuclides of concern in the environment are mainly ^{238}U, ^{232}Th, and ^{40}K [5]. These radionuclides can be classified into primordial, cosmogenic and anthropogenic radionuclides [1]. The cosmogenic radionuclides are formed continuously by the interaction of cosmic rays with matter in space [1, 4] and finally, the anthropogenic radionuclides are a wide variety of radionuclides coming from the activities of man [1, 2, 4]. The primordial radionuclides have the half-lives that stretch to the age of the earth [1, 2, 4]. The decay of ^{238}U and ^{232}Th and their series is of concern because they produce a lot of ionizing radiation [6] .

The agricultural activities also contribute significantly to environmental radioactivity through phosphate fertilizers produced from the phosphate rock that is highly enriched in ^{238}U and ^{232}Th series [7, 8, 9, 10]. These radioisotopes made their way into the rock from dissolved uranyl complex in seawater during the geological formation of the phosphate rocks[9]. Consequently, the workers are exposed to an additional source of external radiation exposure [6] in agricultural fields. Fertilizers provide radiation outside the mines where radon gas inhalation is an issue [11], medical applications [12], fallout from nuclear weapon tests and power plants failures where radiation scatters all over, such as Chernobyl in 1986, and Fukushima Daiichi nuclear power

station on 11 March 2011 [13] and Three Mile Islands [14]. The ^{222}Rn gas contributes hugely in the total background radiation followed by cosmic and terrestrial sources [15]. The terrestrial radiations come from rocks and soils containing heavy metals of varying concentrations [9, 16]. The radiations are not uniform, but depend on the geographical and geological formation of the underlying rocks [4, 6, 5].The farm workers are particularly exposed to radiological hazards because they spend lengthy hours working on land.

The anthropogenic activity in agriculture increases environmental radioactivity over time as compared to barren soils where no plantation takes place except natural growths [9]. There is no scientific assessment on the radioactivity profile found for this area. This motivated the present study to be conducted. The objective of the present study is to evaluate the radiological hazards linked with working agricultural land by estimating the absorbed dose rate, the annual effective dose rate, the external hazard index, and radium equivalent [9]. The results will serve as a benchmark and baseline for future assessment studies on monitoring radioactivity in farmland of Weenen, KwaZulu-Natal, South Africa.

2. Materials and Method

2.1. The soil sample collection and preparation

Two soil samples were collected on 3rd January 2017, Weenen KwaZulu-Natal. One was collected from a spot that was never fertilized (C17) while the other one was regularly nourished with fertilizers (A17). The samples range from the field samples (A17, A1 A2 and A3) to control samples (C17 and A4) sampled at about 200 - 250 meters away from the field (field A1). The entire field was sampled at a depth of 15 – 20 cm and the soils were loaded in 2L containers. In this way, a representative soil sample for each field was obtained. Figure 1 and 3 are Google Earth views of the sampling spots on the 3^{rd} of January 2017 and 9^{th} of August 2018.

This study hypothesizes that the field samples have high radioactivity levels [7, 8] as compared to the control samples. The samples were dried by laying them on a metal sheet for two days. After drying, the samples were kept in 2 Litres containers. On the 9^{th} of August 2018, a collection of four more representative samples took place on the spots shown on Figure 3 as A1, A2, A3 and A4. On 12^{th} June 2018, the crushing and pulverization of samples into powder took place at a milling facility of University of Johannesburg at the Doornfontein campus. They were prepared for analysis at iThemba Labs, Gauteng on Figure 3 below. The homogenized samples

Figure 1: Left: Google Earth views of A17 and C17, middle: The fields that were sampled, and right: LN tank, MCA and HPGe.

were packed in zip-lock plastic bags and taken to iThemba LABS to be analysed. At iThemba LABS, the empty Marinelli beakers were weighed. The difference in mass of the loaded beakers gives the mass of the soil samples contained. The samples were then kept in tightly sealed Marinelli beakers. The samples were kept for 30 days to allow the ^{222}Rn and its daughters to reach secular radioactive equilibrium at ambient temperature prior to γ-spectroscopy analysis. The background radiation of the γ-spectroscopy was determined using an empty Marinelli beaker under identical measured conditions. It was negligible as the detector is covered with thick lead castle.

2.2. The analysis of soil samples

The concentrations of ^{238}U, ^{232}Th and ^{40}K, for the representative soil samples were measured using High Purity Germanium (HPGe) γ-ray spectrometer having 10 cm thick lead shielding on all sides with inner Cu and Sn lining, to reduce the background activity to about 95%. The energy resolution (FWHM) of the detector was 1.9 keV at the 1332 keV γ-ray line of ^{60}Co source. The detector was connected to a data acquisition system applying Genie-2000 analysis software, version 3.3 with both γ-ray energy and radionuclide identification. The prominent -ray lines were identified to find of ^{238}U and ^{232}Th content. Since the analysis was done at after the samples had established secular equilibrium, these γ-ray lines 186.20 keV (^{226}Ra), 351.9 keV (^{214}Pb), and 1765 keV (^{214}Bi) were used to estimate ^{238}U concentration. For ^{232}Th, the γ-lines 583.1 keV (^{208}Tl) and 911.20 keV (^{228}Ac) were used. The singly occurring 1460.80 keV gamma line was used to directly determine the concentration of ^{40}K. Since the ^{238}U and ^{232}Th content are determined from their progenies, their contents are referred to as uranium equivalent (eU) and thorium equivalent (eTh) respectively.

3. Numerical Calculations

3.1. The absolute efficiency of the detector

The ability of detecting gamma rays from a source depends on the resolution and the efficiency of the detector. The emission probabilities of various radionuclides were obtained from different sources in the literature [17]. The absolute efficiency of the HPGe detector was calculated with the known multisource calibration standards. The efficiency calibration curve of the detector was obtained from the standard sources as well and an empirical formula generated was used to find efficiencies of different signals in the ^{238}U, ^{232}Th and ^{40}K and others.

$$\varepsilon_{abs} = 4.148E^{-1.009} \tag{1}$$

where E represents the peak energy of a particular isotope of interest. Eqn (1) is in agreement with [18] and produced a curve similar to those on work by [19, 20] which were simulated curves of standard liquid sources from NMISA and CSIR. The linearity and energy resolution of the detector were tested by using signals from these standard sources. For any γ-ray detector, the most important properties are the energy resolution and the detection efficiency of that detector.

3.2. The activity concentration in soil samples

The background count was determined by counting an empty Marinelli beaker of the same dimension as those containing the samples and subtracting from the gross count. Each sample was counted for 28800 seconds to reduce the statistical uncertainty. The activity concentrations for the natural radionuclides in the measured samples were computed using the following relation [3, 21, 22, 23].

$$A = \frac{C_{net}}{I_\gamma \varepsilon m} \tag{2}$$

where A represents the activity concentration of an isotope of concern in a particular sample in Bq.kg^{-1}, C_{net} is the net peak count rate of the sample corrected for background, then ε is the absolute detector efficiency of the specific γ-ray, I_γ is the emission probability of a specific energy photo peak.

3.3. Evaluation of radiation hazards

The radium equivalent (Ra_{Eq}) quantity was developed to express the gamma yield from the mixture of the radionuclides in a soil sample and it also represents the activity levels due to ^{238}U, ^{232}Th and ^{40}K [2, 3, 23, 24]:

$$Ra_{Eq} = C_U + 1.43C_{Th} + 0.077C_K \quad (3)$$

where Ra_{Eq} is the radium equivalent, C_U, C_{Th} and C_K are the concentrations of ^{238}U, ^{232}Th and ^{40}K in the sample. The concentration of ^{238}U is sometimes replaced by that of ^{226}Ra assuming that there exists equilibrium. Eqn (03) assumes that 370 Bqkg^{-1} of ^{238}U, 259 Bqkg^{-1} of ^{232}Th and 4810 Bqkg^{-1} of ^{40}K produce the same gamma dose rate and its maximum value should not exceed 370 Bqkg^{-1}. The coefficient of C_{Th} and C_K are found by a ratio of expected radium concentration to those of C_{Th} and C_K. From the activity concentrations of ^{238}U, ^{232}Th, and ^{40}K, the total absorbed dose rate due to natural occurring radioactive materials (NORM) in air 1 metre above the ground is calculated using the following formula [2, 25, 26]:

$$D_R = 0.429C_U + 0.666C_{Th} + 0.042C_K \quad (4)$$

where D is the absorbed dose rate, 0.429 for ^{238}U series, 0.666 for ^{232}Th series and 0.042 for ^{40}K, are dose conversion factors in units determined from the ratio of absorbed exposure in air to the activity concentration in the soil [27][7]. The estimate the annual effective dose was estimated using the following equation. So using the calculated dose rate in Eqn (04), the estimates of effective dose rates per annum can be made from this relation [23]:

$$D_{Eff}(mSvy^{-1}) = D_R TF \quad (5)$$

where D is the absorbed (nGyh^{-1}), T is (36524h0,2) and F is conversion coefficient equivalent to (0,7103mSv/109nGy). The UNSCEAR reports used 0,7 Svy^{-1} for the conversion coefficient from an absorbed dose in air to effective dose received by adults, and 0.2 for the outdoor occupancy factor [27, 23, 15] and the effective dose rate per annum should be less than 1 mSvy^{-1} [28, 29]. The external radiation exposure is usually associated with gamma radiation emitted by radionuclides of concern. The external hazard index (H_{Ex}) is obtained from Ra_{Eq} expression [2, 4, 30]:

$$H_{Eff} = \frac{C_U}{370} + \frac{C_{Th}}{259} + \frac{C_K}{4810} \quad (6)$$

where C_U, C_{Th} and C_K are as defined above. For safer limits, this index should be small than a unity.

4. Results and discussion

The isotopic ratio of daughter radionuclides ^{214}Pb/^{214}Bi was used to define the level of radioactive secular equilibrium achieved in the samples analysed. These values are 1.51±0.40, 1.11±0.36, 1.16±0.38, 1.37±0.46, 1.04±0.25 and 1.08±0.36 for the ratio of ^{214}Pb to ^{214}Bi. And the ratio of ^{228}Ac to ^{208}Tl 0.899±0.082, 0.823±0.074, 1.10±0.096, 0.978±0.085, 1.06±0.093 and 0.876±0.088. When the secular equilibrium is established, the decay and production rate of a radionuclide is the same that is, $A_p = A_d$

The distribution of activity concentrations of the daughter isotopes of the primordial radionuclide ^{238}U, ^{232}Th and a singly occurring ^{40}K in the samples is presented in Table 1. The ^{238}U concentration was determined through the ^{226}Ra decay products average concentrations, that is, ^{214}Pb (351.9 KeV) and ^{214}Bi (1764.5 KeV) decay products in the sample. The concentration of ^{232}Th was determined from the average concentrations of ^{212}Pb (583.19 KeV) and ^{228}Ac (911.20 KeV) in the samples. The singly occurring 1460.6 KeV gamma ray signal was used to determine the concentration of ^{40}K in samples. In quantifying ^{226}Ra it was difficult to use 186.2 keV due to the interfering 185.7 keV from ^{235}U [31]. The Activity concentration (Bq kg^{-1}), Radium equivalent (Ra_{Eq}), Dose rate (D_R), Annual effective dose equivalent (D_{Eff}) and External hazard (H_{Ex}) in soil samples. The activity concentrations of ^{238}U, ^{232}Th and ^{40}K in soil

Sample ID			Activity Concentration (Bq/kg)				Radiation Hazard Indices			
Sample		Parameters	^{238}U	^{232}Th	^{40}K	^{226}Ra	Ra_{Eq} ($Bqkg^{-1}$)	D_R ($nGyh^{-1}$)	D_{Eff} ($mSvy^{-1}$)	H_{Ex}
Control	C17	Min	15±4	39±3						
		Max	68±5	44±2						
		Ave ± σ	**18.8±4**	**41.4±3.8**	**430±20**	**67,5±4,8**	**160±8,2**	**69±5,8**	**0,084±0,01**	**0,300±0,07**
	A4	Min	19±6	35±3						
		Max	29±4	39±2						
		Ave ± σ	**20.1±6.4**	**37.3±3.7**	**424±22**	**29.0±4,1**	**115±10**	**66±6,8**	**0,081±0,01**	**0,288±0,97**
Field	A17	Min	20±6	41±3						
		Max	49±4	49±2						
		Ave ± σ	**20.8±6.4**	**45.0±3.8**	**578±24**	**49,1±4**	**158±9,9**	**83±7,2**	**0,102±0,01**	**0,352±0,11**
	A1	Min	19±6	40±2						
		Max	58±4	41±3						
		Ave ± σ	**20.2±6.1**	**40.4±3.7**	**526±23**	**58,4±4,3**	**157±9,8**	**76±6,9**	**0,093±0,01**	**0,322±0,10**
	A2	Min	19±6	48±4						
		Max	42±5	49±2						
		Ave ± σ	**23.0±6.6**	**48.8±4.1**	**556±25**	**41,7±4,9**	**154±11**	**85±7,5**	**0,105±0,01**	**0,369±0,11**
	A3	Min	28±7	42±2						
		Max	60±4	45±3						
		Ave ± σ	**28.8±6.8**	**43.4±3.9**	**550±24**	**60,3±4,4**	**165±11**	**84±7,4**	**0,103±0,01**	**0,362±0,09**
Overall	M ± σ	Min	15±4	35±3	424±22	29.0±4,1	115±10	66±6,8	0,081±0,01	0,288±0,97
		Max	68±5	49±4	578±24	67,5±4,8	160±8,2	85±7,5	0,105±0,01	0,369±0,11
		Ave ± σ	**22±4**	**43±4**	**511±67**	**51,0±14**	**123±18**	**77±8**	**0,095±0,01**	**0,33±0.033**

1.png

Figure 2: Activity concentration (Bq kg-1), Radium equivalent (RaEq), Dose rate (DR), Annual effective dose equivalent (DEff) and External hazard (HEx) in soil samples

samples were measured. ^{40}K was higher in field soil samples (A17, A1, A2, and A3) and was a bit lower for the control samples C17 and A4. The calculated radium equivalent for all the activity was lower than the reference value of $Bqkg^{-1}$ [24, 27] ranging from 115±10 $Bqkg^{-1}$ to 160±8.2 $Bqkg^{-1}$ in control soil samples to 154±11 $Bqkg^{-1}$ - 165±11 $Bqkg^{-1}$ in the field soil samples. The mean equivalent activity concentrations for ^{238}U, ^{232}Th, and single occurring ^{40}K from the field samples were found to be 23.2±3.9, 44.5±3.5 and 552.5±21.4 $Bqkg^{-1}$, respectively. The mean activity concentrations for ^{238}U, ^{232}Th, and single occurring ^{40}K from the control samples were found to be 19.5±0.9, 39.4±2.9 and 427±30 $Bqkg^{-1}$, respectively.

For the field samples, the mean radium equivalent was 158.5±14.5 $Bq.kg^{-1}$ and whereas for the control samples, the radium equivalent was 137.4±12.9 $Bqkg^{-1}$. The external radiation hazard indices were found to be less than unity, which is within a permissible limit. The overall mean dose rate of the samples is 77±8 $nGyh^{-1}$, which is higher than a recommended value of 55-60 $nGyh^{-1}$ [5, 27]. The mean annual effective dose rate for the representative field samples was 0.101±0.049 $mSvy^{-1}, avaluelesserthan1mSvy^{-1}$ recommended by ICRP and UNSCEAR [5] as the limit for the public radiation exposure control. The external hazard index fell below a unity with an overall average of 0.3330.03.

5. Conclusion

The soil samples from different parts of a farm were analysed for natural radionuclides emanating from the soil and continuous application of fertilizers. Only naturally occurring radionuclides were detected in the samples. On average, the equivalent ^{238}U and ^{232}Th were 23.2±3.9 $Bqkg^{-1}$ and 44.5±3.5 $Bqkg^{-1}$ and the activity of the singly occurring ^{40}K peak was 552.5±21.4 $Bqkg^{-1}$ all are presented in Table 1. The absorbed dose rate is higher than the value of 55 $nGyh^{-1}$ .as it was found to be 77±8 $nGyh^{-1}$. The average annual effective dose rate is 0.101±0.0049 $mSvy^{-1}$ that is a value lesser than 1 $mSvy^{-1}$ recommended by ICRP and UNSCEAR for public radiation exposure control.

Again, the control samples C17 and A4 display a slightly lower potassium concentration in agreement with each other. A conclusion can be drawn that the higher potassium concentration in the field samples is due to the application of fertilisers. The results, however, indicate that the radiological dose from the soil is within safe limits. Thus, the application of fertilizers in these agricultural fields that were sampled poses no significant radiological hazard to the farm workers. This claim is primarily due to that the external hazard index and the average annual effective

dose both fall within a unity of their measurements. According to the data on UNSCEAR 2000, the concentrations of ^{238}U, ^{232}Th and ^{40}K from this study are within world average.

6. Acknowledgements

The author would like to acknowledge with great appreciation the service rendered at iThemba LABS, Gauteng by Mr A. Kwelilanga for whose knowledge of gamma spectrometric analysis is outstanding. Thank you again for your eye-opening insights, sir. Dr LP Masiteng, my supervisor, is acknowledged for helping me out.

References

[1] Khandaker M U, Jojo P J and Kassim H A 2012 *APCBEE Procedia* **1** 187–192
[2] Amanjeet, Kumar A, Kumar S, Singh J, Singh P and Bajwa B 2017 *Journal of radiation research and applied sciences* **10** 283–288
[3] Yousef M, El-Ela A A and Yousef H 2007 *Journal of nuclear and radiation physics* **2** 61–68
[4] Thabayneh K M and Jazzar M M 2012 *Open Journal of Soil Science* **2** 7
[5] on the Effects of Atomic Radiation U N S C 2000 *Sources and effects of ionizing radiation: sources* vol 1 (United Nations Publications)
[6] Hamidalddin S *et al.* 2014 *International Journal of Current Microbiology and Applied Sciences* **3** 623–633
[7] Fávaro D 2005 *Journal of Radioanalytical and Nuclear Chemistry* **264** 445–448
[8] Hamamo H, Landsberger S, Harbottle G and Panno S 1995 *Journal of Radioanalytical and Nuclear Chemistry* **194** 331–336
[9] Hameed P S, Pillai G S and Mathiyarasu R 2014 *Journal of Radiation Research and Applied Sciences* **7** 463–471
[10] Ahmed N K and El-Arabi A G M 2005 *Journal of environmental radioactivity* **84** 51–64
[11] Kleinschmidt R, Watson D, Janik M and Gillmore G 2018 *Journal of Sustainable Mining* **17** 120–130
[12] Nassef M and Kinsara A 2017 *Journal of Taibah University for Science* **11** 1259–1266
[13] Yamaguchi N, Taniyama I, Kimura T, Yoshioka K and Saito M 2016 *Soil science and plant nutrition* **62** 303–314
[14] Tomkiv Y, Perko T, Oughton D H, Prezelj I, Cantone M C and Gallego E 2016 *Journal of Radiological Protection* **36** S64
[15] Rafique M, Rahman S U, Basharat M, Aziz W, Ahmad I, Lone K A, Ahmad K and Matiullah 2014 *Journal of Radiation Research and Applied Sciences* **7** 29–35
[16] Ramli A T, Sahrone S and Wagiran H 2005 *Journal of Radiological Protection* **25** 435
[17] Henwood P and McCain R 2006 *Proc. of the 2006 Waste Management Symp., Tucson, AZ* vol 26
[18] Barescut J, Hlatshwayo I, Lindsay R, Ndwandwe O and Newman R 2009 *Radioprotection* **44** 825–830
[19] Joseph A D 2007 *Radiometric study of soil: the systematic effects* Ph.D. thesis University of the Western Cape
[20] Maibane K F 2016
[21] Mohammed N K and Mazunga M S 2013 *International Journal of Analytical Chemistry* **2013**
[22] Tzortzis M, Tsertos H, Christofides S and Christodoulides G 2003 *Radiation Measurements* **37** 221–229
[23] Agbalagba E, Avwiri G and Chad-Umoreh Y 2012 *Journal of environmental radioactivity* **109** 64–70
[24] Unscear S 2000 *United Nations, New York* 453–487
[25] UNSCEAR S 1988 *New York*
[26] Śleziak M, Petryka L, Zych M *et al.* 2010 *Polish J. Environ. Stud* **19** 1095–1099
[27] on the Effects of Atomic Radiation U N S C *et al.* 2011 *Sources and Effects of Ionizing Radiation: Report to the General Assembly with Scientific Annexes. Volume 2. Annex D. Health Effects Due to Radiation from the Chernobyl Accident.(advanced Copy).* (UN)
[28] Mohamed R, Algamdi S and Al-Shamani N 2016 *Journal of Taibah University for Science* **10** 369–374
[29] Leuraud K, Richardson D B, Cardis E, Daniels R D, Gillies M, O'hagan J A, Hamra G B, Haylock R, Laurier D, Moissonnier M *et al.* 2015 *The Lancet Haematology* **2** e276–e281
[30] El Aassy I, El Galy M, Nada A, El Feky M, Abd El Maksoud T, Talaat S and Ibrahim E 2011 *Journal of Radioanalytical and Nuclear Chemistry* **289** 173–184
[31] Issa S, Uosif M and Elsaman R 2013 *Turkish Journal of Engineering and Environmental Sciences* **37** 109–122

Compatibility of a simplified BSM model with the observed excesses in multi-lepton production at the LHC

Phuti Rapheeha[1], Xifeng Ruan[1] and Bruce Mellado[1,2]

[1] School of Physics and Institute for Collider Particle Physics, University of the Witwatersrand, Johannesburg, Wits 2050, South Africa
[2] iThemba LABS, National Research Foundation, PO Box 722, Somerset West 7129, South Africa

E-mail: ntsoko.phuti.rapheeha@cern.ch

Abstract. The discovery of the Higgs boson in 2012 by the ATLAS and CMS experiments at the Large Hadron Collider experiments has opened a window to a wide range of physics searches. The study of a number of features in the Run 1 data has lead to unearthing excesses in the production of multiple-leptons with intermediate transverse momentum in proton-proton collisions. The elevated production of leptons has the potential to provide indirect evidence for new physics Beyond the Standard Model. Here we investigate the compatibility of a simplified BSM model with the observed multi-lepton anomalies in the LHC public data. The BSM model predicts the existence of a heavy scalar H with a mass of about 270 GeV that decays to a SM Higgs boson in association with a scalar singlet S with a mass of about 150 GeV. In particular, here we investigate the invariant mass spectrum of four leptons (e, μ) and two muons in the region of interest.

1. Introduction

The discovery of the Higgs boson at the Large Hadron Collider (LHC) by the ATLAS and CMS Collaborations in 2012 put together the last piece of the puzzle to help understand the mechanism of electroweak (EW) symmetry breaking, and completed the Standard Model of particle physics [1, 2]. The Collaborations have since been making detailed measurements to better understand the couplings of the Higgs boson to other Standard Model (SM) particles. The measurements made by the LHC are compared to SM predictions, and they agree to a great extent. There however exists some discrepancies between the SM predictions and the observed experimental results, especially in events that produce multiple leptons [3, 4].

A number of Beyond the Standard Model (BSM) models interpret the discrepancies between the observed LHC experimental results and SM predictions as signatures of new physics. One of such models, the Madala hypothesis, postulates the existence of a heavy scalar boson H (which may participate in the electroweak symmetry breaking) with a mass of about 270 GeV produced in association with a scalar singlet S which has a mass of about 150 GeV [5, 6].

A study detailed in Reference [7] was performed with the aim of understanding the multi-lepton anomalies in the LHC data and their compatibility with new physics at the EW scale. In the study, the prediction of the Madala hypothesis was compared with public results with

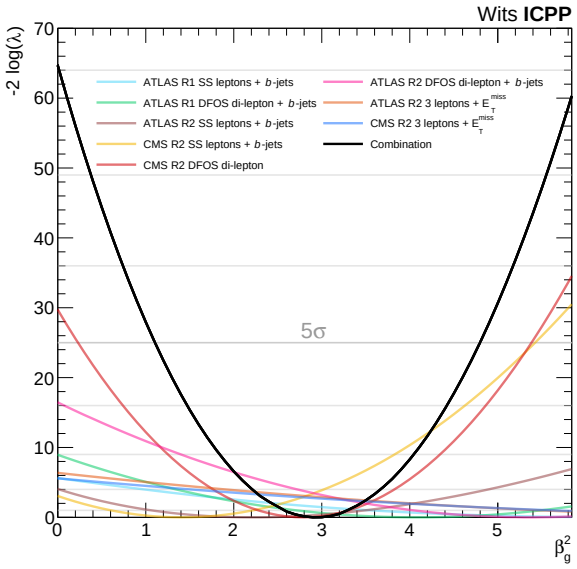

Figure 1. The profile likelihood ratio obtained for each fit result considered in the study in Reference [7]. The black curve is the combination of the results.

multi-lepton final states from ATLAS and CMS Collaborations. The comparison was made by performing a statistical fit with the aim of establishing constraints on the fit parameter β_g^2 (the single degree of freedom of the Madala hypothesis). The parameter β_g^2 controls the Yukawa couplings of H, with $\beta_g^2 = 0$ corresponding to the absence of a BSM signal. The parameter β_g^2 was constrained using the profile likelihood ratio, with the best fit value taken as the β_g^2 value that minimises the negative log likelihood function, $-2 \log \lambda \beta_g^2$.

Figure 1 shows the profile likelihood ratios of each fit result considered in the study in Reference [7]. The combined profile likelihood ratio is obtained by multiplying the profile likelihood ratios obtained for each measurement and the combinations yields $\beta_g^2 = 2.92 \pm 0.35$. The Poisson significance of the fit results is calculated as the square root of the point where $\beta_g^2 = 0$ and the combined profile likelihood ratio has a local significance of 8.04σ, revealing large discrepancies between SM predictions and the LHC experimental data. The discrepancies are observed at a corner of the phase space where different SM processes dominate, indicating that the discrepancies are unlikely to be due to mismodelling of the SM processes.

In the wake of these results, this article aims to perform a direct search of H on the invariant mass spectra of public ATLAS and CMS results containing final states with 4ℓ and 2μ in a mass range 230 to 280 GeV with different natural decay widths, Γ, values ranging from 0 to 10% of the resonant mass.

2. Methodology

The study considers published Run 2 results from both ATLAS and CMS Collaborations containing four leptons [9–11] in their final states and one publication with final state containing two muons [12]. The results were recorded from proton-proton (pp) collisions at $\sqrt{s} = 13$ TeV.

Two of the four publications used are searches of a pair of Z bosons decaying to a final state with four leptons ($\ell^+\ell^-\ell^+\ell^-$). The papers used are published by the ATLAS [9] and CMS [11] Collaborations using pp collisions with integrated luminosity of 36.1 fb^{-1} and 35.9 fb^{-1} for ATLAS and CMS experiments, respectively. The searches considered the production of

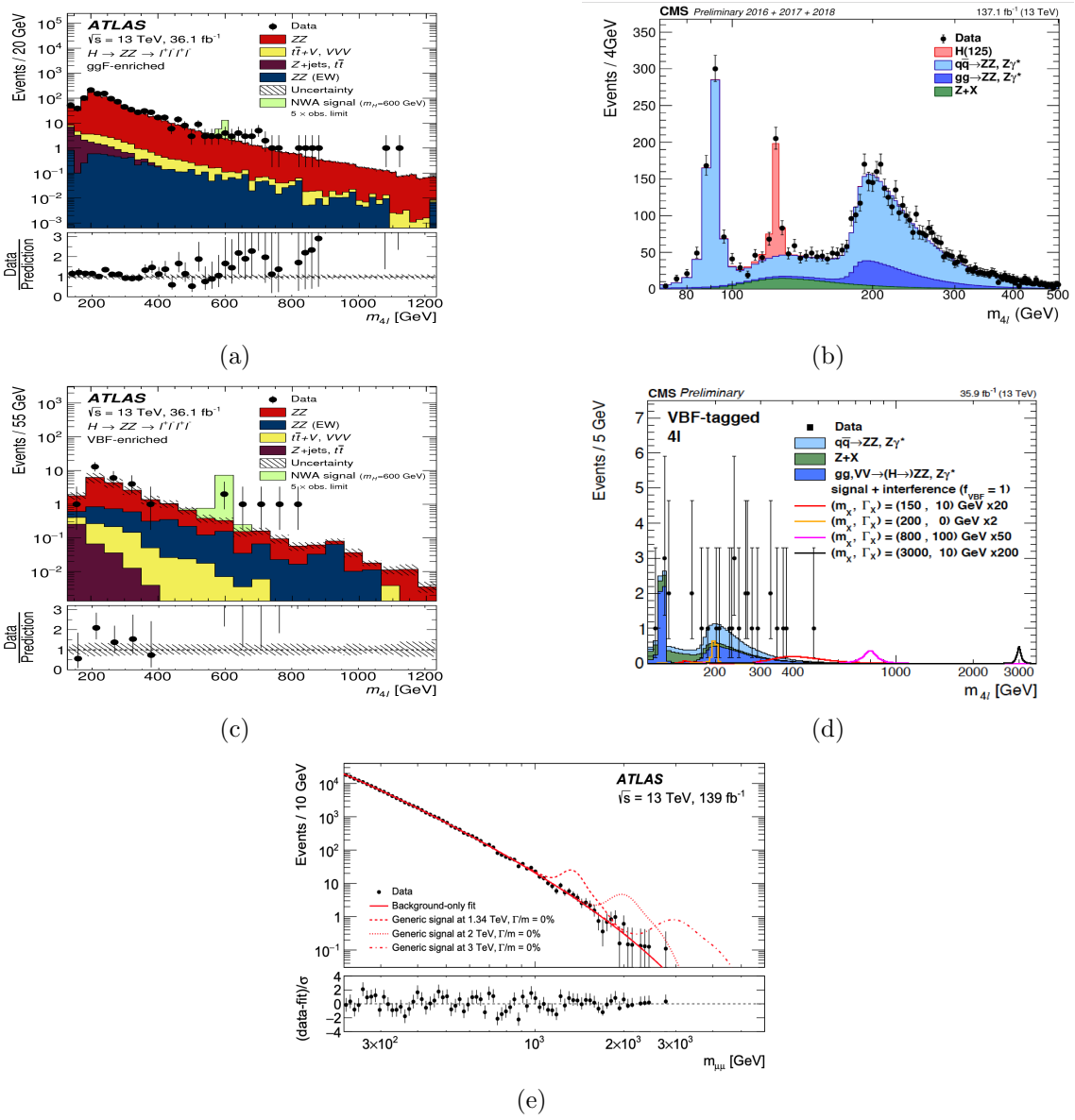

Figure 2. The invariant mass distribution of $ggF \to ZZ \to 4\ell$ published by (a), ATLAS and (b) CMS. (c) ATLAS and (d) CMS invariant mass distribution of the VBF $\to ZZ \to 4\ell$ process. (e) The invariant mass distribution of the 2μ as recorded by ATLAS.

a heavy scalar boson via gluon-gluon fusion (ggF) and an electroweak production dominated by the vector boson fusion (VBF). The heavy scalar then decays to a pair of Z bosons which then decay to a pair of same flavour but oppositely charged lepton ($e^+e^-, \mu^+\mu^-$) pairs. The studies required that the reconstructed Z boson candidates be formed by oppositely charged electron or muon pairs with invariant mass that fall in the mass window $12 < m_{\ell^+\ell^-} < 120$ GeV.

Further selection requirement were applied to categorize the four leptons events produced through the VBF process. The ATLAS search required that selected VBF events should contain at least two jets with transverse momentum $p_T > 30$ GeV, with the leading two jets being well separated in η, $|\Delta\eta_{jj}| > 3.3$, and having an invariant mass $m_{jj} > 400$ GeV [9]. The CMS search required that the four leptons events produced via the VBF process should have two energetic

and forward associated jets and to pass a cut on a matrix-element discriminant sensitive to the VBF signal topology [11].

The third publication considered is a study that measures the properties of the Higgs boson in $h \to ZZ \to 4\ell$ using pp collisions recorded by the CMS detector with an integrated luminosity of 137.1 fb^{-1} [10]. The Z boson candidates formed are with pairs of the same flavour and oppositely charged leptons are required to pass the $12 < m_{\ell^+\ell^-} < 120$ GeV requirement. In the 4μ and $4e$ channels where the four leptons invariant mass, $m_{4\ell}$, is reconstructed from same flavour leptons, the reconstructed invariant mass is required to be greater than 70 GeV. Figure 2 (b) shows the reconstructed $m_{4\ell}$ distribution up to 500 GeV.

The fourth publication considered searches for high-mass dielectron or dimuon resonances using 139 fb^{-1} of pp collision data collected by the ATLAS detector [12]. The reconstructed invariant mass of the dimuon system is required to be greater that 225 GeV, reconstructed from oppositely charged muons. The dimuon system was chosen because it is predicted that at high masses the heavy Higgs boson-like scalars would have a higher decay rate into muon pairs over electron pairs [13].

A statistical fit was performed using RooFit and RooStat statistical tools [14] distributed in Root [15], an object-oriented data analysis framework. The combined background and signal statistical model used to describe the observed experimental data is given by the following expression:

$$N_{\text{bkg}} \times f_{\text{bkg}}(m_H) + N_{\text{sig}} \times \mu \cdot f_{\text{sig}}(m_H, \sigma, \Gamma), \tag{1}$$

where N_{bkg} and N_{sig} are the number of fitted background and signal events, respectively. The parametrized background shape ($f_{\text{bkg}}(m_H)$) and the data points are scanned from the published distributions considered in this study, shown on Figure 2. The generic signal shape is taken to be a Voigtian distribution (convolution of the Breit–Wigner and Gaussian distributions), $V(mass, \sigma, \Gamma)$, where the σ of the Gaussian distribution accounts for the detector resolution and Γ of the Breit-Wigner distribution gives the natural decay width of the resonance. The decay width Γ is given by:

$$\Gamma = a \times m_H, \tag{2}$$

where a is expressed as a percentage. The decay width of the heavy scalar in this study is varied from 0% to 10%, the case where $\Gamma = 0\% \times m_H = 0$ is called the narrow width approximation and the width of H is determined by the detector resolution.

The significance of a SM+BSM signal hypothesis of mass m_H and Γ is summarised by a p-value, the probability of observing a background+signal excess in data using the background-only hypothesis. The local p-value (p_0) for the compatibility of a signal hypothesis of mass m_H and decay width Γ with a background-only hypothesis is obtained by scanning the test statistic, $q_0(m_H, \Gamma)$, given by [16]:

$$q_0(m_H, \Gamma) = -2 \log \frac{L\left(N_{\text{sig}} = 0 | m_H, \Gamma, \hat{\hat{\nu}}\right)}{L\left(\hat{N_{\text{sig}}} | m_H, \Gamma, \hat{\nu}\right)}, \tag{3}$$

where N_{sig} is the parameter of interest and ν is a set of nuisance parameters. The parameter $\hat{\hat{\nu}}$ is chosen to maximise the likelihood L in a background-only fit and $\hat{N_{\text{sig}}}$ and $\hat{\nu}$ are chosen to maximise the likelihood function over the entire parameter space. The local p_0 value of the background only hypothesis is calculated by applying the asymptotic approximation to the test statistic $q_0(m_H, \Gamma)$ distribution. The significance is obtained by taking the square root of the test statistic, $Z = \sqrt{q_0}$.

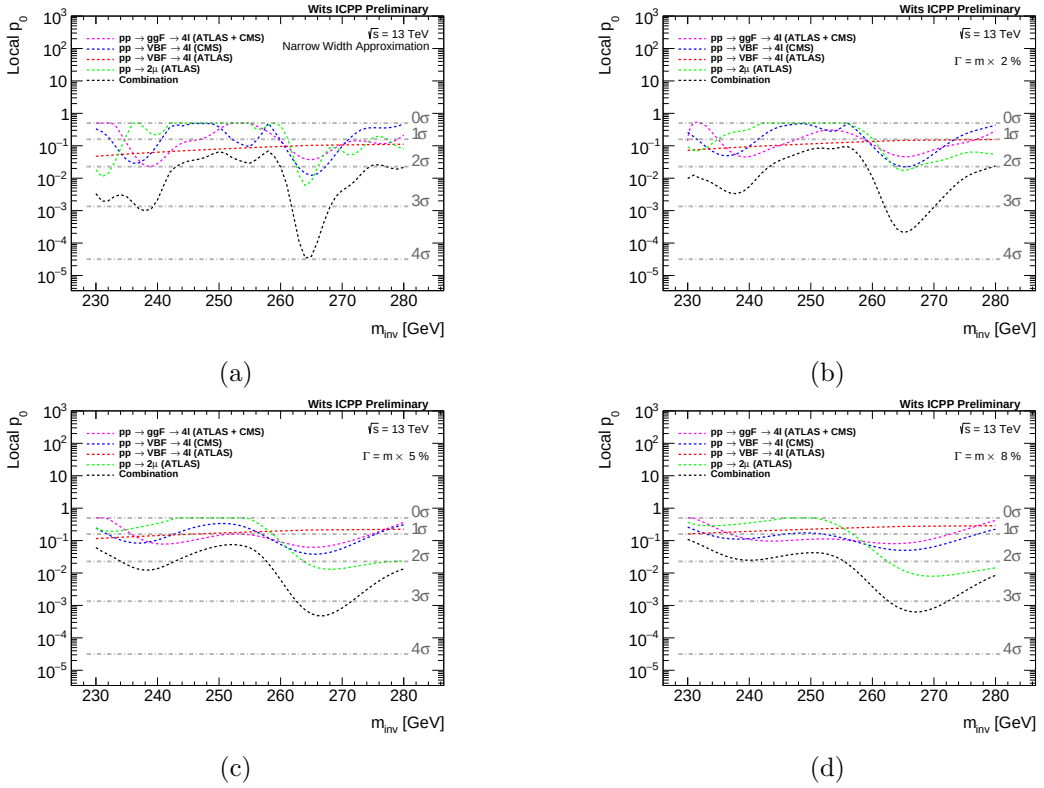

Figure 3. The observed local p_0 values as a function of the hypothesised mass of H with a natural decay width of (a) 0%, (b) 2%, (c) 5% and (d) 8%. The red, blue, green and magenta curves correspond to the observed local p_0 values from fitting the ATLAS $pp \to 4\ell$ VBF produced events, CMS $pp \to 4\ell$ VBF produced events, ATLAS $pp \to 2\mu$ events and ATLAS and CMS $pp \to ggF \to 4\ell$ events, respectively. The black curve corresponds to the quadrature sum of the other curves.

3. Results

For each distribution in Figure 2, a hypothesis test is performed at mass points from 230 GeV to 280 GeV with 1 GeV intervals for decay widths ranging from the narrow width approximation ($0\% \times \Gamma$) to 10% of the resonant mass. The $pp \to ggF \to ZZ \to 4\ell$ results from ATLAS and CMS Collaborations, Figures 2 (a) and (b), were combined into a single dataset and a simultaneous fit was used to do the hypothesis testing. The simultaneous fit took into consideration the different luminosities (36.1 fb^{-1} for ATLAS and 137.1 fb^{-1} for CMS) and the signal model of each dataset. The event selection used in the selection of VBF $\to ZZ \to 4\ell$ events is different for ATLAS and CMS published studies, therefore a simultaneous fit was not performed to combine these measurements.

The final results presented in Figure 3 are a combination of the simultaneous fit results combining the ggF 4ℓ results from ATLAS and CMS, separated ATLAS and CMS VBF fit results and the fit result to the ATLAS dimuon mass distribution used in the high-mass resonance search illustrated in Figure 2 (e). The independent results are combined by adding the significance at each mass point for all the channels in quadrature:

$$Z_{\text{combined}} = \sqrt{(Z_{ggF})^2 + (Z_{\text{VBF,ATLAS}})^2 + (Z_{\text{VBF,CMS}})^2 + (Z_{2\mu})^2}. \quad (4)$$

The observed local p_0-values as a function of m_H at different Γ are shown in Figures 3. The dashed horizontal lines correspond to the local significance levels. Figure 3 (a) shows the a

maximum local 4σ deviation from the SM prediction in favour of SM+BSM hypothesis, with Γ taken as the narrow width approximation ($\Gamma = 0$ GeV). Figures (b), (c) and (d) show the observed local p_0-values as a function of m_H at $\Gamma = 2\% \times m_H$, $5\% \times m_H$ and $8\% \times m_H$ GeV, respectively.

From the results in Figure 3 it can be seen that the heavy scalar resonance seems to be a double humped structure located at around 237 GeV and 265 GeV for small decay widths. The resonance remains above 3σ when the decay width is being increased, hinting that the resonance might also be broad one located between 236 and 280 GeV.

4. Conclusions

From the results shown in the above section it is evident that the published LHC multi-lepton results show discrepancies in the 235 - 280 GeV region. The largest deviation from the SM-only hypothesis is observed at 267 GeV using the narrow width approximation. The observed local 4σ deviation should be treated as a lead to where future searches can optimise their event selection to search for a BSM signal originating from the decay of a heavy scalar boson may participate in the electroweak symmetry breaking mechanism.

The results obtained for small decay widths showed a possibility that the resonance might be a double humped structure located at around 237 GeV and 265 GeV. The signal does not completely disappear when the decay width is increased to larger widths also hinting that it is possible that we are actually looking at a broad excess in the 236-280 region. Further studies will shed light on the nature of these structures.

5. References

[1] Aad G *et al.* (ATLAS) 2012 *Phys. Lett.* **B716** 1–29 (*Preprint* 1207.7214)
[2] Chatrchyan S *et al.* (CMS) 2012 *Phys. Lett.* **B716** 30–61 (*Preprint* 1207.7235)
[3] Ahmad M (CMS) 2016 *Acta Phys. Polon.* **B47** 1365–1377
[4] Gemme C (ATLAS Collaboration) 2016 Latest ATLAS results from Run 2 Tech. Rep. arXiv:1612.01987 CERN Geneva URL http://cds.cern.ch/record/2241217
[5] von Buddenbrock S, Chakrabarty N, Cornell A S, Kar D, Kumar M, Mandal T, Mellado B, Mukhopadhyaya B and Reed R G 2015 (*Preprint* 1506.00612)
[6] von Buddenbrock S, Chakrabarty N, Cornell A S, Kar D, Kumar M, Mandal T, Mellado B, Mukhopadhyaya B, Reed R G and Ruan X 2016 *Eur. Phys. J.* **C76** 580 (*Preprint* 1606.01674)
[7] von Buddenbrock S, Cornell A S, Fang Y, Fadol Mohammed A, Kumar M, Mellado B and Tomiwa K G 2019 (*Preprint* 1901.05300)
[8] von Buddenbrock S, Cornell A S, Fadol A, Kumar M, Mellado B and Ruan X 2018 *J. Phys.* **G45** 115003 (*Preprint* 1711.07874)
[9] Aaboud M *et al.* (ATLAS Collaboration) 2018 *Eur. Phys. J.* **C78** 293 (*Preprint* 1712.06386)
[10] Sirunyan A M *et al.* (CMS Collaboration) 2019 Measurements of properties of the Higgs boson in the four-lepton final state in proton-proton collisions at $\sqrt{s} = 13$ TeV Tech. Rep. CMS-PAS-HIG-19-001 CERN Geneva URL https://cds.cern.ch/record/2668684
[11] Sirunyan A M *et al.* (CMS Collaboration) 2017 Search for a new scalar resonance decaying to a pair of Z bosons in proton-proton collisions at $\sqrt{s} = 13$ TeV Tech. Rep. CMS-PAS-HIG-17-012 CERN Geneva URL https://cds.cern.ch/record/2296714
[12] Aad G *et al.* (ATLAS Collaboration) 2019 *Phys. Lett.* **B796** 68–87 (*Preprint* 1903.06248)
[13] Djouadi A 2008 *Phys. Rept.* **459** 1–241 (*Preprint* hep-ph/0503173)
[14] Cranmer K, Lewis G, Moneta L, Shibata A and Verkerke W (ROOT Collaboration) 2012 HistFactory: A tool for creating statistical models for use with RooFit and RooStats Tech. Rep. CERN-OPEN-2012-016 New York U. New York URL https://cds.cern.ch/record/1456844
[15] Antcheva I *et al.* 2009 *Comput. Phys. Commun.* **180** 2499–2512 (*Preprint* 1508.07749)
[16] Cowan G, Cranmer K, Gross E and Vitells O 2011 *Eur. Phys. J.* **C71** 1554 [Erratum: Eur. Phys. J.C73,2501(2013)] (*Preprint* 1007.1727)

High mass VBF categorization for narrow-width resonance searches in the $H \to ZZ \to 4\ell$ channel with the ATLAS detector

Mzwandile Thabede[1], Theodota Lagouri[1], Xifeng Ruan[1] and Bruce Mellado[1,2]

[1] School of Physics and Institute for Collider Particle Physics, University of the Witwatersrand, Johannesburg, Wits 2050, South Africa
[2] iThemba LABS, National Research Foundation, P.O. Box 722, Somerset West, 7129, South Africa

E-mail: mzwandile.thabede@cern.ch

Abstract. The search for a heavy resonance (H) decaying to four leptons in the $H \to ZZ \to 4\ell$ ($\ell = \mu$ or e) channel can be conducted in at least two main production modes. This analysis channel is also one of the main decay channels for the Higgs boson which was discovered at the Large Hadron Collider (LHC) in 2012. In this proceeding, we categorize four lepton events using a cut-based approach in events with two or more jets (N-jets ≥ 2). This study focuses on the signal optimization for the $H \to ZZ \to 4\ell$ channel and the separation of vector boson fusion (VBF) events from the events produced via the gluon-gluon Fusion (ggF) production mechanism. The study is conducted using the ATLAS full Run 2 Monte Carlo with the total luminosity of 140 fb^{-1}. By defining a leading jet to be a jet with the largest transverse momentum, the optimal selection cuts on the invariant mass (m_{jj}) and the pseudo-rapidity difference between two leading jets ($\Delta\eta_{jj}$) can be obtained using signal selection efficiency and background rejection 2D maps. The new cuts obtained are then compared with the current optimal VBF selection to check if there is any improvement in the sensitivity. It was found that the standard cut-based VBF selection is still good enough to use for event categorization in the four-lepton channel with high selection efficiency and background rejection in the 0.2 TeV $\leq m_H \leq$ 1 TeV mass range.

1. Introduction

After the discovery of the Standard Model Higgs boson in 2012 by ATLAS and CMS collaborations [1, 2], much of the work done has been to perform the measurements of its physical properties and to search for physics beyond the Standard Model. In hadron colliders, heavy Higgs bosons are produced mainly via the gluon fusion and vector boson fusion production mechanisms. This makes it possible to search separately for resonances in each production mode. To this end, it is necessary to distinguish events from each production mode by defining a set of selection requirements (criteria) to be applied on all events that enter the signal region. Given that the ggF production mode is the most dominant one at the LHC in terms of the Higgs boson production cross-section [3], one may ask if the sensitivity of the Higgs boson searches to the VBF production mode can be improved using Run 2 Monte Carlo from the ATLAS detector. This study attempts to answer this question by adopting a cut-based categorization method.

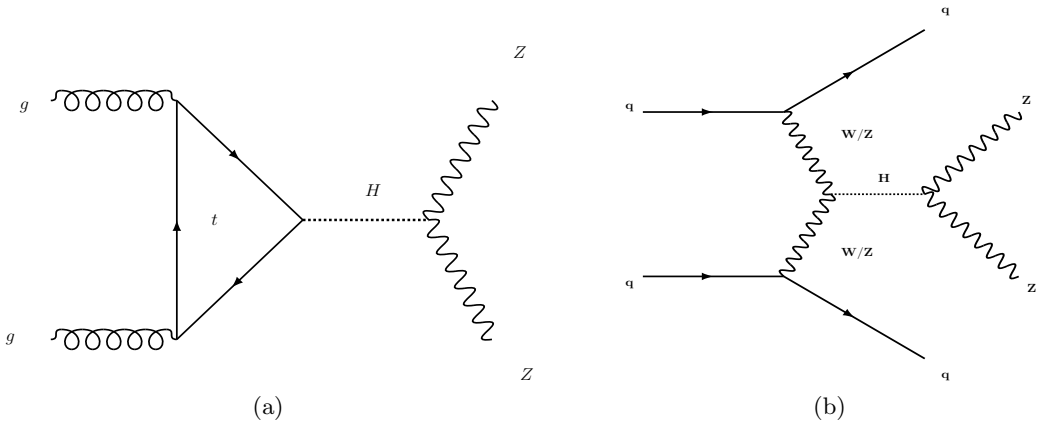

Figure 1: The leading production mechanisms for the Higgs boson in hadron colliders are (a) the gluon fusion and (b) the vector boson fusion production modes.

The selection for the signal events is based on the characteristic 2-jet signature of the VBF production mode ($pp \to H(\to ZZ)jj$), which is an important feature that is used to distinguish between ggF and VBF categories. Details of this selection and optimization study is discussed in this study where we assume the production of a narrow-width resonance (NWA). Searches for heavy resonances in the $H \to ZZ \to 4\ell$ decay channel can be performed separately in the ggF and in the VBF production modes provided that a criteria for selecting clean signal (VBF) events has been clearly defined. To classify events as either VBF or ggF, a method based on the signal selection efficiency and background rejection is adopted. This is achieved by choosing events with two or more jets with p_T greater than 30 GeV. Signal events will also satisfy the optimized cut on the di-jet invariant mass and the separation in η[1] between the two leading jets ($\eta_{j1} - \eta_{j2}$). The categorization method employed in this study provides the optimal selection cuts that can be used for all samples in the mass range considered. The Feynman diagrams for the ggF and VBF production modes are shown in figure 1.

2. Event Selection

This section provides a summary of the event selection [4, 5] as applied to all events in the four lepton channel. All events passing the standard four-lepton event selection are used for categorization. Only events with exactly four electron and/or muon combinations (one quadruplet) in the final state are selected. Events are classified into three different channels according to the flavor of leptons in the final state ($4e$, 4μ and $2\mu 2e$). For high mass studies, both Z-bosons are on-shell so it is only the measurement resolution that decides which way the pairing of leptons occurs. 2μ2e and 2e2μ quadruplets are selected by choosing di-lepton pairs with the invariant mass closest to the mass of the Z-boson (≈ 91.2 GeV) [6] so instead of using four channels in the analysis, 2μ2e and 2e2μ are combined into one channel called 2μ2e.

2.1. Final State Object Selection

To reconstruct the final state objects for the four lepton channel, electrons are required to have $p_T \geq 7$ GeV and with $|\eta| \leq 2.47$. Requirements for muon candidates is $p_T \geq 5$ GeV and with $|\eta| \leq 2.7$. Not more than one calorimeter-tagged, segment-tagged or stand-alone muon candidate in the pseudo-rapidity range $2.5 \leq |\eta| \leq 2.7$ is allowed per quadruplet. A jet is a composite object

[1] The pseudo-rapidity is defined in terms of the polar angle (θ) as $\eta = -\ln\tan(\theta/2)$.

 ISBN: 978-0-620-88875-2

contained in a narrow cone. The identification and reconstruction of an object as a jet begins on the topological clusters of cells in the calorimeter, used as input for the jet-finding algorithms. Jet objects are reconstructed using the Anti-k$_T$ algorithm [7]. This is a clustering algorithm with a radius parameter $R = 0.4$ and is implemented in the FastJet package [8] which uses the particle flow algorithm [9] as input. Jet objects in the four-lepton channel are required to satisfy p$_T \geq 30$ GeV and $|\eta| \leq 4.5$. Pile-up jets can be suppressed by applying a cut on the jet vertex fraction (JVF) [10, 11] which requires that all jet objects must originate from the primary vertex.

2.2. Lepton Pairs and Quadruplet Formation

The Higgs boson candidate is obtained by selecting one quadruplet (two same flavour opposite sign lepton pairs) with $p_T \geq 20, 15, 10$ GeV for the first three leading leptons. The separation requirement of $\Delta R = \sqrt{(\Delta\eta)^2 + (\Delta\phi)^2} \geq 0.10$ (0.20) for same- (different-) flavour leptons are required and all quadruplets containing a pair of leptons with invariant mass smaller than 5 GeV are vetoed. This requirement on the di-lepton invariant mass helps to reduce the contamination from J/ψ mesons in the analysis. The leading lepton pair is chosen by selecting a pair with invariant mass (m_{12}) closest to the mass of the Z-boson and is required to be between 50 GeV and 106 GeV. The invariant mass of the third and fourth leptons in the quadruplet (m_{34}) is required to be in the range ($m_{th} \leq m_{34} \leq 115$ GeV) where m_{th} is the threshold mass and ranges between 12 GeV and 50 GeV, depending on the invariant mass of the quadruplet and it remains 50 GeV for high mass studies ($m_{4l} \geq 190$ GeV). The threshold (m_{th}) increases linearly with m_{4l} from the lower value of 12 GeV to the highest value of 50 GeV in the range 140 GeV $\leq m_{4l} \leq$ 190 GeV.

2.3. Impact Parameter and Isolation Requirements

Leptons are required to be isolated using track-based and calorimeter-based isolation discriminants. The track-based isolation discriminant, defined as the sum of the transverse momenta of all tracks inside a cone of size ΔR = 0.3 around the muon and ΔR = 0.2 around an electron excluding the lepton track, divided by the lepton p$_T$, must not be larger than 0.15. The calorimeter-based isolation discriminant similarly adds up the cluster E$_T$ values used to reconstruct jets within a cone of width ΔR = 0.2 around the barycentre of the candidate lepton. The E$_T$ sum divided by the p$_T$ of the lepton is required to be less than 0.3 for muons and 0.2 for electrons. The requirement on the transverse impact parameter significance $|d_0/\sigma d_0| \leq 3$ (5) for muons (electrons) must also be satisfied [12]. Track-based isolation requirements, calorimeter-based isolation requirements, primary vertex constraint as well as the impact parameter requirements on lepton candidates help with the suppression of the sub-dominant $t\bar{t}$ and $Z + jets$ background contributions [13]. The requirement for tracks to originate from the primary vertex (defined to be a vertex with the largest p$_T$ sum) is used to suppress contribution from pile-up [14] events.

2.4. Overlap Removal

To remove overlap between leptons of different flavors, electrons that share the same Inner Detector track with a muon are removed, unless the muon in question is a segment-tagged muon or a calorimeter-tagged muon with no track in the muon spectrometer. Jet objects that appear within ΔR = 0.2 of an electron or within ΔR = 0.1 of a muon are removed.

3. Optimization of VBF Signal

In this section, we discuss the optimization of the m_{jj} and $\Delta\eta_{jj}$ selection cuts for the four-lepton channel. The method employed in this study is based on the signal selection efficiency ($\epsilon(S)$)

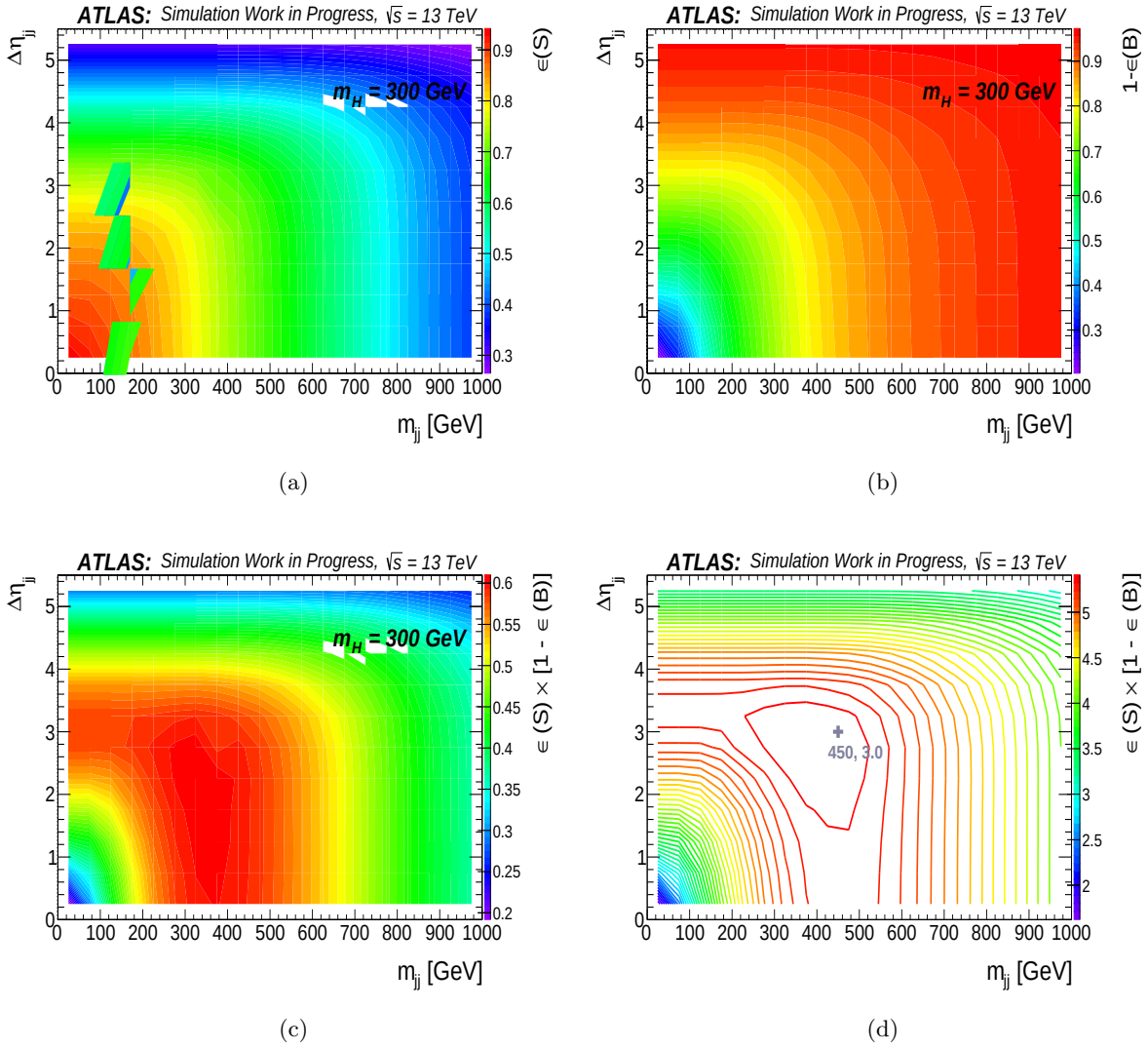

Figure 2: The (a) signal selection efficiency (ϵ(S)), (b) background rejection (1-ϵ(B)), (c) the product ϵ(S)×[1-ϵ(B)] for m_H = 300 GeV mass point and (d) ϵ(S)×[1-ϵ(B)] for all mass points from m_H = 200 GeV to m_H = 1 TeV.

and background rejection (1-$\epsilon(B)$) 2D maps. The signal selection efficiency is calculated as the ratio of the number events after the VBF selection cuts to the number of events before the VBF selection cuts were applied. One efficiency map is displayed in figure 2 for the m_H = 300 GeV mass points. To define background (ggF) rejection in the VBF signal region, a fraction of non-VBF events that are removed during the selection is calculated and it is the measure of the ability of each applied selection cut to reject ggF events in the VBF signal region. Background rejection and selection efficiency are calculated in 0.2 TeV to 1 TeV mass range. Various combinations of m_{jj} (0 GeV to 1000 GeV) and $\Delta\eta_{jj}$ (0 to 5.5) cuts are investigated in figure 2b and the optimal selection for each mass point is chosen by finding the cuts corresponding to the maximum value of the product ϵ(S)×[1-ϵ(B)]. This method provides selection cuts with good ability to reject non-VBF events and still maintain high signal selection efficiency in the given mass range. Choosing a very tight cut may result in excellent background rejection but very low signal efficiency. The opposite is also true, choosing a loose cut may result in high signal selection efficiency but poor background rejection. This trade-off can be seen clearly in figure 3 as a small increase in

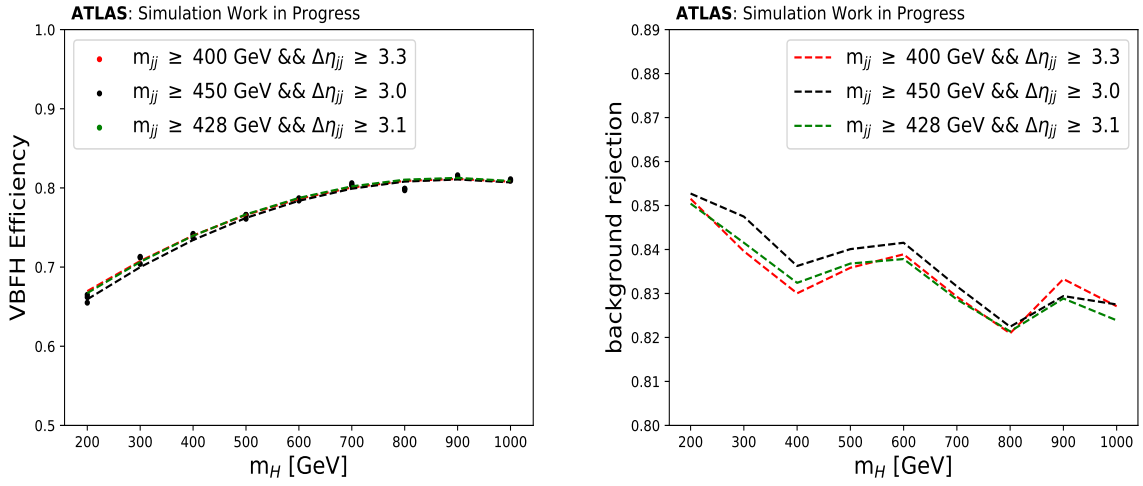

(a) (b)

Figure 3: The (a) Selection efficiency and (b) background rejection as a function of mass of the resonance for the optimal selection in the VBF category.

background rejection and a small decrease in the signal efficiency for the new cuts. The overall selection that can be used for all mass points in the mass range considered in this study can be obtained by combining all ϵ(S)×[1-ϵ(B)] 2D maps. The maximum value of the product ϵ(S)×[1-ϵ(B)] obtained in figure 2d reveals the new optimal selection for all nine mass points that were used. The currently used standard VBF selection requires events with two or more jets with p_T greater than 30 GeV, that are well separated in η and satisfying $m_{jj} \geq 400$ GeV and $\Delta\eta_{jj} \geq 3.3$. Comparison of the new cuts with the standard VBF selection is discussed in section 4.

4. Comparison

To test the overall performance of the VBF selection obtained in section 3, the efficiency and background rejection were calculated for each optimal selection and drawn as a function of the resonance mass. The final optimal selection is decided by comparing the new cuts with the current standard cut-based selection in the VBF category. In figure 3, a third set of cuts ($m_{jj} \geq 428$ GeV and $\Delta\eta_{jj} \geq 3.1$) is included and this was obtained by taking the average of the cut values over all mass points that are used in this study. The black line in figure 3 is the new selection obtained from section 3 by summing all ϵ(S)×[1-ϵ(B)] maps, the green line is a new selection cut obtained by taking the average over all mass points and the red line shows the currently used standard cut which is used here as a reference cut-based selection. This comparison is done to look for improvements in the selection efficiency and background rejection for the chosen optimal selection with respect to the standard cuts. It can be seen in figure 3 that the current selection is still good enough to use as cut-based VBF selection with high signal selection efficiency across all mass points.

5. Summary

The categorization of events into VBF and ggF categories was performed using selection efficiency and background rejection 2D maps for ggFH and VBFH signal samples in the 0.2 TeV $\leq m_H \leq$ 1 TeV mass range. The optimization is done using Monte Carlo samples and by choosing events with two or more jets and requiring that all events passing the optimal

selection be categorized into the VBF-enriched category. The remaining events are classified in any one of the three ggF categories depending on the lepton-flavour composition of the final state. It was found that the currently used selection is still good enough for use in the cut-based categorization of VBF and ggF events with full Run 2 Monte Carlo corresponding to the total integrated luminosity of 140 fb^{-1}. It is recommended therefore to keep the current cuts ($m_{jj} \geq$ 400 GeV and $\Delta\eta_{jj} \geq 3.3$) as optimal cut-based selection to use for narrow resonance searches in the $H \to ZZ \to 4\ell$ channel.

References

[1] Aad G *et al.* (ATLAS) 2012 *Phys. Lett.* **B716** 1–29 (*Preprint* 1207.7214)
[2] Chatrchyan S *et al.* (CMS) 2012 *Phys. Lett.* **B716** 30–61 (*Preprint* 1207.7235)
[3] Hussein M Y 2017 Higgs boson production at the lhc (*Preprint* 1703.03952)
[4] Aad G *et al.* (ATLAS) 2015 *Phys. Rev.* **D91** 012006 (*Preprint* 1408.5191)
[5] Aad G, Abajyan T and et-al 2013 *Physics Letters B* **723** 15 – 32 ISSN 0370-2693
[6] Achard P, Adriani O and et-al 2004 *Physics Letters B* **585** 42 – 52 ISSN 0370-2693
[7] Cacciari M, Salam G P and Soyez G 2008 *JHEP* **04** 063 (*Preprint* 0802.1189)
[8] Cacciari M, Salam G P and Soyez G 2012 *Eur. Phys. J.* **C72** 1896 (*Preprint* 1111.6097)
[9] Aaboud M *et al.* (ATLAS) 2017 *Eur. Phys. J.* **C77** 466 (*Preprint* 1703.10485)
[10] Aaboud M *et al.* (ATLAS) 2017 *Eur. Phys. J.* **C77** 580 [Erratum: Eur. Phys. J.C77, no.10,712(2017)] (*Preprint* 1705.02211)
[11] Tomiwa K 2017 *Journal of Physics: Conference Series* **802** 012012
[12] Aaboud Morad and others (ATLAS) 2017 *JHEP* **10** 132 (*Preprint* 1708.02810)
[13] Sirunyan, Albert M and et-al (CMS) 2017 *JHEP* **11** 047 (*Preprint* 1706.09936)
[14] Marshall Z 2014 *Journal of Physics: Conference Series* **513** 022024

Search for a resonance in the diphoton plus b-jet final states in the ttH and bbH production

Esra Mohammed Shrif[1], **Xifeng Ruan**[1] **and Bruce Mellado**[1,2]

[1] School of Physics and Institute for Collider Particle Physics, University of the Witwatersrand, Johannesburg, Wits 2050, South Africa

[2] iThemba LABS, National Research Foundation, PO Box 722, Somerset West 7129, South Africa

E-mail: shrif.esra@gmail.com

Abstract. We propose a simple analysis to search for resonance in the diphoton and at least one b-tagged jet final states with ttH and bbH models. This region has never been checked and needs to be checked now in run II and in the future run III data. We search for the new resonance in the range above 160 GeV. The analysis uses Run II proton-proton (pp) collision data with an integrated luminosity of 140 fb^{-1} recorded at a centre-of-mass energy of $\sqrt{s} = 13$ TeV with the ATLAS detector. In this work, we discuss event selections and signal optimization. In addition, we compare data to MC simulation in the control region. A 2D scan of the variables, number of central jets N_{cjet} and $\Delta\phi_{\gamma\gamma}$ is made to optimize the search.

1. Introduction

The diphoton channel provides a clean experimental signature with an invariant mass resolution that can be reconstructed with high precision [1, 2]. The Higgs to diphoton decay $h \to \gamma\gamma$ channel was one of the most important channels that led to the discovery of the Higgs boson [3, 4]. Recently, the unconfirmed resonance with mass around 750 GeV also observed in the diphoton channel [5, 6, 7]. An excess in the diphoton spectrum at high-energy, could be interpreted as the decay of a hypothetical particle with spin-0 or spin-2.

The searches for new high-mass resonances decaying into two photons was performed, using CERN Large Hadron Collider (LHC) pp collision data recorded by the ATLAS and CMS detectors since run I [8, 9]. This proceeding presents a search for a resonance in the diphoton plus b-tagged jet final states. In this channel, the QCD background is highly suppressed. These final states can be the result from top or bottom quark associated productions. We search for the diphoton resonance in high mass region, through the $gg/q\bar{q} \to t\bar{t}H$, $b\bar{b}H$ process, examples of tree-level Feynman diagrams are given in Figure 1. Where, H is Higgs like spin zero particle with a mass range [160 GeV, 1 TeV] decaying to diphoton final state in this study. To understand these final states, for instance, the top quark, t, decays to a W^+ boson, and a quark $q = b, s$ or d. Here, W^+ boson decay into a lepton and a neutrino, $t \to W^+q \to \ell^+\nu q$. The case for anti-top quark decay is $\bar{t} \to W^-q \to \ell^-\nu\bar{q}$, where, $\bar{q} = \bar{d}, \bar{b}$ or $\bar{d}$. These quarks will turn into jets as they cannot exist freely. The plan is to search for any resonance of diphoton and setup limits on the production cross-section times branching ratio ($\sigma \times \mathrm{BR}(H \to \gamma\gamma)$) to the ttH and bbH models with $m_H > 160$ GeV.

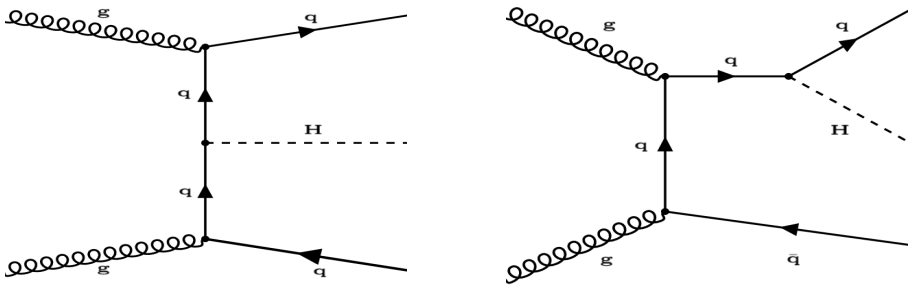

Figure 1. Feynman diagrams show two different production processes of the heavy boson H with a pair of top or bottom quarks, q refers to either top or bottom quark.

2. Samples and Event Selection

Monte Carlo (MC) simulated events are used for the estimation of signal and background processes. The MADGRAPH aMC@NLO [10] event generator interfaced to PYTHIA8 [11] is used to produce the ttH signal samples, while the bbH samples are simulated using PYTHIA8. The dominant background samples that are used here are the SM diphoton production and γ+jet; contributions also come from $bb\gamma\gamma$, $V\gamma$ (W/Z), $V\gamma\gamma$, $tt\gamma\gamma$ and $tt\gamma$ (one fake photon from electron). The γ+jet and diphoton samples are normalised to 20% and 80% respectively of the data at the inclusive case. The dataset used in this analysis encompasses all data that was recorded with the ATLAS detector, between 2015 and 2018, in pp collisions with an integrated luminosity of 140 fb^{-1} at a centre-of-mass energy of $\sqrt{s} = 13$ TeV.

After an event passes the quality selection (after selecting two well identified photons), it has to pass additional kinematic and geometrical requirements to be considered for the analysis. The event are selected with at least two photons, the transverse momentum p_T of the leading and sub-leading photon should be greater than 40 GeV, and 30 GeV, respectively. The invariant mass of the diphoton system $m_{\gamma\gamma} > 130$ GeV. It is required to have at least one b-tagged jet. To avoid the SM Higgs peak events are then categorised into three regions:

- At least one lepton and at least one b-tagged jet.
- Zero lepton and exactly one b-tagged jet.
- Zero lepton and at least two b-tagged jet.

3. Analysis

After the application of the requirements described above over the dataset and the MC (background and signal) samples, we tabulated the number of the events that passed the cuts in Table 1. It's important to note that the signal events are not normalised to anything; they are just entries. The background is normalised with its corresponding cross-section, total weight, efficiency and the data luminosity. The normalizations of the $\gamma\gamma$ and γ+jet contributions are respectively fixed to 80% and 20% of the data yield in the inclusive case. Figures 2 and 3 display the kinematic distributions corresponding to different variables for the inclusive case (just after preselections). The agreement between data and total background is reasonable in both the cores and tails.

Cuts	Data	Total Bkg	ttH180	ttH250	ttH500	ttH750	bbH180	bbH250	bbH500	bbH750
Inclusive	1278499	1301087	68150	78406	91070	98070	20091	23860	28326	29894
$N_{bjet} \geq 1$	30119	30393	52563	59397	67764	69720	7875	10772	16332	18961
$N_{bjet} = 1$ & $N_{leps} = 0$	27658	28045	22437	24468	30630	31478	7246	9954	14892	17034
$N_{bjet} \geq 2$ & $N_{leps} = 0$	2100	1912	14731	16805	17180	18316	623	795	1423	1891
$N_{bjet} \geq 1$ & $N_{leps} \geq 1$	361	436	15395	18122	19953	19924	6	23	16	35

Table 1. The number of events that are survived after the application of the event selections described in section 2 for data and MC corresponding to various regions.

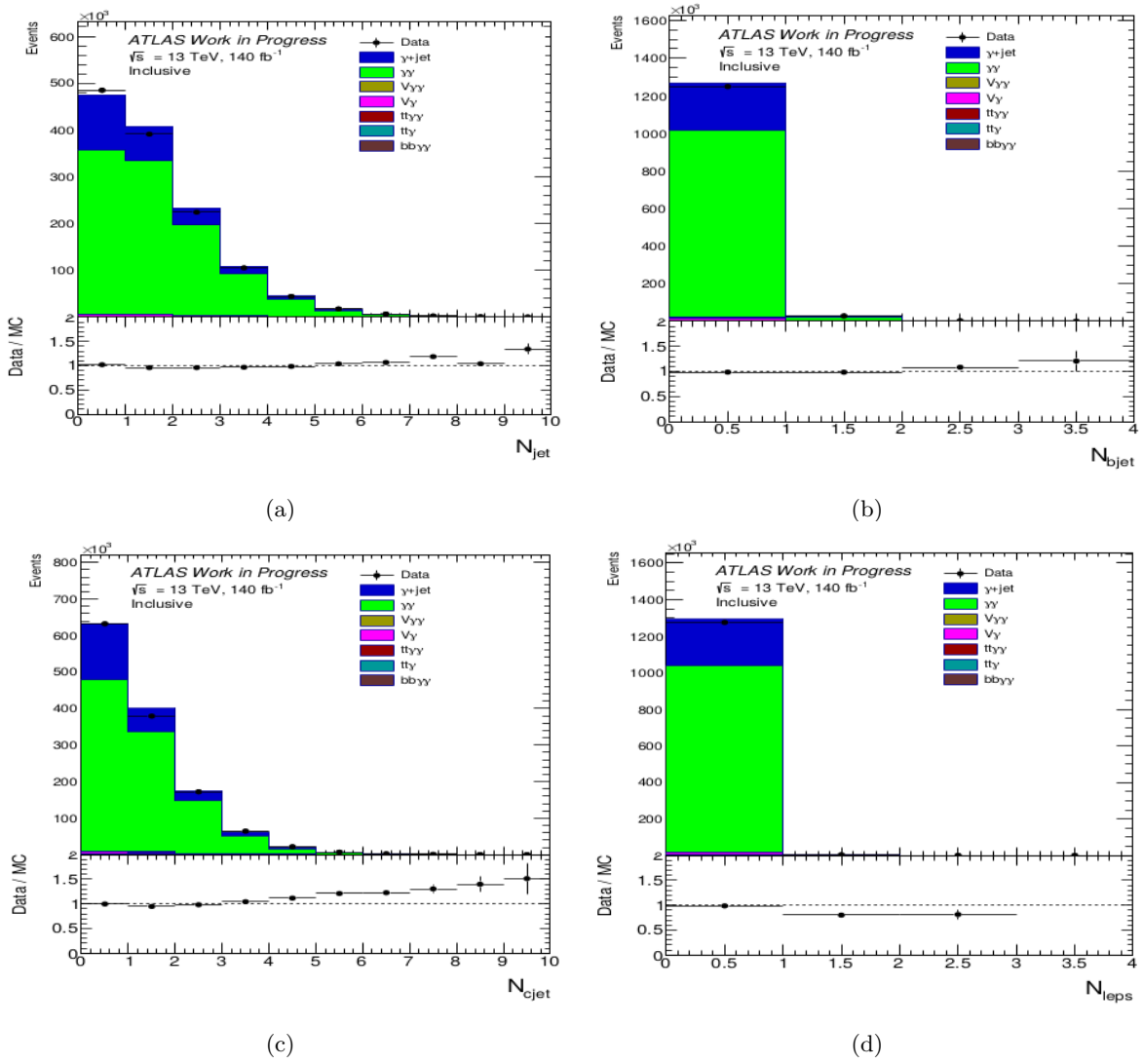

(a) (b)

(c) (d)

Figure 2. Kinematic distributions comparing the data to background at the inclusive case (after selecting two photons with $p_T^{1\gamma} > 40$ GeV and $p_T^{2\gamma} > 30$ GeV and $m_{\gamma\gamma} > 130$ GeV). The multiplicity of (a) jets and (b) b-tagged jets, (c) Number of central jets and (d) Number of leptons.

 ISBN: 978-0-620-88875-2

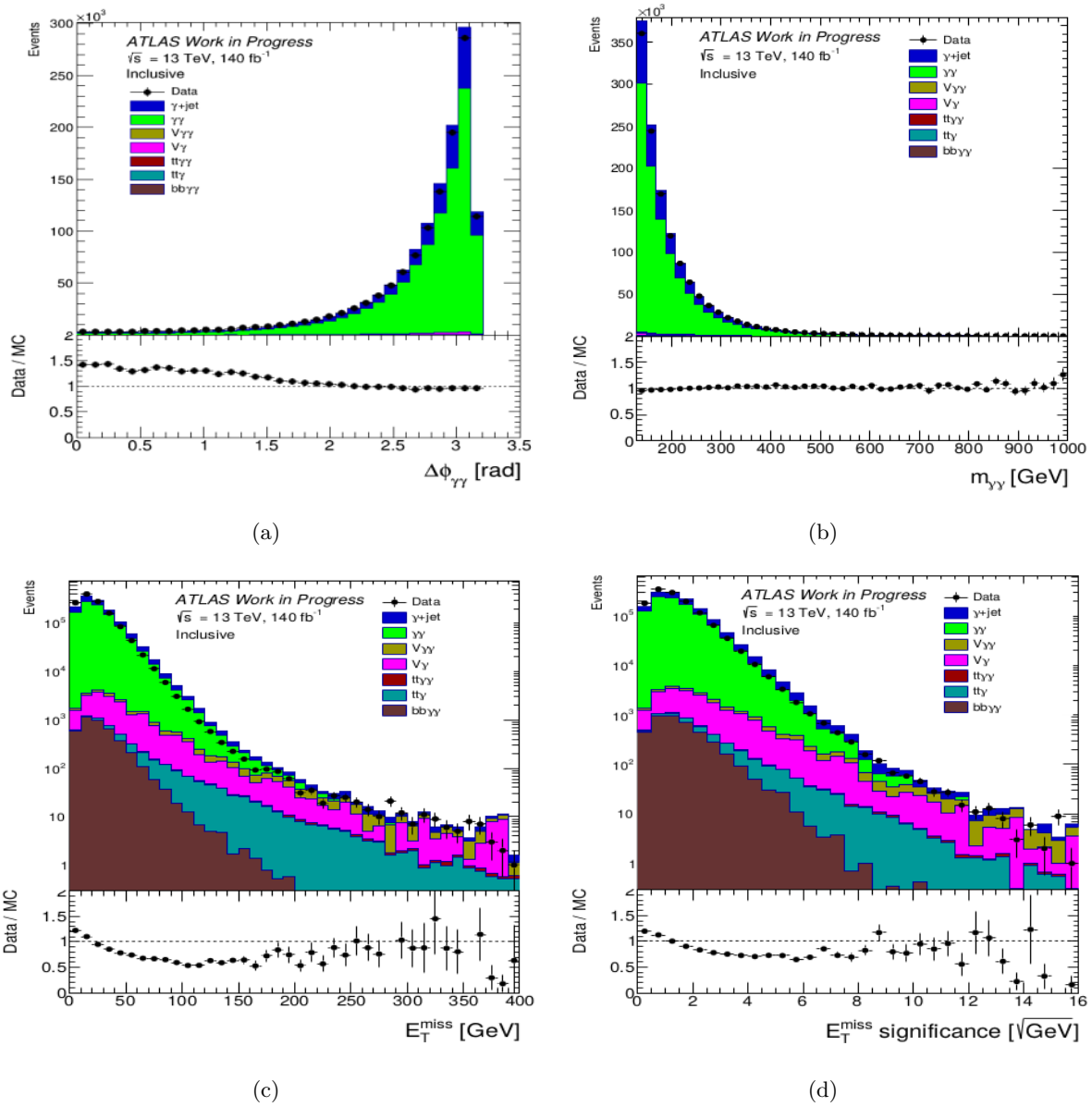

Figure 3. Kinematic distributions comparing the data to background at the inclusive case (after selecting two photons with $p_T^{1\gamma} > 40$ GeV and $p_T^{2\gamma} > 30$ GeV and $m_{\gamma\gamma} > 130$ GeV). (a) the azimuthal angle between the two photons $\Delta\phi_{\gamma\gamma}$, (b) the invariant mass of the diphoton system, (c) the missing transverse energy E_T^{miss} and (d) E_T^{miss} significance ($E_T^{\text{miss}}/\sqrt{\sum E_T^{\text{miss}}}$).

4. Optimization

We use the ttH sample with $m_H = 180\,\text{GeV}$ as the signal sample for optimization. The reason for choosing the ttH sample is because it has events with zero lepton and one or two b-tagged jet, and events with one lepton and one b-tagged jet. It also has more signatures that are different from the background samples. The bbH is almost the same as the background (nothing to optimize). Therefore, we optimize the ttH, and at the same time, we examine the bbH and $Z(bb)H$. Since the ttH with m_H in the range 105 to 160 GeV is examined in the nominal

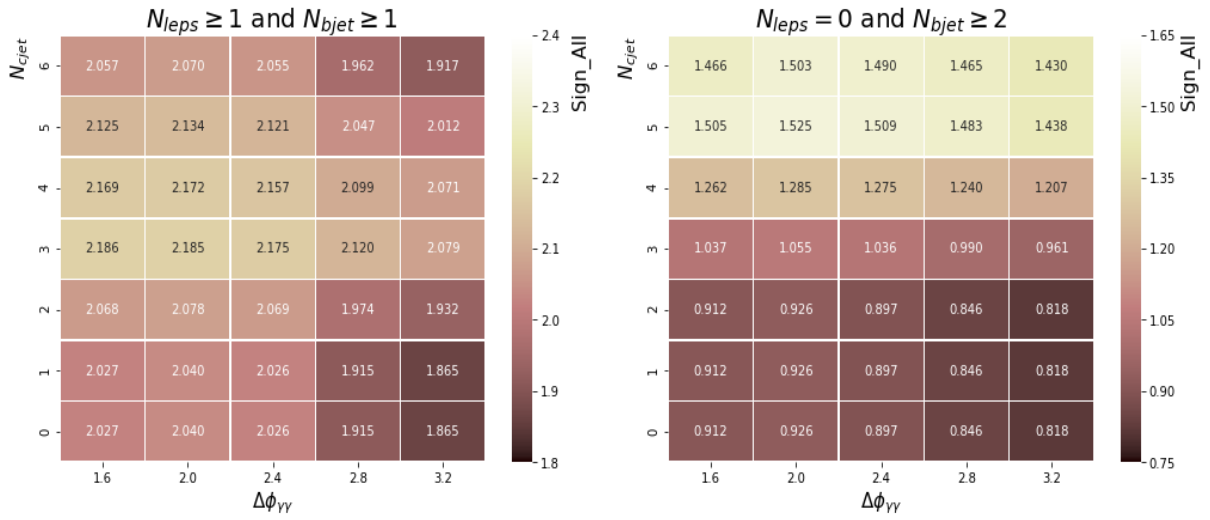

Figure 4. Optimization results for region ($N_{leps} \geq 1$ and $\mathrm{N_{bjet}} \geq 1$) and ($N_{leps} = 0$ and $\mathrm{N_{bjet}} \geq 2$). Sign_All indicate the quadrature sum of significance for all four bins in each region.

Region	$N_{leps} \geq 1$ and $N_{bjet} \geq 1$	$N_{leps} = 0$ and $N_{bjet} \geq 2$	$N_{leps} = 0$ and $N_{bjet} = 1$
NC-Significance	0.87	0.37	0.15
C-Significance	2.19	1.53	1.01
N_{cjet}	3	5	5
$\Delta\phi_{\gamma\gamma}$	1.6	2	2

Table 2. NC and C-significance with the corresponding N_{cjet} and $\Delta\phi_{\gamma\gamma}$ cuts for each region.

Higgs analysis, so that in this optimization, we use the lowest available ttH signal sample which corresponds to the $m_H = 180$ GeV. All background samples are mixed and normalised to 140 fb^{-1} for the optimization.

We optimize the variables N_{cjet} and $\Delta\phi_{\gamma\gamma}$ to select the cut that gives the maximum significance. These variables are chosen because they give better significance compared to the other variables that we tested. In each region (Section 2), we further split events into four bins by making a 2D scan on $\Delta\phi_{\gamma\gamma}$ and N_{cjet}. The significance is calculated using the formula $S/\sqrt{S+B}$, and this is to avoid having infinite significance in the case where B is zero. Where S and B are the signal and background events, respectively. Here, the signal is normalised to 50 events in the inclusive case, while the background is calculated in a small range of the diphoton invariant mass spectrum ($180 \pm 10\,\mathrm{GeV}$). Then we use the quadrature sum of significance for all four bins in each region. Figure 4, shows the result of the optimization for two of our regions. While in Table 2, we show the Non-Categorized "NC" and the maximum categorized "C" significance that we got for all regions together with the corresponding optimal $\Delta\phi_{\gamma\gamma}$ and N_{cjet} cuts for each region. There is a big improvement in the significance after the selection cuts.

5. Summary and Future Work

A simple analysis is proposed to search for a new heavy resonance decaying into two photons in association with at least one b-tagged jet. Kinematic distributions with data to background comparisons have been shown. Optimization on truth sample (preselection) has also been presented, to mimic the analysis procedure and choose the maximum significance cut as the final event selection.

In the future, and each category, a signal plus background fit will be performed to extract the signal from the data. The double-sided crystal ball method will be used for the signal parameterization according to the diphoton mass. In contrast, an analytical function will be used to describe the background of the whole spectrum. We will test the ttH and bbH model and give the limits on the production cross-section times the branching ratio.

Acknowledgment

E. Shrif would like to acknowledge the financial support of the Schlumberger Foundation, Faculty for the Future.

References

[1] Aaboud M *et al.* [ATLAS Collaboration], Phys. Lett. B 775, 105 (2017) [arXiv:1707.04147].
[2] Molinaro E and Vignaroli N, Mod. Phys. Lett. A 32, no. 27, 1730024 (2017) [arXiv:1707.00926].
[3] Aad G *et al.* [ATLAS Collaboration], Phys. Lett. B 716, 1 (2012) [arXiv:1207.7214].
[4] Chatrchyan S *et al.* [CMS Collaboration], Phys. Lett. B 716, 30 (2012) [arXiv:1207.7235].
[5] The ATLAS collaboration, ATLAS-CONF-2015-081.
[6] CMS Collaboration,CMS-PAS-EXO-15-004.
[7] The ATLAS collaboration, ATLAS-CONF-2016-059.
[8] Lenzi B *et al.* [ATLAS Collaboration] PoS ICHEP 2016, 436 (2016) [arXiv:1611.03308].
[9] Khachatryan V *et al.* [CMS Collaboration], Phys. Lett. B 767, 147 (2017) [arXiv:1609.02507].
[10] Alwall J *et al.*, JHEP 1407, 079 (2014) [arXiv:1405.0301].
[11] Sjostrand T, Mrenna S and Skands P Z, Comput. Phys. Commun. 178, 852 (2008) [arXiv:0710.3820].

Top-quark background estimation for BSM physics search $H \rightarrow Sh \rightarrow 2\ell+$ 2 jets with the ATLAS detector at LHC

Jeremiah Kgomotso Monnakgotla[1], Yesenia Hernández Jiménez[1] and Bruce Mellado[1,2]

[1] School of Physics and Institute for Collider Particle Physics, University of the Witwatersrand, Johannesburg, Wits 2050, South Africa
[2] iThemba LABS, National Research Foundation, PO Box 722, Somerset West 7129, South Africa

E-mail: jeremiah.kgomotso.monnakgotla@cern.ch

Abstract. This paper presents the top-quark background estimation for a heavy scalar H that decays to Standard Model Higgs boson (h) and a Higgs-like scalar (S). This work uses the dataset corresponding to an integrated luminosity of 36 fb^{-1} of pp collisions at center-of-mass energy $\sqrt{s}$ =13 TeV. For this analysis the final state consists of two oppositely charged leptons with different flavour ($e^{\pm}\mu^{\mp}$) and jets. In this analysis the dominant Standard Model background is made of the top-quark processes ($t\bar{t}$ and Wt). The top quark control and validation regions are defined in the 1 b-tagged jet and 2 b-tagged jets phase space, respectively. The construction of the top-quark validation region is defined in order to correct the Monte Carlo mismodeling observed in the lepton kinematics.

1. Introduction

A wide range of results validating Standard Model (SM) processes are published by ATLAS [1, 2] and CMS [3] collaborations pertaining the multi-lepton production at the Large Hadron Collider (LHC) which observe discrepancies between data and Monte Carlo (MC). Excesses can be explained by the Madala hypothesis [4, 5, 6, 7]. In that hypothesis, H decays to Sh which subsequently decays into a wide range of possible final states, dominated by leptons and jets.

This paper presents the top-quark background estimation for the $H \rightarrow Sh$ search using a dataset corresponding to an integrated luminosity of 36 fb^{-1} recorded by the ATLAS detector at center-of-mass energy $\sqrt{s}$ = 13 TeV. The Madala hypothesis uses a simplified model that considers gluon-gluon fusion production mode in association with the heavy scalar (H) that decays into a Higgs-like scalar (S) and the Standard Model (SM) Higgs boson (h). The S boson is assumed to have the either of or Higgs boson's branching ratio depending on its mass (m_S).

2. Object Selection

The final state consists of two oppositely charged leptons with different flavor and at least two jets. In this analysis, the main physics objects are the electrons, muons, jets and missing transverse momentum ($E^{\text{miss}}_{\text{T, track}}$). Electron candidates must have pseudorapidity range $|\eta| < 2.47$, excluding the transition region between the barrel and endcaps in the LAr calorimeter ($1.37 > |\eta| > 1.52$). The muon candidates must have pseudorapidity range $|\eta| < 2.5$. The leading lepton to satisfy $p_{\text{T}} > 27$ GeV, sub-leading lepton $p_{\text{T}} > 15$ GeV and veto events having additional leptons with $p_{\text{T}} > 10$ GeV. The leading lepton and sub-leading lepton are the leptons with the highest p_{T} and second highest p_{T}, respectively.

The jets are reconstructed by the anti-k_t algorithm [8] with a distance parameter R=0.4 using a cluster of energy deposit in the calorimeters. The jets are required to have $p_{\text{T}} > 25$ GeV within the range $|\eta| < 2.5$. However, jets with $p_{\text{T}} < 60$ GeV are required to have Jet-Vertex-Tagger (JVT) [9] less than 0.59, where JVT is a technique used to separate jets from pile-up events. In Addition, jets originating from b-hadrons are identified using the MV2c10 b-tagging algorithm [10, 11] with an efficiency of 85%. Finally, b-tagged jets are required to have $p_{\text{T}} > 25$ GeV.

3. Signal Region Definition

Phase space with high signal sensitivity and low background contamination determines the signal region (SR). The top-quark background is reduced by selecting events without b-tagged jets as shown in Figure 1 (a). After applying a b-tagged jet veto, the signal is more dominant at ≥ 2 jets region as shown in Figure 1 (b).

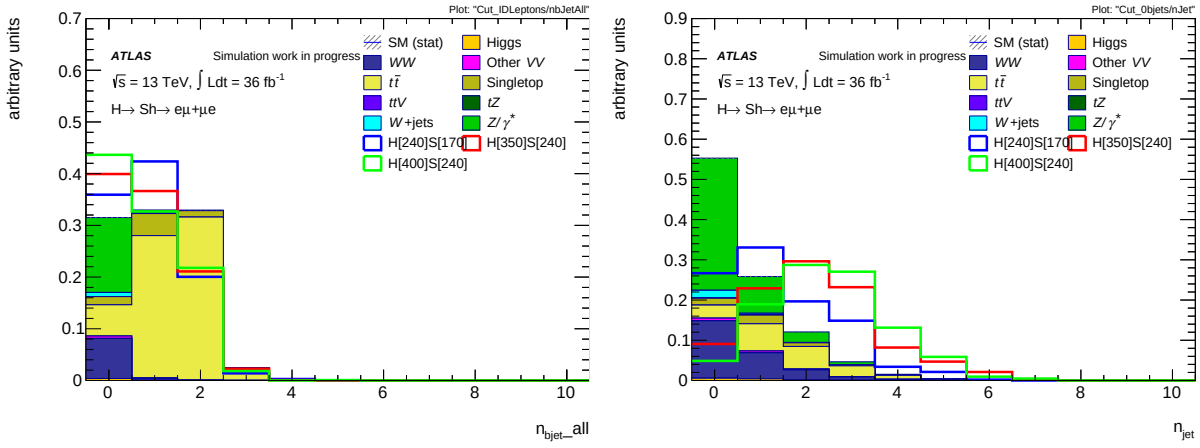

(a) (b)

Figure 1: Shape Comparison of signal and background (both normalized to unity) after selecting events with two high p_{T} leptons: (a) Number of b-tagged jets and (b) Number of jets distributions

4. Top-quark Background Estimation

The top-quark background estimation is based on MC simulation and the experimenta data. In this analysis the top-quark background is dominated by the $t\bar{t}$ events due to its large cross section and the contribution from the single-top (Wt) is relatively small. After applying the requirements discussed in the section 3, the SR is dominated by the top-quark production with 60% contribution. Other relevant background contributions arise from the production of WW, W+jets and Z+jets. The top-quark is estimated by defining a control region (top CR) and a validation region (top VR) to be orthogonal in the SR and required to be signal depleted. The top CR is constructed in order to derive the normalization factors and extrapolate the top-quark contribution to the SR. In order to test the modeling of the top-quark processes a top VR is constructed.

The top CR is selected by applying the SR selection with an additional requirement on the invariant mass of the di-lepton system ($m_{\ell\ell}$) to be greater than 150 GeV in order to achieve a signal depleted region, as shown in Figure 2 (a). The top VR is selected by same SR selection with the exception of the b-tagged jets requirement. Moreover, in order to reduce the signal contamination in the top VR the invariant mass of the two b-tagged jets (m_{bb}) is required to be above 150 GeV as shown in Figure 2 (b). The event selection summary is presented in Table 1 and the contributions from different SM processes are shown in Table 2

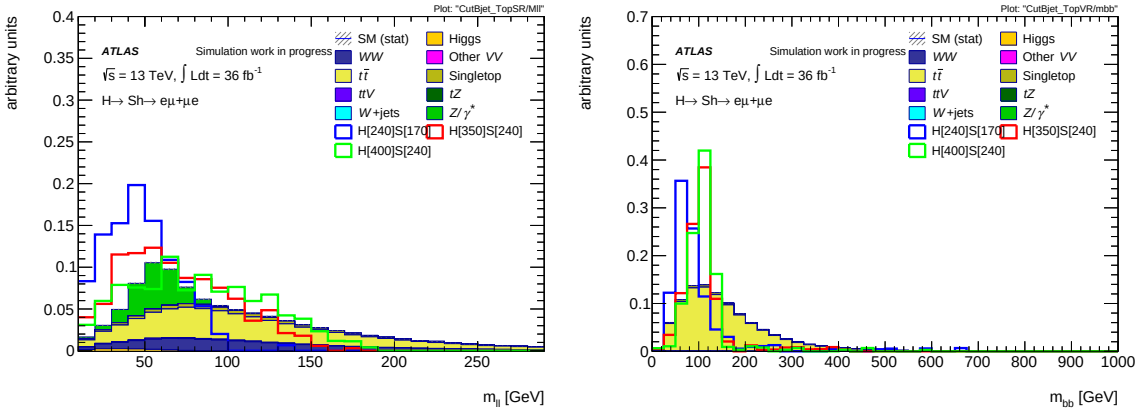

(a) (b)

Figure 2: Comparison shape of signal (normalized to total background) and background after selecting events with two high p_{T} leptons and at least two jets: (a) $m_{\ell\ell}$ and (b) m_{bb} distributions.

Table 1: Analysis selection for SR, top CR and top VR.

Observable	SR	top CR	top VR
Leading lepton p_{T}	>27 GeV		
Sub-leading lepton p_{T}	>15 GeV		
Number of jets	≥ 2		
Number of b-tagged jets	$=0$	$=0$	$=2$
$m_{\ell\ell}$	-	>150 GeV	-
m_{bb}	-	-	>150 GeV

 ISBN: 978-0-620-88875-2

4.1. Kinematic Distributions in the Top Control Region

In this region the agreement between data and MC is good. The ratio of data over MC is 0.97 ± 0.01 with top-quark purity of 72%. The implementation of NLO Electro Weak (EW) corrections (purely based on MC simulation)[12, 13, 14] have a very small impact on the ratio of data over MC, as shown in Figure 3. Other background contributions are from the non-resonant WW which is about 25%, W+jets, other VV, $Z/\gamma*$ processes add up to 3% to the total background.

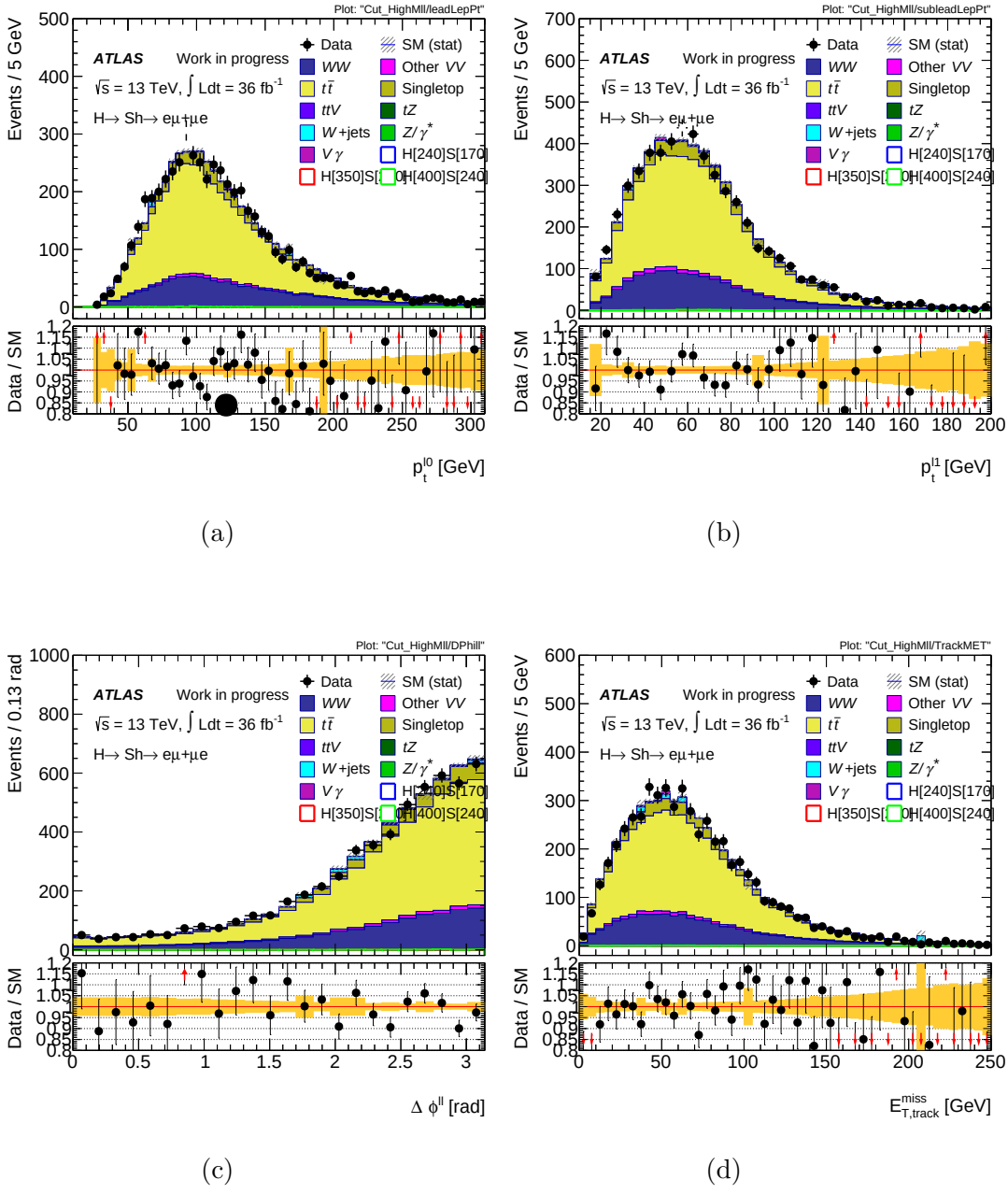

(a) (b)

(c) (d)

Figure 3: Lepton kinematics of data and MC simulation in the top CR after applying requirements shown in Table 1: (a) Leading lepton p_{T}, (b) Sub-leading lepton p_{T}, (c) Angular separation between two leptons ($\Delta\phi^{\ell\ell}$) and (d) $E^{\mathrm{miss}}_{\mathrm{T,track}}$. Uncertainties are statistical only.

4.2. Kinematic Distributions in the Top Validation Region

In this region the agreement between data and MC is reasonable. The ratio of data over MC is 0.95 with top-quark puritiy of 99%. Other non-top-quark background contributions add up to 1%. The implementation of the NLO EW corrections sligthly improves the agreement between data and MC, as shown in the tail of the distributions in Figure 4.

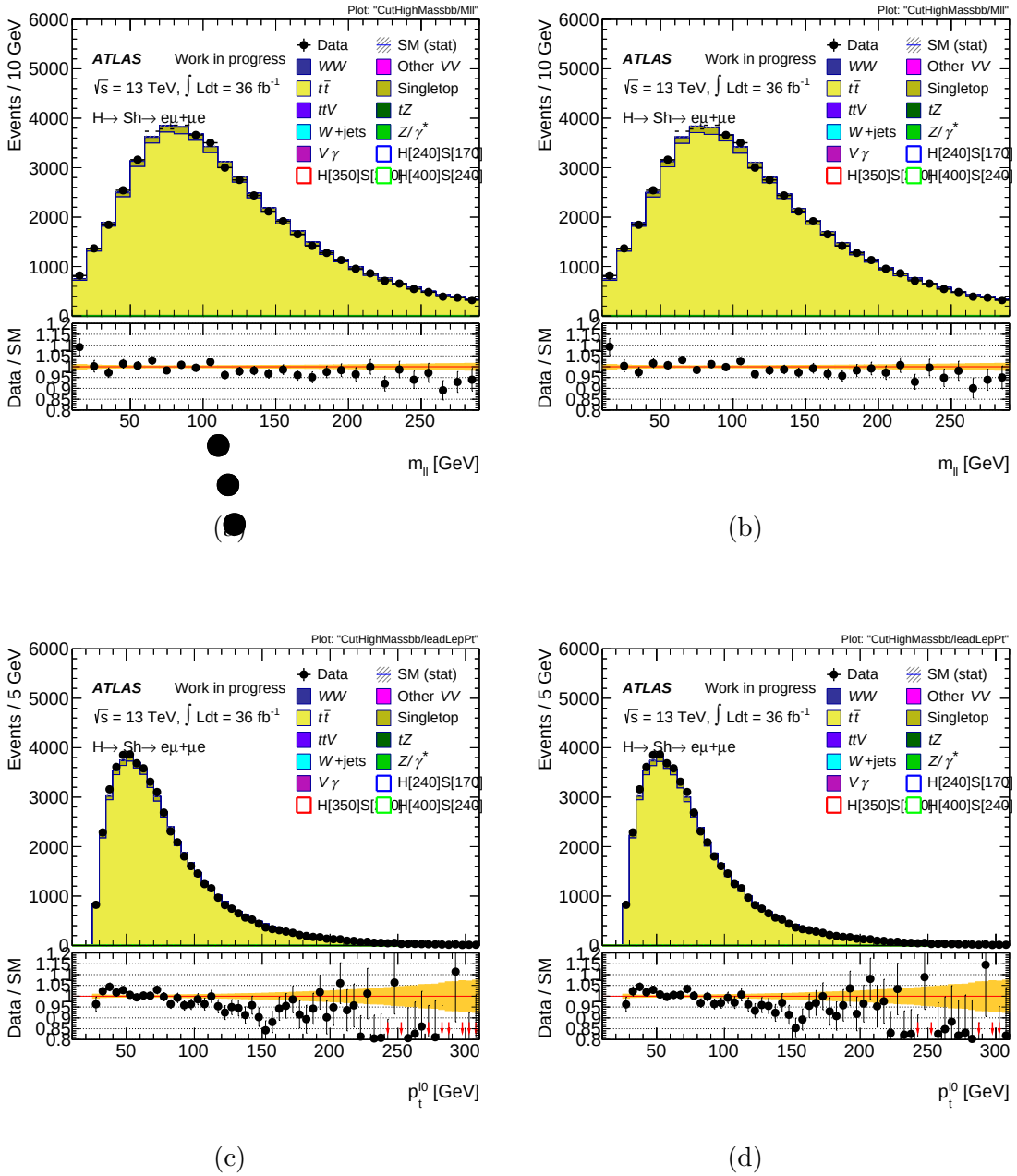

Figure 4: Comparison of data and MC in the top CR after applying requirements shown in Table 1: (a) Di-lepton invariant mass (b) Di-lepton invariant mass after NLO EW corrections (c) Leading lepton p_{T}, (d) Leading lepton p_{T} after NLO EW corrections. Uncertainties are statistical only.

Table 2: Number of events observed in data, compared to the numbers of predicted background events. The analysis is blinded in the SR. Uncertainties are statistical only.

	SR	top CR	top VR
SM Higgs	299.97 ± 1.56	3.19 ± 0.08	25.29 ± 0.24
WW	4789.12 ± 13.38	1355.89 ± 7.01	33.05 ± 0.84
Other VV	421.43 ± 3.63	105.01 ± 1.69	4.56 ± 0.27
$t\bar{t}$	12594.71 ± 32.42	3534.73 ± 17.30	52658.56 ± 64.70
Singletop	1630.74 ± 15.97	469.49 ± 8.66	2134.64 ± 17.98
ttV	22.32 ± 0.41	7.74 ± 0.24	66.83 ± 0.68
tZ	1.96 ± 0.04	0.64 ± 0.02	2.01 ± 0.04
W+jets	115.33 ± 32.44	40.44 ± 20.30	0.00
Z/γ^*	4716.15 ± 57.43	17.77 ± 10.83	62.27 ± 3.76
Total Bkg	24887.97 ± 78.18	5561.66 ± 31.55	54991.04 ± 67.29
Data	-	5376	52217
Data/MC	-	0.97 ± 0.01	0.95 ± 0.00

5. Conclusion

This proceeding presents the top-quark background estimation for the $H \to Sh$ search. This analysis is characterized by two oppositely charged leptons with different flavour and at least two jets. For this search the top-quark is the dominant SM background with 60% contribution in the SR. The top-quark background is normalized in the 0 b-tagged jets bin, with the ratio of data over MC is approximately 0.97 ± 0.01 and top-quark purity of 72%. The modeling of top-quark process is tested in the 2 b-tagged jets bin, the ratio of data over MC is approximately 0.95 and top-quark purity of 99%. Finally, the NLO EW corrections applied on the top-quark MC slightly improve the agreement between data and MC in the top CR and VR.

6. References

[1] ATLAS Collaboration 2016 *JHEP* **09** 029 arXiv:1603.01702
[2] ATLAS Collaboration, Measurement of fiducial and differential W^+W^- production cross-sections at $\sqrt{s}$ =13 TeV with the ATLAS detector 2019 arXiv:1905.04242
[3] CMS collaboration 2018 *JHEP* **10** 117 arXiv:1805.07399
[4] von Buddenbrock S. et al. The compatibility of LHC Run 1 data with a heavy scalar of mass around 270 GeV arXiv:1506.00612 [hep-ph]
[5] von Buddenbrock S. et al. 2016 *Eur. Phys. J.* **C76** 580 arXiv:1606.01674 [hep-ph]
[6] von Buddenbrock S. et al. 2018 *J. Phys.* **G45** 115003 arXiv:1711.07874 [hep-ph]
[7] von Buddenbrock S. et al. The emergence of multi-lepton anomalies at the LHC and their compatibility with new physics at the EW scale 2019 arXiv:1901.05300 [hep-ph]
[8] Cacciari M, Salam G. P., Soyez G 2008 *JHEP* **04** 063 arXiv: 0802.1189 [hep-ph]
[9] ATLAS Collaboration, Tagging and suppression of pileup jets with the ATLAS detector, ATLAS-CONF-2014-018, 2014, https://cds.cern.ch/record/1700870
[10] ATLAS Collaboration, Expected performance of the ATLAS b-tagging algorithms in Run-2, ATL-PHYS-PUB-2015-022, 2015, https://cds.cern.ch/record/2037697
[11] ATLAS Collaboration, Commissioning of the ATLAS b-tagging algorithms using $t\bar{t}$ events in early Run 2 data, ATL-PHYS-PUB-2015-039, 2015, https://cds.cern.ch/record/2047871
[12] Denner A., Mathieu P. 2016 *JHEP* **08** 155 arXiv:1607.05571 [hep-ph]
[13] Actis S. et al. 2017 *Comput. Phys. Commun.* **214** 140-173 arXiv:1605.01090 [hep-ph]
[14] Denner A. et al. 2017 *Comput. Phys. Commun.* **212** 220-238 arXiv:1604.06792 [hep-ph]

A Deep Neural Network for Missing Transverse Momentum Reconstruction in ATLAS

Matthew Leigh

University of Cape Town, South Africa

E-mail: matthew.leigh@cern.ch

Abstract. The missing transverse momentum ($\mathbf{E}_{\mathrm{T}}^{\mathrm{miss}}$) of a proton-proton ($pp$) collision is an important observable as it serves as an experimental proxy for the total momentum carried away by undetected particles in the plane perpendicular to the beam line. Precisely measuring $\mathbf{E}_{\mathrm{T}}^{\mathrm{miss}}$ is critical for the understanding many physical processes which take place at the Large Hadron Collider. The ATLAS experiment currently utilises several algorithms to reconstruct the $\mathbf{E}_{\mathrm{T}}^{\mathrm{miss}}$. These proceedings describe the development of a novel algorithm based on a deep neural network to improve $\mathbf{E}_{\mathrm{T}}^{\mathrm{miss}}$ reconstruction. The network reconstruction had resolution of 22.7 GeV when tested in simulated $t\bar{t}$, improving over than the next best performing algorithm which had a resolution of 27.3 GeV. The new estimate was more robust to an increase in pileup and outperformed all other methods across the full pileup range. The network was also demonstrated to generalise well in real Z events, improving the $\mathbf{E}_{\mathrm{T}}^{\mathrm{miss}}$ resolution from 15.53 to 11.29 GeV.

1. Introduction

The ATLAS detector [1] is an example of a hermetic detector. It was thus designed to observe nearly all possible decay products produced in the high-energy pp collisions provided by the Large Hadron Collider (LHC) at CERN. However, neutrinos and many theorised particles in beyond the Standard Model physics are weakly interacting and are able travel through the detector without leaving any measurable signal. Since the total linear momentum of the colliding protons in the transverse plane is negligible, the presence of these undetectable particles can be inferred by the resultant transverse momentum imbalance of all observable decay products emerging from the collision. The negative vectorial sum of the visible momenta in the transverse plane, $\mathbf{E}_{\mathrm{T}}^{\mathrm{miss}}$, therefore serves as an experimental proxy for the net transverse momentum of undetected particles. This is an essential part of many ongoing physics analyses at the LHC [2,3], and played a role in the discovery of the Higgs boson in 2012 [4]. Reconstructing $\mathbf{E}_{\mathrm{T}}^{\mathrm{miss}}$ requires the output of all detector subsystems, as well as the most complete representation of the hard-scatter[1] which gets obscured by the presence of additional pp interactions in the same bunch crossing, known as "*pileup*". Therefore, the performance of current $\mathbf{E}_{\mathrm{T}}^{\mathrm{miss}}$ reconstruction algorithms are expected to get worse as the luminosity of the LHC increases over the next few years. Monte-Carlo (MC) simulations are used in most analyses to provide a baseline from which one can analyse real data captured by ATLAS. To produce this simulated data, the underlying parton interaction is generated, soft radiation and hadronization modelling is applied, before the passage of the

[1] The hard-scatter is defined in ATLAS as the reconstructed vertex with the highest $\sum(p_{\mathrm{T}}^{\mathrm{track}})^2$.

 ISBN: 978-0-620-88875-2

resultant stable particles through a detector simulation, to estimate the signals they would produce [5]. The event reconstruction process applied to MC is identical to the one applied to real data. In this project we extracted and stored the true transverse momentum of all non-interacting particles in each MC event before the detector simulation, called $\mathbf{E}_{\mathrm{T}}^{\mathrm{miss,\ true}}$. A deep neural network [6] was then trained to learn a mapping from a set of reconstructed observables to $\mathbf{E}_{\mathrm{T}}^{\mathrm{miss,\ true}}$. This mapping was applied and evaluated on real and MC datasets, all of which are orthogonal from those used to train the network.

2. The ATLAS Detector

The ATLAS detector at the LHC is a general purpose particle detector with nearly 4π solid angle coverage and a nominal forward-backward symmetry. It consists of an inner tracking detector (ID) surrounded by a superconducting solenoid magnet which provides a 2 T magnetic field. Encompassing the ID are electromagnetic (EM) and hadronic calorimeters, and a muon-spectrometer (MS). The ID consists of a pixel detector, a semiconductor tracker and a transition radiation tracking detector. It provides tracking information in a pseudo rapidity range of $\eta < |2.5|$[2]. The EM calorimeter provides high granularity energy measurements over a range of $\eta < |3.2|$. Steel-scintillating hadronic calorimeters provide central coverage within $\eta < |1.7|$. End-cap regions of the detector contain additional calorimeters up to $\eta < |4.9|$. The MS is the outermost layer of the ATLAS detector and features three large air-core toroidal superconducting magnet systems with eight coils each. It contains precision tracking chambers covering $\eta < |2.7|$. ATLAS data-taking utilises a two-level trigger system. The Level-1 trigger is hardware-based and reduces the event rate to around 100 kHz. The Level-2 trigger is a software-based high level trigger, which further reduces the rate to approximately 1 kHz.

3. Missing Transverse Momentum Reconstruction at ATLAS

Over the past few years, different algorithms have been developed to reconstruct $\mathbf{E}_{\mathrm{T}}^{\mathrm{miss}}$ at ATLAS [7]. ATLAS currently offers several variants for physics analyses with different requirements, several of which are used in this project [8]. Most definitions are object based and characterised by two contributions. The first one is from "*hard-event*" signals, which are signals associated with identified and calibrated physics objects, such as fully reconstructed jets, photons, electrons, and muons. Dedicated rejection procedures are carried out to ensure that all contributing objects were reconstructed from mutually exclusive detector signals. The second contribution to $\mathbf{E}_{\mathrm{T}}^{\mathrm{miss}}$ is from "*soft-event*" signals. These are the leftover detector signals that were not used to reconstruct the objects mentioned above. Most algorithms use a Track Soft Term (TST), which is created purely from unused particle tracks in the ID which are associated with the hard-scatter. The tracks are required to have passed high-quality reconstruction requirements and have $\eta < |2.5|$ and $p_T > 0.4$ GeV. An example of this algorithm is shown in Equation 1, which show the negative vectorial summation of the terms:

$$\mathbf{E}_{\mathrm{T}}^{\mathrm{miss}} = -\underbrace{\sum_{\substack{\text{selected}\\\text{electrons}}} \mathbf{p}_{\mathrm{T}}^{e}}_{\mathbf{E}_{\mathrm{T}}^{\mathrm{miss},e}} - \underbrace{\sum_{\substack{\text{selected}\\\text{muons}}} \mathbf{p}_{\mathrm{T}}^{\mu}}_{\mathbf{E}_{\mathrm{T}}^{\mathrm{miss},\mu}} - \underbrace{\sum_{\substack{\text{selected}\\\text{photons}}} \mathbf{p}_{\mathrm{T}}^{\gamma}}_{\mathbf{E}_{\mathrm{T}}^{\mathrm{miss},\gamma}} - \underbrace{\sum_{\substack{\text{selected}\\\text{jets}}} \mathbf{p}_{\mathrm{T}}^{\mathrm{jet}}}_{\mathbf{E}_{\mathrm{T}}^{\mathrm{miss,\ jet}}} - \underbrace{\sum_{\substack{\text{unused}\\\text{tracks}}} \mathbf{p}_{\mathrm{T}}^{\mathrm{track}}}_{\mathbf{E}_{\mathrm{T}}^{\mathrm{miss,\ soft}}} \qquad (1)$$

$$\underbrace{\qquad\qquad\qquad\qquad\qquad\qquad\qquad\qquad}_{\text{hard terms}} \qquad \underbrace{\qquad\qquad}_{\text{soft term}}$$

[2] ATLAS uses a right-handed coordinate system with its origin at the nominal interaction point in the center of the detector. The z-axis lies along the beam pipe, the x-axis points towards the center of the LHC ring, and the y-axis points vertically upwards. Cylindrical coordinates are used in the transverse plane where ϕ is the azimuthal angle around the z-axis. The pseudorapidity is defined in terms of the polar angle as $\eta \equiv -\log\tan\frac{\theta}{2}$, where θ is the polar angle off the z-axis.

The total transverse energy in the detector, ΣE_{T}, is a scalar which quantifies the total event activity. This is a crucial variable for understanding the scale and resolution of $\mathbf{E}_{\mathrm{T}}^{\mathrm{miss}}$. It uses the same terms, and follows the same overlap removal procedures, but is created using the scalar sum of the various transverse momenta. Reconstruction of the magnitude of the missing transverse momentum ($|\mathbf{E}_{\mathrm{T}}^{\mathrm{miss}}|$) suffers from a positive observation bias towards non-vanishing values, due to it being strictly positive by definition. This is most noticeable in final states without genuine missing transverse momentum. This means that the recorded $|\mathbf{E}_{\mathrm{T}}^{\mathrm{miss}}|$ is often non-zero even when there are no undetected particles due to mismeasurements.

3.1. Hard Terms

Muons are identified by matching an ID track with an MS track or segment, and are required to have $p_T > 10$ GeV to be included in the muon term for $\mathbf{E}_{\mathrm{T}}^{\mathrm{miss}}$. Electrons are reconstructed from clusters in the EM calorimeter associated with an ID track and must also have $p_T > 10$ GeV to contribute to $\mathbf{E}_{\mathrm{T}}^{\mathrm{miss}}$ or ΣE_{T}. Photons are identified from their distinctive electromagnetic showers in the calorimeters. In this project, photon candidates are required to satisfy a set of tight criteria to reduce backgrounds and must have $p_T > 25$ GeV. Jets are reconstructed from clusters of topologically connected calorimeter cells using the anti-kt algorithm [9] with a radius parameter of $R = 0.4$. All jets are first required to have $p_T > 20$ GeV after calibration and $\eta < |4.5|$. Jets are further decorated using a tagging algorithm to select jets likely from emerging from the hard-scatter, known as jet-vertex-tagging (JVT) [10]. The JVT value attributed to a jet ranges from 0 (likely from pile-up) to 1 (likely from the hard-scatter). All central jets ($\eta < |2.5|$) are required to have either a JVT value greater than 0.59 or $p_T > 60$ GeV.

3.2. Alternate Definitions of $\mathbf{E}_T^{miss}$

Five different algorithms are used and compared in this work. The first three are constructed as mentioned above and only differ in their treatment of forward jets. *Loose* $\mathbf{E}_{\mathrm{T}}^{\mathrm{miss}}$ includes contributions from any forward jet with $p_T > 20$ GeV. *Tight* $\mathbf{E}_{\mathrm{T}}^{\mathrm{miss}}$ removes all forward jets with $p_T < 30$ GeV. *FJVT* $\mathbf{E}_{\mathrm{T}}^{\mathrm{miss}}$ once again uses the same terms as Loose, but all forward jets with $20 > pT > 50$ GeV are required to pass the "Loose" FJVT criteria [11]. *CST* $\mathbf{E}_{\mathrm{T}}^{\mathrm{miss}}$ uses the same jet selection as the Tight, but replaces the TST with a more inclusive soft term created from unused calorimeter clusters [12], and although noise suppression is applied, no additional pileup suppression techniques are used. The fifth and final algorithm used in this work is somewhat distinct from the others. *Track* $\mathbf{E}_{\mathrm{T}}^{\mathrm{miss}}$ is not object based and only employs ID tracks. It is therefore inherently more immune to pileup but ignores all neutral particles.

4. The Deep Neural Network

The main goal of this project was to produce a new definition, *Network* $\mathbf{E}_{\mathrm{T}}^{\mathrm{miss}}$, derived from a non-linear combination of all other algorithms. The form of this combination would be adaptable and unique for each event to maximise accuracy. The model chosen for this work was a dense feed-forward artificial neural network (ANN) [6]. The network did not receive any raw detector signals or even individual particles as inputs. This was due to the desired scope of the project, which was to provide a final level correction to the $\mathbf{E}_{\mathrm{T}}^{\mathrm{miss}}$ of an event only, and not to redefine object selection or identification. 65 variables were chosen to be inputs for the neural network. These included the outputs of the 5 mentioned algorithms, their unique hard and soft terms, and additional variables which might indicate the accuracy of these definitions. These additional variables included the number of reconstructed vertices, which indicates the amount of pileup, the amount of forward jet activity and object based $\mathbf{E}_{\mathrm{T}}^{\mathrm{miss}}$ significance [13].

4.1. Network Training

The network was trained on MC simulated datasets where the target variable on an event by event basis was $\mathbf{E}_{\mathrm{T}}^{\mathrm{miss,\,true}}$. The dataset was made up of 8 million $t\bar{t}$, Wt, $W\bar{t}$ and diboson (WW, WZ, ZZ) processes. Underlying events were generated using Powheg-Box [14] and subsequent parton showers and hadronisation were handled by Pythia [15].

Over the course of this work, more than 3000 different networks architectures were tested and compared. Features that were varied included the network depth, width, hidden layer activation function, loss metric, optimising algorithm, learning rate, and regularisation technique. The final and most accurate network had five hidden layers, each with 1000 neurons featuring a Swish activation function [16]. After each non-linearity a dropout layer with $p = 0.2$ was applied. Gradient descent was performed by the ADAM optimiser [17] based on the Huber loss function [18].

5. Performance on $Z \to ee$ and $t\bar{t}$ events

5.1. Event Selection

Events involving $t\bar{t}$ production provide a good topology to measure $\mathbf{E}_{\mathrm{T}}^{\mathrm{miss,\,true}}$ reconstruction performance in environments with large jet multiplicities. Studies in this region involved MC simulation only. The absence of background allowed for very loose selection criteria, so only standard ATLAS event quality checks were performed [19].

The $Z \to ee$ final state is ideal for the evaluation of $\mathbf{E}_{\mathrm{T}}^{\mathrm{miss}}$ performance in real events. Z boson production is relatively abundant at the LHC, has a well understood topology, and can be selected with high signal to background ratios. In this channel neutrinos are produced only through very rare heavy-flavour decays in the hadronic recoil. In standard ATLAS $\mathbf{E}_{\mathrm{T}}^{\mathrm{miss}}$ evaluations [7, 8, 12], this process is associated with not having any genuine missing transverse momentum. Events were selected for this channel if they fired a single lepton trigger and contained exactly two oppositely charged electrons with $p_T > 25$ GeV, which have an invariant mass between 76 GeV and 106 GeV. Data used in this channel was recorded by the ATLAS experiment in 2017 at $\sqrt{s} = 13$ TeV, and had a total integrated luminosity of 44.3 fb^{-1}. All events had to pass standard detector quality assessment criteria. Monte-Carlo samples of $Z \to ee$ were generated using Sherpa [20]. Background contributions from $t\bar{t}$, single-t and diboson events were generated using Powheg, with Pythia handling the parton shower.

5.2. Results

The resolution is determined by the width of the combined distribution of the differences between the measured $E_{x(y)}^{\mathrm{miss}}$ and the corresponding components of the true $\mathbf{E}_{\mathrm{T}}^{\mathrm{miss,\,true}}$. The width is taken from the of the root mean square error (RMSE) of the distributions,

$$\mathrm{RMSE} = \begin{cases} RMS(E_{x(y)}^{\mathrm{miss}} - E_{x(y)}^{\mathrm{miss,\,true}}) & t\bar{t} \text{ sample } (E_T^{\mathrm{miss,\,true}} > 0) \\ RMS(E_{x(y)}^{\mathrm{miss}}) & Z \to ee \text{ sample } (E_T^{\mathrm{miss,\,true}} \approx 0) \end{cases} \tag{2}$$

The performance of the different algorithms was compared to each other in simulated $t\bar{t}$ events. In Figure 1a, the resolution is plotted with respect to the ΣE_{T}, which can be taken as a measurement of the hardness of the interaction, providing a useful scale for the evaluation of the resolution. The network outperforms all other estimates and shows less degradation with increased event activity. Furthermore, from the plots in Figure 1b, the network shows an excellent resilience to pileup, based on the consistently greater resolution with respect to the number of reconstructed vertices.

Data vs MC simulation comparisons for the Tight and the Network $\mathbf{E}_{\mathrm{T}}^{\mathrm{miss}}$ algorithms in the $Z \to ee$ channel are shown in Figure 2. The error on the ratio points show the uncertainty of the MC samples, accounting for uncertainty in luminosity, cross section and statistics. Systematic

uncertainties have yet to be added to this work. Figure 2b shows good agreement between data and MC in the bulk and the distributions display same overall shape. This shows that the network, which was trained exclusively on MC datasets, is still able to generalise well to real data. Over 99% of events in the MC $Z \to ee$ contribution, which significantly dominates all other processes, have $|\mathbf{E}_{\mathrm{T}}^{\mathrm{miss,\ true}}| < 3$ GeV. Both the Tight and Network $|\mathbf{E}_{\mathrm{T}}^{\mathrm{miss}}|$ distributions show a tail in $Z \to ee$ events extending beyond this value, indicating that they both suffer from the aforementioned observation bias. However, the width of this tail is greatly reduced when using the network, leading to a greater distinction between the signal and background processes. The average resolution using all algorithms applied to both datasets are shown in Table 1.

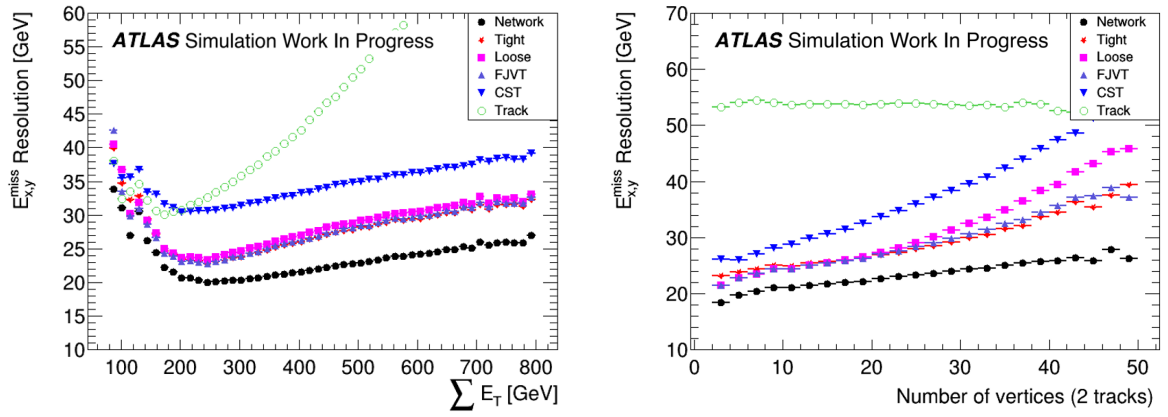

(a) (b)

Figure 1. Comparisons of the $\mathbf{E}_{\mathrm{T}}^{\mathrm{miss}}$ resolution using different algorithms with respect to the ΣE_{T} (a) of the event and the number of reconstructed vertices (b).

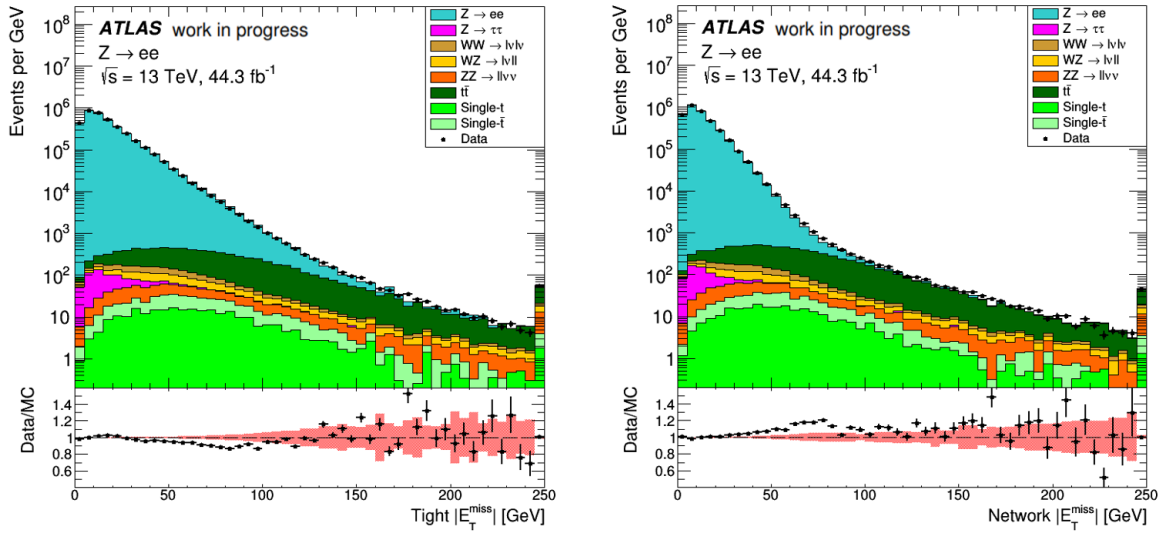

(a) (b)

Figure 2. Data to Monte-Carlo comparisons of the magnitude of the $\mathbf{E}_{\mathrm{T}}^{\mathrm{miss}}$ reconstruction using the Tight (a) and the Network (b) definitions in the $Z \to ee$ channel.

 ISBN: 978-0-620-88875-2

	$t\bar{t}$	$Z \to ee$
Tight	27.30	15.53
Loose	28.20	18.06
FJVT	27.48	16.55
CST	34.31	24.24
Track	53.96	18.48
Network	**22.70**	**11.29**

Table 1. The $\mathbf{E}_{\mathrm{T}}^{\mathrm{miss}}$ resolution, measured in GeV, of the different algorithms measured on the the simulated $t\bar{t}$ and real $Z \to ee$ datasets.

6. Conclusions

The measurement of $\mathbf{E}_{\mathrm{T}}^{\mathrm{miss}}$ is an important contribution to many different physics analyses. The high luminosity at the LHC, however, means that there are large amounts of pileup interactions which degrade its reconstruction quality. Therefore there are a number of existing algorithms to reconstruct and estimate $\mathbf{E}_{\mathrm{T}}^{\mathrm{miss}}$ depending on the topology of the event. A neural network was trained to combine these different definitions and produced a reconstruction method which lead to a greater $\mathbf{E}_{\mathrm{T}}^{\mathrm{miss}}$ resolution in both data and MC, as well as an excellent stability with pileup. While more quantitative analysis still needs to be performed on the resolution improvements, this project reflects the ongoing work to improve reconstruction performance at ATLAS.

7. References

[1] The ATLAS Collaboration 2008 *Journal of Instrumentation* **3** S08003
[2] The ATLAS Collaboration 2019 *Phys. Rev. D* **100**(1) 012006
[3] The ATLAS Collaboration 2018 *Phys. Rev. D* **98**(9) 092002
[4] The ATLAS Collaboration 2012 *Physics Letters B* **716** 1 – 29 ISSN 0370-2693
[5] The ATLAS Collaboration 2010 *The European Physical Journal C* **70** 823–874 ISSN 1434-6052
[6] Goodfellow I and Bengio Y 2016 *Deep Learning* (MIT Press) `http://www.deeplearningbook.org`
[7] The ATLAS Collaboration 2018 *The European Physical Journal C* **78** 903 ISSN 1434-6052
[8] The ATLAS Collaboration 2018 $E_{\mathrm{T}}^{\mathrm{miss}}$ performance in the ATLAS detector using 2015-2016 LHC p-p collisions Tech. Rep. ATLAS-CONF-2018-023 CERN Geneva
[9] Cacciari M, Salam G P and Soyez G 2008 *Journal of High Energy Physics* **2008** 063–063
[10] The ATLAS Collaboration 2016 *The European Physical Journal C* **76** 581 ISSN 1434-6052
[11] The ATLAS Collaboration 2017 *The European Physical Journal C* **77** 580 ISSN 1434-6052
[12] The ATLAS Collaboration 2017 *The European Physical Journal C* **77** 241 ISSN 1434-6052
[13] The ATLAS Collaboration 2018 Object-based missing transverse momentum significance in the ATLAS detector Tech. Rep. ATLAS-CONF-2018-038 CERN
[14] Nason P 2004 *Journal of High Energy Physics* **2004** 040–040
[15] Sjstrand T, Mrenna S and Skands P 2006 *Journal of High Energy Physics* **2006** 026–026
[16] Ramachandran P *et al.* 2017 Searching for activation functions (*Preprint* `1710.05941`)
[17] Kingma D P and Ba J 2014 *arXiv preprint arXiv:1412.6980*
[18] Huber P J 1964 *Ann. Math. Statist.* **35** 73–101
[19] The ATLAS Collaboration 2010 Data-Quality Requirements and Event Cleaning for Jets and Missing Transverse Energy Reconstruction with the ATLAS Detector in Proton-Proton Collisions at a Center-of-Mass Energy of $\sqrt{s} = 7$ TeV Tech. Rep. ATLAS-CONF-2010-038 CERN
[20] Gleisberg T *et al.* 2009 *Journal of High Energy Physics* **2009** 007–007

Anomalies in the production of multiple leptons at the LHC

Stefan von Buddenbrock[1] **and Bruce Mellado**[1,2]

[1] School of Physics and Institute for Collider Particle Physics, University of the Witwatersrand, Johannesburg, Wits 2050, South Africa
[2] iThemba LABS, National Research Foundation, PO Box 722, Somerset West 7129, South Africa

E-mail: stef.von.b@cern.ch,bmellado@mail.cern.ch

Abstract. Based on a number of features from proton-proton collisions taken during Run 1 data taking period at the LHC, a boson with a mass around the Electro-Weak scale was postulated such that a significant fraction of its decays would comprise the Standard Model (SM) Higgs boson and an additional scalar, S. One of the phenomenological implications of a simplified model, where S is treated as a SM Higgs boson, is the anomalous production of high transverse momentum leptons. A combined study of Run 1 and Run 2 data is indicative of very significant discrepancies between the data and SM Monte Carlos in a variety of final states involving multiple leptons with and without b-quarks. These discrepancies appear in corners of the phase-space where different SM processes dominate, indicating that the potential mismodeling of a particular SM process is unlikely to explain them. Here an important aspect of the multi-lepton anomalies based on recent results from the LHC is discussed. In particular it is noted that the di-lepton invariant mass distribution is also discrepant in corners of the phase-space with a full jet veto, where the contribution from top quark processes is suppressed. The state-of-the-art NLO and EW corrections are applied to the yield of events in data.

1. Introduction

An early study in 2015 considered the possibility of a heavy scalar, H, being compatible with several LHC Run 1 measurements [1]. The result of this study had shown that with a single parameter β_g^2 (the scale factor for the production cross section of H) a set of ATLAS and CMS physics results could be fit with a significance of 3σ. Using an effective vertex, the best fit mass of H was found to be at $m_H = 272^{+12}_{-9}$ GeV. This study included, but was not limited to, the production of multiple leptons in association with b-jets, as reported by the search for the SM Higgs boson in association with top quarks. Other multi-lepton final states predicted in Ref. [2] and verified in Refs. [3, 4] were not included in the significance reported in Ref. [1]. Now it seems evident that the multi-lepton final states reported in Refs. [3, 4] displayed sings of discrepancies with respect to SM predictions already in Run 1 data sets. Early discrepancies from Run 1 data sets not considered in Ref. [1] include opposite sign di-leptons and missing transverse energy with a full hadronic jet veto (see Ref. [3]) or di-leptons in association with at least one b-jet [5, 6], among others.

Following a discussion of the results in Ref. [1], the next point of interest was to explore the possibility of introducing a scalar mediator S (instead of using effective vertices), such that H

could decay to Sh, SS, and hh [2]. The S was assumed to have globally re-scaled Higgs-like couplings, such that its branching ratios (BRs) could be fixed. In this setup, and in light of the results in Ref. [7] where the 100% branching ratio of S into Dark Matter was ruled out, multi-lepton final states became a focus. The possibility of embedding H into a Type-II two Higgs doublet model (2HDM) was also discussed, where the allowed parameter space of the model was reported in Ref. [2, 8]. More importantly, a predictive set of potential search channels for the new scalars was shown. Several of these predictions were tested and expanded upon in Refs. [3, 4].

2. Simplified Model

In terms of interactions, H is assumed to be linked to electro-weak symmetry breaking in that it has Yukawa couplings and tree-level couplings the weak vector bosons V ($W^{\pm}$ and Z). After electro-weak symmetry breaking, the Lagrangian describing H is Higgs boson-like. Omitting the terms that are irrelevant in this analysis, H interacts with the SM particles in the following way:

$$\mathcal{L} \supset -\beta_g \frac{m_t}{v} t\bar{t}H + \beta_V \frac{m_V^2}{v} g_{\mu\nu}\, V^\mu V^\nu H. \tag{1}$$

These are the the Higgs-like couplings for H with the top quark (t) and the heavy vector bosons, respectively. The strength of each of the couplings is controlled by a free parameter: β_g for the H-t-t interaction and β_V for the H-V-V interaction. The omitted terms include the Yukawa couplings to the other SM fermions and self-interaction terms for H. It can be expected that the couplings to the other SM fermions would also differ by a factor like β_g, however the effect would not make a noticeable difference to the analysis considered here and therefore these terms are neglected. The vacuum expectation value v has a value of approximately 246 GeV.

The first term in Equation (1) allows for the gluon fusion (ggF) production mode of H. Due to the squaring of the matrix element in width calculations, production cross sections involving this Yukawa coupling are scaled by β_g^2. The value of β_g^2 is used as a free parameter in fits to the data. We have set $\beta_V = 0$, such that the coupling of H to pairs of the weak vector bosons is significantly smaller; the associated production of H with the weak vector bosons and vector boson fusion (VBF) are not-leading production modes. As H mixes with h and the latter displays couplings close to SM values, the couplings of H to weak bosons is suppressed. The dominant production mode of H is therefore ggF, while both single (tH) and double (ttH) top associated production of H are also non-negligible. While single top associated production of a Higgs-like boson is usually suppressed due to interference, the implicit assumption of a significantly small H-V-V coupling allows for a sizeable tH production cross section [9]. It has been shown in previous studies [3, 1] that the tH cross section is enhanced to being approximately that of the ttH cross section. The representative Feynman diagrams for the production modes of H are shown in Figure 1.

The S boson, on the other hand, is assumed not to be produced directly but rather through the decay of H. In principle, it is possible to include S as a singlet scalar that has interactions with H and the SM Higgs boson h. Doing this would allow the H to produce S bosons through the $H \to SS$ and Sh decay modes. Here we assume the $H \to Sh$ decay mode to have a 100% BR (also shown in Figure 1). These assumptions are all achieved by introducing the following effective interaction Lagrangians. Firstly, S is given a vacuum expectation value and couples to the scalar sector:

$$\mathcal{L}_{HhS} = -\frac{1}{2}\, v\Big[\lambda_{_{hhS}} hhS + \lambda_{_{hSS}} hSS + \lambda_{_{HHS}} HHS + \lambda_{_{HSS}} HSS + \lambda_{_{HhS}} HhS\Big], \tag{2}$$

where the couplings are fixed to ensure that the $H \to Sh$ BR is 100%. In order to reduce the parameter space S is assumed to be a SM Higgs-like scalar.

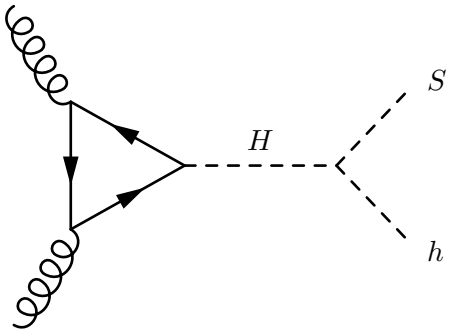

(a) Gluon fusion (ggF).

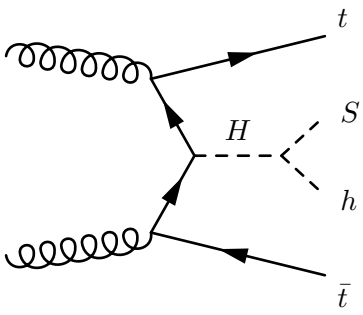

(b) Top pair associated production (ttH).

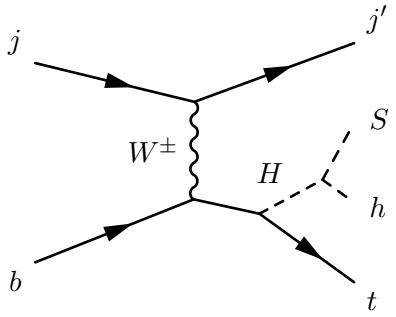

(c) Single top associated production (tH).

Figure 1: The representative Feynman diagrams for the leading order production modes of H and its subsequent decay to Sh.

3. Anatomy of the anomalies

All fits to the LHC data here were performed using a template-based method of performing fits based on maximizing a profile likelihood ratio [4]. The SM components of the fits are always taken directly from the published experimental distributions, along with their associated systematic uncertainties, including those that affect normalization and shape. The BSM component is always constructed using a single mass point ($m_H = 270$ GeV and $m_S = 150$ GeV) and therefore has only one degree of freedom under the assumptions stated in Section 2. The single degree of freedom is β_g^2, which maps directly to the normalisation of the BSM signal with respect to the SM Higgs-like production cross section of H. It is very important to note that the boson masses were not tuned. They were fixed to values obtained with an analysis obtained from different data sets corresponding to Run 1 data, as reported in Ref. [3]. Further, the choice of final states under study here was made based on the predictions of Ref. [2]. In contrast to searching for excesses in a wide span of the phase-space, the excesses identified here are related to a prediction.

The statistical likelihood function $L\left(\beta_g^2 \mid \theta\right)$ is constructed as the product of Poisson probabilities for each bin and in each considered measurement. Systematic uncertainties are incorporated as additional constraint factors in the likelihood, which vary according to their associated nuisance parameters θ. The best-fit value of the parameter of interest β_g^2 is identified as the minimum of $-2\log\lambda\left(\beta_g^2\right)$, where a deviation of one unit in this quantity is equivalent to a 1σ deviation from the best-fit point of the parameter of interest. Since the value $\beta_g^2 = 0$ corresponds to the SM-only hypothesis (the *null* hypothesis), the significance of each fit is

Table 1: A list of the ATLAS and CMS experimental results pertaining to final states with multiple leptons that are considered here. For each result, a simple baseline selection is shown.

Data set	Reference		Selection
ATLAS Run 1	ATLAS-EXOT-2013-16	[10]	SS $\ell\ell$ and $\ell\ell\ell$ + b-jets
ATLAS Run 1	ATLAS-TOPQ-2015-02	[11]	OS $e\mu$ + b-jets
CMS Run 2	CMS-PAS-HIG-17-005	[12]	SS $e\mu$, $\mu\mu$ and $\ell\ell\ell$ + b-jets
CMS Run 2	CMS-TOP-17-018	[13]	OS $e\mu$
CMS Run 2	CMS-PAS-SMP-18-002	[14]	$\ell\ell\ell + E_T^{miss}$ (WZ)
ATLAS Run 2	ATLAS-EXOT-2016-16	[15]	SS $\ell\ell$ and $\ell\ell\ell$ + b-jets
ATLAS Run 2	ATLAS-CONF-2018-027	[16]	OS $e\mu$ + b-jets
ATLAS Run 2	ATLAS-CONF-2018-034	[17]	$\ell\ell\ell + E_T^{miss}$ (WZ)

Table 2: A summary of the SM+BSM fit results for each measurement considered here, along with the result of their combination. DFOS stands for different flavor and opposite sign, in relation to di-leptons.

Selection	Best-fit β_g^2	Significance
ATLAS Run 1 SS leptons + b-jets	6.51 ± 2.99	2.37σ
ATLAS Run 1 DFOS di-lepton + b-jets	4.09 ± 1.37	2.99σ
ATLAS Run 2 SS leptons + b-jets	2.22 ± 1.19	2.01σ
CMS Run 2 SS leptons + b-jets	1.41 ± 0.80	1.75σ
CMS Run 2 DFOS di-lepton	2.79 ± 0.52	5.45σ
ATLAS Run 2 DFOS di-lepton + b-jets	5.42 ± 1.28	4.06σ
CMS Run 2 tri-lepton + E_T^{miss}	9.70 ± 3.88	2.36σ
ATLAS Run 2 tri-lepton + E_T^{miss}	9.05 ± 3.35	2.52σ
Combination	2.92 ± 0.35	8.04σ

calculated as $Z = \sqrt{-2 \log \lambda\,(0)}$.

The fits include searches for the SM production of top quarks decaying to opposite-sign (OS) lepton pairs, searches for Higgs boson production in leptonic final states and BSM searches for the production of same-sign (SS) lepton pairs, to name a few. Many of these searches involve either a signal or dominant background component that contains top quarks in the final state. Therefore, the results are often always dependent on the number of b-jets produced with the leptons (e, μ).

The ensemble of results considered in this article is shown in Table 1. The majority of results come from the Run 2 data sets. Each of the results studied in this article make use of a profile likelihood ratio to constrain the single fit parameter β_g^2 under an SM+BSM hypothesis. With these profile likelihood ratios constructed as a function of β_g^2, it is relatively straightforward to perform a simultaneous fit on all of the results considered and therefore make a combination of the independent data sets under the SM+BSM hypothesis. The combined profile likelihood is constructed by multiplying the profile likelihood ratios for each individual measurement. Then, the best-fit value of β_g^2 and significance can be calculated similarly to the individual results. Doing so constrains the parameter β_g^2 to the value 2.92 ± 0.35, which corresponds to a significance of $Z = 8.04\sigma$ in favour of the SM+BSM hypothesis over the SM-only hypothesis. A summary of all the individual fit results, as well as the combination, can be seen in Table 2. In addition

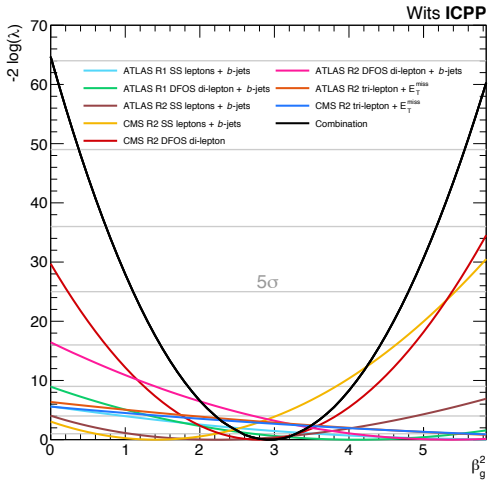

Figure 2: The profile likelihood ratios for each of the individual fit results and their combination [4]. The significance of a result is calculated as the square root of the point which intersects the y-axis.

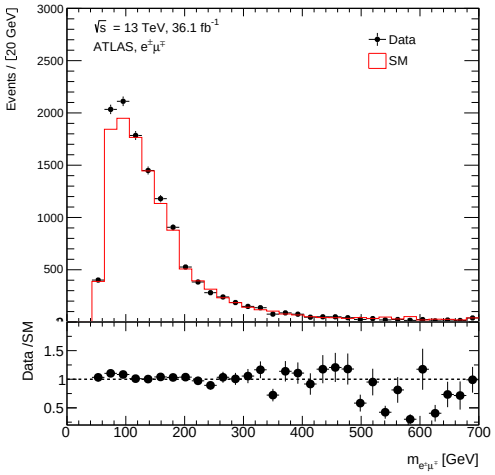

Figure 3: Dilepton invariant spectrum in events with a full hadronic jet veto after the application of NNLO QCD and NLO EW corrections (see text).

to this, each of the individual profile likelihood ratios are shown in Figure 2, with the combined case shown in black. The statistical significance reported here is obtained with a simplified model, which imperfectly describes the deviations of the data with respect to the SM. As such, the significance reported here is a conservative estimate.

Recent results reported by the ATLAS collaboration confirm with more statistics the anomalies described above in di-lepton final states with a full hadronic jet veto [18], where the dominant SM process is the non-resonant production of W pairs. Figure 3 displays the di-lepton invariant mass in $e\mu$ events with a full hadronic jet veto after the application of the aforementioned corrections. Here QCD NNLO corrections to $q\bar{q} \to W^+W^-$ production [19, 20, 21, 22], QCD NLO corrections to non-resonant $gg \to W^+W^-$ [23] and EW NLO corrections [24] have been applied. The SM MC has been normalised to the data with $m_{\ell\ell} > 110\,\text{GeV}$. The discrepancy re-emerges here with $m_{\ell\ell} < 100\,\text{GeV}$, as predicted in Refs. [2, 3], showing similar features compared to the discrepancies in di-lepton final states with b-jets documented in Ref. [4]. The deviation seen in Figure 3 is not included in the excess reported in Figure 2, and neither were those already identified with Run 1 data in Ref. [3].

Table 3 summarises the final states studied here, including basic characteristics and the corresponding dominant SM process. The anomalies described here appear in final states and corners of the phase-space where different SM processes dominate. This important feature renders the possibility of explaining the anomalies by MC mismodelling rather improbable.

4. Conclusions

A number of predictions were made in Refs. [1, 2] pertaining to the anomalous production of multiple leptons at high energy proton-proton collisions. These would be connected with a heavy boson with a mass around the EW scale decaying predominantly into a SM Higgs boson and a singlet scalar. Discrepancies in multi-lepton final states were reported with Run 1 data in Refs [1, 3] have now become statistically compelling with the available Run 2 data [4]. These include the production of opposite-sign, same-sign and three leptons with and without b-jets.

Table 3: A succinct summary of the characteristics of the multi-lepton anomalies studied here.

Final State	**Characteristic**	**Dominant SM process**
$\ell^+\ell^-$ + jets, b-jets	$m_{\ell\ell} < 100\,\text{GeV}$	$t\bar{t}, Wt$
$\ell^+\ell^-$ + jet veto	$m_{\ell\ell} < 100\,\text{GeV}$	W^+W^-
$\ell^\pm\ell^\pm$ + b-jets	Moderate H_T	$t\bar{t}V, (V = Z, W^\pm)$
$\ell^\pm\ell^\mp\ell^\pm$ + b-jets	Moderate H_T	$t\bar{t}V, (V = Z, W^\pm)$
$Z(\to \ell^+\ell^-) + \ell^\pm$	$p_{TZ} < 100\,\text{GeV}$	$W^\pm Z$

Discrepancies emerge in final states and corners of the phase-space where different SM processes dominate, indicating that the potential mismodeling of a particular SM process is unlikely to explain them. The yields of the anomalies and their kinematic characteristics are remarkably well described by a simple ansatz, where $H \to Sh$ is produced via gluon-gluon fusion and in association with top quarks.

Here the event yield of di-lepton events with a full jet veto is presented with the state-of-the-art NLO and EW corrections. In this corner of the phase-space the contribution from top-quark processes is suppressed, where the non-resonant W^+W^- becomes dominant.

References

[1] von Buddenbrock S, Chakrabarty N, Cornell A S, Kar D, Kumar M, Mandal T, Mellado B, Mukhopadhyaya B and Reed R G 2015 (*Preprint* 1506.00612)
[2] von Buddenbrock S, Chakrabarty N, Cornell A S, Kar D, Kumar M, Mandal T, Mellado B, Mukhopadhyaya B, Reed R G and Ruan X 2016 *Eur. Phys. J.* **C76** 580 (*Preprint* 1606.01674)
[3] von Buddenbrock S, Cornell A S, Fadol A, Kumar M, Mellado B and Ruan X 2018 *J. Phys.* **G45** 115003 (*Preprint* 1711.07874)
[4] von Buddenbrock S, Cornell A S, Fang Y, Fadol Mohammed A, Kumar M, Mellado B and Tomiwa K G 2019 *JHEP* **10** 157 iCPP-007 (*Preprint* 1901.05300)
[5] Aad G *et al.* (ATLAS) 2015 *Phys. Rev. Lett.* **114** 142001 (*Preprint* 1412.4742)
[6] Khachatryan V *et al.* (CMS) 2016 *Phys. Rev.* **D93** 052007 (*Preprint* 1601.01107)
[7] Aaboud M *et al.* (ATLAS) 2017 *Phys. Rev.* **D96** 112004 (*Preprint* 1706.03948)
[8] von Buddenbrock *et al* 2019 *Journal of Physics G* ICPP-02 (*Preprint* 1809.06344) URL http://iopscience.iop.org/10.1088/1361-6471/ab3cf6
[9] Farina M, Grojean C, Maltoni F, Salvioni E and Thamm A 2013 *JHEP* **05** 022 (*Preprint* 1211.3736)
[10] Aad G *et al.* (ATLAS) 2015 *JHEP* **10** 150 (*Preprint* 1504.04605)
[11] Aaboud M *et al.* (ATLAS) 2017 *Eur. Phys. J.* **C77** 804 (*Preprint* 1709.09407)
[12] Sirunyan A M *et al.* (CMS) 2017 URL https://cds.cern.ch/record/2264553
[13] Sirunyan A M *et al.* (CMS) 2018 *JHEP* **10** 117 (*Preprint* 1805.07399)
[14] Sirunyan A M *et al.* (CMS) 2018 URL http://cds.cern.ch/record/2628761
[15] Aaboud M *et al.* (ATLAS) 2018 *Submitted to: JHEP* (*Preprint* 1807.11883)
[16] Aaboud M *et al.* (ATLAS) 2018 URL http://cds.cern.ch/record/2628770
[17] Aaboud M *et al.* (ATLAS) 2018 URL http://cds.cern.ch/record/2630187
[18] Aaboud M *et al.* (ATLAS) 2019 (*Preprint* 1905.04242)
[19] Gehrmann T, Grazzini M, Kallweit S, Maierhfer P, von Manteuffel A, Pozzorini S, Rathlev D and Tancredi L 2014 *Phys. Rev. Lett.* **113** 212001 (*Preprint* 1408.5243)
[20] Grazzini M, Kallweit S, Pozzorini S, Rathlev D and Wiesemann M 2016 *JHEP* **08** 140 (*Preprint* 1605.02716)
[21] Hamilton K, Melia T, Monni P F, Re E and Zanderighi G 2016 *JHEP* **09** 057 (*Preprint* 1606.07062)
[22] Re E, Wiesemann M and Zanderighi G 2018 *JHEP* **12** 121 (*Preprint* 1805.09857)
[23] Caola F, Melnikov K, Rntsch R and Tancredi L 2016 *Phys. Lett.* **B754** 275–280 (*Preprint* 1511.08617)
[24] Biedermann B, Billoni M, Denner A, Dittmaier S, Hofer L, Jger B and Salfelder L 2016 *JHEP* **06** 065 (*Preprint* 1605.03419)

Geant4 in a new role - Reactor Physics

A Cilliers[1,2], SH Connell[1], J Conradie[1], MNH Cook[1,3], R Mudau[4], P Naidoo[1], D Nicholls[1]

1. University of Johannesburg, Johannesburg, Mechanical Engineering, South Africa.
2. Kairos Power, USA.
3. Gem Diamonds, South Africa.
4. Nuclear Energy Corporation of South Africa (Necsa), South Africa

E-mail: shconnell@uj.ac.za

Abstract. The accurate modeling of nuclear reactors is essential for design, regulation, safety analysis, operations and forensic analysis. There are two classes of approaches to modeling the neutronics of nuclear reactors. The first is deterministic, where the neutron transport equations are solved using a combination of approximations and numerical methods based on a space-time discretization. This approach currently dominates where computing speed and resource limitations apply. The second class of models is stochastic in nature. Here many statistically independent histories for each neutron event and all secondary events related to its interactions are tracked and various physical data are stored for later statistical analysis. This paper presents several results that establish the proof of principle in the stochastic Monte Carlo (MC) modelling of a nuclear reactor core using the Geant4 framework. The simulation is exercised in the context of a High Temperature Gas Cooled Reactor (HTGCR) with pebble fuel and helium coolant. MCNP and SERPENT are better known codes in this context, however Geant4 promises to be a significant additional coding framework. It has a modern C++ modular architecture, it is multi- threaded and trivially parallel on multiple nodes and the well documented source is readily available. Rather than being input file driven, the user modifies and extends the class structure. It has excellent engines for geometry, materials, physics, tracking, history recording, visualisation and the analysis is readily done with additional frameworks such as ROOT. In this paper we review the implementation of the following aspects in proof of principle form : the basic neutronics (thermalisation and containment), validation of the databases (elementary neutron induced reactions), scalability, thermal neutronics, geometrical discretisation for studying the spatial variation of physical parameters, time slicing and adaptation of Geant4 for correct intra-slice persistence, a scheme of integration with thermal hydraulics by workflow scheduling, the process of fission, burn, decay, and differential energy depositions for the various physics processes, criticality and core follow over multiple time steps. The benchmarking programme against MCNP and Serpent is also discussed.

1. Introduction

The accurate modeling of nuclear reactors is essential for design, regulation, safety analysis, operations and forensic analysis. In the most demanding case, the calculations must usually be sufficiently rapid that they are much faster than natural time for burn and decay processes while still being sufficiently accurate. There are two classes of approaches to modeling the neutronics of nuclear reactors. The first is deterministic, where the neutron transport equations are solved using a combination of approximations and numerical methods based on a space-time discretization [1]. Usually, compromises are made in the accuracy of the model in terms of the level of approximations used, the scale of the discretization and the level of geometric and material detail, in order to achieve a sufficiently fast speed of calculation. The error induced due to the compromises made is offset with often rather unsatisfactory

compensating modifications of the physical description or processes. The second class of models is stochastic in nature. Here many statistically independent histories for each neutron event and all secondary events related to its interactions are tracked and various physical data is stored for later statistical analysis [2–12]. The physics content manifests through the microscopic cross sections (probabilities) for each interaction. The thermal and material information is encoded into thermally averaged macroscopic cross sections, which are assembled together with the microscopic cross sections. The geometrical information is reconstructed using technical drawings of the system, essentially to the desired precision.

The full physics of the reactor are in this way encoded into probability distributions to be sampled on an event-by-event basis in the particle tracking and data extraction process, as various objects tracked are manifested in different regions of the reactor. The particle transport code, Geant4, developed for high-energy physics, has recently been extended to accommodate lower energy nuclear physics and energy scales down to the far sub-eV region. More recently it has been used in areas where several elements of the processes in a nuclear reactor are considered, for example, fission [13], thermal neutrons [14] and spallation [15–17].

The Monte Carlo space for neutronics in nuclear reactors currently has two main players MCNP [5, 6] and Serpent [7], among some others too. The former is very well benchmarked and widely used. It is a general neutron transport code, with far wider application than nuclear reactors. The latter is gaining popularity as a specialist nuclear reactor code. The interest in Geant4 arises as it is written in a modern object oriented language (C++) in contrast to MCNP. It also is a framework, in contrast to the previous mentioned codes, in that it is operated on the basis of user modified mandatory classes from templates, rather than preparation of input files. The user is therefore deeply integrated into the design of the simulation and its operation. Geant4 is open source code, again where the two previous examples are not. Geant4 is free, and MCNP is not. Geant4 has base elements in its geometry construction, materials definition, physics lists, data bases, tracking code and history analysis that are very well benchmarked in very many different scenarios. It is therefore interesting to investigate if it can be adapted also to the nuclear reactor context.

In this work, the application of the Geant4 framework to a new area, that of gas-cooled reactors, is investigated. This approach promises the capacity for a much higher degree of detail in the geometry and material definitions as well as the physics modeling detail. The advent of massively parallel high-performance computing will make it more feasible in terms of the speed of the calculations. The design and manufacturing of small modular reactors will be affordable and feasible for developing countries to meet their energy needs and requirements.

1.1. Gas Cooled Reactors and the TRISO particle fuel

We consider a HTGCR with pebble fuel, helium cooled and graphite moderated. In the simulation below, the fuel characteristics are borrowed from the Pebble Bed Modular Reactor (PBMR) fuel definition [18, 19]. The discrete element of the fuel is about 12000 low enriched uranium triple coated isotropic (LEU-TRISO) particles, each of about 1 mm diameter, all distributed within a spherical graphite matrix of diameter 50 mm. The TRISO particle innermost sphere is a kernel of uranium dioxide. There are subsequent layers of porous carbon, pyrolytic carbon, silicon carbide and then finally pyrolytic carbon again. The first layer acts as a buffer, and the three subsequent layers are primary containment. The 50 mm fuel sphere has a final pure carbon layer, bringing it to a 60 mm outside diameter. The whole is then sintered and annealed and then accurately machined to finish it off.

For the purposes of the proof of principle calculations, the pebbles were chemically homogenised simply as fresh fuel mass fractions with PBMR data to yield uranium dioxide 4.248%, silicon carbide 0.759% and carbon at 94.992%. In a full neutronics treatment, they would of course be subject to a state dependent homogenisation to respect various requirements

such as reaction rates and/or boundary fluxes. In this work we note that the depletion of the fuel and the production of actinides and fission fragments and all their progeny can in principle be tracked and stored for each time slice of operation, so that the composition of the fuel can be modified and followed as in a normal reactor. The dimensions of the fuel sphere could also be modified to respect thermal effects.

1.2. Event Generation and time slices

A summary of the event flow is shown in Figure 1. A time slice consists of neutronic processes and isotope decay events. Neutron events are created either by sampling a neutron density file or reading the previous time slices neutron n-Tuple. The neutrons are tracked, and lead to energy deposits and the creation of isotopes via neutron capture and fission. Reactions that occur within the time slice are simulated, and final isotopes stored in order to update the isotope inventory. Isotope decay events are created by sampling the isotope inventory. The isotope inventory is updated either by recording the simulated daughter isotopes at the end of the time slice, or via a deterministic calculation based on pre-calculated branching ratios. The 3D map of energy deposits, binned according to the appropriate mesh, will then be input to the thermal transport code for the next time slice.

In a standard simulation, Geant4 simulates all particles until their end, for example when they are destroyed or come to rest. For supercritical reactors, the simulation will never terminate. In order to simulate a reaction for a time slice only, a custom physics process was added to the Geant4 physics list, which culls all particles at the end of the time slice. All particles that are not neutrons deposit their kinetic energy at their current position. Neutrons do not deposit kinetic energy, as it is understood that they will be recreated with the same energy at the beginning of the next time slice, so this energy is not lost. The custom particle culling process has priority over the standard radioactive decay process. This means that decays of short-lived isotopes that occur within the time slice are simulated. In this implementation, at the end of the time slice, the radioactive decay process is interrupted, and longer-lived isotopes that are present at the end of the time slice can be culled from the simulation and recorded in order to update the isotope inventory for the next time slice. Each time slice is therefore a Geant4 run, with an updated geometry / materials inventory that has tracked burn and decay and thermal effects. The neutronic code can link to a thermal hydraulic code through the concept of work-flow scheduling, based on the handover of updated state information between timeslices. A reactor time scale is of the order of a minute when it is critical, so time slicing in the millisecond scale is sufficient for this workflow scheduling. Figure 1 suggests where the handover of the updated state information between timeslices would occur.

The context of the simulations described here is a fictitious "cigar reactor" designed to have a length longer the the neutrino mean free path (λ_{mfp}), but to be as small as possible otherwise, so that certain aspects of the physics can be captured, while the calculations are not too resource intensive.

2. Simulation Results

Figure 2 below shows a fictitious cigar reactor (1m cylinder, with radius 9 cm) with 80 pebbles and a superimposed thermal gradient (ranging from a minimum of 300K to a maximum of 1200K). There is no shielding between the pebbles. The aim of this simulation is to validate the neutron thermalisation behaviour and the correct operation of the thermal macroscopic cross sections. To see this, note the neutron flux distribution as a function of energy (inset) can be histogrammed and the energy-time behaviour (main graph) can be recorded locally. One sees fast neutrons rapidly thermalise to the local temperature as revealed by the quasi Maxwellian distributions that result from the long-time behavior for each individual neutron. The temperature recovered from the Maxwellian is 353 ± 29 K, for Probe 1 and 884 ± 65 K

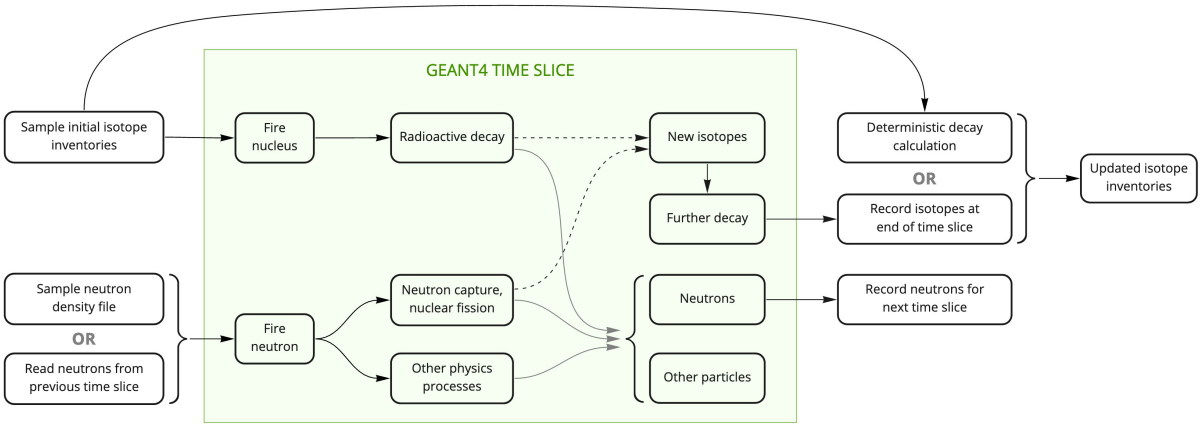

Figure 1. Event flow for a time slice, including both neutron and isotope decay events.

for Probe 2. This matches the temperatures superimposed in the simulation. The differences from the ideal Maxwellian behaviour are expected and accounted for by the energy dependent absorption cross sections and also the energy dependent leakage due the energy dependence of the length of the neutron mean free path. The boundaries were modelled with reflection considering an adjustable albedo as a new Geant4 class to simulate an effective much larger reactor while using a more constrained geometry. A special geometric discretization was placed over the reactor defining virtual local regions where local information could be recovered from the Geant4 simulation.

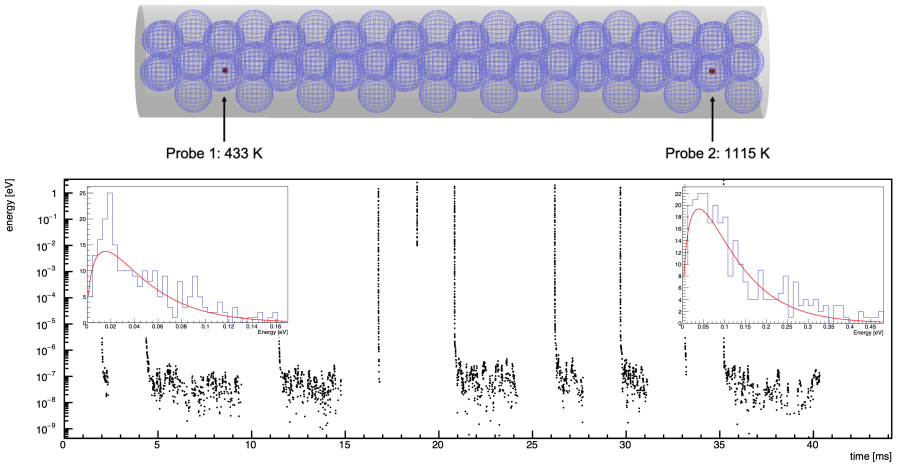

Figure 2. Top: Fictitious cigar reactor with a superimposed thermal gradient. Bottom: The neutron flux distribution as a function of energy (inset) and energy-time (main graph) showing the thermalisation to a quasi Maxwellian distribution where the local temperature is recovered.

The energy deposition per pebble would also depend on temperature through the doppler broadening of the resonance reactions, dominated by the high energy depositions of fission and neutron capture. Part of the physics background is cross section dependence on the CoM which is affected by the thermal motion of the target nuclei as seen in the Laboratory frame. Figure 3 shows this behaviour is effectively modelled, using the same cigar shaped reactor with the superimposed thermal gradient as mentioned above.

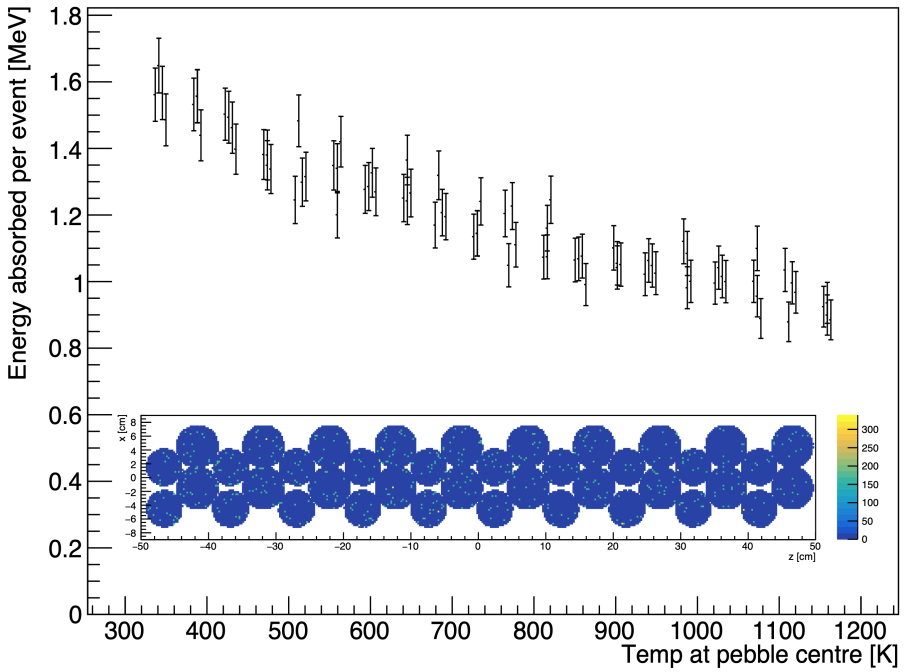

Figure 3. Validation of increased energy deposition per pebble as function of temperature.

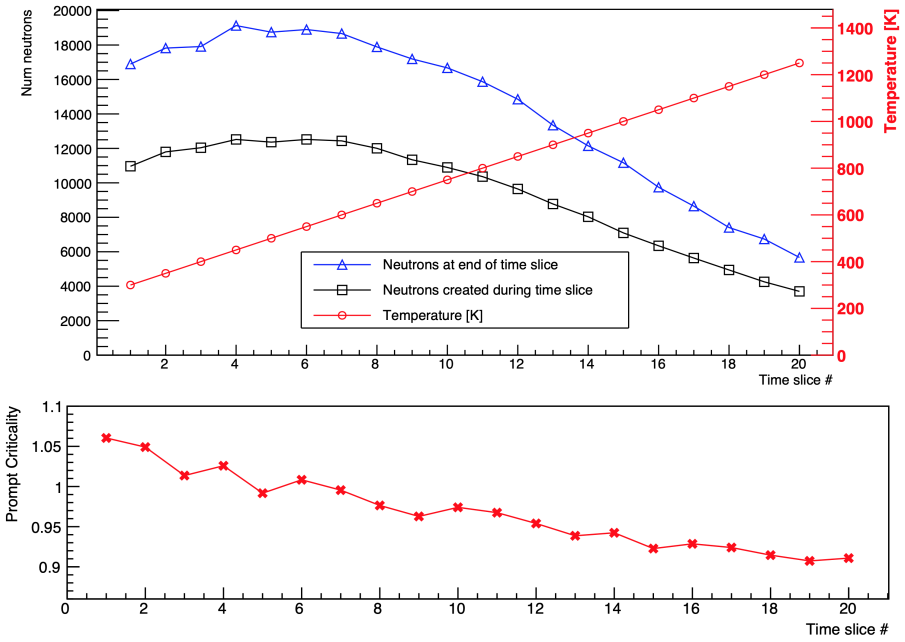

Figure 4. Numbers of neutrons per generation (top) and prompt criticality (bottom) for 20 time slices, with temperature rising by 50K per time slice, from 300K to 1200.

Up to this point, we have only presented results from a single time slice. We now demonstrate the simulations ability to follow and evolve a neutron population. A simulation was set up where the initial temperature and pressure throughout were 300 K and 100 atmospheres respectively. 10,000 neutrons with an energy of 26 meV (roughly corresponds to 300 K) from random positions

and random directions within pebbles. The uranium-235 enrichment was set to 18%, in order to get the criticality of this particular simulation geometry near 1. The neutron population was then followed through 20 consecutive 2 ms time slices. At the end of each time slice, neutrons were stored, then fired again with same position, energy and momentum in the next time step. At each time step, the temperature was increased by 50 K everywhere. This is not meant to represent a realistic reactor scenario, but rather to emphasise the response of the system to temperature changes. The helium density was adjusted in each time slice to maintain a constant pressure of 100 atmospheres as the temperature rose. Figure 4 shows the number of neutrons at the end of each time slice, the number of neutrons created during each time slice, and the prompt criticality calculated for each time slice. All neutrons were prompt, as the simulation did not include delayed neutrons. Figure 4 shows how the neutron population grows at low temperatures, then starts to shrink for at higher temperatures. Based on a comparison between the change in number of neutrons in each time slice, and the criticality (which is calculated based on number of parents and daughters), each 2 ms time slice corresponds to an average of 1.51 neutron generations.

3. Conclusions

In this paper we reviewed the implementation of the following aspects in proof of principle form as preliminary results towards the stated longer term goal: the basic neutronics, geometrical discretisation for studying the spatial variation of physical parameters, time slicing and adaptation of Geant4 for correct inter-slice persistence, a scheme of integration with thermal hydraulics by workflow scheduling, validation of the thermal macroscopic cross section behaviour, the process of fission, burn, decay, and differential energy depositions for the various physics processes, criticality and core follow over multiple time steps. The next step is to validate to other stochastic codes such as MCNP, SERPENT, and to deterministic codes, such as OSCAR for the SAFARI Reactor in South Africa, where there is also experimental data available. Then it would be interesting to select and implement a thermal hydraulic code. It will be necessary to introduce event biasing to improve the variance in rare processes without affecting the physics performance overall.

References

[1] Duderstadt J and Hamilton L 1974 *John Wiley & Sons*
[2] Agostinelli S *et al.* 2003 *Nuclear Instruments and Methods in Physics Research A* **506** 250–303
[3] Allison J *et al.* 2006 *IEEE Transactions on Nuclear Science* **53** 270–278
[4] Allison J *et al.* 186-22 *Nuclear Instruments and Methods in Physics Research A* **835** 2016
[5] Werner C *et al.* 2018 *Los Alamos National Laboratory, report LA-UR-18-20808*
[6] CJ Werner(editor) 2017 *Los Alamos National Laboratory, report LA-UR-17-29981*
[7] J Leppänen et al 2015 *Ann. Nucl. Energy* **82** 142–150
[8] Russell L, Buijs A and Jonkmans G 2014 *Nuclear Science and Engineering* **176:3** 370–375
[9] Russell L, Buijs A and Jonkmans G 2014 *Annals of Nuclear Energy* **71** 451–461
[10] Hansen K 1964 *Massachusetts, Academic Press Inc* 239–277
[11] Sjenitzer B and Hoogenboom E J 2013 *Nuclear Science and Engineering* **175** 94–107
[12] Martin W and Brown F B 2001 *U.S. Department of Los Alamos*
[13] Tana J and Bendahan J 2017 *Physics Procedia* **90** 256–265
[14] Lit G, Bentoumi G, Tun Z, Li L and Sur B 2018 *CNL Nuclear Review* **7-1** 11–17
[15] Heikkinen A *et al.* 2010 *J. Phys.: Conf. Ser.* **219** 032043
[16] Bungau C *et al.* 2009 1351–1353
[17] Malyshkin Y *et al.* 2012 *Nuclear Instruments and Methods in Physics Research Section B: Beam Interactions with Materials and Atoms* **289** 79–90
[18] Koster A, Matzner H D and Nicholsi D 2003 *Nuclear Engineering and Design* **222** 231–245
[19] Martzner D 2004 *2nd International Topical Meeting on High Temperature Reactor Technology, Beijing* A04–1

DIVISION D1 – DIVISION OF ASTROPHYSICS

Multi-messenger hunts for heavy WIMPs

Geoff Beck

School of Physics, University of the Witwatersrand, Private Bag 3, WITS-2050, Johannesburg, South Africa

E-mail: geoffrey.beck@wits.ac.za

Abstract. Heavy neutrinos have a long history of consideration in the literature, in particular related to their role as solutions to the problems of neutrino mass, baryon asymmetry, and possibly dark matter. Interestingly, recent developments in the Madala hypothesis, a standard model extension designed to explain persistent LHC lepton anomalies, may also necessitate a heavy neutrino. This prospect is exciting as a dark matter model consisting of a TeV-scale leptophilic fermionic particle is also invoked to explain the electron-positron excess observed by the DAMPE experiment. The tantalising similarities between these new fermions may allow indirect dark matter detection methods to probe empirically compelling standard model extensions, like the Madala hypothesis. However, the leptophilic nature and large mass mean the expected gamma-ray signatures of annihilation or decay are weaker than those in the traditionally considered heavy quark and tau lepton channels. In this work we explore whether the KM3NeT neutrino detector could take advantage of the leptophilic nature of the added particle to provide an alternative means of exploring such interesting connections between cosmology and collider physics. We demonstrate that dwarf galaxies, in particular highly dense ultra-faint dwarf galaxies like Triangulum II, provide very strong prospects for KM3NeT searches.

1. Introduction

Indirect searches for Dark Matter (DM) have managed to probe below the thermal relic cross-section for Weakly Interacting Massive Particles (WIMPs) with masses below 100 GeV in a variety of environments and frequency ranges [1, 2, 3, 4]. High energy gamma-rays may offer a promising future probe via the up-coming Cherenkov Telescope Array but DM particles that annihilate via muons and electrons in particular produce significantly weaker cross-section constraints in gamma-rays [1] (as can be seen in Figure 1). Models that couple DM to lighter leptons are of particular interest on two grounds: the first being that it has been shown that the DArk Matter Particle Explorer (DAMPE) excess [5] can be explained in terms of these models [6, 7, 8, 9], the second being the persistent lepton anomalies emerging in Large Hadron Collider (LHC) [10, 11] data as discussed in [12, 13, 14]. This second point is linked to the Madala hypothesis, an extension of the standard model designed to explain LHC anomalies that have grown more significant as more data has emerged (see [12, 15, 13, 16] for the original hypothesis). The hypothesis originally contained a coupling to a dark sector, which was used to constrain the properties of additional particles in [17, 18, 19]. However, a necessary reformulation has moved the Madala scenario away from an effective field theory approach [20, 14]. This alteration has also removed the necessity of the original dark sector coupling. However, it does include room for, and may even require, an extra heavy neutrino [21], which may be

employed to resolve the neutrino mass problem [22], as well as both the muon anomalous magnetic moment [23, 24] and anti-baryon asymmetry [22]. Crucially, the mass of this added neutrino is not well constrained, with [21] considering 100 to 1000 GeV. In general, [22] notes that the mass could be anywhere between the eV and GUT scales but that TeV scale neutrinos are of significant interest phenomenologically (see for instance [25]). Interestingly, leptophilic WIMP models proposed to account for the DAMPE excess can also provide a mechanism for producing neutrino masses [6] and typically invoke a fermionic WIMP with a mass around 1 TeV.

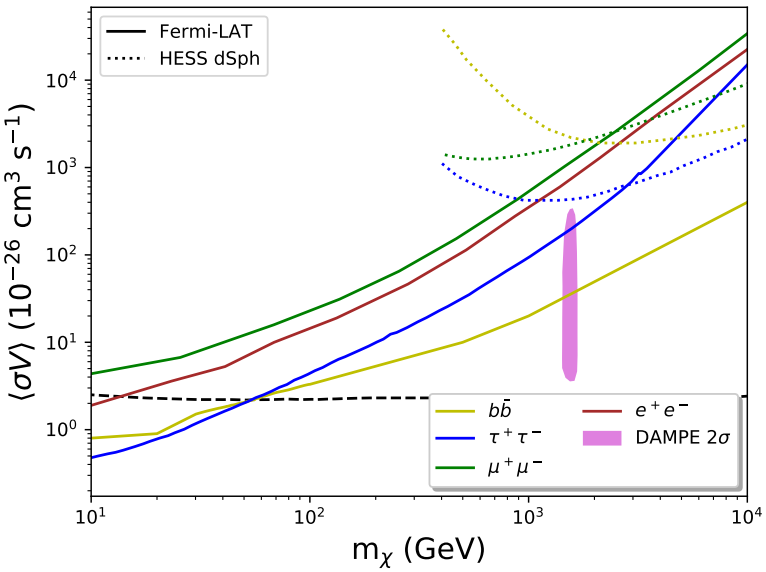

Figure 1. Limits on the DM annihilation cross-section from Fermi-LAT [1, 2] and HESS [26]. The contour from [6] lies well below the muon/electron channel limits. The black dashed line shows the themal relic cross-section [27].

In this work we explore the idea that a neutrino-like particle with a mass around 1 TeV could explain all the aforementioned anomalies. We will do this by considering the potential to detect annihilation of the particle indirectly through up-coming neutrino telescopes such as KM3NeT. We particularly consider annihilation here in order to be relevant to the cross-section parameter space for the DAMPE excess from [6].

In previous works [28, 29] we explored the potential of various approaches to detecting local DM over-densities associated with the DAMPE excess [5, 6, 7, 8, 30, 9] in radio, gamma-rays, and neutrinos. In so doing we found that a promising method of constraint on leptophilic WIMPs would be to employ the KM3NeT detector to search for a neutrino flux from the galactic centre (despite the large angular extension). Since we are looking for heavy WIMPs our aims in this work overlap somewhat with our aforementioned works. However, we will extend the preceding results by looking at the use of neutrino observations to constrain the WIMP parameter space in a larger mass range around 1 TeV. In particular, we will focus upon the potential of dwarf galaxies as neutrino observation targets. This will allow us to both find new environments from which to probe the DAMPE excess models of DM, but will also allow us to investigate the potential of Madala hypothesis associated particles to solve the DM problem. Thus, this work will serve to expand our previous approach [17, 18, 19] to the reformulation of the Madala hypothesis that no longer relies upon an effective field theory [20, 14].

We demonstrate that, in addition to the galactic centre [29], dwarf spheroidal galaxies have strong potential to improve probes on leptophilic WIMP models with masses around 1 TeV. In particular, despite the uncertainties over its J-factor, Triangulum II provides a very prominent candidate for neutrino based searches. This is because, even in the most pessimistic case, it can provide improvements on the constraints obtained by Fermi-LAT, and, in the most optimistic cases, probe the entire DAMPE excess parameter space and encroach upon the thermal relic cross-section. This would allow for significant exploration of the further consequences of the Madala hypothesis, should it be able to accommodate a neutrino-like particle suitable as a DM candidate, and thus determine whether DM and LHC leptonic anomalies can be connected.

This work is structured as follows: in Section 2 we discuss the estimation of neutrino fluxes from DM annihilation, while the target halo properties and KM3NeT sensitivities are discussed in Sections 3 and 4 respectively. Finally, results are presented in Section 5 and discussed in 6.

2. Dark matter emmission of neutrinos

The flux of neutrinos from DM annihilation can be written in terms of the J factor

$$J(\Delta\Omega, l) = \int_{\Delta\Omega}\int_{l}\rho^2(\mathbf{r}')dl'd\Omega' \ , \tag{1}$$

where l is the line of sight and $\Delta\Omega$ is the angular extension of the target. The flux is then found via

$$S_\nu(E) = \frac{1}{2}\langle\sigma V\rangle\sum_f \frac{dN_\nu^f}{dE}B_f J(\Delta\Omega, l) \ , \tag{2}$$

where $\langle\sigma V\rangle$ is the velocity averaged annihilation cross-section, $\frac{dN_\nu^f}{dE}$ is the number of neutrinos produced per annihilation per unit energy via annihilation channel f, B_f is the branching fraction of channel f, and $\rho(\chi)/m_\chi$ is the WIMP number density.

We will follow the standard approach where we set $B_f = 1$ and study each of the tau, muon, and electron leptonic channels individually. The functions $\frac{dN_i^f}{dE}$ will be sourced from [31, 32] including electro-weak corrections.

3. Target halos

In this work we focus upon dwarf galaxies and so present the J-factors for the Draco, Reticulum II, Triangulum II dwarf galaxies. These are chosen as they have all been considered as DM hunting environments in the past [33, 34, 35], with recent attention on the case of Triangulum II in particular [36].

Halo	J-factor (min)	J-factor (median)	J-factor (max)	θ	Reference
Triangulum II	1.86×10^{19}	2.75×10^{20}	4.37×10^{21}	0.5°	[36, 37, 38]
Reticulum II	7.24×10^{16}	5.75×10^{17}	4.90×10^{18}	0.5°	[34, 37, 38]
Draco	5.37×10^{18}	1.23×10^{19}	3.02×10^{19}	0.5°	[37, 38]

Table 1. A summary of the J-factor values used in this work. θ refers to angular radius over which J is calculated. All J-factors are given in units of $\mathrm{GeV}^2\ \mathrm{cm}^{-5}$.

4. KM3NeT sensitivities

We follow [39] in using their calculations for the sensitivity of KM3NeT to extended sources. Note that these only consider muon neutrinos while KM3NeT is expected to be sensitive to all three flavours. To account for this we will consider two cases: a pessimistic one where we only

compare predicted DM muon neutrino fluxes to the sensitivity from [39], and an optimistic one where we use a DM flux with all three flavours. These two extremes should serve to bracket the expected range of non-detection constraints that could be achieved.

5. Results

Here we present the non-detection constraints for the 3 dwarf galaxies considered. These are displayed relative to existing Fermi-LAT results from [1, 2] with the thermal relic value from [27] for comparison. We will display results for annihilation to all lepton channels as we are interested in leptophilic models of DM. However, we note the muon and electron channels are of special interest due to their role in models suggested to explain the DAMPE excess [6] and the significance of these leptons in LHC excesses [14].

In Figure 2 we display the results for the Draco dwarf. Even in the most optimistic case this target can only marginally constrain the DAMPE parameter space via KM3NeT non-observation in the muon channel. However, it produces improvements over Fermi-LAT for $m_\chi > 7$ TeV in the pessimistic case, and $m_\chi > 1$ TeV in the optimistic one (for tau and electon channels this occurs at masses 3 or 4 times larger). Notably, the constraints improve with WIMP mass (at least in the displayed range), unlike those from other high-energy measures like gamma-rays. Importantly, the muon neutrino only case significantly worsens the limit on the electron channel as expected.

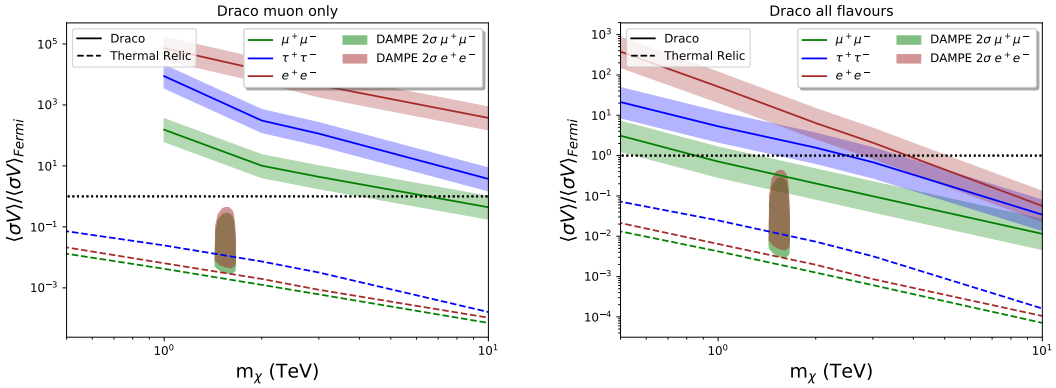

Figure 2. Non-observation upper limits on the annihilation cross-section from the Draco dwarf with KM3NeT. The solid line shows the median J-factor case while shading is between the minimum and maximum values from Table 1. Left: muon neutrinos only. Right: all flavours.

Figure 3 displays the case of the Triangulum II dwarf. This case has substantial uncertainties in the J-factor [36, 37, 38] but manages to improve upon Fermi-LAT substantially in both scenarios for tau and muon channels. Importantly, the optimistic case achieves significant coverage of the DAMPE parameter space and encroaches upon the thermal relic density.

Reticulum II, displayed in Fig. 4 fails to encroach upon the DAMPE parameter space in either case and even at the most optimistic J factors. However, in the optimistic case, it does manage to improve upon Fermi-LAT for $m_\chi > 1.5$ TeV and $m_\chi > 5$ TeV for the maximum and median J factors respectively.

6. Discussion and conclusions

The WIMP mass range > 1 TeV is a difficult regime to probe. However, the results presented here demonstrate that substantial advances can be made in leptonic annihilation channels (specifically relevant to leptophilic DM models) through the use of non-detection constraints

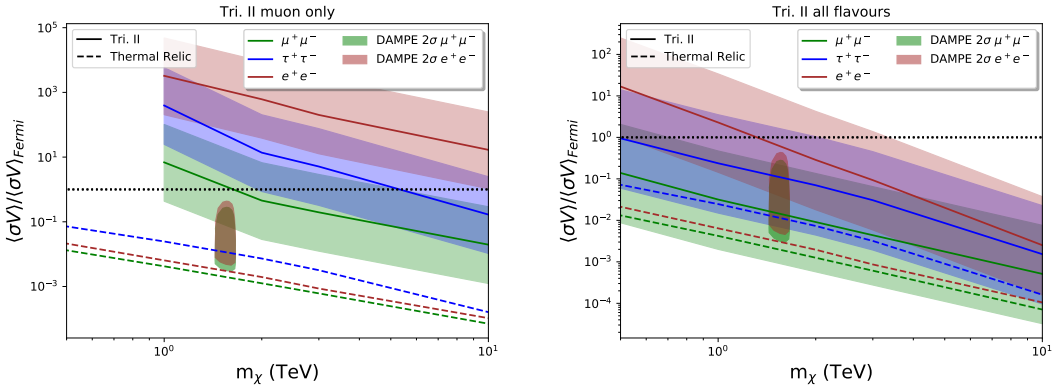

Figure 3. Non-observation upper limits on the annihilation cross-section from the Triangulum II dwarf with KM3NeT. The solid line shows the median J-factor case while shading is between the minimum and maximum values from Table 1. Left: muon neutrinos only. Right: all flavours.

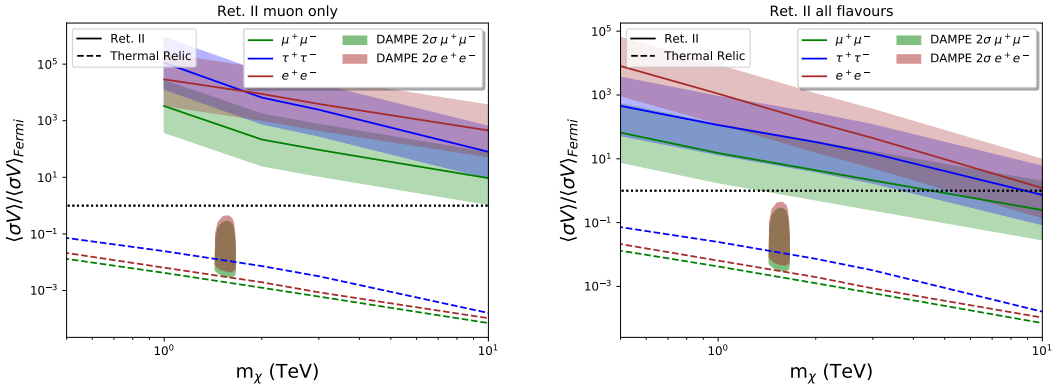

Figure 4. Non-observation upper limits on the annihilation cross-section from the Reticulum II dwarf with KM3NeT. The solid line shows the median J-factor case while shading is between the minimum and maximum values from Table 1. Left: muon neutrinos only. Right: all flavours.

from the up-coming KM3NeT experiment. It is especially notable that the cross-section constraints derived in this manner improve with increasing WIMP mass, in sharp contrast to the behaviour of both radio and gamma-ray limits. These particular annihilation channels are of special interest as they offer a chance to probe models of DM that may have relevance to multiple outstanding issues in modern physics and provide an alternative means of effectively probing standard model extensions, such as the Madala hypothesis, which provide potential leptophilic DM candidates. In future work it may become possible to combine LHC and astrophysical/cosmological constraints to determine if a leptophilic standard model extension can compellingly address anomalies across such vastly different scales.

Acknowledgments

G.B acknowledges support from a National Research Foundation of South Africa Thuthuka grant no. 117969.

References

[1] Drlica-Wagner A *et al.* 2015 *Astrophys. J.* **809** L4

[2] Albert A *et al.* (Fermi-LAT, DES) 2017 *ApJ* **834** 110 (*Preprint* 1611.03184)
[3] Egorov A E and Pierpaoli E 2013 *Phys. Rev. D* **88** 023504 (*Preprint* 1304.0517)
[4] Beck G 2019 (*Preprint* 1905.05599)
[5] Ambrosi G *et al.* 2017 *Nature* **552** 63
[6] Fan Y, Huang W, Spinrath M, Tsai Y S and Yuan Q 2018 *Physics Letters* **B 781** 83
[7] Yuan Q *et al.* 2017 *Preprint* arXiv: 1711.10989
[8] Cao J, Feng L, Guo X, Shang L, Wang F and Wu P 2018 *Phys. Rev. D* **97**(9) 095011 URL https://link.aps.org/doi/10.1103/PhysRevD.97.095011
[9] Yang F, Su M and Zhao Y 2017 *Preprint* arXiv: 1712.01724
[10] Aad G *et al.* (ATLAS) 2008 *JINST* **3** S08003
[11] Bayatian G L *et al.* (CMS) 2006
[12] von Buddenbrock S, Chakrabarty N, Cornell A S, Kar D, Kumar M, Mandal T, Mellado B, Mukhopadhyaya B and Reed R G 2015 (*Preprint* 1506.00612)
[13] von Buddenbrock S 2017 *J. Phys. Conf. Ser.* **878** 012030 (*Preprint* 1706.02477)
[14] von Buddenbrock S, Cornell A S, Fang Y, Fadol Mohammed A, Kumar M, Mellado B and Tomiwa K G 2019 (*Preprint* 1901.05300)
[15] von Buddenbrock S, Chakrabarty N, Cornell A S, Kar D, Kumar M, Mandal T, Mellado B, Mukhopadhyaya B, Reed R G and Ruan X 2016 *Eur. Phys. J.* **C76** 580 (*Preprint* 1606.01674)
[16] Fang Y, Kumar M, Mellado B, Zhang Y and Zhu M 2017 *Int. J. Mod. Phys.* **A32** 1746010 (*Preprint* 1706.06659)
[17] Beck G and Colafrancesco S 2017 *J. Phys. Conf. Ser.* **889** 012006 (*Preprint* 1704.08031)
[18] Beck G and Colafrancesco S 2017 *Proceedings, 62st Annual Conference of the South African Institute of Physics (SAIP2017): Stellenbosch, South Africa, July 3-7, 2017* pp 228–233 (*Preprint* 1707.07940)
[19] Beck G and Colafrancesco S 2018 *PoS* **HEASA2017** 030 (*Preprint* 1812.00691)
[20] von Buddenbrock S, Cornell A S, Iarilala E D R, Kumar M, Mellado B, Ruan X and Shrif E M 2018 (*Preprint* 1809.06344)
[21] von Buddenbrock S, Cornell A S, Fadol A, Kumar M, Mellado B and Ruan X 2018 *J. Phys.* **G45** 115003 (*Preprint* 1711.07874)
[22] Drewes M 2015 *PoS* **EPS-HEP2015** 075 (*Preprint* 1510.07883)
[23]
[24] Grange J *et al.* (Muon g-2) 2015 (*Preprint* 1501.06858)
[25] Akhmedov E, Kartavtsev A, Lindner M, Michaels L and Smirnov J 2013 *JHEP* **05** 081 (*Preprint* 1302.1872)
[26] Abramowski A *et al.* (H.E.S.S.) 2014 *Phys. Rev.* **D90** 112012 (*Preprint* 1410.2589)
[27] Steigman G, Dasgupta B and Beacom J F 2012 *Phys. Rev.* **D86** 023506 (*Preprint* 1204.3622)
[28] Beck G and Colafrancesco S 2018 *Proceedings, 61st Annual Conference of the South African Institute of Physics (SAIP2016): Johannesburg, South Africa, July 4-8, 2016* (*Preprint* 1810.07176)
[29] Beck G and Colafrancesco S 2019 *PoS* **HEASA2018** 013 (*Preprint* 1902.07468)
[30] Athron P, Balazs C, Fowlie A and Zhang Y 2018 *Journal of High Energy Physics* **2018** 121 ISSN 1029-8479 URL https://doi.org/10.1007/JHEP02(2018)121
[31] Cirelli M *et al.* 2011 *JCAP* **1103** 051
[32] Ciafaloni P *et al.* 2011 *JCAP* **1103** 019
[33] Colafrancesco S, Profumo S and Ullio P 2007 *Phys. Rev. D* **75** 023513
[34] Bonnivard V, Combet C, Maurin D, Geringer-Sameth A, Koushiappas S M, Walker M G, Mateo M, Olszewski E W and Bailey III J I 2015 *Astrophys. J.* **808** L36 (*Preprint* 1504.03309)
[35] Regis M, Richter L and Colafrancesco S 2017 *Journal of Cosmology and Astroparticle Physics* **2017** 025 URL http://stacks.iop.org/1475-7516/2017/i=07/a=025
[36] Genina A and Fairbairn M 2016 *Monthly Notices of the Royal Astronomical Society* **463** 3630–3636 ISSN 0035-8711 (*Preprint* http://oup.prod.sis.lan/mnras/article-pdf/463/4/3630/18516441/stw2284.pdf) URL https://doi.org/10.1093/mnras/stw2284
[37] Hayashi K, Ichikawa K, Matsumoto S, Ibe M, Ishigaki M N and Sugai H 2016 *Mon. Not. Roy. Astron. Soc.* **461** 2914–2928 (*Preprint* 1603.08046)
[38] Pace A B and Strigari L E 2019 *MNRAS* **482** 3480–3496 (*Preprint* 1802.06811)
[39] Ambrogi L, Celli S and Aharonian F 2018 *Astropart. Phys.* **100** 69–79 (*Preprint* 1803.03565)

Constraining *f(R)*-gravity models with recent cosmological data

Renier Hough[1], Amare Abebe[2] and Stefan Ferreira[1]

[1]Center for Space Research, North-West University, Potchefstroom 2520, South Africa
[2]Center for Space Research, North-West University, Mahikeng 2735, South Africa

E-mail: renierht@gmail.com

Abstract. In this work, we look at the cosmological constraints of some *f(R)*-modified gravity models such as $f(R) = \beta R^n$ (a toy model) and more realistic ones like the Starobinsky and Hu-Sawicki models. We use 236 intermediate-redshift and 123 low-redshift Type 1A Supernovae data obtained from the SDSS-II/SNLS3 Joint Light-curve Analysis (JLA), with absolute magnitudes, for the B-filter, found on the NASA Extragalactic Database (NED). We then develop a Markov Chain Monte-Carlo (MCMC) simulation to find the best fit (firstly to the ΛCDM model), to obtain the cosmological parameters (Ω_m and $\bar{h}$). We then use the concordance model results to constrain the priors for the *f(R)*-gravity models on the MCMC simulation. We assume a flat universe $\Omega_k = 0$ and a radiation density Ω_r that is negligible in both the ΛCDM model and *f(R)*-gravity models. Thus, the only difference between the ΛCDM model and *f(R)*-gravity models will be dark energy and the arbitrary free parameters. This will tell us if there exist viable *f(R)*-gravity models when we compare them to the results of the ΛCDM model and thus constrain the generic *f(R)*-gravity models with cosmological data.

1. Introduction

Since the theory of General Relativity (GR) was proposed by Einstein in 1915, it has developed into the accepted theory to explain gravity. GR is a generalization of Newtonian gravity in the presence of extreme gravitational fields. The reason behind the acceptance, among others, was due to the discovery by Hubble in 1929 that the Universe is expanding. GR was able to explain this discovery, and this led to the Hot Big Bang theory model, which uses GR as the physical basis. With the observational discovery in more recent times that the expansion of the Universe is accelerating, which is not in line with GR predictions, the Hot Big Bang model had to be improved. An unknown pressure force acting out against gravity, dubbed "dark energy" was added to explain why gravity on cosmological scales is not able to slow down the expansion.

The cosmological field equations in standard cosmology are derived by the using variational principle on the Einstein-Hilbert action

$$A = \frac{c^4}{16\pi G}\int d^4x\sqrt{-g}\big[R + 2(L_m - \Lambda)\big] \ , \tag{1}$$

where Λ is the cosmological constant representing the "dark energy" pressure force, and L_m is the standard matter Lagrangian [1]. These field equations are given by

$$R_{\mu\nu} - \frac{1}{2}Rg_{\mu\nu} + \Lambda g_{\mu\nu} = \frac{8\pi G}{c^4}T_{\mu\nu} \ , \tag{2}$$

where $R_{\mu\nu}$ and R are the Ricci tensor and Ricci scalar respectively, $g_{\mu\nu}$ is the metric tensor and $T_{\mu\nu}$ represents the energy-momentum tensor. The two most important cosmological equations in Eq. (2) are the Friedmann equations (we assume that in the geometric unit system $c = 1 = 8\pi G$),

which in the Friedmann-Lemaître-Robertson-Walker (FLRW) spacetime metric read

$$\left[\frac{\dot{a}(t)}{a(t)}\right]^2 = \frac{\rho(t)}{3} - \frac{\kappa}{a^2(t)} + \frac{\Lambda}{3}\,, \tag{3}$$

$$\frac{\ddot{a}(t)}{a(t)} = -\frac{1}{6}\Big(\rho(t) + 3P(t)\Big) + \frac{\Lambda}{3}\,, \tag{4}$$

where $a(t)$ is the scale factor (describing the relative size of the Universe at a certain time), $\rho(t)$ is the energy density, $P(t)$ is the isotropic pressure, and κ is the 3D (spatial) curvature. To close the above system of expansion equations, we relate ρ and P through the equation of state

$$P(t) = \omega\rho(t)\,, \tag{5}$$

where we assume a perfect-fluid system with a constant equation of state parameter ω.

1.1. Problems faced by GR and proposed solutions ∼ f(R)-gravity

The Friedmann equations are used to mathematically describe the Big Bang theory and the ongoing expansion (with the inclusion of dark energy to explain the late-time acceleration) of the Universe. The inclusion of dark energy provides one of the problems faced by the ΛCDM model, since dark energy is an unknown pressure force acting out against gravity, but have been shown to make up $\sim 68\%$ of the Universe, [2]. Furthermore, an early-time accelerated expansion, called the inflation period, added other problems to the ΛCDM model such as the horizon problem and the coincidence problem. Other arising problems faced by the ΛCDM model also include the Magnetic monopole problem (none has been found) and the Universe's matter/anti-matter ratio, which is expected to be equal to 1, but is close to zero [3].

Due to the problems faced by the ΛCDM model, there exist proposed solutions in the form of modified gravity models. In some of these modified theories, you may add extra fields or go to higher dimensions. We will be looking at a higher-order derivative theory, called *f(R)*-gravity model. For these models, the modification occurs when changing the Ricci scalar in the Einstein-Hilbert action (1) to a function of the Ricci scalar, namely *f(R)*. Re-deriving the Einstein field equations, we obtain

$$f'(R)R_{\mu\nu} + g_{\mu\nu}\Box f'(R) - \nabla_\mu\nabla_\nu f'(R) - \frac{1}{2}g_{\mu\nu}f(R) = T_{\mu\nu}, \tag{6}$$

where $\Box = \nabla_\sigma\nabla^\sigma$ is the covariant d'Alembert operator. As you will notice in equation (6), we do not have a dependency on the cosmological constant, since this modified theory tries to explain the accelerated expansion without the inclusion of dark energy. We can then re-derive the Friedmann equations for *f(R)*-gravity, and obtain

$$\begin{aligned}\left[\frac{\dot{a}(t)}{a(t)}\right]^2 &= \frac{\rho(t)}{3f'(R)} - \frac{\kappa}{a^2(t)} + \frac{1}{6}\Big(R - \frac{f(R)}{f'(R)}\Big) - H\dot{R}\frac{f''(R)}{f'(R)},\\ \frac{\ddot{a}(t)}{a(t)} &= -\frac{\rho(t)}{3f'(R)} + \frac{f(R)}{6f'(R)} + H\dot{R}\frac{f''(R)}{f'(R)}.\end{aligned} \tag{7}$$

2. Supernovae Type 1A data and MCMC simulations

2.1. Distance modulus

To test the *f(R)* Friedmann equations (7), we use Supernovae Type 1A data. The reason for this is due to the fact that Type 1A Supernovae (White Dwarf (WD) accreting a low mass companion star) are regarded as standard candles, since their limunosities are relatively similar to one another. This would mean that the measured flux is only dependent on the distance to

supernovae and not the composition or mass of the WD. We will use redshift to approximated the distance. Thus, an expanding universe, where the distance to the supernovae is changing, can be used to find the best fitting distance modulus for our Friedmann equation. For simplicity, we will assume a flat universe $\Omega_k = 0$, with a negilible radiation density $\Omega_r \approx 0$ [2].

We will be using data obtained from SDSS-II/SNLS3 Joint Light-curve Analysis (JLA). From that particular dataset, we will use 123 are low-redshift supernovae with a redshift between $0.01 < z \leq 0.1$ and 236 supernovae with an intermediate redshift between $0.1 < z \leq 1.1$. The reason we will using low-redshift data, is due to the fact that we will be testing the model for a late-time acceleration, thus a redshift below ~ 0.5. Furthermore, we will be using the calculated absolute magnitudes of these supernovae for the B-filter, that can be found in [4, 5, 6].

The distance modulus can be derived from the *luminosity distance* D_L, which relates two bolometric quantities, namely the luminosity L and the flux f of the distant supernovae. We can then relate D_L to the *transverse comoving distance*, by using redshift and obtaining

$$D_L = (1 + z)D_M. \tag{8}$$

By using the conditions for the *transverse comoving distance* as a function of the curvature of spacetime density (Ω_k) found in [7], we can determine that $D_M = D_c$, where D_c is the *line-of-sight comoving distance*. The *line-of-sight comoving distance* is defined as

$$D_c = \int \frac{cdt}{a} = D_H \int_0^z \frac{dz'}{h(z')}, \tag{9}$$

where $D_H = 3000\bar{h}\frac{km}{s.Mpc}$ is the *Hubble distance* and $h(z)$ is the normalized Hubble parameter in terms of redshift. By using the definition of the *distance modulus* (in *Mpc*), and the aforementioned different distance definitions, we obtain

$$\mu = m - M = 25 - 5 \times \log_{10}\left(3000\bar{h}^{-1}(1 + z)\int_0^z \frac{dz'}{h(z')}\right), \tag{10}$$

where m is the apparent magnitude and M is the absolute magnitude of the measured Supernovae [5]. This method is called supernova cosmology [8].

2.2. Markov Chain Monte Carlo (MCMC) simulations

To fit the data to the distance modulus, we will use MCMC simulations. The MCMC simulation is able to search for the most probable free parameter value, given certain physical constrains. It starts searching at some initial given value, by calculating the likelihood of the distance modulus for that particular initial condition. It then takes a random step for each parameter in the parameter space away from the initial values. Then it calculates the likelihood for the distance modulus for all possible combinations between the initial parameter values and the new parameter values to find the combination with the largest likelihood of occurring. The simulation then finds an acceptance ratio between the initial parameter values and the new largest likelihood combination parameter value. If the ratio is above 1 the new values are accepted and the entire procedure starts over. If the acceptance ratio is below 1, a chance is created for the second combination to still be accepted in ratio to the probabilities for each combination to occur. If it is not accepted, the initial parameter is accepted and the entire procedure starts over. This continues until it converges to the most probable best fit parameter values.

We will use the *EMCEE Hammer Python* package to execute the MCMC simulation. This package uses different random walkers (in most cases we will use 100 random walkers), each starting at a different initial parameter value and each converging on the most probable parameter values. This creates a Gaussian probability distribution. Using the average values

for each probability distribution for each parameter, we will then have the best-fit parameter value for each parameter and their 1σ-value (error bars)[1].

3. Results

3.1. Concordance model ∼ ΛCDM model

We use the ΛCDM model to calibrate our MCMC simulation. We will use the ΛCDM model as the "true" model to which we can compare the *f(R)*-gravity models against, to find if they are viable for being alternative models. We assume a flat universe $\Omega_k = 0$, as well as, neglecting the radiation density of the Universe, since the expected value is in the range of $\Omega_r h^2 = 2.47 \times 10^{-5}$ [10] (they assumed $h = 0.73$). Using these assumptions, we obtain a Friedmann equation in terms of redshift as

$$h(z) = \sqrt{\Omega_m (1+z)^3 + 1 - \Omega_m}, \tag{11}$$

where $h(z) = \frac{H(z)}{H_0}$ is dimensionless parameter, and making the substitution $\Omega_\Lambda = 1 - \Omega_m$. When we execute the MCMC simulation for the ΛCDM model, we obtain the results in Figure (1).

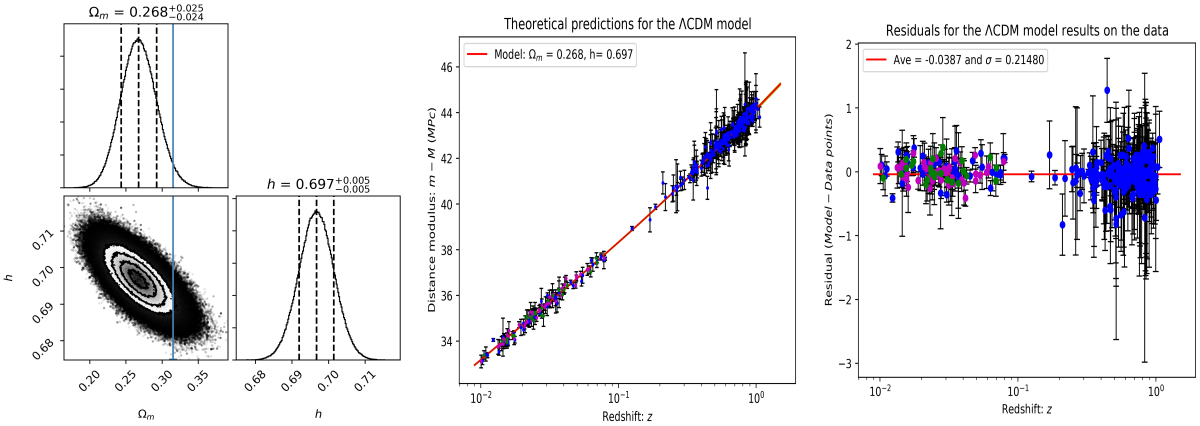

Figure 1. MCMC simulation results (Panel: 1) and the corresponding model fitted to the Supernovae Type 1A data obtained from JLA (Panel: 2). Furthermore, the residuals between the model prediction and the actual data points are also shown (Panel: 3).

From Figure (1), we can confirm that the MCMC simulation works, even though the predicted parameter values are not within 1σ from the Planck2018 result (blue line in Panel: 1). The reason for this is due to the Planck results being determined on Cosmic Microwave Background (CMB) radiation data, and it has been shown that the Supernovae Type 1A data predicts a higher Hubble constant value than the CMB results [11]. The reason for showing the Planck results is just to remind us that we did use Planck results to make our assumptions and also to show the discrepancy between supernovae and CMB results.

3.2. f(R)-gravity model results

Since Figure (1) confirmed that our MCMC simulation works, we can go ahead and test different *f(R)*-gravity models in a similar fashion as done for the concordance model. Thus, we derive a distance modulus equation for each of the chosen *f(R)*-gravity models. These models include 2 toy models, the Starobinsky model and the Hu-Sawicki model, where the latter 2 models are considered as the more realistic models:

- $f(R) = \beta R^n$ - First toy model,

[1] This entire section including the MCMC simulation code is similar to work done in the conference proceedings paper by [9], where they used the code developed in the masters dissertation, which this paper is based on, to test their model.

- $f(R) = \alpha R + \beta R^n$ - Second toy model,
- $f(R) = R + \beta R_c \left[(1 + \frac{R^2}{R_c^2})^{-n} - 1 \right]$ -Starobinsky model,
- $f(R) = R - \alpha R_c \left[\frac{\left(\frac{R}{R_c}\right)^n}{1+\left(\frac{R}{R_c}\right)^n} \right]$- Hu-Sawicki model.

We use the best-fit parameter values for the ΛCDM model to set appropriate priors for the *f(R)* models, to ensure that the resulting cosmological values are close to those found by the ΛCDM model. The best-fit model results (without the MCMC results) are shown in Figures 2 - 5 in the same order as given above. The Starobinsky and Hu-Sawicki model results are preliminary due to having non-solvable Friedmann equations (executing a numerical method).

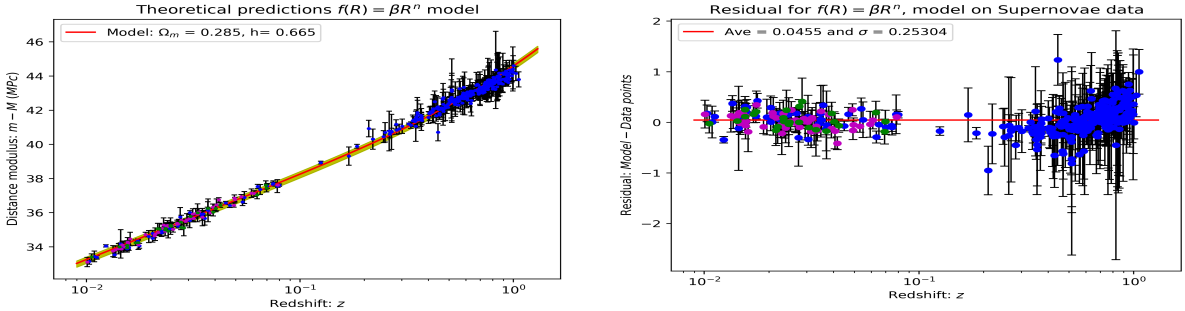

Figure 2. First toy model's best fit to the Supernovae Type 1A data, with cosmological parameter values $\Omega_m = 0.285^{+0.082}_{-0.105}$, $\bar{h} = 0.665^{+0.054}_{-0.045}$, and $q_0 = -0.011^{+0.001}_{-0.002}$. The *f(R)*-model free parameter values are $\beta = 2.687^{+0.968}_{-0.999}$ and $n = 1.270^{+0.000}_{-0.000}$.

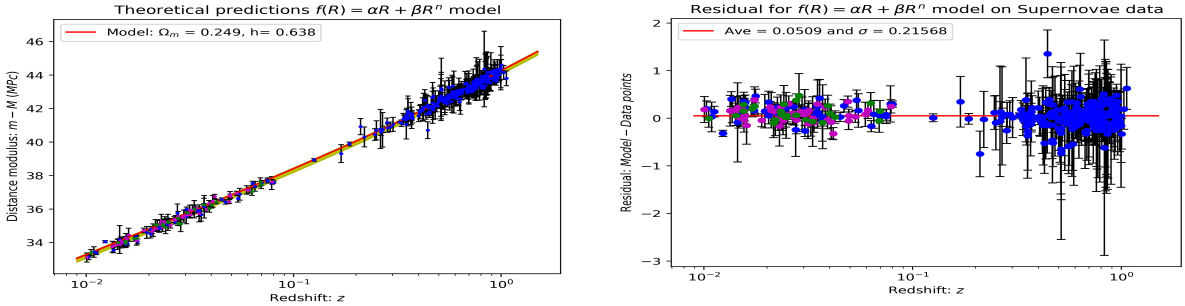

Figure 3. Second toy model's best fit ($n = 2$ and the (-) solution) to the Supernovae Type 1A data, with cosmological parameter values $\Omega_m = 0.249^{+0.102}_{-0.101}$, $\bar{h} = 0.638^{+0.046}_{-0.027}$, and $q_0 = -0.575^{+0.040}_{-0.046}$. The *f(R)*-model free parameter values are $\alpha = 19.642^{+2.967}_{-1.753}$ and $\beta = 0.903^{+0.070}_{-0.107}$.

4. Conclusion

From these results, we can see that these models do fit the data, although each model has a disadvantage in some sense. In the first toy model, the predicted cosmological values are close to the Planck2018 results [2], thus minimizing the discrepancy between CMB and Supernovae Type 1A results, but struggled with predicting the period before the acceleration started ($z > 0.5$), as well as with the deceleration parameter value (q_0) that is expected to be close to ~ -0.5 based on observations. The second toy model fitted the data better, but gave a Hubble constant that is lower than any observed value. The Starobinsky and Hu-Sawicki models (preliminary results) found realistic Hubble constant values compared to the CMB observations, but in both

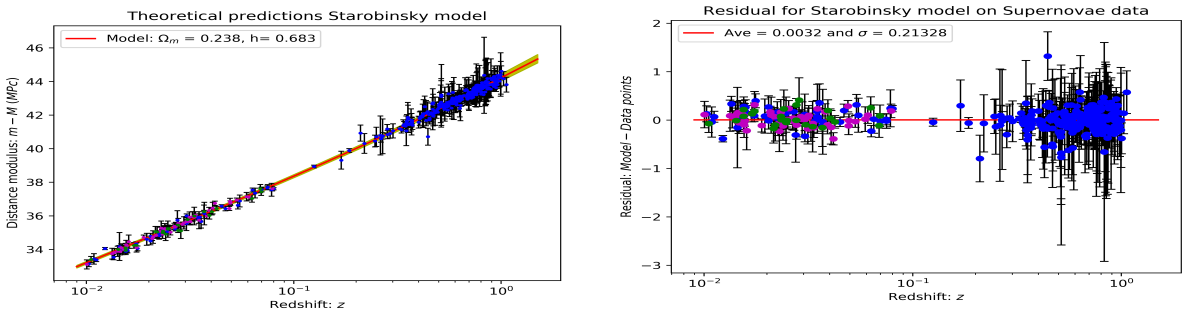

Figure 4. The Starobinsky model's best fit to the Supernovae Type 1A data, with cosmological parameter values $\Omega_m = 0.238^{+0.089}_{-0.087}$, $\bar{h} = 0.683^{+0.026}_{-0.024}$, and $q_0 = -0.494^{+0.298}_{-0.278}$. The *f(R)*-model free parameter values are $\beta = 4.588^{+3.668}_{-2.683}$ and $n = 3.493^{+3.705}_{-2.057}$.

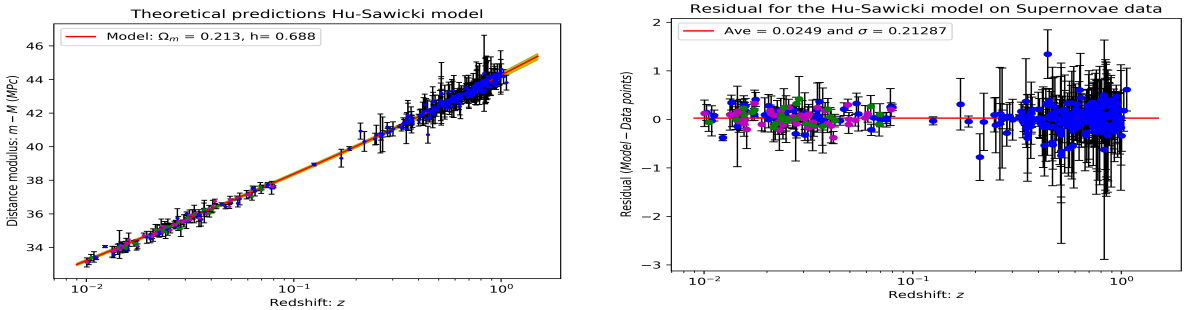

Figure 5. The Hu-Sawicki model's best fit to the Supernovae Type 1A data, with cosmological parameter values $\Omega_m = 0.213^{+0.076}_{-0.038}$, $\bar{h} = 0.688^{+0.024}_{-0.024}$, and $q_0 = -0.538^{+0.144}_{-0.179}$.The *f(R)*-model free parameter values are $\alpha = 4.823^{+0.070}_{-0.092}$, $\beta = 5.012^{+0.087}_{-0.087}$, and $n = 3.500^{+0.038}_{-0.049}$.

cases found matter densities that were lower than observations suggest. Both of these also gave deceleration parameters close to the expected values.

Future work will include doing a statistical analysis on each individual best-fit values by calculating the χ^2-value. Furthermore, we will also calculate the AIC and BIC criterion values of each for the *f(R)*-gravity models and compare them to the ΛCDM model to check if some of these *f(R)*-gravity models are cosmologically viable alternatives or not.

Acknowledgements

RH acknowledge funding through a National Astrophysics and Space Science Program (NASSP) and National Research Foundation (NRF) scholarship (Grant number 117230). AA and SF acknowledge that this work is based on the research supported in part by the NRF (with grant numbers 109257/112131 and 109253 respectively).

References

[1] Gidelew A 2013 *Beyond the concordance cosmology* Ph.D. thesis University of Cape Town
[2] Planck Collaboration 2018 *arXiv e-prints* arXiv:1807.06209 (*Preprint* 1807.06209)
[3] Amaral Vieira F J 2011 *arXiv e-prints* arXiv:1110.5634 (*Preprint* 1110.5634)
[4] Conley A, Guy J, Sullivan M *et al.* 2011 *Astrophysical Journal, Supplement* **192** 1 (*Preprint* 1104.1443)
[5] Neill J D, Sullivan M, Howell D A *et al.* 2009 *Astrophysical Journal* **707** 1449–1465 (*Preprint* 0911.0690)
[6] Hicken M, Challis P, Jha S *et al.* 2009 *Astrophysical Journal* **700** 331–357 (*Preprint* 0901.4787)
[7] Deza M M and Deza E 2009 Encyclopedia of distances *Encyclopedia of distances* (Springer) pp 1–583
[8] Leibundgut B 2008 *General Relativity and Gravitation* **40** 221–248 (*Preprint* 0802.4154)
[9] Swart A M, Hough R, Sahlu S *et al.* 2019 Unifying dark matter and dark energy in Chaplygin gas cosmology, *in preparation.*
[10] Lahav O and Liddle A 2004 *Physics Letters B* **592** 1 (*Preprint* astro-ph/0406681)
[11] Riess A G, Macri L M, Hoffmann S L *et al.* 2016 *Astrophysical Journal* **826** 56 (*Preprint* 1604.01424)

Multi-wavelength study of large-scale outflows from the Circinus galaxy

R Ebrahim[1], A Chen[1], D Prokhorov[1], K Thorat[2 34] , G Jozsa[2 3 5] and P Serra[6]

[1] School of Physics, University of the Witwatersrand, 1 Jan Smuts Ave, Johannesburg, 2000, South Africa
[2] South African Radio Astronomy Observatory, Black River Park, 2 Fir Street, Observatory, Cape Town, 7925, South Africa
[3] Department of Physics and Electronics, Rhodes University, PO Box 94, Makhanda 6140, South Africa
[4] Department of Physics, University of Pretoria, Hatfield, Pretoria, 0028, South Africa
[5] Argelander-Institut für Astronomie, Auf dem Hügel 71, D-53121 Bonn, Germany
[6] INAF- Osservatorio Astronomico di Cagliari, Via della Scienza 5, I-09047 Selargius (CA), Italy

E-mail: 1049197@students.wits.ac.za

Abstract. The Circinus galaxy is a composite starburst/Seyfert galaxy which exhibits radio lobes inflated by kpc scale outflows along its minor axis. It is located 4 Mpc away, which makes it a unique target to study the physical nature of these outflows. Our task will be to investigate if they originate from nuclear star formation activity or if they are jets from an active galactic core. The MeerKAT array can perform 5 arcsecond resolution radio observations, which is in the observed range of the arcminute lobes of the Circinus galaxy. In this work, a multi-wavelength analysis of the radio lobe structures will be conducted using the available MeerKAT observations and Fermi-LAT data, which will aid in the understanding of the origin of these structures. The results can then be compared to the star-formation driven Fermi bubbles in the Milky Way, which have also been observed in both the gamma-ray and the radio bands to determine possible connections to these structures.

1. Introduction

The Circinus galaxy is a spiral galaxy at a distance of 4 Mpc [1]. It is hence one of the closest galaxies to the Milky Way. This galaxy possesses characteristics of both Seyfert and starburst galaxies.

In the AGN (Active Galactic Nucleus) classification scheme Seyfert galaxies feature relatively low luminosity nuclei, and like other AGNs, are powered by massive black holes. In the visible wavelengths, Seyfert galaxies usually appear as spiral galaxies, but at other wavelengths the cores are much more luminous. The core of Circinus is classified as a Seyfert 2 core for several reasons including the presence of characteristic narrow emission lines [2].

Starburst galaxies show very high star formation rates compared to normal galaxies. Circinus is one of the closest starburst galaxies. These galaxies are ideal laboratories to study star formation and its feedback into the interstellar and intergalactic medium. As a consequence of its star formation activity, Circinus hosts one of the brightest type II supernova in the radio

and X-ray, SN1996cr [3]. The significant star-formation rate, starburst characteristic emission lines (HII regions) and the observed nuclear starburst ring in Circinus are further indicators of its starburst nature [2] .

2. Why Circinus?

There are three key reasons why we are interested in studying Circinus:

2.1. Studying the origin of radio lobes

A prominent feature of Circinus is the kpc radio lobe outflows along its minor axis.

Radio lobes are radio emission that is created by outflows from the centre of a galaxy and extends outwards on both sides. The lobes are often much larger in size than the host galaxy.

There are two proposed models commonly used to explain the origins of these radio lobes: (i) *Starburst-driven galactic winds*: The outflows result from supernova explosions in the core whose combined stellar winds form a super-bubble which is observed as a radio lobe. (ii) *AGN-driven jets*: AGNs have super-massive black holes in their centres. The accreting matter surrounding the black holes are often flung out at relativistic speeds in the form of jets . These astrophysical jets move at much higher speeds relative to the surrounding medium, which can result in the formation of shock waves depending on the structure of the surrounding medium. This jet structure terminates at the beam head which is often observed as a radio hotspot and this also depends on the properties of the this medium. The fluid from the jet then passes through a strong shock and spreads in the cocoon. With sufficient energy and momentum this flow can then drive a bow shock, i.e. the shell, through the ambient gas [4]. Both the cocoon and the shell emit in the radio, X-ray, and gamma-ray bands [e.g.,[5]].

Studying the lobes of Circinus in greater detail could provide a better understanding of these emission models.

2.2. Studying Fermi bubbles

There is a similar type of kpc emission in our Milky Way known as the Fermi bubbles. They were first discovered as gamma-ray emitting lobes which extend from the Galactic centre about 8 kpc above and below the Galactic plane [6]. After their discovery in gamma rays in 2010, various features associated with these "gamma-ray" lobes have been observed across the electromagnetic spectrum. In the radio regime they are observed as larger bi-conical lobes with ridges winding along the conical structure [7].

Similar to the origin of radio lobes in Circinus, the origin of Fermi bubbles is still debated: AGN-driven or starburst-driven outflows. A study by Caretti et al. (2013) [7] advocated for a cosmic ray model to explain radio emission from the Fermi bubbles where these particles are transported from the galactic plane outwards and radiate via the synchrotron mechanism to produce the lobes. These bubbles are also observed to have a narrow waist which is consistent with a central star-forming ring of gas and this supports a star-formation driven outflow model [7].

The discovery of Fermi bubbles and the study of its origins demands the observation of other galaxies which feature a similar emission structure. NGC 1068 features lobes which originate from AGN ejecta material [e.g., [8]]. NGC 3079 features large radio lobes and, like Circinus, has both AGN and starburst characteristics [9]. The nearest AGN, Centaurus A, is located at a distance of 3.4 Mpc and features jets, radio lobes and diffuse emission [e.g.,[10]]. The southern inner lobe of Centaurus A also features a shock similar to one observed in Circinus.

Since these galaxies feature similar structures to Fermi bubbles, studying the origin of radio lobes in other galaxies like Circinus could facilitate a better understanding of Fermi bubbles.

2.3. Studying radio lobed spiral galaxies

Radio lobes are usually observed in elliptical galaxies. Unlike elliptical galaxies, spiral galaxies feature a very dense interstellar medium (ISM) making it difficult for the jets to travel far out. These smaller jets mean less energy is being fed into the ISM to produce lobes.

The Milky Way is unusual in that it is a spiral galaxy with large outflows. Other such cases include NGC 1068, NGC 3079 and Circinus which are all spiral galaxies. This makes them excellent objects of study to investigate the interaction of AGN with their environment in spiral galaxies. In addition we choose to study Circinus since it is much closer than the other candidates facilitating the study of the substructure of its lobes in better detail.

3. Research objective

For this project, our task is firstly to observe the radio lobes of Circinus. Then we will investigate their observational properties in order to study the formation of these structures. This will be achieved through a multi-wavelength analysis of the radio lobes using MeerKAT and Fermi-LAT data. Finally, the results will also be compared to the Fermi bubbles to determine possible connections to these structures.

4. Results

For this study we have used MeerKAT observations of the Circinus galaxy 3.6 hours in duration. These data form part of the MeerKAT telescope commissioning observations of the Circinus galaxy, carried out by SARAO.

For the data reduction we used the CARACal pipeline [11] supplemented by our own data imaging and calibration code. We made a radio image of the source from a 150 MHz sub-band of the total bandwidth shown in Figure 1 and wrote python script to perform the spatial analysis.

The measurement of the flux densities for the image made from the complete band as well as the spectral index and detailed astrophysical analysis will be presented in Thorat et al. (2020 in prep) [12]. In this proceeding we report a qualitative analysis identifying structures from the MeerKAT image and comparing it with data at other wavebands.

4.1. Spatial structure of radio lobes

MeerKAT provides deeper and more sensitive images compared to the earlier studies of Circinus with ATCA. This means that the regions of different brightness in Circinus can be identified more clearly, allowing us the opportunity to analyse new information which may have eluded previous efforts.

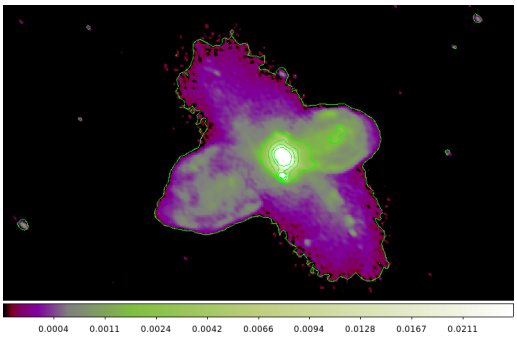

Figure 1. MeerKAT radio map of Circinus [12] with a 7.6x4.4 arcsec^2 beam, a central frequency of 1.375 GHz and in units of Jy/beam (1.3 arcsec/px).

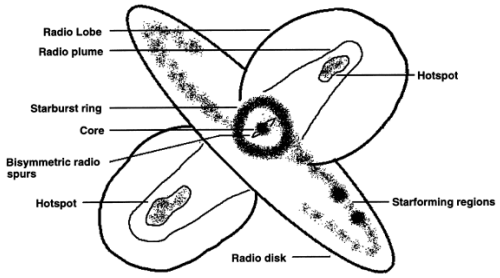

Figure 2. Proposed structure of Circinus from ATCA observations by Elmouttie et al. (1998) [2].

 ISBN: 978-0-620-88875-2

The ATCA study of Circinus by Elmouttie et al. (1998) [2] proposed the structure shown in Figure 2, presenting an unresolved core surrounded by a diffuse radio star-burst ring and radio lobes which are approximately 1.5 kpc in length consisting of a central plume (or a cocoon) and an edge brightened region. A similar ATCA radio map was also produced by Mingo et al. (2012) shown in Figure 3 [13] .

We found a similar morphology when comparing the MeerKAT image to their ATCA image: a bright core region, a visible radio galactic disk, and radio outflows oriented in the north westerly and south easterly directions. There were also star-forming regions at similar locations such as those observed in the southern part of the disk.

4.2. Comparisons between Circinus' lobes and Fermi bubbles

4.2.1. Edge-brightening MeerKAT observations offer a higher sensitivity at a finer angular resolution compared to previous observations of Circinus. This facilitates better observations of the edge-brightening of the lobes. From the MeerKAT image, we identified the bright, thin regions along the edges of the lobes, demonstrating the edge brightening effect shown in Figure 4. The localisation of these regions is more precise owing to the sharpness of the MeerKAT image than previous efforts from ATCA observations (Figure 3).

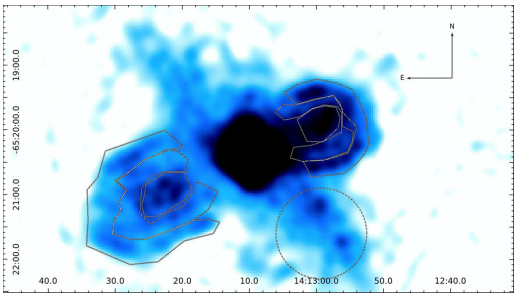

Figure 3. 13cm ATCA radio map of Circinus by Mingo et al (2012) [13].

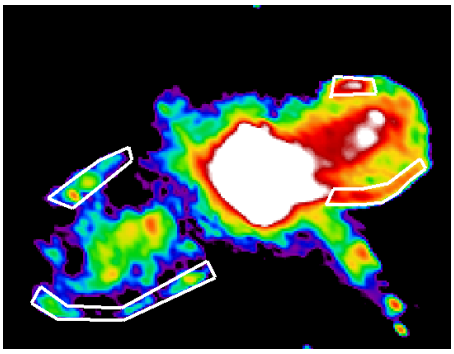

Figure 4. 1.4 GHz MeerKAT radio image of Circinus with edge-brightened regions outlined [12].

This effect has also been observed in X-ray observations of Fermi bubbles in which the edges of the bubbles line up with features in the ROSAT X-ray maps [6]. This is usually interpreted as shock waves.

4.2.2. Plumes Another previously identified feature of the lobes of Circinus are its plumes. We identified these regions from the MeerKAT image as the brightest regions inside each lobe, as shown in Figure 5.

This can be compared to similar regions of enhanced gamma-ray emission found in Fermi bubbles, identified as 'cocoons' by Ackermann et al. (2014) [14], which can be seen in Figure 6. They investigated the possibility of a jet origin for the cocoons but did not find sufficient supporting evidence [14].

5. Future work

5.1. Radio

The MeerKAT observations can also facilitate a spectral analysis which could provide new information on the ageing of electrons along the flow [2] and also help us better understand the structure and origin of the emission in each region, including the possible presence of hotspots.

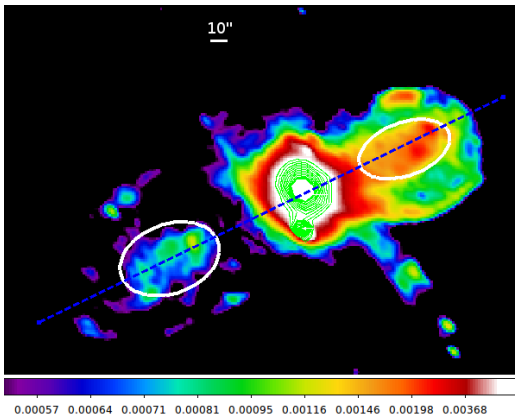

Figure 5. 1.4 GHz MeerKAT radio image of Circinus with plumes outlined [12].

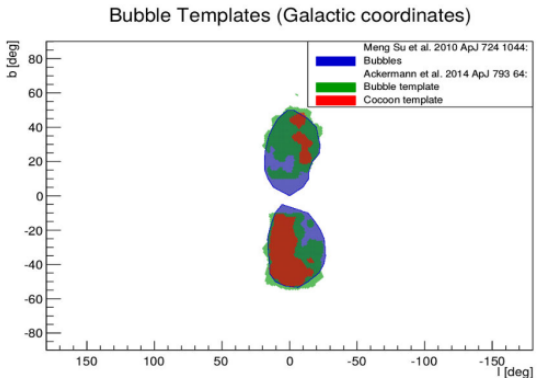

Figure 6. Templates of the Fermi bubbles by Su et al. (2010) [6] and of the Fermi bubbles and cocoons by Ackermann et al. (2014) [14] compiled by S. Hallmann.

We also intend on performing further, in depth, comparisons between the lobes of Circinus and Fermi bubbles to search for similarities.

The quantitative results of our analysis of the MeerKAT observations of the Circinus galaxy will be reported in Thorat et al. (in prep.) [12].

5.2. Gamma-ray

The Fermi-LAT telescope has been performing gamma-ray observations of the whole sky since 2008. In modern gamma-ray telescopes the finest angular resolution is about 5 arcmin which is insufficient to resolve the disk and lobes of Circinus. Instead of the spatial analysis, we will perform a search for variability of the Seyfert nucleus in order to partially decompose the observed gamma-ray emission in the nucleus and diffuse components.

Hayashida et al. (2013) [15] studied the gamma-ray emission from Circinus using Fermi-LAT. Their observations found a 7.3 σ signal above the background emission. There was no signature of temporal variability and no observations of significant spatial structure in their study [15]. The luminosity they found exceeds predictions for interactions of cosmic ray hadrons with the ISM and therefore an additional source of excess emission is needed [15].

Our gamma-ray analysis of Circinus will use a maximum likelihood technique. This involves finding the parameters (flux, position and spectral law of the emission) which best fit the data to a source model inclusive of the Galactic diffuse background. The source model that will be used comes from the 4th LAT catalog (4FGL) based on the first eight years of Fermi observations [16]. Compared to previous catalogs, the latest one features the most data. Previous studies of Circinus, including Hayashida et al. (2013) [15], made use of the older catalog. Given that 11 years of the Fermi-LAT data are now available and that Hayashida et al. (2013) [15] used only 4 years of the data, the chance of finding an AGN core during its low or high states is higher.

All these results could be used to provide support for either a jet, starburst or composite model in explaining the origin of these radio lobes.

Acknowledgements

This work is based on the research supported wholly/in part by the National Research Foundation of South Africa (Grant Numbers: 113833). This work has made use of data from the MeerKAT telescope, provided by the South African Radio Astronomy Observatory (SARAO).

The MeerKAT telescope is operated by the South African Radio Astronomy Observatory, which is a facility of the National Research Foundation, an agency of the Department of Science and Technology.

References

[1] K. C. Freeman, B. Karlsson, G. Lynga, J. F. Burrell, H. van Woerden, W. M. Goss, and U. Mebold. A large new galaxy in Circinus. *A&A*, 55:445–458, Mar 1977.

[2] M. Elmouttie, R. F. Haynes, K. L. Jones, E. M. Sadler, and M. Ehle. Radio continuum evidence for nuclear outflow in the Circinus galaxy. *MNRAS*, 297:1202–1218, Jul 1998.

[3] F. E. Bauer, V. V. Dwarkadas, W. N. Brandt, S. Immler, S. Smartt, N. Bartel, and M. F. Bietenholz. Supernova 1996cr: SN 1987A's Wild Cousin? *A&A*, 688:1210–1234, Dec 2008.

[4] P. A. G. Scheuer. Models of extragalactic radio sources with a continuous energy supply from a central object. *MNRAS*, 166:513–528, Mar 1974.

[5] P. Bordas, V. Bosch-Ramon, and M. Perucho. The evolution of the large-scale emission in Fanaroff-Riley type I jets. , 412(2):1229–1236, Apr 2011.

[6] Meng Su, Tracy R. Slatyer, and Douglas P. Finkbeiner. Giant Gamma-ray Bubbles from Fermi-LAT: Active Galactic Nucleus Activity or Bipolar Galactic Wind? *ApJ*, 724(2):1044–1082, Dec 2010.

[7] E. Carretti, R. M. Crocker, L. Staveley-Smith, M. Haverkorn, C. Purcell, B. M. Gaensler, G. Bernardi, M. J. Kesteven, and S. Poppi. Giant magnetized outflows from the centre of the Milky Way. *Natur*, 493:66–69, Jan 2013.

[8] A. J. Young, A. S. Wilson, and P. L. Shopbell. A Chandra X-Ray Study of NGC 1068. I. Observations of Extended Emission. *A&A*, 556(1):6–23, Jul 2001.

[9] Judith A. Irwin and D. J. Saikia. Giant Metrewave Radio Telescope observations of NGC 3079. *MNRAS*, 346(3):977–986, Dec 2003.

[10] R. P. Kraft, S. E. Vázquez, W. R. Forman, C. Jones, S. S. Murray, M. J. Hardcastle, D. M. Worrall, and E. Churazov. X-Ray Emission from the Hot Interstellar Medium and Southwest Radio Lobe of the Nearby Radio Galaxy Centaurus A. *A&A*, 592:129–146, Jul 2003.

[11] Gyula I. G. Józsa, Sarah V. White, Kshitij Thorat, Oleg M. Smirnov, Paolo Serra, Mpati Ramatsoku, Athanaseus J. T. Ramaila, Simon J. Perkins, Dániel Cs. Molnár, Sphesihle Makhathini, Filippo M. Maccagni, Dane Kleiner, Peter Kamphuis, Benjamin V. Hugo, W. J. G. de Blok, and Lexy A. L. Andati. MeerKATHI – an end-to-end data reduction pipeline for MeerKAT and other radio telescopes. *Conference proceedings of the Astronomical Data Analysis Software and Systems XXIX, to appear in ASPC.* (in press), 2020.

[12] K. Thorat et al. (in prep), 2020.

[13] B. Mingo, M. J. Hardcastle, J. H. Croston, D. A. Evans, P. Kharb, R. P. Kraft, and E. Lenc. Shocks, Seyferts, and the Supernova Remnant Connection: A Chandra Observation of the Circinus Galaxy. *A&A*, 758:95, Oct 2012.

[14] M. Ackermann et al. The Spectrum and Morphology of the Fermi Bubbles. *A&A*, 793(1):64, Sep 2014.

[15] M. Hayashida, Ł. Stawarz, C. C. Cheung, K. Bechtol, G. M. Madejski, M. Ajello, F. Massaro, I. V. Moskalenko, A. Strong, and L. Tibaldo. Discovery of GeV Emission from the Circinus Galaxy with the Fermi Large Area Telescope. *ApJ*, 779:131, Dec 2013.

[16] The Fermi-LAT collaboration. Fermi Large Area Telescope Fourth Source Catalog. *arXiv e-prints*, page arXiv:1902.10045, Feb 2019.

A radiative transfer model for hydrogen recombination line masers

A Prozesky[1] **and D P Smits**[1]

[1] Department of Mathematical Sciences, University of South Africa, Private Bag X6, Florida 1709, South Africa

E-mail: prozea@unisa.ac.za

Abstract. Maser emission arises when spectral lines are enhanced through radiative transfer effects and are observed to be very bright. Molecular astronomical masers have proved to be a very useful tool to probe conditions in a wide variety of sources. Masers are also produced by atomic hydrogen formed by recombination in sufficiently dense HII regions. These hydrogen recombination line (HRL) masers have been observed in a handful of objects to date but the analysis of the atomic physics involved has been rudimentary. In this work a new model of HRL masers is presented that uses an nl-method model to describe the atomic populations interacting with free-free radiation from the plasma, and an escape probability framework to deal with radiative transfer effects. The model is used to describe the general behaviour of radiative transfer of HRLs and to investigate the conditions under which HRL masers form.

1. Background

1.1. Hydrogen recombination line masers

Astronomical masers occur when spectral lines are amplified through stimulated emissions over long path lengths, producing line emission that is much brighter than expected under local thermodynamic equilibrium (LTE) conditions. Traditional astronomical masers occur due to rotational or vibrational transitions of various molecules, and have been studied extensively both observationally and theoretically. More recently, recombination line masers from atomic hydrogen have been observed in a few objects.

[1] showed that recombination lines can be amplified by stimulated emission in the Rayleigh-Jeans limit, even at low optical depths. The theoretical possibility of HRL masers was considered by [2] to account for the anomalous hydrogen line intensities found in dense gasses associated with active galactic nuclei. The first cosmic high-gain HRL maser was discovered in the young stellar object MWC 349A [3, 4]. This maser source has since been studied extensively [5, 6, 7, 8, 9, 10, 11] with the evidence confirming the presence of strongly masing recombination lines. For some time, MWC 349A was the only source in which HRL masers had been detected, but growing interest in the subject has prompted more searches, leading to the identification of a number of HRL masers in other objects, see for example [12], [13], [14] and [15].

The environments in which these atomic masers can form are distinctly different from those of their molecular counterparts. For recombination lines to form, the emitting gas has to be ionized, which for hydrogen requires a temperature of $\sim 10^4\,\mathrm{K}$. The host clouds of molecular masers are necessarily cooler than the molecules' dissociation temperature and, therefore, are relatively cool ($T \leq 10^3\,\mathrm{K}$).

 ISBN: 978-0-620-88875-2

A population inversion occurs in hydrogen over a large range of atomic levels in a recombination nebula, whereas in molecular masers the inversion is often limited to a few levels only. A result of this is that many adjacent HRL lines will exhibit masing behaviour at the same time instead of just a few specific lines, as is the case with molecules. In HRL masers, the pumping scheme for the population inversions is a natural consequence of the capture-cascade processes in the atomic component of the ionized gas, which is discussed in more detail in [16]. In many molecular masers the details associated with the pumping scheme are unclear. It should also be noted that because hydrogen makes up the bulk of almost all astronomical gasses, the hydrogen masing lines can be seen in very high column densities. For molecular masers the relevant constituents have low number densities compared to the H_2 content.

There have been some endeavours to construct a theoretical framework for HRL masers. [17] extended the departure coefficient calculations of [18] to higher densities in response to the discovery of the first HRL maser source. [16] addressed the theoretical foundations of HRL masers and considered conditions necessary for their formation.

Most theoretical models for HRL masers have focused on the morphology of the emitting region [8, 19, 11], leading to the suggestion that the masing is strongly related to the structure and kinematics of the emitting gas [20]. Most notable is the three-dimensional non-LTE radiative transfer code MORELI [21]. MORELI uses pre-calculated departure coefficients of either [17] or [22], but does not solve the statistical balance equations (SBE) in a self-consistent way.

[23] incorporated radiative transfer effects into a capture-collision-cascade (C^3) model to assess the effects of saturation on the level populations. They employed an n-model which neglects the effects of the elastic collisions between angular momentum states, as opposed to an nl-model in which they are included. [23] found that the effects of the radiative transfer on the level populations of hydrogen are important.

2. Radiative transfer

The equation of radiative transfer (ERT) describes the radiation added to and subtracted from a given ray as it travels through a medium and is given by

$$\frac{\mathrm{d}I_\nu}{\mathrm{d}l} = -\kappa_\nu I_\nu + j_\nu, \tag{1}$$

where I_ν is the specific intensity and l is the path along the ray. The volume emission and absorption coefficients at the frequency ν are given by j_ν and κ_ν, respectively. The source function is defined as $S_\nu = j_\nu/\kappa_\nu$.

The line emission coefficient j_{nm} describes radiation added to the spectral line of the $n \to m$ transition due to spontaneous emissions and is given by

$$j_{nm} = \frac{h\nu}{4\pi} \sum_{l=0}^{n-1} \sum_{l'=l\pm1} b_{nl} N^*_{nl} A_{nl,ml'} \tag{2}$$

where h is Planck's constant, b_{nl} is the departure coefficient of level nl, N^*_{nl} is the population of level nl in LTE and $A_{nl,ml'}$ is the Einstein A-value for the $nl \to ml^{'}$ transition.

The line absorption coefficient κ_{mn} gives the contribution of absorptions (B_{mn}) and stimulated emissions (B_{nm}) to the emerging radiation field as

$$\kappa_{mn} = \frac{h\nu}{4\pi} \left(N_m B_{mn} - N_n B_{nm}\right) \tag{3}$$

$$= \frac{h\nu}{4\pi} \sum_{l=0}^{n-1} \sum_{l'=l\pm1} b_{ml'} N^*_{ml'} B_{ml',nl} \left(1 - \frac{b_{nl}}{b_{ml'}} \mathrm{e}^{-h\nu/kT_\mathrm{e}}\right), \tag{4}$$

where k is the Boltzmann constant and $T_{\rm e}$ is the temperature of the free electron gas, which is assumed to have a Maxwellian distribution.

From the definition in equation (3), it is clear that κ_{mn} can become negative if the number of stimulated emissions exceeds the number of absorptions, thereby increasing the line intensity. The term inside brackets in equation (4) is the correction for stimulated emission.

At low enough frequencies, when the continuum is significant, which usually occurs in the Rayleigh-Jeans limit, the line and continuum radiation are formed together. This means the net quantities (indicated by subscripts ν) in equation (1) must take into account the contributions of both the line radiation and the continuum (indicated by subscripts c), so that

$$\kappa_\nu = \kappa_{mn}\phi_\nu + \kappa_{\rm c}, \qquad j_\nu = j_{nm}\phi_\nu + j_{\rm c}\,. \tag{5}$$

where the spectral line shape, assumed to be the same for emission and absorption, is described by ϕ_ν . A box profile with the same line centre maximum as the Doppler profile is assumed for all lines in this work.

The net source function S_ν is given by

$$S_\nu = \frac{j_{nm}\phi_\nu + j_{\rm c}}{\kappa_{mn}\phi_\nu + \kappa_{\rm c}}\,. \tag{6}$$

For an homogeneous medium of thickness L the optical depth is given by

$$\tau_\nu = -L\kappa_\nu\,. \tag{7}$$

In our models, the continuum absorption coefficient $\kappa_{\rm c}$ in the Rayleigh-Jeans regime is calculated using the expression of [24]. The continuum emission coefficient is given by $j_{\rm c} = \kappa_{\rm c} B_\nu(T_{\rm e})$, where B_ν is the Planck distribution function.

3. The escape probability approach

When solving a C^3-type model, such as described in [25], it is standard practice to use the Case A/B assumption of [26]. This assumption has been found to work well for nebular conditions where densities are low and line radiation is optically thin ($\tau \ll 1$) [27]. In the other extreme, the cloud is completely optically thick to all line radiation ($\tau_\nu \gg 1$), so that all the level populations have Boltzmann distributions and the mean intensity $J_\nu = B_\nu$.

The escape probability approximation (EPA) addresses the situation between these two extremes: a portion of the radiation is trapped in the cloud and the rest is allowed to escape. If the fraction of photons with frequency ν that escape the cloud is labeled β_ν, then the mean intensity can be approximated by

$$J_\nu = (1 - \beta_\nu)\, S_\nu\,. \tag{8}$$

Strictly speaking, β_ν depends on the full solution of the ERT and cannot be calculated locally. However, if an approximation can be derived that depends only on the geometry and local properties of the cloud and is independent of intensity, then the original problem is greatly simplified.

The EPA has been used extensively to model molecular masers (see for example [28, 29, 30, 31, 32, 33]). In this work

$$\beta_\nu = {\rm e}^{-\tau_\nu} \tag{9}$$

is used for the escape probability. This form of β_ν does not make any additional assumptions regarding the geometry or the changes in transfer effects throughout the line profile and, therefore, is appropriate to use if these details are not known.

4. The model

The EPA model used here is similar to that of [23] with some important improvements. Most significantly, it includes the effects of the elastic collisions so the calculations are done with a full nl-model. Also, the effects of free-free radiation on the level populations have been incorporated. Nevertheless, we use the same form of the escape probability and general calculational approach.

Our atomic model is based on the C^3 nl-model described in [25] that was adapted to incorporate radiative transfer using the EPA as described in section 3. All atomic rates are as described in [25].

The SBE are solved in the optically thin case ($\beta_\nu = 1$ for all lines) to yield departure coefficients that are equivalent to the ones given in [25] for Case A. From the calculated values of b_{nl}, the net absorption coefficients, emission coefficients and source functions are calculated for each line using equations (2), (4) and (6).

The path length L is then increased and the optical depths and escape probabilities are calculated from equations (7) and (9), respectively. The resulting mean intensities are calculated for each line frequency using equation (8). The SBE are solved again with these values of J_ν incorporated into the rates of the absorption and stimulated processes. The process is repeated for increasing increasing values of L.

values of L.

5. Results and discussion

5.1. Conditions for H masers

The pumping mechanism for hydrogen masers is the ionization-recombination cycle, so it is important that the gas is ionized. Canonically, ionized hydrogen nebulae are taken at $T_e \sim 10^4$, but mechanisms such as forbidden line emission due to high metallicity can cool the gas to much lower temperatures than this while keeping the hydrogen mostly ionized, which occurs in some nova shells. If the electron temperature is too high, the interactions between the free and bound electrons become very fast and the populations of the bound electrons thermalize.

Spectral lines will exhibit high gain maser action if the conditions are such that stimulated emissions become the dominant atomic process and $\tau_\nu < -1$. This requires large column densities along the lines of sight, which can be achieved with either high number densities of hydrogen atoms or long path lengths. Masers require velocity coherence along the amplification path, so there is an upper limit on the path length. The model results show that a path length of $L \sim 10^{16}$ cm is required to have maser action at a density of $10^6\,\mathrm{cm}^{-3}$. Each order of magnitude decrease in N_e results in about an order of magnitude increase required in L to produce the same amplification.

5.2. General trends

Fig. 1 shows how the intensities change as the path length is increased in the model at frequencies of various H$n\alpha$ transitions. For small path lengths, the intensities at all frequencies increase linearly with path length, as is expected for optically thin lines. The behaviour of the line intensities change at the point when $|\tau_\nu| > 1$ in one of two ways, depending on whether τ_ν is positive or negative.

For the conditions shown in Fig. 1, the lines with $n \geq 40$ have positive optical depths. The level populations for these lines are not strictly inverted, but are "overheated" as discussed in [16]. The upper level of these lines are overpopulated with respect to the LTE populations so that the lines are enhanced by stimulated emissions even though the absorption coefficients for these lines are positive. These intensities increase linearly with path length until the cloud becomes larger than their characteristic path length (for which $\tau_\nu = 1$). Once they are optically thick, their intensities remain constant as the size of the cloud is increased, because they cannot be observed from deeper in the cloud than their characteristic path length. The lower frequency

(higher n) lines become optically thick first as L is increased, since the absorption coefficients increase with n beyond the masing lines.

The optical depths of the H15α and H20α lines are negative and their intensities start to increase exponentially with path length when $\tau_\nu < -1$ and maser action sets in. The optical depth of the H5α line is also negative, but $\tau_\nu > -1$ at the path length where the model is terminated.

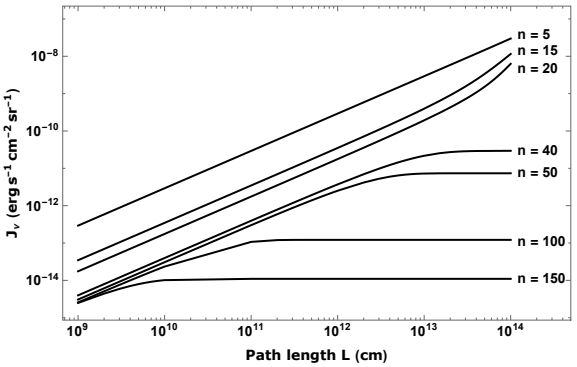

Figure 1. The change of the intensities at frequencies of various H$n\alpha$ transitions with path length for a gas at $T_\mathrm{e} = 10^4\,\mathrm{K}$ and $N_\mathrm{e} = 10^8\,\mathrm{cm}^{-3}$.

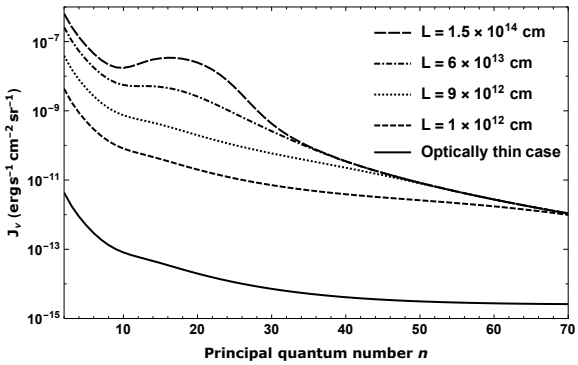

Figure 2. Intensities at the frequencies of H$n\alpha$ transitions with respect to principal quantum number for a gas with $T_\mathrm{e} = 10^4\,\mathrm{K}$ and $N_\mathrm{e} = 10^8\,\mathrm{cm}^{-3}$ for different path lengths.

Fig. 2 shows the intensities at H$n\alpha$ line frequencies for a gas with $T_\mathrm{e} = 10^4\,\mathrm{K}$ and $N_\mathrm{e} = 10^8\,\mathrm{cm}^{-3}$ as a function of n for different path lengths. The intensities increase universally from the optically thin values as L is increased as was also illustrated in Fig. 1. As L increases, the lines become optically thick from high values of n, and then do not increase further. If the path length becomes large enough that $\tau_\nu < -1$ for some lines, a bump starts to appear, indicating maser action in the affected lines. As the path length is increased further, the intensities of the masing lines increase significantly with L as the degree of saturation for the masing lines increases.

6. Conclusions

Hydrogen recombination masers are a relatively new field of study with only a small number of examples detected so far. There are some important differences between molecular and atomic hydrogen masers, both on the macro scale, such as in the environments where they form, and at the atomic level, such as in the pumping mechanism and the mutual interaction of many masing lines. The theoretical framework for these objects is still developing and the aim of this paper is to contribute to our understanding by constructing a theoretical model that specifically focuses on the atomic process rather than the geometry and kinematics.

The modeling of masers has some inherent complexities, due to having to solve simultaneously both the local level populations of the masing species, and the non-local radiative transfer of the line photons. Simplifying assumptions, such as the EPA used here, are often employed to make the solutions tractable.

A model for hydrogen recombination masers using the EPA has been constructed to evaluate the general behaviour of hydrogen emission from clouds with conditions where masing is possible. The model results correspond well to our current understanding of how masers grow with increasing path length.

References

[1] Goldberg L 1966 *ApJ* **144** 1225–1231
[2] Krolik J H and McKee C F 1978 *ApJS* **37** 459–483
[3] Martin-Pintado J, Bachiller R, Thum C and Walmsley M 1989 *A&A* **215** L13–L16
[4] Martin-Pintado J, Thum C and Bachiller R 1989 *A&A* **222** L9–L11
[5] Planesas P, Martin-Pintado J and Serabyn E 1992 *ApJ* **386** L23
[6] Thum C, Martin-Pintado J and Bachiller R 1992 *A&A* **256** 507–518
[7] Martin-Pintado J, Neri R, Thum C, Planesas P and Bachiller R 1994 *A&A* **286** 890–897
[8] Ponomarev V O, Smith H A and Strelnitski V S 1994 *ApJ* **424** 976–982
[9] Thum C, Martin-Pintado J, Quirrenbach A and Matthews H E 1998 *A&A* **333** L63–L66
[10] Gordon M A, Holder B P, Jisonna Jr L J, Jorgenson R A and Strelnitski V S 2001 *ApJ* **559** 402–418
[11] Weintroub J, Moran J M, Wilner D J, Young K, Rao R and Shinnaga H 2008 *ApJ* **677** 1140–1150 (*Preprint* 0801.0608)
[12] Cox P, Martin-Pintado J, Bachiller R, Bronfman L, Cernicharo J, Nyman L A and Roelfsema P R 1995 *A&A* **295** L39–L42
[13] Jiménez-Serra I, Báez-Rubio A, Rivilla V M, Martín-Pintado J, Zhang Q, Dierickx M and Patel N 2013 *ApJ* **764** L4 (*Preprint* 1212.0792)
[14] Aleman I, Exter K, Ueta T, Walton S, Tielens A G G M, Zijlstra A, Montez R, Abraham Z, Otsuka M, Beaklini P P B, van Hoof P A M, Villaver E, Leal-Ferreira M L, Mendoza E and Lépine J D R 2018 *MNRAS* **477** 4499–4510 (*Preprint* 1805.06496)
[15] Murchikova E M, Phinney E S, Pancoast A and Blandford R D 2019 **570** 83–86 (*Preprint* 1906.08289)
[16] Strelnitski V S, Ponomarev V O and Smith H A 1996 *ApJ* **470** 1118–+ (*Preprint* arXiv:astro-ph/9511118)
[17] Walmsley C M 1990 *A&AS* **82** 201–206
[18] Brocklehurst M and Salem M 1977 *Computer Physics Communications* **13** 39–48
[19] Strelnitski V S, Smith H A and Ponomarev V O 1996 *ApJ* **470** 1134 (*Preprint* astro-ph/9511119)
[20] Martín-Pintado J 2002 *Cosmic Masers: From Proto-Stars to Black Holes* (*IAU Symposium* vol 206) ed Migenes V and Reid M J p 226
[21] Báez-Rubio A, Martín-Pintado J, Thum C and Planesas P 2013 *A&A* **553** A45 (*Preprint* 1307.3896)
[22] Storey P J and Hummer D G 1995 *MNRAS* **272** 41–48
[23] Hengel C and Kegel W H 2000 *A&A* **361** 1169–1177
[24] Oster L 1961 *Rev. Mod. Phys.* **33** 525–543
[25] Prozesky A and Smits D P 2018 *MNRAS* **478** 2766–2776 (*Preprint* 1805.02440)
[26] Baker J G and Menzel D H 1938 *ApJ* **88** 52
[27] Osterbrock D E 1962 *ApJ* **135** 195–+
[28] Sobolev A M, Cragg D M and Godfrey P D 1997 *A&A* **324** 211–220
[29] Cragg D M, Sobolev A M and Godfrey P D 2002 *MNRAS* **331** 521–536
[30] Langer S H and Watson W D 1984 *ApJ* **284** 751–768
[31] Chandra S, Kegel W H, Albrecht M A and Varshalovich D A 1984 *A&A* **140** 295–302
[32] Röllig M, Kegel W H, Mauersberger R and Doerr C 1999 *A&A* **343** 939–942
[33] Humphreys E M L, Yates J A, Gray M D, Field D and Bowen G H 2001 *A&A* **379** 501–514

Surface brightness profiles of nearby central group galaxies

S Hattingh[1] **and S I Loubser**[1]

Centre for Space Research, North-West University, Potchefstroom, South Africa

E-mail: sumarihatt@gmail.com

Abstract. Galaxy groups offer an excellent opportunity to study the impact of galaxies on their intergalactic medium (IGM), and vice versa, as the galaxy's heating process effects are more visible due to the groups' lower density and mass compared to clusters of galaxies. This project is part of an optical observational campaign to observe the Complete Local-Volume Groups Sample (CLoGS), which is a statistically-complete sample of 53 groups within 80 Mpc. Radio observations (GMRT & VLA), X-ray bands, and sub-mm (IRAM-30m) data are already available for the entire sample. Here, we are interested in accurate surface brightness (SB) profiles of these central, dominant elliptical galaxies in the groups as this directly relates to their stellar mass profiles. The SB profiles can be used to measure structural parameters e.g. the size of the core, contains detail of the assembly histories of the galaxies, and can ultimately be used to calculate dark matter density profiles if combined with dynamical (total) mass measurements from spectra.

1. Introduction

The location of dominant galaxies in the centres of the groups suggests a particularly extensive evolution history where the stellar mass is buildup through frequent mergers with smaller galaxies [1]. As SB profiles can be used to measure structural parameters and since they directly relate to the stellar mass profiles, it should display several observational signatures of how these galaxies formed. One example of a structural property we can measure from accurate SB profiles is the presence and size of cores. The formation of the most massive early-type galaxies took place by mergers of pre-existing gas free galaxies [2] and it is then suggested that the core is naturally formed as an end-point of this process. This explains why cores are found in nearly all luminous early-types [3];[4].

2. Data

CLoGS is an optically-selected and statistically-complete sample of groups in the nearby Universe, which is specifically chosen and studied with optical observations for this project, since radio and X-ray bands [5] are already available. This provides important physical properties of the IGM such as gas temperature and the total X-ray luminosity, both probing the environment in which the group members are located [6]. Together, the CLoGS observations can be used to investigate the role of active galactic nuclei (AGNs) in maintaining the thermal balance of the IGM, to name one example.
In order to get the SB profiles that we need, we make use of R-band (or equivalent) imaging and the Multi-Gaussian Expansion (MGE) fitting method. We apply the MGE fitting to the R-band images of 35 central group galaxies, from archival Hubble Space Telescope (HST) and Canada-France-Hawaii Telescope (CFHT) MegaCam imaging. For 12 of the 35 groups, we also present new CFHT MegaCam observations obtained in 2018/2019. We will also measure the sizes of the cores of these galaxies and

correlate it with other physical properties of the galaxies and host groups.

We find that the 35 group galaxies of CLoGS have different morphologies. NGC4261, for example, is an elliptical galaxy. However, the Flexible Image Transport System (FITS) [7] image of this central group galaxy, retrieved from the Hubble Legacy Archive, shows a well defined disk of dust in the centre (see Figure 1), well known from an earlier study [8]. We find three more similar disks (refer to Figure 1). All four of these central group galaxies host radio jets [5].

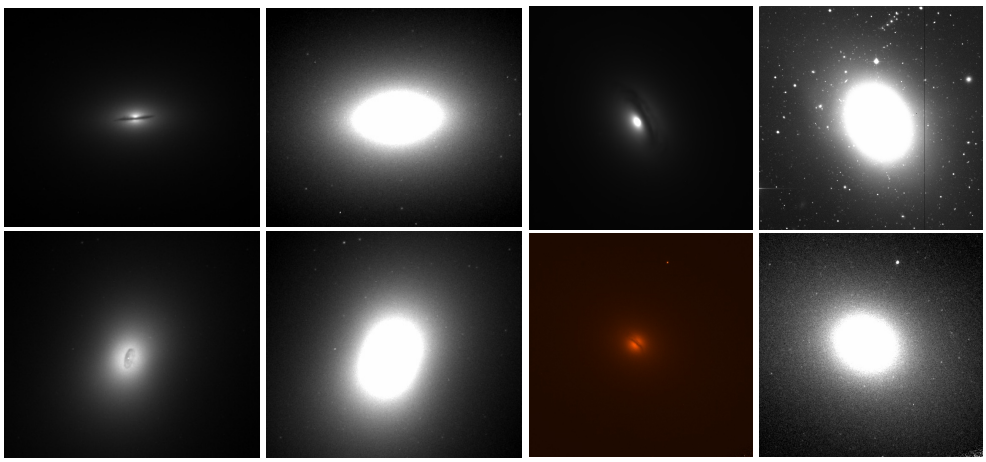

Figure 1. We show the four central group galaxies with two different contrast algorithms applied. *Top row, from left to right:* NGC5322 (HST) in minmax scale, NGC5322 in zscale, NGC3665 (one of the New MegaCam observations) in minmax scale, NGC3665 in zscale. *Bottom row:* NGC4261 (HST) in minmax scale, NGC4261 in zscale, NGC5127 (HST) in minmax scale (heat colour), NGC5127 in zscale.

Figure 1 shows a few examples indicating the different morphologies for some of the central group galaxies that we have analysed. Four central group galaxies, NGC5322, NGC3665, NGC4261 and NGC5127 are shown. These different colours and scales were set in SAO ds9 for each FITS image.

Method

We use the MGE method [9], as implemented by [10]. This method reproduces detailed photometry, which allows for variations of ellipticity. The MGE procedure starts with determining the galaxy's average ellipticity (ε), the orientation (or position angle, PA), and the luminosity-weighted central coordinates (x_{cen}, y_{cen}). Next, the galaxy image is divided into four quadrants, and detailed photometric profiles are measured along sectors which are uniformly spaced in orientation (angle) from the major- to minor axis. The average of the SB profiles from sectors in the four quadrants are taken together, and each is then fitted as the sum of Gaussian components. The best-fitting MGE model SB is determined by convolving it with the instrumental point spread function (PSF) and comparing to the observed SB. The projected MGE surface brightness (Σ) is defined as follows:

$$\Sigma(x', y') = \sum_{j=1}^{N} I'_j exp\left[-\frac{1}{2\sigma'^2_j}(x'^2 + \frac{y'^2}{q'^2_j})\right] \quad (1)$$

with N indicating the Gaussian components that the model is composed, I'_j as the distance-independent surface density, σ'_j the dispersion in units of *arcsec* along the major x'-axis and q'_j the flattening for each Gaussian. The MGE surface density can be de-projected analytically [11] to obtain the intrinsic density $\rho_*(R,z)$ in the galaxy meridional plane, which can be still expressed as the sum of Gaussians, under the assumptions of the MGE method, and for a given inclination i.

The results of the MGE method can be used to convert the total counts of each Gaussian (C_0) into corresponding peak SB with physical units. The equation, to determine the total counts of each Gaussian, C_0, is defined by [10]:

$$C_0 = \frac{TotalCounts}{2\pi SigmaPixels^2 q} \tag{2}$$

with q as the observed axial ratio for each Gaussian component. By making use of standard photometry formulae, the peak SB C_0 can be converted into SB μ_R with units of $mag \cdot arcsec^{-2}$. This is defined by the equation to a first approximation [10]; [12]:

$$\mu_R = zeropoint + 0.1 + 5log(SCALE) + 2.5log(EXPtime) - 2.5logC_0 - A_R \tag{3}$$

for all the R-band images. The parameters used are the photometric *zeropoint* (25.94 for HST images of filter F814W, 26.52 and 26.74 for MegaCam images of filters R.MP9601 and r.MP9601, respectively) in AB magnitude, a correction for infinite aperture of SB measurements (0.1), the spatial scale (0.0455 $arcsec \cdot pixels^{-1}$ for HST images of filter F814W, 0.206 $arcsec \cdot pixels^{-1}$ and 0.187 $arcsec \cdot pixels^{-1}$ for MegaCam images of filters R.MP9601 and r.MP9601, respectively), the exposure time (varying for every galaxy; from 460s to 2460s), the peak SB (C_0) and the galactic extinction (A_R) [13] from the recalibration of the [14] infrared-based dust map.

3. Results

The MGE fitting method was applied to 35 (of the 53) central group galaxies from CLoGS. From the Hubble Space Telescope (HST) archive we obtained 16 central group galaxies, four from the Canadian Astronomy Data Centre (CADC): Canada-France-Hawaii Telescope (CFHT) as stacked MegaCam archival data and 12 from new observations with CFHT MegaCam. Only some of the results from each telescope will be presented here as examples.

3.1. HST images

The MGE method was used for 16 FITS images, retrieved from the Hubble Legacy Archive. The filter of these images is F814W and is less affected by dust. Here, we present the results of the MGE fitting method for one central group galaxy, NGC0315, an elliptical galaxy. Figure 2 shows the determination

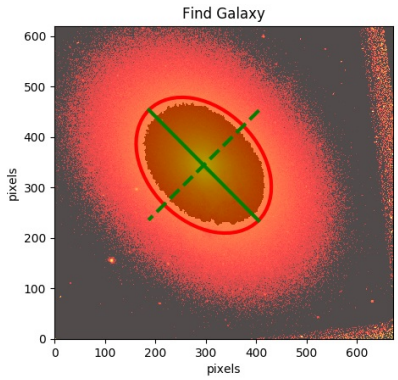

Figure 2. This procedure computes the centre, orientation and ellipticity of NGC0315.

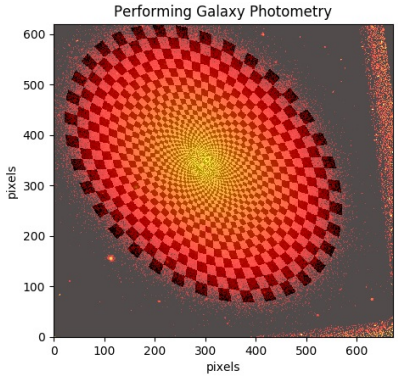

Figure 3. Galaxy photometry is measured along sectors linearly spaced in angle and covering the whole image.

of the precise position of the galaxy's centre as well as the orientation with respect to the image axes

($PA = 44.8deg$) and the ellipticity ($\varepsilon = 0.283$). The galaxy image of NGC0315 is then divided into four quadrants. For the next step of the method, Figure 3 shows detailed photometric profiles measured along (uniformly spaced) sectors in orientation from the major- to minor axis.
The next step of the method is shown by Figure 4 where the best-fitting parameters at the end of the fit are shown. Here, the best-fitting model Gaussians are shown, as well as the deviation from the observed data. This third step takes the average of the SB profiles together, from sectors in all four quadrants, and each is then fitted as the sum of Gaussian components. From the fitting method's output results, it was found that NGC0315 can be described with three nonzero Gaussian components.

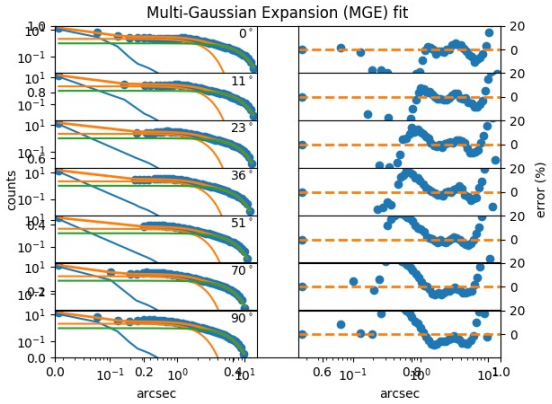

Figure 4. The MGE fit is determined by starting from the photometry at the previous step. *Left:* The best-fit model (solid line) fitted on the counts (blue circles) varying for Gaussian components (in colours of blue, green, orange and yellow). *Right:* The error percentage, showing the goodness of fit of the MGE for NGC0315.

After the best-fitting parameters have been determined from the previous step, the fitting method will use these parameters to produce contour plots that compares the PSF-convolved MGE fit model to the actual (original) fitted image, making use of instrumental units of counts (for intensity) and pixels (for the spatial scale). These results are shown by Figure 5.

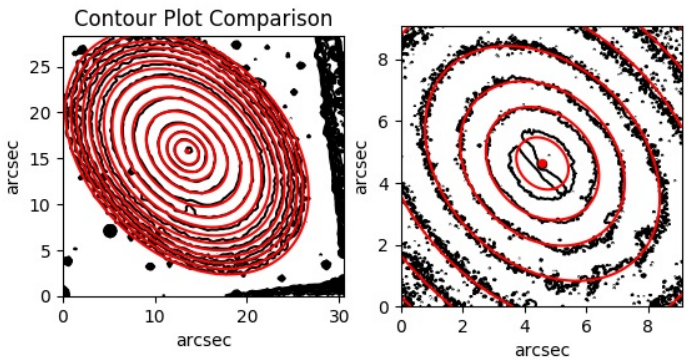

Figure 5. Contours (red colour) expand from the centre outwards. *Left:* PSF-convolved MGE fit. *Right:* MGE fit on original image.*Left:* Contours are superimposed on the MGE fitting model convolved with the PSF. *Right:* Contours are overlaid on the central part of the (original fitted) image of NGC0315 that has been extracted and plotted at high resolution.

3.2. MegaCam archival images
Four R-band images were analysed with the MGE fit method, from the Canadian Astronomy Data Centre (CADC): Canada-France-Hawaii Telescope (CFHT) Science Archive. Stacked MegaCam data was used.

The specific filters for the R-band are R.MP9601 and r.MP9601. Image Reduction and Analysis Facility (IRAF) was used to copy a portion of the CFHT R-band FITS image, consisting of the central group galaxy from a wide field image. Here, we present only the final results of the MGE fitting method of one central group galaxy NGC3613, an elliptical galaxy, as an example.
Figure 6 is the output results of the third step of the MGE fitting method - showing the best-fitting parameters at the end of this fit. The average of the SB profiles taken together were fitted as the sum of Gaussian components. From the fitting method's output results, it was found that NGC3613 can be described by five nonzero Gaussian components. The instrumental units used are the same as indicated previously.

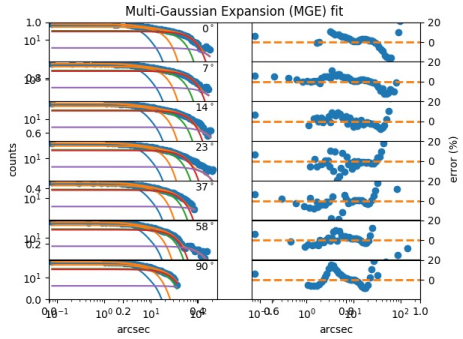

Figure 6. Determines the MGE fit of NGC3613 by starting from the photometry at the previous step. *Left:* The best-fit model (solid line) fitted on the counts (blue circles) varying for Gaussian components (in colours of blue, green, orange an yellow). *Right:* The error percentage, showing the goodness of fit of the MGE.

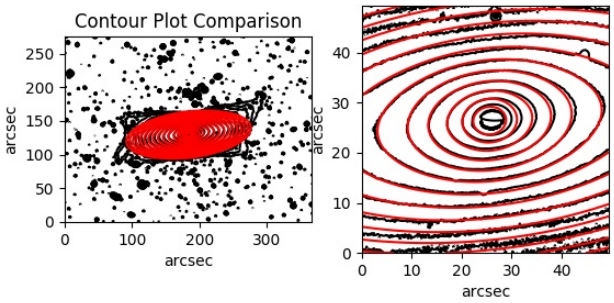

Figure 7. Contours, indicated in red colour, expand from the centre outwards. This visual comparison ensures that the MGE fitting routine focuses on a small central part of the galaxy so that the best-fitted parameters could be produced. *Left*: PSF-convolved MGE fitted model. *Right*: Contours are overlaid on the (original fitted) image of NGC3613 as plotted at high resolution.

3.3. New MegaCam observations

New images were observed with CFHT MegaCam for 12 groups. IRAF was used to copy a portion of the FITS image, consisting of the central group galaxy. After this, the same MGE fitting was executed. Here, we also present only the final results of the MGE fitting method of the central group galaxy, NGC0410, an elliptical galaxy, as an example. For the third step of the method, Figure 8 shows best-fit model (solid line) fitted on the counts (blue circles). After the average of the SB profiles was taken, it was fitted as the sum of Gaussian components (different coloured solid lines) - from which NGC0410 can be described with five nonzero Gaussian components. The plot is shown in Figure 8, and the instrumental units that were used are the same as for Figures 4 and 6.

4. Conclusions

For this project, we have used the MGE fitting method in order to get accurate SB profiles of 35 central group galaxies (of the CLoGS sample) of which the results of only three are presented in this article, as examples.
We firstly show the surprising result that four elliptical central group galaxies show disks of dust in the

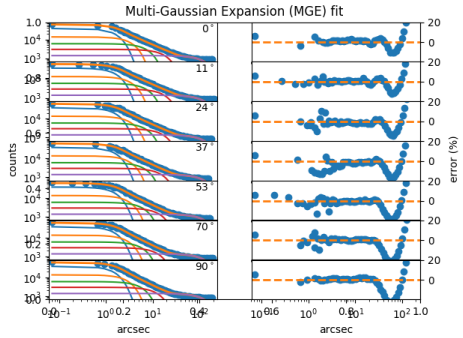

Figure 8. *Left:* The best-fit model (solid line) fitted on the counts (blue circles) varying for Gaussian components (different coloured solid lines). *Right:* The error percentage, showing the goodness of fit of the MGE.

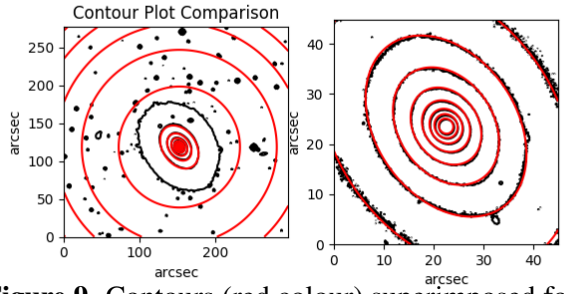

Figure 9. Contours (red colour) superimposed for the PSF-convolved MGE fitted model (left) and overlaid on the (original fitted) image (right) of NGC0410. This comparison shows us that the contour lines are superimposed well onto the original observed image, focusing on the central part of the galaxy.

centre, of which one (NGC4261) was previously known and described in an earlier study [8]. We find a range of morphologies for the 35 central group galaxies ranging from clear spiral arms and bulges to round elliptical galaxies.

The MGE fitting method is effective for these central galaxies, and we will in future work also fit broken power-laws to compare the results in order to get accurate SB profiles we need, and measure size of cores.

Acknowledgments

Acknowledgments SH is supported by the National Astrophysics and Space Science Programme (NASSP). SIL is supported by the National Research Foundation (NRF) of South Africa.

References

[1] Khochfar S, Silk J 2006 On the origin of stars in bulges and elliptical galaxies *MNRAS* **370** 902
[2] Faber S M et al 1997 The centres of early-type galaxies with HST-iv: central parameter relations *AJ* **114** 1771
[3] Laine S et al 2003 Hubble space telescope imaging of brightest cluster galaxies *AJ* **125** 478
[4] Lauer T R et al 2007 The centres of early-type galaxies with Hubble Space Telescope-vi: bimodal central surface brightness profiles *ApJ* **664** 226
[5] Kolokythas K et al 2018 The complete local-volume groups sample-ii: a study of the central radio galaxies in the high-richness sub-sample *MNRAS* **481** 1550
[6] O'Sullivan E et al 2017 The complete local-volume groups sample-i: sample selection and X-ray properties of the high-richness subsample *MNRAS* **472** 1482
[7] Hanisch R J et al 2001 Definition of the flexible image transport system (FITS) *A&AS* **376** 359
[8] Jaffe W et al 1996 The nuclear disk of NGC 4261: hubble space telescope images and ground-based spectra *ApJ* **460** 214
[9] Emsellem E, Monnet G and Bacon R 1994a The multi-gaussian expansion method: a tool for building realistic photometric and kinematical models of stellar systems *A&AS* **285** 723
[10] Cappellari M 2002 Efficient multi-gaussian expansion of galaxies *MNRAS* **366** 1126
[11] Monnet G, Bacon R and Emsellem E 1992 Modelling the stellar intensity and radial velocity fields in triaxial galaxies by sums of gaussian functions *A&AS* **253** 366
[12] Holtzman J A et al 1995 The photometric performance and calibration of WFPC2 *PASP* **107** 1065
[13] Schlafly E F, Finkbeiner D P 2011 Measuring reddening with sloan digital sky survey stellar spectra and recalibrating SFD *ApJ* **737** 103
[14] Schlegel D J, Finkbeiner D P and Davis M 1998 Maps of dust infrared emission for use in estimation of reddening and cosmic microwave background radiation foregrounds *ApJ* **500** 525

Phenomenology of axion-like particles coupling with photons in the jets of active galactic nuclei

Ahmed Ayad and Geoff Beck

School of Physics, University of the Witwatersrand, Private Bag 3, WITS-2050, Johannesburg, South Africa

E-mail: ahmed@aims.edu.gh

Abstract. Axions or more generally axion-like particles (ALPs) are pseudo-scalar particles predicted by many extensions of the Standard Model of particle physics (SM) and considered as highly viable candidates for dark matter (DM) in the universe. If they exist in nature, they are expected to couple with photons in the presence of an external magnetic field through a form of the Primakoff effect. In this work, we examine the detectability of signals produced by ALP-photon coupling in the highly magnetized environment of the relativistic jets produced by active galactic nuclei (AGNs). Furthermore, we use the environment of the M87 AGN jet to test a Cosmic ALP Background (CAB) model, motivated by its explanation of the Coma cluster soft X-ray excess. We then demonstrate the potential of the environment of M87 AGN jet to probe low-mass ALP models and to potentially constrain the CAB model proposed to explain the Coma cluster X-ray excess.

1. Introduction

An outstanding result of modern cosmology is that only a small fraction of the total matter content of the universe is made of baryonic matter, while the vast majority is constituted by dark matter (DM) [1]. However, the nature of such a component is still unknown. Light scalar candidates of DM such as axions and axion-like particles (ALPs) are one of the well-motivated hypotheses to explain the nature of DM. Axions [2, 3] are pseudo-Nambu-Goldstone bosons that appear after the spontaneous breaking of the Peccei-Quinn symmetry. These particles were introduced to solve the CP-violation problem of the strong interaction, which represents one of the serious problems in the standard model of particle physics (SM), for a review see reference [4]. The theory, together with observational and experimental bounds, predicts that such axions are very light and weakly interacting with the SM particles, see reference [5]. For these reasons, they are suggested to be suitable candidates for the DM content of the universe [6, 7, 8]. The observation of a light axion would indeed solve the strong CP-problem and at least would participate in improving our understanding of the origin of the component of the DM in the universe. Furthermore, there are plenty of theories beyond the SM that predict the existence of many other pseudo-scalar particles sharing the same phenomenology of the QCD axions [9, 10, 11]. All of this provides strong motivation that axions or now more generally ALPs [12, 13, 14] are a highly viable candidate for DM in the universe.

If they really exist in nature, ALPs are expected to couple with photons in the presence of an external electromagnetic field through the Primakoff effect [15]. This coupling gives rise to the mixing of photons with ALPs [16], which leads to the conversion between photons and ALPs

and changes the polarization state of photons. Over the last few years, it has been realized that this phenomenon would allow searches for the ALPs in the observations of distant AGNs in radio galaxies [17, 18]. Since photons emitted by these sources can mix with ALPs during their propagation in the presence of an external magnetic field and this might reduce photon absorption caused by extragalactic background light [19]. Recent observations of blazars by the Fermi Gamma-Ray Space Telescope [20] in the 0.1-300 GeV energy range show a break in their spectra in the 1-10 GeV range. In their paper [21, 22], Mena, Razzaque, and Villaescusa-Navarro have modeled this spectral feature for the flat-spectrum radio quasar 3C454.3 during its November 2010 outburst, assuming that a significant fraction of the gamma rays converts to ALPs in the magnetic fields in and around the large scale jet of this blazar.

The main aim of this work is to follow the approach of [21] to explore the capability of a Cosmic ALP Background (CAB) model to produce the soft X-ray excess in the Coma cluster as claimed in [23]. This test is based upon whether the same model survives scrutiny in highly magnetized AGN jet environments. We find that using the environment of M87 AGN jet and without accounting for misalignment between the AGN jet direction and the line of sight, CAB ALPs conversion into photons would over-produce the X-ray spectrum for the M87 environment. This casts doubt on the existence of a CAB with the necessary properties to explain the observed Coma cluster X-ray excess.

The structure of this paper is as follows. We briefly review the theoretical model that describes the photon-ALP mixing phenomena in section 2 and discuss whether this mixing can explain the soft X-ray excess phenomenon in section 3. The results are shown and discussed in section 4. Finally, a summary and conclusion are provided in section 5.

2. ALPs-photon coupling model

The coupling of ALPs with photons in the presence of an external magnetic field $\mathbf{B}$ is represented by the following Lagrangian [15, 16, 24]

$$\mathcal{L}_{a\gamma} = -\frac{1}{4} g_{a\gamma} \mathrm{F}_{\mu\nu} \tilde{\mathrm{F}}^{\mu\nu} a = g_{a\gamma}\, \mathbf{E}\cdot\mathbf{B}\, a\,, \tag{1}$$

where $g_{a\gamma}$ is the ALP-photon coupling constant, $\mathrm{F}_{\mu\nu}$ and $\tilde{\mathrm{F}}^{\mu\nu}$ represent the electromagnetic field tensor and its dual respectively, and a donates the ALP field. While $\mathbf{E}$ and $\mathbf{B}$ are the electric and magnetic fields respectively. The evolution equations that describe the coupling of ALPs with a monochromatic and linearly polarized photon beam of energy ω propagating along the z-direction in the presence of an external and homogeneous magnetic field transverse $\mathbf{B}_T$ to the beam direction (i.e. in the x-y plane), takes the form [16, 17, 21, 22]

$$i\frac{d}{dz}\begin{pmatrix} A_\perp(z) \\ A_\parallel(z) \\ a(z) \end{pmatrix} = -\begin{pmatrix} \Delta_\perp \cos^2\xi + \Delta_\parallel \sin^2\xi & \cos\xi\sin\xi(\Delta_\parallel + \Delta_\perp) & \Delta_{a\gamma}\sin\xi \\ \cos\xi\sin\xi(\Delta_\parallel + \Delta_\perp) & \Delta_\perp \sin^2\xi + \Delta_\parallel \cos^2\xi & \Delta_{a\gamma}\cos\xi \\ \Delta_{a\gamma}\sin\xi & \Delta_{a\gamma}\cos\xi & \Delta_a \end{pmatrix} \begin{pmatrix} A_\perp(z) \\ A_\parallel(z) \\ a(z) \end{pmatrix}\,, \tag{2}$$

where $A_\perp$ and $A_\parallel$ are the photon linear polarization amplitudes along the x and y axis, respectively, and $a(z)$ donates the amplitude of ALPs. The parameter ξ represents the angle between the transverse magnetic field B_T and a fixed y-axis in the x-y plane. For ALP-photon mixing model in the jet of the blazar 3C454.3, Mena and Razzaque in [21] adopted the following transverse magnetic field and electron density profiles

$$\mathbf{B}_T = \phi \left(\frac{R}{10^{18}\mathrm{cm}}\right)^{-1} \mathrm{G}\,, \quad \text{and} \quad n_e = \eta \left(\frac{R}{10^{18}\mathrm{cm}}\right)^{-s} \mathrm{cm}^{-3}\,, \tag{3}$$

where R is the radius from a central supermassive black hole, believed to be at the center of the AGN. The normalization parameters ϕ and η are found in [21] by fitting GeV γ-ray data with

this ALP-photon mixing model for different values of $s = 1, 2$ and 3 corresponding to different electron density profiles. The other different terms of the model, following references [17, 21, 22], are given as

$$\begin{aligned}
\Delta_{\perp} &\equiv 2\Delta_{\rm QED} + \Delta_{\rm pl}\,, \qquad \Delta_{\parallel} \equiv (7/2)\Delta_{\rm QED} + \Delta_{\rm pl}\,,\\
\Delta_{\rm QED} &\simeq 1.34\cdot 10^{-18}\phi^2 \left(\frac{\omega}{\rm GeV}\right)\left(\frac{R}{10^{18}{\rm cm}}\right)^{-2} {\rm cm}^{-1}\,,\\
\Delta_{\rm pl} &\simeq -3.49\cdot 10^{-26}\eta \left(\frac{\omega}{\rm GeV}\right)^{-1}\left(\frac{R}{10^{18}{\rm cm}}\right)^{-s} {\rm cm}^{-1}\,,\\
\Delta_{a\gamma} &\simeq 1.50\cdot 10^{-17}\phi \left(\frac{g_{a\gamma}}{10^{-10}{\rm GeV}^{-1}}\right)\left(\frac{R}{10^{18}{\rm cm}}\right)^{-1} {\rm cm}^{-1}\,,\\
\Delta_{a} &\simeq -2.53\cdot 10^{-19} \left(\frac{\omega}{\rm GeV}\right)^{-1}\left(\frac{m_a}{10^{-7}{\rm eV}}\right)^{2} {\rm cm}^{-1}\,. \qquad (4)
\end{aligned}$$

Using this set of parameters, the evolution equations (2) can be numerically solved to find the two components of the photon linear polarization; $A_{\perp}$ and $A_{\parallel}$. Then the spectrum for a given blazar can be modified by a normalized suppression factor defined as

$$S(E) = |A_{\parallel}(E)|^2 + |A_{\perp}(E)|^2\,. \qquad (5)$$

Then the ALP-photon mixing model able to produce a simulation for the γ-ray energy spectra ($\nu F_{\nu} \equiv E^2 dN/dE$) as a function of the energy of the photons with $\omega \equiv E(1+z)$ where z is the blazar's redshift. In the case of replicating [21] we note that the γ-ray energy spectra read

$$E^2 dN/dE = CE^{-\Gamma+2}S(E)\,. \qquad (6)$$

Here, C and Γ are spectral parameters. Hence, the ALP-photon mixing for the blazar jet model includes six free parameters: the normalization for the magnetic field ϕ, the normalization for the electron density η, the ALP mass m_a, the ALP-photon coupling constant $g_{a\gamma}$, and two spectral parameters C and Γ.

3. Cosmic Axion Background

In [25], the authors motivate the existence of a homogeneous CAB arising via the decay of string theory moduli in the very early universe. The suggestion being that the natural energy for such a background lies between 0.1 and 1 keV. Furthermore, in [26] it was shown that such CAB would have a quasi-thermal energy spectrum with a peak dictated by the mass of the ALP. This CAB is also invoked in [23] to explain the soft X-ray excess on the periphery of the Coma cluster with an ALP mass of 1.1×10^{-13} eV and a coupling to the photon of $g_{a\gamma} = 2 \times 10^{-13}$ GeV^{-1}.

In this work, we assume, for convenience, that the CAB has a thermal spectrum with an average energy of $\langle E_a \rangle = 0.15$ keV. Then we normalize the distribution to the typical example quoted in [26]. We use the thermal distribution as an approximation, as the exact shape of the distribution will not substantially affect the conclusions we draw. We can then determine the fraction of CAB ALPs converted into photons within the environment of the M87 AGN jet and use this to determine a resulting photon flux. This flux can be compared to X-ray measurements to see if such environments can constrain low-mass ALPs and put limits on the ALP explanation of the Coma X-ray excess.

4. Results and discussion

The Fermi Large Area Telescope in the period from 2010 September 1st to December 13th, reported observations of the radio quasar 3C454.3 at a redshift of z=0.895, constitutes of four

epochs [20]: (i) A pre-flare period, (ii) A 13 day long plateau period, (iii) A 5-day flare, and (iv) A post-flare period. The ALP-photon mixing model then has been used in [21] to fit these observation data by plotting the γ-ray energy spectra ($\nu F_\nu \equiv E^2 dN/dE$) as a function of the energy of the photon E to get some constraints on the ALP parameters. To validate the results in [21] , we replicated the model analyses considering the photons to be initially unpolarized, and the following initial condition has been applied: $(A_\parallel(E), A_\perp(E), a(E)) = (\frac{1}{\sqrt{2}}, \frac{1}{\sqrt{2}}, 0)$ at $z \equiv R = 10^{18}\,\mathrm{cm}$. Besides, the angel ξ has been fixed to be $\pi/4$ during the whole calculations. The evolution equations (2) have been solved numerically to produce the spectral feature of the blazer 3C454.3 in its four epochs for three different cases of the electron profile density.

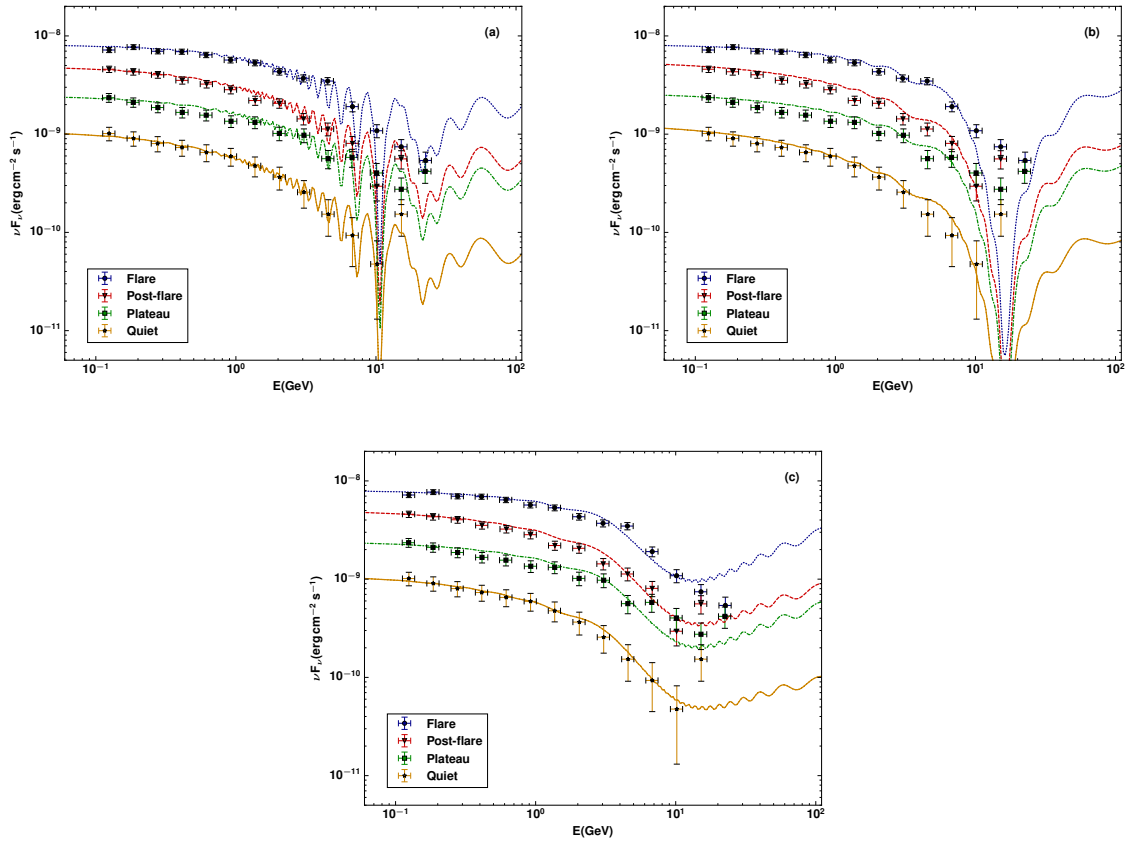

Figure 1. The numerical simulation of the spectral energy fitting observations of blazer 3C454.3 for four different epochs produced using ALP-photon mixing model with electron profile density: (a) $n_e \propto R^{-1}$, (b) $n_e \propto R^{-2}$ and (c) $n_e \propto R^{-3}$.

Figures 1 show the numerical simulation of the spectral energy fitting observations to blazer 3C454.3 for four different epochs (flare, post-flare, plateau, and quiet) using the ALP-photon mixing model with the three different electron density profiles with $s = 1$ (a), 2 (b), and 3 (c). The two spectral parameters C and Γ have been varied from epoch to another as they affected by the γ-ray emission region, while the other four parameters; ϕ, η, m_a, and $g_{a\gamma}$ have been kept fixed. Comparing our results with the one published in [21], allows us to deduce that the spectral energy obtained using the numerical solutions to the evolution equations (2) show a good agreement with these published results. The best fitting of the ALP-photon mixing model for the observation data of blazar jet has been achieved when the transition between photons to

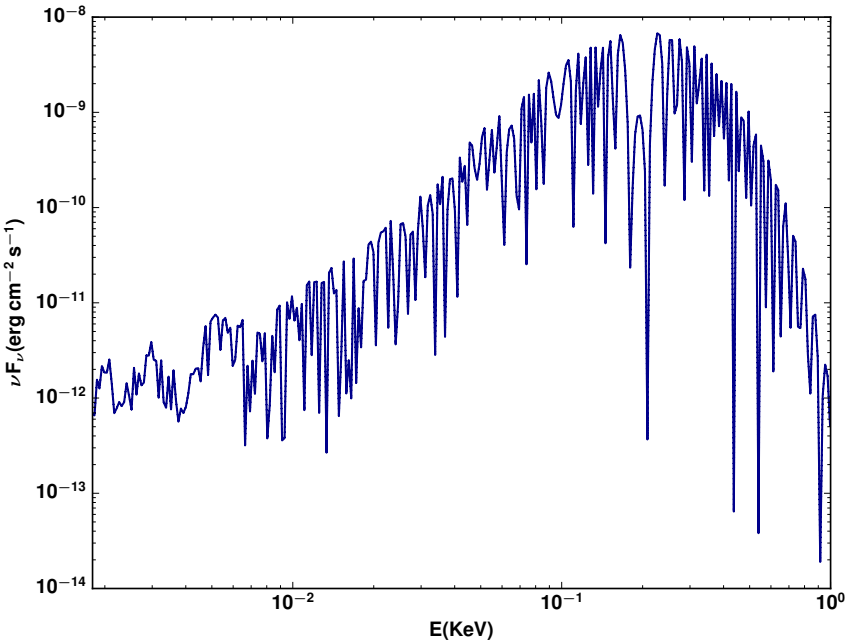

Figure 2. The numerical simulation of the energy spectrum from ALPs conversion to photons in the magnetic field on the jet of M87 AGN.

ALPs take place over different radii, $R \sim 10^{18} - 10^{21}$ cm for $\phi \sim 10^{-2}$, $\eta \sim 10^{9}$, $m_a \sim 10^{-7}$ eV, and $g_{a\gamma} \sim 10^{-10}\,\mathrm{GeV}^{-1}$.

As a step forward, we apply the ALP-photon mixing model to study the probability of CAB ALPs to convert to photons in the magnetic field on the jet of M87 AGN, which is the best characterized AGN in the literature [29, 30]. We use an electron density profile of the first case with $s = 1$. In addition, we set the ALP mass to be 1.1×10^{-13} eV and the ALP-photon coupling to be $g_{a\gamma} = 2 \times 10^{-13}$ GeV^{-1} in agreement with the models derived in [23] to explain the soft X-ray excess on the periphery of the Coma cluster. The environmental parameters are taken as $\phi = 1.4 \times 10^{-3}$ and $\eta = 0.3$ to make sure that the magnetic field and the electron density profiles used for the M87 AGN are consisted with the obtained values in [27]. Preliminary results are shown in figure 2 for the energy spectrum obtained from the numerical simulation for ALP-photon conversion in the magnetic field of the M87 AGN jet. The resulting photon flux between 0.3 and 8 keV obtained from the simulation is $\sim 2.57 \times 10^{-10}$ erg cm^{-2} s^{-1}. This value is about two orders of magnitude greater than the observed flux $\sim 3.76 \times 10^{-12}$ erg cm^{-2} s^{-1} from the M87 AGN in the same energy range [28].

5. Conclusion

In this work, we have examined the ALP-photon model which developed by Mena and Razzaque to fit the spectral features of the flat-spectrum radio quasar 3C454.3 during its November 2010 outburst. This allowed the aforementioned authors to derive constraints on the ALP parameters by assuming that a significant fraction of the gamma rays converts to ALPs in the presence of an external magnetic field in the large scale jet of this blazar. We reproduced their results that have a very good agreement with the observation data for the 3C454.3 blazar. Indeed, this makes us very confident that our simulation is robust. As a step forward, we used the environment of the M87 AGN jet to test whether the CAB ALP conversion to photons which is proposed to explain

the Coma cluster X-ray excess, survives comparison with X-ray data in M87. We find that the environment of the M87 AGN jet provides preliminary suggestions of an X-ray over-production around two orders of magnitude. This casts doubt on whether the Coma X-ray excess CAB model is viable in general. Further effects, such as misalignment between the AGN jet direction and the line of sight, must be considered in future work before we can rule out the CAB model proposed to account for the observed Coma X-ray excess.

6. Acknowledgments

This work is based on the research supported by the South African Research Chairs Initiative of the Department of Science and Technology and National Research Foundation of South Africa (Grant No 77948). A. Ayad acknowledges support from the Department of Science and Innovation/National Research Foundation (DSI/NRF) Square Kilometre Array (SKA) post-graduate bursary initiative under the same Grant. G. Beck acknowledges support from a National Research Foundation of South Africa Thuthuka grant no. 117969. The authors would like also to offer special thanks to Prof. S. Colafrancesco, who, although no longer with us, continues to inspire by his example and dedication to the students he served over the course of his career.

References

[1] Komatsu E, Smith K, Dunkley J, Bennett C, Gold B, Hinshaw G, Jarosik N, Larson D, Nolta M, Page L *et al.* 2011 *The Astrophysical Journal Supplement Series* **192** 18
[2] Peccei R D and Quinn H R 1977 *Phys. Rev. Lett.* **38** 1440–1443
[3] Weinberg S 1978 *Physical Review Letters* **40** 223
[4] Peccei R D 2008 *Axions* (Springer) pp 3–17
[5] Asztalos S J, Rosenberg L J, van Bibber K, Sikivie P and Zioutas K 2006 *Annu. Rev. Nucl. Part. Sci.* **56** 293–326
[6] Preskill J, Wise M B and Wilczek F 1983 *Physics Letters B* **120** 127–132
[7] Abbott L F and Sikivie P 1983 *Physics Letters B* **120** 133–136
[8] Dine M and Fischler W 1983 *Physics Letters B* **120** 137–141
[9] Arvanitaki A, Dimopoulos S, Dubovsky S, Kaloper N and March-Russell J 2010 *Physical Review D* **81** 123530
[10] Cicoli M, Goodsell M D and Ringwald A 2012 *Journal of High Energy Physics* **2012** 146
[11] Anselm A and Uraltsev N 1982 *Physics Letters B* **114** 39–41
[12] Arias P, Cadamuro D, Goodsell M, Jaeckel J, Redondo J and Ringwald A 2012 *Journal of Cosmology and Astroparticle Physics* **2012** 013
[13] Ringwald A 2012 *Physics of the Dark Universe* **1** 116–135
[14] Marsh D J 2016 *Physics Reports* **643** 1–79
[15] Sikivie P 1983 *Physical Review Letters* **51** 1415
[16] Raffelt G and Stodolsky L 1988 *Physical Review D* **37** 1237
[17] Bassan N, Mirizzi A and Roncadelli M 2010 *Journal of Cosmology and Astroparticle Physics* **2010** 010
[18] Horns D, Maccione L, Mirizzi A and Roncadelli M 2012 *Physical Review D* **85** 085021
[19] Harris J and Chadwick P M 2014 *Journal of Cosmology and Astroparticle Physics* **2014** 018
[20] Abdo A A, Ackermann M, Ajello M, Allafort A, Baldini L, Ballet J, Barbiellini G, Bastieri D, Bellazzini R, Berenji B *et al.* 2011 *The Astrophysical journal letters* **733** L26
[21] Mena O and Razzaque S 2013 *Journal of Cosmology and Astroparticle Physics* **2013** 023
[22] Mena O, Razzaque S and Villaescusa-Navarro F 2011 *Journal of Cosmology and Astroparticle Physics* **2011** 030
[23] Angus S, Conlon J P, Marsh M D, Powell A J and Witkowski L T 2014 *Journal of Cosmology and Astroparticle Physics* **2014** 026
[24] Anselm A A 1988 *Physical Review D* **37** 2001
[25] Conlon J P and Marsh M D 2013 *Physical review letters* **111** 151301
[26] Conlon J P and Marsh M D 2013 *Journal of High Energy Physics* **2013** 214
[27] Park J, Hada K, Kino M, Nakamura M, Ro H and Trippe S 2019 *The Astrophysical Journal* **871** 257
[28] Donato D, Sambruna R M and Gliozzi M 2004 *ApJ* **617** 915–929 (*Preprint* `astro-ph/0408451`)
[29] Macchetto F, Marconi A, Axon D J, Capetti A, Sparks W and Crane P 1997 *The Astrophysical Journal* **489** 579
[30] Gebhardt K and Thomas J 2009 *The Astrophysical Journal* **700** 1690

Unifying Dark Matter and Dark Energy in Chaplygin Gas Cosmology

Anna-Mia Swart[1], Renier Hough[2], Shambel Sahlu[1,3,4], Heba Sami[1], Thato Tsabone[1], Rubby Aworka[5], Maye Elmardi[2] and Amare Abebe[1]

[1] Center for Space Research, North-West University, Mahikeng 2735, South Africa
[2] Center for Space Research, North-West University, Potchefstroom, 2520, South Africa
[3] Astronomy and Astrophysics Department, Entoto Observatory and Research Center, Ethiopian Space Science and Technology Institute, Addis Ababa, Ethiopia
[4] Department of Physics, College of Natural and Computational Science, Wolkite University, Wolkite, Ethiopia
[5] African Institute for Mathematical Science (AIMS), Ghana

E-mail: annamiaswart@gmail.com

Abstract. In this paper we study the accelerating expansion of the Universe by unifying dark matter and dark energy with an exotic fluid - the so-called Chaplygin gas. We consider the cosmological background expansion of a universe model filled with a radiation-baryonic matter-Chaplygin gas fluid system and show that such a model can solve the dark matter and dark energy problems, at least at the level of the background expansion. We present the numerical results of the deceleration parameter and luminosity distance, and show that they correlate well with observational data.

1. Introduction

One of the most active areas of research in cosmology today involves trying to understand the nature of dark matter and dark energy. The Universe is made up of different components, amongst them matter, radiation and dark matter. Recently, the Chaplygin gas (CG) model has been proposed. This model mimics the effects of dark energy and dark matter, and can be a possible substitution for our current standard model of cosmology. The negative pressure associated with the CG model is related to a positive energy density by a characteristic equation of state given as

$$p = -\frac{A}{\rho^{\alpha}} \, , \tag{1}$$

where p is the pressure and ρ is the energy density, both in a comoving reference frame with $\rho > 0$. A and α are positive constants. The values for α are given by the generalized Chaplygin gas (GCG) model ($0 < \alpha \leq 1$), and the original Chaplygin gas (OCG) ($\alpha = 1$) [1]. From the above equation of state, the energy density of the exotic fluid reads

$$\rho_{ch}(a) = \left[A + \frac{B}{a^{3(1+\alpha)}} \right]^{\frac{1}{1+\alpha}} \, , \tag{2}$$

where $B = e^{C(1+\alpha)}$ with C a constant of integration, which means that B is a positive constant.

We can now look at equation (2) and determine how the energy density of the CG evolves during different epochs. In the limiting case where $\frac{B}{A} \gg a^{3(1+\alpha)}$ for the early universe, the energy density in OCG can be given by

$$\rho_{ch}(a) \approx \sqrt{\frac{B}{a^6}} = \frac{\sqrt{B}}{a^3} \, . \tag{3}$$

From this we can conclude that the CG corresponds to dust-like matter (or dark matter) in the early Universe as $\rho_{ch} \sim a^{-3}$.

On the other hand, $\frac{B}{A} \ll a^{3(1+\alpha)}$ at late times, and for this case, the energy density becomes

$$\rho_{ch}(a) \approx \pm\sqrt{A} \, . \tag{4}$$

This tells us that $\rho_{ch} \sim$ constant, and thus the CG corresponds to a cosmological constant [2]. In this manuscript, we study different cosmological scenarios and present the numerical solutions describing the evolution of the Universe filled with a CG-radiation-barionic matter system. In this preceding paper we assume a flat universe ($\Omega_k = 0$, where Ω_k is the density due to the curvature of spacetime).

The layout of the manuscript is as follows: in the following section we review the basic Friedmann equation by unifying the exotic fluid with other components like radiation and baryonic matter fluids. In Section 3, we present the numerical analysis of some key cosmological constraints to examine the general evolutionary features of the Universe. We then devote Section 4 to discussions of our results and the conclusions.

2. A Universe consisting of CG, radiation and baryonic matter fluids

We have now concluded that the CG complies to the behaviour of dark matter and dark energy. It thus now becomes necessary to include radiation and baryonic matter so that we can get a comprehensive view of this model to describe the expansion of the Universe. To do this, we will consider a universe in which we assume the energy density to consist of CG, baryons and radiation. The fluid equations for radiation (r), baryonic matter (b) and CG (ch) hold independently as

$$\dot{\rho}_i + 3\frac{\dot{a}}{a}(\rho_i + p_i) = 0 \, , \quad i = \{r, b, ch\}. \tag{5}$$

Here $\rho_b = (\rho_0)_b a^{-3}$ is the energy density of baryonic matter with constant initial value $(\rho_0)_b$ and pressure $p_b = 0$ (the equation of state parameter for baryonic matter is $\omega = 0$). The energy density of radiation is found to be $\rho_r = (\rho_0)_r a^{-4}$, where $(\rho_0)_r$ is the constant initial value for the energy density of radiation, with pressure $p_r = \frac{1}{3}\rho_r$. The values for the pressure and energy density of the CG are given by equations (1) and (2), respectively.

We can write the energy density as the sum of the different energy density components:

$$\rho_{tot}(a) = \left[A + \frac{B}{a^{3(1+\alpha)}}\right]^{\frac{1}{1+\alpha}} + (\rho_0)_r \, a^{-4} + (\rho_0)_b \, a^{-3} \, . \tag{6}$$

The total pressure can also be given in a similar fashion:

$$p_{tot}(a) = -\frac{A}{[\rho_{ch}(a)]^{\alpha}} + \frac{1}{3}\rho_r(a) \, . \tag{7}$$

The fluid equation for the total energy density then becomes

$$\dot{\rho}_{tot} + 3\frac{\dot{a}}{a}(\rho_{tot} + p_{tot}) = 0 \, . \tag{8}$$

We can also make a change of variables and use redshift, z, instead of the scale factor, a, as this is a physically measurable quantity, and the scale factor is not. We do this by substituting $1+z=\frac{a_0}{a}$, where a_0 is the scale factor at the present time which we normalize to 1. The basic Friedmann equation consequently reads as

$$3H^2(z)=\left\{\left[A+B(1+z)^{3(1+\alpha)}\right]^{\frac{1}{1+\alpha}}+(\rho_0)_r\,(1+z)^4+(\rho_0)_b\,(1+z)^3\right\}\,, \tag{9}$$

where $H=\dot{a}/a$ is the Hubble parameter. Dividing equation (9) by $3H_0$ (H_0 being the value of the Hubble parameter today), we obtain

$$h^2=\left[D+E(1+z)^{3(1+\alpha)}\right]^{\frac{1}{1+\alpha}}+(\Omega_0)_r\,(1+z)^4+(\Omega_0)_b\,(1+z)^3\,, \tag{10}$$

where $h\equiv\frac{H}{H_0}$ is the normalized Hubble parameter, and $D=\frac{A}{9H_0^4}$, $E=\frac{B}{9H_0^4}$, $(\Omega_0)_r\equiv\frac{(\rho_0)_r}{3H_0^2}$ and $(\Omega_0)_b=\frac{(\Omega_0)_b}{3H_0^2}$ are dimensionless density parameters. The density parameters for radiation, baryonic matter and CG can be expressed as

$$\Omega_r(z)=(\Omega_0)_r\,(1+z)^4\,,\quad \Omega_b(z)=(\Omega_0)_b\,(1+z)^3\,,\quad \Omega_{ch}(z)=\left[D+E(1+z)^{3(1+\alpha)}\right]^{\frac{1}{1+\alpha}}\,, \tag{11}$$

respectively. The total density parameter for a universe where CG, baryonic matter and radiation dominate can be written as

$$1=\Omega_r(z)+\Omega_b(z)+\Omega_{ch}(z)\,. \tag{12}$$

3. Numerical analysis

In this section, we analyse different cosmological constraints, such as the deceleration parameter and luminosity distance, by considering the CG in addition to the other components of the Universe.

3.1. Deceleration parameter

From the Friedmann equation, we obtain the acceleration equation of the total fluid as

$$\frac{\ddot{a}}{a}=-\frac{1}{6}\left(\rho_{tot}+3p_{tot}\right)\,. \tag{13}$$

With the use of equations (6) and (7), we get the acceleration equation into the form

$$\begin{aligned}\frac{\ddot{a}}{a}=-\frac{1}{6}\Big\{&\left[A+B(1+z)^{3(1+\alpha)}\right]^{\frac{1}{1+\alpha}}-3A\left[A+B(1+z)^{3(1+\alpha)}\right]^{-\frac{\alpha}{1+\alpha}}\\&+2\,(\rho_0)_r\,(1+z)^4+(\rho_0)_b\,(1+z)^3\Big\}\,.\end{aligned} \tag{14}$$

There exists a deceleration parameter, q, which gives us an understanding of the rate of expansion of the Universe:

$$q\equiv-\frac{\ddot{a}}{a}\frac{1}{H^2}\,. \tag{15}$$

By substituting equations (9) and (14), the deceleration parameter can be written as

$$q(z)=\frac{\left[A+B(1+z)^{3(1+\alpha)}\right]^{\frac{1}{1+\alpha}}-3A\left[A+B(1+z)^{3(1+\alpha)}\right]^{-\frac{\alpha}{1+\alpha}}+2\,(\rho_0)_r\,(1+z)^4+(\rho_0)_b\,(1+z)^3}{2\left[A+B(1+z)^{3(1+\alpha)}\right]^{\frac{1}{1+\alpha}}+2\,(\rho_0)_r\,(1+z)^4+2\,(\rho_0)_b\,(1+z)^3}\,. \tag{16}$$

It is now possible to plot the deceleration parameter versus the redshift as shown in Figure 1. This plot shows an accelerated expansion in negative z until $z \sim 0.6$, and a decelerated expansion after this, which means that the Universe's expansion was decelerating early in time, and later (including the present and the future) the expansion is accelerating. This result is consistent with what one would expect the expansion history of the Universe to look like: in the current concordance model, there should be a decelerating matter-dominated phase followed by a dark-energy-driven late time acceleration phase.

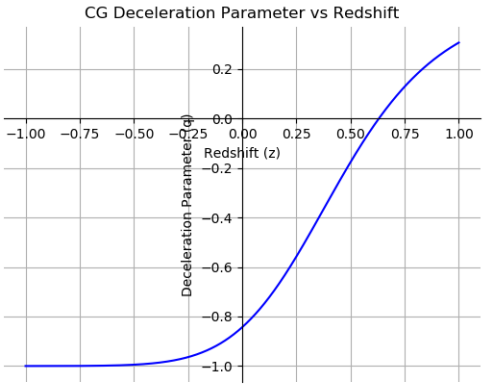

Figure 1. A plot of the deceleration parameter, q, versus the redshift, z.

3.2. Luminosity distance D_L and distance modulus μ

To test our model, equation (10) is useful. We can use the distance modulus, μ, for Supernovae Type 1A data and calculate the corresponding distance modulus for the CG model at different redshifts. The luminosity distance relates two bolometric quantities, namely the luminosity, L, and the flux, f, of a distant object such as a supernova [3]. From the luminosity distance, the distance modulus can be derived as a function of redshift. Since we need the luminosity distance, D_L, in terms of redshift, we have to relate it to the transverse comoving distance, D_M, to obtain

$$D_L = (1+z)D_M, \tag{17}$$

Furthermore, we have D_M as a function of Ω_k [4], given by

$$D_M = \begin{cases} D_H \frac{1}{\Omega_k} \sinh\left(\sqrt{\Omega_k}\frac{D_c}{D_H}\right) & \text{for } \Omega_k > 0, \\ D_c & \text{for } \Omega_k = 0, \text{ and} \\ D_H \frac{1}{|\Omega_k|} \sinh\left(\sqrt{|\Omega_k|}\frac{D_c}{D_H}\right) & \text{for } \Omega_k < 0\ , \end{cases} \tag{18}$$

where Ω_k is the density due to the curvature of spacetime and D_H is the Hubble Distance. Since $\Omega_k = 0$ we have $D_M = D_c$, where D_c is called the line-of-sight comoving distance (LSCD) and is defined as

$$D_c = \int \frac{cdt}{a} = D_H \int_0^z \frac{dz'}{h(z')}\ , \tag{19}$$

where z' is the redshift of the supernova you are observing. From the LSCD definition, in conjunction with equation (10), we can calculate the distance modulus. Using the above given

distance definitions, the resulting distance modulus (in Mpc), is given as

$$\mu = m - M = 25 - 5 \times \log_{10}\left[3000\bar{h}^{-1}(1+z)\int_0^z \frac{dz'}{h(z')}\right] , \tag{20}$$

where m is the apparent magnitude and M is the absolute magnitude of the object [5]. We use the Hubble distance as $D_H = 3000\bar{h}\ \frac{km}{s \cdot Mpc}$, where $\bar{h}$ is the Hubble uncertainty parameter.

Now that we have a way of relating the Chaplygin gas model to data, we need to discuss the dataset that we will use. We obtained the Supernovae Type 1A dataset from the SDSS-II/SNLS3 Joint Light-curve Analysis (JLA). It contains 123 low-redshift ($0.01 < z < 0.1$) supernovae and 236 intermediate redshift ($0.01 < z < 1.1$) supernovae. We used the B-filter magnitudes, and found the absolute magnitudes of these particular supernovae in the research papers [6], [7], and [8]. The reason we use these types of supernovae is due to the fact that their luminosity is relatively similar to one another, since all White Dwarfs (WD) are known to have a relative size and composition. This particular type of supernovae is caused by a WD accreting a low-mass companion main sequence star. Since their luminosity is relatively the same, the difference in the flux received, from one WD to another, is a direct consequence of the distance the light had to travel. We can use redshift to approximate the distance.

To fit the distance modulus to the data, we will use a Markov-Chain-Monte-Carlo (MCMC) simulation[1]. The MCMC simulation is able to search for the most probable free parameter value, given certain physical constrains. The *EMCEE Hammer Python* package was used to execute the MCMC simulation. Furthermore, the MCMC calculates the most probable best fit by calculating the likelihood function for the given free parameters. We assumed that the data has a Gaussian distribution. The best fit calculated free parameters for the CG model on the supernovae data is shown in Figure 2.

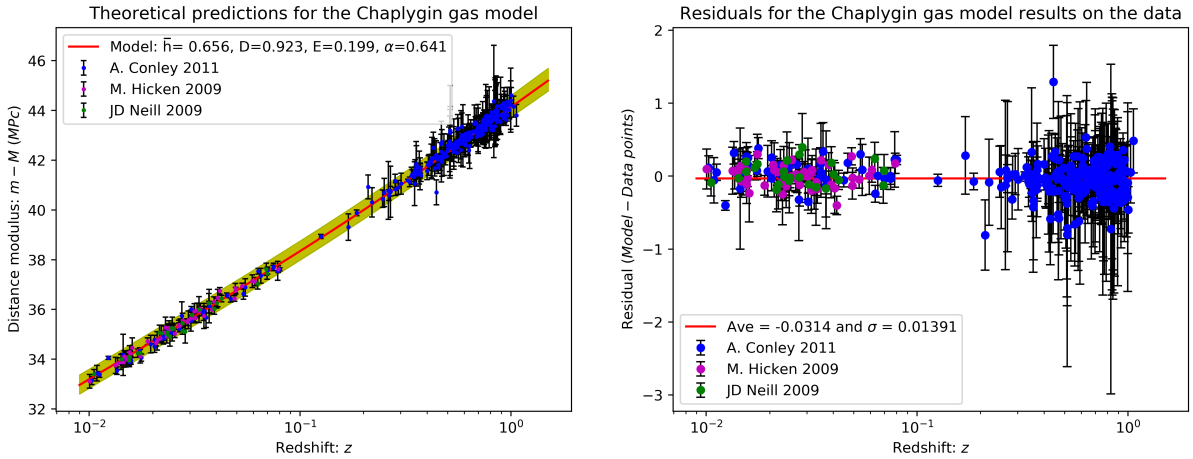

Figure 2. The Chaplygin gas model's (10) best fit free parameters to the Supernovae Type 1A data with cosmological parameter values $\bar{h} = 0.6561^{+0.074}_{-0.041}$, $D = 0.9226^{+0.251}_{-0.263}$, $E = 0.1986^{+0.059}_{-0.064}$, and $\alpha = 0.6411^{+0.255}_{-0.362}$ as calculated by the MCMC-simulation (L.H.S. panel). The cosmological parameter values were fixed to $\Omega_b = 0.049$ and $\Omega_r(0.674)^2 = 2.47 \times 10^{-5}$. The R.H.S panel shows the residuals between the predicted model values and the data points.

Figure 2 clearly shows in the R.H.S panel that we have obtained the best fit model for equation (10), since the average residual deviation is $\bar{x}_{res} = -0.0314$ with a standard deviation

[1] This entire section, including the MCMC simulation code, is similar to work done in the conference proceedings paper [9]. We used the code developed in that paper to test the model.

of $\sigma_{res} = 0.0139$. Furthermore, the residuals show no over- or under-estimation on either low-redshift or intermediate redshift. This suggests that the CG model can accurately predict the late-time accelerated expansion. However, it is worth noting that the best fit Hubble constant parameter for the CG model includes within the error approximation, the measured Hubble constant found by [10]. This is an interesting result, since it is known that the predicted Hubble constant values between Cosmic Microwave Backgroud (CMB) related results, such as Planck2018 [10], and supernovae results have a discrepancy between them with the latter's results for the ΛCDM model predicting a higher value for the Hubble constant [11].

Thus the CG model is able to give, not only realistic values for the Hubble constant, but it also lowers the discrepancy between cosmic microwave background (CMB) radiation and supernovae results. From this we can conclude that the CG model is a viable alternative model to explain the late-time acceleration.

4. Conclusion

In this paper, we examined the accelerating expansion of the Universe using a theoretical exotic fluid which mimics dark energy and dark matter. After we reviewed the background of the Universe, we presented the numerical results of some important cosmological parameters like the deceleration parameter and luminosity distance by unifying this exotic fluid with the usual cosmological fluids (baryonic matter and radiation). From the numerical results, we concluded that the CG is an alternative candidate to explain the current accelerating universe and that this model is a possible way to solve the dark matter and dark energy problems. It would be possible to get a more accurate model by adding more constraints on the A, B and α terms using observational data, and this is a task we plan to undertake in the near future.

Acknowledgements

AS and RH acknowledge funding through the National Astrophysics and Space Science Program (NASSP) scholarship. HS and TT have been funded through the National Research Foundation (NRF) free-standing scholarship. SS gratefully acknowledges financial support from Wolkite University, Entoto Observatory and Research Center and Ethiopian Space Science and Technology Institute, as well as the hospitality of the Physics Department of North-West University (NWU) during the preparation of part of this manuscript. ME acknowledges that this work is supported by an NWU/NRF postdoctoral fellowship. AA acknowledges that this work is based on the research supported in part by the National Research Foundation (NRF) of South Africa with grant numbers 109257 and 112131. RH acknowledges funding through National Research Foundation (NRF) scholarship (Grant number 117230).

References

[1] Elmardi M and Abebe A 2017 *Journal of Physics: Conference Series* **905** 012015
[2] Kamenshcik A, Moschella U and Pasquier V 2008 ArXiv:gr-qc/0103004v2
[3] Gidelew A 2013 *Beyond the concordance cosmology* Ph.D. thesis University of Cape Town
[4] Deza M M and Deza E 2009 Encyclopedia of distances *Encyclopedia of distances* (Springer) pp 1–583
[5] Riess A G, Filippenko A V, Challis P *et al.* 1998 *The Astronomical Journal* **116** 1009
[6] Conley A, Guy J, Sullivan M *et al.* 2011 *The Astrophysical Journal Supplement Series* **192** 1 (*Preprint* 1104.1443)
[7] Neill J D, Sullivan M, Howell D A *et al.* 2009 *The Astrophysical Journal* **707** 1449–1465 (*Preprint* 0911.0690)
[8] Hicken M, Challis P, Jha S *et al.* 2009 *The Astrophysical Journal* **700** 331–357 (*Preprint* 0901.4787)
[9] Hough R, Abebe A and Ferreira S 2019 *in preparation*
[10] Planck Collaboration, Aghanim N, Akrami Y *et al.* 2018 *arXiv e-prints* arXiv:1807.06209 (*Preprint* 1807.06209)
[11] Riess A G, Macri L M, Hoffmann S L *et al.* 2016 *The Astrophysical Journal* **826** 56 (*Preprint* 1604.01424)

Perturbations in a Chaplygin gas Cosmology

Shambel Sahlu[1,2,3], Heba Sami [3], Anna-Mia Swart[3], Thato Tsabone[3], Maye Elmardi[4] and Amare Abebe[3]

[1] Astronomy and Astrophysics Department, Entoto Observatory and Research Center, Ethiopian Space Science and Technology Institute, Addis Ababa, Ethiopia.
[2] Department of Physics, College of Natural and Computational Science, Wolkite University, Wolkite, Ethiopia.
[3] Center for Space Research, North-West University, Mahikeng 2735, South Africa.
[4] Center for Space Research, North-West University, Potchefstroom 2520, South Africa.

E-mail: hebasami.abdulrahman@gmail.com

Abstract. In this paper we study the perturbations of a cosmic multi-fluid medium consisting of radiation, dust and a Chaplygin gas. To do so, we follow the $1+3$ covariant formalism and derive the evolution equations of the fluctuations in the energy density for each species of fluid in the multi-fluid system. The solutions to these coupled systems of equations are then computed in both short-wavelength and long-wavelength modes. Our preliminary results suggest that unlike most dark energy models that discourage large-scale structure formation due to the rapid cosmological expansion (which gives little time for fluctuations to coalesce), the Chaplygin-gas model supports the formation of cosmic structures. This is manifested in the solutions of the perturbation equations which show the growth of density fluctuations over time.

1. Introduction

In the last two decades, it has become apparent that the standard cosmological model (ΛCDM) fails to explain the accelerating expansion of the Universe [1], the existence of dark matter in galaxy clusters [2], the formation of the large-scale structure [3],the inherent inhomogeneity and anisotropy of the Universe on the small scales [4] and so forth. To solve the first two problems, scholars have proposed an exotic fluid, the so-called Chaplygin gas (CG), which acts as a cosmological fluid with an equation of state of the form $p = -\frac{A}{\rho^{\alpha}}$, where p and ρ are the pressure and energy density, and A and α are constants such that $A > 0$ and $0 < \alpha \leq 1$ [5]. The purpose of this fluid is to substitute the dark matter and dark-energy components of the Universe. This model acts as dark-matter in the early Universe and dark-energy in the late times of the cosmos. In a universe in which we assume the energy density to consist of matter and CG fluids, the conservation equation reads as

$$\dot{\rho}_t + 3\frac{\dot{a}}{a}(\rho_t + p_t) = 0, \tag{1}$$

where ρ_t is the energy density and p_t is the pressure for the total fluid[1], a is the cosmological scale factor and the subscript t stands for total (matter+CG) fluids[2]. From this equation, the energy

[1] When referring to matter, we mean either radiation or dust.
[2] w_m is the equation of state parameter for the matter fluid.

density becomes $\rho_{tot}(z) = \left[A + B(1+z)^{3(1+\alpha)}\right]^{\frac{1}{1+\alpha}} + \rho_m(1+z)^{3(1+w_m)}$, where $B = e^{C(1+\alpha)}$ with C a constant of integration.

Whereas much has been said of the Chaplygin gas as an alternative to a unified dark matter and dark energy model that mimics the cosmic expansion history of a Friedmann-Lemaître-Robertson-Walker (FLRW) background, to our knowledge there is no work in the literature that considered the cosmological perturbations of this fluid model in the 1+3 covariant formalism [6–8]. Here we derive the density perturbation equations and present the solutions both analytically and numerically. From the results, we analyse cosmological implications as far as large-scale structure formation is concerned on both sub- and super-horizon scales [8].

The outline of the manuscript is as follows: in the following section we review the basic spatial gradient variables. In this section, we also derive the linear evolution equations, applying the scalar and harmonic decomposition techniques and obtain the wave-number dependent energy density fluctuations for both CG and matter fluids. In Sec. 3, we present the analytical and numerical solutions of density perturbations by considering radiation-CG, dust-CG and CG like fluids for both wave-length ranges. We then devote Sec. 4 to discussions of our results and the conclusions.

2. Perturbations

We define the spatial gradient variables for the energy density of the individual matter components ρ_m, the Chaplygin-gas energy density ρ_{ch}, the total energy density ρ_t and the volume expansion Θ respectively as

$$D_a^m = \frac{a}{\rho_m}\tilde{\nabla}_a\rho_m \ , \quad D_a^{ch} = \frac{a}{\rho_{ch}}\tilde{\nabla}_a\rho_{ch} \ , \qquad D_a^t = \frac{a}{\rho_t}\tilde{\nabla}_a\rho_t \ , \qquad Z_a = a\tilde{\nabla}_a\Theta \ .$$

For a perfect-fluid system, the following fluid equations hold:

$$\dot{\rho}_t = -\Theta(\rho_t + p_t) \ , \tag{2}$$

$$(\rho_t + p_t)\dot{u}_a + \tilde{\nabla}_a p_t \ , \tag{3}$$

from which one can conclude for the 4-acceleration

$$\dot{u}_a = \alpha\frac{\omega_{ch}\rho_{ch}D_a^{ch}}{a(\rho_t + p_t)} - \frac{w_m\rho_m D_a^m}{a(\rho_t + p_t)} \ , \tag{4}$$

where w_{ch} is the equation of state parameter of the CG fluid. Another key equation for a general fluid is the so-called Raychaudhuri equation and it can be expressed as

$$\dot{\Theta} = -\frac{1}{3}\Theta^2 - \frac{1}{2}(\rho_t + 3p_t) - \tilde{\nabla}^a\dot{u}_a \ . \tag{5}$$

After defining the comoving gradients of the cosmological expansion and the comoving fractional density gradient of the matter components in a covariant and gauge-invariant way and taking the harmonically decomposed scalar parts, it can be shown that the scalar perturbations in the

matter and CG energy densities evolve according to

$$\begin{aligned}
\ddot{\Delta}^k_m = \quad & \Theta(\omega_m - \frac{2}{3})\dot{\Delta}_m + \Bigg\{(1+\omega_m)\Bigg[\frac{1}{2}(1+3\omega_m) + \frac{\Theta^2\omega_m}{3\rho_t(1+\omega_t)} \\
& + \frac{w(1+3\omega_t)}{2(1+\omega_t)} + \frac{k^2\omega_m}{a^2\rho_t}\Bigg]\rho_m + \Bigg[\frac{1}{3}\omega_m\Theta^2 - \frac{\omega_m}{2}(1+\omega_t)\rho_t\Bigg\}\Delta^k_m + (1+\omega_m) \\
& \Bigg[\frac{1}{2} - \frac{3\omega_{ch}}{2} - \frac{\Theta^2\omega_{ch}}{3\rho_t(1+\omega_t)} - \frac{\omega ch(1+3\omega_t)}{2(1+\omega_t)} + \frac{k^2\omega_{ch}}{a^2\rho_t}\Bigg]\rho_{ch}\ \Delta^k_{ch}\ , \qquad (6) \\
\ddot{\Delta}^k_{ch} = \quad & -\Theta\left(\omega_{ch} + \frac{2}{3}\right)\dot{\Delta}^k_{ch} + (1+\omega_{ch})\Bigg[\frac{1}{2}(1+3\omega) + \frac{\Theta^2\omega}{3\rho_t(1+\omega_t)} + \frac{\omega(1+3\omega_t)}{2(1+\omega_t)} \\
& + \frac{k^2\omega_m}{a^2\rho_t}\Bigg]\rho_m\Delta^k_m + \Bigg\{(1+\omega_{ch})\Bigg[\frac{1}{2} - \frac{3\omega_{ch}}{2} - \frac{\Theta^2\omega_{ch}}{3\rho_t(1+\omega_t)} - \frac{\omega_{ch}(1+3\omega_t)}{2(1+\omega_t)} \\
& + \frac{k^2\omega_{ch}}{a^2\rho_t}\Bigg]\rho_{ch} - \omega_{ch}\left(\frac{1}{3}\Theta^2 + \frac{1}{2}(1+3\omega_t)\rho_t\right) + \Theta^2\omega_{ch}\left[2(1+2\omega_{ch})\rho_{ch} + \frac{2}{3}\right]\Bigg\}\Delta^k_{ch}\ , \qquad (7)
\end{aligned}$$

where

$$\Delta^k_m = a^2\frac{\nabla^2\rho_m}{\rho_m}\ , \qquad \Delta^k_{ch} = a^2\frac{\nabla^2\rho_{ch}}{\rho_m}\ , \qquad k = \frac{2\pi a}{\lambda}\ , \qquad (8)$$

k being the comoving wave-number and λ the wavelength of the perturbations. In redshift space, the corresponding equations can be recast as

$$\begin{aligned}
\Delta''_m = \quad & \frac{1}{1+z}(\frac{1}{2} - 4\omega_m)\Delta'_m + \Bigg\{\frac{(1+\omega_m)}{(1+z)^2}\Bigg[\frac{1}{2}(1+3\omega_m) + \frac{\omega_m}{(\Omega_{ch}+\Omega_m)(1+\omega_t)} + \\
& \frac{\omega_m(1+3\omega_t)}{2(1+\omega_t)} + \frac{9\pi^2(1+\omega_m)^2\omega_m}{3\lambda^2(1+z)^{3(1+\omega_m)}(\Omega_{ch}+\Omega_m)}\Bigg]3\Omega_m + \Bigg[3\omega_m - \frac{3}{2}\omega_m(\Omega_{ch}+\Omega_m)(1+\omega_t)\Bigg\}\Delta^k_m \\
& + \frac{(1+\omega_m)}{(1+z)^2}\Bigg[\frac{1}{2} - \frac{3\alpha\omega_{ch}}{2} - \frac{\alpha\omega_{ch}}{(\Omega_{ch}+\Omega_m)(1+\omega_t)} - \frac{\alpha\omega_{ch}(1+3\omega_t)}{2(1+\omega_t)} + \\
& \frac{9\pi^2(1+\omega_m)^2\alpha\omega_{ch}}{3\lambda^2(1+z)^{3(1+\omega_m)}(\Omega_{ch}+\Omega_m)}\Bigg]3\Omega_{ch}\Delta^k_{ch}\ , \qquad (9) \\
\Delta''_{ch} = \quad & \frac{3\sqrt{4}-6}{\sqrt{4}(1+z)}\left(\omega_{ch}(1+\alpha) - \omega_{ch} + \frac{2}{3}\right)\Delta'_{ch} + \frac{(1+\omega_{ch})}{(1+z)^2}\Bigg[\frac{1}{2}(1+3\omega_m) + \frac{\omega_m}{3(\Omega_m+\Omega_{ch})(1+\omega_t)} \\
& + \frac{\omega_m(1+3\omega_t)}{2(1+\omega_t)} + \frac{9\pi^2(1+\omega_m)^2\omega_m}{3\lambda^2(1+z)^{3(1+\omega_m)}(\Omega_{ch}+\Omega_m)}\Bigg]3\Omega_m\Delta^k_m + \frac{1}{(1+z)^2}\Bigg\{(1+\omega_{ch})\Bigg[\frac{1}{2} - \frac{3\alpha\omega_{ch}}{2} \\
& - \frac{\alpha\omega_{ch}}{(\Omega_m+\Omega_{ch})(1+\omega_t)} - \frac{\alpha\omega_{ch}(1+3\omega_t)}{2(1+\omega_t)} + \frac{9\pi^2(1+\omega_m)^2\alpha\omega_{ch}}{\lambda^2(A+B(1+z)^{3(1+\alpha)})^{\frac{1}{1+\alpha}}(\Omega_{ch}+\Omega_m)}\Bigg]3\Omega_{ch} \\
& - \omega_{ch}\left(3 + \frac{3}{2}(1+3\omega_t)(\Omega_m+\Omega_{ch})\right) + 9\omega_{ch}\left[(1+\alpha)(1+2\omega_{ch})3\Omega_{ch} + \frac{2}{3}\right]\Bigg\}\Delta^k_{ch}\ , \qquad (10)
\end{aligned}$$

respectively. In GR with normal forms of matter, one would obtain a closed second-order equation of the density fluctuations and the equations are generally easier to solve. But here we get a coupled system of second-order equations in the density fluctuations of both matter and CG, the solutions to which are are more complicated to compute analytically. As such, we consider short-wavelength ($k/aH \gg 1$) and long-wavelength ($k/aH \ll 1$) limits of the perturbations [8] and analyse large-scale structure implications of the resulting solutions.

3. Results and Discussion

For further discussion of the growth of the energy density fluctuations with redshift, we assume that the Universe has two major non-interacting fluids, namely radiation associated with CG and dust associated with CG[3], and CG fluids in the following subsections.

3.1. Radiation-CG dominated Universe

The equation of state parameter for radiation fluid is $w_r = 1/3$, and the equation of state parameter for CG reads

$$\omega_{ch} = -\frac{A}{A + B(1+z)^6} \,,$$

The equation of state parameter of the total fluid is then given as

$$\omega_t = \frac{\rho_{0,r}(1+z)^4 - 3\frac{A}{\sqrt{A+B(1+z)^6}}}{3\rho_{0,r}(1+z)^4 + 3\sqrt{A + B(1+z)^6}} \,.$$

In the early universe, the redshift is large. If, in this case, we take B to be a small value, then $\omega_{ch} \approx -1$. The equation of state parameter for the total fluid consequently reads as

$$\omega_t \approx \frac{\rho_{0,r}(1+z)^4}{3\rho_{0,r}(1+z)^4 + 3\sqrt{B}(1+z)^3} = \frac{3H_0^2\Omega_{0,r}(1+z)}{9H_0^2\Omega_{0,r}(1+z) + 3\sqrt{B}} \,.$$

Now, if we again make the same assumptions of large redshift, z, and small values of B, then the total equation of state parameter becomes $\omega_t \approx 1/3 = \omega_r$.

If we assume radiation fluctuations in the background of the CG fluid, we have $\Delta_r \gg \Delta_{ch}$, i.e., $\Delta_{ch} \approx 0$, similar analysis is done in [8] for dust-radiation system. Then solutions of our leading equation, Eq. (9), for the short-wavelength range becomes

$$\begin{aligned} \Delta(z) = \quad & C_1(1+z)^{\frac{1}{12}}\mathrm{BesselJ}\left(\frac{\Sigma}{24(\Omega_{ch}+\Omega_r)}, \frac{4\pi\sqrt{\Omega_r}}{3\lambda\sqrt{\Omega_{ch}+\Omega_r}(1+z)^2}\right) + \\ & C_2(1+z)^{\frac{1}{12}}\mathrm{BesselY}\left(\frac{\Sigma}{24(\Omega_{ch}+\Omega_r)}, \frac{4\pi\sqrt{\Omega_r}}{3\lambda\sqrt{\Omega_{ch}+\Omega_r}(1+z)^2}\right) \,, \end{aligned} \tag{11}$$

where $\Sigma = \sqrt{624\Omega_r^2 - 96\Omega_{ch}^2 + 528\Omega_{ch}\Omega_r + 145\Omega_{ch} + 289\Omega_r(\Omega_{ch}+\Omega_r)}$, C_1 and C_2 are integration constants and BesselJ and BesselY are the first- and second-order Bessel functions.

The solution of Eq. (9) for the long-wavelength range is given as

$$\Delta(z) = C_3(1+z)^{\Omega_{ch}+\Omega_r+\frac{\psi}{12(\Omega_{ch}+\Omega_r)}} + C_4(1+z)^{-(\Omega_{ch}+\Omega_r-\frac{\psi}{12(\Omega_{ch}+\Omega_r)})} \,, \tag{12}$$

where $= \sqrt{432\Omega_{ch}^2\Omega_r + 1152\Omega_{ch}\Omega_r^2 - 96\Omega_{ch}^3 + 624\Omega_r^3 + 145\Omega_{ch}^2 + 289\Omega_r^2 + 434\Omega_{ch}\Omega_r}$. We assume initial conditions given as $\Delta_{in} \equiv \Delta^k(z_{in} = 1100) = 10^{-3}$ and $\Delta'_{in} \equiv \Delta'(z_{in} = 1100) = 0$ for every mode, k, to deal with the growth of matter fluctuations [8]. Therefore, we determine the integration constant C_i (i = 1,2,3,4,...) by imposing those initial conditions.

The numerical result of Eq. (11) is presented in Fig. 1. In this figure we observe the oscillatory motions of the density perturbations in the short-wavelength modes. The results of Eq. (12) are shown in Fig. 2 for the case of the long-wavelength modes. In this figure, we clearly observe the density fluctuations growing up through time.

[3] For all analysis, we consider the original CG model, $\alpha = 1$.

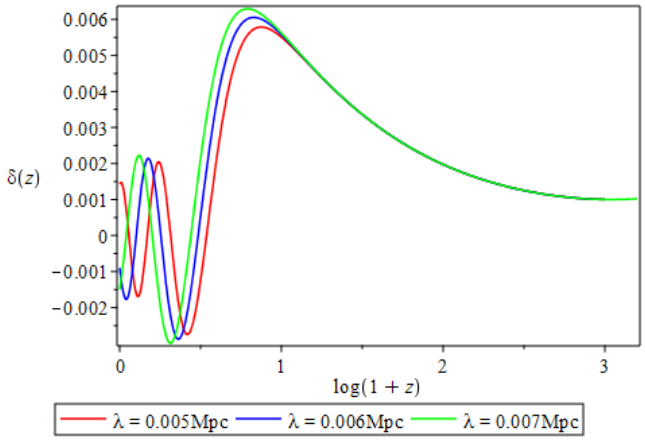

Figure 1. $\delta(z)$ versus z for short wavelengths for $\Omega_r = 1 - \Omega_{ch}$. Every colour represents a different wavelength.

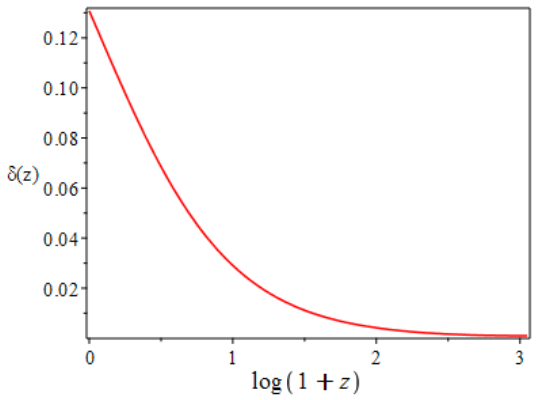

Figure 2. $\delta(z)$ versus z for long wavelengths for $\Omega_r = 1 - \Omega_{ch}$. We used $\Omega_r = 4.48 \times 10^{-5}$ [10].

3.2. Dust-CG dominated Universe

The equation of state parameter for dust fluid is given as $\omega_d = 0$, and the equation of state parameter of the total fluid then becomes $\omega_t = \frac{-\frac{A}{\sqrt{A+B(1+z)^6}}}{3\rho_{0,d}(1+z)^3+3\sqrt{A+B(1+z)^6}} \approx 0$, for large value of z. The solutions of our evolution equations for the density perturbations, which is given by Eq. (9), in a dust-CG system reads

$$\Delta(z) = C_5(1+z)^{\frac{3}{4}+\frac{1}{4}\sqrt{9+24\Omega_d}} + C_6(1+z)^{\frac{3}{4}-\frac{1}{4}\sqrt{9+24\Omega_d}} \,. \tag{13}$$

This solution is represented graphically in Fig. 3.

3.3. CG-dominated Universe

Considering the growth of the CG fluctuations as a background of matter fluids, we can let $\Delta_{ch} \gg \Delta_m$, causing $\Delta_m \approx 0$. The solution of our leading equation, Eq. (10), then reads as

$$\Delta(z) = C_7 \log(1+z)\sin(\Omega_r + \Omega_d + \Omega_{ch} + 5) + C_8 \log(1+z)\cos(\Omega_r + \Omega_d + \Omega_{ch} + 5) \,. \tag{14}$$

The numerical results are represented in Fig. 4 to depict the growth of CG density fluctuations in terms of redshift, and the role of CG fluid for the formation of large-scale structure.

What our current results show is that even at the level of the perturbations, the CG fluid offers an excellent alternative to the narrative of large-scale structures formation. This is because, contrary to what one would expect in a dark-energy-dominated universe where there would be less chance of large-scale structure formation due to the rapid cosmological expansion, we see the growth of the density perturbations with time.

4. Conclusions

In this work, we explored the solutions of cosmological perturbations in a multi-fluid cosmic medium where one of the fluids is a Chaplygin gas. We applied the $1+3$ covariant and gauge-invariant formalism to define the spatial gradient variables and applied scalar and harmonic decomposition methods to analyse the scalar perturbations of the different energy densities involved. We considered different systems such as radiation-CG, dust-CG and CG fluids in

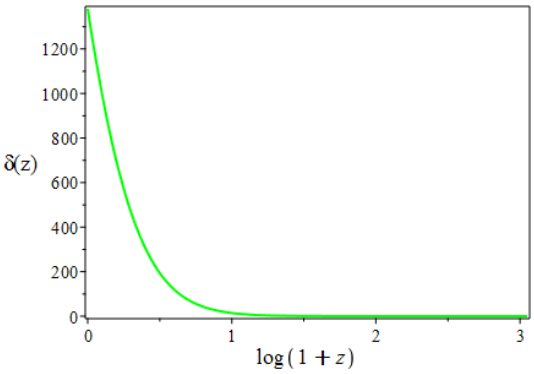

Figure 3. $\delta(z)$ versus z for dust and for $\Omega_d = 1 - \Omega_{ch}$. We used $\Omega_d = 0.32$ [11].

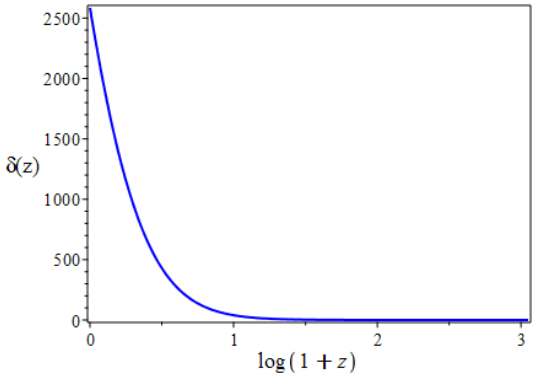

Figure 4. $\delta(z)$ versus z for CG, using $1 - \Omega_r - \Omega_d = \Omega_{ch}$.

both short- and long-wavelength modes to present the numerical and analytical solutions to the perturbation equations. Our results show that at least in the simplest CG model, the formation of large-scale structures is enhanced, rather than discouraged (as one would expect from dark energy fluid models), since all our preliminary calculations show the growth of density fluctuations with time.

Acknowledgments

SS gratefully acknowledges financial support from Wolkite University, Entoto Observatory and Research Center and Ethiopian Space Science and Technology Institute, as well as the hospitality of the Physics Department of North-West University (NWU) during the preparation of part of this manuscript. HS acknowledges the financial support from the Mwalimu Nyerere African Union scholarship and the National Research Foundation (NRF) free-standing scholarship. TT has been funded through the National Research Foundation (NRF) free-standing scholarship. AS acknowledges funding through the National Astrophysics and Space Science Program (NASSP) scholarship. ME acknowledges that this work is supported by an NWU/NRF postdoctoral fellowship. AA acknowledges that this work is based on the research supported in part by the NRF of South Africa with grant numbers 109257 and 112131.

References

[1] Riess A G *et al.* 1998 *The Astronomical Journal* **116** 1009
[2] Fall S M and Efstathiou G 1980 *Monthly Notices of the Royal Astronomical Society* **193** 189–206
[3] Blumenthal G R, Faber S, Primack J R and Rees M J 1984 *Nature* **311** 517
[4] Rees M J 1980 *Physica Scripta* **21** 614
[5] Bento M, Bertolami O and Sen A A 2002 *Physical Review D* **66** 043507
[6] Ellis G F, Hwang J and Bruni M 1989 *Physical Review D* **40** 1819
[7] Dunsby P K 1991 *Class. Quant. Grav.* **8** 1785
[8] Abebe A, Abdelwahab M, De la Cruz-Dombriz Á and Dunsby P K 2012 *Class. Quant. Grav.* **29** 135011
[9] Dunsby P K, Bruni M and Ellis G F 1992 *The Astrophysical Journal* **395** 54–74
[10] Chavanis P H 2015 *Physical Review D* **92** 103004
[11] Ade P, Aghanim N, Arnaud M, Arroja F, Ashdown M, Aumont J, Baccigalupi C, Ballardini M, Banday A, Barreiro R *et al.* 2016 *Astronomy and Astrophysics* **594**

DIVISION E – DIVISION OF PHYSICS EDUCATION

An evaluation of the impact of scientific explanation model on pre-service teachers' understanding of basic concepts in electricity

M N Khwanda and P Molefe

Physics Department, P. O. Box 524, University of Johannesburg, Auckland Park 2006, South Africa.

mkhwanda@uj.ac.za

Abstract. Electricity as a topic is regarded as challenging worldwide because students from different countries around the world are reported to have the same pattern of learning difficulties in understanding electricity due to misconceptions associated with it. The current study explored the impact of the scientific explanation model commonly known as CER, as an instructional strategy, on bridging the conceptual gap about some basic concepts of the DC circuit. A two-tier test was developed and then used as an instrument for data collection. The results revealed that the CER model as an instructional strategy has the potential of diagnosing and minimizing misconceptions students have. However, some misconceptions were still available after instruction. The results of this study is consistent with literature that previously concluded that the teaching of electric circuits for qualitative understanding is challenging to students from secondary to tertiary levels

Keywords: Preservice teachers, charge, misconceptions, language of science, scientific explanation

1. Introduction and background

Electricity as a topic is regarded as challenging worldwide because students from different countries around the world are reported to have the same pattern of learning difficulties in understanding electricity due to misconceptions associated with it [1]. For example, "when resistors are connected in series, the one with higher resistance has lower current" [2], which is a misconception. This misconception is sometimes caused by the incorrect mathematical interpretations of Ohm's law. The other misconception "*current is consumed by circuit elements"* was reported in most studies [3], is sometimes caused by the incorrect understanding of current convention. These are just few examples of misconceptions, there are many and are obstacles to learning. The literature on misconceptions suggested further research to determine if instructors are able to prescriptively address students' misconceptions in such a way that learning is improved significantly and also if teachers are gathering insights into students' preconceptions and thought processes. The understanding of students' preconceptions and thought processes is believed to be helpful in planning for future interventions. As an attempt to bridge the conceptual gap in students' understanding of basic electric circuits, literature advised university lectures to pay more attention into students' misconceptions [4] by developing instructional strategies or materials that will enhance students' understanding. In bridging the gap, a two-tier test was developed guided by selected designed principles adopted from knowledge building theory [5]. The current study explored the impact of the scientific explanation model, which has elements; claim, evidence and reasoning abbreviated (CER) [6] as an instructional strategy, on bridging the conceptual gap about some basic concepts of the Direct Current (DC) circuit. The study was guided by the following research questions:

(a) Does the CER model as instructional strategy helped in minimising the target misconceptions students have?
(b) Which targeted misconception(s) resisted instruction?

2. Motivation for the study

The usage of words in physics is different from how the same words are used in our everyday language [7] According to [8]: *Often a student can listen to, or read a statement in science and make sense of it by using the everyday interpretation of the word*. For example, the meaning of power in everyday language is different from the meaning in physics. Based on the fact that students have challenges regarding the languages of physics it is necessary to evaluate the actual students' understanding of the physics concepts. In other words, the identifications of students' conceptions or misconceptions should be done prior to instruction. Misconceptions are classified as robust if they are present before instruction, common to a significant percentage of students in a particular class, reproducible in form and structure across different classes at different institutions in different contexts, and resistant to instruction [9]. In the context of this study, the operational definition of misconception was based on the comparison of the model used by students with the model that is used by a scientific community in explaining the phenomena. A misconception is said to exist if: "the model constructed by an individual fails to match the model accepted by the mainstream science community in a given situation"[10]. Even specialists in the field can have misconceptions, for example, our famous Newton who formulated the three laws of motion once had a misconception. According to [11], one of the misconception held by Newton through his many years of research was that: *space is not an absolute void, but rather is continuously filled with ether* (a hypothetical elastic type of gas which has no mass).

2. he Scientific Explanation Framework: CER Model

From constructivist view point, teachers are expected to use "certain strategies and methods which involve students in constructing the desired meaning of scientific concepts and which help the students undergo the desired conceptual change"[12]. The Scientific explanation model CER [6] in fig 1 was adopted as the strategy to facilitate conceptual change when students construct their own understanding.

Figure 1: The Scientific Explanation Framework taken from fig 2.2 in McNeill and Krajcik (2012)

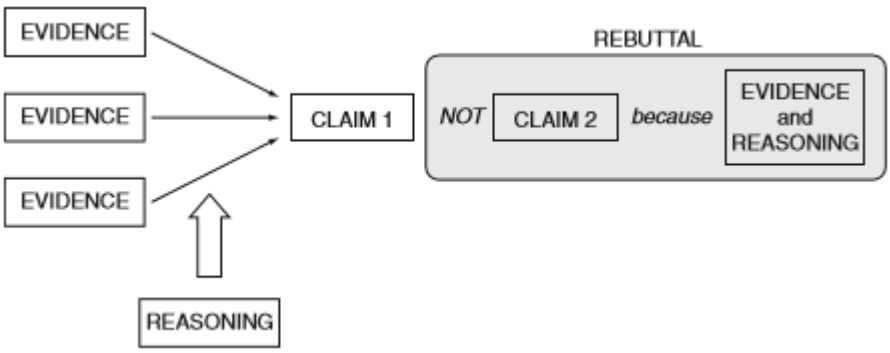

According to the CER model [6], any scientific explanation consists of a Claim, Evidence and Reasoning. A claim (abbreviated C in CER) was defined as *a conclusion to a question or problem* that is investigated, evidence (abbreviated E in CER) was defined as *scientific data that supports the claim* and reasoning (abbreviated R in CER) was defined as *a justification that links the evidence to the claim.* The last stage, rebuttal in figure 1 is an additional stage that is included only after students have mastered how to claim and to give evidence justifying with reasons to support their claim. During intervention, students were introduced to the CER model and were also advised to apply the model while answering all questions.

3. Methodology

3.1 Participants

The participants in the study were students registered for B.ED (FET) second year pre-service teachers taking physics with code PSFTOA2 as one of the major. The participants are formally registered in the faculty of education and only doing physics in the faculty of science. The minimum requirement to register for first year students is a score of 3 which is very low. The total numbers of participants were 45 but only 39 were considered when analysing the concept tests results since they wrote both pre and posttests. The course PSFTOA2 was offered during the first semester.

3.2 Instrument for data collection

Guided by literature on students' understanding of basic electric circuits [3],[13] and personal experience teaching the topic, a the test instrument consisting of four questions probing students' understanding of charges in electric circuit was formulated. Questions were designed to illuminate students' conception/misconceptions about charges in electric circuit. The instrument consisted of multiple choice questions with free response answers. The answer to the multiple choice questions constitute a claim, while the free response answers constitute evidence and reasoning. The test instrument can be classified as a two tier test [9.Table 1 that follows show question items of the developed test with their targeted conception/misconception..

Table 1: Instrument Question Items and their targeted misconception

Question item no	Statement of the Question	Conception/misconception targeted
1	When a battery/ cell no longer works, ***it is out of charge*** and ***must be recharged***.	*Conservation of charges*
2	The charge that flows through the circuit ***originate from the battery.***/	*Battery as the source of charges*
3	Charges ***become used up*** as they flow through a circuit and the amount of charges that exit the light bulb is always less than that enters the bulb.	*Conservation of charges / current consumption.*
4	The electrical utility company like ESKOM, ***supplies millions of electrons*** to our home every day so that we can have current.	*Conservation of charges*

To allow simple scoring, a rubric adapted from [6] was converted to table 2. Table 2 categorized students' explanations into two four categories labelled A to D. The instrument was administered before and after instruction. During intervention, students were familiarized on how to answer questions based on CER. They were shown examples of how to support a claim with correct evidences and reasoning.

Table 2: Classifications of students' conceptual understanding

Category A	Correct Claim Correct evidence & reasoning	→	**Understanding**
Category B	Incorrect Claim Correct evidence & reasoning	→	**Partially Understanding**
Category C	Correct Claim Incorrect evidence & reasoning	→	**Guess**
Category D	Incorrect Claim Incorrect evidence & reasoning	→	**Do not Understanding**

4 Results and Discussion per question

Question item 1: When a battery/ cell no longer works, it is out of charge, must be recharged. The term "recharge" according to Thesaurus, means to renew, refresh, boost, revive, revitalise, restore etc. In terms of physics, are we restoring charges when we recharge a battery? Do our physics students understand the term recharge in the context of recharging a battery scientifically? The answers about students' understanding are shown in table 3 that follows.

Table 3: Battery runs out of charge responses

	Understand	***Partially understand***	***Guess***	***Do not understand***
Before Instruction	2.6 %	7.7 %	28 %	62 %
After Instruction	28 %	26 %	28 %	21 %

To show an understanding of the physics concept in this question, students were expected to choose false as the correct *claim* and use the *principle of conservation of charge* to conclude that a battery can't run out of charge because they are always within a material (*evidence and reasoning*). From the results, before intervention, only 1 (2.56 %) student had a clear understanding of the principle of conservation of charge and make use of it to conclude correctly, 3 (7.69%) students had what we call a false negative explanation (partially understanding), 11 (28%) students guessed their answers(correct claim) because their explanation showed that they believe in the misconceptions *that the battery can run out of charges* and , lastly the majority of students 24 (62%) did not have an idea about the concept being tested. After intervention, there was a slight improvement in terms of choosing the correct answer and the correct explanation. A notable observation was that the percentage number of those who guessed remained unchanged and lastly the number of those who did not understand the concept at all decreases to 8 (21 %). Some of those in 21 % still retain that *their everyday usage of the word recharge* meaning *to return or restore* etc. Based on the contexts mentioned from the dictionary, one can conclude that students associate the word charge with that of some unscientific definition from dictionary. This can be seen as the origin of the association of charge with energy (38.46%). Some of those who did not use the everyday context in explaining mentioned the following two statements: (a) *The battery runs out of charge because the bulb consumes charges when lighting which is a common misconception (33.3%).*
(b) Since the battery has positive and negative terminals and charges are positive and negative hence the charges are from the terminals of the battery, which means that they are from the battery (38.46 %)

Question Item 2: The charge that flows through the circuit originate from the battery. All the participants passed the chemistry module where the origin of charges was introduced using the atomic models. The question was included to test if students are associating the terminals of the battery charges of the battery because a battery consists of a positive terminal and a negative terminal, and at the same time charges are electrons (positive charge) and protons (positive charge). The results of this question item are shown in Table 4 that follows.

Table 4: Charges from battery responses

	Understand	***Partially understand***	***Guess***	***Do not understand***
Before Instruction	8 %	8 %	15 %	69 %
After Instruction	36 %	38 %	13 %	13 %

Based on the fact that to define what a charge is was challenging as observed during the pre-instructional activity, and given that a battery consist of positive and negative terminals, it seems logical but unscientific to think that charges are from the battery or alternatively " *a battery is the source of charges*". Those who understand the concept were expected to answer false, and to mention that all materials have charges, furthermore the number of charges in the material can also help to identify the type of the materials. The results in table 4 show that there was an improvement from 8 to 36 % in terms of understanding. After instruction, only 13 % of students guessed and another 13% still do not understand the origin of charges and stick to their original conviction that charges originate from the battery.

Question item 3: Charges used up in circuit. The question was aimed at assessing students' knowledge of the common science principle: The principle of conservation of charges. It was in response to the common misconception that many students think charges are used up in the circuit which contradicts the principle of conservation of charges. According to the principle, charges are conserved in an isolated system. The results in table 5 revealed that, before instruction, (2.6%) understood, 5.1 % partially understood, 20.5% guessed while the majority (71.8%) did not understand the principle in context. After instruction, it can be claimed that the CER model helped many students to understand the principle but with only few (2. 8 %) that retained their original understanding. The results is consisted with literature that says some misconceptions resist instruction.

Table 5: Question 3 responses

	Understand	*Partially understand*	*Guess*	*Do not understand*
Before Instruction	2.6 %	5.1 %	20.5 %	71.8 %
After Instruction	66.7 %	7.7 %	2.8 %	2.8 %

Some of the notable explanations used by students before instruction were as follows:

- *Charges are used up and converted to light and heat in order for light bulb to shine"*
- *Resistance of the wires decreases the amount of charges*
- *When charges light the bulb the amount of energy reduces because of resistors which try to block the movement of charges which makes the existing charges less than the starting charges.*
- *When the bulb is brand new, it is more brighter than when it is old, bulb used up charges*
- *Some charges are used by the bulb to light, energy is converted to heat, which causes the bulb to light up*
- *Resistor reduces the amount of charges*

Question item 4: Utility Company supply electrons

The question was again the principle of conservation of charges, and to test if students are able to differentiate qualitative terminologies that are reported to be confusing students. The terminologies are: current, energy, potential difference, charges, power and resistance. We expected them to say the municipality only maintain or create the potential difference to enable the charge to move, and when a charge move, there will be current.

Table 6: Question item 4 responses

	Understand	*Partially understand*	*Guess*	*Do not understand*
Before Instruction	12.8 %	2.6 %	51.2 %	33.3 %
After Instruction	7.7 %	7.8 %	30.8 %	48.7 %

Some of the 5 sampled students' notable responses that revealed elements of misconceptions before and after instructions are shown in table 7.

Table 7: Students responses to question item 4

St #	*Before Instruction*	*After Instruction*
S1	*It supplies millions of electrical energy so that we can have current*	*It supplies millions of electric charges*
S2	*Electrons are not the one sent to our homes, the circuit* ***carries charges*** *which are provided by the supplier, ie box, main switch or so forth*	*Current is the* ***movement of charges not the movement of electrons***
S3	*Electrons are electricity conductors, for the current we need electrons so that we can conduct electricity. The electrons are negatively charged and enhance the movement of energy or voltage*	*We need electrons to have current*
S4	*They don't supply electrons* ***but charges which we use in our electric circuit***	*Electrons alone cannot form current, current is defined as the flow of charges not electrons*

Students' responses suggest that the student did not understand the distinction /similarity between an electron and the charge even after intervention. This was regarded as a very difficult question, because most students was unable to differentiate a charge and an electron as shown when one said: *Electrons*

*are not the one sent to our homes, the circuit **carries charges** which are provided by the supplier, ie box, main switch or so forth. The results revealed that some students, refers potential difference as energy*

5. Conclusion

In answering the first research question, the results suggest that the CER model was very helpful in identifying conceptions/misconceptions students have. Some of the notable misconceptions were the following:

- *Resistor reduces the amount of charges in the circuit*
- *The battery as the source of charge*
- *When the bulb is brand new, it is more brighter than when it is old, bulb used up charges*

The misconceptions that students have prior to instruction but that resisted instruction by many students, were the ones that deals with electrons and electricity, especially the one that say the Eskom supply electrons as indicated on the following explanations:

- *Electrons are electricity conductors, for the current we need electrons so that we can conduct electricity*
- *At our homes, we have power stations nearby each township, so utility company supply the power stations with electrons so that we can have electricity*

The results of this study is consistent with [1] that previously concluded that the teaching of electric circuits for qualitative understanding is challenging to students from secondary to tertiary levels. Based on the results of this study, it can be suggested that further interventions be done to help students to discern terminologies that are used to define electricity in our daily lives.

References

[1] Jaakkola, T., & Nurmi, S. (2008). Fostering elementary school students' un derstanding of simple electricity by combining simulation and laboratory activities. *Journal of Computer Assisted Learning, 24*, 271-2

[2] Bilal, E., & Erol, M. (2009). Investigating Students' conceptions of some electricity concepts. *Lat. Am .J. Phys.Educ. 3*(2), 193-201.

[3] Küçüközer, H. and Kocakülah, S. (2007). Secondary school students' misconceptions about simple electric circuits, *Journal of Turkish Science Education* 4, 101-115.

[4] Soong, B. (2008). Learning through computers: Uncovering students' thought processes while solving physics problems. *Australasian Journal of Educational Technology, 24*(5), 592-610.

[5] Scardamalia, M., & Bereiter, C. (2006). Knowledge building: Theory, pedagogy, and technology. In K. Sawyer, *Cambridge Handbook of Learning Sciences* (pp. 97-118). New York: Cambridge University Press.

[6] McNeill, K., & Krajcik, J. (2012). *Supporting Grade 5-8 Students in Constructing Explanations in Science: The Claim, Evidence, and Reasoning Framework for Talk and Writing.* Pears

[7] Harlow, D., & Otero, V. (2006). Talking to Learn Physics and Learning to Talk Physics. In P. H. McCullough, & J.Marx (Ed.), *Physics Education Research Conference Proceedings. 818*, pp. 53-56. merican Institute of Physics.

[8] Gilbert, J.K., Osborne, R.J. & Fensham, P.J. (1982). Children's Science and Its Consequences for *Teaching. Science Education,* 66(4), 623-633.

[9] Ekici, E. (2016). "Why Do I Slog Through the Physics?" Understanding High School Students' Difficulties in Learning Physics. *Journal of Education and Practice, 7*(7), 95-107.

[10] Clerk, D., & Rutherford, M. (2000). Language as a confounding variable in the diagnosis of misconceptions. *International Journal of Science Education, 22*(7), 703-717.

[11] Nussbaum, J. (2005). History and Philosophy of Science and the Preparation for Constructivist Teaching: The Case of Particle Theory . In J. Mintzes, J. Wandersee, & J. Novak, *Teaching Science for Understanding: A Human Constructivist View* (pp. 165-194). Academic Press

[12] Tsai, C., & Chou, C. (2002). Diagnosing students' alternative conceptions in science through a networked two-tier test system. *International Journal of Computer Assisted Learning, 18*(2), 157-165.

[13] Lee, Y. and Law, N., (2001) Explorations in promoting conceptual change in electrical concepts via ontological category shift, *Int. J. Sci. Educ.* 23, 111-149

DIVISION F– DIVISION OF APPLIED PHYSICS

 ISBN: 978-0-620-88875-2

Density functional theory study of copper zinc tin sulphide (Cu_2ZnSnS_4) doped with calcium and barium

TM Mlotshwa[1], NE Maluta[1], RR Maphanga[2]
[1] Department of Physics, University of Venda, P/Bag X 5050, Thohoyandou, 0950
[2] Council for Scientific and Industrial Research, P.O. Box 395, Pretoria, 0001

E-mail: thokozanimxolisi@gmail.com

Abstract. The sun is the most important source of renewable energy today. Producing energy from sunlight using cheap, abundant and non-toxic materials is considered a major challenge in the field of solar-electrical energy conversion. To harvest solar energy, a thin film solar cell composed of the Cu_2ZnSnS_4 (CZTS) semiconductor is a candidate to harvest as much energy as possible. Some of its advantages include optical direct band gap and high absorption coefficient. The structural, electronic and optical properties of pure and doped CZTS structure were calculated using density functional theory (DFT) as implemented in the Cambridge Serial Total Energy Package (CASTEP) codes. An adsorption doping mechanism was used to dope the structure with alkali earth metals, Calcium (Ca) and Barium (Ba). The dopants were adsorbed on the structure rather than replacing one of the atoms. Doping using different elements is expected to yield improved the conversion efficiency of the CZTS based solar cells.

1. Introduction

The quaternary CZTS is a promising material for thin film solar cell application [1]. It has been intensively examined as an alternative photovoltaic (PV) material due to its similarity in material properties with copper indium gallium selenide (CIGS), which has attained the conversion efficiency of 20% and its relative abundance of its constituent raw materials. Although GIGS has reached a very high efficiency amongst thin film solar cells, it contains expensive materials (Indium and Gallium) and the band gap is usually not optimal, hence there is a strong desire to discover novel, high efficiency, low cost solar cell absorber materials to replace GIGS [2]. CZTS is a compound semiconductor of $(I_2)(II)(IV)(VI_4)$ with a high absorption coefficient (>104 cm^{-1}) and a desirable bandgap (~ 1.45 eV) and thus considered an excellent PV material. The cost of raw materials for CZTS PV technology is much lower than that of the existing thin film PV technologies. Theoretical calculations have shown that conversion efficiency as high as 32% are possible for CZTS thin film solar cell, with a CZTS layer of several micrometres [3].

CZTS is a promising candidate for efficient solar cell materials as it inherits all the merits of CIGS while possessing other significant features such as being solely composed of abundant, non-toxic and economic elements in the earth's crust [4] [5]. CZTS film has gained much interest in recent years since its optical property is optimum for PV application. Current thin film technologies are not as effective as crystalline silicon, but they are cheaper to manufacture and have several other important

advantages including good performance in incident light, less sensitivity to temperature-related efficiency reduction and flexibility. The main advantages of CZTS is the relatively high absorption coefficient for the solar spectrum and its tuneable bandgap to make an optimum match to the solar spectrum [6]. The most basic component of a PV cell is the semiconductor. There is a reasonable number of first principle studies on doping of CZTS with different atoms. Some of the atoms used to enhance the efficiency of CZTS through doping include Cadmium (Cd) [7], Sodium (Na) [8], Chromium (Cr) [9], Oxygen (O_2) [10], Antinomy (Sb) [11], Potassium (K) [12], etc. Out of all the dopants that have been used generally, there is no viable improvement on the efficiency of CZTS-based photovoltaic solar cells reported so far. The doped semiconductor develops an excess of free electrons (leading to n-type material) or develops vacancies (called holes) and giving rise to a p-type material. These n-type and p-type materials combine to form a photovoltaic cell. Better understanding of the properties of CZTS is encouraged by improving efficiencies and has drawn interest in the development of these cells through experimental and theoretical means. This study seeks to investigate photovoltaic properties of CZTS material using computer modelling techniques for application in solar cells.

2. Computational method

In this work, first principle calculations were implemented in the framework of density functional theory within the generalized gradient approximation (GGA) using the PBE exchange correlation potential and utilizing the plane wave total energy pseudopotential method as implemented in CASTEP code [13]. The structure was modelled in material studio using the 3D Atomistic window in which space group representing the tetragonal structure of I - 4 was used. Lattice parameters of a = b = 5.430 Å and c = 10.890 Å were used to draw the external skeleton of the structure. Copper (Cu) atoms were placed in separate positions, 2a (0, 0, 0) and 2c (0, 0.5, 0.25). Zinc (Zn) atoms placed at position 2d (0.5, 0, 0.25), the tin (Sn) atom at position 2b (0.5, 0.5, 0) and sulphur (S) in position 8g (0.7560, 0.7566, 0.8722) respectively [14].

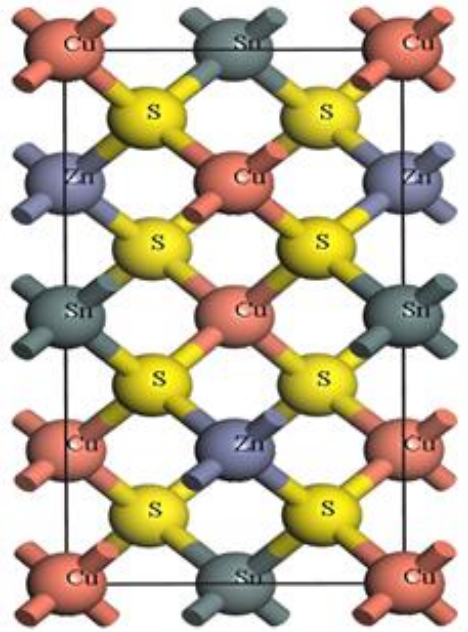

Figure 1. CZTS crystal structure indicating the atomic positions for Cu, Zn, Sn and S respectively

The structure was doped with three elements, the first of which was sodium (group one element) which will act as a basis to validate the study as it has been studied extensively in both experimental and theoretical studies, and hence results of the study will be monitored using sodium. The other two dopants which were used to give identity to the study were the two alkaline earth metals, calcium and barium (they exhibit low toxicity, combines with several metals, abundant, environmentally friendly and they have very high chemical reactivity).

3. Results and discussion

The band gap obtained for the bulk structure was found to be 1.447 eV which is not far off from the expected experimental value of 1.5 eV for CZTS kesterite structure [15]. Kesterite is a sulphide mineral with a formula $Cu_2(Zn,Fe)SnS_4$. The band gap is obtained accurately by making use of the scissors operator because the internal structural parameters are relaxed in the GGA functional and thus this method underestimates the band gap. The scissors operator describes the difference between the theoretical and experimental values of the band gap. It is applied to make the theoretical band gap match the experimental value. To further justify the use of scissors operator, the Heyd−Scuseria−Ernzerhof (HSE06) hybrid density functional was used to determine the band gap because of its accuracy for typical semiconductors. The hybrid HSE06 functional most certainly gives a better value for the band gap. The HSE06 includes short-range, exact Hartree-Fock exchange. It shifts the conduction band to higher energies similar to a scissor correction. The band gap obtained by using the HSE06 functional was 1.495 eV which agrees very well with the experimental value. As seen from figure 2 and 3, it is evident that CZST has a direct band gap and thus favorable for application in the photovoltaics solar cells for improved and efficient solar technologies.

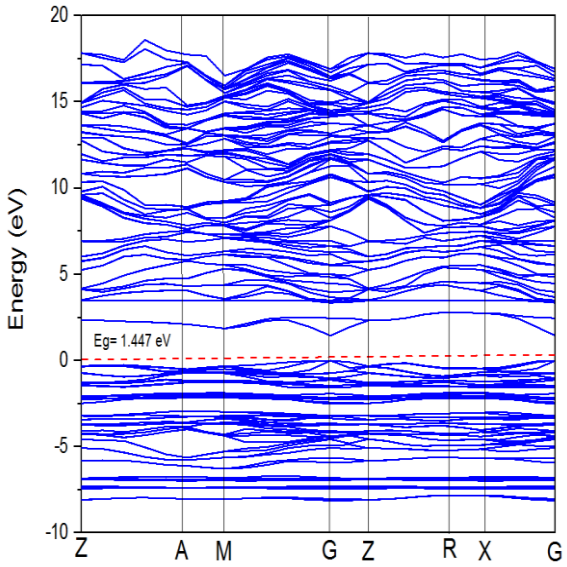

Figure 2. Band structure for bulk CZTS calculated through the GGA-PBE functional

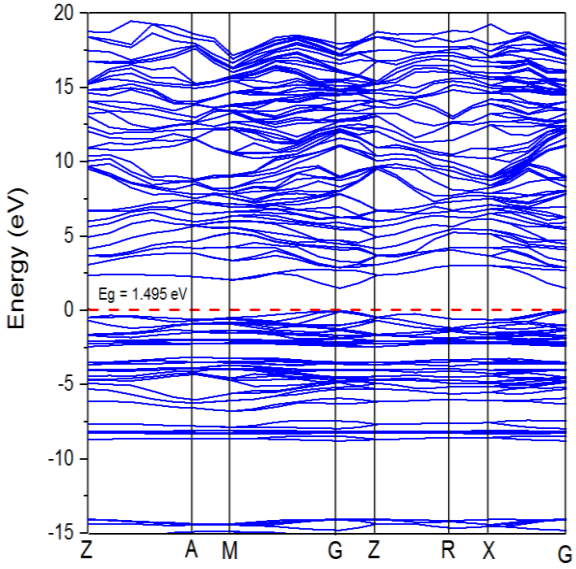

Figure 3. Band structure for bulk CZTS calculated through the HSE06 functional

The band gap calculated using GGA-PBE functional are obviously underestimated while the band gap calculated using HSE06 function are very comparable to other computational results as well as experimental works. It is also clear that CZTS possesses a direct band gap as it is clearly shown on the G Brillouin zone. This is because the conduction band minimum (CBM) and the valence band maximum (VBM) are located at the G point of the Brillouin zone.

It is evident that the conduction band is made of single band due to the Sn-5s and Cu-3d states while the valence band has several bandwidths. One bandwidth is observed at energies from -2 to -3 eV

which is dominated by the Cu-3d states and another one at energies from -6 to -7 eV which is dominated by S-3p states. From -8 eV there is a huge bandwidth of about 4 eV on the valence band which is due to the S-3s state. There are a few short energy gaps on the valence band lying between - 2 eV to - 3 eV and - 6 eV to - 7 eV which are closest to the Fermi level. The conduction band has energy gap from 2 eV to 3 eV matching the energy gap in the valence band. The Cu-3s states is almost vanishing with a slight appearance in the energy range from 4 to 8 eV. It has the lowest density of states on both the valence and the conduction band. The valence atomic configurations of the CZTS structure are $3d^{10}4s^1$ for Cu, $3d^{10}4s^2$ for Zn, $5s^25p^2$ for Sn and $3s^23p^4$ for S. The total and the partial density of states considering the last two atomic orbitals are presented in Figure 4 as they are the key players in the band gap.

The valence band is composed mostly of the S-3p and Cu-3d states while the conduction band is composed mostly of the Sn-5s and S-3p states respectively. The conduction band is dominated by the Sn atom with its Sn-5s and Sn-5p states clearly visible, a proper Sn content could adjust all the formation energies of the Sn-related defects in an appropriate range as suggested by Xiao *et al* [16]. The s-states for Cu, Zn and S are the lowest available states on the valence and conduction bands respectively. The valence band of CZTS is mainly composed of the hybridization between Cu-3d states and S-3p states.

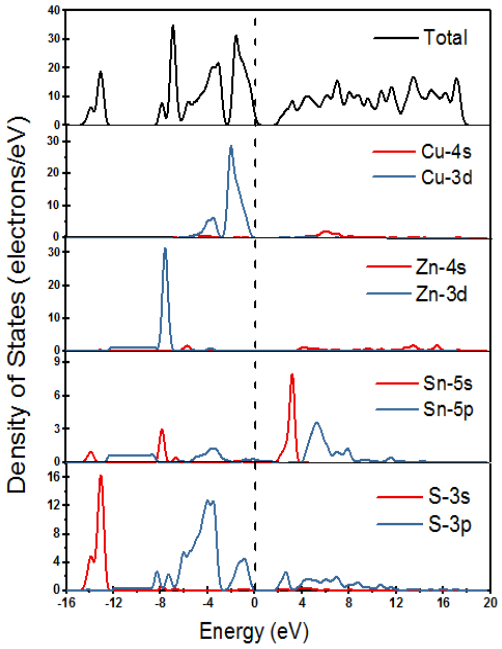

Figure 4. CZTS bulk structure density of states showing contribution of atomic states on the band gap

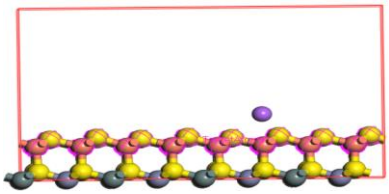

Figure 5. CZTS (112) sodium doped surface

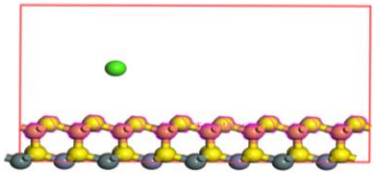

Figure 6. CZTS (112) barium doped surface

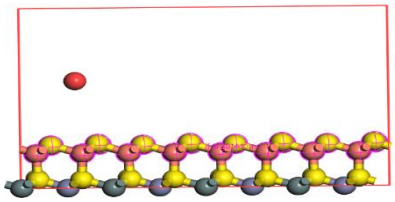

Figure 7. CZTS (112) calcium doped surface

The Zn-4s state is very low on both the valence and conduction bands and therefore there are no states available to be occupied by the dopant elements. There is a slight presence of the Sn-5s and 5p orbitals on both the valence and conduction bands as well as a strong presence of S-3s and 3p states on the valence band. The valence band is dominated by the 3d states while the conduction band is dominated by the 5s states from the Sn element. Figure 5 through Figure 7 shows the attachment of the dopants, sodium, calcium and barium on the (112) surface of CZTS. It is noticeable from the structures that the low energy regions on the surface are mostly found on the central atoms hence the dopants are

attached around the central regions. One important feature of the surface is that the energy is not uniformly distributed throughout the surface hence the presence of lowest energy regions. Absorption coefficient gives information about the solar energy conversion of material and how far light of specific frequency can penetrate the material before being absorbed. The visible region indicates more absorption activity for the spectra with barium being the highest and sodium taking the lowest compared to the total. There is an impressive improvement of absorption from the total CZTS (112) surface for Na, Ca and Ba doped surface on the visible region with the differences clearly visible.

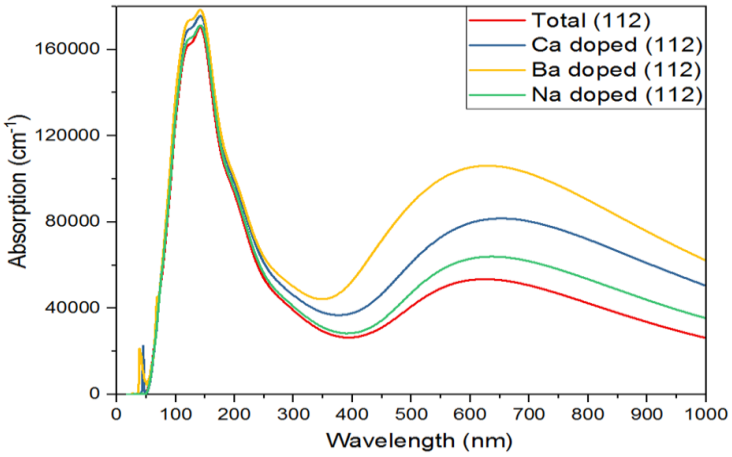

Figure 8. Absorption spectra of pure and doped CZTS (112) surface

CZTS was identified as kesterite type and it is said to have a direct band gap of 1.51 eV with an optical absorption coefficient of $1x10^4$ cm^{-1} [17]. The highest absorption coefficient for the doped structures is for barium with $10x10^4$ cm^{-1}. Calcium and sodium have absorption coefficients of $8x10^4$ cm^{-1} and $6x10^4$ cm^{-1} respectively. Barium doped surface gives the highest absorption peak in the visible region followed by calcium and sodium. These peaks can be credited to the position of the elements in the periodic table and their photo electrolytic properties. Doping of CZTS with Ba can improve the absorption coefficient of CZTS-based solar cells for application in renewable energy.

4. Conclusion

In this work we studied the optical and electronic properties of CZTS. The ground state conditions for the bulk structure were successfully determined and comparable. Semiconductors having band gaps of ~ 1.5 eV are capable of creating electron-hole pairs in the visible region. Most of the solar light falls on the infrared and visible regions and has a maximum value in the visible region. The bulk CZTS (112) plane band gap is lower than the bulk CZTS structure thus indicating the flat band existence and eliminating chances of having electron traps on the band gap. It is evident that doping CZTS (112) surface with either Ca, Ba or Na reduces the band gap and could improve the efficiency of CZTS based solar cells. The material class of kesterite to which CZTS belongs has crystal structure very similar to that of chalcopyrite's and therefore similar electronic properties were expected. CZTS shows a p-type semiconducting behavior with a carrier concentration ~10^{17} cm^{-3}, optical absorption coefficient ~ 10^4 cm^{-1} and direct band gap ~1.4 eV. New thin-film solar cell materials and a greater understanding of their properties are needed to meet the urgent demand for sustainable, lower cost and scalable photovoltaics. Doping of semiconductors is expected to decrease the bandgap and improve its optical response for application in renewable energy technologies. The decrease of the bandgap size can be understood from the hybrid orbital interactions. For kesterite solar cells to present a commercially viable solution it will certainly be necessary to reach 15% efficiency.

5. Acknowledgments
This work is financially supported through the National Research Foundation (NRF). We would also like to thank the University of Venda for the support in carrying out this research and the Centre for High Performance Computing (CHPC) for using their facilities. Special thanks to the DST energy and fuel cell division.

6. References

[1] S. Shauddin, "Comparison among Various Emerging PV Cells with History, Current Status and Future Challenges," *Energy and Power*, vol. 3, no. 6, pp. 91–105, 2013.
[2] D. B. Mitzi, O. Gunawan, T. K. Todorov, K. Wang, and S. Guha, "The path towards a high-performance solution-processed kesterite solar cell," *Sol. Energy Mater. Sol. Cells*, vol. 95, no. 6, pp. 1421–1436, 2011.
[3] C. G. Granqvist, "Transparent conductors as solar energy materials: A panoramic review," *Sol. Energy Mater. Sol. Cells*, vol. 91, no. 17, pp. 1529–1598, 2007.
[4] Z. Zhao and X. Zhao, "Electronic, optical, and mechanical properties of Cu_2ZnSnS_4 with four crystal structures," *J. Semicond.*, vol. 36, no. 8, p. 83004, 2015.
[5] R. J. Deokate, A. D. Adsool, N. S. Shinde, S. M. Pawar, and C. D. Lokhande, "Structural and optical properties of spray-deposited Cu_2ZnSnS_4 thin films," *Energy Procedia*, vol. 54, pp. 627–633, 2014.
[6] H. S. Min, "Optical properties of ternary thin films ($Ni_3Pb_2S_2$) prepared by chemical bath deposition technique," 2017.
[7] T. Maeda, S. Nakamura, and T. Wada, "First-Principles Study on Cd Doping in Cu_2ZnSnS_4 and $Cu_2ZnSnSe_4$," *Jpn. J. Appl. Phys.*, vol. 51, p. 10-11, 2012.
[8] O. P. Singh, A. Sharma, K. S. Gour, S. Husale, and V. N. Singh, "Fast switching response of Na-doped CZTS photodetector from visible to NIR range," *Sol. Energy Mater. Sol. Cells*, vol. 157, pp. 28–34, 2016.
[9] C. Tablero, "Electronic and photon absorber properties of cr-doped Cu_2ZnSnS_4," *J. Phys. Chem. C*, vol. 116, no. 44, pp. 23224–23230, 2012.
[10] C. Tablero, "Effect of the oxygen isoelectronic substitution in Cu_2ZnSnS_4 and its photovoltaic application," *Thin Solid Films*, vol. 520, no. 15, pp. 5011–5013, 2012.
[11] X. Zhang, Miaomiao Han, Zhi Zeng, and Y. Duan, "The role of Sb in solar cell material Cu_2ZnSnS_4," pp. 1–22, 2017.
[12] H. S. Craft, R. Collazo, Z. Sitar, and J. P. Maria, "A novel strategy to control defects and secondary phases of CZTS by surfactant Potassium," vol. 4, pp. 2105–2110, 2006.
[13] S. J. Clark, M. D. Segall, C. J. Pickard, and P. J. Hasnip, "First principles methods using CASTEP," *Zeitschrift für Krist.*, vol. 220, no. 5, pp. 567–570, 2005.
[14] S. R. Hall, J. T. Szymanski, and J. M. Stewart, "Kesterite, $Cu_2(Zn,Fe)SnS_4$ and Stannite $Cu_2(Zn,Fe)SnS_4$, structurally similar but distinct minerals," *Can. Mineral.*, vol. 16, no. 2, pp. 131–137, 1978.
[15] K. N. Basri, N. A. Zabidi, H. Abu Kassim, and A. N. Rosli, "Density Functional Theory (DFT) Calculation of Band Structure of Kesterite," *Adv. Mater. Res.*, vol. 1107, pp. 491–495, 2015.
[16] W. Xiao, J. N. Wang, X. S. Zhao, and J. W. Wang, "Intrinsic defects and Na doping in CZTS: A density-functional theory study," *Sol. Energy*, vol. 116, pp. 125–132, 2015.
[17] S. Das, K. C. Mandal, and R. N. Bhattacharya, Earth-Abundant $Cu_2ZnSn(S,Se)_4$ (CZTSSe) Solar Cells, vol. 4, pp. 25-74, 2016.

Construction and testing of a magneto-optical trap for laser cooling of rubidium atoms

Kessie Govender, Adrian Wyngaard and Rory Pentz

Quantum Physics Research Group, Dept. of Electrical, Electronic and Computer Engineering, Cape Peninsula University of Technology , Symphony Way, Bellville, Cape Town, South Africa

E-mail: govenderk@cput.ac.za

Abstract. We describe in this paper details of the design, development and testing of a device to cool and trap neutral Rubidium atoms. The system consists of an ultra high vacuum chamber having a number of view ports, plus vacuum pumps, piping, vacuum gauge and valves. Rubidium atoms stored in a getter material are released into the vacuum chamber by means of electrical heating. Three pairs of counter propagating laser beams, each pair positioned on opposite sides of the chamber along three orthogonal axes, are used for cooling of the atoms in the chamber. The cooled atoms are trapped using a pair of anti-Helmholtz magnetic coils positioned on either side of the vacuum chamber. Optical sensors such as CCD cameras and avalanche photo detectors for measuring the light emitted by the trapped atoms are used to estimate parameters of the trapped atom cloud.

1. Introduction and background information

A quantum optics laboratory is currently being developed at the Cape Peninsula University of Technology by the Quantum Physics Research Group within the Department of Electrical Engineering. The group is engaged in laser-atom interaction research, particularly the study of interaction of lasers with cold and ultra cold atoms.

Cold atoms are produced in a device called a magneto-optical trap (MOT)[1, 2]. Atoms that are used in these experiments are alkali atoms (Group I elements of the periodic table). These atoms have a closed shell configuration plus one unpaired electron. Rubidium and Cesium are more common candidates these days, as there are readily available laser sources in the form of diode lasers that could be used for cooling these atoms [3, 4].

In this paper we focus on the design, development and testing of the magneto-optical trap. This exercise requires constructions skills in electronic, mechanical and optical systems. The only other institutions in South Africa that are involved in similar research are the University of KwaZulu-Natal who have reported preliminary findings in cooling ^{85}Rb and University of Stellenbosch who are conducting research into cold ions.

This paper is organised as follows. The basic theory of laser cooling and trapping is presented in Section 2. In Section 3 an overview of the design of the magneto-optical trap is described. The performance of the trap is given in Section 4. The summary and conclusion is given in Section 5.

 ISBN: 978-0-620-88875-2

2. Theory of laser cooling and trapping

In this section we explain the basic principle of cooling atoms using laser beams and trapping them using magnetic fields.

2.1. Electronic structure of Rubidium

Rubidium has 37 electrons and lies in the first group of the periodic table. There are two naturally occurring isotopes, ^{85}Rb and ^{87}Rb with an abundance of 70% and 30%, respectively. There is one unpaired electron which exits in the 5s orbital. Although we have managed to cool both ^{85}Rb and ^{87}Rb, we will discuss laser cooling using ^{87}Rb. The ground state and first few excited states of ^{87}Rb are shown in Figure 1. This figure shows the fine and hyperfine splitting of the 5s and 5p orbitals relevant for laser cooling.

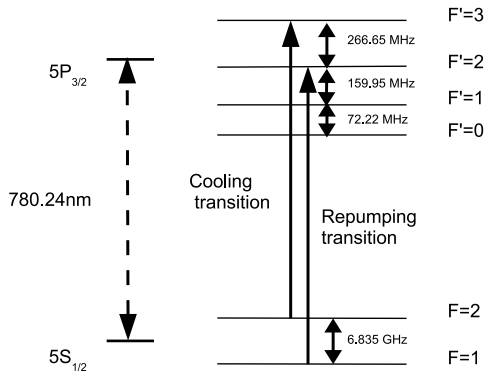

Figure 1. Electronic structure of ^{87}Rb.

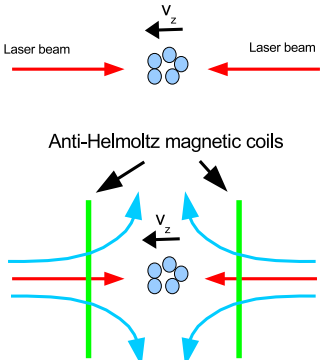

Figure 2. Laser cooling in 1D (top) and laser cooling and trapping arrangement (bottom). The vertical green bars represent anti-Helmholtz magnetic coils and the blue lines are the magnetic fields.

The transitions used for cooling are from F=2 to F′=3. For every thousand or so transitions the atom will decay to the lower ground state, thus taking it out of the cooling cycle. To bring atoms back into the cooling cycle a repumping laser is used to pump them to the upper F′ state as shown in Figure 1. From there they have a higher a chance to decay to upper ground state.

2.2. Doppler cooling and trapping

We will illustrate laser cooling using a one dimensional situation as shown in Figure 2. A cloud of atoms is subjected to two counter propagating laser beams as shown. The laser frequencies are set to be slightly lower than the resonant transition of the atoms, i.e. the lasers are detuned with respect to the atomic transition.

Let's assume that the atoms are moving to the left with velocity v_z as shown. Atoms see the left approaching laser beam to have a higher frequency, due to a Doppler shift, closer to resonance and it is more likely to absorb photons from that beam. Energy and momentum are absorbed. With each photon absorption, the atom gets a momentum kick in the opposite direction thus slowing down the atom in the process. For the atoms moving to the left the right laser beam is further detuned (due to the Doppler shift) and the atoms are less likely to absorb photons coming from the right laser. The opposite happens for atoms moving to the right.

For speeds close to zero there is an inverse linear relation between the force F and speed v_z and it can be shown that [5]:

$$F = -\gamma v_z \tag{1}$$

where γ is a damping factor that depends on the decay rate of the excited state, mass of the atom, detuning of the cooling laser, Planck's constant and the wave number of the laser. The above equation represents a force that is similar to viscous damping. To achieve cooling in 3D, three counter propagating laser beams intersecting at right angles are used.

There is a lower temperature limit to which cooling can be achieved using Doppler cooling [2, 5]

$$T_{Dop}^{min} = \frac{\hbar\Gamma}{2k_B} \tag{2}$$

where Γ is decay rate of the excited state and k_B is the Boltzmann constant. For ^{87}Rb the above formula gives $T_{Dop}^{min} = 146$ μK. In practice, lower temperatures are achievable due to other mechanisms that come into play such polarization gradient cooling/Sisyphus cooling [2].

Although the lasers reduce the atomic velocities, they do not trap or change the density of the atomic cloud. Atoms can still drift out of the laser beam even when cooled. To achieve trapping, a pair of anti-Helmholtz coils (vertical green bars in Figure 2) are used to create a quadrupole magnetic field and the laser beams are left and right circularly polarized. The equation describing the force on the atoms due to the laser beam and the magnetic field is the same as for a damped harmonic oscillator. The atoms are thus attracted to both $v_z = 0$ in velocity space and $z = 0$ in physical space.

3. Overview of the magneto-optical trap

In this section we provide an overview of the vacuum system and optics for generating the laser beams for cooling. The schematic of the vacuum system is shown in Figure 3 and Figure 4 shows a simplified schematic of the optics for generating the cooling laser beams.

3.1. Vacuum system

As shown in Figure 3, the system consists of an octagonal vacuum chamber connected to three vacuum pumps, viz. ion, turbo and rotary pumps. The atoms are cooled in the octagonal vacuum chamber. Rubidium atoms stored in a getter material are released into the vacuum chamber by means of electrical heating. Three pairs of counter propagating laser beams, each pair positioned on opposite sides of the chamber along three orthogonal axes, are used for cooling the atoms in the chamber. These are shown as thick red arrows in Figure 3. The chamber has a number of view ports to allow for optical access. Three stages of pumping (i.e. rotary, turbo and ion pumping) are used to reduce the pressure from atmospheric down to approximately 10^{-10} mbar. The rotary pump is used first to reduce the vacuum pressure from atmospheric to around 10^{-3} mbar, and the turbo pump is then switched on to reduce the pressure to around 10^{-8} mbar. Finally the ion pump is turned on to reduce the pressure to around 10^{-10} mbar.

When the system was first put together a bake out was done over a period of three days to get rid of residual gases stored in the walls of the system. The system was gradually heated to a temperature of 160 ^{o}C during the first day, kept constant at this temperature for the second day and gradually reduced from 160 ^{o}C to ambient on the last day. Only the rotary and turbo pumps were used during the bake out period. The ion pump was only turned on, on the last day of bake out when the system temperature was below 80 ^{o}C.

3.2. Optical system

A simplified schematic of the optical system is shown in Figure 4. A single laser is used to generate the three pairs of counter propagating beams needed for cooling. The major portion of

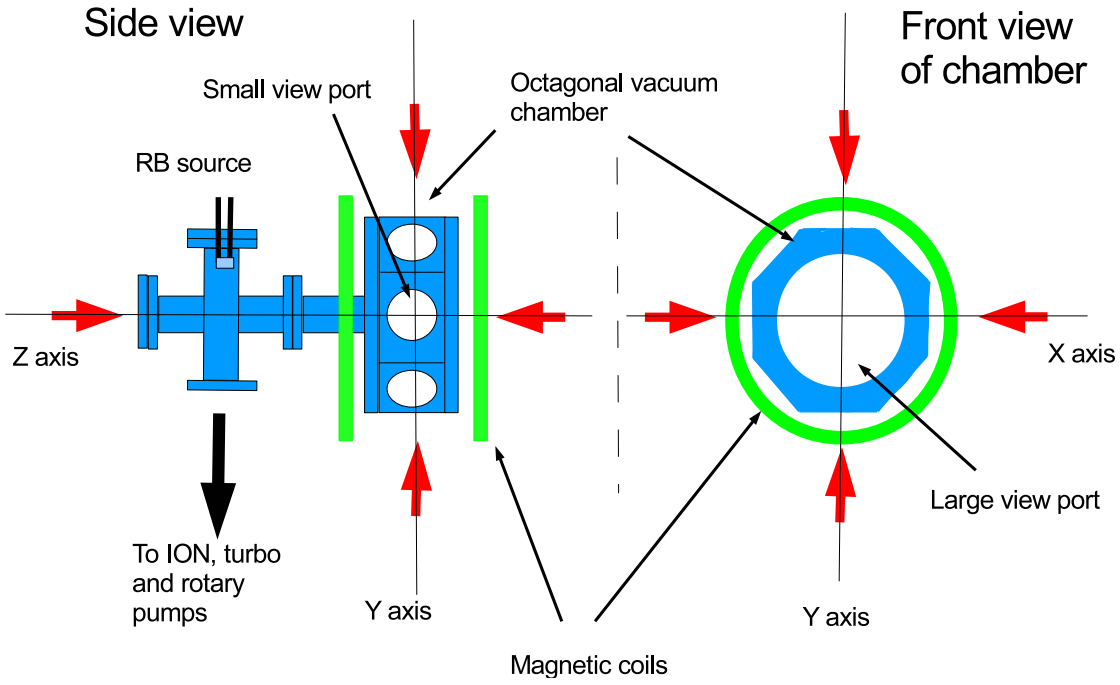

Figure 3. Schematic of the vacuum system. The system consists of an octagonal chamber having a number of view ports on the side and a large view port in front. Also shown in this figure are the counter propagating laser beams (red arrows) entering the chamber along the three axes. Positioned on either side of the chamber are the anti-Helmholtz magnetic coils.

the beam that emerges from the frequency stabilization set up passes through a half wave plate and then gets split three ways using polarizing beam splitter (PBS) and a 50/50 beam splitter. The half wave plate rotates the direction of linear polarization of the incoming laser beam and depending on the orientation it controls the amount of power that emerges in the arms of the PBS. One arm of the PBS produces the cooling beam on one of the axes. The other arm of the PBS goes to a 50/50 beam splitter which splits the remaining power equally between the other two cooling axes. The beams before entering the chamber are expanded using a set of lenses and passes through a quarter wave plate. The expanded beams have diameter of approximately 8 mm. Each beam is reflected back onto itself passing through a second quarter wave plate. The first quarter wave plate converts linear polarized light to circular polarized light. The second half wave plate changes the direction of circular polarization so that the overlapping beams in between the two quarter wave plates have counter rotating circular polarization. A repumping laser beam is combined with the cooling laser using a half wave plate and another PBS as shown.

The cooling and repumping laser frequencies are locked to the specific transition of Rubidium using a feedback system that consists of a saturated absorption setup (SAS) and servo-lock PID controller [3].

4. Results

The process to create cold atoms is quite involved: the two lasers first have to be locked to the correct frequency and this takes some trial and error before the lasers are locked. The Rb dispensers have to be turned on gradually and then the magnetic field is switched on. All of

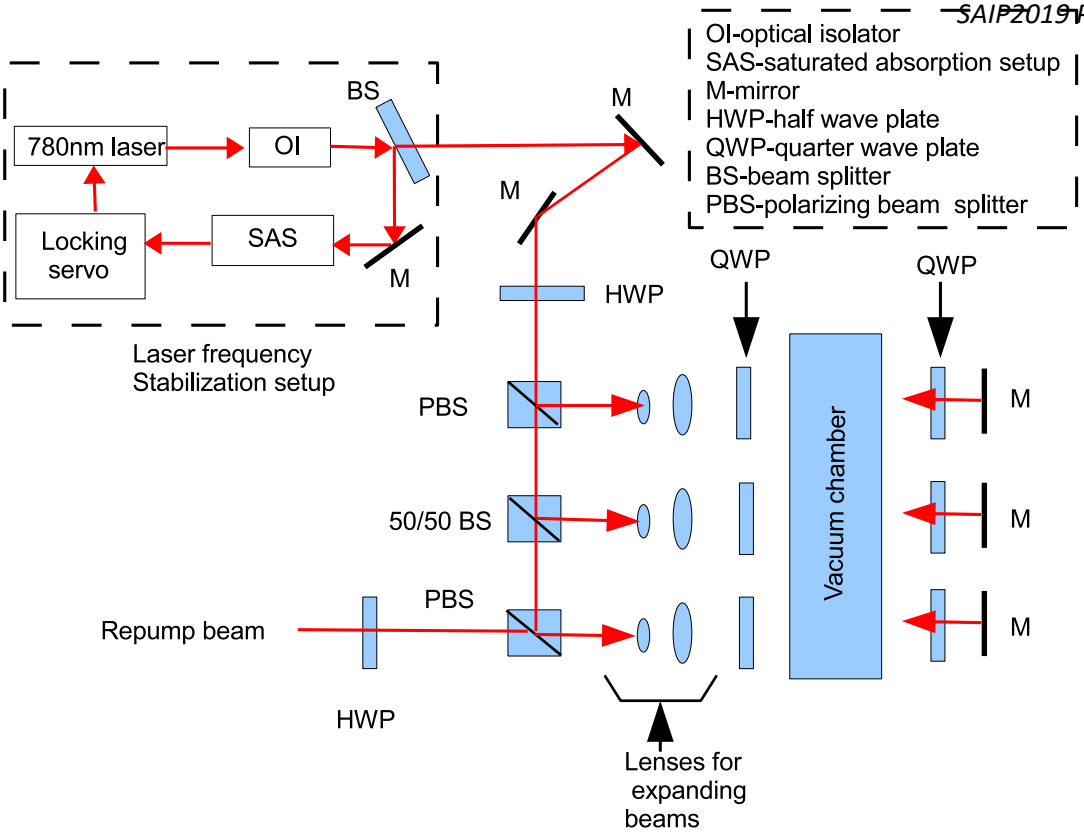

Figure 4. Optical setup.

these are done manually at the moment and usually takes two people to run and monitor all instruments at the same time. A cloud then forms within thirty seconds of everything being switched on. The images of the cloud are captured using monochrome CCD cameras. Figure 5 shows one of the images, looking through the large viewport in Figure 3.

Figure 6 shows a sequence of images spaced 200 ms apart showing growth of the cold atomic cloud (from left to right starting from top left) as soon as the magnetic field is turned on. These images are viewed via the side viewport in Figure 3. The width of each sub-image in Figure 6 is 11.5m. From this the size of the cloud is estimated to be approximately 3 mm in diameter. Figure 7 shows a plot of the integrated image intensity as a function of time, showing the growth of the cloud from the time the cooling lasers are turned on. These measurements were done using a magnetic field current of 4 A which gave a gradient at the centre of the trap of approximately 10 G/cm and the laser power on each beam entering the vacuum chamber was of the order of 3 mW.

To estimate the temperature of the cloud we have used a very simple method for now; the cooling laser is interrupted for a very short period and we monitor the integrated image of the cloud before and after the interruption of the beam. This is shown in Figure 8. The temperature of the cloud can be related to the integrated cloud intensity before and after the beams are interrupted [6]. Our estimate of the temperature is $\approx 17\mu$K.

5. Summary and conclusion

In this paper we have described the construction and testing of a magneto-optical trap for laser cooling of rubidium atoms. The overall performance of the trap was analysed and a cloud of cold ^{87}Rb atoms was created having an approximate diameter of 3 mm and a temperature of

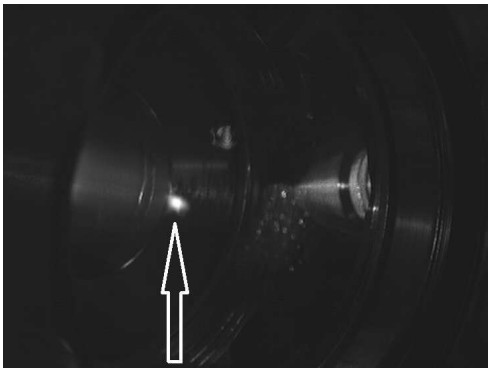

Figure 5. Image of the cloud viewed through the large viewport in Figure 3. The arrow points to the cloud.

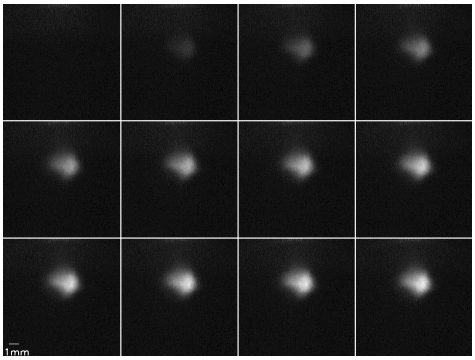

Figure 6. Sequence of images spaced 200 ms apart of the cloud showing growth from the time the system is activated.

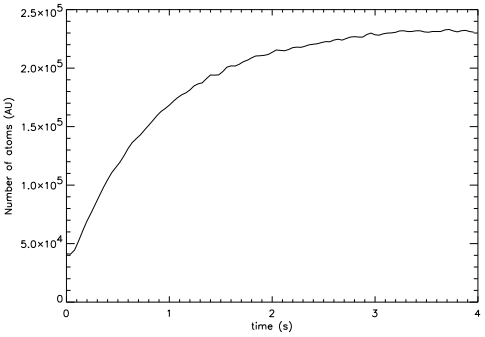

Figure 7. Integrated image intensity of the cloud as a function of time showing growth of the cloud of cold atoms from the time the system is started.

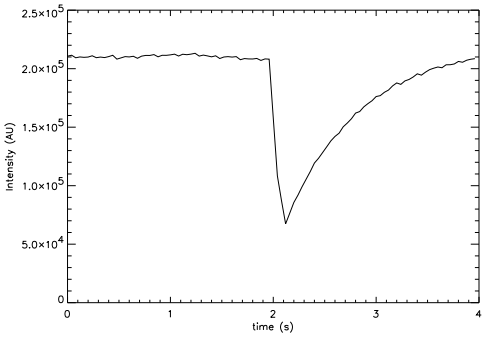

Figure 8. Integrated image intensity of the cloud as a function of time showing cloud growth after lasers are interrupted for a short duration.

around 17 μK.

References

[1] Wienman C and Flowers G 1995 *Am. J. Phys.* **63** (4) 317-30
[2] Metcalf H J and van der Straten P 1999 *Laser cooling and trapping* (New York: Springer)
[3] MacAdam K B Steinbach A and Wieman C 1992 *Am. J. Phys.* **60** (12) 1098-1111
[4] Wienman C and Hollberg L 1991 *Rev. Sci. Instrum.* **62** (1) 1-20
[5] Grynberg G, Aspect A and Fabre C, 2010 *Introduction to quantum optics* (UK: Cambridge University Press)
[6] Arora P, Swatilekha Chowdhury S, Agarwal A, Pant K and Gupta A S 2011 *Indian J. Pure and Applied Phys.* **49** 590-5

Density functional theory study of Cyanidin (Cy) dye molecule adsorbed on (100) TiO_2 anatase surface for application in DSSCs

T S Ranwaha[1], N E Maluta [1,2] and R R Maphanga [2,3]

[1].University of Venda, Department of physics, P/Bag X 5050, Thohoyandou, 0950, South Africa
[2].National Institute for Theoretical Physics (NITheP), Gauteng, South Africa.
[3].Council for Scientific and Industrial Research, Modelling and Digital Science, P.O Box 395, Pretoria, 0001, South Africa.

E-mail: funawahau@gmail.com

Abstract. Density functional theory (DFT) has been used to study the geometric, electronic and optical properties of Cyanidin (Cy) dye and its adsorption behaviour on (100) TiO_2 anatase surface. The generalized gradient approximation (GGA) was used in the scheme of Perdew-Burke Ernzerhof to describe the exchange -correlation function as implemented in the CASTEP package in material studio of BIOVIA. Our results show a redshift absorption of cyanidin dye adsorbed on (100) anatase TiO_2 surface, with a shift of Valence band towards the conduction band illustrating the reduction of band gap. The calculated adsorption energy of Cyanidin dye on (100) TiO_2 anatase surface was found to be $24.51\ \mathrm{K\ cal\ mol^{-1}}$ suggesting a stable grafting of the cyanidin dye onto the surface of the semiconductor. The highest percentage of light harvesting efficiency was found to be 14% at maximum wavelength. The adsorption results show a spontaneous electron injection followed by efficient regeneration of the oxidized dye molecules by the electrolyte and strong binding ability to the TiO_2 surface.

1. Introduction

The demand for reliable and economically viable alternatives to fossil fuels and the search for low cost renewable energy photovoltaics technologies have boosted the research on new materials. The solar cells used in harvesting the solar power are commonly categorized into different types in respect to the composition of their material (organic solar cells, non-crystal, multiple crystal, and single crystal silicon solar cells).The production cost of the solar cells based on silicon crystal material is high compared to the organic solar cells, which uses low temperature technologies and available materials [1]. The dye sensitized solar cells (DSSCs) is one on the current studied type of solar cells due to its lower cost of manufacturing, flexibility, high photon to energy conversion efficiency and its ability to be used as skylight windows [2]. DSSCs are devices that convert solar to electric energy by light sensitization established on wide energy band gap semiconductors [3].Typically a DSSCs architecture contains a transparent conductive oxide (TCO) on a glass or plastic substrate, a mesoporous nanocrystalline layer of the semiconductor (TiO_2), a sensitizer monolayer (dye) adsorbed on the surface of the semiconductor, an electrolyte with a redox couple (i.e. I^-/I_3^-) and a metal counter electrode where the redox mediator is regenerated[1-3].The dye which acts

as sensitizers in DSSCs plays an important task in absorption and conversion of incident light ray to electricity[4,5] . Recently, more attention has been directed to the use of metal-free organic dyes in DSSCs because of no noble metal resource restriction, high molar absorption coefficient, relatively easy synthetic procedure, several structures, tuneable absorption spectral response from the visible to the near infrared area and economical production techniques [6]. In this study we reported on the DFT studies of Cyanidin dye molecule on the (100) TiO_2 anatase surface, we reported our results on the light harvesting efficiency, HOMO-LUMO energy levels for electron injection of the dye, and the optical properties and electronic properties of (100) TiO_2 anatase/Cyanidin dye complex.

2. Computational method

The structure of the dye molecule was built using Material Studio of BIOVIA on a 3D atomic window [7]. The dye molecule structure was cleaned so that the atoms are reoriented in their lattice positions. Geometrical optimization of the dye molecule was performed by CASTEP package in material studio of BIOVIA using density functional theory (DFT) which uses a plane-wave pseudopotential method generalized gradient approximation (GGA) in the scheme of Perdew-Bruke-Ernzerhof (PBE) to describe the exchange-correlation functional using the coarse quality and all band/EDFT as electronic minimizer. The ground state structures obtained through geometrical optimization was imported into a new 3D atomic window and the optical absorption properties were calculated using Material Studio of BIOVIA Vulnerability Analysis Methodology Program (VAMP) [7]. Anatase TiO_2 bulk structure was optimized using CASTEP code within the framework of the Material Studio of BIOVIA to obtain its ground state properties. The GGA-PBE functional were used for geometrical optimizations. The convergence parameters of anatase TiO_2 structure were calculated and the k-points were obtained to be 7 x 7 x 3 and the cut-off energy to be 650 eV, the fixed basis set and ultra-soft pseudopotential were used throughout the study. The ground state structures obtained through geometrical optimization were imported into a new 3D atomic window and the (100) surface was cleaved from the structures and a vacuum slab of appropriate size built for the structures. After this process, the surfaces were optimized using the same convergence parameters obtained for the bulk structures and the electronic and optical properties calculated. The dye/ TiO_2 complex were also optimized to obtain the ground state structures, and the electronic properties calculated using CASTEP code

3. Results and discussion

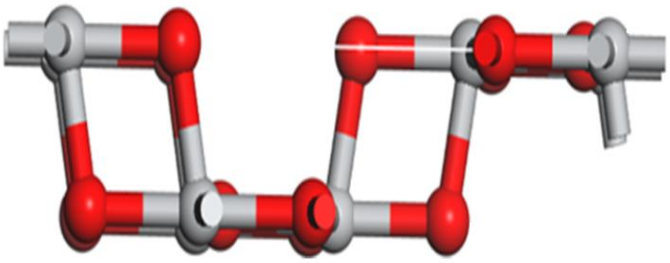

Figure 1: Structure of TiO_2 anatase (100) surface, red represent oxygen and grey represent titanium

Figure 1 illustrate the structure of TiO_2 anatase (100) surfaces cleaved from anatase TiO_2 bulk structure. The atoms in this surface are having some cleaved bonds in the termination position, while terminating with both oxygen and titanium. The surfaces were optimized by relaxing atoms to eliminate surface tension.

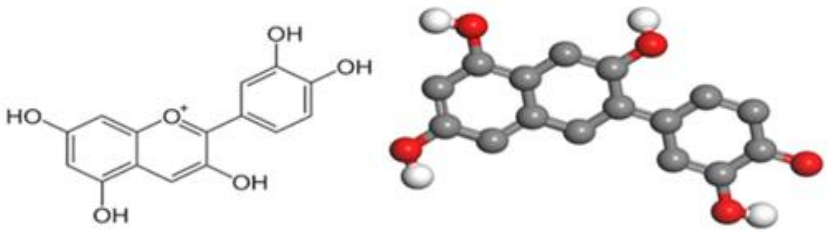

(a) (b)

Figure 2: The molecular structure of Cyanidin dye molecule [6] (a) and optimised geometry structure, red balls represent oxygen, grey balls represent carbon, and white balls represent hydrogen.

The molecular structure of Cynadin dye molecule is shown in figure 2, it is understandable that this dye has a widely delocalized p-conjugate electronic system on its skeleton plane and a highly symmetric structure [8].

3.1. Energy levels and isodensity surfaces of the dyes

The cyanidin sensitizer dye molecules structure was optimized for ground state energy level in vacuum and the E_{HOMO}, E_{LUMO} and HLG (E_{LUMO} - E_{HOMO}) were obtained as follows: E_{HOMO} = -8.081 eV, E_{LUMO}= -6.424 eV and HLG =1.657 eV respectively.

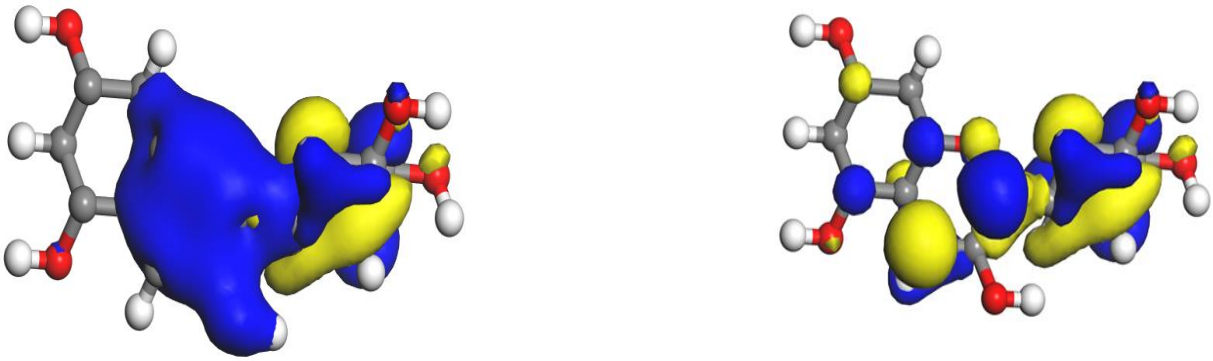

(a) (b)

Figure 3: Isodensity surfaces of the molecular orbitals (a) highest occupied molecular orbital (b) lowest unoccupied molecular orbital of Cyanidin dye molecule

The lower value of the HOMO-LUMO energy gap of sensitizer, illustrate the enhancement absorption of dye at higher wavelength and photocurrent response of DSSCs. Usually the energy gap between the LUMO of the dye and the conduction band must be more than 0.2 eV for effective electron injection. The calculated results show that the LUMO energy level of cyanidin dye is higher than the TiO_2 conduction band edge (4.0 eV) and energy gap between them is more than 0.2 eV. Thus, cyanidin has strong ability to inject electron into TiO_2 conduction band.

3.2. Absorption spectrum and light harvesting efficiency of the Dyes

Figure 4 illustrates UV-Vis spectra of Cyanidin dye molecules obtained using VAMP code on material studio package. The absorption maxima of the cyanidin dye molecules is situated at 304 nm.

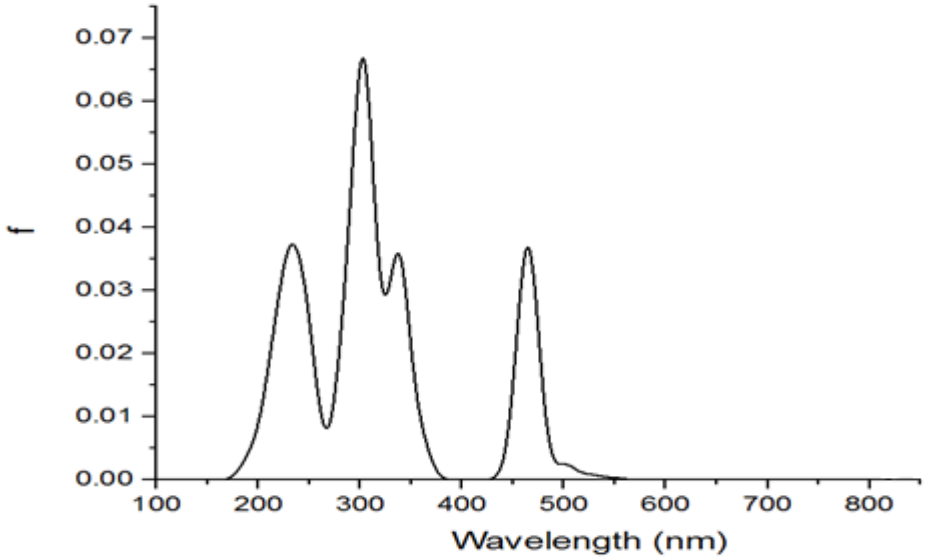

Figure 4: Calculated UV-Vis spectrum for cyanidin dye molecule

The light harvesting efficiency (LHE) at the absorption peaks was calculated using the following equation:

$$LHE(\lambda) = 1 - 10^{-f} \quad (1)$$

where f denotes the absorption or the oscillator strength of sensitizer at a given wavelength (λ) [9]. LHE becoming 0 for zero oscillator strength and 1 for infinite oscillator strength. The LHE values of Cyanidin dye calculated at respective λ_{max} are shown on table 1. It can be observed from the figure 4 and table 1 that the highest absorption of the dye molecule is at 304 nm with the LHE percentage of 14.0 which shows that the cyanidin adsorb more photons at visible light.

Table 1. Calculated light harvesting efficiency of cyanidin dye molecule

Wavelength	f	LHE	LHE (%)
235	0.037	0.082	8.20
304	0.066	0.140	14.0
339	0.035	0.077	7.70
464	0.036	0.081	8.10

3.3. Adsorption of cyanidin dyes on TiO_2 anatase (100)

Figure 5 shows the cyanidin dye adsorbed on TiO_2 anatase (100) surface to form TiO_2/dye complex, which is the structure formed when the dye molecule is adsorbed on the surface of TiO_2, the substance being absorbed is an adsorbate and the absorbing substance, an adsorbent. In this study an adsorbate is a cyanidin dye molecule and the adsorbent is TiO_2 anatase (100) structure.

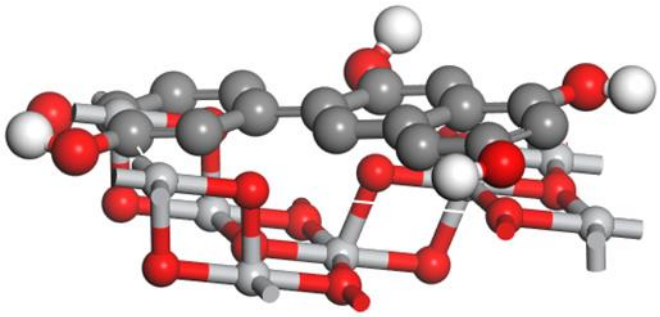

Figure 5: Structure of Cyanidin dye molecule adsorbed on TiO_2 anatase (100) surface

3.3.1. Electronic property (Density of State)

The total density of states (TDOS) shown in figure contains broad surface valence band and conduction bands separated by a wide band gap for TiO_2 anatase (100). A great TDOS at a given energy state means that there are numerous available states for occupation by electrons while a TDOS of zero represents that there are no states that can be occupied by electrons.

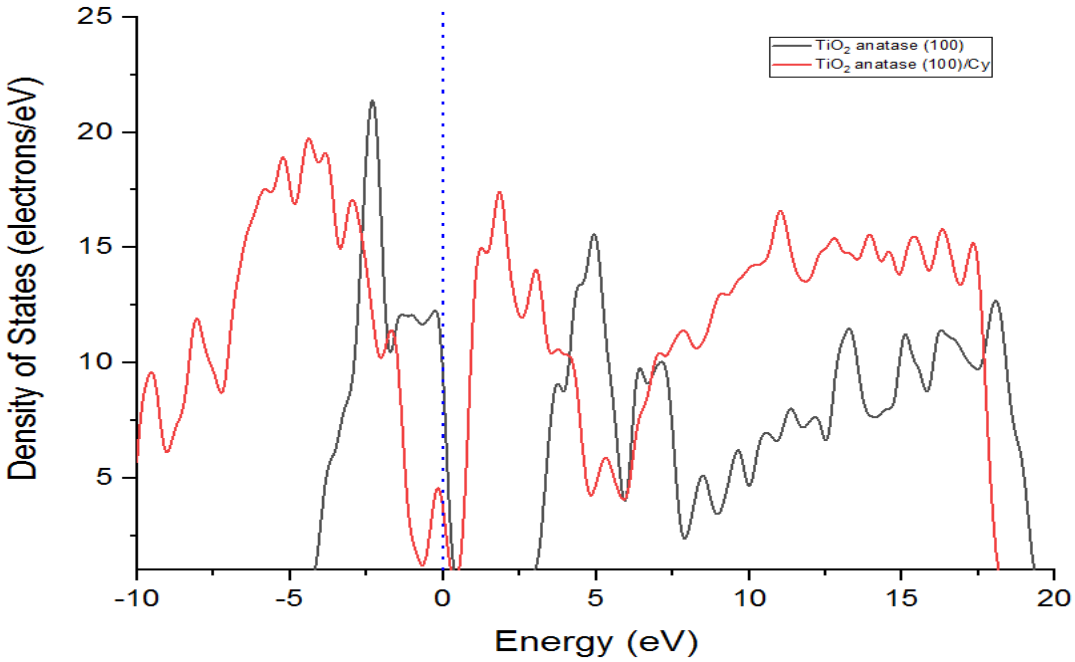

Figure 6: The total density of states of TiO_2 anatase (100) and TiO_2 anatase (100)/Cy complex

The TDOS curves Figure 6, shows that after adsorption, the dyes introduce sharp occupied molecular energy levels in the band gap. When comparing the pure TiO_2 anatase (100) surface to the TiO_2 anatase (100)/Cyanidin complex, the TDOS, point out a shift of the conduction band edge of TiO_2 towards the valence band, hence the band gap of TiO_2 anatase (100)/Cyanidin complex is smaller than that of the pure TiO_2 anatase (100) surface.

3.4. Adsorption energy of TiO_2 /dye complex

The adsorption energies of cyanidin on TiO_2 are computed using equation 2 [9]:

$$E_{ads} = [E_{dye} + E_{(TiO2)}] - [E_{(dye+TiO2)}] \quad 2$$

where E_{ads} is the adsorption energy, E_{dye} is the energy of the dye, $E_{(TiO2)}$ is the energy of the TiO_2 slab

and $E_{(dye+TiO2)}$ is the total energy of the dye-TiO_2 complex [9]. The calculated adsorption energy was found to be 24.51 K cal mol^{-1}. The adsorption energy denotes the binding ability of the dye molecules, and the positive value obtained shows that Cyanidin binds stronger when adsorbed on to TiO_2 anatase, and the TiO_2/dye complex is stable.

4. Conclusion

First-principles DFT has been used to systematically investigate, the HOMO-LUMO energy gap, UV-Vis spectrum and light harvesting efficiency of cyanidin dye molecules. The HOMO-LUMO energy gap found to be 1.657 eV, which shows an effective electron injection and the shift of the absorption to near infrared region. The calculated results show that light harvesting efficiency depend on the absorption (oscillator strength) of the dyes. The obtained adsorption energy of cyanidin dye on anatase TiO_2 (100) surface clearly points out to large value of around 24.51 K cal mol^{-1} which shows that the complex is stable and has a strong binding ability., The TDOS illustrate that after adsorptions, the dyes introduce sharp occupied molecular energy levels in the band gap.

5. Acknowledgement

This work is financially supported through the NRF Thuthuka, DST Renewable Energy Funding, merSETA and the National institute for theoretical Physics (NiTheP). We would also like to thank the University of Venda for the support to carry out this research and Centre for High performance Computing (CHPC) for using their computing facilities.

6. eferences

[1] Adedokun, O., Titilope, K., & Awodugba, A. O. (2016). Review On Natural Dye-Sensitized Solar Cells (Dsscs).

[2] O'regan, B., & Grätzel, M. (1991). A Low-Cost, High-Efficiency Solar Cell Based On Dye-Sensitized Colloidal Tio2 Films. *Nature*, ***353*(6346),** 737.

[3] Ozuomba, J. O., Ekpunobi, A. J., & Ekwo, P. I. (2011). The Viability Of Prophyrin Local Dye In The Fabrication Of Dye Sensitized Solar Cells. *Digest Journal Of Nanomaterials & Biostructures (Djnb)*, ***6*(3).**

[4] Chitumalla, R. K., Lim, M., & Jang, J. (2015). Substituent Effects On The Croconate Dyes In Dye Sensitized Solar Cell Applications: A Density Functional Theory Study. *Journal Of Molecular Modeling*, **21(11),** 297

[5] Luceño-Sánchez, J. A., Díez-Pascual, A. M., & Peña Capilla, R. (2019). Materials For Photovoltaics: State Of Art And Recent Developments. *International Journal Of Molecular Sciences*, ***20*(4),** 976.

[6] Rahnasto-Rilla, M., Tyni, J., Huovinen, M., Jarho, E., Kulikowicz, T., Ravichandran, S., ... & Moaddel, R. (2018). Natural Polyphenols As Sirtuin 6 Modulators. *Scientific Reports*, ***8*(1),** 4163

[7] Clark, S. J., Segall, M. D., Pickard, C. J., Hasnip, P. J., Probert, M. I., Refson, K., & Payne, M. C. (2005). First Principles Methods Using Castep. *Zeitschrift Für Kristallographie-Crystalline Materials*, ***220*(5/6),** 567-570.

[8] Matsui, M., Hashimoto, Y., Funabiki, K., Jin, J. Y., Yoshida, T., & Minoura, H. (2005). Application Of Near-Infrared Absorbing Heptamethine Cyanine Dyes As Sensitizers For Zinc Oxide Solar Cell. *Synthetic Metals*, ***148*(2),** 147-153.

[9] Puyad K.R Chitumella, And K Bhanuprakash. Adsorption Of Croconate Dyes On Tio_2 Anatase (101) Surface: A Periodic Dft Study To Understand The Binding Of Diketo Groups, *Journal Of Chemical Sciences*, **124**, 1, 301-310, (2012).

Development and testing of a photon detector for Quantum optics experiments.

R A Pentz[1] and K Govender[2]
[1,2] Department of Electrical, Electronic and Computer Engineering, Cape Peninsula University of Technology, Bellville, Cape Town, 7535, South Africa

E-mail:[1] pentzr@cput.ac.za

Abstract. Quantum communications and computing rely heavily on the use of single photons. Thus there is a need for generating single photons and detecting single photons. In this research, we focus on the detection of single photons. We employ an avalanche photodiode (APD) for this purpose. APD's are special electrical diodes that are operated in reverse bias, beyond the breakdown voltage in the Geiger mode. In the Geiger mode, the device is still non-conducting. Upon receiving a single photon an avalanche breakdown occurs, resulting in a large current. The device then needs to be quenched before it can detect another photon. This can be done using passive or active quenching methods. In this paper, we provide the methodology followed in developing a single photon detector and the challenges associated with developing such a single-photon detector. Some experimental results are also provided.

1. Introduction

Quantum cryptography is currently being investigated at the Cape Peninsula University of Technology with the focus being on developing a quantum key distribution system. The whole project aims to develop and construct a basic, cost-effective, quantum key distribution system, based on the BB84 protocol [1]. One of the main components of such a system is single-photon detectors (SPD). The two main devices that can be used for this application is a photo-multiplier tube (PMT) and an APD. Silicon APD is well researched and well developed, and therefore it is the 1st choice when it comes to selecting a detector [2]. The APD is referred to as a single-photon avalanche diode (SPAD) when it is used to detect a single photon and when it is used in the Geiger mode [3]. Developing a SPAD comes with its challenges and trade-offs.

This paper is organised as follows: The basic theory of developing a SPAD is presented in section 2. Section 3 gives an overview of the experimental setup. The results obtained are presented in section 4, followed by the conclusion in section 5.

2. Single Photon Detection

In a system where one uses photons to communicate, it is important to be able to detect each photon with 100% accuracy. SPAD is used to detect photons, but they have practical limitations, called dead-time and dark-count rates [4].

A SPAD is manufactured with three different types of materials, functioning at different wavelengths: Silicon (Si) (750 nm-900 nm), Geranium (Ge) (1000 nm-1350 nm), and Indium Gallium Arsenide (InGaAs) (950 nm – 1550 nm). These SPAD can be operated in linear or Geiger mode. Geiger

mode is when the diode is operated beyond the reverse breakdown voltage, which results in a huge current gain during an incident photon [5].

The SPAD (D in figure 1) is reversed biased (V_{bias}) to be above the breakdown voltage, V_{bias}, with a DC power supply. At this high V_{bias}, the electric field is so high that a single photon, absorbed within the junction of the SPAD, can trigger a self-sustaining avalanche. When a photon triggers an avalanche, there is a rapid increase in the current to be above the trigger current, I_t, of the diode. In this mode, quenching is required to reset the diode to its original state [3].

Three types of quenching methods are available:

- Passive quenching is achieved by connecting a large resistor (R), 50 kΩ-500 kΩ, in series with the SPAD so that there is a reduction in voltage across the SPAD as soon as the avalanche occurs (figure 1) [6].
- Active quenching utilizes a complex circuit that actively lowers the biasing voltage to a voltage below the reverse breakdown voltage as soon as the avalanche occurs, controlling the dead time and reducing it to a shorter effective quenching time [2].
- Gated mode entails keeping the biasing voltage below the breakdown voltage and increasing it to the required voltage just before an expected photon arrives. The count rate of this method is similar to active quenching but reduces the complexity of the electronic circuit [5].

A Silicon avalanche photo-diode, utilizing passive quenching, will be used, as this is the most cost-effective way to produce a photon detector. Quenching the SPAD is done by introducing a quenching resistor R (figure 1). The quenching resister will force the voltage across the SPAD to decrease rapidly as the current increase, reducing the current to below I_t, therefore resetting the SPAD to a non-conductive state. The reverse bias voltage, V_{bias}, is chosen to be slightly higher than the V_{BD}.

$$V_{excess} = V_{bias} - V_{BD} \tag{1}$$

V_{excess} is the additional voltage above the breakdown voltage [3].

The value of R can be calculated as follows:

$$R = \frac{V_{bias} - V_{BD}}{I_t} \tag{2}$$

The value of R is normally large and is in the order of hundreds of kΩ.

The recovery time is the time required for the SPAD to change from a conduction state to a non-conduction state. This recovery time is also referred to as the dead time, as during this time the SPAD can't detect the next photon. The recovery time τ is a product of the total capacitance C, consisting of the junction capacitance C_j and the stray capacitance C_s, of the SPAD and the quenching resistor R [3].

Dark-counts can be created due to two main causes: Firstly, thermal energy contained within the SPAD can cause an avalanche to occur, creating a current pulse, without an incident photon [3]. Secondly, dark-counts can occur due to after-pulse. After-pulses occur, due to carriers trapped within the junction's depletion layer and when released, an avalanche can occur [3]. High dark-counts will decrease the accuracy of the detector to detect when a photon is arriving. There is also an increase of dark-counts with the increase of V_{bias}. Dark-counts can be reduced by a factor of 50 by cooling the SPAD down to -25 °C, as the dependence of dark-count rate on temperature, is exponential. Dark-current is the current due to dark-count and therefore this current also increases with the increase of V_{bias} [7]. According to Robert Brown *et al.* a V_{excess} of 3-3.5 V is an acceptable voltage to be used when the SPAD is cooled [8].

3. Experimental Setup

The basic setup, depicted in figure 2, is used. The photon source is pulsed with optical switches, which are mechanically synchronized. The photons are channeled via free air into the SPAD and photodiode (PD). The SPAD is an APD10-8-150-T52 from OSI Optoelectronics with a trigger current, I_t, of 10 µA and a breakdown voltage, V_{BD}, 156.6 V was used. V_{excess} of 1.4 V was used to determine R=142 kΩ. V_{excess} was selected to be small, as the dark-current should be as little as possible and the SPAD is not cooled and was used at room temperature.

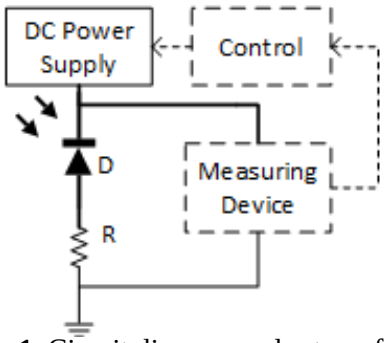

Figure 1. Circuit diagram and setup of the single-photon detector.

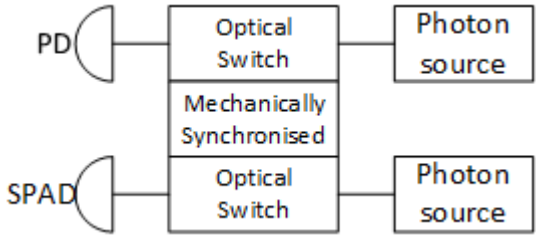

Figure 2. Experimental setup to characterize a single-photon detector.

A reference pulse was created, by measuring the voltage across the limiting resistor of the led. This reference pulse will show us how the current through the led changes and will be used to determine the position of the pulse generated by the SPAD. The wavelength for the photon source for the SPAD is 780 nm and the power of the photon source was reduced to a point where the photon source can just produce light. The light power was measured to be 0.65 nW and a light power meter was used. The electrical pulses generated by the SPAD was measured by an oscilloscope. The purpose of the reference pulse is to determine when a pulse is expected from the SPAD, as the pulse is very small and can be embedded within the noise. The passive quenching circuit and DC power supply are illustrated in figure 1. The current measuring device is an oscilloscope and will be replaced by a comparator circuitry, that will detect any pulses from the SPAD. This will be done in conjunction with a control circuit, as it is crucial to obtaining maximum gain and a low dark-current from the SPAD.

4. Results

4.1. Gain and Dark-current

The gain of the SPAD and the dark-current was measured by varying the intensity of the photon source so that the entire range of measurements can be done without saturating the SPAD. The optical switch was set to function at a steady rate of 50 Hz. The biasing voltage was increased from 0-160 V, in steps of 1 V, while documenting the voltage across R. The voltage measured with a biasing voltage of 0 V, was used as a reference, as the SPAD will produce a gain of one at no biasing voltage, and function like a normal photodiode.

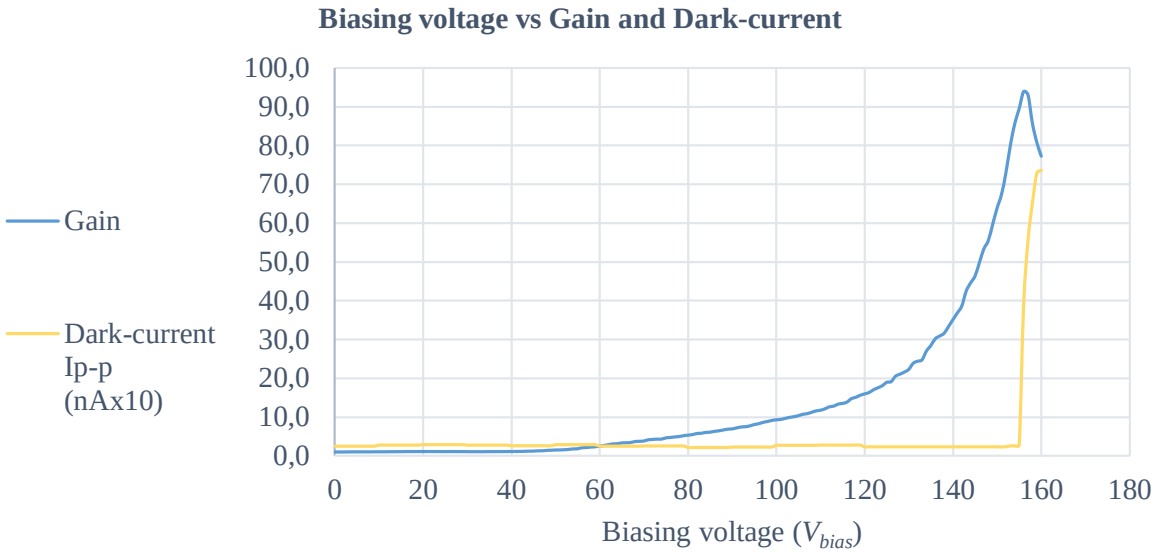

Figure 3. Graph representing biasing voltage vs gain and dark-current.

 ISBN: 978-0-620-88875-2

Gain is the ratio of the output voltage and the reference voltage. The photon source for the SPAD was switched off and the voltage across *R* was measured and converted to a current, which represents the dark-current. Figure 3 shows the results of dark-current and gain, versus biasing voltage.

The SPAD, according to the manufacturer, has a maximum gain of 100, but in practice, a gain of 93.9 was achieved. Observe the increase of dark-current while the gain is at a maximum. Take note that the gain reduces after reaching a peak. This shows that selecting V_{bias} incorrectly will result in low gain and an increased dark-current.

4.2. Photon Counting

Figure 4 shows the pulses measured from the APD (orange, top) and the reference signal from the PD (blue, bottom).

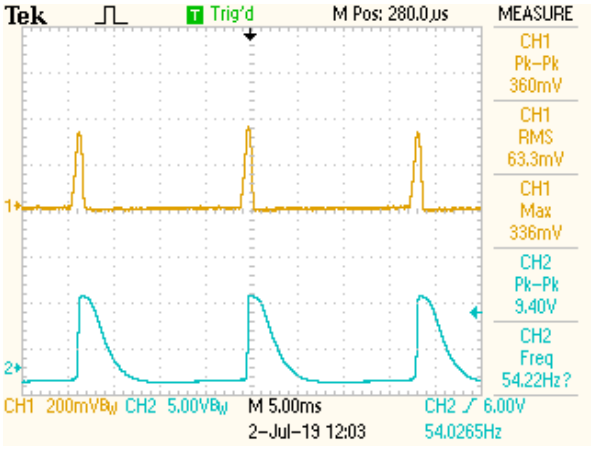

Figure 4. Output waveforms from the APD and PD

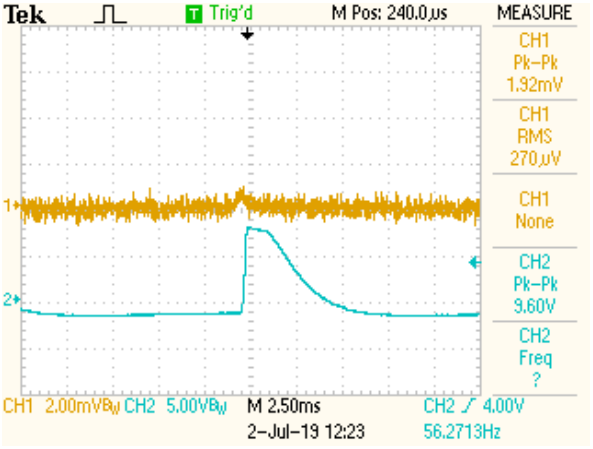

Figure 5. Smallest pulse measured from the APD

Selecting V_{bias} as 158 V, as determined above, will result in a voltage gain of 85.6, with a dark-current of 652.78 nA. Using figure 3, one can reduce the dark-current by selecting a lower biasing voltage of 155 V, and therefore reduce the dark-current to 27.78 nA, with a gain of 89.5. By doing this, one maximizes the gain, while keeping the dark-current to a minimum. It should be mentioned that the manufacturer included a specification sheet for the device, stating that V_{BD} was 156.6 V. Figure 5 shows the reference pulse (blue, bottom) and therefore the position of the output pulse of the APD (orange, top) is identified, even though it is hidden by the noise. The power of the light was measured with a light power meter and, with the aid of the following equation, the number of photons could be calculated:

$$N = \frac{P \times T \times \lambda}{h \times c} \tag{3}$$

N is the number of photons, *P* is the power measurement of the light, *T* is the period of the pulse, λ is the wavelength, *h* is Planck's constant, and *c* is the speed of light. The number of photons calculated was 51.01×10^6 photons. Therefore, each pulse in figure 5 represents a large number of photons. We still need to optimize the setup to be able to detect just one photon.

4.3. Quenching

The junction capacitance of the SPAD is 6 pF from the datasheet, and the stray capacitance, measured of the circuit, is 0.5 nF. The resistor, *R*, has a value of 142 kΩ, and therefore a quenching time (or dead-time) was calculated to be 71.85 µs. Figure 6 shows the pulse of the SPAD (blue, bottom) with the measurement of a fall time of 80.8 µs, which is a good approximation of the time taken to quench the APD.

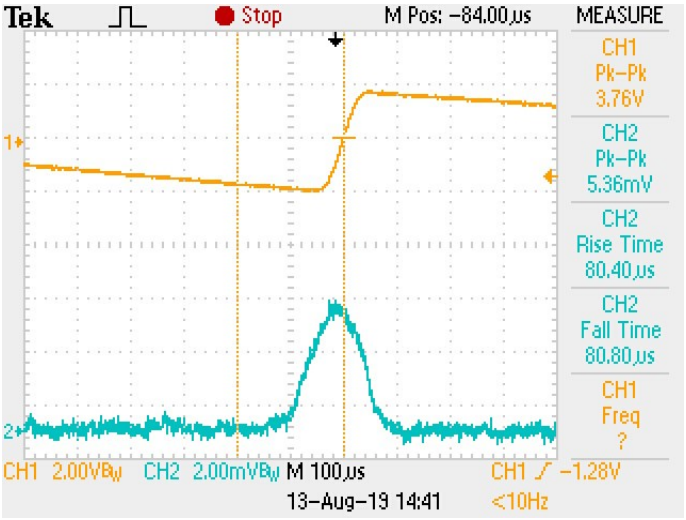

Figure 6. Measurement of the quenching time for an APD

5. Conclusion

A simple photon detector was developed to get acquainted with the challenges, related to such a device. While it is still necessary to optimize the circuit so that we can detect single photons, we have demonstrated the operation of the detector at very low light levels. The detector was constructed, characterised and measurements were shown. It was shown that, by applying attention to the gain/dark-current versus bias voltage, one can select an optimal reverse biasing voltage to obtain a maximum gain, with minimum dark-current. It is still a challenge to obtain single-photon results, due to the rising noise floor and a lack of sufficient gain. Care should be taken to keep circuit and radiation noise to a minimum.

References

[1] Bennett C H and Brassard G *1984 Proc. of IEEE Int. Conf. on Computers Systems and Signal Processing* **1/3**, 175-179
[2] Bennett C H and Brassard G 1984 *Proc. of IEEE Int. Conf. on Computers Systems and Signal Processing* **1/3**, 175-179
[3] Cova S, Ghioni M, Lotito A, Rech I and Zappa F 2004 *J. Modern Optics* **51**, 1267-1288
[4] Cova S, Ghioni M, Lacaita A, Samori C and Zappa F 1996 *Appl. Optics* **35**, 1956-1976
[5] Shenoy-Hejamedi A, Pathak A and Radhakrishna A 2007 *Quanta* **6,** 22
[6] Gisin N, Ribordy G, Tittel W and Zbinden H 2002 *Rev. of Modern Phys.* **74**, 145-195
[7] PerkinElmer Inc. 2000 *High-Speed Solid State Detectors for Fiber Optic and Very Low Light-Level Applications, Silicon Avalanche Photodiodes C30902E, C30902s, C30921E and C30921S datasheet*
[8] Brown R G W, Ridley K D and Rarity J G 1986 *Appl. Optics* **22** 4122-4126

The Diagnostics and Verification System for the Tile Calorimeter Trigger and Data Acquisition framework of the ATLAS Detector

Nthabiseng Miranda Lekalakala[1], Thabo Masuku[1] and Bruce Mellado[1,2]

[1] School of Physics and Institute for Collider Particle Physics, University of the Witwatersrand, Johannesburg, Wits 2050, South Africa
[2] iThemba LABS, National Research Foundation, PO Box 722, Somerset West 7129, South Africa

E-mail: 673507@students.wits.ac.za

Abstract. During the maintenance period of the Front-End electronics of the Tile Calorimeter of the ATLAS detector, the state of the electronics has to be assessed, first by confirming existing problems, and secondly by assessing the validity of the repairs. The Diagnostics and Verification System (DVS) tests are composed of checks that are used to verify the functionality of the TileCal front-end (FE) electronics and is used mostly during the maintenance period. The DVS implements similar tests to the Mobile Integrity Check (MobiDick) in an embedded system. MobiDick is the first level tests after repairs, and the DVS follows at the second level when the module is inserted back into position and connected to the TDAQ system. The current high-precision DVS tests available for the TileCal are run from the command-line using two separate programs executed on separate computers. This is not efficient and is mostly understood by TileCal Data Acquisition (DAQ) experts.

1. Introduction

The ATLAS (A Toroidal LHC Apparatus) detector is one the two multipurpose experiments at the Large Hadron Collider and it is utilized for the search of new physics. It consists of four main components namely the inner detector, calorimeter, muon spectrometer and magnet system. The hadronic Tile Calorimeter is a sampling calorimeter that resides in the innermost part of the ATLAS detector and it is used to measure energies carried by charged and neutral particles. It uses steel as an absorber medium and scintillating tiles as the active medium. It consists of two extended barrels (EB) and one central long barrel (LB). The system is split into four partitions such as EBA and EBC for the extended barrel and LBA and LBC for the long barrel [1]. Each partition constitutes 64 azimuthally segmented modules which are commonly known as the super-drawers. The super-drawer consists of Front-End electronics such as the digitizer boards, adder boards, interface boards, photo-multiplier tubes, 3-in-1 cards and High voltage divider boards that needs to assessed and maintained during the Long and Short Shut-down.

The ATLAS Online Software is in charge of the overall experimental configuration of the AT-

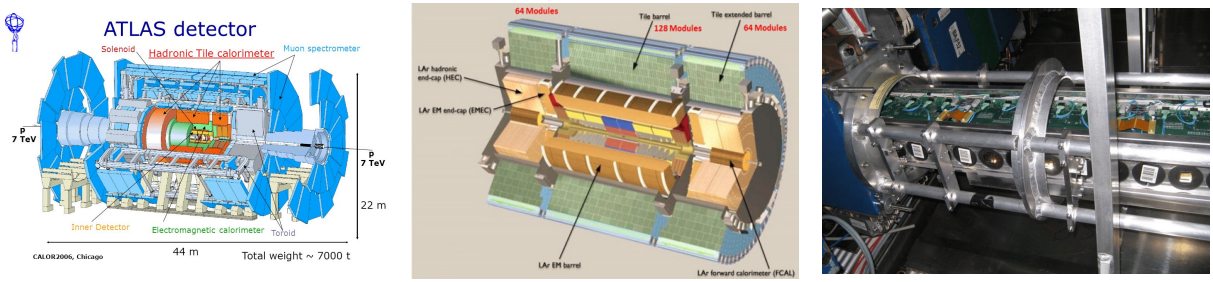

Figure 1. ATLAS Detector (left) , Tile Calorimeter (middle) and Super-Drawer (right)

LAS detector including the run control. It monitors the Trigger and Data Acquisition systems software (TDAQ), which is a system that reduces the vast amount of data from the collisions to a manageable amount. The trigger system checks the data and selects events with distinguishing characteristics that makes them suitable for the physics analysis. The data acquisition system channels the data from the detector to storage. The main purpose of the online software is to readout, transport, and to store data that originates from the proton-proton collisions. It must synchronize and collaborate with the other ATLAS sub-systems, in particular, interfaces are required for the data-flow, triggers, processor farms, event builder, detector read-out crate controllers and Detector Control System (DCS) [2, 3].

The Control subsystem of the ATLAS detector supervises the individual detector components as well as the experimental infrastructure. The DCS includes a number of software packages that enables equipment supervision using operator commands, reads, processes and archives the operational parameters of the detector, allows for error recognition and handling, manages the communication with external control systems, and provides a synchronization mechanism with the physics data acquisition system. The Diagnostics and Verification system is part of the software packages of the DCS. It is utilized for checking and diagnosing faults in the front-end components of the detector [3].

2. The Diagnostics and Verification System

The DVS is part of the ATLAS Online TDAQ software. It is a supporting structure that allows TDAQ developers and experts to combine tests and knowledge into it, thus making it user-friendly for a non-experienced shift operator to be able to diagnose problems within the TDAQ component. There are two types of TDAQ users namely the TDAQ operator and the TDAQ expert. The TDAQ Expert is mainly involved in the implementation, configuration and storing tests in the database while the role of the TDAQ operator is to perform tests on the components [3, 4].

The DVS tests are a set of digital checks that examines the functionality of the components of the super-drawer. They are similar to the Mobile Drawer Integrity Checking System (MobiDick) in the sense that they check assess the functionality of the individual components of the super-drawer. The MobiDick and DVS tests differs in aspects of how the test is being performed. For the MobiDick testing the drawer has to be opened while the drawer has to remain closed for the dvs testing. DVS are second level tests that follows immediately after MobiDick to verify the faults found in the components.

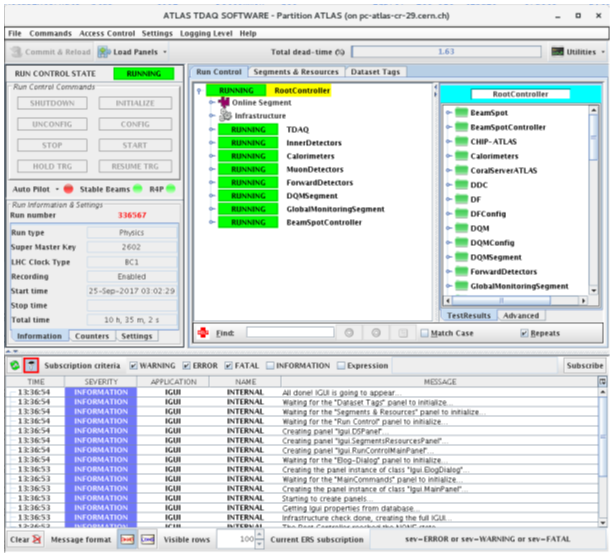

Figure 2. The DVS GUI

2.1. DVS Implementation and Graphical User Interface

The DVS can be accessed by human users (TDAQ operator) via the DVS Graphical User Interface (GUI) or by online software packages (TDAQ supervisor) via the Application Programming Interface (API). To be able to implement the required functionality, the DVS reads the TDAQ configuration via the configuration databases service, it then launches the tests via the test manager and then use the CLIPS ("C" language Integrated Production System) packages to implement the expert system [3]. The DVS has an internal architecture that is composed of the following:

- A Test Repository Database: A database that describes the attributes of a test in the configuration database. The test attributes are described in the form of classes in this case the classes are *Test, Test4Object or Test4Class*
- A knowledgeable Base: Store specific Knowledge about component functionality.
- An Expert System Engine: Available via the C/C++ API.
- C++ and Java Libraries
- A Graphical User Interface application: The user interface used for DVS is the partition. The hardware components are described in the configuration database of the ATLAS TDAQ. Tests are configured using the Test Manager which reads the OKS (Object Kernel System) configuration database to select tests to be executed. Tests have to be collected in Test Repositories and linked to the Partition or one of its Segments [3]. The user can select any component on the partition and perform tests specific for that component.

2.2. DVS Tests

There are several types of DVS tests:

- Charge Injection Scan (CIS): This test checks the existence of a pulse inside some bands for high and low gains.
- Pedestal Test: This test checks the low and high frequency values and compares it to nominal values.

- Data Management Unit (DMU) Memory: This is a test whereby a bitwise pattern is written to the DMU memory and then pattern data is read out and checked for errors.
- Stress: This is a test whereby a 100 kHz random trigger and a full busy logic is used to reject the acquisition. Data is processed inside the Digital Signal Processor. The number of the Cyclic Redundancy Check (CRC) errors found in the data is reported.
- Digitizer Address: The test checks the correct address of the digitizer board [4].

Although there are a number of the DVS tests. The TDAQ experts focuses only on the CIS and Pedestal tests.

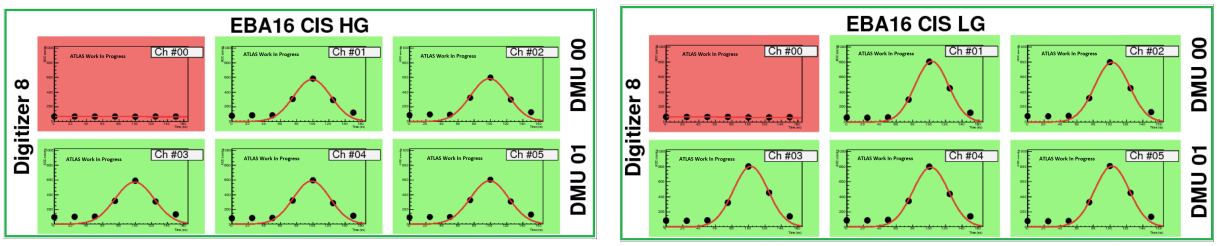

Figure 3. Results for the charge injection scan for high and low gains for EBA16

Figure 3 displays the results for the Charge Injection Scan DVS test for the sixteenth Extended Barrel (EBA16) module in the low and high gain. A Gaussian function is fit through the samples for pulse recognition. The plots are also color coded, green means everything is fine, and red means that something is wrong with that particular channel i.e channel 0. A channel is associated with the photo-multiplier tube number and the Data Management Unit (DMU). Finding a problem in a certain channel makes it easy to determine which electronic is faulty. After testing the module using dvs, the module is repaired and tested again to confirm the repair.

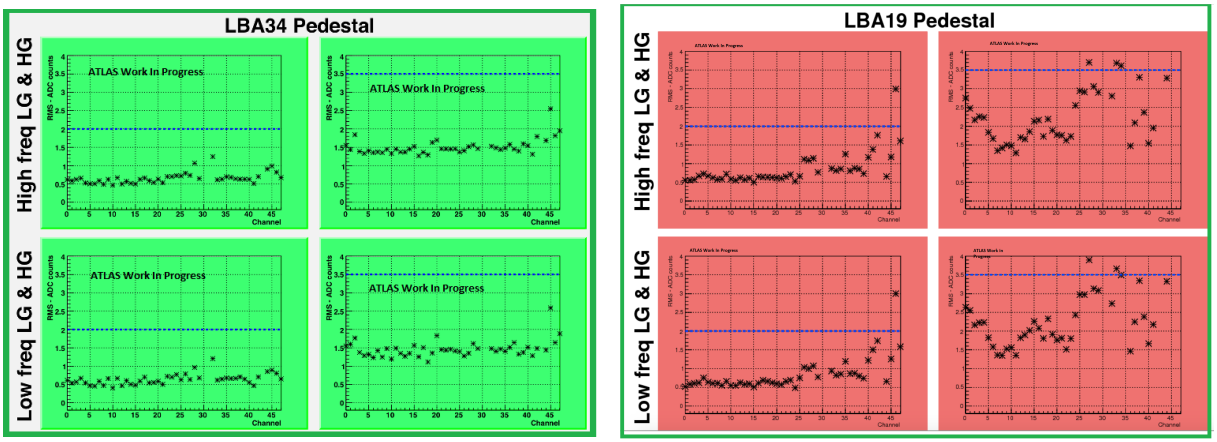

Figure 4. Results for the high and low frequency noise pedestal tests

Figure 4 displays the high and low frequency noise for the Long Barrel number 17 and 34 (LBA19 and LBA34) . LBA19 had a bad response in both the low and high gains. LBA34 had a good response in both gains. The low and high gains refers to the Analogue to Digital Converter (ADC) gains. The gains are chosen automatically by the DMUs. If the number of ADC counts in High Gain (HG) is 1023 for at least 1 of the data samples, then the gain is switched to Low Gain (LG). If the number of ADC counts in HG is 0, then the gain is switched to LG.

3. Conclusion

The Diagnostics and Verification tests are implemented to check the functionality of the super-drawer as well as its components. DVS tests are digital tests that checks for faults in the drawer while the drawer is closed. They are designed similar to MobiDick tests but are carried out later to assess the Tile FE electronics later on after the maintenance period. Sometimes after a drawer repair, negative feedback comes one day later from the offline team about specific errors that both DVS and MobiDick are not designed to detect. More DVS tests are currently being implemented to be able to improve the quality assurance procedure after the repairs. In particular, a stuckbit test is currently being implemented by the author, which is currently not available in DVS but it is in MobiDick.

References

[1] The ATLAS Collaboration. The ATLAS Detector and Technology *Online Accessed 8 August 2019* https://atlas.cern/discover/detector

[2] The ATLAS TDAQ Collaboration. The ATLAS Data Acquisition and High Level Trigger system, *J.Inst.: Conf.Ser.* **11**06: P06008 http://stacks.iop.org/1748-0221/11/i=06/a=P06008

[3] Soloviev I, et al. Verification and Diagnostics Framework in ATLAS Trigger/DAQ *Geneva: CERN;2003* ATL-DAQ-2003-033 https://cds.cern.ch/record/685565

[4] Hlaluku D, ATLAS Tile Calorimeter Online Software Reorganization and Phase-II test-beam campaigns, *Cern, MSc Thesis 2017.*

The development of test stations for the ATLAS Tile Calorimeter Low Voltage Power Supplies

Thabo James Lepota[1], **Bruce Mellado**[1,2]

[1] School of Physics and Institute for Collider Particle Physics, University of the Witwatersrand, Johannesburg, Wits 2050, South Africa

[2] iThemba LABS, National Research Foundation, PO Box 722, Somerset West 7129, South Africa

E-mail: thabo.james.lepota@cern.ch

Abstract. This paper describes the development of test stations at the University of the Witwatersrand for the ATLAS Tile Calorimeter Low Voltage Power Supplies (LVPS) of the Large Hadron Collider (LHC). As part of the phase II cycle, South Africa will produce and test, half of the LVPS bricks that will power up the front-end electronics of the detector. We describe procedures and parameters used to verify the functionality of the LVPS bricks using the Test and Burn-in stations. The upgraded LVPS bricks have improved reliability, reduced noise which reduces the trips due increase in luminosity. The Test station is functional, while the Burn-in station development still in progress.

1. Introduction

The expected elevated radiation from higher luminosity of a factor of five on the Large Hadron Collider (LHC) [1] and the reduction of the lifespan of the current electronics in the detectors indicates that all electronics of the Hadronic Tile Calorimeter (TileCal) must be upgraded as part of the Phase II upgrade cycle [3]. The TileCal [2] of the ATLAS experiment [3] is designed to measure the energy and time of arrival of hadronic jets and isolated single hadrons that are produced in the detector from proton-proton collisions at the LHC CERN. The calorimeter is constructed from long wedge-shaped modules, as shown in figure 1. Each module is composed of alternating layers of steel absorber and scintillating tiles as the active media. Light produced in the scintillators is routed to photo-multiplier tubes (PMTs) using wavelength-shifting fibers. The PMTs reside in the outer section of each module called drawers as shown in the lower part of figure 1, which also contain the front-end electronics, digitizers, and read-out electronics. Generally, there are 45 PMTs in each drawer, although the number varies depending on location. The power supplies that provide power for the drawer electronics are mounted at the end of the drawer, as shown in figure 1. The TileCal is designed as a 6-m-long barrel section with each mechanical module containing two electronics drawers, and two 3-m-long extended barrel sections with each module containing one electronics drawer. Each section contains 64 independent modules in azimuth, for a total of 256 electronics

drawers. The drawer electronics are powered by full-custom switching power supplies, called the Finger Low Voltage Power Supply (fLVPS or LVPS).

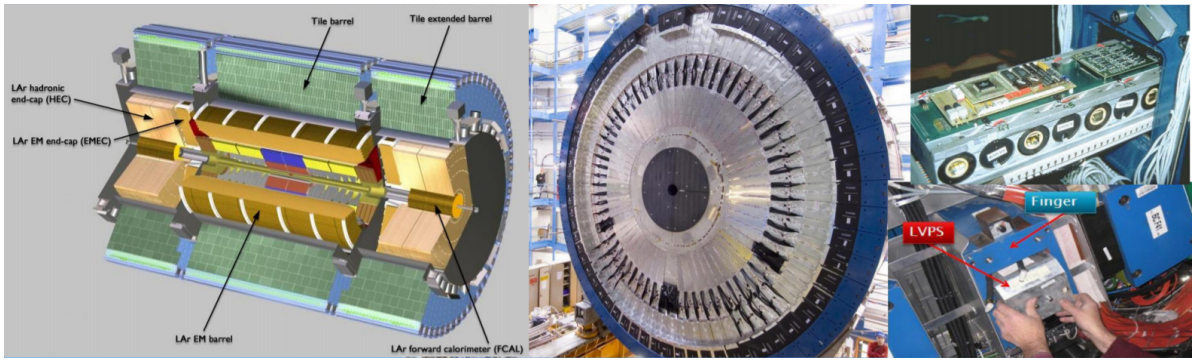

Figure 1. Shows the cross sectional view of the TileCal, modules, electronic drawer and the fLVPS [5].

1.1. Readout Architecture

Replacement of the readout electronics is mandatory because the current readout architecture is not compatible with the new fully digital Trigger/DAQ (Data AcQuistion) system of ATLAS. Figure 2 shows the upgraded readout architecture which will be suitable to sustain the higher trigger rate (> 1 MHz) and the larger event buffer (latency $> 10\mu s$). Some main guidelines were adopted: move buffers and pipelines off detector, read out data at 40 MHz (LHC bunch-crossings frequency), and improve reliability through redundancy to limit the impact of component failures. A total of 9852 PMTs are used to readout the TileCal cells. The PMT signals are amplified, shaped, and digitized at 40 Msps (Mega Samples Per Second) using a clock synchronous with the LHC beam crossing. The analogue signals are converted to digital signals using the Analogue Digital Converter (ADC) on the main board (MB). The digitized data are sent to a Daughter Board (DB). The MB also provides the control of the High Voltage. The DB synchronizes the digitized data and sends them to the Pre-Processor (PPr) via optical links [6].

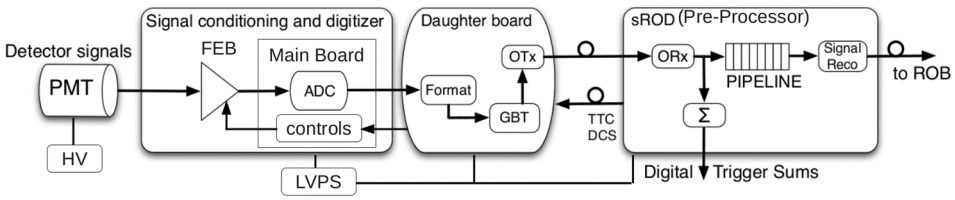

Figure 2. Block diagram of the TileCal readout architecture at the HL−LHC [7].

2. Low Voltage Power Supply for the TileCal

The power supply bricks that were installed on the detector functioned well up until there was a rise in the luminosity, the system showed sensitivity to trips at a rate that

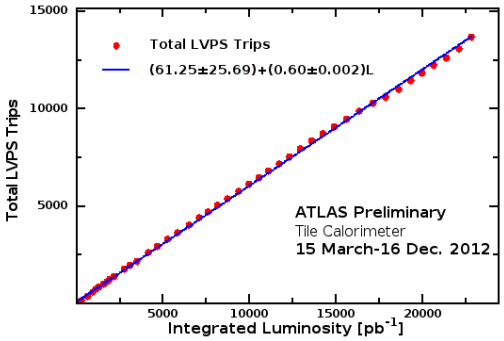

Figure 3. Number of power supply trips observed versus delivered luminosity [8].

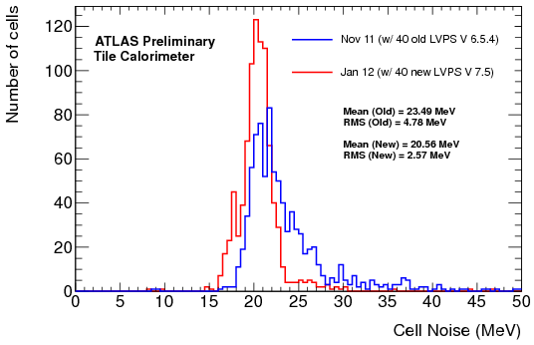

Figure 4. RMS of the electronic noise for all cells noise in relation to the LVPS bricks [9].

scales with the luminosity of the beam. A plot of the observed trips versus luminosity during 7.5 months of operation in 2011 is shown in figure 3. In these cases, an individual LVPS box trips off, it's then restarted after a period of 2 minutes. Most often the recovery is automatic through software control, but sometimes the recovery required human intervention. These trips are usually not debilitating, but do cause a loss of data from that particular module for several minutes. Also, a great deal has been learned about the low-voltage power system and the performance of the bricks, and we will take this opportunity to implement other improvements to the design. From figure 4, it clearly shows that there is a significant decrease in the RMS noise cells on the new LVPS bricks compared to its predecessor.

3. LVPS Production testing

As part of the Phase II upgrade, South Africa is responsible for producing and testing half of the LVPS bricks, which will power the ATLAS detector electronics. For a prototype of LVPS bricks see figure 5 - produced in South Africa and tested, where small issues were encountered and resolved for the next production phase. LVPS system consists of eight identical power supply (bricks). The combination of the harsh operating environment (radiation hardness) and the high reliability necessitated the custom design of a switching power supply. Because of the environment in which LVPS is located in, LVPS must remain radiation hardened to single-event upsets and total dose accumulated over several years. LVPS also contains custom designed magnetic components to operate reliably within the magnetic field of ATLAS. The LVPS bricks which step down 200 V to 10 V to power all the detector electronics are nominally rated at 100 W each. Additional control circuitry (with a quick response time) has been synthesized outside of the main controller to shut down the brick in any event of over current, over voltage or temperature.

3.1. Testing Station

The test station in figure 5 is controlled by a custom-based computer software (LabVIEW) figure 6, which controls and performs readout of certain parameters to

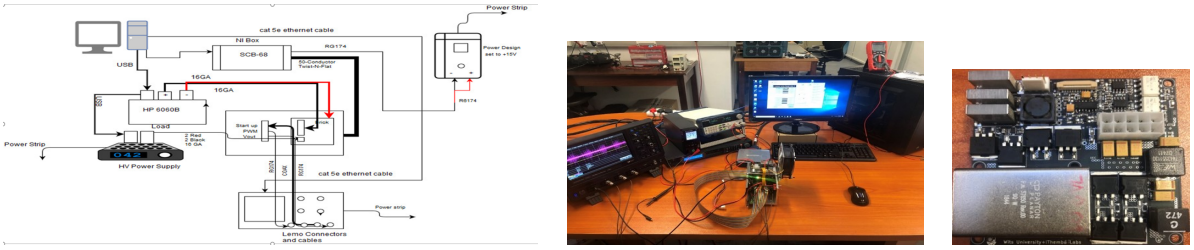

Figure 5. Functional block diagram of the LVPS test station (left), Test station setup at Wits (middle), and LVPS prototype manufactured in South Africa (right).

accomplish tests. The station consists of a high voltage power supply, oscilloscope, electronic load and personal computer. The only custom component is a metal case that acts as brick support and administers the interface to the computer and the ground connections. The data is acquired primarily through a data acquisition card connected to the computer using a Peripheral Component Interconnect interface. A few noticeable metrics which we are measuring are the system clock and its jitter. A presence of clock in LVPS can alter system stability and scale down the functioning domain of the system duty cycle. The stations authenticates the protection circuitry of the LVPS brick shield in contrast to over voltage, temperature and current. A testing program procedure is in place, which provides us a guideline to examine the functionality of an LVPS brick. In all there are 11 tests that each brick has to pass in order to be deemed good enough to passed to another testing station (burn-in). The figure 6 shows a testing program developed using the graphical programme framework called LabVIEW. The following list shows the tests that need to carried out:

- Minimum Stable Current
- Minimum Output Voltage
- Output Over Voltage Trip Point (validates fail safe features of the Bricks.)
- Output Over Current Trip Point (validates fail safe features of the Bricks)
- Output Analysis (more metrics)
- Start-up Verification (turn-on delay)
- output Voltage / Voltage input monitor vs Trim (feedback signal: slope, offset, linearity)
- output Voltage / Current input monitor vs Load (feedback signal: slope, offset, linearity)
- Input Voltage Monitor (Validates feedback signals used for remote monitor)
- Input Current Monitor (Validates feedback signals used for remote monitor)
- Temperature Measure

3.2. Burn-in Station

During the burn-in process, components are exposed to harsh settings whereby both temperature and load are high. These settings stress the electronics under test and

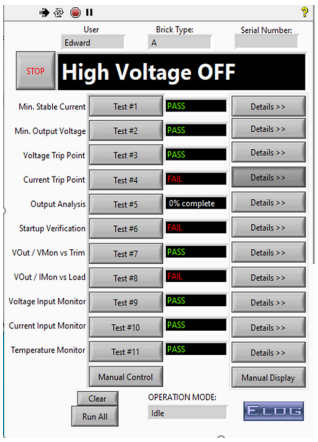

Figure 6. LabVIEW testing program framework for the test station.

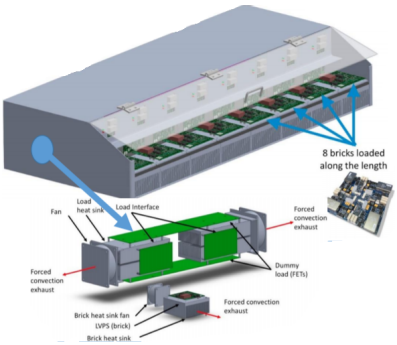

Figure 7. Burn-in Station and its components.

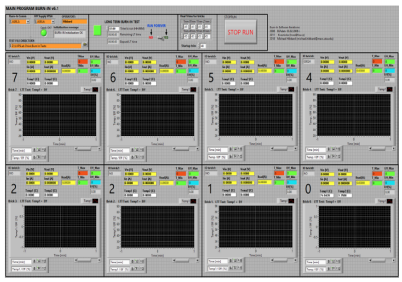

Figure 8. Front graphical panel of the LabView program for burn-in station.

causes components that would fail prematurely, to deteriorate rapidly during the duration of this test before they can be manufactured and installed on the TileCal, where there is limited space to access them if they fail during the operation of the detector. The previous Burn-in station used a cooling circuit, to lower the temperature of the bricks by reducing capacity from the load of eight bricks. With the new model, the electronic load uses a forced-convection cooling mechanism to maintain temperature of the bricks compared to the previous model which used a water circuit. Also in this new model, each brick has its own heat sink, that's forced-convection cooled to regulate temperature independently for each brick.

Duration	8 hours
Temperature	$60°C$
Brick load	100 $W/10.5$ A, nominal is 2.5 A
Start-up Cycles	30+

Table 1. LVPS Brick Burn-in operating parameters.

The burn-in station in figure 7 and 8 consists of a desktop PC with software that controls eleven compartmentalized microprocessors placed within the burn-in station. A LabVIEW software program [4] is used to control and do the test on the LVPS bricks.

The high voltage power supply will power up the burn-in station populated with eight bricks with 1kW while supplying 200 V voltage across all the bricks. The high voltage power supply is controlled by the LabVIEW software using a VISA communication link over Ethernet. The infant mortality stage will be used to detect early failures on the components and this needs to be done in a timely manner. It's ideal to conduct the test above $40°C$, and marginally below the lowest maximum temperature of any device on the brick, which is assumed to be $60°C$. The parameters in table 1 will be implemented to test the bricks on the burn-in station and the following measurements are used to indicate the behaviour of the bricks: temperature, efficiency, input and output voltages and current.

4. Summary

The TileCal Phase II upgrade design is well advanced and a prototype for the LVPS has been tested and it shows improved reliability and reduced noise levels compared to the previous design. The prototypes manufactured in South Africa have been tested using the developed Test station situated at Electronics Lab, University of the Witwatersrand. The development of the Burn-in station will commence shortly after all the technical details are finalised. This station will play a vital role when South Africa go to a mass production of LVPS bricks in 2021.

5. References

[1] LHC webpage, http://lhc.web.cern.ch/lhc/

[2] ATLAS Collaboration, 2010, *Readiness of the ATLAS Tile Calorimeter for LHC collisions,* in European Physics Journal C, Vol. 70, Issue 4,pp. 1193-1236

[3] ATLAS Collaboration, 2017, *Technical Design Report for the Phase-II Upgrade of the ATLAS Tile Calorimeter*,CERN-LHCC-2017-019.

[4] National Instruments, 2001, Laboratory virtual instrument engineering workbench (labview)., [Online]., Available: http://www.ni.com/en-us/shop/labview/labview-details.html

[5] ATLAS Experiment webpage, http://atlasexperiment.org/photos/calorimeters-tile-barrel.html

[6] Drake G, 2015, *The new front-end electronics for the ATLAS tile calorimeter phase 2 upgrade*, 2015 IEEE Nuclear Science Symposium and Medical Imaging Conference, pp. 1-6 (NSS/MIC), 10.1109/NSSMIC.2015.7581864.

[7] Anderson J et al.,2015 FELIX: a High-Throughput Network Approach for Interfacing to Front End Electronics for ATLAS Upgrades, ATL-DAQPROC-2015-014, https://cds.cern.ch/record/2016626.

[8] Lundberg O, 2012 *"Eta dependence of electronic noise and noise in a single channel, with changed LVPS."*, ATLAS Collaboration, ATLAS-PLOT-TILECAL-2012-005, https://cds.cern.ch/record/1442284

[9] Lundberg O, 2012 *"Electronic Noise of the Tile Calorimeter"*, ATLAS Collaboration, ATLAS-PLOT-TILECAL-2012-002, https://cds.cern.ch/record/1414789

Low Voltage Power Supply production, hardware upgrade and testing for the ATLAS TileCal Front-End Electronics system

Edward Nkadimeng[1],Thabo Lepota[1], Roger van Rensburg[1],Charles Sandrock[1], and Bruce Mellado[1,2]

[1] School of Physics and Institute for Collider Particle Physics, University of the Witwatersrand, Johannesburg, Wits 2050, South Africa
[2] iThemba LABS, National Research Foundation, PO Box 722, Somerset West 7129, South Africa

E-mail: edward.khomotso.nkadimeng@cern.ch

Abstract. The large-scale production of the LVPS bricks will involve the complete replacement of all power supply "bricks" in the TileCal (Tile Calorimeter) front-end electronics for the LHC-HL upgrade. A total of 1024 LV bricks (half needed for the entire detector) will be produced by the University of the Witwatersrand. Such an operation comprises of several steps which include the development of two new custom quality assurance test stations. The initial test station will quantify a multitude of performance metrics of a LVPS brick, whereas the Burn-In test station would perform an endurance type test and subject the LVPS brick to a stressed environment. Both these custom test stations ensure the reliability and quality of a new LVPS which will power the next generation of the upgraded hardware system of ATLAS at CERN.

1. Introduction

At the European Laboratory, CERN, the ATLAS detector is a general-purpose proton-to-proton collider designed to exploit the full discovery potential of the Large Hadron Collider (LHC) [1]. The Tile Calorimeter is the hadronic calorimeter of the ATLAS detector, based on an iron scintillator and provides coverage in the central rapidity region ($|\eta| < 1.7$) behind the electromagnetic calorimeter [2]. The Tile Calorimeter is designed as a 6-m-long barrel section with each mechanical module containing two electronics drawers, and two 3-m-long extended barrel sections with each module containing a super-drawer. Each section contains 64 independent modules for a total of 256 electronics drawers. The electronics of the super-drawers are powered by a switch-mode power supply and referred to as a Low Voltage Power Supply (LVPS) [3]. Eight LVPSs are mounted inside an aluminium box to supply power to a super-drawer. The LVPS box provides stable power to the front-end electronics of the super-drawer and interfaces with a Distributed Control System (DCS) for remote monitoring and control [3].

2. Overview of the Tile Calorimeter readout system

The LVPS system supplies power to all the front-end electronics of the ATLAS TileCal and

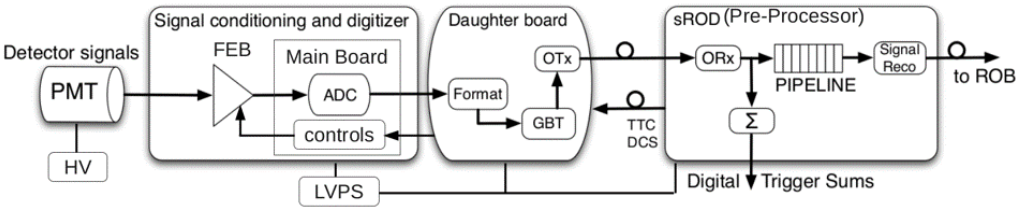

Figure 1: Upgraded TileCal readout architecture [2].

provides feedback through a monitoring system. The power for each super-drawer is supplied by one LVPS box which powers up to four mini-drawers of one module of the TileCal. Modules of the long barrel have 4 mini-drawers powered from the LVPS box, and modules of the extended barrel have 3 minidrawers powered from the LVPS box. In total, there are 256 LVPS boxes in the TileCal, which consists of eight or six individual power supply boards called bricks (for boxes located in long barrel and extended barrel, respectively), a fuse board, and a monitoring/control board [4]. The fuse board has filtering elements for the 200 V DC line and individual fuses for the individual bricks [5]. There is also a cold plate that runs laterally through the middle of the LVPS box to provide water-cooling for the bricks. Compared to the design used in the initial TileCal, the Phase-II design is different in two important ways (see Figure 1). Each LVPS box will consist of eight bricks supplying 10 VDC through a step-down transformer that needs a forward converter and buck regulator with negative feedback control.
The main boards and daughterboards have two independent sides and a left right symmetry so that in case of the failure of the electronics on one side, the other side is still operational. Each side is served by a separate brick. Each calorimeter cell is read out by two photo-multiplier tubes (PMTs) [5] and both PMTs are connected to the two opposite sides of the front end electronics. Therefore, in case of loss of one side of the front end electronics or brick, the other side is still active and the calorimeter cell is still read out by one PMT. A second redundancy is envisioned in case one brick fails. With the help of fast fuses and diode-OR circuit located on the main board the role of a failing brick can be taken over by the brick serving the other left/right side. In this situation the remaining brick sees its load increase from 3 A to 6 A. For this reason, the bricks are required to be able to deliver 3 to 6 A. The LVPS box specifications contain additional fail-safe and redundancy electronics to still provide power if certain bricks fail.

3. Detailed Functional Description and Specification

The brick Printed Circuit Board (PCB) is a 6 layer board with dimensions of 80.26 mm by 80.26 mm and has mounting holes for attachment to the cooling plate inside the LVPS box. A shielded transformer is produced by PAYTON following our custom specifications. The transformer is used to step down an alternating high voltage produced from the forward controller depicted in Figure 2a to a lower an alternating voltage for DC-DC regulation. Ceramic cylinders made from Aluminium Nitride, called thermal posts, are used to transfer heat from brick components to the cooling plate. The metallized cylinders have one metallized face, which will be in contact with the pad of the switches and diodes on the PCB. A 4 pin connector is used to receive the 200 V DC from the fuse board, with two pins for +200 V and two pins for return. There is a 10 pin output connector to deliver the 10V output of the brick to the Harting connector on the LVPS box. (see Figure 2b). The is also a small 20 pin connector, which connects the brick to the Embedded Local Monitor Board (ELMB) motherboard with a ribbon cable. This connector is used to receive the control signals from the ELMB motherboard, and send the monitoring signals in Differential Analog format to ELMB motherboard.

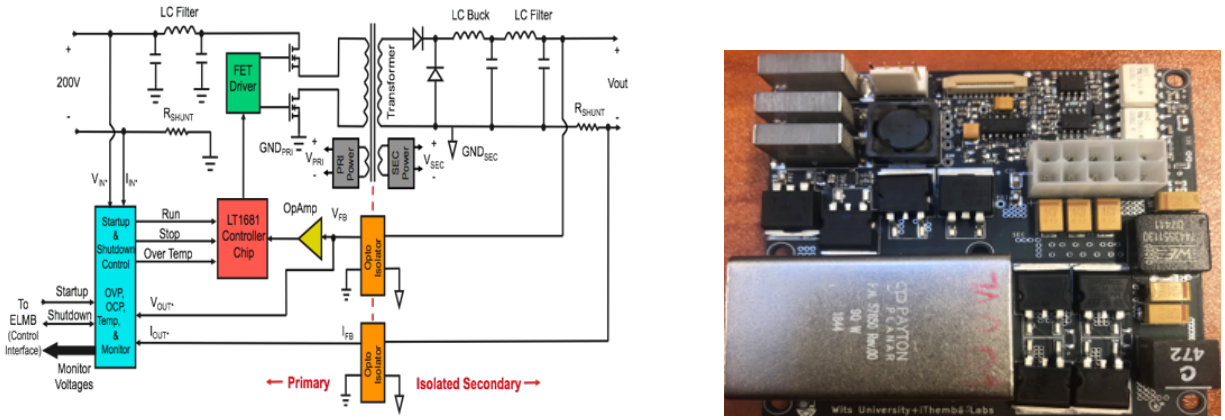

(a) LVPS schematic [2]

(b) Wits Low Voltage Power Supply brick

Figure 2: (a) LVPS block diagram control system illustrating the LT1681 forward controller operating at 300 kHz, (b) Wits LVPS brick manufactured in South Africa.

3.1. Low Voltage Power Supply monitoring system

The brick is an isolated switching DC-DC converter, that converts the 200 V input to a 10 V output. The isolation is provided by a step-down transformer, which also has additional windings for other auxiliary power supplies on the brick, required for control and monitoring purposes [2]. A summarized schematics of the converter with the transformer is given in Figure 2a. The switching frequency of the brick is constant at 300 kHz, and it benefits from a two switch Forward converter topology. The brick measures six analog signals and sends them to the ELMB motherboard, which includes input voltage and current, output voltage and current, and the temperature readings from two points on the brick (primary and secondary side switches), measured using thermistors. The brick receives an Enable signal and a start-up pulse from ELMB motherboard. The start-up pulse provides temporary power to the control circuits of the brick to power it on. When the Enable signal is high, the brick will power on after a short delay after receiving the start-up pulse. The brick provides a nominal output current of 3 A, should be able to provide twice of the nominal current (6 A), and has built-in automatic over current protection (at 10.5 A) and over temperature protection (at 70°C), in addition to over voltage protection (at 12 V). Each brick will be tested according to a specific procedure and must pass different criteria. Table 1 also lists this criteria for the LVPS bricks.

3.2. Development of the Wits test-station for LVPS Production

Pre-production and production of the bricks will entail testing and subsequent testing. Testing procedures will take place at the University of Witwatersrand School of Physics, High-throughput lab. The testing ensures that bricks meet the criteria listed in Table 1. Bricks that pass these test procedures will then be shipped for assembly at CERN, and for further radiation testing of the LVPS components. The 'Wits test-station' quantifies a multitude of performance metrics of a LVPS brick. This station would also verify protection circuitry of the LVPS brick, to guard against over temperature, over current and over voltage. Custom PC based software was synthesized to perform the tests and graphically display and record onto file these performance metrics [5]. The desktop PC is connected to the data acquisition using a National Instrument (NI) and B-type USB to the electronic load as well as the high voltage power supply. The Data Acquisition uses a 50 pin ribbon cable twist and flat to connect to the brick as can be seen in Figure 3. Coaxial cables will be used for the start up and voltage output of the LVPS and recorded.

Parameter	Minimum	Maximum
Frequency Standard Deviation	0	1000
Duty Cycle Standard Deviation	0	0.1
Frequency Max	350000	290000
Frequency Min	250000	310000
Minimum Stable Load	2.1	2
Minimum Output Voltage	9.8	10.2
Over Voltage Protection Trip Point	11.5	12
Over Current Protection Trip Point	10.25	10.75
Output root mean square Voltage	0	0.5
Output Peak to Peak Voltage	0	0.5
Clock Duty Cycle Average	0	40
Clock Duty Cycle Standard Deviation	0	0.15
Start-up Delay (Max)	0.2	0.08

Table 1: Minimum and maximum of testing parameters. Parameters are used in the test station software to test individual bricks.

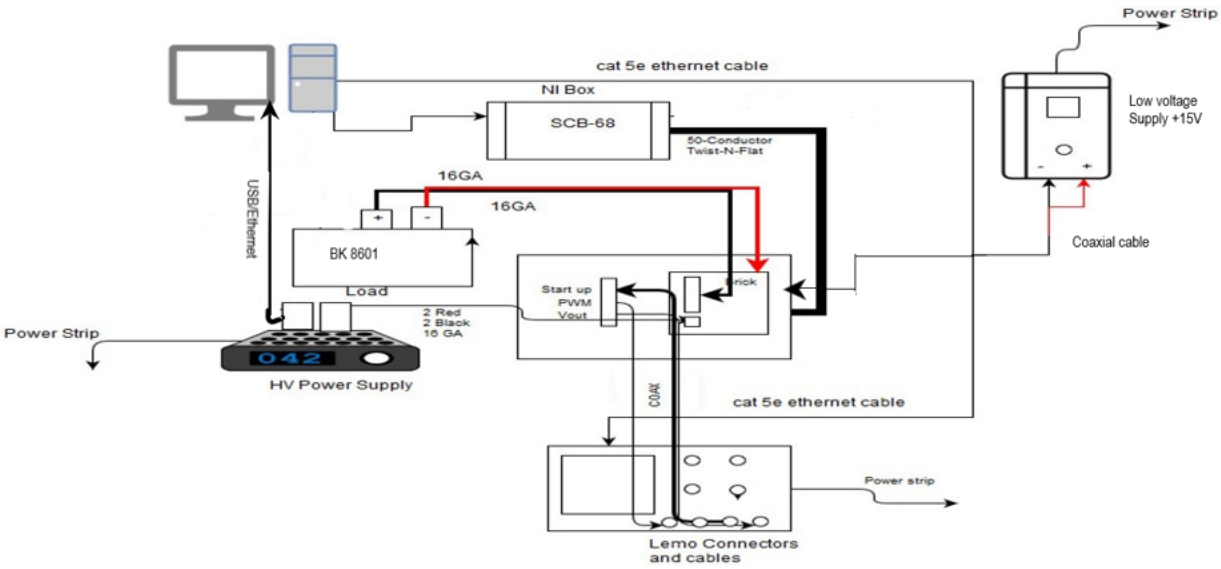

Figure 3: Wits test-station block diagram.

4. Quality Assurance test results

The testing ensures that bricks meet the criteria listed in Table 2. So far sixteen bricks were assembled and produced in South Africa. We have already done a rigorous analysis using sophisticated LabVIEW software programs developed by the University of Texas and Arlington (UTA) group. The feasibility of the design regarding electrical parameters of specification was verified using a test-station that was assembled at the University of the Witwatersrand. The test stand performs several tests on the bricks to ensure all of the parameters are according to the specification [5]. Various tests determine whether the protection circuitry of the LVPS are functioning correctly. In the test results as can be seen in Figure 4b the over-voltage protection and the current trip point are assessed. Similarly to the protection circuitry results, we also monitor the output voltage range and a function of output voltage settings operating at nominal

Parameter	Value	Status of test
Minimum stable current (0.5-2A)	1.700A	Pass
Minimum Output voltage (9.8-10.2V)	10.0484V	Pass
Voltage trip point (11.5-12V)	11.8092V	Pass
Current Trip point (10.25-10.75A)	10.1901A	Fail
Voltage input Monitor(0.95-1.05V)	1.04901V	Pass
Current Input monitor(-0.015 -0.005A)	-0.01032A	Pass
Temperature monitor(10-93°C)	57°C	Pass

Table 2: Test status and summary of voltages and currents for the different brick types.

load as can be seen in Figure 5b.

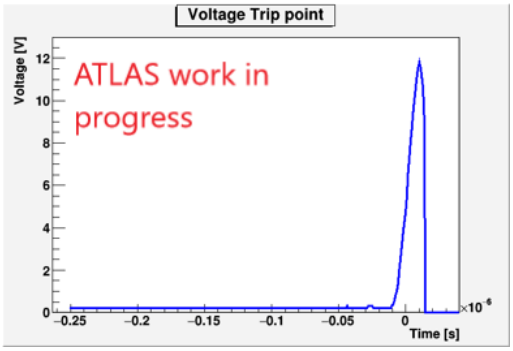

(a) Voltage trip point of the Wits LVPS brick.

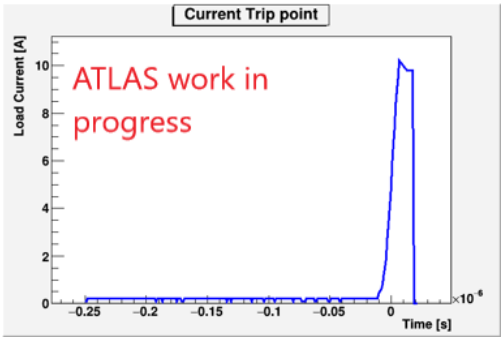

(b) Current trip voltage of the Wits LVPS brick.

Figure 4: (a) While operating at minimum stable load, the output voltage is increased by decreasing the trim voltage, until the built-in over voltage protection shuts down the brick. (b) The load current is increased, until the built-in over current protection shuts down the brick

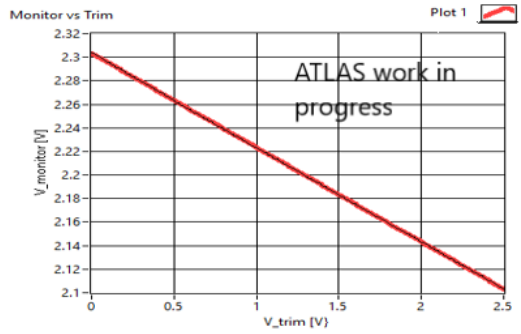

(a) Voltage monitoring and trim voltage.

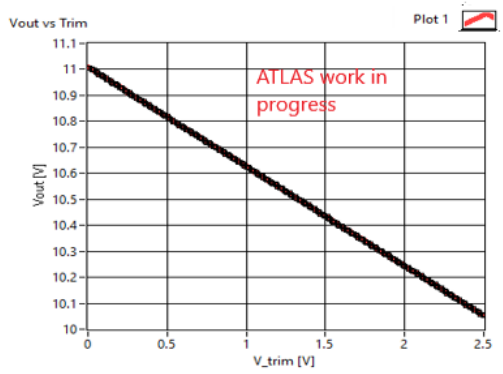

(b) Output voltage and trim voltage.

Figure 5: Operating at nominal load, the trim voltage is changed to change the output voltage. Then, a linear plot is produced to show the output voltage vs trim voltage.

 ISBN: 978-0-620-88875-2

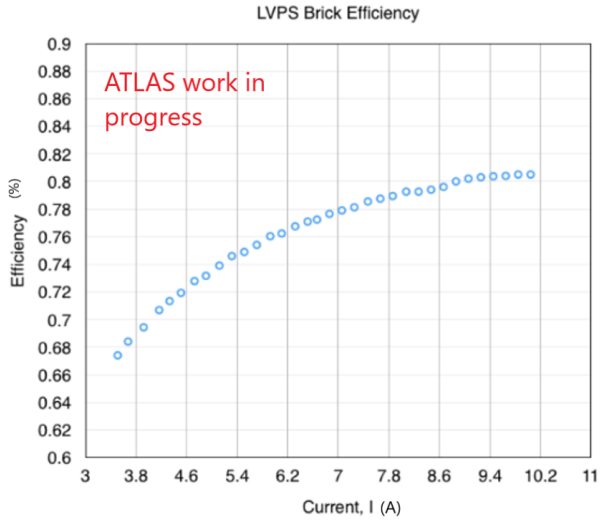

Figure 6: The total losses of the brick is 19.7 W, while supplying 100 W on the output. The measured efficiency of the brick operating at 10.19 A is 80.5%.

5. Overall performance and reliability analysis

We have undertaken a project to develop a test-station according to UTA's design requirements. We are manufacturing half of the bricks in South Africa for the next run. The primary goals are to improve noise performance, reliability, and tolerance to single-event upset, while retaining the physical layout, interface to the detector control system, and other infrastructure. There are various efficiencies in power supplies as a function of output load that meet manufacturer specifications input/output conditions,The LVPS prototype guarantees over 80.5 efficiency at 10A load at 200V / 55Hz input and able to withstand harsh environments from the overall design.The total power loss and efficiency of the LVPS can be seen in Figure 6.

6. Summary and Outlook

We have built and tested the LVPS bricks which are manufactured in South Africa and tested at Wits (using the Wits LVPS test-station). The reliability and stability of the system has been visibly improved with respect to the previous design [2]. A few notable metrics we are measuring is the efficiency of the brick operating at nominal load (see Figure 6). The analyses that follow assume that the bricks are in the normal operating portion of the lifetime curve, where components exhibit a constant failure rate as a function of time. The calibration systems of the ATLAS TileCal have been presented, analysis of the LVPS bricks can be used to gain detailed insight in what causes variations in detector response. Once a brick passes the Quality Assurance tests from above it will be sent to component stress testing on the 'burn-in' test-station which elevates the temperature of the bricks to 60°C for 8 hours.

References

[1] Clement C. et al. General Requirements for the Tile Calorimeter Front-End Electronics in the HL-LHC Environment, ATL-COM-TILECAL-2019-004,2019, *cds.cern.ch/record/2654796*
[2] Anderson K. et al. Design of the front-end analog electronics for the ATLAS tile calorimeter, Nucl. Instrum. Meth. A 551 (2005) 469.
[3] Einsweiler K, ATLAS Tile Calorimeter Phase-II TDR, *edms.cern.ch/document/2040955/1*
[4] Moayedi S, Hadavand H.K, ATLAS TileCal, LVPS Upgrade Hardware and Testing, cds.cern.ch/record/2624126
[5] Popeneciu G. et al. Minidrawer mechanics specification document, edms.cern.ch/document/2040955/1

A case study on monitoring Potential Induced Degradation (PID) recovery in multi-crystalline modules

I M Kwembur[1], J L Crozier McCleland[1], F J Vorster[1] and E E van Dyk[1]

[1] Nelson Mandela University, Port Elizabeth, South Africa

E-mail: s21379446@mandela.ac.za

Abstract

Potential Induced Degradation (PID) causes significant module degradation leading to decreased power output in photovoltaic (PV) power plants. Many PV power plants are constructed using transformerless inverters and may be susceptible to issues associated with the galvanic connection between the PV configuration and the power grid. This increases the likelihood of a leakage current between the PV system`s active circuit and the ground. The resulting electric field causes sodium (Na^+) ions to drift to the cell and some at a certain concentration may diffuse into the PN junction creating shunting paths. The PID detection tools employed in this work are maximum power measurements, comparison of open circuit voltage (V_{oc}) at low irradiance (200 $W.m^{-2}$) and high irradiance (1000 $W.m^{-2}$) and Electroluminescence (EL) imaging at 10% of Short-circuit current (I_{sc}). These techniques are used to assess the degree of PID and to monitor the module recovery. This work explores two recovery methods for PID affected modules, forced recovery and natural recovery. Forced recovery involves reverse biasing the module terminals for a few hours while natural recovery, modules are left unbiased for several months. This yields a maximum power recovery of approximately 95% and 94% for forced and natural recovery respectively. These techniques are used to assess the degree of PID and to monitor recovery. This paper demonstrates that PID recovery on modules depends on two mechanisms, viz. drift or diffusion, or combined.

1. Background

Photovoltaic (PV) solar power is a promising renewable source due to the abundance and inexhaustible nature of solar energy. Most of the first solar power plants to be constructed were fitted with high frequency transformers between the grid and PV system resulting in galvanic isolation [1]. This came at a cost since transformers are expensive, large and results in power conversion losses due to the several levels of conversion [2]. To solve these issues transformerless inverters were deployed with topologies that attempt to maintain the required galvanic isolation between the PV system and the power grid [1]. Inadequate galvanic isolation, however, made the PV power plants vulnerable to leakage current flowing between the PV active circuit and the ground resulting in potential induced degradation (PID) [1]. The electric field that developed between the module active circuit and the frame causes Na^+ ions (present in soda lime glass) [3] to migrate through the encapsulation to the surface of the cell and in some cases, when a sufficient concentration is attained, Na^+ ions are caused to diffuse into the PN junction [4]. The

accumulation of Na^+ ions in the PN junction results in a significant shunting leading to a decrease in shunt resistance (R_{sh}) and an increase in series resistance (R_s) which in turn, results in a decreased module power output [5]. The module closer to the negative side of the string (-V) are often more affected in comparison to modules on the positive side of the string (+V) because they are at the higher negative potential in relation to the ground [6]. The extent of PID damage depends on, the system voltage (potential between the active circuit and the earthed frame), humidity levels [7], ambient temperature [3], type of the glass used in module fabrication [8] and resistivity of the solar cell encapsulation [6].

Detection of PID shunted cells on a module is made possible by way of Electroluminescence (EL) imaging [9]. The EL imaging set up comprises of EL camera, programmable power supply and computer controls. EL imaging involves forward biasing the module, while the EL camera is placed at some optimised distance from the front surface of the module in a dark environment to eliminate interference from stray light. Under normal conditions, cells are detected with uniform brightness except inter-cell spaces, busbars and dark sports within the cells which appear darker [10]. For a module that has PID, the EL brightness varies depending on the degree of shunting, such cells or regions appear dark. The variation in brightness of the cell is commensurate to the number of minority charge carriers flowing into individual cells in a module. For PID affected cells the number of minority charge carriers are reduced due to increased R_s resulting in the dark appearance of PID affected cells [11].The main objective of this work is to induce PID in modules and compare two PID recovery procedures, (i) natural recovery and ii) reverse polarization on several module samples.

2. Modelling module current leakage pathways

In a typical PV system, a high electric potential difference between an active circuit and the aluminium frame induces a leakage current to flow through sections of the PV module. In a standard p-type crystalline silicon module seven current leakage pathways can be described and are depicted in figure 1. The pathways are; 1) along the glass surface, 2) through the glass substrate, 3) through the interface between the glass and the encapsulant, 4) through the encapsulation, 5) through the interface between the encapsulation and the back sheet, 6) through the back sheet substrate and 7) along the surface of the back sheet [3, 4]. For n-type modules, the PID stress set up is reversed biased in relation to that of figure 1.

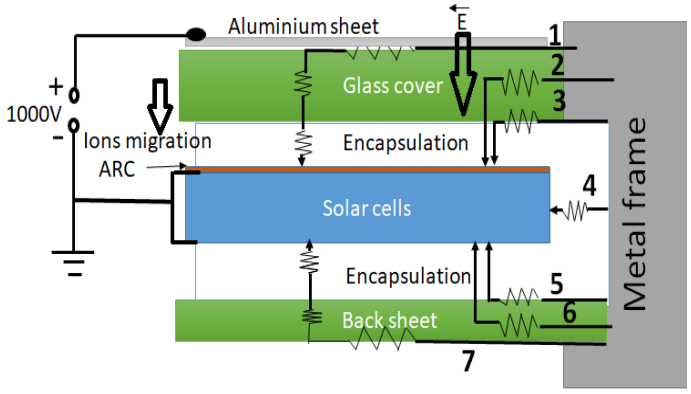

Figure 1. A cross section of mc-Si PV module constructed to indicate current modelled current leakage: 1) along the glass surface, 2) through the glass substrate, 3) through the interface between glass and the encapsulation, 4) through the encapsulation substrate, 5) through the interface between the back encapsulation and the back sheet, 6) through the back sheet and 7) along the back sheet surface [3].

The magnitude of the leakage current increases with an increase in humidity [7], as such the leakage current is high in the morning owing to dew condensation on the glass surface in the morning hours. On days with low humidity, the conductivity is limited to the edges of the modules and not the surface as it would be the case for high humidity. This explains why cells along the frame are highly susceptible to PID. Over a long period of time, moisture may ingress into the module resulting in reduced encapsulant bulk resistivity which may enhance PID progression. In extreme humidity conditions in case of modules fabricated with EVA encapsulation, acetic acid may develop resulting corrosive irreversible PID [7].

3. Experimental set and procedure

3.1 PID induction in multi-crystalline modules

In this study five PV modules were used, four 60-cell multi-crystalline modules (X, A, B, C) and a 72-cell multi-crystalline module (D). The five modules from different manufacturers were subjected to PID stressing by applying a bias voltage of 1000V for 24 hours while placed in an environmental chamber that was kept at 35 ± 1 °C, with relative humidity < 40% RH throughout the induction period. Biasing was achieved by applying a positive voltage to either a 3 mm thick aluminium plate resting on the entire surface of the module's cover glass without touching the frame as illustrated in figure 1, or to the frame itself. The negative voltage was connected to the shorted module connector terminals.

3.2 PID detection light IV measurements and EL imaging

PID is confirmed by a drop in power measured by an indoor solar simulator. The measurements are taken when the simulator is set at STC (standard test condition of 25°C temperature, Irradiance of 1000 $W.m^{-2}$). For purposes of PID detection the second power measurement was taken when irradiance is set at 200 $W.m^{-2}$ and temperature of 25°C. This is because at low irradiance, PID affected module experience greater carrier losses to the shunted paths with reduction in photocurrent as compared to 1000 $W.m^{-2}$ where the carrier losses go undetected because of abundance of photocurrents [3].

In addition to power loss, PID in a module can be detected from power measurements by comparing the open circuit voltage (V_{oc}) obtained at solar irradiance of 1000 $W.m^{-2}$ and 200 $W.m^{-2}$. If the V_{oc} drops by more than 10% between 200 $W.m^{-2}$ and 1000 $W.m^{-2}$, the module may have PID and may experience PID shunting [6]. For module X used in this section, the V_{oc} drop is 7.9% before PID and 36.2% after PD stress (see table 1). The increase in the low-high irradiance V_{oc} difference may be indicative of the presence of PID shunting otherwise, for any other PV performance limiting defect the V_{oc} ratio may be within a small increase. PID affected cells on a module in an EL image appear darker/less bright as compared to the rest as observed in figure 3 and figure 5. EL images in this work were recorded at 10% of I_{sc} because PID shunted cells appear distinctively less bright as compared to those taken at I_{sc}[10].

Table 1: Table of V_{oc} and P_{mpp} taken at 1000 $W.m^{-2}$ and 200 $W.m^{-2}$ irradiance for module X.

	Before PID		After PID	
Irradiance	1000 $W.m^{-2}$	200 $W.m^{-2}$	1000 $W.m^{-2}$	200 $W.m^{-2}$
V_{oc} (V)	37.3	34.3	36.0	22.9
P_{mpp} (W)	230.0	40.5	149.6	12.4

3.3 Module recovery Procedure

It is possible that modules can recover from induced PID by reversing the degradation caused by PID shunting [3]. This was done in two ways; 1) forced reverse polarity of a module for 120 minutes or 2) by way of unbiased natural recovery in the dark at the open circuit over a period up to 12 months at room temperature. The recovery percentage is calculated based on the initial power measurements of the module. The recovery procedure was monitored by periodically measuring maximum power output using a class AAA of a solar simulator, (spectral mismatch of 0.75-1.25 times the ideal spectral range, spatial uniformity ≤ 2% and temporal instability on measurements of 0.5% on short term and < 2% on the long term) [12]. EL images are recorded at a current corresponding to 10% of I_{sc}.

4. Results and Discussion

4.1 Module recovery

The modules were subjected to PID stress and evaluated using the techniques discussed in section 3.2. The modules showed varying degrees of PID and the characteristics are summarized in table 2. In the table, the initial and degraded power of the modules is listed together with the associated % drop in power (the ratio of the difference between initial and final power and initial power), post recovery power and % recovery (ratio of power recovered to power lost). The rate of the recovery is determined based on recovery period which was quoted either as per minute or per day, depending on the duration of recovery time. Module A underwent forced reversed biased recovery and after 120 minutes the module power recovered up to 94.8% of the degraded power. Module B was subjected to natural recovery at room temperature in the dark at open circuit voltage and after 8 months the power recovery level was 94.0% of the degraded power. Module C which belongs to the same class as module A underwent extreme PID, with a power loss of 88.5%. After 7 months of natural recovery, the module has recovered 45.1% of the lost power. Module D degraded by 18.3% and underwent natural recovery for a period of 12 months with 74.6% recovery, making its recovery relatively slow compared to the other modules.

Table 2: Module characteristics of modules subjected to PID stress.

Module	Initial P_{mpp} (W)	Post PID stress P_{mpp} (W)	P_{mpp} drop (%)	Duration	Post recovery P_{mpp} (W)	P_{mpp} recovery (%)	Rate of recovery	Type of Recovery
A	233.9	148.7	36.4	120 minutes	229.5	94.8	0.67 $W.min^{-1}$	Reverse Polarization
B	265.9	187.1	29.6	8 months	261.2	94.0	0.31 $W.day^{-1}$	Natural
C	229.5	26.1	88.5	7 months	116.2	45.1	0.44 $W.day^{-1}$	Natural
D	294.4	240.5	18.3	12 months	280.9	74.6	0.11 $W.day^{-1}$	Natural

In addition to assessing PID recovery based on power measurement, EL images are a good indicator of recovery. The PID and subsequent recovery of modules A and B serve to illustrate this for excessive degradation and recovery via two different methods. Figures 2 and 4 show the respective I-V curve measurements for Modules A and B, taken before PID, after PID and after PID recovery. Figures 3 and 5, show the EL images for modules A and B, taken before PID, after PID and after PID recovery. From figures 2 and 4, the I-V curves show that modules have recovered substantially, but not to initial power level, although the curves appear to overlap. The EL images shown in figures 3 and 5, exhibits the expected checkerboard pattern of varying luminescence with the cells affected by PID appearing dark, and the subsequent absence of this pattern in the images after recovery.

The module recovery may not be 100% because Na^+ ions may not have been completely migrated from defect sites within the PN junction. In the case of natural recovery procedure, the procedure is slow since it only depended on diffusion as the mechanism to cause migration of Na^+ ions from the defect sites within the PN junction and cell surface. Forced recovery is quick since it combines both drift and diffusion of sodium ion Na^+ ions hence it is quick taking approximately 120 minutes (module A) as compared to 8 months in the case of natural recovery (module B). Different PV manufacturers use different types of encapsulation with varied resistivity properties the same applies to the glass cover [13]. In addition, different mechanisms have been used in module fabrication to limit PID progression in modules, as such modules will exhibit a varied response to PID progression effect and power recovery [14]. PID shunting can easily be detected at infancy using EL imaging taken at low current and power measurements at low irradiance.

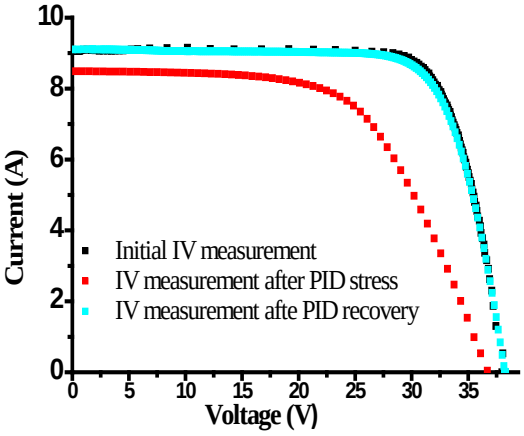

Figure 2. Light I-V measurements for Module A.

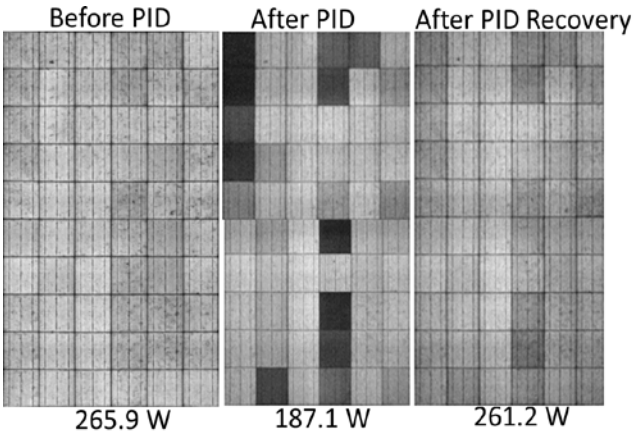

Figure 3. EL-images of module A recorded 10% I_{sc} with the measured P_{mpp} listed.

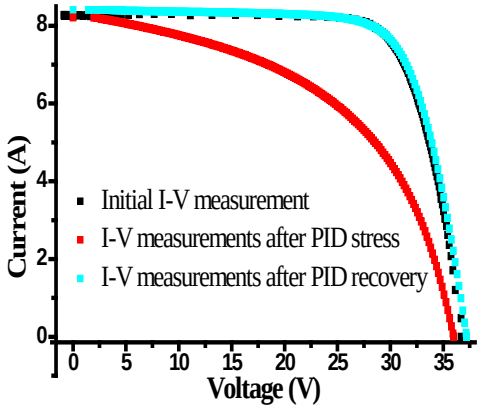

Figure 4. Light I-V measurements for Module B.

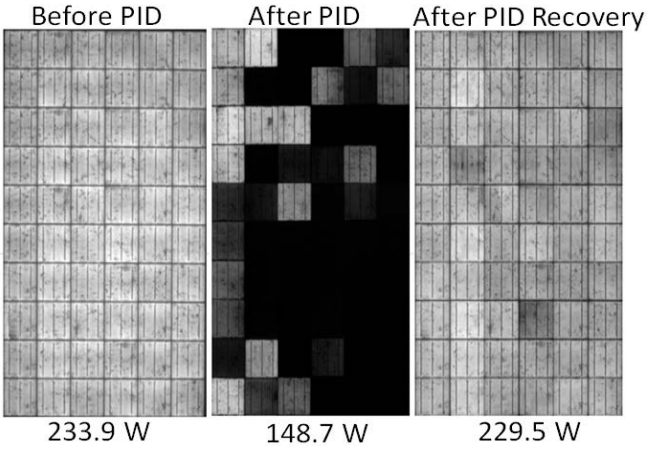

Figure 5. EL-images of module B recorded at 10% of I_{sc} with the measured P_{mpp} listed.

5. Conclusion

PID if left undetected can greatly affect the performance of modules in a string, hence need to detect and undertake module recovery procedures. PID in modules is caused when an electric field between the frame and active circuit of the PV modules causes a leakage current to flow. In the process, Na^+ ions are forced to drift from the glass to the cells and at the right concentration, the Na^+ ions are forced to diffuse into PN junction resulting in increased R_s. Under low irradiance PID affected cells generate less charge carriers because of increased recombination resulting in less power output as compared to the PID free cells. The PID affected cells also appear less bright in comparison to the rest of the cells in an EL image. EL imaging and power measurement at low irradiance are two complementary methods used to successfully detected presence of PID in a PV module. Module power recovery procedures by way of forced recovery over a short period of time or unbiased natural conditions in the dark over a long period of time were deployed. The PID recovery occurred because Na^+ ions were forced to migrate from the cells back to the glass by a strong electric field in reverse to the PID inducing electric field and diffusion over a long period of time for the unbiased method. In both the procedures more than 94% of power lost was recovered in modules A and B. However, incomplete Na^+ ions removal from the PN

junction may be responsible for not attaining 100% P_{mpp} recovery. Solar PV power plant operators can employ a simple procedure to partly recover modules affected by PID by disconnecting the modules in situ, effectively keeping them under open circuit condition for an extended period of time that can be optimally determined by the solar plant operator.

Acknowledgements
The authors gratefully acknowledge the South African National Research Foundation (NRF), PVinsight (Pty) Ltd, National Laser Centre (NLC), African Laser Centre (ALC), the South African Department of Science and Technology (DST), ESKOM and Nelson Mandela University (NMU) for the financial support and providing necessary facilities for research.

References

[1] Shayestegan M. Overview of grid-connected two-stage transformer-less inverter design. *J Mod Power Syst Clean Energy* 2018; **6**: 642–655.
[2] Kumar LA, Kumar S. Design and Analysis of Highly Efficient and Reliable Single-Phase Transformerless Inverter for PV Systems. *Int J Energy Power Eng* 2014; **8**: 1405–1410.
[3] Luo W, Khoo YS, Hacke P, Naumann V, Lausch D, Harvey SP, Singh JP, et al. Potential-induced degradation in photovoltaic modules: a critical review. *Energy Environ Sci* 2017; **10**: 43–68.
[4] Luo W, Hacke P, Singh JP, Chai J, Wang Y, Ramakrishna S, Aberle AG, et al. In-Situ Characterization of Potential-Induced Degradation in Crystalline Silicon Photovoltaic Modules Through Dark I-V Measurements. *IEEE J Photovoltaics* 2017; **7**: 104–109.
[5] Pingel S, Frank O, Winkler M, Oaryan S, Geipel T, Hoehne H, Berghold J. Potential Induced Degradation of Solar Cells and Panels. In: *35th IEEE PVSC.*, pp. 2817–2822.
[6] Schwark M, Berger K, Ebner R, Ujvari G, Hirschl C, Neumaier L, Muhleisen W. Investigation of potential induced degradation (PID) of solar modules from different manufacturers. *IECON Proc (Industrial Electron Conf* 2013; **8**: 8090–8097.
[7] Hoffmann S, Michael K. Effect of humidity and temperature on the potential-induced degradation. *Prog Photovolt Res Appl* 2014; **22**: 173–179.
[8] Burrows K, Fthenakis V. Glass needs for a growing photovoltaics industry. *Sol Energy Mater Sol Cells* 2015; **132**: 455–459.
[9] Fuyuki T, Kitiyanan A. Electroluminescence Characterization of Crystalline Silicon Solar Cells. *Appl Phys A Mater Sci Process* 2009; **96**: 189–196.
[10] Kwembur IM, Crozier McCleland JL, van Dyk EE, Vorster FJ. Detection of Potential Induced Degradation in mono and multi-crystalline silicon photovoltaic modules. *Phys B Condens Matter* 2020; **581**: 1–6.
[11] International Electrotechnical Commission. *Electroluminescence of photovoltaic modules*. IEC TS 60904-13, Geneva, www.iec.ch (2019).
[12] Droz C, Fakhfouri V, Pelet Y, Roux J, Peguiron N, Beljean P-R. Evaluation of Commercial Large Area Solar Simulator: Features Exceeding the IEC Standard Class AAA. In: *25th European Photovoltaic Solar Energy Conference and Exhibition / 5th World Conference on Photovoltaic Energy Conversion, 6-10 September 2010, Valencia, Spain*, pp. 3884–3888.
[13] Koch S, Berghold J, Okoroafor O, Krauter S, Grunow P. Encapsulation Influence on the Potential Induced Degradation of Crystalline Silicon Cells with Selective Emitter Structures. In: *27th European Photovoltaic Solar Energy Conference and Exhibition*. Frankfurt, Germany, pp. 1991–1995.
[14] S. Pingel, Janke S, O. Frank. Recovery Methods for Modules Affected by Potential Induced Degradation (PID). In: *27th European Photovoltaic Solar Energy Conference and Exhibition*, pp. 3379–3383.

Investigating the feasibility of using neutron activation to measure elemental pollution in the Richards Bay area

Sizwe Mhlongo[1], Sifiso Ntshangase[1], Peane Maleka[2] and Ntombizikhona Ndlovu[2]

[1]Department of Physics, University of Zululand, Private Bag X1001, KwaDlangezwa, 3886, KwaZulu-Natal, South Africa
[2]Department of Subatomic Physics, iThemba LABS, PO Box 722, Somerset West 7129, South Africa

E-mail: sizwesmhlongo@gmail.com

Abstract. Neutron Activation Analysis (NAA) is among the most reliable analytical techniques that can be used for the simultaneous analysis of multiple elements present in a sample. The technique involves exposing samples to a flux of neutrons for a predetermined period of time and then measuring the emanating characteristic γ-rays from the activated elements using a calibrated γ-ray spectrometer. A successful analysis depends on various factors, such as the neutron energy, neutron flux, and the sample matrix. The aim of this study was to investigate the feasibility of the NAA technique for routine analysis as a result of industrial pollution in the Richards Bay area, Kwa-Zulu Natal, South Africa. Richards Bay is an industrialized area and consists of industries that can potentially release elements such as aluminum, iron, lead, arsenic and others. Experiments with a test sample of mixed metals were made at the facility prior to analyzing the collected samples and they revealed that Al and Fe could be determined accurately with D-T generator, while the Am-Be source was sensitive to Al.

1. Introduction

Neutron Activation Analysis (NAA) is considered as one of the most reliable analytical techniques, because of its rapidness and accuracy [1, 2]. The technique has been well developed since it was first introduced in the 1940s, a few years after the discovery of neutrons by James Chadwick in 1932 [3]. The wide range of applications using the NAA technique spans various fields, including industries such as chemical and mining industries. The technique is also employed in archeology and the arts, education, as well as in the environmental pollution applications [4], which is the focus of this study. In this study the feasibility of using the technique to measure elemental pollution in the environment of the Richards Bay area was investigated. The area of Richards Bay is heavily industrialized and there is a possibility of contamination due to industrial activities.

Richards Bay is located in the Northern coast of KwaZulu-Natal, South Africa. The town is one of the industrialized areas in the country; the available heavy industrial activities in the

area include aluminium smelting, a phosphate fertilizer plant, sand dune mining, a kraft-process paper-mill and coal mining [5]. All the mentioned industries have typical elements associated with the waste they produce. Phosphate fertilizer industries may release cadmium (Cd), zinc (Zn) and strontium (Sr) into the environment; aluminium smelting activities may release aluminium (Al), lead (Pb), iron (Fe) and manganese (Mn), while a Kraft process paper-mill industry may release sulfur (S) and chlorine-based compounds [6, 7, 8]. The presence of these industries thus necessitates the need for routine soil and water elemental analysis as a means to monitor elemental contamination in the environment; only a few of such studies have been conducted in the area, with the most recent being in 2016 [9]. The analytical method used by Masok et. al. [9] was the method known as the inductively coupled plasma mass spectrometry (ICP-MS). In this study the aim is to investigate the feasibility of using the NAA in the area to measure the above mentioned elements, which can accumulate in the environment due to the available industrial activities. The motivation behind the choice of NAA is that it has many advantages over most of the commonly used analytical methods. Some of the advantages of the technique are that it is relatively fast and the samples are not destroyed during analysis. This makes it possible to analyze samples multiple times with NAA, or with other methods to benchmark the attained NAA results [1, 2]. Furthermore, although it is not the first time that the technique is used to conduct a study in the area [10], but it has never been used for the purpose of measuring environmental pollution, which makes this study a first attempt to do so.

2. Experimental Method

For the study, certified reference materials (CRMs) of soil and water were obtained from Waters ERA, an organization that provides both CRM and proficiency testing (PT) products. Environmental soil and water samples were also collected from three locations around the area of Richards Bay. The water samples were obtained from two water bodies (Mzingazi Dam and a pond situated next to one of the industries) and from a drinking water tap in Esikhawini township using 500 mL polyethylene bottles. Soil samples were collected next to the water bodies and one from one of the residential homes in Esikhawini, using the same 500 mL polyethylene bottles used to collect water samples. The collected water samples were prepared inside 100 mL cylindrical polyethylene bottles; the soil samples were prepared inside 30 mL cylindrical polyvials. In order to be able to quantify the identified elements using NAA, various standardization methods are used [1]. The comparator method, in which a standard is irradiated along with the sample, was considered because it allows simultaneous analysis of multiple elements. Therefore, the CRMs were also prepared according to the guidelines given in the accompanying certificates. Furthermore, a sample of mixed metals containing 9.0651 % of Al, 27.0174 % of Fe, 23.5691 % of Zn and 40.3484 % of nickel (Ni) was prepared inside a glass sample holder and was used for test runs in order to determine the elements the facility would be more sensitivity to.

The irradiation was done at the Department of Physics at University of Cape Town (UCT). The neutron sources available are the MP320 sealed tube neutron generator (STNG), which was purchased from Thermo Fisher Scientific [11]; the neutron facility was commissioned in 2017 with just the STNG [12]. The Americium-Beryllium (Am-Be) is also available as an additional neutron source. The STNG available is the deuterium-tritium based generator which produces neutrons by accelerating deuterium (^{2}H) ions towards a tritium (^{3}H) target. This causes a fusion reaction between ^{3}H and ^{2}H, which produces 14 MeV neutrons. As such, the facility is capable of providing a near monoenergetic beam of 14 MeV neutrons with a beam intensity of 10^8 neutrons per second [12]. The STNG is placed inside a vault where it is shielded with high density polyethylene blocks and beads.

The Am-Be source was initially stored inside a box with dimensions of 150cm×150cm×150cm, in which some of the samples were irradiated. The source has since been moved to the same vault where the STNG is also installed. Generally, the neutron energies of Am-Be sources range from about 2.5 MeV to 11 MeV, with the average energy being 4 MeV. Also, the neutron flux of a Am-Be source is specified to be 2.2×10^8 n/cm^2/s.

Out of the total number of samples prepared only three samples were irradiated using the STNG. These were the mixed metals sample, environmental water sample and a water CRM. This is a result of not observing the γ-rays from the elements of interest in the spectrum of the irradiated water CRM. Another reason for not irradiating any further is that the STNG has a limited lifetime of about 1200 hours [11]. The samples were irradiated for 1 hour and were then counted using the HPGe detector. The samples were also irradiated using the Am-Be source while it was still stored inside the box, the remaining samples were irradiated inside the vault where the STNG is installed. The summary of the irradiation times (t_i), decay times (t_d) and counting times (t_c) is given in tables 1-2.

Table 1. List of samples activated using the STNG.

Sample name	t_i(h)	t_d(s)	t_c(h)
Water-CRM	1	74.13	1
Metallic sample	1	60	1
Art-Road-Water	1	82.94	1

Table 2. List of samples irradiated using the Am-Be source.

Sample Name	t_i(h)	t_d(s)	t_c(s)
Soil-CRM	3.4	135	10800
Art-Road-Soil	3.5	55	7116.442
Metallic sample	5	60	7500.489
ESK-soil	3	180	7220.305
ESK-tapwater	2	180	7213.505
Mz-Soil	2	270	1982.992
Mz-water	9	120	7376.970
Water-CRM	5	60	7500.481

3. Results and discussion

The irradiation of the mixed metals sample, using the STNG, showed a significant response from Fe and Al. Fe was identified using γ-rays from ^{56}Mn, a radioactive product resulting from the ^{56}Fe(n,p)^{56}Mn reaction. The γ-rays used to identify Fe in the spectrum are 846 keV, 1810 keV and 2113 keV full-energy peaks. The spectrum is presented in Fig. 1. The identification of Al was done through the 1368 keV γ-ray from the decay of the isotope of sodium, ^{24}Na,

which is one of the γ-rays with a high intensity (I_γ) of 99% [13]. The other two elements in the mixed metals sample, Ni and Zn, were not easily identified from the background contribution of the reported spectrum. The activation of water CRM and the environmental water sample (Art-Road soil sample) did not show any recognizable γ-ray peaks above the background. The water CRM contained 22 elements which were all present in the order of parts per billion (ppb), and this was suspected to be one of the reasons why the water CRM sample was not activated. The spectra of the water environmental sample and that of the water CRM are superimposed in one plot in Fig. 2, where it can be seen that the peaks are dominated by background contribution.

Following the results from the irradiation of samples using the STNG, the then remaining samples were irradiated using the Am-Be source. The irradiation of the soil CRM using the Am-Be source in the collimator resulted in the activation of Al. The soil CRM contained 29 elements present in parts per million (ppm) concentration levels. Al was identified in the soil CRM via the 1368 keV and 2754 keV γ-ray peaks from the decay of ^{24}Na; this indicating that Al was activated by the fast neutron region of the Am-Be source. The spectrum resulting from the soil CRM was superimposed to the background spectrum in order to identify peaks that are non background contribution.

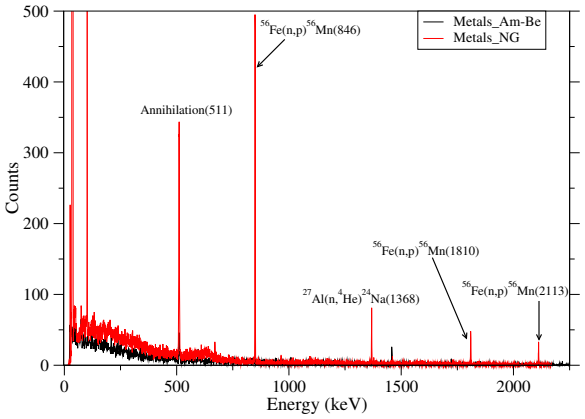

Figure 1. Superimposed spectra of the mixed metals sample.

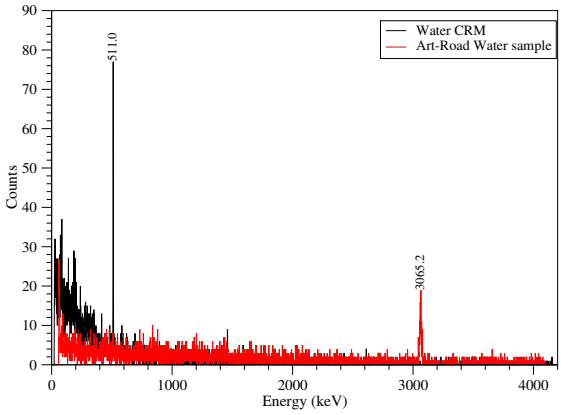

Figure 2. Spectrum of environmental water sample (Art-Road water) irradiated with the STNG superimposed to the spectrum of the water CRM.

The environmental samples that were irradiated using the Am-Be source were dominated by background contribution, and peaks of interest with very low count rates. As a result, the analysis procedure did not reach the quantification stage. Furthermore, even if there were high count rates for the energy peaks of interest, it was still not going to be possible to quantify the elements using the comparator method, since the suspected peaks were not present in the CRMs. As explained under the experimental method section, the quantification of elements using the comparator method requires that the elements that are being analyzed for must be present in the CRM as well, and must be activated in both the sample and CRM under similar experimental conditions. The spectra of environmental soil and water samples from Esikhawini are shown in Fig. 3 and Fig. 4, respectively. The spectra of environmental soil and water samples from Mzingazi are shown in Fig. 5 and Fig. 6.

 ISBN: 978-0-620-88875-2

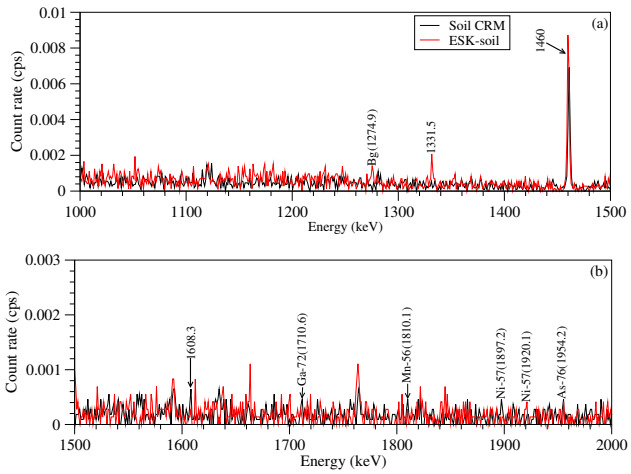

Figure 3. The spectrum of Esikhawini soil sample superimposed to the soil CRM spectrum. The figure shows only the 1000-2000 keV region of the two spectra.

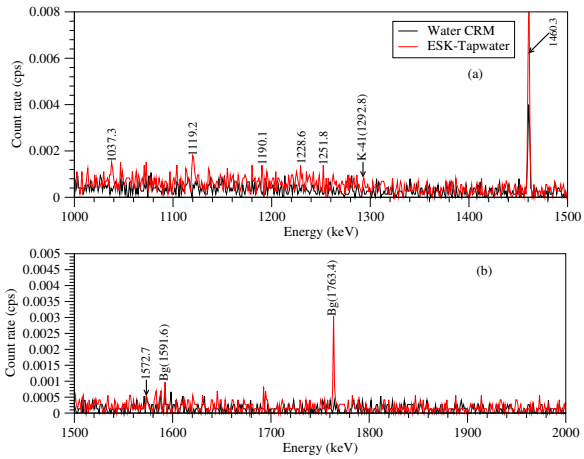

Figure 4. Spectrum of Esikhawini tap water sample (ESK-Tapwater) superimposed to that of the water CRM. The figure shows only the 1000-2000 keV region of the two spectra.

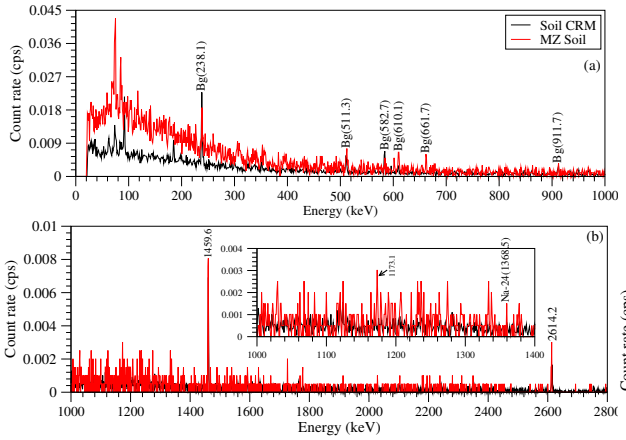

Figure 5. The spectrum of Mzingazi soil sample (Mz-soil)superimposed on the soil CRM spectrum. The figure shows only the 1000-2000 keV region of the two spectra.

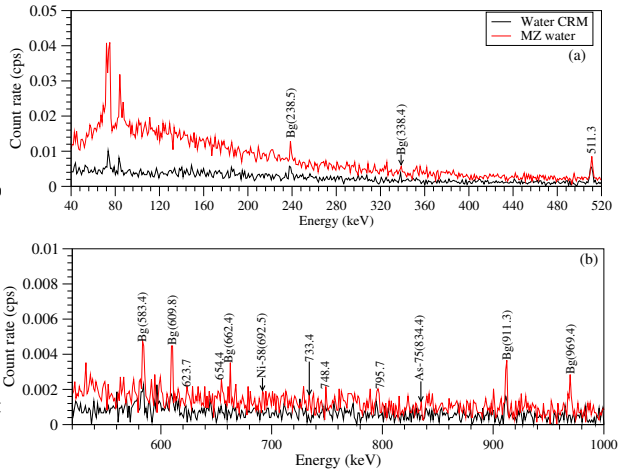

Figure 6. Spectrum of Mzingazi water sample (Mz-water) superimposed on that of the water CRM. The figure shows only the 1000-2000 keV region of the two spectra.

4. Conclusion

The spectra of the mixed metals irradiated at the facility shows that 14 MeV neutrons can be used to analyze for Al and Fe using high intensity γ-rays from ^{24}Na and ^{56}Mn, respectively. However, the successful activation of Al and Fe is attributed to the fact that they were were present in high concentrations. Since it was also possible to activate Al in the soil CRM, this meant that the facility is capable of identifying Al present in ppm concentration levels using the available Am-Be source. However, Fe was not successfully activated even though it was present in the CRM. Thus, a conclusion that can be drawn from this study is that the use of the technique is feasible for Al analysis in soils using fast neutrons from the neutron facility at UCT. For other elements of interest, there is a need for further studies as it is suspected that they were present in concentration levels that are below the limits of detection of the facility. This is

mostly true for the elements in the water CRM, in which they were present in ppb concentration levels. The challenges of sensitivity can be overcome through employing other types of NAA, such as those involving chemical separation; alternatively, a different neutron facility with high sensitivity to the elements of interest can be used.

5. Acknowledgements

This work is supported by the University of Zululand and the National Research Foundation (NRF), through the MANUS/MATSCIE program, iThemba LABS and under grant number 106012. The authors also wish to thank the following people for their contribution to this work: Dr. Tanya Hutton, Prof. Andy Buffler, Mr. Michael Van Heerden (Department of Physics, UCT) and Mr. Graham Daniels (NECSA).

References

[1] Kharfi, F. L. (Ed), 2013, *Imaging and Radioanalytical Techniques in Interdisciplinary Research - Fundamentals and Cutting Edge Applications*.

[2] Guinn, V.P. and Hoste, J., et al., 1980, *Analytical Techniques For Trace and Minor Elements in Biological Materials: Current Problems and Techniques. With Special Reference to Trace Elements*, iaea.org, viewed on 4 February 2017 from http://www.iaea.org/inis/collection/nclcollectionstore/_public/-11/564/11564331.pdfpage=115.

[3] Chadwick, J., 1932, "Possible Existence of a Neutron", Nature 129, 312.

[4] Mulhauser, F. (ed), "Neutron Generators for Analytical Purposes", Vienna, 2012, International Atomic Energy Agency, IAEA.

[5] Okello, N. & Allan, C., 2015, "The Richards Bay Clean Air Association: A Case Study for Success in Participatory Air Quality Management", The Clean Air Journal 25(1), 35 − 37, viewed on 4 February 2017, from http://www.cleanairjournal.org.za/download/caj_vol25_no1_2015_p34.pdf.

[6] Rotimi, A., Umo N. et al., *Environmental Pollution Induced by an Aluminium Smelting Plant in Nigeria*, researchgate.net, viewed on 19 May 2017, from www.researchgate.net/publication/268265647_Environmental_Pollution-_induced_By_an_Aluminium_Smelting_Plant_in_Nigeria.

[7] Mumford, M. & Engelhardt C n.d., "Pulp and Paper mill Pollution Effects on Estuarine Environments", Coastal Carolina University, Conway.

[8] Kassir, L., Lartiges B. et al., *Effects of Fertilizer Industry Emissions on Local Soil Contamination: A case study of a phosphate plant on the east Mediterranean coast*, iahr.tandfonline.com, viewed on 19 May 2017, from www.iahr.tandfonline.com/doi/abs/10.1080/09593330.2011.601765.

[9] Masok, F.B., Masiteng, P.L., Mavunda, R.D. and Maleka, P.P., 2016, "Chemical Contamination and Radiological Risk Assessment of Water Sources in Richards Bay", Journal of Physical Science and Application 6(5).

[10] Masok, F.B., Masiteng, P.L., Mavunda, R.D. and Maleka, P.P., 2016, "Health Effects Due to Radionuclides Content of Solid Minerals within Port of Richards Bay, South Africa", Int. J. Environ. Res. Public Health, 13, 1180.

[11] ThermoFisher Scientific n.d.,Thermo Scientific MP 320: Lightweight, Portable Neutron Generator, viewed 14 April 2019, from https://www.thermofisher.com/order/catalog/product/1517021A.

[12] Hutton, T, and Buffler, A., 2017 J. Phys.: Conf. Series 62 324330.

[13] Chu, S.Y.F., Ekstrom, L.P. and Firestone, R.B., computer software, viewed March 2018 from http://nucleardata.nuclear.lu.se/toi/index.asp.

Low Dose Radiation Damage in Diamond from High Energy Electrons and Photons

T Nemakhavhani[1], R Andrew[1], JE Butler[2], SH Connell[1], MN Cook[1,3], R Erasmus[4], J Van Rooyen[5]

1. University of Johannesburg, Johannesburg, Mechanical Engineering, South Africa
2. Cubic Carbon Ceramics - Huntingtown Md, USA
3. Gem Diamonds, South Africa
4. School of Physics and Microscopy and Microanalysis Unit, Wits University, South Africa
5. Necsa, South Africa

E-mail: tnemakhavhani@uj.ac.za

Abstract. Radiation damage is of great interest in diamond. Diamond is so-called radiation hard and is a candidate for passive and active electronics in high radiation environments. Further, it is possible to treat diamond by radiation and annealing stages, so as to change its colour or introduce a favoured colour. The study of radiation damage is therefore well advanced in diamond. More recently, so-called quantum diamond is engineered by a low dose damage and ion implantation process. Our own interest in the matter of radiation damage in diamond arises from natural diamond recovery using the MinPET technique. This has a high energy photon irradiation stage to produce internal Positron Emission Tomography (PET) emitters, whose subsequent transient PET radiation yields 3D quantitative local carbon density distributions within kimberlite rock. We have therefore made a study of radiation damage in diamond in the limit of very low dose derived from a high energy mixed radiation field of photons and electrons. The process has also been modelled using Geant4. The major mechanism for displacement of carbon atoms is ballistic collisions derived from the primary and secondary electrons. One must also consider the damage due to the secondary carbon recoils. Then there is the various nuclear reactions and the secondary consequences of these. The primary damage created is the single neutral vacancy (GR1 defect). There are also the primary interstitials which can be the single dumbbell interstitial on cubic face centre (R2 defect) or the self-trapped pair of these (R1 defect). Finally there can be aggregates of these defects with each other as well as with pre-existing defects in the diamond (if these were present not too far from the radiation induced defect). As most of these defects are optically active, measurements were performed using UV-VIS absorption spectroscopy, IR absorption spectroscopy and very sensitive photo-luminescence (PL) spectroscopy at 77K. The results will be presented and discussed. The low dose experiments to characterise the MinPET diamond discovery system showed the damage creation was too low to be quantified.

1. Introduction

Radiation damage in diamond is a much studied subject, due to its importance as mentioned in the abstract, and also due to its complexity. For example, diamond does not anneal to a high quality lattice as silicon does, as one might have at first expected. If this were the case, there would be very high quality diamond both for the gem industry and for scientific and industrial applications on the market. Instead, one achieves high quality either by very superior and particular synthesis conditions in the case of synthetic diamond, or in the case of gems, there must be selection of the rarest specimens. Diamond is a metastable allotrope of carbon, and high temperatures require stabilising high pressure and inert environments to prevent surface reactions. However, even annealing experiments at high temperature and pressure (up to 2000

K and 5 GPa) do not mange to anneal the lattice to high quality [1]. Point defects that can be mobilised during annealing tend to form complexes or trap at other point and extended defects that are less mobile. The annealing behaviour of radiation damaged diamond is therefore strongly dependent on any pre-existing defects. This means that annealing can improve diamond to some extent, but usually, it is a treatment for colour enhancement. For example, a yellow diamond has single substitutional nitrogen (impurity) at trace levels. If vacancies are introduced by irradiation, and an annealing stage follows, then single vacancies which become mobile may then be trapped at the nitrogen (NV centre) and will endow the diamond with a pinkish colour. One does not entirely anneal out the nitrogen or the vacancies. Instead one has complexation and aggregation of defects. Experiments to understand primary radiation defects in diamond were therefore not entirely successful until they were carried out under conditions of low defect mobility (well below room temperature during irradiation) and in very pure and very high quality crystal specimens. It is now known that the most significant primary radiation induced defects are the single vacancy, known as GR1 (general radiation defect 1) and then the single interstitial, followed by complexes of these, such as the divacancy, the double interstitial, known as R2, V_2 and R1 respectively [2, 3, 4, 5, 6]. Then of course, with some annealing, there are yet higher order complexes of these, and depending on the presence of other pre-existing defects, complexes with them as well. The most important class of pre-existing defects which trap radiation damage is the nitrogen related defects. These are the single substitutional nitrogen mentioned earlier, N_s, the A-centre, which is two neighbouring substitutional nitrogen atoms and the B-centre, which is four nearest neighbour substitutional nitrogen atoms surrounding a vacancy. Of course the list is really very much longer. More recent articles on radiation damage in diamond can be studied [7, 8] including the references therein to track and expand on the statements made here.

These references and the references therein reflect many studies using low energy (few MeV range) electron irradiation; other charged particles; photon induced radiation damage, also in the low energy regime; and neutron induced damage, similarly with low energy neutrons. One may also find some studies at a very high energy, such as that relevant to the Tevatron or the Large Hadron Collider (GeV range). An interesting theoretical study using Monte Carlo style modelling of the damage may be found in the references [9, 10]. These studies connect to the low energy damage regime and progress out to 10 MeV.

In this paper we are interested in a very low dose regime, to understand the limits of detection of radiation damage in diamond. The presence of detectable defects is in a separate dose regime to that which could lead to an "altered" or a "treated" diamond, as might affect the natural diamond's properties or value as a gem. The energy regime of diamond radiation is raised to the 40 MeV level, and the theoretical modelling is much further developed than previously, deploying the well established particle tracking code, Geant4 [11, 12]. The relevant low dose is that dose that is used in the MinPET system [13] which activates Positron Emission Tomography (PET) isotopes within kimberlite rock for the later PET detector based sorting of diamondiferous from barren kimberlite in a online run-of-mine context. Here the primary electron beam energy is 40 MeV with a dose of $< 3 \times 10^{12}$ e^-/cm^2, and where a mixed radiation field (shower) of electrons, photons and nuclear reaction products develops within the kimberlite and the diamond. We shall call this mixed integral flux the "MinPET Dose" for the purposes of this paper.

2. Simulations, Experiments, and Results

The irradiation system consist of a primary electron beam energy with an energy of 40 MeV, which firstly impacts a thin (3 mm) tungsten slab leading to an electromagnetic shower, which develops further in the diamond target. There is also a hadronic component to the shower, or cascade, due to nuclear reactions (elastic and inelastic), delayed recoil following nuclear decay and also elastic coulomb scattering secondaries. The tungsten acts as a primary converter for bremsstrahlung radiation. It optimises the yield of photons in the Giant Dipole Resonance energy regime for the reaction $^{12}C(\gamma,n)^{11}C$, so that the photo-transmutation reaction yielding

the ^{11}C PET isotope is maximised, so that ultimately, diamonds can be discovered in kimberlite as carbon density hot spots in a PET tomograph. Geant4 is used to track the histories of a large ensemble of such high energy electron initiated showers. The most important damage producing hadronic component is the carbon recoils themselves.

2.1. SRIM study of vacancy production by C-recoils

In the circumstances of this study, these are typically less than 1 keV in energy, but they are very effective as a secondary source of additional vacancy production, as they will have a large Rutherford cross-section and are very heavy. Figure 1 below shows how the SRIM [14] programme was used to generate the specific vacancy production as a function of incident projectile energy by these recoils as an interpolable set of points.

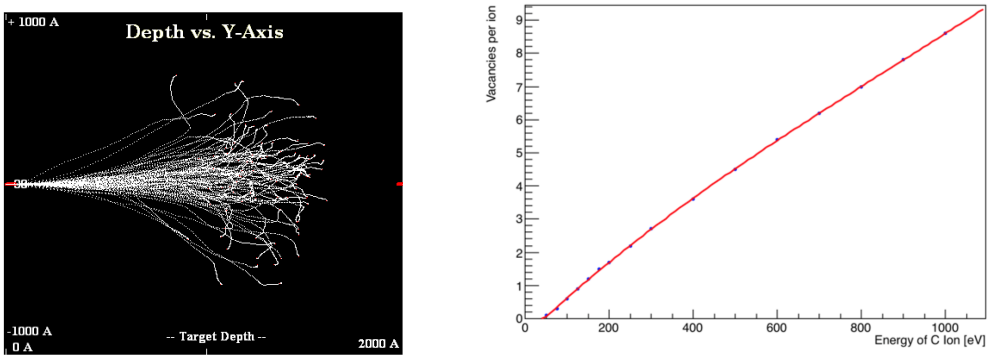

Figure 1: Left: A typical SRIM cascade for 100 keV carbon in diamond. There are 99 events with 215 vacancies per ion. The axes represent depth and transverse position in Angström units. Right: A section of the curve for vacancy production as a function of incident projectile energy.

2.2. Geant4 study of shower development and damage production

Geant4 can now be used to model the damage production. This includes the electromagnetic physics of the shower formation, and also the physics of the electron (and positron) components of the shower as they deposit energy and transfer momentum into the lattice, considering especially the screened relativistic non-ionising energy loss (SR-NIEL) [15]. The SRIM result discussed above is used in conjunction with Geant4. The Geant4 simulation gives the energy distribution of ion recoils, and the curve in Figure 1 then gives number of primary knock-on vacancies that are created from these recoils. Figure 2 below shows a visualisation of the primary electron beam and the shower development in the system described, and then also a 3D rendering of vacancy production in the diamond. Currently the hadronic component is not switched on in the simulation. A careful process of identifying which reactions are most significant to include is being done in parallel using the code FISPACT [16]. It is currently estimated that the nuclear hadronic component will contribute 20% to the vacancy production.

2.3. Experimental study of vacancy production using photo-luminescence

A synthetic diamond (type IIa) grown by the High Pressure High Temperature (HPHT) method with a low nitrogen concentration (around 10 ppb) and a high quality lattice (only a few dislocations overall) was used. It was irradiated as described above where the energetic core of the shower had an elliptical footprint with dimensions smaller than the sample. The dose was 600 times the "MinPET dose" described above. After irradiation the photo-luminescence (PL) signal from the single neutral vacancy (GR1) signal was studied. This is a peak at 741 nm. The excitation was via a 514.5 nm confocal laser / detector system and the samples were

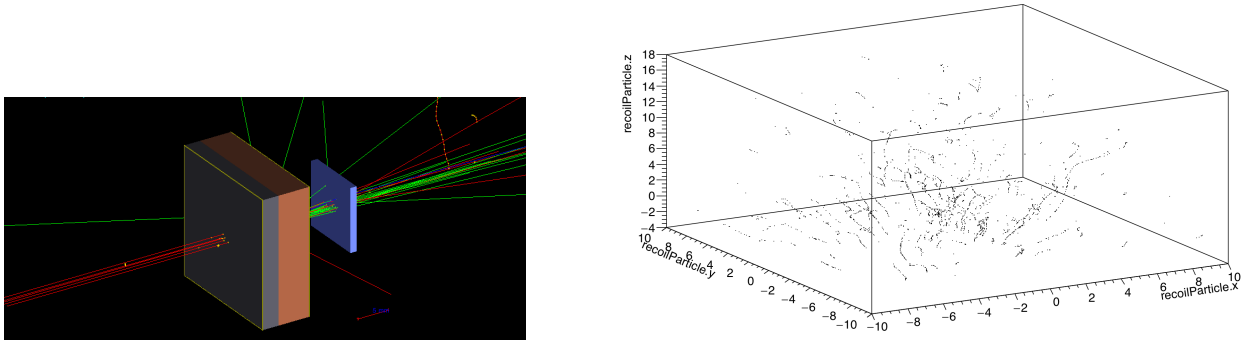

Figure 2: Left: A visualisation of the primary electron 40 MeV beam incident on the tungsten slab and the diamond with the shower development, and then also a 3D rendering of vacancy production in the diamond. Red - e^-, Blue - $^+$, Green - γ.

maintained at a temperature of 77K in order to enhance the intensity of the Zero Phonon Line (ZPL) relative to the phononic sideband components during the acquisition time of each spot. Spot analyses were conducted on a grid as shown in Figure 3 with acquisition times in the range of seconds per spot. This represents a near maximal sensitivity to the GR1 via PL. The GR1 PL peaks for each spot are also shown in the figure.

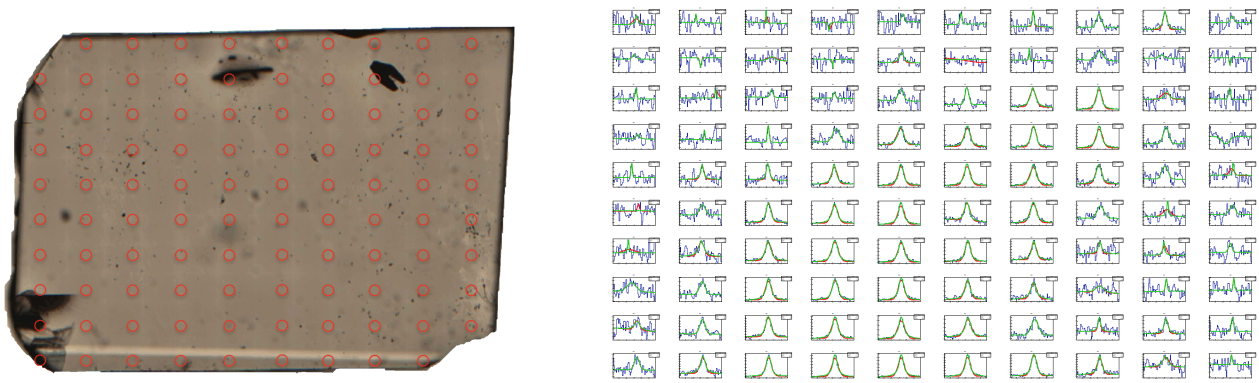

Figure 3: Left: The diamond sample (4mm×5.5mm) with positions indicated where the photo-luminescence (PL) spot analyses were carried out. Right: The GR1 PL peaks for each spot. This represents a map of vacancy production by the electromagnetic shower.

The Figure 4 below shows the GR1 PL peak at 741 nm arising from a primary electron beam dose of 2×10^{15} e^-/cm^2 (600 MinPET doses). By scaling the noise statistics and considering a peak 600 times smaller, the conclusion is the GR1 concentration is near or below the minimum detection limit (MDL) in these experimental conditions. Figure 4 also shows a 3D reconstruction of the GR1 production concentration in arbitrary units. There is an effort to convert the production to absolute units. One method relies on the use of the Raman peak intensity acquired during the same experiment to normalise the intensity of the ZPL. There are several systematics to be considered. Another method involves the use of a standard sample. There is currently a tension of a factor of 10 between the Geant4 simulation of the absolute vacancy production and the GR1 PL measurement. Continuing experiments aim to remove the tension. In this case the Geant4 simulation will become a tool that connecting all the different damage production experiments at different energies, reconciling the effects of shower development, which allows

 ISBN: 978-0-620-88875-2

then the sensible comparison of data points across all energies and primary projectile types.

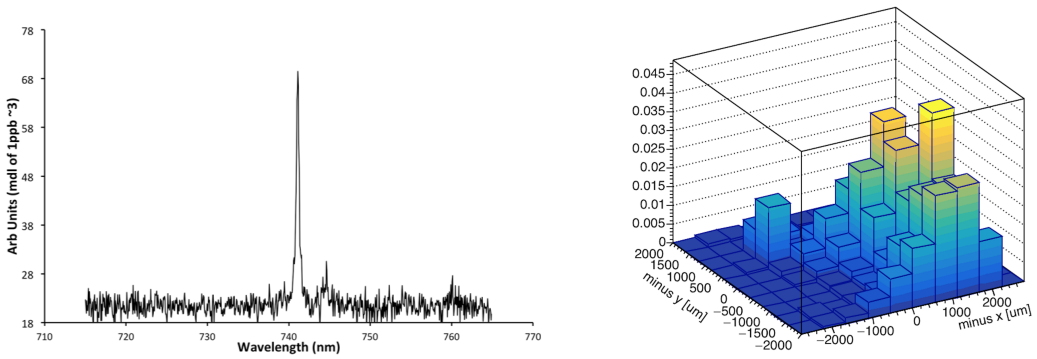

Figure 4: Left: Detail of the GR1 PL peak at 741 nm arising from a primary electron beam dose of 2×10^{15} e^-/cm^2. Right: 2D reconstruction of GR1 production concentration (arb. units).

2.4. Very low dose damage studies at high defect detection sensitivities

A selection of 10 natural diamonds was made, representing a variety of types (pre-existing defects). These are tabulated in Table 1. Essentially they will contain nitrogen impurities at different levels of aggregation in terms of A, B and N_s defects. These diamonds were studied by Optical Absorption (UV-Vis) as well as low temperature PL with different wavelengths of excitation as shown, and with different power levels. The irradiation was once again as in section 2. The characterisation was done before and after irradiation, to the dose shown in the table in "MinPET dose" units. The analysis conditions were chosen to provide maximal sensitivity in few spot analyses to a wide range of defects, those known to be associated with irradiation damage, and also as yet uncharacterised spectral features. It is not likely that the same spot was probed, before and after irradiation. This data will be discussed in more detail elsewhere. Many of these lines require aggregation of the radiation induced damage and the pre-existing defects. It is not considered reasonable that there could have been annealing conditions present in the experiments to enable this. One also considers that these diamonds have had a several billion year residence in the continental mantle. Here they would have had long term exposure to low dose irradiation from Naturally Occurring Radioactive Material (NORM). Calculations indicate this dose is about 1000 times the "MinPET dose". However, the physical conditions during the irradiation are very different. As such, on an aggregated defect molecular level, there will still be differences in the MinPET irradiation compared to the natural irradiation. Keep in mind that with some defects, for example the NV centre, it is possible to study a single isolated one of them by highly optimsed confocal PL techniques. This means the sensitivity to some defects is extreme, perhaps representing the finest example of the capacity to locate a needle in a haystack in all science. Accordingly, one notes by studying the table that there is a story that could be told of both pre-existing and new radiation related features, which for some stones contradicts others. As a whole, it is not certain one could say scientifically that the stones show evidence of non-natural irradiation. For example, in a gem scenario, one would not have the pre-irradiated information. Even with this information, the situation is not sufficiently clear.

3. Conclusion

We have presented a review of the main features of radiation damage in diamond. Following this we shown that one can model the spatial distribution of the production of vacancies, and also measure it, and that these two processes are converging. In due course, the tension in

Table 1: Summary of noticeable spectral changes due to the irradiation (PL at 77K).

Stone	Dose	Carats	Type	UV-Vis	488 laser PL	514 laser PL	633 laser PL
9	0	8.04	Ia		H3 slight incr, 787 appear	vvw 577 appearance	
2	0	3.55	Ia		H3 present		
6	1.6	8.06	IIa		3H appearance; stronger GR1, no NV, NV-	weaker NV,NV-, 612, weak broad 555, 630, stronger GR1	stronger GR1
8	1.9	7.12	IaA		H3, 700 stronger, 787 appear, No GR1	612 appearance	
5	2.1	4.75	IIa	weak 540 band	496, 3H, 612, 637 vvw, H3, slight GR1 Incr	GR1 vvw, broad 555, 600	weaker GR1?
7	2.6	5.83	Ia		H3 incr, No GR1		
3	2.6	7.9	Ia		H3 incr and ZPL splits?, 612, 676 appear, No GR1	612, 676 appear	787, 794 both present, no change
1	2.9	1.18	Ia		H3 always present, new band comes in on higher energy side after. Splitting or 3H? No GR1	weak broad band ca. 560 nm	679, 700, 787 appearance; 676 disappearance
10	3.5	3.58	IaAB		No GR1	535, 603, 640 appearance, 700 incr.	stronger 700;793 appearance
4	4	0.91	Iia	weak 540 band	broad at 555 appear, 496, 498.1, H3 incr, weaker NV-, GR1	weaker NV-, GR1, broad 555, 600 appear	no 787, 794 in either

the model and the measurement will not be significant, and at this stage one has a tool to compare all damage studies across all projectile types and energies, and come to a universal understanding of the primary damage creation. This is a significant contribution. Furthermore, we have shown that in the extreme low dose case, of the "MinPET dose", it is not yet possible to be sure a diamond was recovered by the MinPET technique. However, as knowledge of the damage mechanisms increases, and the technology for analysing these at low levels increases, it may ultimately become possible. This is a reflection of the extreme sensitivity at which defects can be detected by advanced techniques, as well as the complexity of the defect aggregation mechanisms. The total number of defects induced remains many orders of magnitude below the point at which any kind of alteration takes place that can be significant gemologically, for example changes that could be detected by any reasonable gemologically available instrument.

4. Acknowledgements

We thank Gem Diamonds for their interest in this project. The IAEA, TIA (SA) and the NRF (SA) also contributed to the work.

References

[1] Kazuchitsa T N M, Rusetskya M S *et al.* 2019 *Diamond & Related Materials* **91** 156–164
[2] Collins A T 2007 *New Diamond Front. Carbon Technol* **17** 47
[3] Clark C, Ditchburn R and Dyer H 1956 *Proc. R. Soc. A* **234** 363
[4] Davies G 1977 *Nature* **269** 498500
[5] Twitchen D, Newton M, Baker J T A, Anthony T and Bahnzoler W 1996 *Phys. Rev. B* **54** 6988
[6] Hunt D *et al.* 2000 *Phys. Rev. B* **61** 3863
[7] Zaitsev A, Moe K and Wang W 2017 *Diamond & Related Materials* **71** 38–52
[8] Buchan J T *et al.* 2015 *J. Appl. Phys.* **117** 245901
[9] Campbell B and Mainwood A 2000 *Phys. stat. sol. (a)* **181** 99
[10] Campbell B and Mainwood A 2002 *Nuclear Instruments and Methods in Physics Research A* **476** 680685
[11] Agostinelli S *et al.* 2003 *Nuclear Instruments and Methods* **A 506** 250–303
[12] Allison J, Amako K, Apostolakis J, Araujo H, Dubois P *et al.* 2006 *IEEE Trans.Nucl.Sci.* **53** 270–8
[13] Nemakhavhani T *et al.* 2017 *The Proceedings of SAIP2017, 62nd Annual Conf. of the South African Institute of Physics, edited by J. Engelbrecht http://events.saip.org.za* **ISBN: 978-0-620-82077-6** 355–360
[14] Ziegler J, Ziegler M D and Biersack J P 2010 *Nuclear Instruments and Methods in Physics Research B* **268** 1818–1823
[15] Boschini M *et al.* 2011 *Proc. of the 13th ICATPP Conference, October 3-7 2011, Villa Olmo, Como, Italy, World Scientific, Singapore, IBSN: 978-981-4405-06-5;* 961–982
[16] Sublet J C *et al.* 2017 *Nuclear Data Sheets* **139** 77–137

DIVISION G – DIVISION OF THEORETICAL & COMPUTATIONAL PHYSICS

 ISBN: 978-0-620-88875-2

The Equation of State (EoS) of hadronic matter from the microscopic Ultra-relativistic Quantum Molecular Dynamics (UrQMD) model

T.E Nemakhavhani[1], M Younus[2], A Muronga[3]

[1]Physics Department, University of Johannesburg, P.O.Box 524. Auckland Park 2006, Johannesburg, RSA
[2] Department Physics , Nelson Mandela University, Summerstrand, Port Elizabeth, 6031, South Africa
[3] Faculty of Science, Nelson Mandela University, Summerstrand, Port Elizabeth, 6031, South Africa

E-mail: tenemakhavhani@gmail.com

Abstract. The Equation of State (EoS) of a hot and dense hadron matter is studied using a microscopic transport model which can support the Large Hadron Collider energies of up to $\sqrt{s_{nn}}$= 14 TeV, namely the Ultra-relativistic Quantum Molecular Dynamics (UrQMD). The molecular dynamics simulation is performed for a system of light meson species (π; ρ and K) in a box with periodic boundary conditions. The equilibrium state is investigated by studying the chemical equilibrium and the thermal equilibrium of the system. The particle multiplicity equilibrates with time, and the energy spectra of different light meson species have the same slopes and common temperatures when thermal equilibrium is reached. The solution of the EoS allows for better understanding of the final state of interactions, which is dominated by hadrons produced during ultra-relativistic heavy ion collisions.

1. Introduction

A large number of studies in heavy ion physics and high energy physics have been done using the results from the Relativistic Heavy Ion Collider (RHIC). Now with the restart of the Large Hadron Collider (LHC) physics programme, the field of high energy nuclear physics, and especially heavy ion physics, has gone into a new era. It is now possible to explore the properties of Quantum-Chromo-Dynamics (QCD) at unprecedented particle densities and temperatures, and at much higher energies than that produced at RHIC, from $\sqrt{s} = 200$ GeV to $\sqrt{s} = 14$ TeV at the LHC [1].

High energy heavy ion reactions are studied experimentally and theoretically to obtain information about the properties of nuclear matter under extreme conditions at high densities and temperatures, as well as about the phase transition to a new state of matter, the quark-gluon plasma (QGP) [2, 3, 4, 5]. This work reports on the equation of state of hadronic matter extracted using the UrQMD model. The knowledge of the equation of state (EoS) is important for better understanding of the final state of interactions which is dominated by hadrons produced during ultra-relativistic heavy ion collisions. The EoS of nuclear matter is one of the key points to gain further understanding since EoS directly provides the relationship between the pressure and the energy at a given net-baryon density [6]. The thermodynamic

properties, transport coefficients and EoS for hadron gas are a major source of uncertainties in dissipative fluid dynamics [4, 7, 8].

In order to study the EoS we look at the system in equilibrium. Equilibration of the system is studied by evaluating particle number densities from chemical equilibrium, energy spectra as well as the temperatures from thermal equilibrium of different light meson species in a cubic box, which imposes periodic boundary conditions. The infinite hadronic matter is modelled by initializing the system with light meson species namely, the pion (π), the rho (ρ) and the kaon (K).

We focus on the hadronic scale temperature (100 MeV $< T <$ 200 MeV) and net zero baryon number density, which are expected to be realized in the central high energy nuclear collisions [9]. We then change energy density from ε = 0.1 - 2.0 GeV/fm^3 and for each energy density we run the system with n-number of events while keeping the volume and baryon number density constant until the equilibrium state is reached.

The rest of the paper is organized as follows: In section 2 we study the description of the UrQMD model. In section 3 we study equilibration properties of the system. In section 4 we study the equation of state (EoS) of the hadron matter.

2. Brief Description of the UrQMD Model

The Ultra-relativistic Quantum Molecular Dynamic model (UrQMD) is a microscopic model based on a phase space description of nuclear reactions. We use version 3.3 of the UrQMD model for this study. The UrQMD 3.3 hybrid approach extends previous ansatzes to combine the hydrodynamic and the transport models for the relativistic energies. The combination of these approaches into one single framework, it is done for a consistent description of the dynamics

The UrQMD model describes the phenomenology of hadronic interactions at low and intermediate energies from a few hundreds MeV up to the new LHC energy of $\sqrt{s}$ =14 TeV per nucleon in the centre of mass system [10, 11]. The UrQMD collision term contains 55 different baryon species and 32 meson species, which are supplemented by their corresponding anti-particles and all the isospin-projected states [10, 12]. The properties of the baryons and the baryon-resonances which can be populated in UrQMD can be found in [12], together with their respective mesons and the meson-resonances. A collision between two hadrons will occur if

$$d_{trans} \leq \sqrt{\frac{\sigma_{tot}}{\pi}}, \qquad \sigma_{tot} = \sigma(\sqrt{s}, type), \tag{1}$$

where d_{trans} and σ_{tot} are the impact parameter and the total cross-section of the two hadrons respectively [10]. In the UrQMD model, the total cross-section σ_{tot} depends on the isospins of colliding particles, their flavour and the centre-of-mass (c.m) energy $\sqrt{s}$. More details about the UrQMD model is presented in [10, 11, 12].

3. Equilibration of Hadronic Matter

To investigate the equilibrition of a system, the UrQMD model is used to simulate the ultra-relativistic heavy ion collisions. A multi-particle production plays an important role in the equilibration of the hadronic gas [4]. The cubic box used for this study is initialised according to the following numbers of baryons and mesons: zero protons, 80 pions, 80 rhos and 80 kaons. For this study a cubic box with volume V and a baryon number density n_B = 0.00 fm^{-3} is considered. The energy density ε, volume V and the baryon number density n_B in the box are fixed as input parameters and are conserved throughout the simulation. The energy density is defined as $\varepsilon = \frac{E}{V}$, where E is the energy of N particles and the three-momenta p_i of the particles in the initial state are randomly distributed in the centre of mass system of the particles as shown in the equations below.

$$E = \sum_{i=1}^{N} \sqrt{m_i^2 + p_i^2}, \qquad \sum_{i=1}^{N} p_i = 0. \tag{2}$$

3.1. Chemical Equilibrium

In this subsection the chemical equilibrium is studied from the particle number densities of different light meson species in a box with $V = 1000$ fm^3, zero net baryon number density $n_B = 0.0$ fm^{-3} at different energy densities using UrQMD box calculations. Figure 1 (a) and (b) represents the time evolutions of the various meson number densities at $\varepsilon = 0.3$ and 0.4 GeV/fm^3 energy densities.

In figures 1 (a) and (b), the meson species indicate that the system does indeed reach chemical equilibrium. It is observed that the pions have large particle number densities and the reason could be the decay in the heavier mesons and other particles produced in the system to form pions. The saturation of the particle number densities indicate the realization of a local equilibrium. In conclusion, the chemical equilibrium of the system has been reached, as in both figures the saturation times are the same for all three mesons, regardless of the shape of each meson. In figure 1 (a) where $\varepsilon = 0.3$ GeV/fm^3, the equilibrium time for all meson species is around $t = 22$ fm/c and for figure 1 (b) at a higher energy density of $\varepsilon = 0.4$ GeV/fm^3, the equilibrium time is observed to have increased to $t = 32$ fm/c. These results show that an increase in energy density influences the particle multiplicity inside the periodic box, which affect the equilibration time.

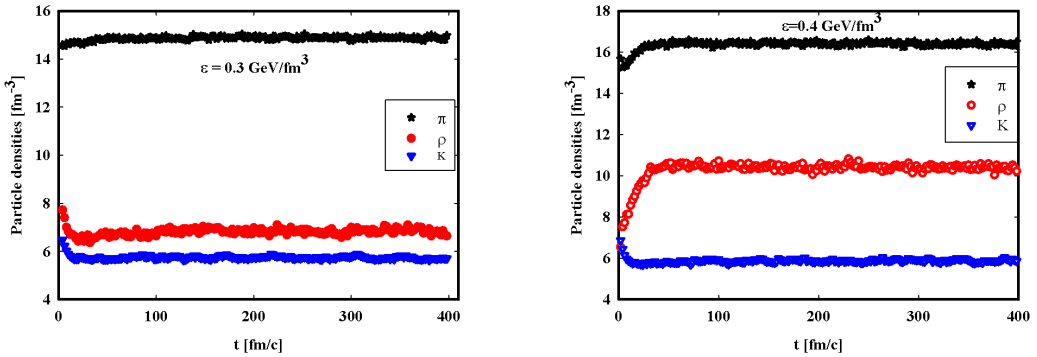

Figure 1: The time evolution of particle number densities of light meson species (π, ρ and K) at (a) $\varepsilon = 0.3$ GeV/fm^3 and (b) $\varepsilon = 0.4$ GeV/fm^3.

3.2. Thermal Equilibrium and Temperature

In this subsection the thermal equilibrium and the temperature from the energy distributions of different light meson species are studied. The possibility of the thermal equilibrium of the hadronic matter is studied by examining the energy distribution of the system in a box with periodic boundary conditions using the UrQMD model. The particle spectra are given by the momentum distribution as [13]

$$\frac{dN_i}{d^3p} = \frac{dN}{4\pi E p dE} \propto Ce^{(-\beta E_i)}. \tag{3}$$

Figure 2 (a) and (b) represent the time evolutions of energy spectra of different meson species. The linear lines are fitted using the Boltzmann distribution, which is aproximated by $C\exp(-\beta E_i)$ from Eq. 3, where $\beta = 1/T$ is the slope parameter of the distribution and E_i is the energy of particle i. The results are plotted as a function of kinetic energy $K = E - m$, so that the horizontal axes for all the particle species coincide [14]. In figure 2 (a) and (b) it is observed that the slopes of the energy distribution converge to common values of temperatures at different times above $t = 180$ fm/c for $\varepsilon = 0.2$ GeV/fm^3 and above $t = 250$ fm/c for $\varepsilon = 0.3$ GeV/fm^3. In thermal equilibrium the system is characterized by unique temeperature T [14]. The thermal temperatures were extracted from the equilibriumn state using the Boltzmann distribution such that $T = 118.3$ MeV for $\varepsilon = 0.2$ GeV/fm^3 and $T = 150.1$ MeV for $\varepsilon = 0.3$ GeV/fm^3.

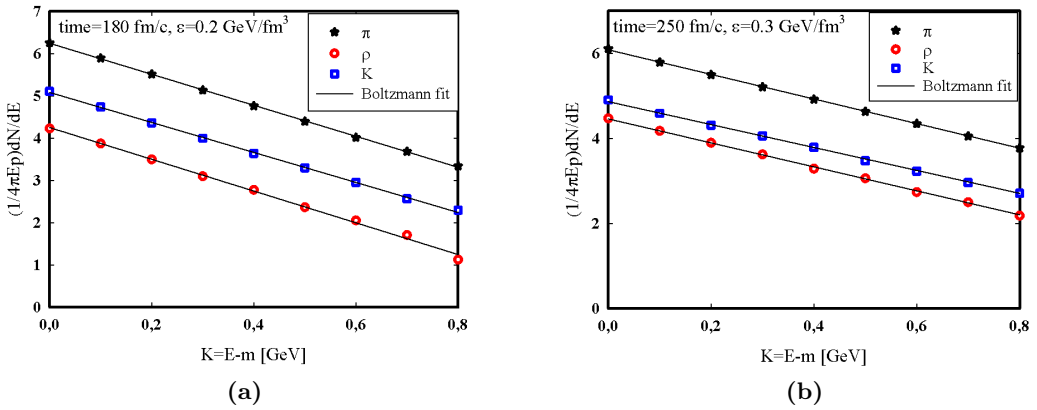

Figure 2: The energy distributions of light meson species (π, ρ and K) at (a) $\varepsilon = 0.2$ GeV/fm^3 and $t = 180$ fm/c and (b) $\varepsilon = 0.3$ GeV/fm^3 and $t = 250$ fm/c. The lines are the Boltzmann fit which gives the extracted temperatures of $T = 118.3$ MeV for (a) and $T = 150.1$ MeV for (b).

4. Hadronic gas model (Equation of State)

The hadron abundances and the ratios have been suggested as the possible signatures for the exotic states and the phase transitions of the nuclear matter [15]. The equation of state of hot and dense hadron matter provides the valuable information regarding the nature of the hadron matter. These signatures have been applied to the study of chemical equilibration in the relativistic heavy ion reactions. The properties like the temperatures, the entropies and chemical potentials of the hadronic matter have been extracted assuming thermal and chemical equilibrium [10].

In this section the EoS for a hadron matter is studied from the UrQMD simulation. The equation of state can be studied using a statistical model which is described by the grand canonical ensemble of non-interacting hadrons in an equilibrium sate at temperature T as presented in [4, 12]. A large number of studies have been done to study EoS of hadron matter [4, 12, 16, 17]. For this study the focus is only on the EoS of hadrong matter made out of the π, the ρ and the K calculated from the UrQMD model. This is done through studying the evolution of pressure and energy density with temperature. The thermodynamic quantities used to calculate EoS are the energy density given by

$$\varepsilon = \frac{1}{V} \sum_{i=1}^{all-particles} E_i \,, \tag{4}$$

 ISBN: 978-0-620-88875-2

and the pressure which is given by

$$P = \frac{1}{3V} \sum_{i=1}^{all-particles} \frac{p_i^2}{E_i}. \quad (5)$$

Figure 3 represent the EoS of hadronic matter namely (a) the pressure and, (b) the energy density as function of temperature. The energy density used here Eq. (4) is the same energy density used as an input parameter during the initialization of the simulation. The pressure is then calculated from the collision results using Eq. (5). The thermal temperatures used here are extracted from the thermal equilibrium (subsection 3.2) using the Boltzmann distribution function given as $C\exp(\frac{E}{T})$ [18].

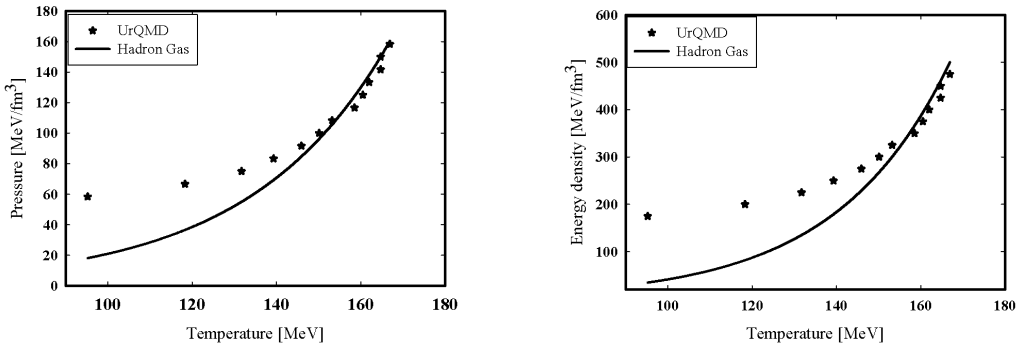

Figure 3: The equation of state of a mixed hadron gas of the π, the ρ and the K at finite temperature (100 MeV $< T <$ 200) (a) the pressure of hadronic matter is plotted as a function of temperature (b) the energy density of hadronic matter is plotted as a function of temperature.

From the above figure 3 (a) and (b), both pressure and energy density increase with an increase in the temperature. The results are in good agreement with those obtained in [4, 12]. The fitted line in both figure 5 and figure 6 represents the power law fit. The focus is on the hadronic scale temperature of (100 MeV $< T <$ 200 MeV) and the zero net baryon number density which is expected to be realized in the central high energy nuclear collisions [4]. The pressure and energy density grow with temperature and start to saturate just after $T = 150$ MeV which might indicate that there is a change in phase transition of the hadron gas. In figure 3 (a) and (b) at low temperatures between $T = 90$ MeV to $T = 150$ MeV the power law T^2 of hadron gas behaves differently than the power law T^4 at high temperature between $T = 155$ MeV to $T = 170$ MeV. The power law of the solid line fit is T^4 which start to behave in the same way as that of hadron matter at high temperatures [18].

5. Conclusion

The results shows that the EoS from the UrQMD model also behaves like results reported by other studies where different model and statistical method was used. The results behaves as expected where we find that the hadronic matter exisit between temperature range 100 MeV $< T <$ 170 MeV. Figure 3 (a) and (b) show that the pressure and the energy density increases exponentially with temperature. The temperature values indicates the phase transion to a new state of matter the QGP at around T = 170 MeV.

6. Acknowlegments

We would like to thank everyone who helped us with this paper in terms of corrections and discussions. Financial support from UJ Department of Physics is acknowledged.

References

[1] Campbell J M, Ellis R K and Williams C 2011 *Journal of High Energy Physics* **2011** 1–36
[2] Bratkovskaya E, Cassing W, Greiner C, Effenberger M, Mosel U and Sibirtsev A 2000 *Nuclear Physics A* **675** 661–691
[3] Demir N and Wiranata A 2014 *Journal of Physics: Conference Series* vol 535 (IOP Publishing) p 012018
[4] Muronga A 2004 *Physical Review C* **69** 044901
[5] Chen Z, Greiner C, Xu Z and Zhuang P 2019 *Physical Review C* **100** 014906
[6] Li Q, Steinheimer J, Petersen H, Bleicher M and Stöcker H 2009 *Physics Letters B* **674** 111–116
[7] Bleicher M, Endres S, Steinheimer J and van Hees H 2015 *arXiv preprint arXiv:1503.07371*
[8] Muronga A 2007 *Physical Review C* **76** 014910
[9] Mitrovski M, Schuster T, Gräf G, Petersen H and Bleicher M 2009 *Phys. Rev. C* **79**(4) 044901 URL `http://link.aps.org/doi/10.1103/PhysRevC.79.044901`
[10] Bleicher M, Zabrodin E, Spieles C, Bass S A, Ernst C, Soff S, Bravina L, Belkacem M, Weber H, Stöcker H *et al.* 1999 *Journal of Physics G: Nuclear and Particle Physics* **25** 1859
[11] collaboration P *et al.* 2005 *Technical Progress Report, GSI, Darmstadt*
[12] Bass S A, Belkacem M, Bleicher M, Brandstetter M, Bravina L, Ernst C, Gerland L, Hofmann M, Hofmann S, Konopka J *et al.* 1998 *Progress in Particle and Nuclear Physics* **41** 255–369
[13] Zabrodin E, Arsene I, Bleibel J, Bleicher M, Bravina L, Burau G, Faessler A, Fuchs C, Nilsson M, Tywoniuk K *et al.* 2009 *Journal of Physics G: Nuclear and Particle Physics* **36** 064065
[14] Sasaki N 2001 *Progress of theoretical Physics* **106** 783–805
[15] Bleicher M, Reiter M, Dumitru A, Brachmann J, Spieles C, Bass S A, Stöcker H and Greiner W 1999 *Physical Review C* **59** R1844
[16] Belkacem M, Brandstetter M, Bass S A, Bleicher M, Bravina L, Gorenstein M I, Konopka J, Neise L, Spieles C, Soff S *et al.* 1998 *Physical Review C* **58** 1727
[17] Pal S 2010 *Physics Letters B* **684** 211–215
[18] Nemakhavhani T E 2016 *Using the ultra-relativistic quantum molecular dynamics (UrQMD) model to extract the thermal conductivity transport coefficient of hadron gas* Ph.D. thesis University of Johannesburg

Computation of the effective potential in the gauge-Higgs unification model with an $SU(3)$ representation

A S Cornell[a,1], A Deandrea[b,2], C Cot[c,2], and M O Khojali[d,3]

[1]Department of Physics, University of Johannesburg, PO Box 524, Auckland Park 2006, South Africa

[2] Université de Lyon, Université Lyon 1, CNRS/IN2P3, UMR5822 IPNL, F-69622 Villeurbanne, France

[3]Physics Department, Faculty of Science, University of Khartoum, Sudan

E-mail: [a]acornell@uj.ac.za, [b]deandrea@ipnl.in2p3.fr, [c]cot@ipnl.in2p3.fr, [d]khogali11@gmail.com

Abstract. Gauge-Higgs unification models give interesting solutions to the hierarchy problem in particle physics. The common study of this type of model is done by using a decomposition of 5-dimensional particles in 4-dimensional Kaluza-Klein modes, which is a handy way to compute the infinite sums appearing in the model. In order to take into account the running of coupling constants in these models, we propose in this proceedings a different decomposition using winding modes around the fifth dimension, which is compactified. This decomposition not only permits us to take running into account, but also gives a faster converging series in all the quantities when summing over these modes.

1. Introduction

Since the discovery of a Higgs boson at the Large Hadron Collider (LHC) in 2012, a lot of questions have emerged concerning its mass and couplings, as they are close to the electroweak (EW) symmetry breaking scale. One such issue relates to the Planck scale being 10^{24} times higher than the EW scale, and that this scale enters the quantum loop corrections to the Higgs boson mass, giving rise to the hierarchy problem. This problem can be solved for gauge theories in more than four-dimensions [1], which can also give an interesting unification of gauge and Yukawa couplings with the running in the renormalisation group [2], where we can see that all the coupling constants run towards a common value at a large energy scale.

These theories include the Higgs boson as a component of a multidimensional gauge boson, rather than via an *ad hoc* addition to the model. In a previous work by some of the authors, an interesting toy model was developed, that of a flat 5-dimensional space-time compactified as a S^1/Z_2 [2]. In this model there exists different methods for studying the 5-dimensional fields, where the most common is to decompose the fields in an infinite tower of 4-dimensional fields (as a Fourier decomposition) called Kaluza-Klein modes (KK modes). This decomposition is convenient, as it allows us to compute (in simple cases) the infinite sums, and is the most common approach used in the literature [3, 4].

In order to introduce the running of the coupling constants in this kind of decomposition, we need to add contributions it at the right energy scale for each KK mode, and this complicates the calculation. We will present a different decomposition, in terms of winding modes, allowing a simpler physical interpretation. Whilst this method may appear to be harder to work with, as each term can be taken at a specific energy scale, it does enable a full running calculation to be done. This winding mode approach is further explained in references [5, 6]. Moreover, we will see that this decomposition brings advantages in terms of not just renormalisation, but also for the convergence of the infinite sums. As such, in section 2, we will see how the gauge-Higgs model can be described in an $SU(N)$ representation, deriving the effective Higgs potential in terms of winding modes in section 3. Finally, in section 4, we will study the effective potential and what can be done to improve the $SU(3)$ model studied here.

2. Gauge-Higgs unification with an S^1/Z_2 orbifold

According to reference [3], we can develop a gauge-Higgs unification model on a five-dimensional orbifold $M^4 \times (S^1/Z_2)$, where M^4 is the 4-dimensional Minkowski-space and S^1/Z_2 is obtained by identifying two points on the compactified fifth dimension S^1 by parity for $x = 0$ and $x = \pi R$. Our model is defined by the boundary conditions and by the parity operators defined as:

$$\begin{aligned} U : A_M(x, y + 2\pi R) &= U A_M(x, y) U^\dagger \,, & (1)\\ P_0 : A_\mu(x, -y) &= P_0 A_\mu(x, y) P_0^\dagger \,, & (2)\\ P_0 : A_y(x, -y) &= -P_0 A_y(x, y) P_0^\dagger \,, & (3)\\ P_1 : A_\mu(x, \pi R - y) &= P_1 A_\mu(x, \pi R + y) P_1^\dagger \,, & (4)\\ P_1 : A_y(x, \pi R - y) &= P_1 A_y(x, \pi R + y) P_1^\dagger \,, & (5) \end{aligned}$$

where A_M is a gauge field in 5-dimensions, with the convention that we use Greek letters for the 4-dimensions of M^4 and Latin letters for 5-dimensions (or just 5 for the fifth dimension). Normally we have $U = e^{i\alpha} P_1 P_0$, but as it does not affect the results, and for simplicity, we will take $U = P_1 P_0$.

From these operators it is possible to define the boundary conditions for the other fields in our model, where for a scalar field ϕ we have

$$\begin{aligned} \phi(x, y + 2\pi R) &= e^{i\pi\beta_\phi} T_\phi[U] \phi(x, y) \,, & (6)\\ \phi(x, -y) &= \pm T_\phi[P_0] \phi(x, y) \,, & (7)\\ \phi(x, \pi R - y) &= \pm e^{i\pi\beta_\phi} T_\phi[P_1] \phi(x, \pi R + y) \,, & (8) \end{aligned}$$

where $T[U]$ represents an appropriate representation matrix. For instance, if ϕ belongs to the fundamental or adjoint representation of the group, then $T_\phi[U]\phi$ is $U\phi$ or $U\phi U^\dagger$, respectively. Note that $e^{i\pi\beta_\phi}$ must be equal to either +1 or -1.

For Dirac fields ψ we have

$$\begin{aligned} (x, y + 2\pi R) &= e^{i\pi\beta_\psi} T_\psi[U] \psi(x, y) \,, & (9)\\ (x, -y) &= \pm T_\psi[P_0] \gamma^5 \psi(x, y) \,, & (10)\\ (x, \pi R - y) &= \pm e^{i\pi\beta_\psi} T_\psi[P_1] \gamma^5 \psi(x, \pi R + y) \,, & (11) \end{aligned}$$

where as before, we must have $e^{i\pi\beta_\psi}$ to be equal to +1 or -1.

The following Lagrangian is then used in order to compute the effective potential:

$$\mathcal{L} = \mathcal{L}_{gauge} + \mathcal{L}_{matter} \,; \qquad (12)$$

$$\mathcal{L}_{gauge} = -\frac{1}{2}\mathrm{Tr}(F_{MN}F^{MN}) - \frac{1}{\alpha}\mathrm{Tr}(F[A]^2) - \mathrm{Tr}\left(\overline{\eta}\frac{\delta F[A]}{\delta A_M}D^M\eta\right) , \tag{13}$$

$$\mathcal{L}_{matter} = \overline{\psi}i\gamma_M D^M\psi + |D_M\phi|^2 . \tag{14}$$

We then split the gauge field A_M into its classical part A^0_M, and its quantum part A^q_M, from which we have the gauge-fixing condition $F[A^0] = 0$, such that

$$F[A] = D_M(A^0)A^{qM} = \partial_M A^{qM} + ig[A^0_M, A^{qM}] = 0 . \tag{15}$$

Note that the notation $D_M(A^0)$ is often denoted D^0_M for short. This means that $\mathcal{L}_{gauge}$ can be rewritten as:

$$\mathcal{L}_{gauge} = -\mathrm{Tr}(A^q_M M^g_{MN} A^{Nq}) - \mathrm{Tr}(\overline{\eta}M^{gh}\eta) , \tag{16}$$

$$\begin{aligned} \text{where} M^g_{MN} &= -\eta_{MN}D^0_L D^{0L} - 4igF^0_{MN} , & (17)\\ M^{gh} &= D^0_L D^{0L} . & (18) \end{aligned}$$

Integrating out the quantum fields A^q_M, η, $\overline{\eta}$, and ϕ, we obtain the one-loop effective potential for A^0_M:

$$V_{eff}[A^0] = V_{eff}[A^0]^{g+gh} + V_{eff}[A^0]^{fermion} + V_{eff}[A^0]^{scalar} ; \tag{19}$$

$$V_{eff}[A^0]^{g+gh} = -(D-2)\frac{i}{2}\mathrm{Tr}(\ln(D^0_L D^{0L})) , \tag{20}$$

$$V_{eff}[A^0]^{fermion} = h(D)\frac{i}{2}\mathrm{Tr}(\ln(D^0_L D^{0L})) , \; h(D) = 2^{D/2} , \tag{21}$$

$$V_{eff}[A^0]^{scalar} = -2\frac{i}{2}\mathrm{Tr}(\ln(D^0_L D^{0L})) , \tag{22}$$

where we have supposed that $F_{MN} = 0$ and ϕ-fields are massless. From the next section onwards we shall focus on a particular group to compute the effective potential.

3. Functional method in $SU(3)_w$

As described in reference [7], it is possible to take $P_1 = P_2 = \mathrm{diag}(1, -1, -1)$ to break the group $G = SU(3)_w \times SU(3)_c$ to $G_{SM} = SU(2)_w \times U(1) \times SU(3)_c$, which is exactly the Standard Model group. In this configuration we only have a doublet for A_y, belonging to G/G_{SM}, which has a zero-mode. This doublet can be identified as our Higgs, such that $H = (A^{1(0)}_y + iA^{2(0)}_y, A^{4(0)}_y + iA^{5(0)}_y)^t$ where the index i in the notation A^i_y refers to the $SU(3)$ generator index. The vacuum expectation value (VEV) is a finite calculable quantity, which is determined by the minimisation of the one-loop induced effective potential as the function of a constant background field, $\langle A_y\rangle \equiv B_y$. In this case, keeping only the non-vanishing zero-modes and using the global $SU(2) \times U(1)$ symmetry, we can set the VEV in the form of $B^a_y = (B^1_y, 0, 0, 0, 0, 0, 0, 0)$, which leads to the effective potential formula:

$$V_{eff} = V^{g+gh}_{eff} + V^f_{eff} ; \tag{23}$$

$$\begin{aligned} V^{g+gh}_{eff} &= \frac{3}{2}\frac{1}{2\pi R}\int\frac{d^4p}{(2\pi)^4}\sum_{n=-\infty}^{\infty}\left[\ln\left(-p^2 + \frac{n^2}{R^2}\right) + \ln\left(-p^2 + \left(\frac{(n-\alpha)}{R}\right)^2\right)\right. \\ &\qquad \left. +2\ln\left(-p^2 + \left(\frac{(n-\alpha/2)}{R}\right)^2\right)\right] , \end{aligned} \tag{24}$$

$$V_{eff}^{f} = -N_f \frac{1}{2\pi R} \int \frac{d^4p}{(2\pi)^4} \sum_{n=-\infty}^{\infty} \left[\ln\left(-p^2 + \frac{n^2}{R^2} \right) + 2\ln\left(-p^2 + \left(\frac{(n-\alpha/2)}{R} \right)^2 \right) \right] . \quad (25)$$

The variable α is proportional to the VEV of B_y where $B_y = \alpha/gR$ [7]. N_f is the number of fermions we consider in this model, and the sum over n is over the full KK tower.

As explained in reference [6], it is possible to replace the KK modes in the previous expression by the winding modes we want to use. To do this we can identify in the propagator expression for the KK decomposition:

$$\sum_{n=-\infty}^{+\infty} \ln\left[-p^2 + \left(\frac{n-m_0}{R} \right)^2 \right] = -\int dp^2 \sum_{n=-\infty}^{+\infty} \frac{1}{-p^2 + \left(\frac{n-m_0}{R}\right)^2} = \int dp^2 \tilde{G}_{KK}(p, m_0) , \quad (26)$$

where m_0 represents the mass of the zero-mode and $\tilde{G}_{KK}(p, m_0)$ represents the KK propagator of a scalar particle. From this we can replace the propagator in KK modes by the propagator in S^1/Z_2 in terms of winding modes, such that:

$$\int dp^2 \tilde{G}_{KK}(p, m_0) = \int dp^2 \int_0^{\pi R} dy \sum_{n=0}^{+\infty} [\tilde{G}_{Winding}(p, 2n\pi R, m_0) \pm \tilde{G}_{Winding}(p, 2y + 2n\pi R, m_0)] , \quad (27)$$

where $\tilde{G}_{Winding}(p, |y - y'|, m_0)$ is the winding mode propagator and can be written as:

$$\tilde{G}_{Winding}(p, |y - y'|, m_0) = \frac{e^{i\chi|y-y'|}}{2\chi} , \quad (28)$$

with $\chi = \sqrt{p^2 - m_0^2}$.

We can now do a different type of regularisation here by just taking out the winding mode $n = 0$, which removes the whole divergent part of the effective potential. From this, we can replace the propagators by their simplified integrals:

$$\int dp^2 \int_0^{\pi R} dy \sum_{n=0}^{+\infty} [\tilde{G}_{Winding}(p, 2n\pi R, m_0) \pm \tilde{G}_{Winding}(p, 2y + 2n\pi R, m_0)] = \int dp^2 \sum_{n=0}^{+\infty} \left[\frac{\pi R e^{i\chi 2\pi R n}}{2\chi} \pm \frac{e^{i\chi 2\pi R(n+1)} - e^{i\chi 2\pi n R}}{4i\chi^2} \right] . \quad (29)$$

We now perform a Wick rotation ($i\chi \to -\chi_E$) to perform a Euclidian integral. We also have that $dp^2 = d\chi^2 = 2\chi d\chi = -2\chi_E d\chi_E$, which means that

$$\int dp^2 \sum_{n=1}^{+\infty} \left[\frac{\pi R e^{i\chi 2\pi R n}}{2\chi} \pm \frac{e^{i\chi 2\pi R(n+1)} - e^{i\chi 2\pi n R}}{4i\chi^2} \right] = \int d\chi_E \sum_{n=1}^{+\infty} e^{-\chi_E 2\pi R n} \left[\pi R \mp \frac{e^{-\chi_E 2\pi R} - 1}{2\chi_E} \right]$$
$$= -\sum_{n=1}^{+\infty} \left(\frac{e^{-\chi_E 2\pi R n}}{2n} \pm \pi R (E_i(-2\pi R(n+1)\chi_E) \mp E_i(-2\pi R n \chi_E)) \right) , \quad (30)$$

where $\chi_E = \sqrt{p_E^2 + m_0^2}$ and $E_i(x)$ is the exponential integral function defined as

$$E_i(x) = -\int_{-x}^{+\infty} \frac{e^{-t}}{t} .$$

From this, we finally have that:

$$-3\frac{i}{2}\int \frac{dp^4}{(2\pi)^4} \frac{1}{2\pi R}\left\{\sum_{n=-\infty}^{+\infty}\ln\left[-p^2+\left(\frac{n-m_0}{R}\right)^2\right]\right\} = \\ -\frac{3}{4} \int dp_E \frac{p_E^3\Omega(4)}{(2\pi R)^4}\sum_{n=1}^{+\infty}\left(\frac{e^{-\chi_E 2\pi R n}}{2\pi R n} \pm (E_i(-2\pi R(n+1)\chi_E) \mp E_i(-2\pi R n\chi_E))\right) , \tag{31}$$

where $\Omega(4)$ is the volume of the 4-dimensional sphere, which is equal to $\pi^2/2$. We define the function $f(m,n)$ such that:

$$f(m_0,n) = -\frac{3}{128}\int dp_E \frac{p_E^3}{\pi^2 R^4}\left(\frac{e^{-\chi_E 2\pi R n}}{2\pi R n} \pm (E_i(-2\pi R(n+1)\chi_E) \mp E_i(-2\pi R n\chi_E))\right) . \tag{32}$$

Now we can rewrite the effective potential with winding modes decomposition, using the f function which is defined for all m_0 and $n > 0$ as:

$$V_{eff}(\alpha) = \sum_{n=1}^{\infty}\left[f(0,n) + f\left(\frac{\alpha}{R},n\right) + 2f\left(\frac{\alpha}{2R},n\right) - \frac{2}{3}N_f\left(f(0,n) + 2f\left(\frac{\alpha}{2R},n\right)\right)\right] . \tag{33}$$

The advantage of this expression is that, in each mode n, the running coupling constant can be taken at the energy scale of the mode, so that we can easily take into account the running developed in reference [2] for this $SU(3)$ model of gauge-Higgs unification. Moreover, each term in n can be calculated numerically and the series converges much faster than for the KK mode approach. For example, the evaluation for $n = 1$ and $n = 2$ shows that there is a factor of 100 between them, due to the exponential dependence on n in each term. This can be compared to the KK sum, which only converges as $1/n^5$. As such, it is possible to effectively study the global evolution of the effective potential with α only with the first term $n = 1$, or with the first few terms.

In figure 1 we find that for $N_f = 1$ the effective potential is symmetric in α, and the only minimum for the first term of $V_{eff}(\alpha)$ is for $\alpha = 0$. This means that we don't have any spontaneous symmetry breaking in this model. We can argue that the shape of the potential is different from the one using KK modes in reference [7], however, this is due to the different approximations used for the KK modes, such as the regularisation method, which means

$$\int \frac{d^4 p_E}{(2\pi)^4}\sum_{n=1}^{\infty}\log\left(p_E^2 + \frac{(n-\alpha)^2}{R^2}\right) \to \sum_{n=1}^{\infty}\frac{1}{n^5}\cos(2\pi n\alpha) . \tag{34}$$

Note that the periodicity of the effective potential comes from this approximation.

4. Conclusion

In this paper we have described a new method for computing the effective Higgs potential in a gauge-Higgs unification model. This method allows us to take into account the running of the coupling constants inside each term of the effective potential. In our toy model with $SU(3)$ the running doesn't have a great deal of impact, because the coupling constants decrease when n goes up, which means that the running makes the sum converge even faster, and so the shape of the effective potential with $n = 1$ does not change much compared to the full effective potential. As such, it seems that this simple model gives a potential that does not provide spontaneous symmetry breaking. On the other hand, this method does permit a simple

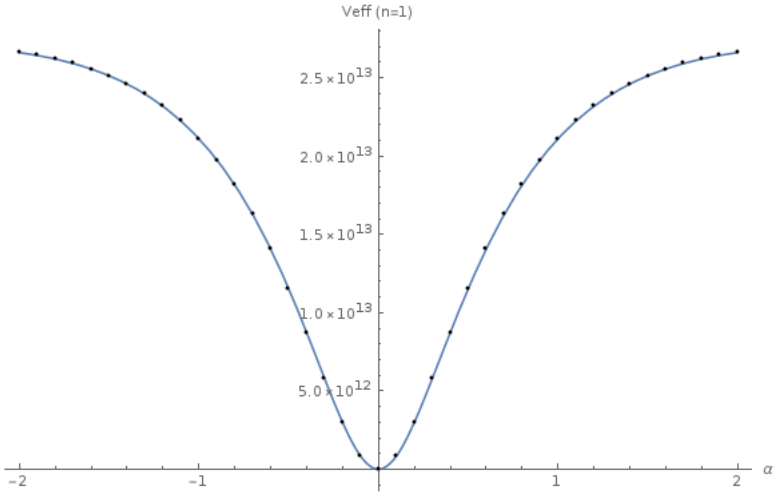

Figure 1. First term ($n = 1$) of the effective potential with $N_f = 1$ for different values of α.

elimination of divergences by removing the $n = 0$ mode, and the convergence of the sum is faster than with KK modes. Moreover, we didn't use any approximation on the VEV compared to the compactification scale to do the calculation, which means that our effective potential remains accurate for higher values of α, that is, it will remain a valid effective description.

To extend beyond this work we have begun using this method with an $SU(5)$ model, along with attempts with other methods: such as diagrammatic computation of the effective potential with winding modes, functional computation with KK modes, differential computation of the effective potential. Note that each of these other methods have major drawbacks making it difficult to include the running of coupling constants. A discussion of these methods shall be the focus of a future work [8].

Acknowledgements
ASC is supported in part by the National Research Foundation of South Africa. This work is partially supported by a PROTEA Campus France project.

References

[1] Hosotani Y 1983 *Phys. Lett.* **126B** 309-313
[2] Abdalgabar A, Khojali M O, Cornell A S, Cacciapaglia G and Deandrea A 2018 *Phys. Lett.* **B776** 231-235
[3] Haba N, Harada M, Hosotani Y and Kawamura Y 2003 *Nucl. Phys.* **B657** 169-213
[4] Haba N, Hosotani Y, Kawamura Y and Yamashita T 2004 *Phys. Rev.* **D70** 015010
[5] Puchwein M and Kunszt Z 2004 *Annals Phys.* **311** 288-313
[6] Da Rold L 2004 *Phys. Rev.* **D69** 105015
[7] Kubo M, Lim C S and Yamashita H 2002 *Mod. Phys. Lett.* **A17** 2249-2264
[8] Abdalgabar A, Cacciapaglia G, Cornell A S, Cot C, Deandrea A and Khojali M O *in preparation*

The ubiquitous pseudo-scalar in composite Higgs models

A S Cornell[a,1], A Deandrea[b,2], B Fuks[c,3,4] and L Mason[d,1,2]

[1] Department of Physics, University of Johannesburg, PO Box 524, Auckland Park 2006, South Africa,
[2] Université de Lyon, F-69622 Lyon, France: Université Lyon 1, Villeurbanne CNRS/IN2P3, UMR5822, Institut de Physique Nucléaire de Lyon,
[3] Laboratoire de Physique Theorique et Hautes Energies (LPTHE), UMR 7589, Sorbonne Université et CNRS, 4 place Jussieu, 75252 Paris Cedex 05, France,
[4]Institut Universitaire de France, 103 boulevard Saint-Michel, 75005 Paris, France.

E-mail: [a]acornell@uj.ac.za, [b]deandrea@ipnl.in2p3.fr, [c]fuks@lpthe.jussieu.fr, [d]220031336@student.uj.ac.za

Abstract. We focus on composite models with a fermion-gauge underlying description, in which the Higgs boson is identified as a Goldstone mode of a larger broken symmetry group. Such an extension of the scalar sector offers solutions to several conceptual issues with the Standard Model, and phenomenological model building of non-minimal theories will provide an important input for further studies. A generic prediction of these models is the presence of additional resonances, which arise as pseudo-Nambu-Goldstone bosons of a broken global symmetry. In the following, the light singlet pseudo-scalar ubiquitous to all such composite Higgs theories is modelled, paving the way for non-minimal composite Higgs studies.

1. Introduction

In 2012 the ATLAS and CMS experiments at CERN announced the discovery of the Higgs boson [1, 2], measured to have a mass of 125 GeV. However, while this discovery has completed the spectrum predicted by the Standard Model (SM), it has brought into focus several issues with the theory, whose Higgs sector is now faced with a variety of problems. Spontaneous symmetry breaking (SSB), widely accepted as the method of mass generation for the electroweak gauge bosons, is modelled rather than explained as a consequence of the theory. A second question is presented by the hierarchy problem, which describes the way in which the Higgs boson, which sits at the electroweak scale unshielded from higher energies [3], receives quadratically large loop corrections to its mass.

A composite Higgs (CH) model replaces the SM Higgs sector with fundamental gauge dynamics by postulating the existence of a new strong sector. In the following, we will describe a class of CH models which are based on a gauge theory featuring fermionic matter. The models are defined in terms of a confining gauge interaction called hypercolour, where the fundamental fermions are irreducible representations of this hypercolour group [4]. CH models will undergo chiral symmetry breaking of a global group of the fundamental fermions G to a subgroup H, whose pattern will depend on the underlying gauge dynamics [3], as the breaking is achieved through the bilinear condensate of the underlying fermions [5]. The symmetry breaking produces

pseudo-Nambu-Goldstone Bosons (pNGBs), including the Higgs doublet. These models, which notably do not include fundamental scalars, are considered for the reason that they may provide a UV-complete theory [6].

The confining dynamics governing the Higgs sector in a CH model solve the hierarchy problem [4], as the tension due to naturalness is removed by allowing these quadratically diverging contributions to the Higgs boson mass only up to some compositeness scale. The Higgs is modelled as a bound state of a new strongly interacting force with a TeV confinement scale, and continues to receive contributions to its mass by low energy virtual quanta as would an elementary scalar. However, the shorter wavelengths of higher energy quanta are able to resolve the finite size of the CH boson. As the energy of the mass contributions surpasses the compositeness scale, the CH boson is transparent to the quanta [7], screening the quadratic growth and resulting in a steep fall in the contributions with energy. The ability of the theory to naturally generate the Higgs boson mass allows us in turn to explain the scale of electroweak symmetry breaking (EWSB).

In CH models of this nature there always exists an anomaly-free $U(1)$ global symmetry, acting on all species of fermions [4]. Condensates of the underlying fermions result in SSB of $U(1)$ symmetries, which are also explicitly broken by the fermion masses and the gauging of the SM symmetries [10]. The CH models that we will consider postulate the existence of additional resonances, which are bound states of the underlying fermions [8]. While the details of these additional resonances depend on the model structure, the Higgs boson and a pNGB a are always present [10, 11]. The pNGB a, a pseudo-scalar and a singlet under the gauge symmetries of the SM, is the subject of this work. We will consider the case where a is light. The postulated existence of such additional resonances may be used in direct physics searches at the Large Hadron Collider (LHC) and at future colliders, and may be considered as a first indication for the mechanism of partial compositeness. In the following, a new model has been produced in order to simulate the production and dynamics of the light a, which paves the way for further non-minimal CH studies.

2. A Composite Higgs Model

The SM Higgs potential can be written as [9]

$$V(h) = -\mu^2|H|^2 + \lambda|H|^4, \tag{1}$$

where $\langle H\rangle = v/\sqrt{2}$ is the vacuum expectation value (vev), with $v = 246$ GeV [9], and where the vev is obtained by minimising the scalar potential. As SSB may only arise if the vacuum of the field in question is non-vanishing under the symmetry, the vev of the Higgs field is crucial for the pattern of EWSB.

When the global symmetry group is broken by the underlying gauge dynamics, a number of pNGB are produced. For a model to be considered a CH model, we must have a Higgs doublet generated in the coset. We must therefore have that $SU(2) \times U(1)$ is embeddable within H. In a CH scenario we observe two separate phase transitions; first, at the higher compositeness scale, the free fundamental fermions condense into composite states. This is the scale at which the global symmetry group G, which governs the fundamental fermions, is broken to some subgroup H. The usual transition then occurs at the electroweak scale, where the Higgs boson develops a vev [12]. The pattern of chiral symmetry breaking in a given CH model is governed by the dimension of the underlying gauge group (the number of fermionic matter fields), and the subgroup to which the symmetry breaks [3].

In completing a CH model, it is necessary to provide mass to the fermions, as well as to break the electroweak symmetry [3]. One method of providing mass to SM particles is that of partial compositeness, which is constructed by the inclusion of a second species of fermion χ in a separate irreducible representation of the hypercolour group. In a CH model with a

fermion-gauge completion which includes the mechanism of partial compositeness, we must then include at least two species of underlying fermions, ψ and χ, belonging to different irreducible representations of the confining group G [13].

2.1. Symmetry breaking

The CH model requires a global symmetry breaking to occur, through which the vector bosons are given mass and a Higgs boson is generated. Goldstone's theorem states that there shall arise at least one massless scalar boson whenever there is a spontaneously broken global symmetry, written $G \to H$. These (massless) bosons, called Goldstone bosons (GBs) or Nambu-Goldstone bosons (NGBs), span the coset G/H [14]. However, when the initial symmetry was originally explicitly broken by some small amount, the spontaneous breaking of this symmetry will give rise to a pNGB, which will have a non-zero mass.

In a given CH model, when G is dynamically broken to some subgroup H, there will be $n = \dim(G) - \dim(H)$ NGB produced in the G/H coset [7]. Several of the NGB are "eaten" in order to provide longitudinal degrees of freedom to the electroweak gauge bosons, as in conventional EWSB.

For a theory with a given species of N_f Dirac fermions, we may only have two possible unbroken global flavour symmetries; $SU(2N_f)$ for a (pseudo-)real fermion representation, or $SU(2N_f) \times SU(2N_f)$ for a complex fermion representation [3]. For a given representation, the chiral symmetry breaking may then follow

$$SU(2N_f) \to SO(2N_f) \tag{2}$$

in the case of a real representation, and

$$SU(2N_f) \to Sp(2N_f) \tag{3}$$

for pseudo-real [3]. We are therefore able to discard the generally recognised minimal CH model [16] which follows the coset structure $SO(5)/SO(4)$, as the global symmetry cannot be constructed using an underlying fundamental fermionic matter theory [3].

The most minimal cosets which may give rise to a CH scenario are then [3]

$$SO(6) \sim SU(4) \to Sp(4) \sim SO(5), \tag{4}$$

obtained with an underlying $SU(2)$ gauge theory, where the coset contains 5 pNGBs; the Higgs doublet and an additional CP-odd singlet, which is the pNGB a.

$$SU(5) \to SO(5), \tag{5}$$

which produces 14 GBs, and

$$SU(6) \to SO(6), \tag{6}$$

which features two Higgs doublets. The pNGB a arises in each case.

2.2. Particle content

In a CH model we expect a low energy spectrum which includes, as the name indicates, a Higgs boson which is expected to be composite. This is accompanied by exotic composite scalars, some of which are ubiquitous to all CH models. All models contain at least two species of underlying fermions, χ and ψ, belonging to different irreducible representations of the confining hypercolour group [13]. During the breaking of the global symmetry we may have the electroweak coset ($\psi\psi$ condensate), the QCD coset ($\chi\chi$ condensate) and two $U(1)$ singlets, a and η' [4]. These singlets, associated with the Abelian symmetries $U(1)_{\chi,\psi}$, occur if both species of fermion condense [10].

The two mass eigenstates, a and η', are then subject to some mixing, and their masses receive contributions from the masses of the underlying fermions, ψ and χ, and the anomalous $U(1)$ combination [4].

The light pNGB on which we focus, a, is associated to the global $U(1)$ symmetry, and occurs when at least one fermion species condenses. It results from the breaking of a non-anomalous $U(1)$ charge by the chiral condensate in the Higgs sector, and will therefore carry electroweak quantum numbers [4]. The pNGB η' expected in addition to the a is a coloured octet, associated to the anomalous $U(1)$ charge, which may arise as a result of the underlying fermions χ which are responsible for the mechanism of partial compositeness [13]. The mechanism of partial compositeness may therefore be indicated by the presence of pNGBs.

The light a can be produced at the LHC via gluon-gluon fusion. By specifying the underlying theory we can predict the couplings to other states [4]. We are interested in the case where only the non-anomalous pseudo-scalar is light, but the anomalous $U(1)$ scalar may also be light in other theories.

3. Model construction

In this first implementation, the composite pseudo-scalar a is added to the SM. This new resonance is self-conjugate, and expected to have a mass of less than 100 GeV. In order to describe it, the SM Lagrangian is augmented with the following effective Lagrangian [10]

$$\begin{aligned}\mathcal{L} =& \frac{1}{2}\left(\partial_\mu a\right)\left(\partial^\mu a\right) - \frac{1}{2}m_a^2 a^2 - \Sigma_f \frac{iC_f m_f}{f_a} a\bar{\Psi}_f\gamma^5\Psi_f \\ &+ \frac{g_s^2 K_g}{16\pi^2 f_a} aG^a_{\mu\nu}\tilde{G}^{a\mu\nu} + \frac{g^2 K_W}{16\pi^2 f_a} aW^i_{\mu\nu}\tilde{W}^{i\mu\nu} + \frac{g'^2 K_B}{16\pi^2 f_a} aB_{\mu\nu}\tilde{B}^{\mu\nu},\end{aligned} \tag{7}$$

where C_f, K_g, K_W and K_B are model-specific parameters determining the coupling to gauge bosons, and f_a and f_ψ are the decay constants of the pseudo-scalar and Higgs boson respectively. The models are numbered M1 - M12, and are based upon the underlying fermionic representation, featuring a variety of hypercolour and flavour cosets. The parameters of the models are described in Ref. [10]. They are based upon a class of theories with two distinct cosets associated respectively to the electroweak quantum numbers and colour [10].

The fermion coupling term can be examined via an expansion in its component spinors

$$\begin{aligned}\bar{\Psi}_f\gamma^5\Psi_f &= (\bar{\Psi}_L + \bar{\Psi}_R)\gamma^5(\Psi_L + \Psi_R) \\ &= \bar{\Psi}_L\Psi_R - \bar{\Psi}_L\Psi_L + \bar{\Psi}_R\Psi_R - \bar{\Psi}_R\Psi_L \\ &= \bar{\Psi}_L\Psi_R - \bar{\Psi}_R\Psi_L\end{aligned} \tag{8}$$

where the terms composed of two $SU(2)$ singlets disappear. The two remaining terms, composed of a doublet and a singlet under $SU(2)$, are not gauge invariant. In order to construct the model it is then necessary to couple to them the Φ field as in a SM Yukawa Lagrangian, after which we obtain additional interactions of the type $Ha\bar{\Psi}_f\Psi_f$.

Additionally, couplings to the Higgs boson and Z bosons are included at loop level, and are written as [10]

$$\mathcal{L}_{haa} = \frac{3C_t^2 m_t^2 \kappa_t}{8\pi^2 f_a^2 v}\log\frac{\Lambda^2}{m_t^2} h\left(\partial_\mu a\right)\left(\partial^\mu a\right), \tag{9}$$

$$\mathcal{L}_{hZa} = \frac{3C_t m_t^2 g_A}{2\pi^2 f_a v}\left(\kappa_t - \kappa_V\right)\log\frac{\Lambda^2}{m_t^2} h\left(\partial_\mu a\right) Z^\mu. \tag{10}$$

The pseudo-scalar Lagrangian therefore depends on the free parameters m_a, f_a and f_ψ.

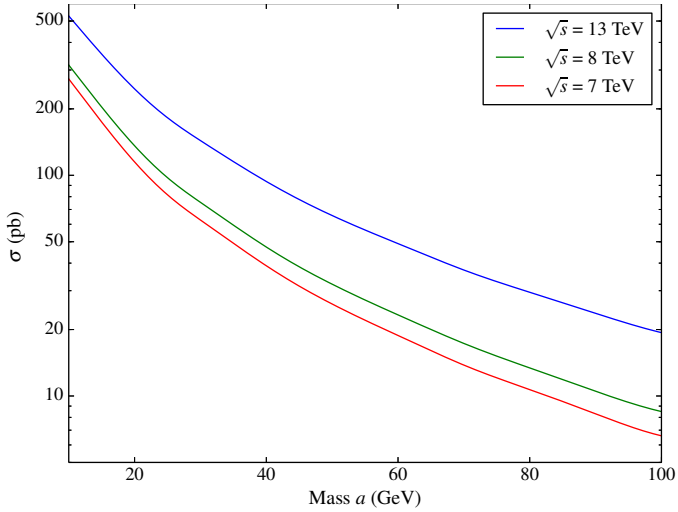

Figure 1. The gluon gluon fusion cross section for a range of LHC energies over the mass range of the light pNGB a.

3.1. FeynRules implementation

In this work we have constructed a new FeynRules [17] implementation of an additional pseudo-scalar a. The model includes small a couplings to SM leptons, quarks, and gauge bosons, where the gauge boson couplings are anomalous couplings which include contributions by top loops. The implementation of the model includes a scan over the mass of the pseudo-scalar, which is free, where the results have been verified by comparison to those of Ref. [10], with good initial agreement.

This light pNGB is expected to be produced copiously via gluon-gluon fusion, where the cross section is plotted in figure 1 for a sample of LHC energies. In this figure the coupling of the pseudo-scalar to gluons has been considered as an effective vertex, but in reality we may expect significant contributions from top and bottom quark loops, particularly for higher masses of a. Branching ratios to quarks and leptons have been calculated, a sample of which are plotted in figure 2.

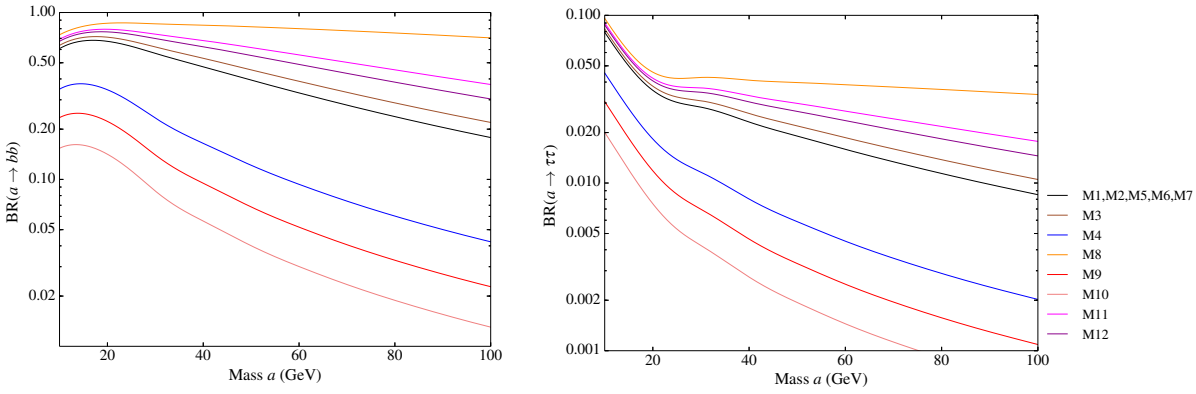

Figure 2. Branching ratios of a to b quarks (left) and τ leptons (right) for each model.

The model, which has been implemented here, offers the possibility of extensions to larger

symmetry groups and non-minimal CH models, as well as forming the basis of phenomenology on which LHC investigations may be based. As a next step, the effective couplings may be replaced by the complete leading order vertices by the inclusion of top and bottom loops, which may afford a better understanding of the couplings of the pseudo-scalar to gauge bosons.

Acknowledgements
ASC and LM are supported in part by the National Research Foundation of South Africa.

References

[1] Aad, G *et al.*, "Observation of a new particle in the search for the Standard Model Higgs boson with the ATLAS detector at the LHC," *Phys. Lett.*, vol. B716, pp. 1–29, 2012.
[2] Chatrchyan, S *et al.*, "Observation of a new boson at a mass of 125 GeV with the CMS experiment at the LHC," *Phys. Lett.*, vol. B716, pp. 30–61, 2012.
[3] Cacciapaglia, G and Sannino, F, "Fundamental Composite (Goldstone) Higgs Dynamics," *JHEP*, vol. 04, p. 111, 2014.
[4] Cacciapaglia, G, Ferretti, G, Flacke, T, and Serodio, H, "Light scalars in composite Higgs models," *Front.in Phys.*, vol. 7, p. 22, 2019.
[5] Cacciapaglia, G, Cai, H, Deandrea, A and Kushwaha, A, "Fundamental Composite Higgs model in SU(6)/SO(6)," 2019.
[6] Barnard, J, Gherghetta, T, and Ray, T S, "UV descriptions of composite Higgs models without elementary scalars," *JHEP*, vol. 02, p. 002, 2014.
[7] Panico, G and Wulzer, A "The Composite Nambu-Goldstone Higgs," *Lect. Notes Phys.*, vol. 913, pp. pp.1–316, 2016.
[8] Arbey, A, Cacciapaglia, G, Cai, H, Deandrea, A, Le Corre, S, and Sannino, F, "Fundamental Composite Electroweak Dynamics: Status at the LHC," *Phys. Rev.*, vol. D95, no. 1, p. 015028, 2017.
[9] Bellazzini, B, Csáki, C and J. Serra, "Composite Higgses," *Eur. Phys. J.*, vol. C74, no. 5, p. 2766, 2014.
[10] Cacciapaglia, G, Ferretti, G, Flacke, T, and Serodio, H, "Revealing timid pseudo-scalars with taus at the LHC," *Eur. Phys. J.*, vol. C78, no. 9, p. 724, 2018.
[11] Buarque Franzosi, D, Cacciapaglia, G, and Deandrea, A, "Sigma-assisted natural composite Higgs," 2018.
[12] Dugan,M J, Georgi, H, and Kaplan, D B, "Anatomy of a Composite Higgs Model," *Nucl. Phys.*, vol. B254, pp. 299–326, 1985.
[13] Belyaev, A, Cacciapaglia, G, Cai, H, Ferretti, G, Flacke, T, Parolini, A and Serodio, H "Di-boson signatures as Standard Candles for Partial Compositeness," *JHEP*, vol. 01, p. 094, 2017. [Erratum: JHEP12,088(2017)].
[14] Csáki, C, Lombardo, S and Telem, O, "TASI Lectures on Non-supersymmetric BSM Models," in *Proceedings, Theoretical Advanced Study Institute in Elementary Particle Physics : Anticipating the Next Discoveries in Particle Physics (TASI 2016): Boulder, CO, USA, June 6-July 1, 2016*, pp. 501–570, WSP, WSP, 2018.
[15] Contino, R, "The Higgs as a Composite Nambu-Goldstone Boson," in *Physics of the large and the small, TASI 09, proceedings of the Theoretical Advanced Study Institute in Elementary Particle Physics, Boulder, Colorado, USA, 1-26 June 2009*, pp. 235–306, 2011.
[16] Agashe, K, Contino, R and Pomarol, A "The Minimal composite Higgs model," *Nucl. Phys.*, vol. B719, pp. 165–187, 2005.
[17] Alloul, A, Christensen, N D, Degrande, C, Duhr, C and Fuks, B, "FeynRules 2.0 - A complete toolbox for tree-level phenomenology," *Comput. Phys. Commun.*, vol. 185, pp. 2250–2300, 2014.

Third order dissipative fluid dynamics and the Bjorken scaling solution

M Younus[1], A Muronga[2]

[1]Department of Physics, Nelson Mandela University, Port Elizabeth, 6031, South Africa
[2]Faculty of Science, Nelson Mandela University, Port Elizabeth, 6031, South Africa

E-mail: younus.presi@gmail.com

Abstract. Third order hydrodynamics equations have been developed using thermodynamics approach. Present calculations are based on entropy principle and the differential equations have been developed in Eckart frame and Bjorken (1+1)D scenario. Energy density, and pressure isotropization etc. as function of proper time have been calculated for massless relativistic fluids. The present calculations have been compared to earlier calculations by A. El et al. and A. Jaiswal et al. An initial QGP formation time of $\tau_0 = 0.4$ fm/c and temperature of $T_0 = 500$ MeV have been used for calculations.

1. Introduction

Heavy ions colliding at relativistic speed form quark gluon plasma (QGP) and give us a scenario similar to early Universe scenario [1]. QGP which is a relativistic fluid with observables such as particle production, elliptic flow are being studied experimentally at RHIC-BNL and LHC-CERN [2–4]. Theoretical transport models on the other hand help us to study the time evolution of particle distributions from the point of collision to freeze-out times when all interaction and production of particles stop. Transport theories include particle interaction and resulting processes such as dissipations, collisions and radiations and are successful in simulating heavy ion collisions and in explaining numerous experimental findings. Earliest works on relativistic fluid dynamics with the first order theories are due to Eckart et al [9]. and to Landau and Lifshitz [10]and Fourier-Navier-Stokes equations were consequently developed. The solutions to first order equations have led to non-causal effects and would propagate viscous and thermal signals with speed greater than that of light. To meet the causality conditions, second order theories were developed by Muller and Israel and Stewart. This is also known as second order dissipative theories or Muller-Israel-Stewart theories (M-IS) [11–13] and [8]. Recent works to include higher order corrections have been done by A. Muronga [14–17], A. El et. al. [18, 19], G. S. Denicol et al. [20], A. Jaiswal et al. [21, 22] etc. using either thermodynamics approach or kinetic Boltzmann equation (BE) to solve the dissipative equations. The results from these various approaches are complimentary to each other [23]. In the current work we have extended the work done by A. Muronga et al. to third order equations for the dissipative fluids [24]. The calculations are shown briefly in section 2. We have compared our calculations and results with earlier calculations by A. El et al. and A. Jaiswal et al. [25–27] who also extended their calculations from second order to third order. The results and discussions are reported in section. 3 of the current manuscript, followed by conclusions.

2. Formalism

The basic formulation of relativistic hydrodynamics can be found in the references mentioned in introduction. Following the prescription by A. Muronga in Ref. [24], we have considered a simple fluid with massless particles and no external electromagnetic fields. The equations for the conservation of net charge $N^\mu(x)$ (particle $4-$current), and energy-momentum $T^{\mu\nu}(x)$ (energy $-$ momentum tensor) are then written as

$$\partial_\mu N^\mu = 0, \text{ and } \partial_\mu T^{\mu\nu} = 0. \tag{1}$$

Also, the second law of thermodynamics dictates for entropy 4-current, S^μ is given by,

$$\partial_\mu S^\mu \geq 0 \tag{2}$$

The genralized form of net charge 4-current might be written in the form,

$$N^\mu = nu^\mu + v^\mu \tag{3}$$

where $n = \sqrt{N^\mu N_\mu}$ is the net charge density in fluid rest frame and we have considered Eckart's frame where particle flux v^μ=0. Then we can calculate $u^\mu = \dfrac{N^\mu}{\sqrt{N^\mu N_\mu}}$ as the fluid 4-velocity. In Bjorken (1+1)D expansion it can be shown that $u^\mu u_\mu = 1$. The energy momentum tensor can be shown to be,

$$T^{\mu\nu} = \varepsilon u^\mu u^\nu - (P + \Pi)\Delta^{\mu\nu} + 2q^{\langle\mu} u^{\nu\rangle} + \pi^{\langle\mu\nu\rangle}\,, \tag{4}$$

where $\varepsilon = u_\mu u_\nu T^{\mu\nu}$ is the energy density, P is the pressure in fluid rest frame, Π is the bulk viscous pressure, q^μ is the heat 4-current and $\pi^{\langle\mu\nu\rangle}$ is shear stress tensor.

In present calculations for relativistic fluid dynamics, we consider a system of gluons and massless quarks that departs slightly from the local thermal distribution. The distribution for particles in that system can then be written as

$$f(x,p) = f^{eq}(x,p)[1 + \Delta^{eq}\phi(x,p)]\,, \tag{5}$$

where

$$f^{eq}(x,p) = A_0 \frac{1}{e^{\beta_\nu p^\nu - \alpha} - a}\,, \tag{6}$$

and $\Delta^{eq} = 1 + aA_0^{-1} f^{eq}(x,p)$ and $\phi(x,p)$ is the deviation/departure function to be discussed shortly. The factor $A_0 = g/(2\pi)^3$, where g is the degeneracy factor.

The entropy 4-current can be divided into an equilibrium part and an non-equilibrium part as follows,

$$S^\mu(x) = S^\mu_{eq}(x) + \delta S^\mu(x) \tag{7}$$

To calculate the non-equilibrium part δS^μ, we use Grad's 14-field theory with $S^\mu(x)$ defined as,

$$S^\mu(x) = -\int dw\, p^\mu \psi(f), \tag{8}$$

where

$$\psi(f) = f(x,p)\ln[A_0^{-1} f(x,p)] - a^{-1} A_0\, \Delta(x,p) \ln \Delta(x,p) \tag{9}$$

The function $\psi(f)$ has been expanded around equilibrium distribution function $f^{eq}(x,p)$. $\psi(f^{eq})$ in the expansion gives the equilibrium part of the entropy while the rest of the expansion

is used to derive its' non-equilibrium part. A small linear departure function $\phi(x,p)$ is used in $f(x,p)$, with quadratic dependence on 4-momentum as (for detail calculation see Ref. [28]),

$$\phi(x,p) \approx \epsilon(x) - \epsilon_\mu(x)p^\mu + \epsilon_{\mu\nu}(x)p^\mu p^\nu \tag{10}$$

The moments ϵ, ϵ_μ and $\epsilon_{\mu\nu}$ are assumed small.

After integration, the entropy 4-current can be written up to third order or cubic in dissipative fluxes as,

$$\begin{aligned} S^\mu &= S_1^0 u^\mu + S_1^1 \Pi u^\mu + S_2^1 q^\mu + \left(S_1^2\Pi^2 - S_2^2 q^\alpha q_\alpha - S_3^2 \pi^{2\langle\alpha\alpha\rangle}\right) u^\mu + S_4^2 \Pi q^\mu \\ &+ S_5^2 \pi^{\langle\mu\alpha\rangle} q_\alpha + \left(S_1^3\Pi^3 - S_2^3 \Pi q_\alpha q^\alpha + S_3^3 \Pi \pi^{2\langle\alpha\alpha\rangle} + S_4^3 q_\alpha q_\beta \pi^{\langle\alpha\beta\rangle} + S_5^3 \pi^{3\langle\alpha\alpha\rangle}\right) u^\mu \\ &+ \left(S_6^3\Pi^2 - S_7^3 q_\alpha q^\alpha + S_8^3 \pi^{2\langle\alpha\alpha\rangle}\right) q^\mu + S_9^3 \Pi \pi^{\langle\mu\alpha\rangle} q_\alpha + S_{10}^3 \pi^{2\langle\mu\alpha\rangle} q_\alpha \end{aligned} \tag{11}$$

where the coefficients S_n^m are calculated as functions functions of (ε and n) and will be shown elsewhere. The coeffcients will be shown elsewhere. The superscript in the coefficients denotes the order and the subscript labels the coefficient number in that order. For thermodynamic processes, the entropy principle suggests, $\partial_\mu S^\mu \geq 0$. The dissipative fluxes can be obtained either from the equations of the balance of the fluxes or from entropy principle.

The calculations are done in Bjorken (1+1)D scenario where $u^\mu = (\frac{t}{\tau}, 0, 0, \frac{z}{\tau})$ and a baryon chemical potential free, $\mu_c = 0$ has been considered. Eckart frame has been assumed and also in Bjorken scaling solution heat flow can be shown to be $q^\mu = 0$ [18]. In the case of massless particles, bulk viscosity can also be neglected while bulk pressure equation does not contribute.

Thus from the entropy principle, the transport equation for shear viscous pressure could be reduced to (see Ref. [28] for detailed calculation)

$$\begin{aligned} \pi &= \frac{4}{3}\frac{\eta}{\tau}, \ (1^{\text{st}} \text{ order}) \\ \dot{\pi} &= -\frac{\pi}{\tau_\pi} - \frac{1}{2}\frac{\pi}{\tau} + \frac{3}{10}\frac{\varepsilon}{\tau} - \frac{3}{2}\frac{\pi^2}{\varepsilon\tau} + \frac{5}{8}\frac{\pi}{\varepsilon}\dot{\varepsilon} + \frac{27}{8}\frac{\pi^2}{\varepsilon^2}\dot{\varepsilon} - \frac{6}{5}\frac{\pi}{\varepsilon}\dot{\pi}, \ (\text{upto } 3^{\text{rd}} \text{ order}) \end{aligned} \tag{12}$$

For the (1+1) dimensional Bjorken flow in (3+1) dimensions the energy equation is given by,

$$\dot{\varepsilon} = -\frac{4}{3}\frac{\varepsilon}{\tau} + \frac{\pi}{\tau}. \tag{13}$$

where $\tau_\pi = 2\eta S_3^2$ is relaxation time for the shear pressure. The coefficient, S_3^2 is taken to be $\sim 9/4\varepsilon$ in the ultra-relativistic limits. We have used equation of state (EoS) due to assumed ultra-relativistic scenario to be, $\varepsilon = 3P$. Next we move to results and discussion section.

3. Results and Discussion

In Fig. 1 we have shown pressure isotropy ratio, P_L/P_T and compared the results from present model by A. Muronga with earlier third order models by A. El et al. and A. Jaiswal et al which is based on kinetic theory approach to Boltzmann transport equation in relaxation time approximation. The shear equations in the current model have been derived from full entropy 4-current expression without neglecting any shear terms (*viz.* non-linear terms neglected in Israel-Stewart theory have been included). Two different values of $\eta/s = 0.1$ and 0.5 have been taken to illustrate the differences between these three models. For $\eta/s = 0.1$, the present

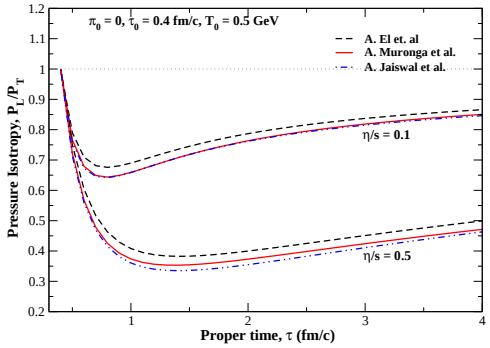

Figure 1: Comparison of models on pressure isotropy ratio for two different values of η/s.

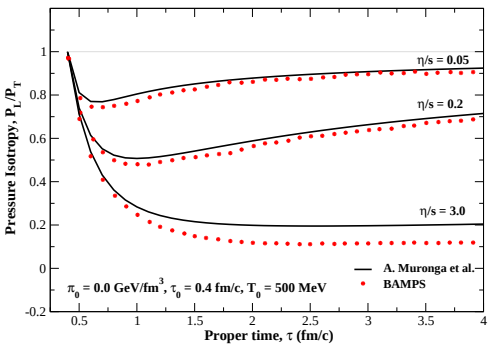

Figure 2: η/s dependence of pressure isotropy ratio from current model/work

calculation is closer to results from A. El et al. While for modestly high value of $\eta/s = 0.5$, the results from present calculation appear to be closer to A. Jaiswal's model. However it should be noted that the values of the coefficients in shear equations are different in all three models. The solutions to the equations depends on the values of the coeffcients although the differences are not considerable. The differences might arise from various initial approximations and assumptions. They tend to bring in uncertainties in the final solutions and outputs. It can also be noted that the models of A. Muronga et al and A. El differ in the number of terms considered for the shear differential equation. Various values of η/s parameter could be taken to illustrate the differences in the models.

In Fig. 2, we have shown the ratio η/s calculated from present model (A. Muronga) for three different values of viscosity to entropy ratio of 0.05, 0.2 and 3.0. The current work has been compared to BAMPS transport calculation. We have also chosen initial shear pressure, $\pi_0 = 0$. This particular initial condition for shear gives ideal scenario for the system initially with P_L/P_T being unity at starting point. Thereafter system develops shear pressure immediately and goes out of equilibrium. However the particles within the system interact and bring down the shear effects with time and the system tends to return to equilibrium once again. We find that for lower values of the parameter the isotropy ratio tends to return to unity which suggests that the system may return to equilibration if given enough time. While for a large value of $\eta/s = 3.0$, thee ratio is almost flat after 2 fm/c and system may not return to equilibrium within the lifetime of QGP. The present third order model also underestimate the transport results due to BAMPS by a small magnitude but the shape of the curves are similar.

In Fig. 3, we have shown energy density of quark gluon plasma as a function of proper time. A modest value for viscosity to entropy ratio, $\eta/s = 6/4\pi$ has been used. We have also used two different initial values for $\pi_0 = 4\eta/3\tau_0$ and 0.0 GeV/fm^3. The ideal fluid equation gives energy density which fall as $\sim \frac{1}{\tau^{4/3}}$ [29]. The first order dissipative equation gives a rise in the energy density initially and then falls the slowest. The higher orders bring down the rise in energy density with third order being closest to ideal scenario. However the time evolution of energy density shows a strong dependence on values chosen for initial shear pressure, π_0.

4. Conclusion

Third order shear equations have been developed after extending earlier calculations by A. Muronga. The energy density as function of proper time shows effect of different ordered theo-

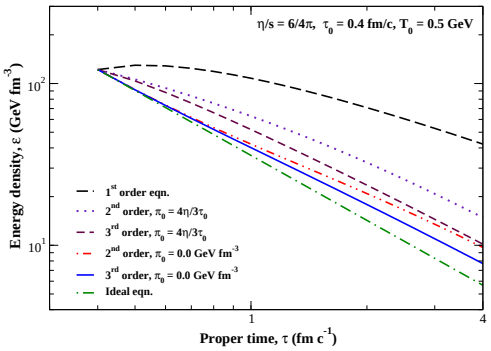

Figure 3: Comparison of orders on energy density

ries. Ideal equations brings down the evolving energy density quickest while first order theory is slowest. Both second and third order theories brings down the magnitude quit close to ideal scenario but choice of initial conditions have considerable effect on the observable. A systematic study of dependence of solutions on initial conditions will be conducted. It is also shown that dissipative fluxes tend to put the system out of local thermal equilibrium but system tends to go back to being ideal state. The value of η/s play a vital role in this. The present calculations have also been compared to other third order models and transport theory of BAMPS. The difference in the outputs with third order models are due to different values of coefficients in the equations and also due to different number of terms considered within the differential equations. This particular aspect is interesting and will be studied in detail.

Acknowledgments
One of the authors (MY) wishes to thank SAIP 2019 conference organizers, advisory committees, faculties and University of Venda (host institute) for allowing me to participate in the conference and write the proceeding.

References

[1] J. W. Harris and B. Muller, Ann. Rev. Nucl. Part. Sci. **46**, 71 (1996).
[2] S. S. Adler *et al.* [PHENIX Collaboration], Phys. Rev. Lett. **91**, 182301 (2003).
[3] Q. Li, C. Shen and M. Bleicher, Central Eur. J. Phys. **10**, 1131 (2012)
[4] B. B. Abelev *et al.* [ALICE Collaboration], JHEP **1506**, 190 (2015).
[5] H. Stoecker and W. Greiner, Phys. Rept. **137**, 277 (1986).
[6] S. A. Bass, M. Gyulassy, H. Stoecker and W. Greiner, J. Phys. G **25**, R1 (1999).
[7] M. Bleicher *et al.*, J. Phys. G **25**, 1859 (1999).
[8] J. I. Kapusta, Phys. Rept. **88**, 365 (1982).
[9] C. Eckart, Phys. Rev. **58**, 919 (1940).
[10] L. D. Landau and E. M. Lifshitz, Fluid Mechanics (Pergamon, New Yourk, 1959).
[11] I. Muller, Z. Phys. **198**, 329 (1967).
[12] W. Israel, Annals Phys. **100**, 310 (1976).
[13] J. M. Stewart and S. W. Hawking, Proc. R. Soc. Lond. A, 357 (1977); W. Israel and J. M. Stewart, Annals Phys. **118**, 341 (1979).
[14] A. Muronga, Phys. Rev. Lett. **88**, 062302 (2002) Erratum: [Phys. Rev. Lett. **89**, 159901 (2002)].
[15] A. Muronga, Phys. Rev. C **69**, 034903 (2004).
[16] A. Muronga, Phys. Rev. C **76**, 014909 (2007).
[17] A. Muronga, Phys. Rev. C **76**, 014910 (2007).
[18] A. El, A. Muronga, Z. Xu and C. Greiner, Phys. Rev. C **79**, 044914 (2009).
[19] A. El, A. Muronga, Z. Xu and C. Greiner, Nucl. Phys. A **848**, 428 (2010).
[20] G. S. Denicol, T. Koide and D. H. Rischke, Phys. Rev. Lett. **105**, 162501 (2010).
[21] A. Jaiswal, Phys. Rev. C **87**, no. 5, 051901 (2013).
[22] A. Jaiswal, B. Friman and K. Redlich, Phys. Lett. B **751**, 548 (2015).
[23] R. S. Bhalerao, A. Jaiswal, S. Pal and V. Sreekanth, Phys. Rev. C **89**, no. 5, 054903 (2014).
[24] A. Muronga, J. Phys. G **37**, 094008 (2010).
[25] A. El, Z. Xu and C. Greiner, Phys. Rev. C **81**, 041901 (2010).
[26] A. Jaiswal, Phys. Rev. C **88**, 021903 (2013).
[27] A. Jaiswal, Nucl. Phys. A **931**, 1205 (2014).
[28] M. Younus and A. Muronga, "Third order viscous hydrodynamics in Bjorken scenario," arXiv:1910.11735 [nucl-th] (2019).
[29] J. D. Bjorken, Phys. Rev. D **27**, 140 (1983).

Fluctuating open heavy flavour energy loss in a strongly coupled plasma with observables from rhic and the lhc

B A Ngwenya[1] and W A Horowitz[1]

[1]Department of Physics, University of Cape Town, Rondebosch 7700, South Africa

E-mail: blessedarthurngwenya@gmail.com, wa.horowitz@uct.ac.za

Abstract. Heavy ion collisions at RHIC and at the LHC produce an enormous amount of energy that enables the nuclei and its constituent particles to melt, thus releasing gluons, quarks and antiquarks, travelling in different directions with different momenta. Studies of these collisions have shown that low transverse momentum observables describe a strongly coupled plasma (quark-gluon plasma), an almost perfect liquid that evolves hydrodynamically and flows with almost no viscosity [1, 2]. We make predictions for the suppression of these heavy quarks and thus describe the energy loss of the heavy quarks as they interact with the plasma; we show that these predictions are in good agreement with experimental data.

1. Introduction

One of the big questions of Physics is 'what happened shortly after the big bang?' Theory predicts that the early universe was composed of a hot mixture of particles (mainly weakly bound quarks and gluons) moving at nearly the speed of light [3]. Powerful particle accelerators can be used to recreate conditions of the early universe through colliding heavy ions. RHIC collides beams of ^{197}Au nuclei, each with a total energy of approximately 17TeV [4] while the LHC collides ^{208}Pb nuclei with a centre of mass energy of approximately 1000TeV [5].

Through these heavy-ion collision experiments, we can quantitatively extract the properties of nuclear matter and through some theoretical predictions, we can understand the properties of this nuclear matter better with the ultimate goal being to construct the phase diagram of nuclear matter [3]. This is a complicated task given that emergent phenomenon is not well understood practically, for example, we cannot predict the behaviour of a single water molecule (in a bucket of water) by simply applying Newton's laws and Maxwell's equations to it.

In these heavy-ion collisions, the temperatures of the material produced is in the order of a trillion Kelvin [3, 6, 7] and the best way of understanding it theoretically is yet to be known. This material is a new phase of matter called the quark-gluon plasma (QGP) [3] and is produced due to the very high temperatures. It is a state of strongly interacting matter where quarks and gluons are no longer confined to the colour-neutral hadrons [8]. In the formation of QGP, there has to be a phase transition and this comes as a natural consequence of the composite nature of hadrons in quantum chromodynamics (QCD) [3]. This phase transition has been found to

be at a critical temperature $T_c \simeq 170MeV$, with an energy density $\epsilon_c \simeq 600MeV/fm^3$ [3, 9]. Hadronization starts to occur almost immediately after the collision, so the QGP has a very short lifetime (on the order of 4fm/c) at RHIC and on the order of 10fm/c at the LHC [3]. QGP can be understood better by looking at its coupling strength.

The interactions in Quantum Chromodynamics (QCD) are strong at low energy and decrease at high energy (asymptotic freedom) [10]. As a result, the strong interactions between quarks, antiquarks and gluons persist in the QGP and the dominant degrees of freedom in the QGP are thus light quarks, antiquarks and gluons [3]. Due to asymptotic freedom, the interaction strength weakens when large energies are exchanged in inter-particle collisions and interactions with a large momentum transfer can be treated in a perturbative way [11]. This asymptotic freedom regime is achieved when the temperature, $T \gg \Lambda_{QCD}$ (where $\Lambda_{QCD} \cong 200MeV$ is the QCD scale parameter) and the QGP is a weakly-interacting gas of slightly modifeid quarks and gluons that yields a plasma relatively transparent to hard probes[11] and calculations are performed using perturbative quantum chromodynamics (pQCD) [12, 13].

We're interested in the high transverse momentum particles because they are decay products of high transverse momentum partons and these are the most direct probe of the relevant degrees of freedom in a quark-gluon plasma [12, 14]. In the low momentum observables, QGP appears as a strongly coupled plasma that evolves hydrodynamically [15] and has almost no viscosity, making it the most perfect liquid observed. In this strong coupling regime, non-perturbative approaches such as AdS/CFT [16] need to be used to perform calculations and in this paper, we look at the energy loss of heavy flavour strongly-coupled to the medium.

Heavy flavour is more interesting because it puts more experimental constraints on the energy loss model and as a result, on the potential properties of the quark-gluon plasma [12]. It is important to compare our theoretical predictions to a wide range of experimental data, for example, by looking at the suppression of heavy flavour at different energies (i.e RHIC and the LHC) through the nuclear modification factor [13]. Some early results of the energy loss in the higher order strong coupling regime (AdS/CFT calculations) have shown favourable results of the measured nuclear modification factor $R_{AA}(p_T)$ of electrons from heavy flavour decay at RHIC [12, 17] but generally over-suppressed $R_{AA}(p_T)$ for D mesons at the LHC by a factor of approximately 5 [12, 18].

In this paper, we compute the nuclear modification factor ($R_{AA}(p_T)$) for bottom quarks at 5.5TeV and thus quantitatively describe the suppression of these heavy quarks at high transverse momentum.

2. Particle Geometry with the Optical Glauber Model

The Glauber model [19] is used to model the geometry of nuclei before a heavy-ion event. The Optical limit approximation of the Glauber model assumes that at high energies, the nucleons carry a sufficiently large momentum that they will be undeflected as nuclei pass through each other. As a result, for calculations, the nucleus is assumed to comprise of a smooth/continuous nucleon density (ρ). Assuming a spherical nuclei, the nucleon charge density (inside the nucleus) is given by the Woods-Saxon distribution [19]

$$\rho(r) = \frac{\rho_0}{1 + e^{\left(\frac{r-R}{a}\right)}} \quad (1)$$

where ρ_0 is the nucleon density in the centre of the nucleus, $r = \sqrt{x^2 + y^2 + z^2}$, R is the nuclear radius and a is the "skin depth". For ^{208}Pb these parameters are; $R = 6.624 \pm 0.035fm$ and $a = 0.549 \pm 0.008fm$ respectively [20].

Perturbative QCD calculations are only valid for transverse momentum, $p_T \geq 1GeV/c$ [21] and thus can't be used to determine the inelastic nucleon-nucleon cross section (σ_{inel}^{NN}) since the cross section involves processes with low momentum transfer (diffractive and elastic processes). As a result, the model takes in the experimental measured cross section data and this provides the only nontrivial beam-energy dependence for Glauber calculations. Table 1 gives the inelastic nucleon-nucleon cross section at collision energies appropriate for RHIC and the LHC.

Table 1: Values of the nucleon-nucleon inelastic cross section (σ_{inel}^{NN}) for collision-energies ($\sqrt{s}$) appropriate for RHIC and the LHC [20]

$\sqrt{s}(TeV)$	σ_{inel}^{NN} (mb)	σ_{inel}^{NN} (fm^2)
0.2	41.6 ±0.6	4.16
0.9	52.2 ±1.0	5.22
2.76	61.8 ±0.9	6.18
5.02	67.6 ±0.6	6.76
5.44	68.4 ±0.5	6.84
5.5	68.5 ±0.5	6.85

We consider two heavy-ions (target A and projectile B) colliding at relativistic speeds with impact parameter b. We focus on two flux tubes located at a displacement $(x - b/2, 0, 0)$ with respect to the center of the target nucleus and a displacement $(x + b/2, 0, 0)$ from the center of the projectile. During the collision these tubes overlap. The probability per unit transverse area of a given nucleon being located in the target/projectile flux tube is given by equation 2, while the joint probability per unit area of finding nucleons located in the respective overlapping target and projectile flux tubes is given by what is defined as the **thickness function** (equation 3).

$$T_{A/B}(x, y) = \int_{-\infty}^{\infty} \rho(x, y, z_{A/B}) dz_{A/B} \quad (2)$$

$$T_{AB}(b) = \int T_A\left(x - \frac{b}{2}, y\right) T_B\left(x + \frac{b}{2}, y\right) dxdy \quad (3)$$

where $\rho(x, y, z_{A/B})$ is the probability per unit volume (normalised to unity), of finding a nucleon at a point $(x, y, z_{A/B})$ in the nucleus of projectile (A) or target (B).
We compute the total number of binary nucleon-nucleon collisions at impact parameter b (equation 4), the number of participants, which is the number of nucleons in the target and projectile nuclei that interacted at least once in a collision (equation 5) as well as the total geometric cross section (equation 7).

$$N_{coll}(b) = ABT_{AB}(b)\sigma_{inel}^{NN} \quad (4)$$

$$N_{part} = A \int T_A^-(1 - [1 + T_B^+]^B) dxdy + B \int T_B^+(1 - [1 + T_A^-]^A) dxdy \quad (5)$$

$$T_X^{\pm} = T_X\left(x \pm \frac{b}{2}, y\right) \quad (6)$$

$$\frac{d\sigma}{db} = 2\pi b(1 - [1 - T_{AB}(b)\sigma_{inel}^{NN}]^{AB}) \quad (7)$$

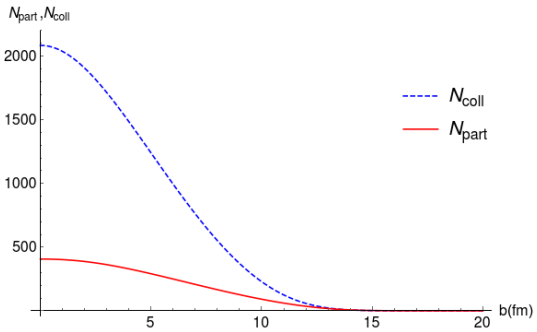

(a) N_{coll} and N_{part} as a function of impact parameter

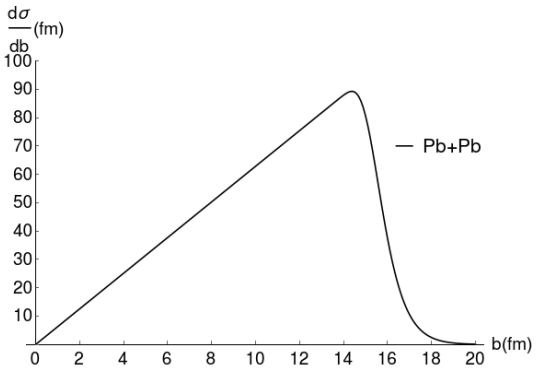

(b) Total geometrical cross section as a function of impact parameter

Figure 1: Some geometric quantities in the optical limit of the Glauber model for Pb-Pb at 5.5TeV

3. Langevin Energy Loss

In the strong coupling regime, the dynamics of heavy quarks interacting with QGP is described by a stochastic differential equation known as the Langevin equation. In the fluid's rest frame, this equation is given by [22, 23]:

$$\frac{dp_i}{dt} = -\mu p_i + F_i^L + F_i^T \quad (8)$$

$$\mu = \frac{\pi\sqrt{\lambda}T^2}{2M_Q} \quad (9)$$

where p^i is the three-momentum of an on-shell heavy quark moving at constant velocity in a thermal bath, μ is the drag loss coefficient of a heavy quark, M_Q is the mass of the heavy quark in a plasma of temperature T and λ is the Hooft coupling constant. F_i^L and F_i^T are longitudinal and transverse momentum kicks with respect to the quark's direction of propagation. The energy loss model is described in detail in [23, 24] and is the first of its kind to include thermal fluctuations. The fluctuating momentum kicks are correlated as [24]

$$< F_i^L(t_1)F_j^L(t_1) > = \kappa_L \hat{p}_i\hat{p}_j g(t_2 - t_1) \quad (10)$$

$$< F_i^T(t_1)F_j^T(t_1) > = \kappa_T(\delta_{ij} - \hat{p}_i\hat{p}_j)g(t_2 - t_1) \quad (11)$$

where $\hat{p}_i = p_i/|\vec{p}|$ and g is a function only known numerically,

$$\kappa_T = \pi\sqrt{\lambda}T^3\gamma^{1/2} \quad (12)$$

$$\kappa_L = \gamma^2\kappa_T \quad (13)$$

The longitudinal direction of the heavy quark is the most important one for calculations of suppression observables and the detailed energy loss model is given by [24]. As mentioned earlier, our energy loss model requires the heavy quark to be moving at a constant velocity, as a result, we need to provide the quark with power to compensate for the momentum lost. Due to the restrictions around that power provided to the heavy quark, we end up with a speed limit on the heavy quark set-up given by,

$$\gamma < \gamma^{sl}_{crit} = \left(1 + \frac{2M_Q}{\sqrt{\lambda}T}\right) \sim \frac{4M_Q^2}{\lambda T^2} \tag{14}$$

4. Results

The main result of this paper is shown in Figure 3: which shows predictions for the nuclear modification factor ($R_{AA}(p_T)$) for bottom quarks at the LHC. We see a clear suppression of open heavy flavour at high transverse momentum for the various centrality classes studied, given with statistical uncertainties from the transverse momentum bins. It is also clear that the suppression is more pronounced for central collisions.

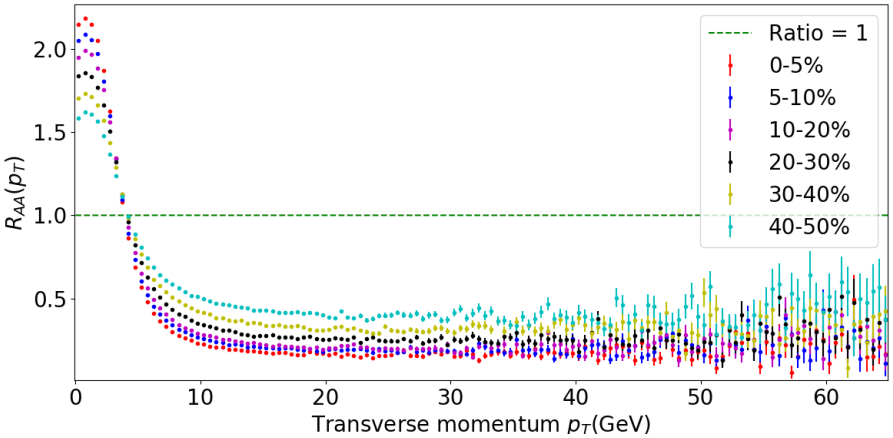

Figure 2: Nuclear modification factor ($R_{AA}(p_T)$) for bottom quark suppression at 5.5TeV

5. Conclusion and Outlook

Heavy flavour energy loss is crucial in understanding the properties of nuclear matter and thus trying to put together the phase diagram of nuclear matter. The Langevin energy loss model used in this paper is the first in the formulation of AdS/CFT correspondence to include thermal fluctuations and has been shown to be a success in computing several quantities from heavy ion collisions [15, 24, 25]. The results presented in this paper have shown that heavy flavour is largely suppressed for high transverse momentum.

The next steps of this work will be to look at the hadronization process decribed in [26] and compute predictions for the suppression of B mesons that these heavy quarks decay to, then compare the results to experimental data. Using this energy loss model, we will also look at the suppression of charm quarks and thus the suppression of D mesons. We will then be able to make predictions for higher energies of the upcoming runs of the LHC and potentially the FCC.

Acknowledgments
The authors would like to acknowledge Valumax Projects (Pty) Ltd, SA-CERN, the South African National Research Foundation and the University of Cape Town for their generous financial contributions towards this work.

References

[1] Riordan M and Zajc W A 2006 *Scientific American* **294** 34A–41
[2] Johnson C V and Steinberg P 2010 *Phys. Today* **63** 29–33
[3] Hands S 2001 *Contemporary Physics* **42** 209–225
[4] Schaefer T 2003 *Physics world* **16** 31
[5] Jowett J and Carli C 2006 *Proceedings of the 2006 European Particle Accelerator Conference, Edinburgh, Scotland* pp 550–552
[6] Shen C, Heinz U, Huovinen P and Song H 2011 *Physical Review C* **84** 044903
[7] Gale C, Jeon S, Schenke B, Tribedy P and Venugopalan R 2013 *Physical Review Letters* **110** 012302
[8] Satz H 2011 *arXiv preprint arXiv:1101.3937*
[9] Pumplin J 2002 *J. High Energy Phys.* **2002** 012
[10] Ho-Kim Q and Pham X Y 1998 *Elementary Particles and Their Interactions* (Springer) pp 505–548
[11] Mrowczynski S 1999 *arXiv preprint nucl-th/9905005*
[12] Horowitz W 2013 *Nuclear Physics A* **904** 186c–193c
[13] Majumder A and Van Leeuwen M 2011 *Progress in Particle and Nuclear Physics* **66** 41–92
[14] Casalderrey-Solana J 2014 *Gauge/string duality, hot QCD and heavy ion collisions* (Cambridge University Press)
[15] Horowitz W 2015 *Physical Review D* **91** 085019
[16] Hubeny V E 2015 *Classical and Quantum Gravity* **32** 124010
[17] Bass S A, Gale C, Majumder A, Nonaka C, Qin G Y, Renk T and Ruppert J 2009 *Physical Review C* **79** 024901
[18] Altarelli G and Parisi G 1977 *Nuclear Physics B* **126** 298–318
[19] Miller M L, Reygers K, Sanders S J and Steinberg P 2007 *Annu. Rev. Nucl. Part. Sci.* **57** 205–243
[20] Loizides C, Kamin J and d'Enterria D 2018 *Physical Review C* **97** 054910
[21] Adams J, Aggarwal M, Ahammed Z, Amonett J, Anderson B, Anderson M, Arkhipkin D, Averichev G, Badyal S, Bai Y *et al.* 2006 *Physics Letters B* **637** 161–169
[22] Moore G D and Teaney D 2005 *Physical Review C* **71** 064904
[23] Gubser S S 2008 *Nuclear physics B* **790** 175–199
[24] Hambrock R and Horowitz W A 2018 *EPJ Web of Conferences* vol 171 (EDP Sciences) p 18002
[25] Hambrock R and Horowitz W 2017 *Nuclear and particle physics proceedings* **289** 233–236
[26] Cacciari M, Nason P and Oleari C 2006 *Journal of High Energy Physics* **2006** 006

Impact-response study of lattice waves and phonons in metallic FCC nanoclusters using the Sutton-Chen potential

R.O. Ocaya[1], **J.J. Terblans**[2]

[1] Univ. of the Free State (Qwaqwa), P.Bag X13, Phuthaditjhaba 9866, RSA.
[2] Univ. of the Free State (Bloemfontein), P.O. Box 339 Bloemfontein 9300, RSA.

E-mail: ocayaro@ufs.ac.za

Abstract. We suggest a novel approach to investigate phonon propagation in an FCC lattice through bond-length oscillations in response to a single atom velocity perturbation. The lattice is modelled using the Sutton-Chen embedded atom model (EAM) without any energy loss mechanisms. We begin by showing that the concept of the cut-off distance must be abandoned to meaningfully simulate the transient behavior of nanoclusters. Oscillations are shown to arise and propagate through the lattice as a result of the interatomic potential. The waves, which have fundamental frequency and velocity, are put into the context of Debye theory and are shown to aptly postulate bulk and surface phonons. Calculations of the C_{11}, C_{12} and C_{44} directional moduli of elasticity calculated along the <100> direction on a thin, nano-sized slab-shaped Cu lattice consisting of 2281 Cu atoms are in good agreement with the literature values at the attained simulated temperature. We also show how the cluster temperature is affected by the passage of the wave.

1. Introduction

Simulation is today central to computational materials science [1, 2, 3]. It is useful to ascertain material properties that are difficult to determine experimentally [4, 5]. The simulated particle system scales range from nano to micro and beyond. Metallic nano-clusters are gaining prominence in many applications, notably in the area of fast, new electronic devices. These devices communicate using metallic interconnects on scales where quantum physics laws dominate. It is necessary to establish whether clusters can still be modelled using the traditional pairwise potentials that routinely applied to the macro-material [6, 7, 8, 9, 10, 11, 12].

In this article, we show, through simulation, that elastic oscillations arise in mechanically perturbed lattices. We then develop a phonon-method by extending these oscillations. We restrict the article to the [100] direction for illustration. Using a previously developed Sutton-Chen (SC) potential toolkit for face-centered cubic (FCC) metals [13], we simulate a system of 2281 copper particles and follow its transient and frequency responses. We then correlate the atomic displacements and velocities with the spectral densities in the material within the elastic-phonon dispersion model of Debye theory. Comparison of the results with the literature w.r.t the calculated elastic moduli and thermal properties show good agreement, indicating feasibility of the approach [14, 15].

1.1. Impulse-oscillation approach

Real lattice atoms vibrate about their equilibrium positions, with a character that depends on lattice defects [16]. An understanding of the energy states $E(\omega)$ and spectral density $g(E(\omega))$ is possible through lattice resonant frequency, ω. In this work, we suggest a *low-strain elastic* phonon method that can be simulated directly using standard MD [16]. The calculation of bulk and surface wave dispersion relies on inter-atomic elasticity, which is implicit in the pairwise potential. Figure (1) shows the simplest, homogeneous particle system. It is possible to model more advanced systems by using position and mass perturbations. Here, we consider only the unbounded, homogeneous mono-atomic, "hard-ball" atom system. Figure (2) shows the proposed harmonic mass-spring oscillator model. The initial, low-amplitude impulse is applied under the following assumptions.

(i) Energy and momentum are conserved,

(ii) The impacting atom remains uncoupled after impact,

(iii) The ensuing waves can be transverse or longitudinal.

Like other pairwise potentials, the SC potential has three regions, i.e. attractive, equilibrium, and repulsive. For Cu, it shows strong repulsion at 2.0 Å. In Figure (1), the wave $e^{i\bar{k}\cdot\bar{r}}$ of wave

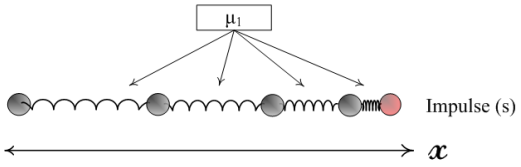

Figure 1. Mass-spring analogy of FCC structure along the x axis.

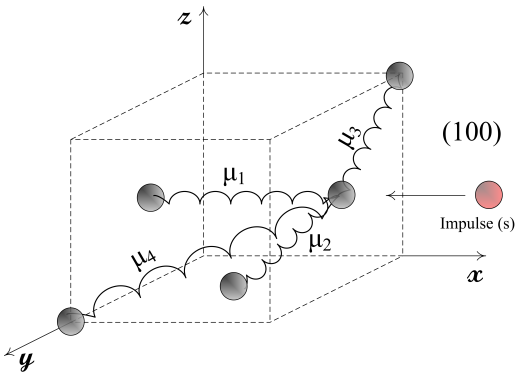

Figure 2. Homogeneous mass-spring analogy of FCC structure.

vector $\bar{k}$ at position $\bar{r}$ is clearly complex for even the simplest lattices due to the superposition from other directions. However, the simulation of such a model can describe the elastic and thermal properties of the lattice reasonably well [17, 18]. The dispersion relation for a 1-D lattice of atomic force constant μ and wave vector k is:

$$\omega^2 = (4\mu/m)\sin^2(ka/2), \tag{1}$$

where a is a lattice parameter. In the first Brillouin zone, the waves are bounded at $k{=}\pm\pi/a$ [16]. Here, we have discarded the idea of "cut-off" distance (r_{cut}), since the forces extend well beyond the boundaries of our small clusters.

2. The simulation model

The SC potential can be written as [19, 3]:

$$E_{tot} = \frac{1}{2}\sum_{ij}^{N} V(r_{ij}) + \sum_{i}^{N} F(\bar{\rho}_i), \tag{2}$$

 ISBN: 978-0-620-88875-2

where $V{=}V(r_{ij})$ is the pairwise interaction potential given by:

$$V = \varepsilon \sum_{i=1}^{N} \left(\sum_{j=i+1}^{N} \left(\frac{\sigma}{r_{ij}}\right)^{n} - c\sqrt{S_i} \right), \tag{3}$$

where

$$S_i = \sum_{j=1, j\neq i}^{N} \left(\frac{\sigma}{r_{ij}}\right)^{m}. \tag{4}$$

The term $F{=}F(\bar{\rho}_i)$ denotes the energy required to embed an atom into the array, and $\bar{r}_{ij}$ is the displacement vector between particles i and j. The force on particle i of mass m is readily shown to be

$$\overline{F}_i = -\overline{\nabla} V(r) = \varepsilon \sum_{j=1,\ j\neq i}^{N} \left[n\left(\frac{\sigma}{r_{ij}}\right)^{n} - \frac{cm}{2}\left(\frac{1}{\sqrt{S_i}} + \frac{1}{\sqrt{S_j}}\right)\left(\frac{\sigma}{r_{ij}}\right)^{m} \right] \frac{\bar{r}_{ij}}{r_{ij}^2}. \tag{5}$$

The constant ε is a dimensionless energy scaling parameter for the system, σ is the equilibrium lattice constant of the structure and c is a fitting parameter. Table 1 shows the potential and simulation parameters.

Table 1. SC and simulation parameters.

Parameter	
ε	0.012382 eV
m, n, c	6, 9, 39.432
δt	91.75 fs
t_{start}, t_{end}	0, 250 ps
T	0 K (bulk)

2.1. Simulation parameters and conditions

The thermal modelling of the system was done using energy-partitioned, independent harmonic oscillators near 0K, to limit thermal noise [20, 21]. The average atom speed v_j and temperature T are related by

$$v_j = \left(\frac{k_B T}{m}\right)^{1/2} = \left(\frac{2E_{kin}}{N_f m}\right)^{1/2}, \tag{6}$$

where E_{kin} is the total kinetic energy of all the atoms, and N_f are the available degrees of freedom. We model only irrotational translation motion, hence $N_f{=}N$. Temperatures higher than 0K but lower than melting point [20, 16] were simulated with time-step velocity equilibration [22, 23, 24, 25]. For a monoatomic lattice a density of state function, $g(\omega)$, describes available degrees of freedom up to ω_D. Its typical Debye frequencies are in the acoustic region ($\sim 10^{13}$/s) while a heterogeneous lattice has an additional branch at optical frequencies, i.e. there is now an energy band gap. We assumed an infinite lattice placed in vacuum and having no energy loss mechanism.

3. Results and Discussions

The Visual Molecular Dynamics (VMD) program [26] was used for output visualization.

3.1. Bond-length oscillations

Figures (3)-(6) show the perturbed, transient bond-length variations in the Cu lattice and their resolved discrete Fast Fourier Transforms (FFT). The equilibrium distances are 2.553 Å and 3.610 Å respectively. A comparison of the Figures (4) and (6) shows that the main peak

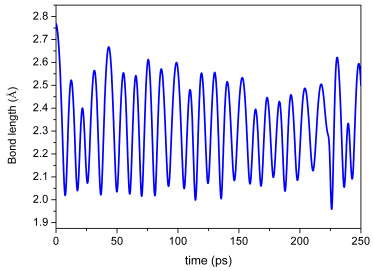

Figure 3. Amplitude transient response.

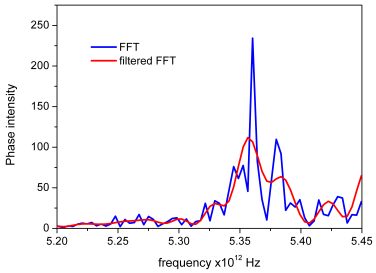

Figure 4. Phase-frequency response.

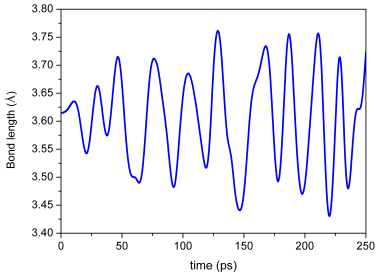

Figure 5. Amplitude transient response along [100] deep in the lattice.

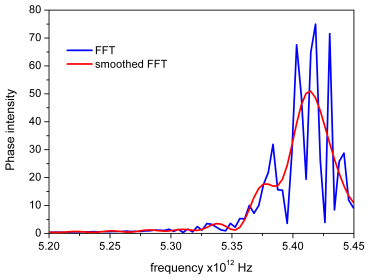

Figure 6. Phase-frequency response [100] deep in the lattice.

frequencies differ by almost 5.38 THz for two major crystal directions. The plots correspond to $\omega \approx 3.4 \times 10^{13}$/s, or phonon energy $\hbar\omega \approx 22.3$ meV, which is within the range reported empirically [27, 28]. The expected maximum vibrational frequency is $2(\mu/m)^{1/2}$ and occurs at the boundary of the first Brillouin zone [16]. We find, for Cu ($m = 63.5$ amu), that $\mu \approx 30.8$ N/m using $\omega_m \approx 3.4 \times 10^{13}$/s. The literature value is 35.32 N/m at 296K [16, 28] .

3.2. Wave propagation and the elastic constants

The moduli of elasticity $C_{\alpha\beta}$ for a cubic crystal in the Hooke's law approximation are related to the directional strain components (e_{ij}). Accepting the solution of the wave equation:

$$u(x,t) = u_0\, e^{i(kx-\omega t)}, \tag{7}$$

in terms of amplitude u_0 and wave vector $k = 2\pi/\lambda$, for the [100] direction we get

$$\omega^2\rho = C_{11}k^2 \quad \text{and} \quad \omega^2\rho = C_{44}k^2, \tag{8}$$

for a longitudinal and transverse waves, respectively.

 ISBN: 978-0-620-88875-2

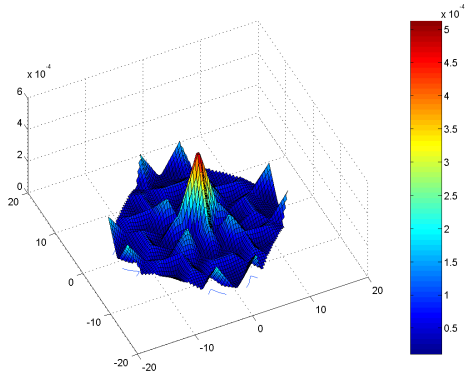

Figure 7. 3D-surface atom neighborhood.

3.2.1. Estimation of C_{11} and C_{44} Applying $\omega(k)=\omega_m$ at $k=\pi/a$ in Equation (8) gives $C_{11} = (\omega_m a/\pi)^2 \rho = (2\omega_m/\pi)^2 M/a$, with $a=b\sqrt{2}$. Using Figure (4), we get $C_{11} = 139.2 \pm 1.4$ GPa at 5.44 THz. Experimental values of 176.2 to 168.4 GPa at 0K and 300K respectively have been reported [16, 28]. The simulated diagonal bond-length (b) is 2.5487Å. The simulated bulk density of 9058 kg/m^3, as determined from $(M\sqrt{2}/b^3)$, differs from the known by less than 2%.

3.2.2. Expected temperature rise The above perturbation of the static lattice by an adatom induces propagating bulk and surface phonons [29, 30]. One therefore expects that the temperature of the overall system will increase. Figure (7), which is a 3-D thermogram of the opposite [100] face taken at the end of the simulation, shows that temperature does indeed rise.

4. Conclusions

In this article, we have suggested a standard MD method based on the Sutton-Chen embedded atom potential to simulate phonon propagation in a metallic FCC lattice. Our test bed consisted of 2281 Cu atoms. We correlated the temporal and spatial displacements with the spectral distribution. The calculated values of resonance frequencies, the elastic and other bulk constants of the lattice are in excellent agreement with empirical, literature values. Future work using the method could ascertain the effects of higher impacting energies, defects, atomic non-homogeneity and energy loss mechanisms. The method could prove valuable in the study of heat conduction of nano-clusters, with interesting implications for nano-device applications.

References

[1] Abraham MJ, Murtola T, Schulz R, Pall S, Smith JC, Hess B, Lindahl E, Gromacs: High performance molecular simulations through multi-level parallelism from laptops to supercomputers, SoftwareX 101 (2015) 88–95.
URL `http://dx.doi.org/10.1016/j.softx.2015.06.001`

[2] Ocaya R, Terblans JJ, Addressing the challenges of standalone multi-core simulations in molecular dynamics, in P. Ramasami (ed.), Computational Sciences, De Gruyter (2017) 1–21.
URL `https://doi.org/10.1515/9783110467215-001`

[3] Koleske DD, Sibener SJ, Phonons on fcc (100), (110), and (111) surfaces using Lennard-Jones potentials, Surface Science 268 (1992) 407–417.

[4] Chen ET, Barnett RN, Landman U, Crystal-melt and melt-vapor interfaces of nickel, Phys. Rev. B 40 (2) (1989) 924–932.
URL `https://doi.org/10.1103/PhysRevB.40.924`

[5] Chen ET, Barnett RN, Landman U, Surface melting of Ni(110), Phys. Rev. B 41 (1) (1990) 439–450.
URL https://doi.org/10.1103/PhysRevB.41.439
[6] Car R, Parrinello M, Unified approach for molecular dynamics and density functional theory, Phys. Rev. Lett. 55 (22) (1985) 2471–2474.
[7] Car R, Parrinello M, The unified approach for molecular dynamics and density functional theory, in simple molecular systems at very high density, in NATO ASI Series, Series B, Physics, P.P. Loubeyre and N. Boccara (Eds.) 186 (1989) 455–476.
[8] Remler DK, Madden PA, Molecular dynamics without effective potentials via the Car-Parrinello approach, Mol. Phys. 70 (6) (1990) 921–66.
[9] Tuckerman ME, Ab initio molecular dynamics: basic concepts, current trends and novel applications, J. Phys.: Condens. Matter.
URL stacks.iop.org/JPhysCM/14/R1297
[10] Rassoulinejad-Mousavi SM, Mao Y, Zhang Y, Physical contributions to the heat capacity of nickel, Journal of Applied Physics 119 (244304) (2016) 861–871.
URL https://doi.org/10.1063/1.4953676
[11] Chistyakova N, Tran TMH, A study of the applicability of different types of interatomic potentials to compute elastic properties of metals with molecular dynamics methods, AIP Conference Proceedings 1772 (060019) (2016) 1–7.
URL https://doi.org/10.1063/1.4964599
[12] Rushton MJD, Chroneos A, A critical assessment of interatomic potentials for ceria with application to its elastic properties revisited, Journal of Materials Science: Materials in Electronics 24 (11) (2013) 4590–4592.
URL https://link.springer.com/article/10.1007%2Fs10854-013-1447-0
[13] Ocaya R, Terblans JJ, Temperature specification in atomistic molecular dynamics and its impact on simulation efficacy, J. Phys.: Conf. Ser 905 (012031).
URL https://dx.doi.org/10.1088/1742-6596/905/1/012031
[14] Allen RE, Alldredge GP, de Wette FW, Studies of vibrational surface modes. I. General formulation, Phys. Rev. B 4 (6) (1971) 1648.
[15] Allen RE, Alldredge GP, de Wette FW, Studies of vibrational surface modes. II. Monatomic fcc crystals, Phys. Rev. B 4 (6) (1971) 1661.
[16] Kittel C, Introduction to Solid State Physics, John Wiley & Sons, New Jersey, 2005.
[17] Mohapatra M, Tolpadi S, Effects of lattice dispersion and elastic anisotropy on the thermal properties of fcc metals, Pramana 35 (2) (1990) 159–165.
[18] Meschter PJ, Wright JW, Brooks CR, Kollie TG, Physical contributions to the heat capacity of nickel, Journal of Physics and Chemistry of Solids 42 (9) (1981) 861–871.
[19] Sutton AP, Chen J, Long-range Finnis-Sinclair potentials, Philosophical Magazine 63 (1) (1990) 139–156.
[20] Schommers W, in Schommers W, von Blankenhagen P (Eds.) Structure and Dynamics of Surfaces, Springer, Berlin, 1986.
[21] Pathak LP, Rai RC, Hemkar MP, Lattice vibrations and Debye temperatures of transition metals, Journal of the Physical Society of Japan 44 (6) (1978) 1834–1838.
[22] Knuth D, The art of computer programming, seminumerical algorithms, Addison-Wesley, 1997.
[23] Box G, Muller M, A note on the operation of random normal deviates, Ann. Math Stat. 29 (1958) 610–611.
[24] Marsaglia G, The role of surface and interface structure in crystal growth, Proc. Nat. Acad. Sci. 61 (1968) 25–28.
[25] Ocaya R, Terblans JJ, Coding considerations for standalone molecular dynamics simulations of atomistic structures, J. Phys.: Conf. Ser 905 (012018).
URL https://dx.doi.org/10.1088/1742-6596/905/1/012018
[26] Theoretical and Computational Biophysics Group, Visual Molecular Dynamics, accessed: 2017-11-02.
URL http://www.ks.uiuc.edu/Research/vmd/allversions/what_is_vmd.html
[27] Ditlevsen Peter D, Nømskov Jens K, Vibrational properties of aluminum, nickel and copper surfaces, Surface Science 254 (1991) 261–274.
URL http://dx.doi.org/10.1.1.718.7356
[28] Behari J, Tripathi BB, Frequency spectra and heat capacities of copper, nickel and aluminium, Aust. J. Phys. 23 (1969) 311–318.
URL http://adsabs.harvard.edu/full/1970AuJPh..23..311B
[29] Chopra KK, Bouarab S, Off-symmetry phonon frequencies of copper, Physica status solidi (b) 125 (2) (1984) 449–504.
[30] Jani AR, Gohel VB, On the phonon frequencies of copper in off symmetry directions, Solid State Communications 41 (5) (1982) 407–411.

Modified hummers synthesis and structural characterisation of graphene oxide

MW Makgoba[1], TE Mosuang[1] and G Ndlovu[2]

[1]Department of Physics, University of Limpopo, Private Bag x1106, Sovenga, 0727, Limpopo Province, South Africa.
[2]Advanced Materials Division/MINTEK, Private Bag X3015, Randburg 2125, Gauteng Province, South Africa.
makgoba.walter@gmail.com, amos.akande@ul.ac.za

Abstract. Graphene oxide (GO) was synthesised using modified hummers method. X-Ray Diffraction (XRD), Scanning Electron Microscopy (SEM), Transmission Electron Microscopy (TEM), Fourier Transform Infrared Spectroscopy (FTIR), Raman Spectroscopy (RM) and Atomic Force Microscopy (AFM) was utilised to acquire the structural properties of GO. Each spectroscopic technique reveals unique features about the surface morphology of graphene oxide. XRD confirmed the crystalline nanosheets stacking of a carbon honeycomb. SEM and TEM revealed wrinkles and folding of planar honeycomb layers. FTIR and RM indicated the presence of carbonyl, alkoxy, epoxy, and hydroxyl functional groups. AFM further confirmed the surface roughness and the thickness of GO layer.

1. Introduction

Graphene oxide (GO) is a new interesting material which is derived from graphene and the oxygen functional group(s) [1]. GO is known to possess some interesting properties such as high surface area, high mechanical stiffness, high Young's modulus and exceptional thermal conductivity [2-3]. Due to these properties GO has attracted enormous great research interest. Nowadays, the synthesis and modification of GO has been one of the major focus and interesting part of graphene related research. The structure of graphene oxide can be defined as a layer of graphene with a number of oxygen functional group(s), such as hydroxyl (OH), epoxy (C-O), carbonyl (C=O) and alkoxy (C–O–C) distributed on the graphene surface [4]. GO is a promising material for future technologies due to the oxygen functional group as well as their minute size and shape [5]. This material has been identified as a potential candidate for advanced semiconducting applications such as water treatment as well as gas sensing [1].

The presence of the oxygen containing functional groups in GO influence this material's hydrophilic behaviour and its polar nature, as a results of which GO can be easily dispersed in several solvents such as water [6], in the process gaining advantage in terms of other peculiar properties over its precursor graphene. These functional groups highlight the opportunities for surface modification in GO which is very much suitable for nanocomposite materials.

This paper is focused on the synthesis and structural characterisation of graphene oxide. Accordingly, the synthesis of graphene oxide is more favourable over other graphene materials due to its low cost, easy access and its ability to be easily converted to graphene [7]. Graphite which is defined as a packed layers of graphene is the main source of graphene oxide [8]. GO has been synthesised using modified hummers method and was further characterised using various spectroscopic instruments including X-

Ray Diffraction (XRD), Scanning Electron Microscopy (SEM), Transmission Electron Microscopy (TEM), Fourier Transform Infrared Spectroscopy (FTIR), Raman Spectroscopy (RM), and Atomic Force Microscopy (AFM).

2. Materials and Methods

2.1 Reagents used for the synthesis of graphene oxide

The materials used in this study were purchased from Sigma Aldrich. The materials are: graphite (99% purity), sodium nitrate (99% $NaNO_3$), potassium permanganate (99% $KMnO_4$) and sulphuric acid (98% H_2SO_4), hydrogen peroxide (50% H_2O_2), hydrochloric acid (35% HCl).

2.2 Synthesis of graphene oxide

The modified hummers method was used to synthesise graphene oxide (GO) [9]. This method involves the treatment of graphite flakes with a mixture of sodium nitrate ($NaNO_3$), potassium permanganate ($KMnO_4$) and sulphuric acid (H_2SO_4). During the synthesis of GO, 120 ml of concentrated H_2SO_4 was measured and cooled to the temperature below 5°C in an ice bath. In the process 2.5 g of $NaNO_3$ and 2 g of graphite were slowly added to the H_2SO_4. The mixture was then allowed to stir for a maximum of 30 min under an ice bath at 300 rpm (revolution per minutes). 15 g of $KMnO_4$ was then added slowly to the mixture after 30 min with continuous stirring at 300 rpm. The temperature of the mixture was always kept below 5 °C. After $KMnO_4$ was successfully stirred into the mixture, the ice bath was replaced with an oil bath. The temperature of the mixture was increased and maintained in the range of 60 - 70 °C in the oil bath. The mixture was further allowed to stir for extra 30 min at 300 rpm. Furthermore, after 30 min of stirring, the mixture was then allowed to react whilst stirring for 24 h under room temperature in the oil bath still at 300 rpm.

After the full complete 24 h reaction, the mixture was cooled to a temperature below 5 °C in an ice bath, followed by gradual addition of 220 ml of de-ionized water drop by drop wise in the mixture to increase the temperature to 55 °C maximum while stirring at 300 rpm. Subsequent the gradual addition of 220 ml of de-ionized water, the mixture was further heated in an oil bath and refluxed for 24 h at a temperature below 60 °C. The mixture was then cooled to room temperature and 50 ml of hydrogen peroxide (H_2O_2) was slowly added to eliminate excess of $KMnO_4$. The exothermic reaction occurred during the addition of H_2O_2 and the mixture changed to bright yellow. The mixture was then filtered and the obtained product (graphite oxide) was washed continuously with 0.1 M of hydrochloric acid (200 ml) to remove the metal ions. The graphite oxide was further washed with the de-ionized water for several times using centrifuge, until the pH value of the supernatant was approximately close to the pH of the water. Then, the graphite oxide was dried up in a vacuum oven at a temperature of 60 °C for 24 h. Finally, 5 mg of graphite oxide was exfoliated by sonication in a 100 ml of deionized water to yield several graphene oxide nanosheets.

2.3 Characterization of graphene oxide

X-ray diffraction pattern of GO was conducted using Bruker D2 Phaser Diffractometer (λ = 0.15418 nm) which uses secondary graphite monochromated with CuKα radiation. The surface of GO was investigated using ZEISS SEM and Perkin Elmer TEM. The presence of the oxygen functional groups on the hexagonal honeycomb sheet was confirmed by Perkin Elmer FTIR TWO spectrometer at the spectral wavenumber range of 400 cm^{-1} to 4000 cm^{-1}. Perkin Elmer Raman Spectrometer was used to analyse the structural characteristics of GO at a laser voltage of 50% with a beam exposure of 10 s. Images of GO layers were further explored and obtained using Veeco-nano scope AFM in a contact mode.

3. Results and Discussion

3.1 X-ray diffraction analysis

The x-ray diffraction spectrum confirms that GO crystallise into nanosheet form with a sharp peak at $2\theta = 11.1^0$ which corresponds to the interlayer spacing of 0.791 nm as depicted in figure 1. In addition,

the diffraction peak correspond with the (001) plane of GO. However, the x-ray diffraction of the well-ordered graphene usually depicts a sharp peak at $2\theta = 26.7^0$ [10]. This simply suggests that the sudden changes in the GO peak is due to the presents of the oxygen containing functional groups lying on the graphene surface. Commonly, the interlayer spacing of GO is known to range from 0.6 to 1.0 nm depending on the oxidation process involved during the synthesis procedure [11]. Therefore, since the obtained interlayer spacing for GO (0.791nm) lies between 0.6 and 1.0 nm, this shows that the synthesised GO is highly oxidized. The Bragg law [12] has been used in the determination of the interlayer spacing. The oxygen functional groups lying on the graphene sheets are also responsible for the increase in the interlayer spacing of GO [13]. The observed value for the sharp peak of GO approximately corresponds with the values reported in the literature [14]. The crystal size of this material was calculated to be 4.7 nm (47 Å). The Debye-Scherrer [15] equation was used to calculate the crystal size.

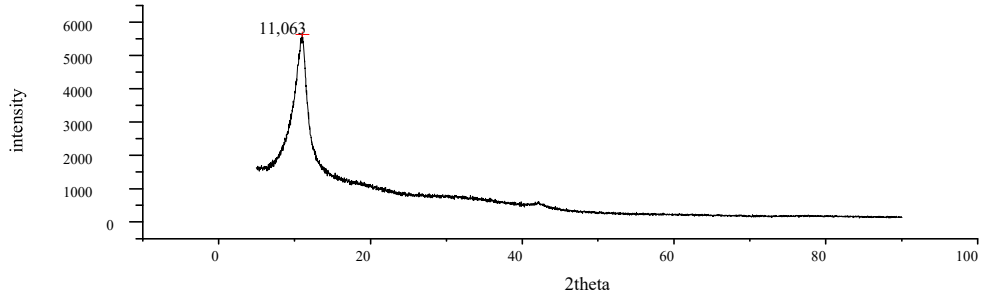

Figure 1. X-ray diffraction of GO.

3.2 Scanning and Transmission Electron Microscopy

The SEM micrograph suggests, the folding or piling of the layers with the surface morphology which is wrinkled, as shown in figure 2. This could be due to oxygen functional groups and other structural defects [16]. Based on the synthesis of GO by improved method, the wrinkles in GO are also caused by the folding of the GO sheets [17].

The TEM micrograph in figure 3 further shows evidence of the wrinkles in the middle of the GO nanosheets. The wrinkles further extend towards the edges. The same observations are noted and reported by Singh et al. [18]. It must be noted that the TEM image was taken in the bright field mode of the microscope where only transmitted electrons are allowed to pass through the aperture. The dark region at the middle and the edges of the GO nanosheets may be caused by the presence of wrinkles.

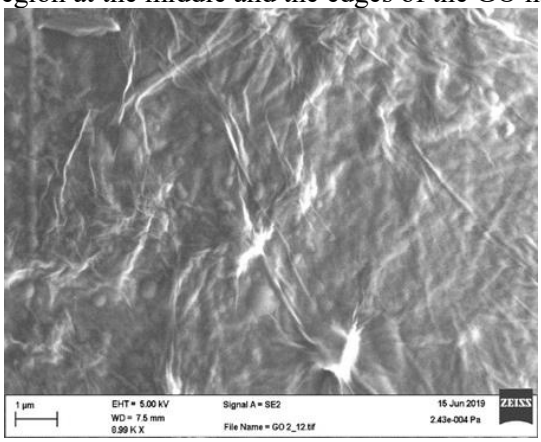

Figure 2: SEM micrograph of GO.

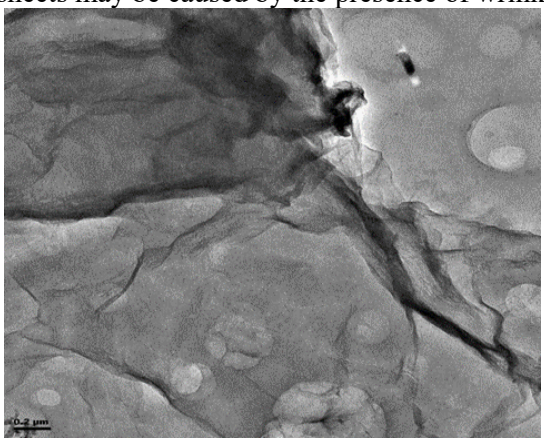

Figure 3: TEM micrograph of GO.

3.3 Fourier Transform Infrared Spectroscopy

In figure 4, the FTIR spectra of GO is shown. The spectra indicate the existence of various functional groups: hydroxyl (OH), carbonyl (C=O), epoxy (C-O), and alkoxy (O-C-O). The hydroxyl (OH) and carbonyl (C=O) groups stretching vibrations can be identified by the bands appearing at 3358 cm^{-1} and 1728 cm^{-1} respectively. Furthermore, the bands appearing at wavenumbers 1224 cm^{-1} and 1050 cm^{-1} correspond to epoxy (C-O) and alkoxy (O-C-O) stretching vibrations respectively. The obtained FTIR results are in good agreement with literature reports as outlined by Zhang et al. [19] and confirms the oxidation of graphite during the synthesis of GO via modified hummers method.

3.4 Raman Spectroscopy

According to many studies, the Raman spectra of graphene oxide usually exhibits two strong peaks, the D and the G peaks at approximately 1343 cm^{-1} and 1598 cm^{-1} respectively [20]. In this study, the D and the G peaks are observed at 1308 cm^{-1} and 1596 cm^{-1} respectively as illustrated in figure 5. The G-peak is usually because of the carbon-carbon bond stretching and the D-peak is associated with the presents of the oxygen functional groups on the graphene sheets [20]. If the intensity of the D peaks is (ID) and that of the G peak is (IG), the increase in the intensity of the ratio of the D and the G (ID/IG) peaks usually indicates the decrease in the average size of carbon-carbon bonds [21]. The ratio of the intensity of GO is 0.82 as compared to the theoretical value of 0.84, which suggests an increase in the average size of the carbon-carbon bonds stretching on the graphene sheets. Consequently, an increased aromaticity in the GO structure which is related with enlarged surface area and improved stability. As a results, Raman spectroscopy was successfully conducted to confirm the chemical changes in the graphitic structure.

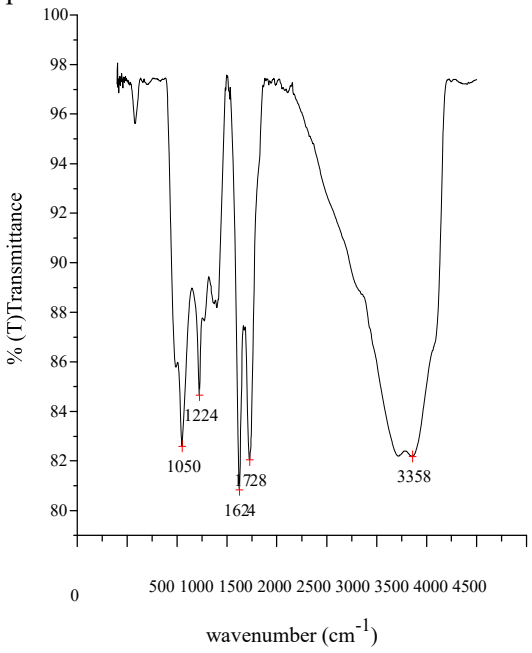

Figure 4. FTIR spectra of GO.

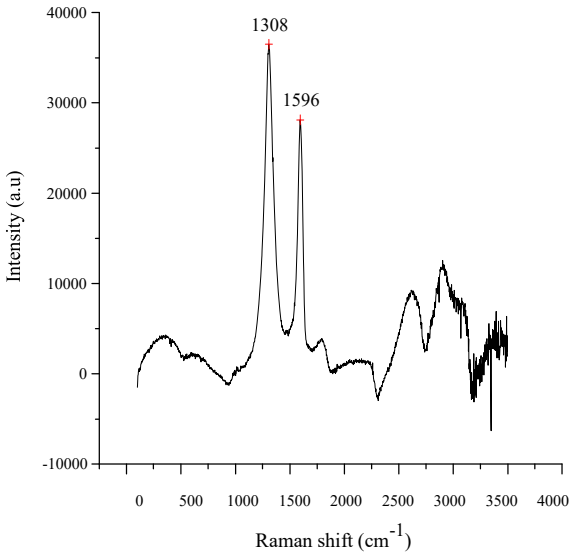

Figure 5. Raman Spectroscopy of GO.

3.5 Atomic Force Microscopy

Figures 6 and 7 shows that the AFM GO layers have different lateral sizes as well as different layer thickness. The folding or piling of the layers can also be observed which could have resulted when drying GO on the glass substrate as observed in figure 7. A typical height profile in figures 6 and 8 reveals the thickness of 2.993 nm of a single GO layer with the root mean square (RMS) value of the surface roughness of 1.134 nm due to the oxygen functional groups as reported in the literature. The thickness of graphene is approximated to range from 0.34 to 1.27 nm [22]. Therefore, since the obtained

thickness for GO (2.993 nm) is out of the approximated range of graphene, this could be attributed to the presence of the oxygen atoms laying on the graphene sheets causing the folding of GO nanosheets. As a result, GO is expected to be thicker than graphene because of the surface oxygen functional groups. However, this spectroscopic technique has difficulties in determining the exact number of layers in graphene and graphene oxide [23], hence this could also introduce difficulties in obtaining the exact thickness of GO.

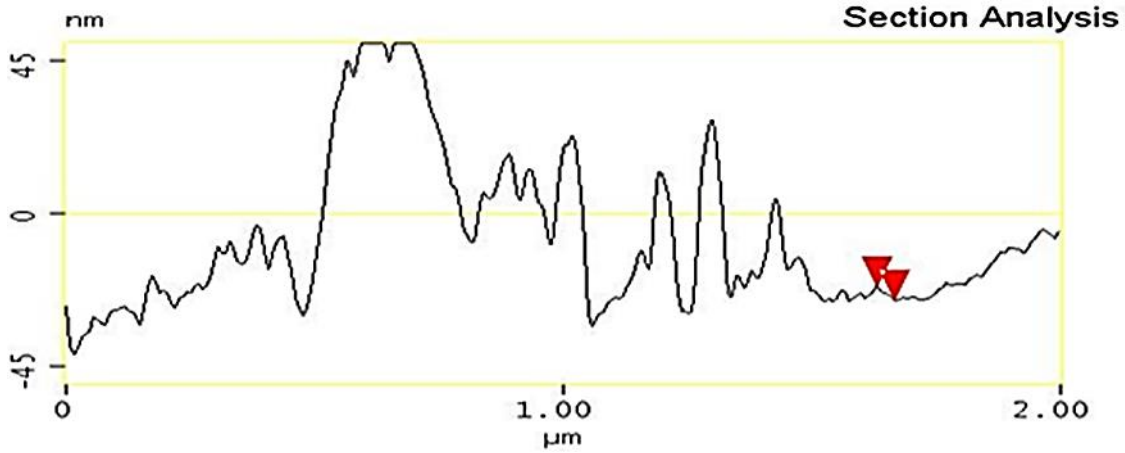

Figure 6: The sectional analysis of the GO nanosheets.

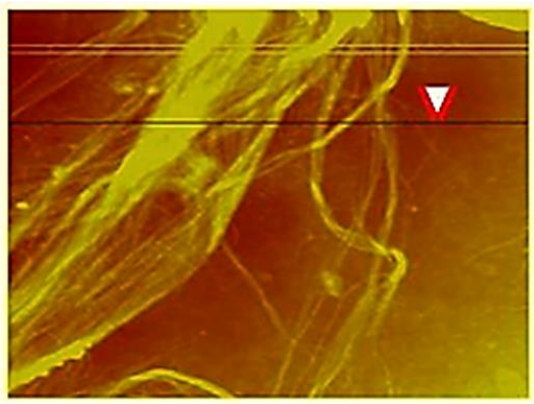

Figure 7: The AFM micrograph of GO nanosheets.

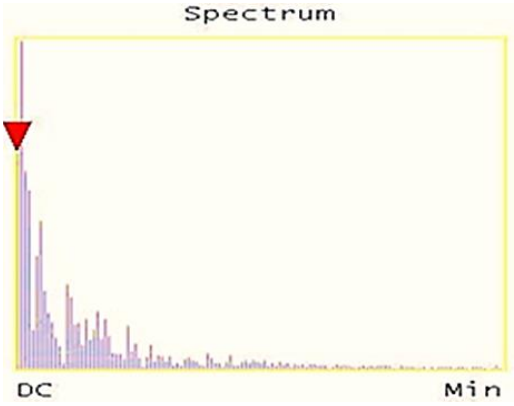

Figure 8: The spectral analysis of GO height profile.

4. Conclusion

Graphene oxide was successfully synthesised via modified hummers method. An acceptable interpretation of the surface morphology of graphene oxide through the spectroscopic instrument was successfully achieved. Correspondingly, SEM and TEM complement each other on the wrinkles and folding of the GO layers. The FTIR and RM results suggest the presence of the oxygen functional groups in the honeycomb sheets and AFM confirms that the synthesised GO is a nanomaterial with a rough surface due to the oxygen functional groups.

5. Reference

[1] Chen H, Feng H and Li J 2012 *Chem. Rev* **112** 6027.
[2] McAllister MJ, Li JL, Adamson DH, Schniepp HC, Abdala AA, Liu J, Herrera-Alonso M, Milius DL, Car R, Prud'homme RK and Aksay IA 2007 *Chem. Mater* **19** 4396.
[3] Ramanathan T, Abdala AA, Stankovich S, Dikin DA, Herrera-Alonso M, Piner RD, Adamson DH, Schniepp HC, Chen X, Ruoff RS, Nguyen ST, Aksay IA, Prud'Homme RK and Brinson LC 2008 *Nat. Nanotechnol* **3** 327.
[4] Raccichini R, Varzi A, Passerini S and Scrosati B 2015 **14** 271.
[5] Huang X, Yin Z, Wu S, Qi X, He Q, Zhang Q, Yan Q, Boey F and Zhang H 2011 *Small* **7** 1876.
[6] Pendolino F and Armata N Springer Briefs in Applied Sciences and Technology.
[7] Bai H, Li C, Wang, X and Shi G 2011 *J. Phys. Chem. C* **115** 5545.
[8] Brodie BC 1859 *Philosophical Transactions of the Royal Society of London* **149** 249.
[9] W.S. Hummers WS and Offeman RE 1958 *J. Am. Chem. Soc.* **80** 1339.
[10] Ashori A, Rahmani H and Bahrami R 2015 *Polym. Test*. **48** 82.
[11] Ramesh P, Bhagyalakshmi, S and Sampath S 2004 *J. Colloid Interface Sci*. **274** 95.
[12] Li J, Zeng X, Ren T, and Van Der Heide E 2014 *Lubricants* **3** 137.
[13] Shen JF, Hu YZ, Shi M, Lu X, Qin C, Li C and Ye M.X 2009 *Chem. Mater* **21** 3514.
[14] Ruiguang X and Yanan L.Y 2016 *Chem. Commun*, **52** 390.
[15] Fischer HE, Barnes AC and Salmon PS 2006 *Rep. Prog. Phys*. **69** 233.
[16] Mungse HP and Khatri O.P 2014 *J. Phys. Chem*. *C* **118** 14394.
[17] Yu H, Zhang B, Bulin C, Li R, and Xing R 2016 *Sci. Rep* **6** 36143.
[18] Singh M, Kaushal S, Singh P and Sharma J 2018 *J. Photochem. Photobiol A*. **364** 130.
[19] Zhang L, Lu Z, Zhao Q, Huang J, Shen and Zhang Z 2011 *Small* **7** 460
[20] Kudin KN, Ozbas B, Schniepp HC, Prud'homme RK, Aksay IA and Car R 2008 *Nano Lett.* **8** 36.
[21] Dresselhaus MS, Dresselhaus G, Saito R and Jorio A 2005 *Phys. Rep*. **409** 44.
[22] Li D, Muller MB, Gilije S, Kaner RB and Wallace GG 2008 *Nat. Nanotechnol*. **3** 101.
[23] Liu WW, Chai SP, Mohamed AR and Hashim U 2014 *J. Ind. Eng. Chem*. **20** 171.

Bottomonia suppression in heavy-ion collisions from AdS/CFT

N N Barnard and W A Horowitz

Department of Physics, University of Cape Town, Private Bag X3, Rondebosch 7701, South Africa

E-mail: brnnad007@myuct.ac.za

Abstract. We compute for the first time the suppression of bottomonia in a strongly coupled QGP and compare the results to those from a weakly coupled QGP and to data. Using imaginary time techniques we numerically determine the real and imaginary parts of the binding energy of ground state bottomonia in a potential computed from AdS/CFT and another computed from pQCD. We implement the complex binding energies in a suppression model to determine the Υ(1S) nuclear modification factor in $\sqrt{s}_{NN} = 2.76$ TeV Pb+Pb collisions. This simplest strong-coupling, p_T-independent potential leads to a significant oversuppression of Υ(1S) compared to data while the results from the pQCD-derived potential are consistent with data. We also investigate the validity of using complex heavy quark potentials from AdS/CFT for all quark separation r by independently computing the meson spectrum using semiclassical, rotating open strings attached to the D7-brane.

1. Introduction

The relativistic heavy-ion collisions at the Large Hadron Collider (LHC) and the Relativistic Heavy Ion Collider (RHIC) are sufficiently energetic for hadrons to transition into a new phase of colored matter, known as the quark-gluon plasma (QGP) [1]. In vacuum, quarkonia are bound states of a heavy quark and its anti-quark pair [2]. Embedded in a medium, the properties of quarkonia change. Matsui and Satz [3] were the first to propose that quarkonia may theoretically exist in conjunction with the QGP at $T > T_c$, where T_c is the critical temperature required for QGP formation, due to its small binding radii relative to the screening radius, whereas lighter hadrons dissociate at $\sim T_c$. At some T, the screening radius becomes smaller than the typical quarkonia radii, leading to their dissolution. In addition, excited states of quarkonia dissociate before the ground state [4]. The suppression of the bound states of quarkonia in heavy-ion collisions is hence a valuable indicator of the formation of QGP, and the comparison of the quarkonia spectra in high multiplicity collisions to that in minimum bias $p + p$ collisions where no QGP is formed is a useful probe of the QGP's properties.

Potential models can be used to describe the interaction of the quark and antiquark in the $q\bar{q}$ pair to calculate the suppression of quarkonia production in heavy-ion collisions [3]. This potential at finite temperature contains not only a standard real Debye-screened term, but also an imaginary part which gives the thermal width of the state, and hence its suppression [5]. One of the first to show this was [6], which made use of perturbative methods to find the static potential of quarkonia at finite temperature. They concluded that the thermal width of the

state increases with T, suggesting that at high T the dissociation due to the effect described by the imaginary part of the potential occurs before color screening can even come into effect.

The complex-valued potential was explored further using non-perturbative lattice QCD by [5], among others, allowing for the study of strongly-coupled quarkonia as well. An important consideration in finding heavy quarkonium suppression is the velocity of the $q\bar{q}$ in relation to the surrounding QGP, however, while perturbative and lattice QCD calculations generally consider the $q\bar{q}$ meson to be at rest in the medium.

The suppression of quarkonia moving at velocity in a QGP hence requires holographic techniques such as the Anti-de Sitter/Conformal Field Theory (AdS/CFT) correspondence. Liu, Rajagopal and Wiedemann (LRW) [7] were the first to present a quantitative description from AdS/CFT of the consequences of velocity on the screening length of charmonium, suggesting that for strongly coupled J/ψ, velocity could result in a significant additional source of suppression at high transverse momentum p_T in the form of a decrease in dissociation energy with increased velocity. Since then, many have performed similar investigations, and while the aforementioned are limited in their scope of application, it is interesting to note that [8] in particular concludes that the effect of velocity may not be as consequential as postulated in LRW.

We would ultimately like to investigate the consequences of these different velocity dependence pictures from AdS/CFT compared to pQCD. Here we have a more modest goal: to compare the experimentally measurable consequences of pQCD vs. AdS/CFT pictures.

2. Potential Models

The potential model for weakly coupled quarkonia is taken from [9]. We plot the real and imaginary parts of the weakly coupled potential as a function of quark separation r for various temperatures in figures 1a and 1b, respectively.

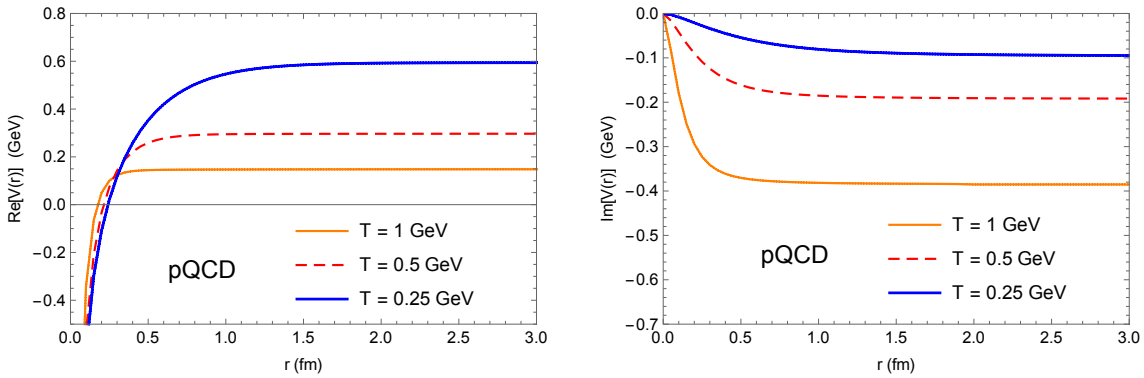

(a) (b)

Figure 1. Plot of the (a) real part and the (b) imaginary part of the weakly coupled potential, as a function of the distance r between the quark and anti-quark in the $b\bar{b}$, for various T.

We modeled the strongly coupled quarkonia at rest in a QGP with the potential given in Albacete et al. [10], which was derived in $\mathcal{N} = 4$ super Yang-Mills at finite temperature using AdS/CFT. Note that the potential becomes complex for $r > r_c \simeq 0.870/\pi T$. Considering that both weakly coupled pQCD and non-perturbative lattice QCD methods yield complex heavy quark potentials, it is sensible to expect the same using AdS/CFT methods. We provide further supporting evidence for our procedure in Section 4, which gives an independent calculation of the binding energies for $\Upsilon(1S)$ using semiclassical, rotating open strings attached to the D7-brane.

Figure 2a and 2b show the real and imaginary parts of the strongly coupled potential as a function of quark separation r taking $\lambda = 10$.

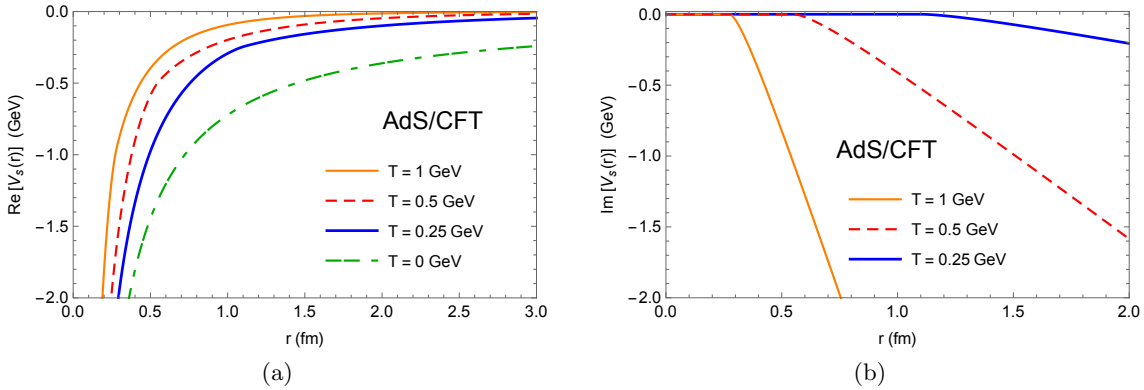

Figure 2. The (a) real part and the (b) imaginary part of the strongly coupled potential, as a function of the distance r between the quark and anti-quark in the $b\bar{b}$, for various temperatures T.

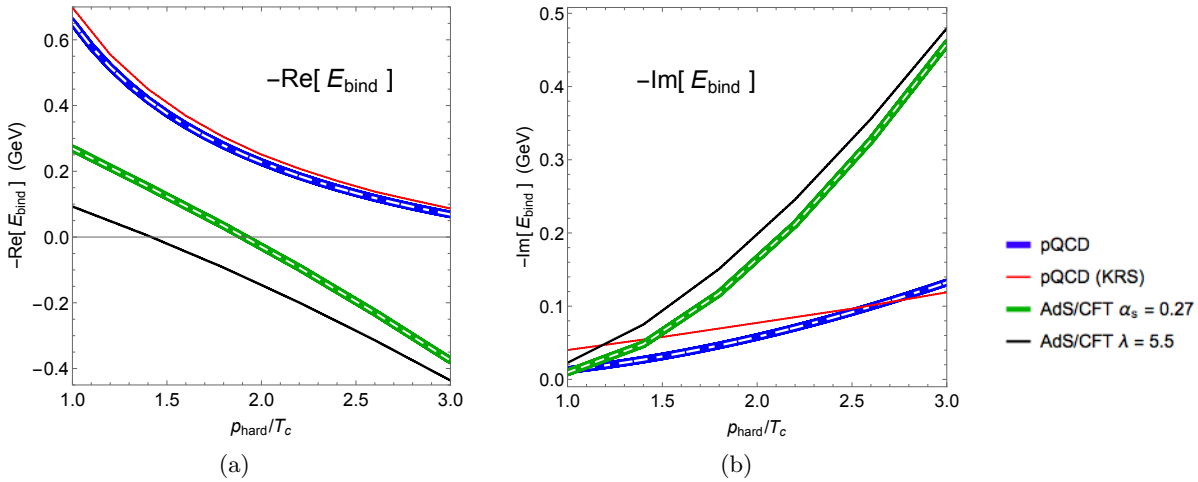

Figure 3. The (a) negative real part and (b) negative imaginary part of $E_{\rm bind}$ for Υ(1S). The dashed white curves inside the blue and green curves are from the independent evaluation using the complex variational method.

3. Binding Energies

The imaginary time numerical method used to calculate the binding energies from the potential models given in Section 2 follows that of [9, 11], with modifications (see [12] for details). Figure 3a gives the real part of the binding energy of Υ(1S) from the pQCD potential and AdS/CFT potential, as a function of temperature. Figure 3b gives the imaginary part of $E_{\rm bind}$.

For the AdS/CFT results, we show the binding energy both for the case where the coupling constant is $\lambda = 10$ (labeled as $\alpha_s = 0.27$) and where $\lambda = 5.5$; the reasoning behind the choice of these values is explained in [12]. The binding energy results for bottomonium from [11] are labeled "pQCD (KRS)" and are included for comparison.

Both the binding energy results presented for the pQCD potential and the AdS/CFT potential taking $\lambda = 10$ were independently confirmed using a complex variational method; see Appendix A of [12] for details.

The binding energy found from our adapted methodology for the pQCD potential differs quantitatively from that presented in [11], which was used in Krouppa et al. [9] to calculate suppression. In the case of Υ(1S), this difference does not change the qualitative behavior of the quarkonia, since both results suggest that the quarkonia remain bound up to at least $T = 3\,T_c$.

However, we will see in Section 5 that the small quantitative differences in the derived binding energies lead to a significant quantitative difference in the predicted suppression.

4. Comparison to an Independent Alternative Method: Hanging, Rotating Strings

We seek an independent confirmation of the binding energies given in Section 3 computed using the non-relativistic imaginary time numerical method [12], using the potential from AdS/CFT as given in figure 2.

Kruczenski et al. [13] computes the energy spectrum of mesons at $T = 0$ from semiclassical, rotating open strings attached to a D7-brane. In particular, in the limit $J \gg \sqrt{\lambda}$, where J is the spin, [13] notes that the spectrum corresponds to that of a non-relativistic $q\bar{q}$-pair bound by a Coulomb potential. We extended the results from [13] to $T > 0$. In addition, we generalized the complex strongly coupled potential from Albacete et al. [10], which was derived in the infinite mass limit, to finite mass. We then compared the binding energies found using this generalized finite mass potential with the non-relativistic numerical regime (NRQM) with the binding energies from the semiclassical string method (SSM).

For the simplest $T = 0$ case, both the binding energies from the SSM and NRQM are purely real. These binding energies are shown in figure 4a for a range of quark masses. The binding energies from the two methods agree for large J. At small J, however, $E_{\text{bind}}^{\text{NRQM}} > E_{\text{bind}}^{\text{SSM}}$.

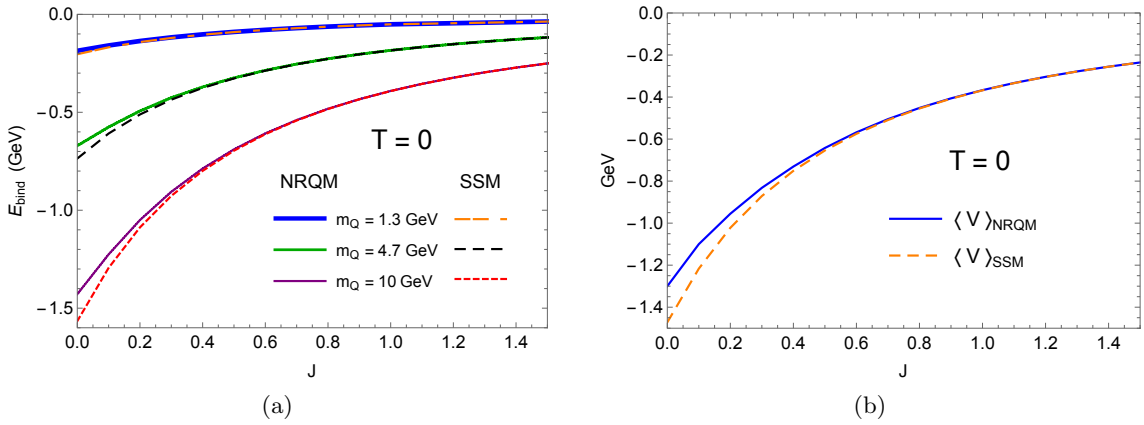

Figure 4. (a) The binding energies from NRQM and SSM for a range of quark masses m_Q. (b) The average potential $\langle V \rangle_{\text{NRQM}}$ from NRQM and $\langle V \rangle_{\text{SSM}}$ from the SSM for $m_Q = 4.7$ GeV.

This discrepancy occurs since the imaginary time numerical method takes into account quantum spreading of the wavefunction, whereas the SSM does not. We may explicitly demonstrate the effect of this quantum spreading by investigating the potential probed by the two methods. We show in figure 4b the average potential felt by the heavy quarks in the two methods. It is evident from figure 4b that $\langle V \rangle_{\text{NRQM}} > \langle V \rangle_{\text{SSM}}$: the average potential experienced by the heavy quarks is deeper at small J for the SSM as opposed to NRQM. We may understand the ordering of potentials from the quantum spreading – the NRQM wavefunction preferentially explores the potential at larger r due to uncertainty. As a result, the binding energies are therefore less negative when quantum effects are taken into account, i.e. the quarkonia is less strongly bound, as expected.

Figure 5a and 5b show the real and imaginary parts, respectively, of the binding energies from NRQM and the SSM for $\Upsilon(1S)$ for a range of temperatures. At small J, the real part of the NRQM binding energy is slightly larger than the real part of the binding energy from the SSM, as was the case for $T = 0$.

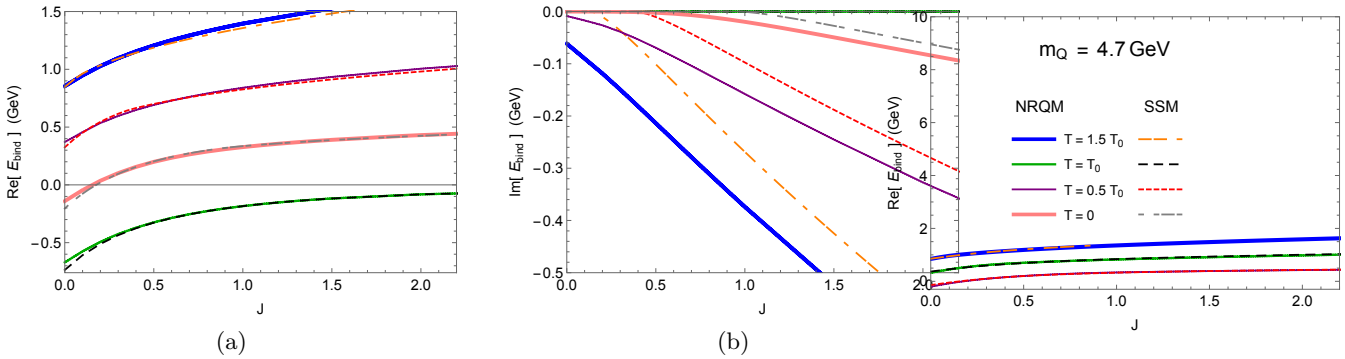

(a) (b)

Figure 5. The (a) real and (b) imaginary parts of E_{bind} of Υ(1S) for a range of T.

The imaginary part of the E_{bind} echo the conclusions drawn regarding the difference in the real parts. The binding energies from NRQM become complex at smaller J than those from the SSM. The larger the imaginary part of the binding energy, the greater the tendency for the quarkonia to fall apart: the Υ(1S) in the NRQM picture is again less tightly bound than SSM.

For large J, however, the binding energies converge as expected. The excellent agreement of these binding energies shows that the use of complex heavy quark potentials to compute binding energies is consistent with the independent semiclassical string method.

5. Suppression

We would lastly like to make quantitative predictions for the suppression of bottomonia in heavy ion collisions and compare to measured data. The nuclear modification factor R_{AA} is calculated following [9] – see [12] for details.

Figure 6a gives the nuclear modification factor R_{AA} for each of the sets of binding energies shown in figure 3a and 3b as a function of the number of participating nucleons N_{part}. Figure 6b shows $R_{AA}(p_T)$, where all centrality classes are included, weighed by the number of binary nucleon-nucleon collisions N_{coll}. Suppression results for mid-rapidity ($|y| < 2.4$) Pb+Pb collisions at $\sqrt{s_{\text{NN}}} = 2.76$ TeV from the CMS Collaboration [14] are included in figure 6a and 6b for comparison.

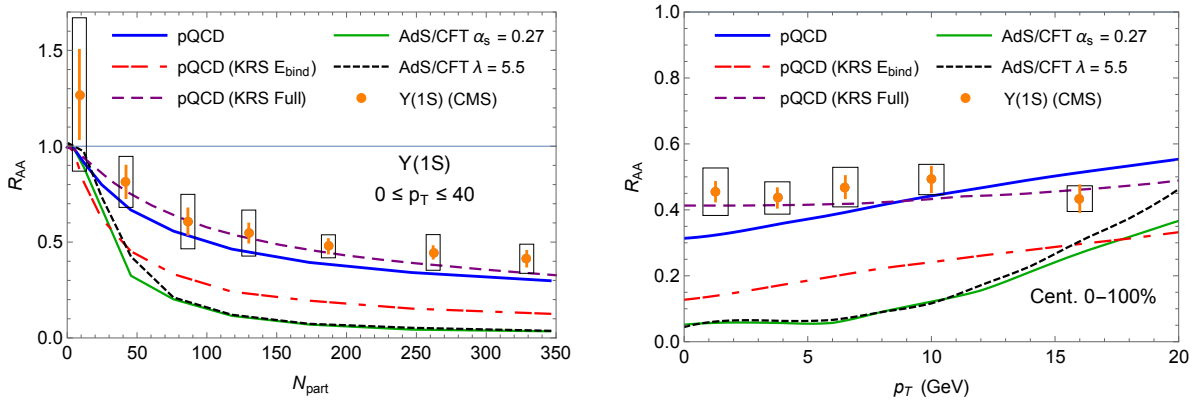

(a) (b)

Figure 6. (a) Nuclear modification factor R_{AA} as a function of the number of participating nucleons N_{part} for $0 \leq p_T \leq 40$. (b) Nuclear modification factor R_{AA} as a function of transverse momentum p_T for combined centrality classes. Data from CMS [14] is included in orange.

6. Discussion and Outlook

We present the suppression of $\Upsilon(1S)$ computed for the first time in an isotropic strongly coupled QGP, compare the results to those from a weakly coupled QGP, and to data [14].

Our first results for $\Upsilon(1S)$ strongly coupled to a strongly coupled plasma show binding energies with much larger imaginary parts than those found from the pQCD potential, as well as real parts that become positive within the T_c to $3\,T_c$ range considered. Thus, for the potential models considered here, a strongly coupled $\Upsilon(1S)$ interacting with a strongly coupled plasma melts at a *lower temperature* than a weakly coupled $\Upsilon(1S)$ interacting with a weakly coupled plasma. The $\Upsilon(1S)$ hence appears more strongly bound at weak coupling than at strong coupling, which is surprising.

Quantitatively, our full model—comprised of the potential, the resulting quarkonia $E_{\rm bind}$, and the translation to R_{AA}—significantly overpredicts the suppression of strongly coupled $\Upsilon(1S)$ compared to data. Our predictions for weakly coupled $\Upsilon(1S)$ are consistent with data.

We note that our model for the medium is significantly less sophisticated compared to that used in [9]: our background is an optical Glauber model as opposed to the 3+1D viscous anisotropic hydrodynamics in that work. Our medium incorporates only Bjorken expansion, whereas the background in [9] includes transverse expansion and entropy production. Therefore the plasma in [9] cools faster than ours, leading to our model showing more dissociation for the same binding energies. The extent of the sensitivity of R_{AA} to the background used is surprisingly large. With the only difference being the background geometry used, we ran the binding energies from [11] through our suppression model and found an R_{AA} a factor of two smaller than that shown in [9].

In contrast to the favorable comparison between the pQCD-based results of [9] and the CMS data [14], if we assume our weak coupling binding energies are more accurate than those of [11], then computing R_{AA} with the more sophisticated background from [9] would likely yield a significant underprediction of the suppression of bottomonia.

At strong coupling, with a potential derived from AdS/CFT as described in [10], it seems unlikely that the use of a more sophisticated background would reduce the suppression of bottomonia enough that the predicted R_{AA} would be consistent with data; however, the differences from using a more sophisticated background, suppression model, and velocity dependent potential may ultimately be sufficient for future strongly coupled quarkonia predictions to be consistent with current data.

Acknowledgments

The authors thank the South African National Research Foundation and SA-CERN Consortium for their financial support. The authors also thank Michael Strickland for useful discussions.

References

[1] Gyulassy M and McLerran L 2005 *Nucl. Phys.* A **750** 30–63
[2] Patrignani C et al. (Particle Data Group) 2016 *Chin. Phys.* C**40** 100001
[3] Matsui T and Satz H 1986 *Phys. Lett.* B **178** 416–22
[4] Karsch F, Kharzeev D and Satz H 2006 *Phys. Lett.* B **637** 75–80
[5] Rothkopf A, Hatsuda T and Sasaki S 2012 *Phys. Rev. Lett.* **108** 162001
[6] Laine M, Philipsen O, Romatschke P and Tassler M 2007 *J. High Energy Phys.* JHEP03(2007)054
[7] Liu H, Rajagopal K and Weidemann U A 2007 *Phys. Rev. Lett.* **98** 182301
[8] Finazzo S I and Noronha J 2015 *J. High Energy Phys.* JHEP01(2015)051
[9] Krouppa B, Ryblewski R and Strickland M 2015 *Phys. Rev.* C **92** 061901
[10] Albacete J L, Kovchegov Y V and Taliotis A 2008 *Phys. Rev.* D **78** 115007
[11] Margotta M, McCarty K, McGahan C, Strickland M and Yager-Elorriaga D 2011 *Phys. Rev.* D **83** 105019
[12] Barnard N N and Horowitz W A 2017 arXiv:1706.09217
[13] Kruczenski M, Mateos D, Myers R C and Winters D J 2003 *J. High Energy Phys.* JHEP07(2003)049
[14] Khachatryan V *et al* (CMS) 2017 *Phys. Lett.* B **770** 357–9

Non-Abelian Corrections for Radiation in QCD

W. A. Horowitz

Department of Physics, University of Cape Town, Private Bag X3, Rondebosch 7701, South Africa

E-mail: wa.horowitz@uct.ac.za

Abstract. We seek to compute the emission spectrum of soft and collinear gluon bremsstrahlung radiation associated with the hard scattering of a quark by a gluon in QCD for one, two, and three gluons. In QED, multiple photon emissions are independent, which is to say they are emitted according to a Poisson distribution. In QCD, the non-Abelian nature of the theory leads to interactions between the emitted gluons. Hence the emissions are not independent, and there are therefore corrections to the Poisson distribution of these radiated particles. We demonstrate how ideas from maximal helicity violating techniques will allow a calculation of these corrections and their potential relevance for heavy ion collision phenomenology.

1. Introduction

There is enormous interest in the scientific community in understanding better non-trivial, emergent, many-body dynamics. These emergent phenomena occur across vastly different materials, as varied as the constituent matter at the center of neutron stars to colonies of ants. Of the four fundamental forces—the gravitational, electromagnetic, weak, and strong—the strong force provides a unique laboratory to explore simultaneously both the theoretical and experimental implications for the emergent phenomena in a non-Abelian gauge theory.

One of the key observables in heavy ion collision phenomenology is jet quenching [1, 2]. In the collision of ultrarelativistic nuclei that provide experimental insight into the collective behavior of the strong force, rare high momentum particles are created that then propagate through the medium that is simultaneously created by the collision of nuclei. The interaction of these high momentum particles with the medium probes the emergent properties of the quark-gluon plasma (QGP); these interactions imprint themselves on the momentum distribution of the measured final state particles measured by detectors.

We therefore seek a theoretical understanding of these interactions in order to invert the measured observables to determine the properties of the quark-gluon plasma. If we assume that the coupling between these very high momentum particles and the medium is perturbatively calculable, then we expect that the dominant form of energy loss is radiative: the propagation of the high momentum particles is disturbed by the presence of the medium, which then leads to the emission of bremsstrahlung gluons. Calculations of the spectrum of these radiated gluons has been performed; see, e.g., [1, 2] for reviews. These derivations have so far involved only the single inclusive gluon emission spectrum. What one finds is that the expected number of emitted gluons is larger than one, more like three [3]. We expect the non-Abelian nature of

QCD to lead to non-trivial correlations between these emitted gluons which are not currently captured in the single inclusive derivations performed so far.

Theoretical calculations with multiple gluon emission using standard perturbative QCD (pQCD) techniques is highly non-trivial; see, e.g., [4]. We therefore seek new methods for gaining insight into these multi-gluon emission processes. Amplitude and helicity techniques [5–8], which are often referred to as maximial helicity violation (MHV) techniques, appear to be one such promising tool.

2. A Model Problem

Performing pQCD calculations in the presence of a deconfined medium of quarks and gluons as is expected in the QGP produced in heavy ion collisions is a formidable problem. We thus seek to first apply amplitude techniques to the problem of $2 \to 2$ hard scattering of partons that also induces the emission of an additional n gluons. Significant progress was made in this problem using traditional pQCD techniques, especially for the case of collinear emission of 1 and 2 gluons [9]. Additional significant progress has been made applying MHV techniques to this process, with the successful determination of $g + g \to g + g + n\,g$ for n arbitrary when the emitted gluons are either fully symmetric or fully antisymmetric under interchange [10] and for $q + g \to q + g + n\,g$ where $n = 1$, 2, or 3 [11].

In this work we'll consider specifically the process of hard quark-gluon scattering with the emission of an additional gluon bremsstrahlung. One may find a number of reviews in the literature including, e.g., [6]. For the sake of clarity, we note some slight notational differences taken here. In this work we take

$$\varepsilon^{ab} \equiv \begin{pmatrix} 0 & 1 \\ -1 & 0 \end{pmatrix} \equiv \varepsilon^{\dot{a}\dot{b}}; \qquad \varepsilon_{ab} \equiv \begin{pmatrix} 0 & -1 \\ 1 & 0 \end{pmatrix} \equiv \varepsilon_{\dot{a}\dot{b}}. \tag{1}$$

and define

$$p_a = \varepsilon_{ab} p^b \qquad p_{\dot{a}} = \varepsilon_{\dot{a}\dot{b}} p^{\dot{b}} \tag{2}$$

$$p^a = \varepsilon^{ab} p_b \qquad p^{\dot{a}} = \varepsilon^{\dot{a}\dot{b}} p_{\dot{b}}, \tag{3}$$

consistent with $p^{\dot{a}} = (p^a)^*$ and $p_{\dot{a}} = (p_a)^*$. Then

$$\langle pq \rangle \equiv p^a q_a = \varepsilon_{ab} p^a q^b = -\varepsilon_{ab} p^b q^a = -q^a p_a = -\langle qp \rangle \tag{4}$$

$$[pq] \equiv p_{\dot{a}} q^{\dot{a}} = \varepsilon^{\dot{a}\dot{b}} p_{\dot{b}} q_{\dot{a}} = -\varepsilon^{\dot{a}\dot{b}} p_{\dot{a}} q_{\dot{b}} = -q_{\dot{a}} p^{\dot{a}} = -[qp]. \tag{5}$$

Since the angle and square brackets are antisymmetric, we have that $\langle pp \rangle = [pp] = 0$ for massless particles. Further, we have that

$$\langle pq \rangle^* = (\varepsilon_{ab} p^a q^b)^* = (\varepsilon_{ab})^* (p^a)^* (q^b)^* = \varepsilon_{\dot{a}\dot{b}} p^{\dot{a}} q^{\dot{b}} = p^{\dot{a}} q_{\dot{a}} = [qp]. \tag{6}$$

We then have the extremely important identity

$$\langle pq \rangle [qp] = p^a q_a q_{\dot{a}} p^{\dot{a}} = \varepsilon_{ab} p^a q^b \varepsilon_{\dot{a}\dot{b}} q^{\dot{b}} p^{\dot{a}} = \varepsilon_{ab} \varepsilon_{\dot{a}\dot{b}} p^\mu \bar{\sigma}_\mu^{\dot{a}a} q^\nu \bar{\sigma}_\nu^{\dot{b}b} = 2\eta_{\mu\nu} p^\mu q^\nu = 2p \cdot q \equiv s_{pq}, \tag{7}$$

where we've defined a generic Mandelstam variable $s_{pq} \equiv (p + q)^2$. Notice that the angle and square brackets are essentially square roots of dot products.

We work in $SU(N)$ and take $N \to 3$ at the end of the calculation. We follow the usual MHV conventions for the normalization of the Hermitian color generators T^a [6, 7], where a runs from 1 to $N^2 - 1$: $[T^a, T^b] = i\sqrt{2} f^{abc} T^c$ with $\mathrm{tr}(T^a T^b) = \delta^{ab}$. The introduction of this square root

simplifies the representation of polarization vectors for external gluons. Let's define the color Casimir $\tilde{C}_F \equiv \frac{N^2-1}{N}$, which is twice the value of the usual Casimir, $\tilde{C}_F = 2C_F$, and for future use we define the second color Casimir $\tilde{C}_A \equiv N$.

For the purposes of applying MHV techniques, we define all lines as incoming in the amplitudes. In this way final-state momenta are assigned the negative of their physical momenta. Then momentum conservation for an n-point process takes the crossing symmetric form $\sum_{i=1}^{n} k_i = 0$. We also label the helicity as if the particle are incoming. For incoming particles this label is the physical helicity; for outgoing particles it is the opposite. In order to connect with the physical process of interest, $qg \to qg + ng$, we must apply crossing symmetry. Recall that when fermion lines are crossed, one must multiply by an overall minus sign to the result [12].

For the case of interest in this work, one finds that the full amplitude can be decomposed as [6, 7]

$$\mathcal{A}^{tree}_{\bar{q}g^n qg^m}(p_{\bar{q}}^{h_{\bar{q}}}, k_1^{h_1}, \ldots, k_n^{h_n}, p_q^{h_q}, \ell_1^{h_1}, \ldots, \ell_m^{h_m}) = g_s^{n+m+2} \sum_{\sigma \in S_n, \tau \in S_m} (T^{a_{\sigma(1)}} \cdots T^{a_{\sigma(n)}} T^{a_{\tau(1)}} \cdots T^{a_{\tau(m)}})_{\alpha\beta} \times A^{tree}_{\bar{q}g^n qg^m}(p_{\bar{q}}^{h_{\bar{q}}}, \sigma(k_1^{h_1}), \ldots, \sigma(k_n^{h_n}), p_q^{h_q}, \tau(\ell_1^{h_1}), \ldots, \tau(\ell_m^{h_m})). \quad (8)$$

where the sum is performed over all possible permutations of the $n+m$ gluons and g_s is the usual strong coupling constant, $\alpha_s \equiv g_s^2/4\pi$. In this expression, $A^{tree}_{\bar{q}g^n qg^m}$ is known as a partial or color-stripped amplitude, which is gauge invariant. In the literature, various other names have been given to this gauge invariant component, such as color-ordered amplitude and dual amplitude [6, 7, 13]. Each partial amplitude in the sum corresponds to a particular color flow, which can be naively thought as the ordering in which the gluons are emitted. That the above decomposition is valid is a highly non-trivial result and depends on trading structure constants for color generators through the relationship $\tilde{f}^{abc} \equiv i\sqrt{2} f^{abc} = \mathrm{tr}\left(T^a[T^b, T^c]\right)$ [6]. The color kinematic decomposition is especially powerful because the computation of the partial amplitude is significantly easier than the full amplitude. In particular, partial amplitudes have an extremely compact and simple form when they maximally violate helicity conservation. These MHV amplitudes have exactly two negative helicity external particles while all other external particles have positive helicity. This generalizes to the notion of N^{k}MHV amplitudes when $(k+2)$ external particles have negative helicity. The case where exactly two particles have positive helicity while all the other particles have negative helicity are called anti-MHV, ($\overline{\mathrm{MHV}}$).

Using the spinor helicity formalism and the Britto–Cachazo–Feng–Witten (BCFW) on-shell recursion relation [14], one can show that a general MHV partial amplitude for a process which involves an arbitrary number of gluons and a quark-antiquark pair is given by [7]

$$A^{MHV}_{\bar{q}qg^n}(p_{\bar{q}}^-, p_q^+, 1^+, \ldots, k^-, \ldots, n^+) = \frac{\langle p_{\bar{q}} k\rangle^3 \langle p_q k\rangle}{\langle p_{\bar{q}} p_q\rangle \langle p_q 1\rangle \cdots \langle n p_{\bar{q}}\rangle}. \quad (9)$$

The partial amplitude for our MHV helicity configuration expressed in Eq. (9) is remarkably simple and only a function of the angle brackets. The $\overline{\mathrm{MHV}}$ partial amplitude can be derived from Eq. (9) by swapping all helicities, which results in changing the angle brackets into square brackets and multiplying by an overall sign depending on the number of external legs. Thus $|A(\{h_i\})|^2 = |A(\{-h_i\})|^2$.

3. Results

Armed with Eq. (9) we may immediately compute the dominant soft and collinear emission of a single bremsstrahlung gluon radiation associated with $qg \to qg$ scattering. The relevant

amplitude is

$$\mathcal{A}(1^-5^+2^+3^-4^+) \simeq g^3\langle 13\rangle^3\langle 23\rangle\Big(T^5T^3T^4\frac{1}{\langle 15\rangle\langle 52\rangle\langle 23\rangle\langle 34\rangle\langle 41\rangle} + T^5T^4T^3\frac{1}{\langle 15\rangle\langle 52\rangle\langle 24\rangle\langle 43\rangle\langle 31\rangle}\Big), \tag{10}$$

where we have used the shorthand $T^i \equiv T^{a_i}$. We are able to drop the additional contributions to the amplitude $\mathcal{A}(1^-5^+2^+3^-4^+)$ from Eq. (8) for the following reason. We are interested in radiation soft and collinear to the outgoing quark, which is particle 1. Since angle brackets can be thought of as something akin to the square root of a dot product, $\langle 15\rangle$ is therefore very small when particle 5, the associated bremsstrahlung radiation for the hard scattering $qg \to qg$ process, is soft and collinear to the outgoing quark, particle 1. None of the other permutations of the three gluons will have a $\langle 15\rangle$ in the denominator and will therefore be small in comparison to the two terms included in Eq. (10).

Comparing to the $qg \to qg$ amplitude, one readily sees for radiation emitted soft and collinear to the outgoing quark that

$$\mathcal{A}(1^-5^+2^+3^-4^+) \simeq gT^5\frac{\langle 12\rangle}{\langle 15\rangle\langle 52\rangle}\mathcal{A}(1^-2^+3^-4^+). \tag{11}$$

The same logic follows for all other helicity configurations of the hard scattering subprocess; i.e. for helicities $\{h_i\}$ with $h_2 = +$ that are MHV,

$$\mathcal{A}(1^{h_1}5^+2^{h_2}3^{h_3}4^{h_4}) \simeq gT^5\frac{\langle 12\rangle}{\langle 15\rangle\langle 52\rangle}\mathcal{A}(1^{h_1}2^{h_2}3^{h_3}4^{h_4}). \tag{12}$$

When the emitted gluon has a negative helicity, the amplitude is severely suppressed by $\langle 15\rangle^3$ in the numerator when the diagram is MHV, i.e. when the other two gluons have positive helicity. However, when the emitted gluon has negative helicity and one of the hard gluons also has negative helicity, then the non-zero amplitudes (i.e. when the quark and anti-quark have opposite helicities) are $\overline{\text{MHV}}$. Thus for helicities $\{h_i\}$ with $h_2 = -$ that are $\overline{\text{MHV}}$,

$$\mathcal{A}(1^{h_1}5^-2^{h_2}3^{h_3}4^{h_4}) \simeq gT^5\frac{[12]}{[15][52]}\mathcal{A}(1^{h_1}2^{h_2}3^{h_3}4^{h_4}). \tag{13}$$

Upon squaring, these contributions will be the same as the squared contributions from the positive helicity emitted gluon MHV amplitudes; we will therefore simply multiply our final squared, summed result by 2 to account for these additional contributions.

We therefore have that

$$\langle|\mathcal{A}_5|^2\rangle = 2g^2\tilde{C}_F\frac{s_{12}}{s_{15}s_{52}}\langle|\mathcal{A}_4|^2\rangle, \tag{14}$$

$$\equiv |\mathcal{J}_g^{(1)}|^2\langle|\mathcal{A}_4|^2\rangle \tag{15}$$

where $\langle|\mathcal{A}_4|^2\rangle$ is given by the square of the $qg \to qg$ amplitude and we have defined the single gluon emission kernel $|\mathcal{J}_g^{(1)}|^2$ in the second line. Notice in the first line the critical overall factor of 2 due to the $\overline{\text{MHV}}$ contributions.

One may write the outgoing parton momenta in the usual way for high energy QCD processes and find that the emission spectrum derived above gives

$$\frac{dN_g^{(1)}}{d^3k} \simeq C_F\frac{\alpha_s}{\pi^2}\frac{1}{x}\frac{1}{k_\perp^2}, \tag{16}$$

in exact agreement with the single gluon radiation spectrum of [15] associated with the scattering of a hard quark, in the limit of a massless quark.

Now consider the same process with two gluons soft/collinear with the outgoing fermion. We have that to leading order in kinematics, i.e. for terms enhanced by inverses of $\langle 15\rangle$, $\langle 16\rangle$, and/or $\langle 56\rangle$,

$$\begin{aligned} &i\mathcal{M}(1_{\bar{q}}^{-}2_{q}^{+}3^{-}4^{+}5^{+}6^{+}) \\ &\quad=\sum_{\sigma} T^{\sigma(3)}\cdots T^{\sigma(6)} i M\big(1_{\bar{q}}^{-}2_{q}^{+}\sigma(3^{+})\cdots\sigma(6^{+})\big) \\ &\quad= i g^{4}\langle 14\rangle^{3}\langle 24\rangle\left[\frac{T^{3}T^{4}T^{5}T^{6}}{\langle 12\rangle\langle 23\rangle\langle 34\rangle\langle 45\rangle\langle 56\rangle\langle 61\rangle}+\frac{T^{3}T^{4}T^{6}T^{5}}{\langle 12\rangle\langle 23\rangle\langle 34\rangle\langle 46\rangle\langle 65\rangle\langle 51\rangle}+(3\leftrightarrow 4)\right] \end{aligned} \tag{17}$$

Just as in the previous case we have that

$$\begin{aligned} \frac{1}{\langle 12\rangle\langle 23\rangle\langle 34\rangle\langle 45\rangle\langle 56\rangle\langle 61\rangle} &= \frac{1}{\langle 12\rangle\langle 23\rangle\langle 34\rangle\langle 41\rangle}\frac{[34]}{[34]}\frac{\langle 41\rangle}{\langle 45\rangle\langle 56\rangle\langle 61\rangle} \\ &\simeq -\frac{1}{\langle 12\rangle\langle 23\rangle\langle 34\rangle\langle 41\rangle}\frac{\langle 21\rangle}{\langle 25\rangle\langle 56\rangle\langle 61\rangle}. \end{aligned} \tag{18}$$

The above equation will also hold for $5\leftrightarrow 6$ and $3\leftrightarrow 4$. Therefore we find that

$$\begin{aligned} i\mathcal{M}(1_{\bar{q}}^{-}2_{q}^{+}3^{-}4^{+}5^{+}6^{+}) &\simeq i g^{4}\frac{\langle 14\rangle^{3}\langle 24\rangle}{\langle 12\rangle}\left[\frac{T^{3}T^{4}}{\langle 23\rangle\langle 34\rangle\langle 41\rangle}\quad\frac{T^{5}T^{6}}{\langle 25\rangle\langle 56\rangle\langle 61\rangle}+\frac{T^{6}T^{5}}{\langle 26\rangle\langle 65\rangle\langle 51\rangle}\right)+(3\leftrightarrow 4)\Bigg] \\ &= i\mathcal{M}_{4}(1_{\bar{q}}^{-}2_{q}^{+}3^{-}4^{+})\mathcal{S}_{2}(5,6), \end{aligned} \tag{19}$$

where the two particle soft factor is

$$\mathcal{S}_{2}(5,6)\equiv\sum_{\sigma} T^{\sigma(5)}T^{\sigma(6)}S_{2}(\sigma(5),\sigma(6)), \tag{20}$$

where we'd defined the two particle soft factor partial amplitude

$$S_{2}(5,6)\equiv\frac{g^{2}\langle 12\rangle}{\langle 25\rangle\langle 56\rangle\langle 61\rangle}. \tag{21}$$

One may straightforwardly brute force square the amplitude

$$\begin{aligned} |\mathcal{S}_{2}(5,6)|^{2} &= \left|\frac{g^{2}\langle 12\rangle}{\langle 56\rangle}\left(T^{5}T^{5}\frac{1}{\langle 25\rangle\langle 61\rangle}-T^{6}T^{5}\frac{1}{\langle 26\rangle\langle 51\rangle}\right)\right|^{2} \\ &= \frac{g^{4}s_{12}}{s_{56}}\left[\tilde{C}_{F}^{2}\left(\frac{1}{s_{16}s_{25}}+\frac{1}{s_{26}s_{15}}\right)-\tilde{C}_{F}(\tilde{C}_{F}-\tilde{C}_{A})\left(\frac{1}{\langle 25162]}+\text{c.c.}\right)\right] \end{aligned} \tag{22}$$

We may simply this last expression to find

$$|\mathcal{S}_{2}(5,6)|^{2}=g^{4}\left[\tilde{C}_{F}^{2}\frac{s_{12}^{2}}{s_{15}s_{25}s_{16}s_{26}}+\tilde{C}_{F}\tilde{C}_{A}\frac{s_{12}}{s_{56}}\frac{\text{tr}(2516)}{s_{15}s_{25}s_{16}s_{26}}\right]. \tag{23}$$

One can clearly see that the first term is, up to an (important!) factor of 2, the "square" of the one gluon bremsstrahlung emission kernel:

$$\tilde{C}_{F}^{2}\frac{s_{12}^{2}}{s_{15}s_{25}s_{16}s_{26}}=\frac{1}{2}|\mathcal{S}_{1}(5)|^{2}|\mathcal{S}_{1}(6)|^{2}. \tag{24}$$

The second term is the non-Abelian correction to the "trivial" Poisson convolution that one finds in QED. (Notice that the non-Abelian correction goes to 0 as $\tilde{C}_{A}=N$ goes to 0.)

4. Conclusions

The non-trivial challenge in using amplitude techniques on $qg \to qg + n\,g$ scattering for $n > 1$, as was shown here, is that next to maximal helicity violating diagrams must be included: including only the MHV (and $\overline{\text{MHV}}$) contributions as in [11] misses $1/2^{n-1}$ contributing helicity configurations. The calculation of these additional diagrams requires the use of the BCFW recursion relation. Although difficult, and perhaps somewhat tedious, these methods will produce results, and the number of diagrams that must be considered is significantly smaller than when using traditional pQCD techniques. There is therefore hope that we may be able to adapt these techniques to the physical processes that we believe are relevant in heavy ion collisions.

5. Acknowledgments

The author gratefully acknowledges financial support from the South African National Research Foundation, the South Africa-CERN Collaboration, and from the University of Cape Town.

References

[1] Wiedemann U A 2010 521–562 [Landolt-Bornstein23,521(2010)] (0908.2306)

[2] Majumder A and Van Leeuwen M 2011 *Prog. Part. Nucl. Phys.* **66** 41–92 (1002.2206)

[3] Gyulassy M, Levai P and Vitev I 2002 *Phys. Lett.* **B538** 282–288 (nucl-th/0112071)

[4] Arnold P, arXiv:1904.04264

[5] Dreiner H K, Haber H E and Martin S P 2010 *Phys. Rept.* **494** 1–196 (0812.1594)

[6] Dixon L J 2014 A brief introduction to modern amplitude methods *Proceedings, 2012 European School of High-Energy Physics (ESHEP 2012): La Pommeraye, Anjou, France, June 06-19, 2012* pp 31–67 (1310.5353)

[7] Henn J M and Plefka J C 2014 *Lect. Notes Phys.* **883** pp.1–195

[8] Elvang H and Huang Y t 2015 *Scattering Amplitudes in Gauge Theory and Gravity* (Cambridge University Press) ISBN 9781316191422, 9781107069251

[9] Catani S and Grazzini M 2000 *Nucl. Phys.* **B570** 287–325 (hep-ph/9908523)

[10] Rasoanaivo A N and Horowitz W A, arXiv:1712.06292

[11] Rabemananajara T R and Horowitz W A 2017 *J. Phys. Conf. Ser.* **889** 012021

[12] Peskin M E and Schroeder D V 1995 *An Introduction to quantum field theory* (Reading, USA: Addison-Wesley) ISBN 9780201503975, 0201503972 URL `http://www.slac.stanford.edu/~mpeskin/QFT.html`

[13] Johansson H and Ochirov A 2016 *JHEP* **01** 170 (1507.00332)

[14] Britto R, Cachazo F, Feng B and Witten E 2005 *Phys. Rev. Lett.* **94** 181602 (hep-th/0501052)

[15] Djordjevic M and Gyulassy M 2004 *Nucl. Phys.* **A733** 265–298 (nucl-th/0310076)

Quantum secret sharing with Greenberger Horne Zeilinger states

Comfort Sekga and Mhlambululi Mafu

Department of Physics and Astronomy, Botswana International University of Science and Technology, P/Bag 16, Palapye, Botswana

Abstract. We propose a scheme for sharing an unknown three-particle quantum state to n agents by using Greenberger-Horne-Zeilinger states. Firstly, we introduce the five party quantum state sharing scheme of arbitrary three particle unknown quantum states where Alice starts by sharing four Greenberger-Horne-Zeilinger entangled states with her four agents and performs three Greenberger-Horne-Zeilinger state measurements on her particles followed by two single particle measurements on the Hadamard basis. One of the agents Bob1 performs single measurement on her particle and three other agents each perform unitary transformations on their particles to recover the unknown state. Subsequently, we propose the generalized multiparty quantum state sharing scheme for an arbitrary three particle state.

1. Introduction

Quantum secret sharing (QSS) is a useful procedure of quantum information which involves the splitting and distribution of a secret message to multiple agents. The split message is sent to untrusted parties who have to collaborate to recover the message [1]. A certain subset of agents can recover the message whilst other participants cannot get the full information about it. QSS is divided into two areas, the first one is based on sharing classical information with the secret distributed among all agents with help of quantum mechanics [2]. The second area deals with the distribution of quantum information with the secret being an arbitrary unknown quantum state [3]. This distribution of quantum state was referred as quantum state sharing (QSTS) by Lance *et. al* in 2004 [4]. QSTS has wide range of applications which include joint sharing of quantum money, quantum error correction and quantum information networks [5]. Various protocols of QSTS have been realized both experimentally and theoretically. These protocols exploit various quantum resources which includes entanglement to distribute an arbitrary single particle, two particle and multiple particle state [6, 7, 8].

To date several entangled states such as Bell states [5, 9] and GHZ states [10] have been featured in QSTS protocols. The first QSS scheme was proposed by Hillery *et. al* which used three and four particle Greenberger-Horne-Zeilinger (GHZ) state to distribute private message to two and three agents respectively [1]. Thereafter, Einstein, Podolsky and Rosen (EPR) pair of entangled states has been extensively used to share an arbitrarily unknown single and two-particle quantum state. Deng *et. al* proposed a scheme with an ordered n pairs of EPR states for multiparty quantum secret splitting [11]. Recently, Yuan *et. al* developed a protocol for tripartite QSTS of an arbitrary unknown quantum state which has the advantage of consuming less quantum and classical resources [12].

In this work, we propose a scheme for sharing an unknown three-particle quantum state to n agents by using GHZ states. In section II, we introduce the five party quantum state sharing scheme of arbitrary three particle unknown quantum state, where Alice starts by sharing four GHZ entangled states with her four agents, and performs three GHZ state measurements on her particles followed by two single particle measurements on the Hadamard basis. One of the agents, Bob1, performs a single measurement on her particle and the three other agents each perform unitary transformations on their particles to recover the unknown state. This is followed by section III where we propose the generalized multiparty quantum state sharing scheme for an arbitrary three particle state. In this section, we show that our proposed scheme fairly performs better than other existing schemes. Finally, we provide concluding remarks in the last section.

2. Five party QSTS of an arbitrary three particle unknown state using GHZ states
In our proposed scheme, Alice shares an arbitrary three particle of an unknown quantum state with four agents referred to as Bob1, Bob2, Bob3 and Bob4 as shown in the steps in Figure 1. Bob4 acts as the controller whilst the remaining three parties act as retrievers of the unknown state. They each have to perform a unitary transformation to their particle to recover the state. The unknown quantum state is expressed as;

$$|\Psi\rangle_{x,y,z} = (a|000\rangle + b|011\rangle + c|101\rangle + d|001\rangle + e|110\rangle + f|010\rangle + g|100\rangle + h|111\rangle)_{xyz}, \quad (1)$$

where x, y and z are three particles in the state $|\Psi\rangle$ and a, b, c, d, e, f, g and h are complex numbers that satisfy the normalization condition

$$|a|^2 + |b|^2 + |c|^2 + |d|^2 + |e|^2 + |f|^2 + |g|^2 + |h|^2 = 1. \quad (2)$$

For sharing an arbitrary three qubit state, Alice first share four 3 particle-GHZ states $|\phi\rangle$ with her four agents as indicated on the first block in Figure 1. The three particle-GHZ states can be generalized as follows:

$$\begin{aligned}
|\phi^{\pm}\rangle_{1,2} &= 1/2\sqrt{2}(|000\rangle \pm |111\rangle) \\
|\phi^{\pm}\rangle_{3,4} &= 1/2\sqrt{2}(|011\rangle \pm |100\rangle) \\
|\phi^{\pm}\rangle_{5,6} &= 1/2\sqrt{2}(|101\rangle \pm |010\rangle) \\
|\phi^{\pm}\rangle_{7,8} &= 1/2\sqrt{2}(|001\rangle \pm |110\rangle). \quad (3)
\end{aligned}$$

Assuming that all 3 particle-GHZ states prepared by Alice are

$$|\phi^{\pm}\rangle = \frac{1}{2\sqrt{2}}(|000\rangle + |111\rangle), \quad (4)$$

then the whole system of 15 particles can be written as

$$\begin{aligned}
|\Phi\rangle_{xyz123456789101112} &= |\psi\rangle_{xyz} \otimes |\phi^{+}\rangle_{123} \otimes |\phi^{+}\rangle_{456} \otimes |\phi^{+}\rangle_{789} \otimes |\phi^{+}\rangle_{101112} \\
&= |\psi\rangle_{xyz}(a|000\rangle + b|011\rangle + c|101\rangle + d|001\rangle + e|110\rangle + f|010\rangle + g|100\rangle \\
&+ h|111\rangle)_{xyz} \otimes \frac{1}{2\sqrt{2}}(|000\rangle + |111\rangle)_{123} \otimes \frac{1}{2\sqrt{2}}(|000\rangle + |111\rangle)_{456} \\
&\otimes \frac{1}{2\sqrt{2}}(|000\rangle + |111\rangle)_{789} \otimes \frac{1}{2\sqrt{2}}(|000\rangle + |111\rangle)_{101112}. \quad (5)
\end{aligned}$$

After sharing the 4 GHZ states, Bob1, Bob2, Bob3 and Bob4 are in possession of particle 3, 6, 9 and 12 respectively whilst Alice retains other particles. She then applies the CNOT gate

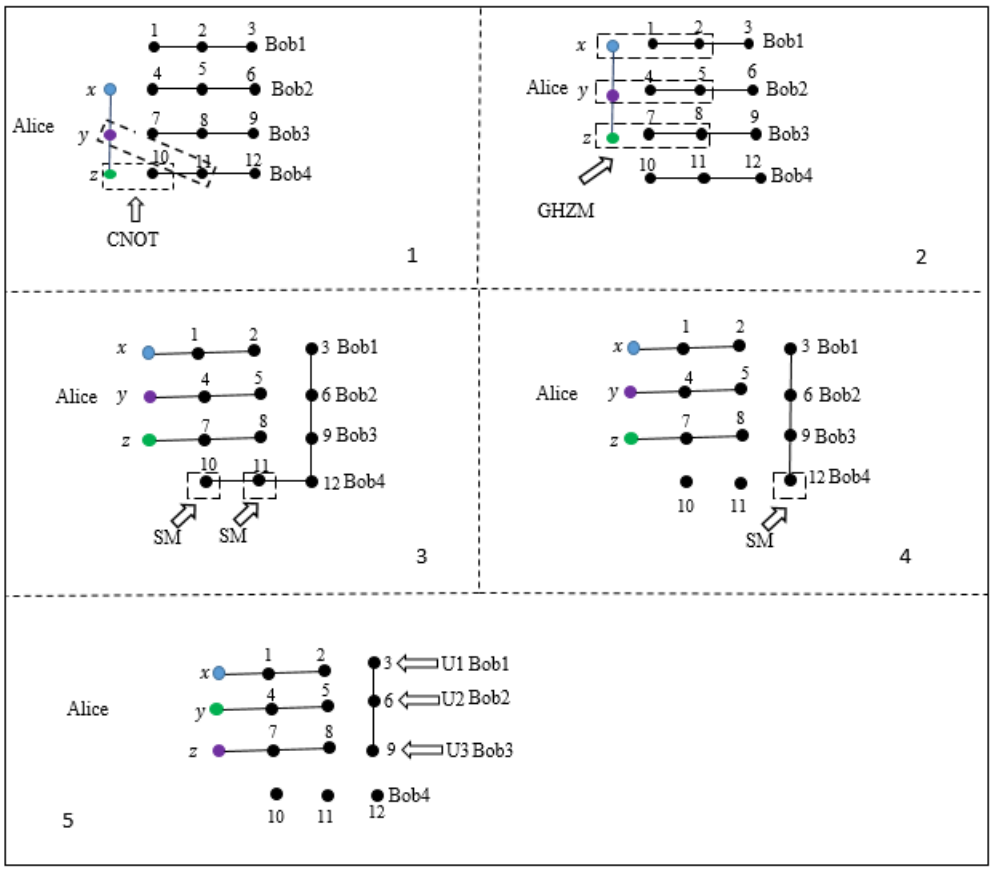

Figure 1. The steps for the proposed five party QSTS of unknown three particle quantum state. In block 1 Alice starts by sharing 4 GHZ states with Bob1, Bob2, Bob3 and Bob4 and then performs a Controlled-Not gate operation (CNOT) on particles $(y, 11)$, $(z, 10)$. In block 2 Alice then carries out GHZ state measurement (GHZM) on particles $(x, 1, 2)$, $(y, 4, 5)$ and $(z, 7, 8)$. In block 3 Alice executes single particle measurements(SM) on particle 10 and 11. In block 4 Bob4 performs a single particle measurement(SM) on particle 12. Finally, in block 5 Bob1, Bob2 and Bob3 perform unitary operations (U1, U2 and U3) on their particles.

operation on four particles $x, y, 10$ and 11. In the proposed scheme, x and y acts as control particles whilst 10 and 11 are target particles. Thereafter, Alice carries out three GHZ state measurements on the particles $(x, 1, 2), (y, 4, 5)$ and $(z, 7, 8)$ respectively as illustrated in second block of Figure 1. Without loss of generality, if Alice's measurements results are $|\phi^+\rangle$ then the collapsed state of the remaining particles can be written as

$$\begin{aligned}|\Psi\rangle_{369101112} &= {}_{x12}\langle\phi^+| \otimes {}_{y45}\langle\phi^+| \otimes {}_{x78}\langle\phi|\Psi\rangle_{123456789101112} \\ &= (a|000000\rangle + a|000111\rangle + b|011110\rangle + b|011001\rangle + c|101101\rangle + c|101010\rangle \\ &+ d|001010\rangle + d|001101\rangle + e|110100\rangle + e|110011\rangle + f|010100\rangle + f|010011\rangle \\ &+ g|100000\rangle + g|100111\rangle + h|111110\rangle + h|111001\rangle. \end{aligned} \quad (6)$$

Alice then executes two single measurements on particles 10 and 11 with the basis X $\{|+x\rangle = \frac{1}{\sqrt{2}}(|0\rangle + |1\rangle), |-x\rangle = \frac{1}{\sqrt{2}}(|0\rangle - |1\rangle\}$ (ref. block 3 of Figure 1). If she obtains

$|+x\rangle$ as her measurement result, then the collapsed state becomes

$$\begin{aligned}|\Phi\rangle_{36912} &= {}_{10}\langle +x|_{11}\langle +x|\Phi\rangle_{369101112} \\ &= (a|0000\rangle + a|0001\rangle + b|0110\rangle + b|0111\rangle + c|1011\rangle + c|1010\rangle + c|0010\rangle + d|0011\rangle \\ &+ e|1100\rangle + e1101 + f0100 + f0101 + g|1000\rangle + g|1001\rangle + h|1110\rangle + h|1111\rangle. \end{aligned} \quad (7)$$

Alice reveals her measurement results to her agents via a classical channel. To reconstruct the original state, Bob4 performs a single measurement on the standard basis and publicly informs Bob1, Bob2 and Bob3 about his results as shown in block 4 of Figure 1. Bob1, Bob2 and Bob3 then collaborate to recover the unknown state by performing appropriate unitary transformations on their particles. This is depicted in block 5 of Figure 1. The required unitary operators are $(\sigma_z, \sigma_x, \mathbb{1})$, where $\sigma_z = |0\rangle\langle 0| - |1\rangle\langle 1|, \sigma_x = |0\rangle\langle 1| + |1\rangle\langle 0|$ and $\mathbb{1} = |0\rangle\langle 0| + |1\rangle\langle 1|$.

For instance, if Alice's measurement results are $|\phi^+\rangle_{x12}, |\phi^+\rangle_{y45}, |\phi^+\rangle_{x78}, |-x\rangle_{10}, |+x\rangle_{11}$ and Bob's results are $|1\rangle_{12}$, then the collapsed state can be described as

$$|\Phi\rangle_{369} = (-a|000\rangle + b|011\rangle - c|101\rangle - d|001\rangle + e|110\rangle + f|010\rangle - g|100\rangle + h|111\rangle)_{369}. \quad (8)$$

To recover the original state then Bob1, Bob2 and Bob3 have to perform the following unitary operations $(\mathbb{1} \otimes \sigma_z\sigma_x \otimes \mathbb{1})$, that is, Bob1 and Bob3 have to do nothing on their particle whilst Bob2 has to do the phase flip operation followed by the bit flip on his particle. This can be explicitly shown as;

Bob1's operation:

$$(|0\rangle\langle 0| + |1\rangle\langle 1|) \otimes (-a|000\rangle + b|011\rangle - c|101\rangle - d|001\rangle + e|110\rangle + f|010\rangle - g|100\rangle + h|111\rangle)_{369}$$

This yields;

$$(-a|000\rangle + b|011\rangle - c|101\rangle - d|001\rangle + e|110\rangle + f|010\rangle - g|100\rangle + h|111\rangle)_{369}.$$

Bob2 has to carry out the phase flip and bit flip on his particle,

$$(|0\rangle\langle 1| - |1\rangle\langle 0|) \otimes (-a|000\rangle + b|011\rangle - c|101\rangle - d|001\rangle + e|110\rangle + f|010\rangle - g|100\rangle + h|111\rangle)_{369},$$

which gives,

$$|\Phi\rangle_{369} = (a|010\rangle + b|101\rangle + c|111\rangle + d|011\rangle + e|100\rangle + f|000\rangle + g|110\rangle + h|101\rangle)_{369},$$

which is the original states sent by Alice to her agents.

3. QSTS of an Arbitrary m-Particle State with n Agents

Subsequently, this three-particle scheme can be generalised to the case of sharing m-particle state with n agents (as shown in Figure 2). Alice start by sharing n GHZ states with Bob$i$ $(i = 1, \ldots, n)$ and hence the whole system can be written as

$$\begin{aligned}|\Psi\rangle \equiv (\sum_{ij\ldots k} \alpha_{\underbrace{ij\ldots k+}_{m}} |\underbrace{ij\ldots k+}_{m}\rangle_{x1x2\ldots xm}) \otimes \frac{1}{2\sqrt{2}}(|000\rangle + |111\rangle)_{123} \otimes \frac{1}{2\sqrt{2}}(|000\rangle + |111\rangle)_{456} \otimes \\ \cdots \otimes \frac{1}{2\sqrt{2}}(|000\rangle + |111\rangle)_{n-2,n-1,n}, \end{aligned} \quad (9)$$

where $i, j, \ldots, k \in \{0, 1\}andx1, x2, \ldots, xm$ are the m particles in the unknown state.

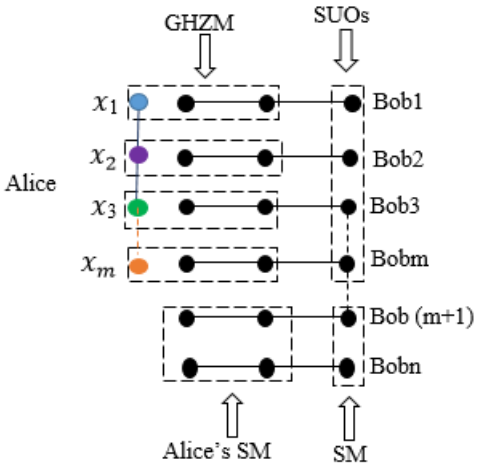

Figure 2. The principles of our proposed QSTS scheme of an arbitrary m-particle state. Alice performs m GHZ state measurements (GHZM) and $2(n-m)$ single particle measurements (SM). Controllers carries out $(n-m)$ single particle measurements and other agents performs single particle unitary operations (SUOs) to recover the unknown state.

Alice then carries out $2(n-m)$ CNOT operations and performs m GHZ state measurements followed by $2(n-m)$ single particle measurements on her particles. Consequently, the unknown state is transferred into the particles in the possession of her agents. The controllers then executes $(n-m)$ single particle measurements in the standard basis and publishes their results. The m agents collaborate to recover the unknown state by performing the unitary operations to their particles(see Figure 2).

In our scheme, the quantum channel is set up using the decoy-photon technique to detect eavesdropping as explained in [7]. The proportion of the decoy photons is so negligible that the intrinsic efficiency of qubits in our scheme approaches 100% as given by the formula [13];

$$\eta_q \equiv \frac{q_u}{q_t}, \tag{10}$$

where q_u is the number of useful qubits in the QSTS and q_t is the number of transmitted qubits. The total efficiency of QSTS scheme is defined as

$$\eta_t = \frac{q_s}{q_u + b_t}, \tag{11}$$

where q_s is the number of qubits that consists of the quantum information to be shared, q_u is the number of useful qubits in the QSTS and b_t is the number of classical bits transmitted. In our scheme $q_u = 3n$, $q_s = 3$ and $b_t = 3n$ which gives the total efficiency, η_t, as $1/2n$. This is equivalent to $1/8$ for a five party QSTS. This efficiency greater than that in the QSTS by Deng et al [11, 9] as depicted in Table 1. Though these schemes in reference [11, 9] uses EPR pairs which are easier to prepare practically as compared to GHZ states in our scheme, they involve a lot operations performed by the parties which increases the difficulty of the schemes. For instance, Alice needs to perform 10 joint GHZ states measurements in reference [11] which is practically difficult to implement in the present moment. The scheme by Sheng et al in ref [10] has better efficiency as compared to our scheme. However, considering the fact that 6 GHZ states are

needed to be prepared, our scheme is more convenient in terms of resource consumption as only 4 GHZ states are required.

Moreover, there are other existing schemes which uses non maximally entangled states which are robust against environmental effects and easier to implement [6]. However, these schemes are asymmetric, therefore only one agent can retrieve the unknown state as compared to our scheme in which any of the agents can act as a receiver. The symmetry created by maximally entangled states allows any of the agents to act as a receiver of the unknown state with the help of other agents.

Table 1. The comparison between our scheme and the other previous schemes for sharing three particle state and two particle state with five parties. QR-quantum resources, NO-necessary operations, CR-Classical resources, GHZM-GHZ state joint measurement, BM-Bell state measurement, SM- single particle measurement, Single particle unitary operation, η_t-total efficiency

Schemes	QR	NO	CR	η_t
Sheng et al[10]	6 GHZ States	3 GHZM, 9 SMs and 3SUOs	15 bits	1/6
Deng et al[11]	8 EPR pairs	10 GHZM, 6 SMs and 2 SUOs	10 bits	1/13
Deng et al[9]	5 EPR pairs	5 BMs and 3 SUOs	10 bits	1/10
Our scheme	4 GHZ States	3 GHZM, 3 SMs and 3 SUOs	12 bits	1/8

4. Conclusion

In this work we presented a scheme for sharing an unknown three particle state with n agents by using GHZ states. Our scheme shows that three particle state can be reconstructed by agents with 100% probability provided that they act honestly. The security of this scheme against eavesdropping can be accomplished by using the decoy state methods proposed in refs [7]. Our scheme uses less quantum resources as only n-GHZ states are required and has few quantum operations achieving the total efficiency of $\eta_t = 1/2n$. Further, we proposed the generalized multiparty quantum state sharing scheme for an arbitrary three particle state. Our proposed schemes indicate a better performance than existing schemes and also use less resources.

Acknowledgements

The authors would like to acknowledge with thanks the funding from Botswana International University of Science and Technology Research Initiation Grant R00015.

References

[1] Hillery M, Bužek V and Berthiaume A 1999 *Physical Review A* **59** 1829
[2] Sergienko A V 2005 *Quantum communications and cryptography* (CRC Press)
[3] Cerf N J, Leuchs G and Polzik E S 2007 *Quantum information with continuous variables of atoms and light* (Imperial College Press)
[4] Lance A M, Symul T, Bowen W P, Sanders B C and Lam P K 2004 *Physical Review Letters* **92** 177903
[5] Shi R H, Huang L S, Yang W and Zhong H 2011 *Quantum Information Processing* **10** 231–239
[6] Jiang M, Huang X, Zhou L, Zhou Y and Zeng J 2012 *Chinese Science Bulletin* **57** 1089–1094
[7] Xi-Han L, Fu-Guo D and Hong-Yu Z 2007 *Chinese Physics Letters* **24** 1151
[8] Cleve R, Gottesman D and Lo H K 1999 *Physical Review Letters* **83** 648
[9] Deng F G, Li X H, Li C Y, Zhou P and Zhou H Y 2006 *The European Physical Journal D-Atomic, Molecular, Optical and Plasma Physics* **39** 459–464
[10] Sheng Y B, Deng F G and Zhou H Y 2008 *The European Physical Journal D* **48** 279–284
[11] Deng F G, Li X H, Li C Y, Zhou P and Zhou H Y 2006 *Physics Letters A* **354** 190–195
[12] Yuan H, Liu Y M, Zhang W and Zhang Z J 2008 *Journal of Physics B: Atomic, Molecular and Optical Physics* **41** 145506
[13] Cabello A 2000 *Physical Review Letters* **85** 5635

Solving the Schrödinger Equation using Sinc Functions in one and two dimensions, employing Python and Numpy

Obiageli Lovenda Ezenwachukwu and Moritz Braun
Department of Physics, UNISA, PO Box 392, Pretoria 0003

Abstract. In this contribution orthonormal sinc basis function are used to numerically solve the Schrödinger equation in one and two dimensions for a number of potentials. The calculations are done using Python and the numpy module. The convergence is found to be quick and, for the Morse potential, also agrees with the theoreticallly expected behaviour. In the two dimensional case code optimizations lead to a large speed-up.

1. Introduction

Sinc functions as a basis set have been used extensively for obtaining the approximate solutions of ordinary differential equations, partial differential equations and integral equations [1, 2]. The sinc numerical method is easily implemented and the results obtained are of good accuracy [3, 4]. It has been shown that sinc numerical methods are distinguished by exponentially decaying errors [5, 6]; they have convergence rates of $O\left(\exp\left(-k\sqrt{N}\right)\right)$ with some $k > 0$, [7], where N is the number of nodes or basis functions used.
In this contribution the numerical solution of the Schrödinger equation for a variety of potentials in both one and two dimensions is demonstrated using the scripting languange Python[8] together with the module numpy[9].

2. Solving the one dimensional Schrödinger equation using Sinc Basis Functions

The normalized sinc function is on the line $-\infty < x < \infty$ defined by

$$\mathrm{sinc}(x) = \frac{\sin(\pi x)}{\pi x}, \qquad \int_{-\infty}^{\infty} \mathrm{sinc}(x)dx = 1. \tag{1}$$

The zeroes of this function are all integer values of x. An orthonormal set of functions can be obtained from the sinc function by shifting it by all positive and negative integers. In order to make this basis set also suitable for the expansion of quickly varying functions, we define the basis functions, also introducing a stretching parameter h, as

$$s_i(x) = \frac{1}{\sqrt{h}} \frac{\sin(\pi(\frac{x}{h} - i))}{\pi(\frac{x}{h} - i)}\,. \tag{2}$$

 ISBN: 978-0-620-88875-2

Here h is the distance between subsequent zeroes of these basis functions, i is the index running in principle over all integer values from $-\infty$ to ∞ and the first factor on the right hand side provides for normalization.
We now restrict i to the interval $[-n, n]$ and define the basis functions for numerical calculations by

$$f_j(x) = s_{-n+j-1}(x), \tag{3}$$

with $j = 1, 2, ...2n+1$. This is a orthonormal basis of dimension $N = 2n+1$. Choosing n and h is equivalent to a cut-off at $x_{max} = nh$. This fixes the boundary conditions and determines the accuracy.
Thus the ansatz for the solution of the Schrödinger equation is given by

$$\psi(x) = \sum_{i=1}^{N} c_i f_i(x)\,. \tag{4}$$

The Schrödinger equation

$$\left\{-\frac{d^2}{dx^2} + V(x)\right\}\psi_\nu(x) = e_\nu \psi_\nu(x) \tag{5}$$

is now solved via the variational method, leading to the eigenvalue problem

$$H\mathbf{u}_\nu = e_\nu \mathbf{u}_\nu \tag{6}$$

with

$$h_{ij} = k_{ij} + v_{ij}\,, \tag{7}$$

$$k_{ij} = \int f_i'(x) f_j'(x) dx = \begin{cases} \frac{\pi^2}{3h^2} & i = j; \\ (-1)^{|i-j|}\frac{1}{h^2}\frac{2}{|i-j|^2} & i \neq j. \end{cases} \tag{8}$$

and

$$v_{ij} = \int_{-x_{\max}}^{x_{\max}} f_i(x) V(x) f_j(x) dx\,. \tag{9}$$

The analytic expression for the kinetic energy matrix elements has been obtained by using the Fourier expansion of the sinc function and the Parseval theorem. The potential matrix was evaluated by repeated Gauss-Legendre integration, where the intervals are coinciding with the intervals between subsequent zeroes of the sinc basis functions. For this integration we used $N_{\mathrm{GL}} = 10$ points and weights in each interval, resulting in a total number of Integration points of $20n$.

3. Numerical Results for one Dimension

3.1. Numerical calculations for the one dimensional harmonic oscillator

For verification purposes we first considered the harmonic oscillator. The energy eigenvalues of the quantum harmonic oscillator with the Hamiltonian

$$H = -\frac{d^2}{dx^2} + x^2 \tag{10}$$

are

$$E_\nu = 2\nu + 1\,, \tag{11}$$

i.e. all odd numbers 1, 3, 5, 7,$\cdots$.
Employing Python and numpy, and using the sinc basis functions for $x_{\max} = 8$, the results of the numerical calculations obtained are shown in table 1, and the lowest eigenvalues $1, 3, 5, 7$ are obtained very accurately. The calculations were done for $nh = x_{max} = 8$. Convergence is seen to be rather quick as function of n.

Table 1. Results of numerical calculations for harmonic oscillator

n	h	E_0	E_1	E_2	E_3
8	1.0	1.00013274618	3.00388708934	5.01965658349	7.1426916954
9	0.8889	1.00001043728	3.00040366538	5.00262094231	7.026576271
10	0.8	1.00000059941	3.00002946274	5.00023921435	7.00326643666
11	0.7273	1.00000002524	3.00000153079	5.00001518651	7.00026666304
12	0.6667	1.00000000078	3.00000005692	5.00000067774	7.00001475924
13	0.6154	1.00000000002	3.00000000152	5.00000002142	7.00000056346
14	0.5714	1.0	3.00000000003	5.00000000048	7.000000015
15	0.5333	1.0	3.0	5.00000000001	7.00000000028
16	0.5	1.0	3.0	5.0	7.0

3.2. Numerical calculations for Morse potential

The Morse potential has been used to model the vibrational excitations of a chemical bond for diatomic molecules. The potential is in this model given by[10]

$$V_{\text{Morse}}(x) = D(e^{-2x/a} - 2e^{-x/a}). \tag{12}$$

i.e. the Hamiltonian becomes

$$H = -\frac{1}{2\mu}\frac{d^2}{dx^2} + D(e^{-2x/a} - 2e^{-x/a}) \tag{13}$$

and, for $\mu = 1/2$ and a =1, the eigenvalues are given by[10]

$$E_\nu = -D\left\{1 - \frac{1}{\sqrt{D}}\left(\nu + \frac{1}{2}\right)\right\}^2 \tag{14}$$

with ν restricted by the condition, that the contents of the curly bracket must be positive. Employing the Python code for the sinc basis function for $D = 9$ and $x_{\max} = 15$, the results as shown in table 2 are obtained.

From the theoretical convergence studies [7] we expect the following to hold for the ν-th

Table 2. Results of numerical calculations for Morse potential

n	h	E_0	E_1	E_2
10	1.5	-3.76039	-0.25006	0.07333
15	1.0	-5.61145	-1.35904	0.00106
16	0.9375	-5.78207	-1.54867	-0.02423
17	0.88235	-5.91164	-1.70946	-0.05513
18	0.83333	-6.00860	-1.84134	-0.08795
19	0.78947	-6.08010	-1.94651	-0.11947
20	0.75	-6.13196	-2.02827	-0.14810
22	0.68182	-6.19503	-2.13663	-0.19210
25	0.6	-6.23361	-2.21183	-0.22830
27	0.55555	-6.24283	-2.23225	-0.23947
30	0.5	-6.24798	-2.24473	-0.24679

eigenvalue resulting from the calculations as function of N:

$$E_\nu(N) = E_\nu + b_\nu \exp(-c_\nu\sqrt{N})\,. \tag{15}$$

Gnuplot was used both for creating the figures as well as fitting the results to the expected convergence behaviour. From figure 1 and figure 2 it is evident, that the eigenvalues agree reasonably well with the fits to equation (15).

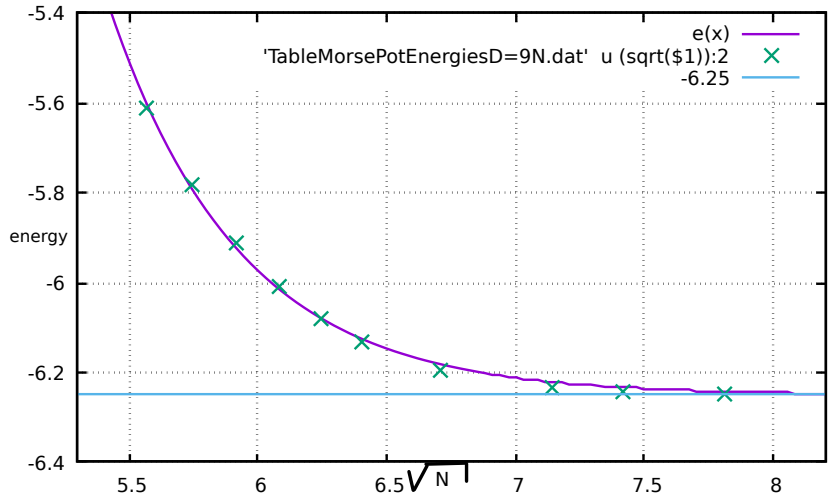

Figure 1. Convergence for ground state of Morse potential

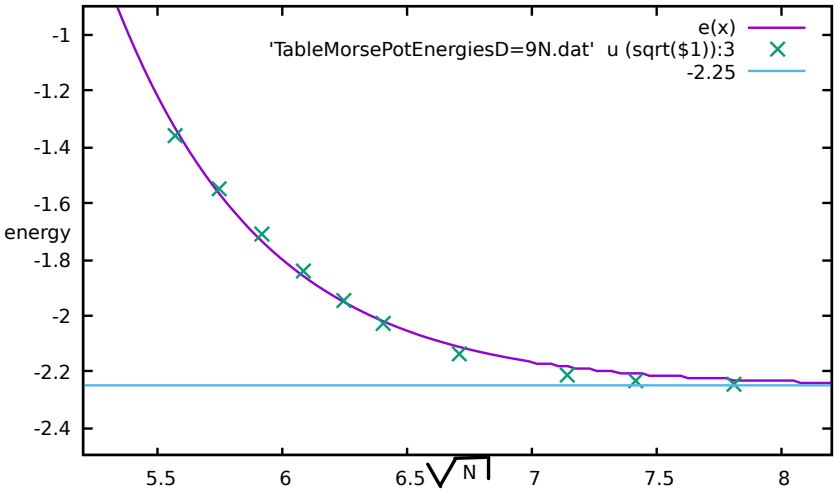

Figure 2. Convergence for first excited state of Morse potential

4. Solving the two dimensional Schrödinger equation

The two dimensional Schrödinger equation was solved numerically by expanding the wave function $\psi(x, y)$ in terms of products of one dimensional basis functions, i.e.

$$\psi(x, y) = \sum c_\alpha f_{i_\alpha}(x) f_{j_\alpha}(y)\,, \tag{16}$$

where i_α and j_α are suitably defined functions of α. Thus the basis functions used in x and y are indentical, the domain of expansion is $[-x_{\max}, x_{\max}] \times [-x_{\max}, x_{\max}]$, and the total number of basis functions becomes N^2.

In two dimensions the Hamiltonian is given by

$$H = -\frac{\partial^2}{\partial x^2} - \frac{\partial^2}{\partial y^2} + V(x, y)\,. \tag{17}$$

 ISBN: 978-0-620-88875-2

Evaluation of the matrix elements $h_{\alpha\beta}$ then proceeds analytically for the kinetic energy term and numerically for the potential energy term in a simliar fashion as in one dimension. It should be be noted, that the numerical integration requires much more CPU time, since there are now $4n^2N_{\rm GL}^2$ integration points.

5. Numerical Results for two Dimensions

5.1. Results for two dimensional harmonic oscillator

Numerical Calculations were done for $nh = x_{max} = y_{max} = 8$ and $N_{\rm GL} = 10$ and the results are given in table 3

Table 3. Results of Numerical Calculations for 2-D Harmonic Oscillator

n	h	E_0	E_1	E_2	E_3	E_4	E_5
7	1.1429	2.002428	4.027192	4.027192	6.051474	6.099747	6.100884
8	1.0	2.000262	4.003994	4.003994	6.007651	6.019370	6.019519
9	0.8889	2.000021	4.000412	4.000412	6.000794	6.002584	6.002597
10	0.8	2.000001	4.000030	4.000030	6.000058	6.000236	6.000237
11	0.7273	2.000000	4.000002	4.000002	6.000003	6.000015	6.000015
12	0.6667	2.	4.000000	4.000000	6.000000	6.000000	6.000000
13	0.6154	2.	4.	4.	6.	6.000000	6.000000
14	0.5714	2.	4.	4.	6.	6.	6.
15	0.5333	2.	4.	4.	6.	6.	6.

Table 4. Parameters of Numerical Calculations for Harmonic Oscillator for $N_{\rm GL} = 10$

n	h	$N_{\rm EVP}$	$N_{\rm int}$	$T_{Eval.of B.F.}$	$T_{Eval.of vmat}$	$T_{\rm EVP}$
7	1.1429	225	19600	18.5929	1.4714	0.1197
8	1.0	289	25600	31.1685	3.1726	0.1915
9	0.8889	361	32400	48.4563	6.2601	0.3513
10	0.8	441	40000	73.5441	11.5954	0.6294
11	0.7273	529	48400	109.2896	20.1906	1.0501
12	0.6667	625	57600	154.8675	33.5829	1.7290
13	0.6154	729	67600	211.3824	53.5678	2.6635
14	0.5714	841	78400	279.7736	82.5839	3.9894
15	0.5333	961	90000	389.9374	123.8101	5.9517

Table 5. Results of Numerical Calculations for HO for $N_{\rm GL} = 10$ with code optimization

n	h	$N_{\rm EVP}$	$N_{\rm int}$	$T_{Eval.of B.F.}$	$T_{Eval.of vmat}$	$T_{\rm EVP}$
7	1.1429	225	19600	0.1613	1.4806	0.0969
8	1.0	289	25600	0.2341	3.1731	0.1933
9	0.8889	361	32400	0.3343	6.2837	0.3545
10	0.8	441	40000	0.4597	11.5784	0.6382
11	0.7273	529	48400	0.6081	20.1427	1.0403
12	0.6667	625	57600	0.8030	33.3005	1.6976
13	0.6154	729	67600	1.0367	53.4464	2.6106 .
14	0.5714	841	78400	1.3088	82.2574	3.9483
15	0.5333	961	90000	1.6377	122.7418	5.8455

Table 6. Results of Numerical Calculations for HO for $N_{\rm GL} = 4$ with code optimization

n	h	$N_{\rm EVP}$	$N_{\rm int}$	$T_{Eval.of B.F.}$	$T_{Eval.of vmat}$	$T_{\rm EVP}$	E_0	E_1	E_2	E_3
7	1.1429	225	3136	0.0626	0.2395	0.0954	2.002419	4.027176	4.027176	6.051453
8	1.0	289	4096	0.0934	0.5131	0.1923	2.000261	4.003997	4.003997	6.007657
9	0.8889	361	5184	0.1260	1.0041	0.3553	2.000021	4.000412	4.000412	6.000795
10	0.8	441	6400	0.1699	1.8476	0.6252	2.000001	4.000030	4.000030	6.000058
11	0.7273	529	7744	0.2202	3.2080	1.0613	2.000000	4.000002	4.000002	6.000003
12	0.6667	625	9216	0.2857	5.3602	1.7419	2.	4.000000	4.000000	6.000000
13	0.6154	729	10816	0.3621	8.4907	2.6021	2.	4.	4.	6.
14	0.5714	841	12544	0.4483	13.1560	4.0709	2.	4.	4.	6.
*15	0.5333	961	14400	0.5563	19.5872	5.8239	2.	4.	4.	6.

From table 3 it is evident tat there is fast convergence of the energy levels, also showing the expected degeneracy. However from table 4 it is clear, that a lot of time was spent evaluating the basis functions at all integration points. Splitting one time consuming python loop into

two small loops, i.e. unrolling, for code optimization, resulted in the time spent with these evaluations to be vastly reduced, as shown in table 5. In addition, via changing N_{GL} to 4, the time for evaluating the basis functions was reduced even further, while the eigen values remained the same as shown in table 6.

6. Conclusions

Convergence for the energies of ground state, first, second and third excited states was very fast for the harmonic oscillator, irrespective of the dimension. For the Morse potential, the error of the eigenvalues showed good agreement with the theoretically expected behaviour. The two dimensional Python and numpy code was accelerated via unrolling a loop.
Further development of the method and the Python code is currently underway to calculate the ground state of the hydrogen molecular ion H_2^+ and also to extend the code to three dimensions.

Acknowledgments

O.L. Ezenwachukwu acknowledges financial support from UNISA.

References

[1] Esmail Hesameddini and Elham Asadolahifard. Solving systems of linear volterra integro-differential equations by using Sinc-collocation method. *International Journal of Mathematical Engineering and Science*, 2, July 2013.
[2] John Lund and Kenneth L. Bowers. *Sinc Methods for Quadrature and Differential Equations*. ISBN, 1992.
[3] Abbas Saadatmandi Mehdi Dehghan. The numerical solution of a nonlinearsystem of second-order boundary value problems using the sinc-collocation method. *Mathematical and Computer Modelling, Issue 11-12*, 46:1434–1441, December 2007.
[4] Jennifer L. Mueller and Thomas S. Shores. A new Sinc-Galerkin method for convection-diffusion equations with mixed boundary conditions. *Mathematical Subject Classification*, 1991.
[5] Frank Stenger. summary of sinc numerical methods. *Journal of computational and applied mathematics*, 121:379–420, 2000.
[6] T. Matsuo M. Sugihara. Recent developments of the Sinc numerical methods. *Journal of Computational and Applied Mathematics*, pages 164–165, 673 – 689, April 2003.
[7] Frank Stenger. Numerical Methods based on Whittaker Cardinal, or Sinc Functions. *Society for Industrial and Applied Mathematics*, 23(2):165–224, April 1981.
[8] *http://www.python.org*, 2013.
[9] *http://numpy.scipy.org*, 2013.
[10] Philip M. Morse. Diatomic molecules according to the wave mechanics. ii. vibrational levels. *Phys. Rev.*, 34:57–64, Jul 1929.

A 2+1D Monte Carlo generator for jets in heavy ion collisions

I Kolbé[1,2,a], J G Milhano[3,4,5], U A Wiedemann[5] and K C Zapp[5,6]

[1] iThembaLABS, Old Faure Road, Faure, Cape Town, 7131, South Africa
[2] Physics Department, Brookhaven National Laboratory, Upton, NY 11973-5000, United States of America
[3] LIP, Avenida Prof. Gama Pinto 2, 1649-003 Lisboa, Portugal
[4] Instituto Superior T ecnico, Universidade de Lisboa, Avenida Rovisco Pais 1, Lisbon, Portugal
[5] CERN, Theoretical Physics Department, CH-1211 Geneva 23, Switzerland
[6] University of Lund, Department of Physics, Professorsgatan 1, Lund, Sweden

E-mail: [a]isobel.kolbe@gmail.com

Abstract. At the Large Hadron Collider (LHC) in Geneva, Switzerland and the Relativistic Heavy Ion Collider (RHIC) at Brookhaven National Laboratory in the United States, it is widely believed that a new state of matter, the Quark-Gluon Plasma (QGP), is routinely created by colliding the nuclei of heavy elements such as gold or lead at nearly the speed of light. In head-on collisions between heavy nucleii, it is not uncommon to create tens of thousands of particles and the patterns they produce in the detectors can be very complex. In order to connect theoretical predictions to experimental measurements, it is useful to create a computer algorithm which uses Monte Carlo techniques to simulate the collisions. Such 'Monte Carlo Generators (MCG)' may be programmed to contain much of the known physics, but the development of MCG's in heavy ion physics has been hampered by the complexity of the interplay between different physics effects. Heavy-ion MCG's have, therefore, often been forced to make simplifying assumptions. JEWEL is one such an MCG, attempting to focus primarily on the physics of highly energetic particles that traverse the QGP. We present an extension of JEWEL which allows JEWEL to consider a dynamical background which evolves in time and has no symmetry in the plain transverse to the beam direction. We also show preliminary results from a variety of analyses.

1. Introduction

The standard model of Cosmology presents a largely consistent theory of the evolution of the universe, but relies almost entirely on deductions made from the observation of light at different wavelengths [1]. The evolution of our universe is therefore only traceable by astrophysical means in so far as photons are able to escape the early stages of the evolution and travel to our detectors, placing a limit on how far into the universe's history observational astronomers can see. However, until about a microsecond after the big bang, the universe was entirely opaque to photons [2], so that this epoch of the universe's evolution must be studied differently [2].

One such method is to attempt to recreate the extraordinarily hot and dense conditions that prevailed by colliding the nuclei of heavy atoms such as lead or gold at ultra-relativistic energies. In doing so, it is now widely believed that colossal colliders, the largest of which is the Large Hadron Collider (LHC) in at CERN in Switzerland, create a new state of matter by bringing the

nucleons within the nucleii of these atoms to temperatures and pressures that are reminiscent of the early universe [3]. This new state of matter is called the quark-gluon plasma (QGP) because the degrees of freedom are no longer those of nucleonic matter, but rather those of the constituent particles of protons and neutrons, known within the standard model of particle physics as quarks and gluons.

The QGP that is created in nucleus-nucleus (also referred to as "AA") collisions, is very short lived [4], with a life-span on the order of 1 fm/c in natural units (or 10^{-28} s). For this reason, studying the QGP relies on the study of constituents of the QGP and probes of the QGP that are created along with the QGP in the collision. Such studies require a detailed theoretical understanding of the properties and evolution of the QGP, as well as the various decay products and their signatures in the detectors that are placed around the point at which the collision occurs. One important probe of the QGP is the manner in which a hard parton (a quark or a gluon) that is created at the same time as the quarks and gluons that make up the QGP, but which has an energy at least an order of magnitude or two higher than the average QGP constituent, traverses and interacts with the lower energy partons within the QGP. Such "hard partons" will lose energy as they interact with the QGP via the strong nuclear force, eventually arriving at the detector with less energy than expected [5], and depositing a characteristic collimated spray of particles in the detector, known as a "jet".

2. Monte Carlo generators and JEWEL

The paradigm within which the properties of a jet in the presence of a QGP are studied is cognisant of the fact that the evolution of the jet has a number of different stages [6]: first, the hard parton is produced via a hard scattering process which may be computed directly via quantum chromo-dynamics (QCD); second, even in the absence of a QGP, it is known that the hard parton will radiate energy according to well-understood evolution equations; the presence of the QGP medium will also induce additional radiation, the modelling of which has a rich literature; finally, the hard quark or gluon does not appear in the detector as a free quark or gluon, but rather as hadrons, and one must therefore also consider the manner in which the quark or gluon hadronizes and produces a variety of decay products that eventually leave a signature in the detector.

In addition to the complicated, multi-scale problem that is the production and evolution of the jet, the entire heavy ion collision is itself a multi-scale problem involving a number of different stages that are studied individually [7, 8]: initially, the two heavily Lorentz contracted nucleii approach each other, each with its own individual distribution of partons that are all highly boosted, presenting a considerable challenge to the determination even of the initial state of the collision. Once one has modeled the initial distribution of the deposited energy, one is faced with a system that is very far out of equilibrium, the out of equilibrium evolution of which needs to be understood in order to provide a realistic initial condition for the equilibrated evolution of the QGP. The QGP itself (within which the jet will propagate as described above) now evolves in a manner which is well described by viscous hydrodynamics before finally expanding and cooling sufficiently for hadronization to set in.

It is clear that the physics of a heavy ion collision is rich and varied, but in order to extract meaningful information regarding the QGP from the manner in which a jet is modified, it is necessary to collect all of the information and produce theoretical predictions that are sophisticated enough to involve the major components of the jet and QGP evolution, but may also be easily compared to data. This problem is ideally suited to a Monte Carlo generator. Monte Carlo generators use random number generators to simulate a heavy ion collision and may encode a variety of different physics effects without the need for fully inclusive first principles analytical calculations. Monte Carlo generators have been used extensively in the particle physics community [8], but the complexity of heavy ion collisions has, until recently, hampered the

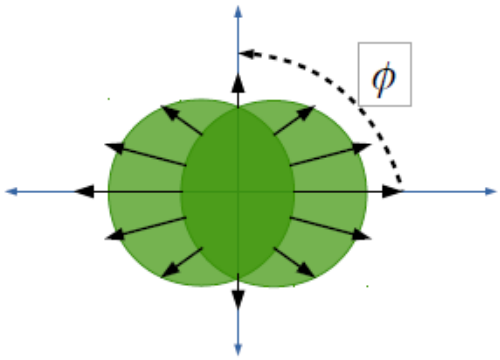

Figure 1. The overlap region of two nuclei as seen in the plane transverse to the beam and the azimuthal angle ϕ as measured in the event plane. Black arrows indicate the emmission of high-momentum particles in plane ($\phi \sim 0, \pi$) and lower-momentum particles out-of-plane ($\phi \sim \frac{\pi}{2}, \frac{3\pi}{2}$. (Drawn by author))

development of a dedicated heavy ion Monte Carlo. JEWEL (Jet Evolution With Energy Loss) is a Monte Carlo generator specifically designed to study the evolution of a jet in a heavy ion collision [9, 10, 11, 12].

JEWEL is a sophisticated generator with many features, the details of which are not important for the present discussion. The reader is referred to the current manual [13] and references therein for further discussions. In essence, JEWEL uses a Glauber distribution for the colliding nucleii to determine the kinematics of a straight forward $2 \to 2$ QCD scattering process for the production of the jet. JEWEL then evolves the jet using the DGLAP evolution equations along with additional $2 \to 2$ scatterings to model the energy loss by sampling a model for the medium, before passing the evolved jet constituents to a modified version of PYTHIA (a widely used generator that has the ability to model the hadronization of partons in order to create a realistic sample of events). JEWEL is freely available for download and ships with two medium options: vacuum jet evolution and jet evolution with a simple classical gas model for the medium which is radially symmetric in the plane transverse to the beam.

3. Generalizing JEWEL

Although a radially symmetric medium is not a bad approximation for head-on collisions, the experimental reality is that the vast majority of collisions are slightly off-center, resulting in an initially almond shaped spatial distribution of the energy density [14]. There is also ample evidence for rich physics related to the evolution of such an asymmetric QGP [15] and it is therefore important to incorporate, within JEWEL, the ability to consider a background medium which contains non-trivial information in at least one temporal direction and two spatial directions (the evolution of the medium in the direction of the beam is, on the time scales considered in a heavy-ion collision, well approximated by a simple scaling mechanism called Bjorken scaling).

We have generalized JEWEL to include the ability to sample a 2+1D background medium when evolving a jet and are in the process of producing Monte Carlo simulated events that will illustrate its usefulness. One possibility for further study is to investigate the path-length dependence of the energy loss of a hard parton by considering the angular distribution of jets given a particular orientation of the almond-shaped background medium. This situation is depicted in fig. 1. If the energy loss does indeed depend heavily on the distance traveled through

the medium (as is expected from a number of perturbative QCD calculations), then it is likely that jets emitted out-of-plane (along the long direction of the almond) will be "quenched" with respect to jets emitted in-plane (along the short direction). One would perform such an analysis event-by-event, but combine the results from many events in order to obtain an emission spectrum. Due to the steeply falling spectrum of jets, such quenching will be visible as a modulation of the number of jets with a particular p_T as a function of the azimuthal angle ϕ. This analysis is does not require a control event in which there is not QGP with which to compare, which is a major hurdle in understanding jet quenching in small colliding systems.

The generalization of JEWEL presented here is based on an existing JEWEL routine that is not yet publicly available and which was used to investigate the effects of including a hydrodynamic profile for the medium in JEWEL [16, 17]. The routine allows JEWEL to read in the temperature and velocity profile of time-snapshots in the hydrodynamical evolution of the background and sample this data in order to construct appropriate four-momenta for the scattering centers. However, the existing routine is only able to read in radially symmetric data.

In order to create the possibility to read in data that is azimuthally asymmetric, a number of changes were made to the existing hydrodynamic medium routine. These changes include, but were not limited to, allowing the dynamical allocation of memory, rewriting the read-in routines so as to allow for a variety of differently formatted hydrodynamical data, and expanding two-dimensional (τ, r) interpolation to three-dimensional (τ, x, y) interpolation. No substantial changes were made to the main JEWEL program.

4. Conclusions

We have presented an argument for studying the quenching of highly energetic partons that traverse the QGP as well as described the need for dedicated Monte Carlo generators that model jet quenching. We have presented a need to generalize a commonly used jet Monte Carlo, JEWEL, in order to include the use of azimuthally asymmetric hydrodynamic profiles for the modeling of the background that the jet interacts with. We have, lastly, briefly described the changes made to an existing, radially symmetric, hydrodynamic routine for JEWEL and an example of a useful analysis that may be done with the data produced with the new routine.

5. Acknowledgments

IK wishes to thank Michael L. Knichel and Jasmine T. Brewer for illuminating discussions as well as CERN for their generous hospitality while working on this project. IK also gratefully acknowledges financial support from the SA-CERN collaboration that made it possible for this collaboration to exist.

References

[1] A. R. Liddle, Chichester, UK: Wiley (1998) 129 p
[2] G. W. Gibbons, S. W. Hawking and S. T. C. Siklos, Cambridge, Uk: Univ. Pr. (1983) 480p
[3] D. J. Schwarz, Annalen Phys. **12**, 220 (2003) doi:10.1002/andp.200310010 [astro-ph/0303574].
[4] D. H. Rischke and M. Gyulassy, Nucl. Phys. A **597**, 701 (1996) doi:10.1016/0375-9474(95)00447-5 [nucl-th/9509040].
[5] J. D. Bjorken, FERMILAB-PUB-82-059-THY, FERMILAB-PUB-82-059-T.
[6] U. A. Wiedemann, Landolt-Bornstein **23**, 521 (2010) doi:10.1007/978-3-642-01539-7_17 [arXiv:0908.2306 [hep-ph]].
[7] H. Petersen, J. Steinheimer, G. Burau, M. Bleicher and H. Stocker, Phys. Rev. C **78**, 044901 (2008) doi:10.1103/PhysRevC.78.044901 [arXiv:0806.1695 [nucl-th]].
[8] T. Sjöstrand *et al.*, Comput. Phys. Commun. **191**, 159 (2015) doi:10.1016/j.cpc.2015.01.024 [arXiv:1410.3012 [hep-ph]].
[9] K. Zapp, G. Ingelman, J. Rathsman, J. Stachel and U. A. Wiedemann, Eur. Phys. J. C **60**, 617 (2009) doi:10.1140/epjc/s10052-009-0941-2 [arXiv:0804.3568 [hep-ph]].

[10] K. C. Zapp, J. Stachel and U. A. Wiedemann, JHEP **1107**, 118 (2011) doi:10.1007/JHEP07(2011)118 [arXiv:1103.6252 [hep-ph]].
[11] K. C. Zapp, F. Krauss and U. A. Wiedemann, JHEP **1303**, 080 (2013) doi:10.1007/JHEP03(2013)080 [arXiv:1212.1599 [hep-ph]].
[12] R. Kunnawalkam Elayavalli and K. C. Zapp, JHEP **1707**, 141 (2017) doi:10.1007/JHEP07(2017)141 [arXiv:1707.01539 [hep-ph]].
[13] K. C. Zapp, Eur. Phys. J. C **74**, no. 2, 2762 (2014) doi:10.1140/epjc/s10052-014-2762-1 [arXiv:1311.0048 [hep-ph]].
[14] B. Abelev *et al.* [ALICE Collaboration], Phys. Rev. C **88**, no. 4, 044909 (2013) doi:10.1103/PhysRevC.88.044909 [arXiv:1301.4361 [nucl-ex]].
[15] C. Loizides, Nucl. Phys. A **956**, 200 (2016) doi:10.1016/j.nuclphysa.2016.04.022 [arXiv:1602.09138 [nucl-ex]].
[16] S. Floerchinger and K. C. Zapp, Eur. Phys. J. C **74**, no. 12, 3189 (2014) doi:10.1140/epjc/s10052-014-3189-4 [arXiv:1407.1782 [hep-ph]].
[17] K. C. Zapp and S. Floerchinger, Nucl. Phys. A **931**, 388 (2014) doi:10.1016/j.nuclphysa.2014.09.037 [arXiv:1408.0903 [hep-ph]].